



UNIVERSITÀ
DEGLI STUDI
DI PADOVA

Sede Amministrativa: Università degli Studi di Padova

Centro di Ateneo di Studi e Attività Spaziali "Giuseppe Colombo" - CISAS

SCUOLA DI DOTTORATO DI RICERCA IN : Scienze, Tecnologie e misure spaziali

INDIRIZZO: Scienze e Tecnologie per applicazioni satellitari e aeronautiche (STASA)

CICLO: XXVIII

Atmosphere in a test tube: laboratory investigations about exoplanet atmospheres

Direttore della Scuola : Ch.mo Prof. Giampiero Naletto

Coordinatore d'indirizzo: Ch.mo Prof. Giampiero Naletto

Supervisore: Dott. Prof. Riccardo Claudi

Dottorando : Marco Erculiani

Abstract

The aim of this thesis is to understand if cyanobacteria, grown on an Earth-like planet orbiting around the habitable zone of an M star can survive and use the light coming from the star in a fruitful way, in particular analyzing their gaseous by-products. The organisms chosen usually don't have photopigments capable to photosynthesize the NIR part of the radiation, but can modify their photosynthetic apparatus in order to adapt to different light conditions if exposed in NIR light conditions, producing chlorophyll d and f. The two bacteria highlighted for our purpose are *Chlorogloeopsis fritschii* and *Cyanobacterium Aponinum*. The first is known to be able to change its photosynthetic apparatus to cope with new radiation conditions. In particular is capable to generate chlorophyll d and f if exposed to NIR light (720 nm). This feature is called FarLip acclimation. The second bacterium is a well known bacterium but no one has ever tried to understand if it has the same capability. Efforts have been done in order to find the best culture medium and the best growth conditions of temperature and pH.

In order to understand how photosynthetic life can handle different radiation doses we ideated and realized a novel and pioneering LED radiation source with dynamical features. Its wavelength intervals (365nm-940nm) overlap the limits of photosynthetic pigment absorption range (280-850 nm) of most common photosynthetic bacteria. Our simulator is composed by an array of 25 different channels corresponding to 25 different wavelengths. Each channel can host a maximum of about 15 LEDs. This simulator has been built thinking to modularity. In fact it is endowed by a mosaic of circuit boards arranged in a pie-chart shape, on the surface of which will be welded the LEDs. This solution allows a rapid change of the damaged LEDs and an easy implementations with other wavelengths.

This simulator is capable to reproduce the spectra of main sequence F, G, K and M stars as well as the most common commercial lamps within its wavelength intervals. The control system is composed by a Laptop which controls a LED box and an STS-VIS spectrograph from Ocean Optics with cosine corrector. The first system generate the best fit of the input spectrum and give information to the simulator on how to reproduce it. The spectrometer has the task to control the goodness of the fit and, by means of a closed loop system, to adjust it tuning the LED's power in real time. The stellar simulator has been subjected to several tests. The power emanated from the radiation source has been estimated to be 106.22 W while the thermal power has been calculated to be 434.05 W. The stellar simulator have been characterized in flux, analyzing the radiation at different distances from the device, from the exit of the source up to 25 cm. Then uniformity measurements have been done, analyzing the flux on a distance of 6.5 cm from the centre. Finally, I calculated the absorption of the optics of the radiation source analyzing the spectra coming out from the stellar simulator and compared it with respect to the spectrum of the single LEDs.

In order to lodge the bacteria we built new concept incubator made of a stainless steel cell with the potential to flux a desired gaseous mixture inside it and fill the cell with the desired gas mixture. Four wedged optical windows opens on the lateral surface and needs to test the oxygen and carbon dioxide concentration inside by means of a Tunable Diode Laser Absorption Spectroscopy (TDLAS) system. The cell is topped by a BOROFLOAT uncoated window to collect the light from the stellar simulator. The cell has been characterized in void and oxygen and carbon dioxide detecting limits.

Bacteria have been grown in white light conditions at for 24 days at 20 $\mu\text{mol photons/m}^2/\text{s}$ and at 30°C in order to understand the growth times and the behaviour in optimal conditions. After that, a new growth experiment have been performed by growing both cyanobacteria species at 30°C and 20 $\mu\text{mol photons/m}^2/\text{s}$

and oxymetric measurements have been done after 6 days from the culture start, thus during their exponential growth phases.

Then, for the main part of the experiment, eight samples have been used. Two samples of *Cyanobacterium aponinum* have been grown at 20 $\mu\text{mol photons/m}^2/\text{s}$ in white light for 6 days and then at 100 $\mu\text{mol photons/m}^2/\text{s}$ for the residual 3 days in white light. Two samples of *Chlorogloeopsis fritschii* have been grown at 20 $\mu\text{mol photons/m}^2/\text{s}$ for 6 days in white light and then at 100 $\mu\text{mol photons/m}^2/\text{s}$ for the residual 3 days in white light. Two samples of *Cyanobacterium aponinum* have been grown at 20 $\mu\text{mol photons/m}^2/\text{s}$ for 6 days in white light and then at 100 $\mu\text{mol photons/m}^2/\text{s}$ for the residual 3 days using the radiation spectrum of an M7 type star. Two samples of *Chlorogloeopsis fritschii* have been grown at 20 $\mu\text{mol photons/m}^2/\text{s}$ for 6 days in white light and then at 100 $\mu\text{mol photons/m}^2/\text{s}$ for the residual 3 days using the radiation spectrum of an M7 type star.

The temperature has been kept at 30°C for the samples not exposed to M7 light and at a temperature oscillating from 35°C to 38°C for the samples exposed to M7 light. The higher environmental temperature under the stellar simulator has been due to the over-heating of the LEDs. During the 3 days of different exposure measurements of optical density have been done in order to collect data about the different growth curves. Moreover, O₂ production have been calculated for each sample.

Finally, a chromatic response have been done, in order to understand if the colour would reflect the vitality of the bacteria.

Sommario

Sulla Terra, la vita può rivelare la sua presenza mostrando una straordinaria varietà di caratteristiche, ma sarebbero discernibili se il nostro mondo fosse osservato da una grande distanza e orbitasse intorno ad altre stelle? In particolare, cosa accadrebbe se una stella M fosse la sorgente di radiazione principale?

In questa tesi mi propongo di rispondere a questa domanda, analizzando l'argomento da diversi punti di vista. Partendo dall'analisi di nuovi metodi usati per trovare esopianeti, ho sottolineato quelli più comuni e fruttuosi a partire dall'albero di Perryman.

Questi metodi posso essere divisi in diretti e indiretti. L'immagine diretta è un metodo diretto mentre velocità radiale e transiti sono metodi indiretti. Dopodichè ho fatto il punto delle missioni spaziali e degli strumenti più famosi dedicati alle osservazioni e caratterizzazione di esopianeti e ho introdotto i concetti base della fisica delle atmosfere come l'altezza di scala, i più comuni modelli atmosferici partendo da quello base alla descrizione di Kasting.

Quindi ho illustrato i differenti tipi di albedo (albedo geometrica e albedo Bond) e il metodo per determinare la temperatura effettiva, la temperatura all'equilibrio e la temperatura di luminosità.

Dopo ciò segue una breve introduzione ai concetti di Indice di Similarità Terrestre e delle più comuni biofirme. Per trovare la vita come noi la conosciamo, la presenza dell'acqua liquida è indispensabile. Partendo da questa dichiarazione è nato il concetto di Zona Abitabile (HZ). La Zona Abitabile è compresa tra un limite superiore dove il pianeta è così vicino alla propria stella che tutta l'acqua è in forma gassosa, e un limite inferiore dove l'eccessiva distanza dalla propria stella implica che tutta l'acqua è in forma di ghiaccio. Oltre a questo, anche i parametri geologici del pianeta possono influenzare il contenuto di acqua e il bilancio energetico. Questo è il caso della tettonica delle placche e del vulcanesimo così come del campo magnetico.

Affinchè sia chiaro se e come la vita possa svilupparsi su un pianeta, ho illustrato le basi della vita, a partire dagli aminoacidi, le proteine e i lipidi e le proteine per capire la varietà di nicchie fotosintetiche e di organismi che vi vivono. Gli organismi fotosintetici riescono a sopravvivere in differenti condizioni di temperatura, pH, pressione, radiazione e danno foto-ossidativo, salinità e disseccamento, gravità e abbondanza o meno di nutrienti. Il processo di raccolta della luce è il cardine che regola il sostentamento degli organismi fotosintetici (siano essi ossigenici od anossigenici) e che trasforma la radiazione in energia. Il prodotto di scarto, l'ossigeno, è una delle frecce al nostro arco per rilevare la presenza di vita su altri pianeti attraverso lo studio delle biofirme. Fra le più comuni e potenti si può annoverare il fenomeno del *red edge*, una caratteristica spettroscopica che mostra come gli organismi fotosintetici possiedano un picco nello spettro di riflettanza fra 680 nm e 730 nm. Questa caratteristica intrinseca può aiutare a capire l'interazione fra lo spettro luminoso che impatta sugli organismi ed i pigmenti fotosintetici, con particolare attenzione alla riflettanza. La luce oltre che essere la principale forma di sostentamento degli organismi fotosintetici può essere tuttavia anche una minaccia. In particolar modo pianeti orbitanti attorno a stelle attive, come le stelle M, presentano degli aumenti casuali o ripetuti di radiazione molto energetica come i *flare*, che sono potenzialmente dannosi per la vita. È altresì vero che sulla terra la vita si è sviluppata anche in posti dove normalmente non ci aspetterebbe di trovarne. È proprio questa asserzione che ci ha guidati nella scelta degli organismi da usare nella nostra ricerca, usando come setaccio l'abilità degli organismi di fotosintetizzare la luce vicino-infrarossa (700 nm;850nm). Pertanto abbiamo isolato due macrogruppi di batteri. I primi sono organismi che presentano al loro interno fotopigmenti in grado di metabolizzare la luce vicino-infrarossa, possedendo clorofilla d ed f, come *Halomicronema hongdechloris* o *Acaryochloris marina*. Gli altri sono batteri che normalmente non possiedono pigmenti che fotosintetizzano nel vicino infrarosso ma sono in grado di modificare il loro apparato fotosintetico in modo da adattarsi alle differenti condizioni di radiazione. È questo il caso di *Chlorogloeopsis fritschii* and *Cyanobacterium Aponinum*.

Per capire inoltre le proprietà dei pigmenti fotosintetici in riflessione sono stati scelti tre organismi noti: la micro-alga *Chlamydomonas reinhardtii* ed i cianobatteri *Synechococcus* PCC 7002 e *Chroococcus* sp. e sono stati fatti degli spettri di riflettanza e l'analisi dei pigmenti.

Entrando nel vivo di questa ricerca ci siamo chiesti come gli organismi fotosintetici possano manipolare le differenti componenti spettrali a cui vengono sottoposti e abbiamo voluto capire se tali organismi, presenti su un pianeta di tipo terrestre ed orbitante attorno alla zona di abitabilità della sua stella madre, potrebbero contribuire ad una sostanziale modifica dell'atmosfera, tale da essere rilevata dalla terra. Per far ciò abbiamo ideato una nuova sorgente di radiazione che abbiamo chiamato simulatore stellare. Il concetto che sta alla base del progetto è stato quello di creare un illuminatore di tipo dinamico. Per questo abbiamo scelto dei LED al posto delle comuni lampade. Il simulatore è stato dotato di 25 differenti canali corrispondenti a 25 diverse lunghezze d'onda LED. Ogni canale può sopportare una tensione massima di 45 V, che corrisponde a circa 15 LED per canale usati alla tensione di 3 V. Un altro criterio per la costruzione dell'illuminatore è stata l'idea di modularità. Ciò ci ha condotto a pensare ad un sistema composto da più parti in forma di anelli, ognuno dei quali presenta come in mosaico a spicchi su cui vengono saldati i LED. I moduli permettono anche di sostituire soltanto una parte della palette di LED qualora si bruciasse o di implementare l'illuminatore con altre lunghezze d'onda all'occorrenza.

In tabella sono mostrati i LED utilizzati e le lunghezze d'onda di picco. L'intervallo di lunghezze d'onda (365nm-940nm) si sovrappone ampiamente ai limiti imposti per la fotosintesi (280-850 nm) della maggior parte dei batteri.

LED	Lunghezza d'onda del picco (nm)
Luxeon LZ1-00U600	365
Luxeon LHUV-0380-0200	380-385
Luxeon LHUV-0400-0500	400-405
Luxeon LHUV-0420-0650	420-425
Luxeon LXZ1-PR01	447,5
Luxeon LXZ1-PB01	470
Olson LB CRBP-HXJX-47-1	485
Luxeon LXZ1-PE01	505
Luxeon LXZ1-PM01	530
Luxeon LXZ1-PX01	567,5
Luxeon LXZ1-PL01	590
Luxeon LXZ1-PD01	627
Philips Lumileds 997-LXZ1-2280-5	(2200K)
Luxeon LXZ1-PA01	655
Roithner SMB1N-680	680
Roithner smb1n-700	700
Roithner SMB1N-720D	720
Luxeon LZ1-00R300	740
Roithner SMB1N-760D	760
Roithner SMB1N-780N	780
Roithner SMB1N-810D-02	810
Roithner SMB1N-830D	830
Osram SFH 4715(S)	850-870
Roithner SMB1N-880	880
Oslon SFH 4725S	940

L'illuminatore viene gestito da un sistema di controllo per mezzo di un PC ed uno spettrometro ha il compito di controllare che il flusso rimanga stabile. Lo spettrometro, modello STS-VIS della Ocean Optics, è dotato di correttore di coseno. Lavorando in loop chiuso garantisce stabilità al flusso ed evita le disomogeneità

dovute agli effetti termici. L'illuminatore emana una potenza complessiva di 106.22 W corrispondente ad una potenza termica di 434.05 W, che è cruciale venga dissipata in maniera adeguata. Per far ciò è stato scelto un raffreddatore 0.06K/W 12V 6W della ditta Thermo Electric Devices, con dimensioni 200 x 135 x 98mm e un rumore complessivo di 77±2 db, 34±2 db sopra il rumore ambientale. Per pilotare i LED sono stati usati dei driver ALD Buck Led della Cincon Electronics poichè, essendo queste componenti multicanale, compatibili DALI e dimmerabili è possibile gestire al meglio e facilmente l'intensità di ogni canale.

Per collegare il PC all'illuminatore attraverso porta seriale è stata usata un'interfaccia DALI RS232 PS/S. Lo spettrometro, dotato di fibra ottica, è collegato via USB al PC. Un trasformatore HLG-320H-54A della ditta Mean Well fornisce l'energia necessaria. Il simulatore stellare è stato caratterizzato in flusso, analizzando la radiazione a diverse distanze (da 0 a 25 cm) dalla bocca di uscita della luce. Inoltre sono state fatte misure di uniformità del flusso ad una distanza di 6.5 cm attorno al centro. Infine è stato calcolato l'assorbimento delle ottiche dell'illuminatore analizzando gli spettri reali con quelli dei singoli LED presi con la sfera integratrice. Fino ad ora nessuno strumento di questo tipo è mai stato progettato. Per confinare i batteri abbiamo pensato ad un incubatore in acciaio inox con due ugelli da 1/8" per il flussaggio di gas all'interno. L'incubatore è dotato di quattro finestre ottiche, due a zeppa da 1" con un'inclinazione di 2° e banda passante 650 - 1050 nm mentre le altre due finestre sono uguali alle precedenti tranne che per il rivestimento. Tali finestre sono state pensate per monitorare la concentrazione di ossigeno e di anidride carbonica all'interno dell'incubatore attraverso un sistema denominato TDLAS (Tunable Diode Laser Absorption Spectroscopy). I due laser usati saranno attaccati all'incubatore attraverso due piastre da 30 mm della ditta Thorlabs spesse 0.35" e due tubi ottici SM1 da 1". Sopra la cella di incubazione è situato un vetro in borosilicato da 125x6.5 mm della ditta Edmund Optics per far passare all'interno della cella la radiazione dell'illuminatore. La cella è stata caratterizzata sia termicamente che in pressione. Le misure sono state effettuate riempiendo al cella di una miscela contenente 84.3% di N e 15.7% di CO₂ ed analizzando la concentrazione di O₂, risultata essere di (1.45x10⁻⁴) con un sigma pari a 1.79x10⁻⁵ e di CO₂ risultata essere 0.0498 con un sigma di 7.057x10⁻⁴. Gli stessi dati per l'aria hanno dato una concentrazione di O₂ pari a 4.23x10⁻⁴ con un sigma di 1.44x10⁻⁵ e una concentrazione di CO₂ pari a 5.72x10⁻⁴ con un sigma di 3.12x10⁻⁵. I risultati del test hanno mostrato un limite inferiore di rilevazione di O₂ pari all'1% e 54 per la CO₂. Una volta testato a fondo i dispositivi abbiamo scelto i batteri: *Chlorogloeopsis fritschii* e *Cyanobacterium aponinum*. Il primo organismo è in grado di modificare il suo apparato fotosintetico a differenti lunghezze d'onda. In particolare è in grado di generare clorofilla d e f se esposti a luce NIR (720 nm). Questa caratteristica è chiamata acclimatazione FarLip. Il secondo batterio è molto ben conosciuto, ma nessuno ha mai provato a capire se ha le stesse capacità. Per questi batteri sono stati scelti i terreni di coltura più appropriati, le migliori condizioni di crescita e di pH e quindi sono state calcolate le curve di crescita. I batteri sono stati cresciuti in luce bianca per 24 giorni a 20 µmol fotoni/m²/s a 30°C per capire il loro comportamento in condizioni ottimali. Le curve di crescita hanno evidenziato una veloce crescita di *Cyanobacterium aponinum* rispetto a *Chlorogloeopsis fritschii* il quale a sua volta presenta una più lunga fase stazionaria. Dopodichè è stato effettuato un nuovo esperimento facendo crescere i batteri a 30°C e 20 µmol fotoni/m²/s e sono state prese misure di produzione di ossigeno dopo sei giorni dall' inizio della coltura e durante le varie fasi di crescita. I risultati per *Chlorogloeopsis fritschii*, presi da due differenti campioni e cresciuti in luce bianca hanno mostrato una produzione media di ossigeno di $224.45 \frac{\mu\text{mol O}_2}{\text{mg Chl} \cdot \text{h}}$ mentre gli stessi risultati per *Cyanobacterium aponinum* hanno mostrato una produzione di O₂ pari a $174.41 \frac{\mu\text{mol O}_2}{\text{mg Chl} \cdot \text{h}}$. Per la parte principale dell'esperimento sono stati utilizzati otto campioni: due campioni di *Cyanobacterium aponinum* fatti crescere a 20 µmol fotoni/m²/s in luce bianca per sei giorni e quindi a 100 µmol fotoni/m²/s per i restanti tre giorni sempre in luce bianca. Due campioni di *Chlorogloeopsis fritschii* sono cresciuti a 20 µmol fotoni/m²/s per sei giorni in luce bianca e quindi a 100 µmol fotoni/m²/s per i restanti tre giorni sempre in luce bianca. Due campioni di *Cyanobacterium aponinum* fatti crescere a 20 µmol fotoni/m²/s in luce bianca per sei giorni e quindi a 100 µmol fotoni/m²/s per i restanti tre giorni usando lo spettro di una stella di tipo M7. Due campioni di

Chlorogloeopsis fritschii sono cresciuti a 20 $\mu\text{mol fotoni/m}^2/\text{s}$ per sei giorni in luce bianca e quindi a 100 $\mu\text{mol fotoni/m}^2/\text{s}$ per i restanti tre giorni in luce M7. La scelta di usare la luce bianca a 20 $\mu\text{mol fotoni/m}^2/\text{s}$ per i primi 6 giorni e quindi di aumentare la dose di radiazione a 100 $\mu\text{mol fotoni/m}^2/\text{s}$ per il restante tempo è stata fatta per avere le stesse condizioni di crescita negli ultimi tre giorni, mantenendo lo stesso numero di fotoni, sia in luce visibile che in luce M7. In particolare, durante questa fase dell'esperimento i batteri sono stati posti sotto l'illuminatore con un flusso costante. La temperatura in questa fase è stata mantenuta a 30 °C per i campioni non esposti a luce M7, mentre tra i 35- 38 °C per quelli esposti a luce M7. Questa variazione di temperatura è stata causata dal surriscaldamento parziale dei LED. Durante gli ultimi tre giorni sono state fatte misure di densità ottica per produrre delle curve di crescita. Inoltre è stata calcolata la produzione totale di ossigeno per ciascuno dei campioni. *Chlorogloeopsis fritschii* ha prodotto $80.1065 \frac{\mu\text{mol O}_2}{\text{mg Chl} \cdot \text{h}}$ dopo 48 h in luce M7 rispetto agli stessi esemplari cresciuti in luce bianca che hanno mostrato una produzione di $79.572 \frac{\mu\text{mol O}_2}{\text{mg Chl} \cdot \text{h}}$. Gli stessi dati per *Cyanobacterium aponinum* sono risultati essere $70.525 \frac{\mu\text{mol O}_2}{\text{mg Chl} \cdot \text{h}}$ e $43.944 \frac{\mu\text{mol O}_2}{\text{mg Chl} \cdot \text{h}}$. Comparando quanto ottenuto con le curve di crescita, si evince che *Chlorogloeopsis fritschii* è in grado di rispondere molto bene alla variazione di luce da bianca a M7, continuando a crescere anche in differenti condizioni di irradiazione e confermando l'ipotesi che i cianobatteri con proprietà FarLip possono anche utilizzare la luce di stelle M. *Cyanobacterium aponinum* non tollera bene il nuovo tipo di radiazione aumentando la sua respirazione cellulare e portando ad una decrescita nella produzione totale di ossigeno. Questo si può ben vedere nella tabella seguente dalla comparazione fra produzione netta e totale di ossigeno.

Campione	[Chl]mg/ml	$\mu\text{mol O}_2/\text{mg Chl}/\text{h}$ totale	Evoluzione netta $\text{O}_2/\text{mgChl}/\text{h}$
<i>Cyanobacterium Aponinum</i> 1 Vis 48h	0.0053	47.479	23.0097
<i>Cyanobacterium Aponinum</i> 2 Vis 48h	0.0066	40.409	22.3289
<i>Cyanobacterium Aponinum</i> 1 M7 48h	0.0035	70.525	-29.2421
<i>Cyanobacterium Aponinum</i> 2 M7 48h	0.0042	3.311	-25.4770
<i>Chlorogloeopsis fritschii</i> 1 Vis 48h	-	-	-
<i>Chlorogloeopsis fritschii</i> 2 Vis 48h	0.0051	79.572	50.3176
<i>Chlorogloeopsis fritschii</i> 1 M7 48h	0.0053	89.716	65.8067
<i>Chlorogloeopsis fritschii</i> 2 M7 48h	0.0056	70.497	48.0808

Infine è stata fatta una analisi cromatica dei vari campioni per capire se i campioni riflettessero nella colorazione la loro vitalità. Negli esperimenti futuri, i batteri saranno alloggiati nell'incubatore, per poter modulare anche la miscela di gas e la temperatura all'interno. Inoltre la sorgente di radiazione, migliorata ed affinata, sarà utile per creare un database di organismi capaci di vivere sottoposti a spettri di diverse stelle. Un'altra proposta per i lavori futuri è quella di capire se la caratteristica della "red edge" e la pigmentazione dei batteri possa essere influenzata dalla variazione di lunghezza d'onda. Questo può essere fatto, facendo crescere gli organismi in differenti condizioni di luminosità e studiando gli spettri di riflettanza dei pigmenti che vi si sviluppano. Potranno essere utilizzati altri organismi, in particolare il muschio *Physcomitrella patens* che rappresenta l'anello di congiungimento tra le piante acquatiche e quelle terrestri. In questo modo potremmo fare nuova luce su quali colori potrebbero avere gli organismi fotosintetici e come queste caratteristiche possano essere inserite nel patrimonio delle biofirme. Da ultimo potranno essere fatte delle analisi di chiralità negli spettri di riflessione degli organismi fotosintetici e capire se questa caratteristica possa essere rilevate dai futuri strumenti astronomici.

Summary

On Earth life can reveal its fingerprint showing a great variety of features, but what would happen if our world would be observed from a great distance and would orbit around other stars? Will we notice the same features? In particular, what would happen if an M star would be the main radiation source?

In this thesis i have treated the problem from different points of view. I started from the analysis of the discovery methods used to find exoplanets, illustrating the Perryman's tree and underlining the most common and fruitful ones. Among these, direct imaging is a direct method while indirect ones are radial velocity and transits. Then i made an overview of the most famous instruments and space missions dedicated to the observation and characterization of exoplanets and introduced the basic concepts of atmospheric physics like the scale height, the most common atmospheric models starting from the basic ones to the Kasting description. Then i illustrated the different types of albedo (geometric albedo and Bond albedo) and the retrieval of the effective temperature, the equilibrium temperature and brightness temperature. After this a brief introduction to the concept of Earth Similarity Index and a quick analysis of the most common biosignatures. In order to find life as we know it, one of the basic constraint is the presence of liquid water. Starting from this statement has born the concept of Habitable Zone (HZ). Habitable zone is enclosed between an inner edge where the planet is so close to its parent star that all the water is in gaseous form, and an outer edge, where the excessive distance from the parent star implies that all the water is in the form of ice. Other than this, even the planetary geological constraint can drive the water content and influence the energetic balance. This is the case of plate tectonics and volcanism as well as the magnetic field. In order to understand if and how life could develop on a planet i had to illustrate the basis of life, such as amino-acids, lipids and proteins and understand the varieties of photosynthetic niches and the organisms that live inside them. Photosynthetic organisms can survive in different conditions of temperature, pH, pressure, irradiation doses and damages, salinity and dessiccation, nutrients and gravity. Light harvesting is the chief process that photosynthetic organisms (oxygenic and anoxygenic) use to transform radiation into energy. A waste product, O₂, is one of our best weapons in order to understand if life could be present on other planets through the study of biomarkers. Among these, the vegetation red edge is a spectroscopic feature of the photosynthetic organisms that shows a peak in flux in the NIR part of the reflectance spectrum, between 680 nm and 730 nm. As said before light is the co-feed of photosynthetic organisms, but it can be a threat too. In particular active M stars have some energetic features like flares, variability and energetic emissions that are dangerous for life. On the other hand we know that life can develop even in the harshest places on Earth, adapting to their conditions. And is this concept that led us to highlight organisms for our research. The main characteristic that they would have was to be able to metabolize NIR light (from 700 nm to about 850nm). We searched among two different types of bacteria. The first are organisms that have photo-pigments like Chld and Chl f that can transform the NIR part of the radiation into energy. Some organisms like these are *Halomicronema hongdechloris* and *Acaryochloris marina*. These second organisms are the ones that usually don't have these photopigments but can modify their photosynthetic apparatus in order to adapt to different light conditions, and in particular to NIR light conditions. One of them is *Chlorogloeopsis fritschii*. It is known to be able to change its photosynthetic apparatus to cope with new radiation conditions. In particular is capable to generate chlorophyll d and f if exposed to NIR light (720 nm). This feature is call FarLip acclimation. *Cyanobacterium Aponinum*, another chosen organism is a well known bacterium but no one has ever tried to understand if it has the same capability.

Moreover, in order to evaluate the reflectance spectra of organisms, some model organisms have been considered too, such as the moss *Physcomitrella patens*, the green micro alga *Chlamydomonas reinhardtii* and the cyanobacterium *Synechococcus* PCC 7002. For two of them the pigment analysis have been done (*Chlamydomonas reinhardtii* and *Synechococcus* PCC 7002) and compared with another reference model

(*Chroococcus sp.*). In order to understand how photosynthetic life can handle different radiation doses, and to understand how the presence of photosynthetic organisms, if grown there, would affect the atmospheric composition of an Earth-like exoplanet in the habitable zone of M an star we started to think about a novel and pioneering radiation source, a starlight simulator. The concept behind this is to endow this source with dynamical features, and this is the reason why we preferred the use of LEDs instead of lamps. Our simulator is composed by an array of 25 different channels with different kind of LEDs. The wavelength intervals chosen for this stellar simulator, that is enclosed between 365nm and 940nm, overlap the limits of photosynthetic pigment absorption range 280-850 nm present inside the most common photosynthetic bacteria. Hereafter in the table are shown the wavelengths of each LED.

LED CODE	Peak wavelength (nm) from datasheet
Luxeon LZ1-00U600	365
Luxeon LHUV-0380-0200	380-385
Luxeon LHUV-0400-0500	400-405
Luxeon LHUV-0420-0650	420-425
Luxeon LXZ1-PR01	447,5
Luxeon LXZ1-PB01	470
Olson LB CRBP-HXJX-47-1	485
Luxeon LXZ1-PE01	505
Luxeon LXZ1-PM01	530
Luxeon LXZ1-PX01	567,5
Luxeon LXZ1-PL01	590
Luxeon LXZ1-PD01	627
Philips Lumileds 997-LXZ1-2280-5	(2200K)
Luxeon LXZ1-PA01	655
Roithner SMB1N-680	680
Roithner smb1n-700	700
Roithner SMB1N-720D	720
Luxeon LZ1-00R300	740
Roithner SMB1N-760D	760
Roithner SMB1N-780N	780
Roithner SMB1N-810D-02	810
Roithner SMB1N-830D	830
Osram SFH 4715(S)	850-870
Roithner SMB1N-880	880
Osram SFH 4725S	940

List of LEDs chosen and peak wavelength

The idea of modularity led us to think a multi-plate LED system shaped in the form of annuli, with mosaic of circuit boards arranged in a pie-chart shape. This simulator is capable to reproduce the spectra of main sequence F, G, K and M stars as well as the most common commercial lamps within its wavelength intervals. The power emanated from the radiation source has been estimated to be 106.22 W while the thermal power has been calculated to be 434.05 W. We dissipated the heat using a cooling aggregate 0.06K/W 12V 6W from Thermo Electric Devices. Its dimensions are 200 x 135 x 98mm. The noise produced by the whole dissipation system is 77 ± 2 db, 43 ± 2 db over environmental noise. We decided to drive the LEDs through an ALD Buck Led Driver by Cincon Electronics. The reason is that this component is multichannel, DALI

compatible and dimmable, so we can easily specify the needed intensity of the entire channel. A DALI RS232 PS/S interface is needed to connect the laptop to the LED box through serial port. The control system is composed by a Laptop which controls a LED box and an STS-VIS spectrograph from Ocean Optics with cosine corrector. The first system generate the best fit of the input spectrum and give information to the simulator on how to reproduce it. The spectrometer has the task to control the goodness of the fit and, by means of a closed loop system, to adjust it tuning the LED's power in real time. The power is granted to the LEDs by a HLG-320H-54A from Mean Well LED power supply.

The stellar simulator have been characterized in flux, analyzing the radiation at different distances from the device, from the exit of the source up to 25 cm. Then uniformity measurements have been done, analyzing the flux on a distance of 6.5 cm from the centre. Finally, I calculated the absorption of the optics of the radiation source analyzing the spectra coming out from the stellar simulator and compared it with respect to the spectrum of the single LEDs.

Up to now no such devices have been developed. In order to lodge the bacteria a new concept incubator has been built, composed of a stainless steel cell and our wedged optical windows that opens on the lateral surface. Two windows are 1" Round Wedge Prisms, with 2° Beam Deviation, and AR Coating: 650 - 1050 nm from Thorlabs. The other two windows are 1" Round Wedge Prisms, with 2° Beam Deviation without Coating. The windows were projected to test the gas concentration inside the closed cell by means of a TDLAS (Tunable Diode Laser Absorption Spectroscopy) system and the channels used are two: one for oxygen and one for carbon dioxide. The cell has been characterized in void and oxygen and carbon dioxide detecting limits. We filled the cell with a 84.3% N and 15.7% CO₂ gas mixture and revealed an O₂ concentration of 1.45x10⁻⁴ arbitrary units with a sigma 1.79x10⁻⁵ as well a CO₂ concentration of 0.0498 arbitrary units with a sigma 7.057x10⁻⁴. The same data for the air are an O₂ concentration of 4.23x10⁻⁴ arbitrary units with a sigma 1.44x10⁻⁵ and a CO₂ concentration of 5.72x10⁻⁴ arbitrary units with a sigma 3.12x10⁻⁵. The results are 1% for O₂ and 54 ppm for CO₂. The bacteria incubator has been tested even from the thermal point of view.

Once thoroughly tested the hardware we found the best culture medium for the bacteria *Chlorogloeopsis fritschii* and *Cyanobacterium aponinum* and the best growth conditions of temperature and pH. Bacteria have been grown in white light conditions at for 24 days at 20 μmol photons/m²/s and at 30°C in order to understand the growth times and the behaviour in optimal conditions. The growth curves have evidenced a quicker growth of *Cyanobacterium aponinum* with respect to *Chlorogloeopsis fritschii* that in comparison have a longer lag phase time. After that, a new growth experiment have been performed by growing both cyanobacteria species at 30°C and 20 μmol photons/m²/s and oxymetric measurements have been done after 6 days from the culture start, thus during their exponential growth phases. The results for *Chlorogloeopsis fritschii*, taken from two different samples and grown in white light conditions have highlighted a mean O₂ production of 224.45 $\frac{\mu\text{mol O}_2}{\text{mg Chl}\cdot\text{h}}$ while results for *Cyanobacterium aponinum* have shown the total O₂ production of 174.41 $\frac{\mu\text{mol O}_2}{\text{mg Chl}\cdot\text{h}}$. Then, for the main part of the experiment, eight samples have been used. Two samples of *Cyanobacterium aponinum* have been grown at 20 μmol photons/m²/s in white light for 6 days and then at 100 μmol photons/m²/s for the residual 3 days in white light. Two samples of *Chlorogloeopsis fritschii* have been grown at 20 μmol photons/m²/s for 6 days in white light and then at 100 μmol photons/m²/s for the residual 3 days in white light. Two samples of *Cyanobacterium aponinum* have been grown at 20 μmol photons/m²/s for 6 days in white light and then at 100 μmol photons/m²/s for the residual 3 days using the radiation spectrum of an M7 type star. Two samples of *Chlorogloeopsis fritschii* have been grown at 20 μmol photons/m²/s for 6 days in white light and then at 100 μmol photons/m²/s for the residual 3 days using the radiation spectrum of an M7 type star. The choice to use white light at 20 μmol photons/m²/s for the first 6 days and then a radiation dose of 100 μmol photons/m²/s for the next 3 days was made in order to compare the same initial common growth conditions with the different radiation conditions for the next 3 days, but keeping the number of photons the same: 100 μmol photons/m²/s in white

light in one case and 100 $\mu\text{mol photons/m}^2/\text{s}$ of M7 light in the second case. During this part of the experiment bacteria irradiated with the M7 radiation have been put under the stellar simulator and let grow, while a spectrometer was monitoring the correct input spectrum to remain constant. The temperature has been kept at 30°C for the samples not exposed to M7 light and at a temperature oscillating from 35°C to 38°C for the samples exposed to M7 light. The higher environmental temperature under the stellar simulator has been due to the over-heating of the LEDs. During the 3 days of different exposure measurements of optical density have been done in order to collect data about the different growth curves. Moreover, O_2 production have been calculated for each sample. A mean O_2 production of $80.1065 \frac{\mu\text{mol O}_2}{\text{mg Chl} \cdot \text{h}}$ has been found for *Chlorogloeopsis fritschii* grown for 48 h in M7 radiation conditions with respect to samples grown in white light conditions (both at 100 $\mu\text{mol photons/m}^2/\text{s}$) that were $79.572 \frac{\mu\text{mol O}_2}{\text{mg Chl} \cdot \text{h}}$. The same measurements for *Cyanobacterium aponinum* give $70.525 \frac{\mu\text{mol O}_2}{\text{mg Chl} \cdot \text{h}}$ and $43.944 \frac{\mu\text{mol O}_2}{\text{mg Chl} \cdot \text{h}}$. These data compared with the growth curves in different light conditions shows that while *Chlorogloeopsis fritschii* is able to respond very well to the change from white light to M7 light, and continue to grow even at in different light conditions, confirming our hypothesis that cyanobacteria with FarLip properties could also exploit M-star light), *Cyanobacterium aponinum* suffers the new type of radiation and increase its cellular respiration decreasing the total oxygen production, as can be well seen in the table comparing net and total oxygen production.

Sample	[Chl]mg/ml	Total $\mu\text{mol O}_2/\text{mg Chl}/\text{h}$	Net evolution $\text{O}_2/\text{mgChl}/\text{h}$
<i>Cyanobacterium Aponinum</i> 1 Vis 48h	0.0053	47.479	23.0097
<i>Cyanobacterium Aponinum</i> 2 Vis 48h	0.0066	40.409	22.3289
<i>Cyanobacterium Aponinum</i> 1 M7 48h	0.0035	70.525	-29.2421
<i>Cyanobacterium Aponinum</i> 2 M7 48h	0.0042	3.311	-25.4770
<i>Chlorogloeopsis fritschii</i> 1 Vis 48h	-	-	-
<i>Chlorogloeopsis fritschii</i> 2 Vis 48h	0.0051	79.572	50.3176
<i>Chlorogloeopsis fritschii</i> 1 M7 48h	0.0053	89.716	65.8067
<i>Chlorogloeopsis fritschii</i> 2 M7 48h	0.0056	70.497	48.0808

Finally, a chromatic response have been done, in order to understand if the colour would reflect the vitality of the bacteria. For the future experiments the bacteria will be lodged inside the environmental chamber in order to modulate even the gaseous mixture and temperature. Moreover, this radiation source, improved and sharpened could be useful to build a database of organisms capable to resist in different planetary conditions. Another proposal for future works is to understand if the feature of the "red edge" and pigmentation could be influenced by the extended undergoing to a radiation spectrum different from the Sun's one. This can be done growing organisms in different light conditions and studying the different reflectance spectra of the pigments developed and present inside them. Other than these two bacteria other photosynthetic organisms could be used, in particular the moss *Physcomitrella patens* that is the direct link between aquatic and land plants. Using these data we will give new light to the understanding of the "colors" that photosynthetic organisms could show and how these feature can impact on the biomarker panorama. Finally, chirality of organisms could be detected inside the reflectance spectra of the samples and compared with the absence of this feature in non-photosynthetic organisms.

INDEX

1. Introduction	p.1
2. Extrasolar planets characterization	p.3
2.1 Discovery methods: Radial velocity, Transits, Direct imaging	p.3
2.2 Exoplanet characterization: past present and future ground and space missions	p.7
2.2.1 Ground based projects	p.7
2.2.2 Space missions	p.10
2.3 Exoplanet atmospheres: key concepts	p.12
2.3.1 Scale height	p.13
2.3.2 Exoplanet atmospheric models	p.13
2.3.3 Albedo	p.19
2.3.3.1 The geometric Albedo $A_{g(v)}$	p.19
2.3.3.2 The Bond Albedo A_B	p.19
2.3.4 The effective temperature	p.20
2.3.5 Equilibrium Temperature	p.21
2.3.6 The Brightness Temperature	p.21
2.4. Earth similarity index	p.22
2.5 Biosignatures	p.27
3. Habitable planets.	p.29
3.1 The Habitable Zone (HZ)	p.29
3.1.1 The inner edge (IHZ)	p.31
3.1.2 The outer edge	p.32
3.1.3 The effect of planetary properties on HZ	p.33
3.1.4 Gravity and the HZ	p.35
3.1.5 Habitable limits calculation	p.39

3.1.6 The galactic HZ	p.43
3.2 Life on other planets: the basis	p.43
3.2.1 Lipids, proteins and other requirements	p.44
3.2.2 Adaptability of the organisms to hostile environments	p.45
3.2.2.1 Temperature	p.46
3.2.2.2 pH	p.48
3.2.2.3 Pressure	p.49
3.2.2.4 Irradiation	p.49
3.2.2.5 UV damages	p.50
3.2.2.6 Salinity	p.51
3.2.2.7 Dessiccation	p.52
3.2.2.8 Rock dwelling	p.52
3.2.2.9 Nutrients	p.53
3.2.2.10 Gravity	p.54
3.3 Photosynthesis: model and description (oxygenic vs non anoxygenic)	p.54
3.3.1 Pigments, metabolism and environmental limits: photosynthetic organisms evolution	p.55
3.3.2 Light harvesting	p.55
3.3.3 Photosynthetic pigments	p.57
3.4 Oxygenic and anoxygenic photosynthesis on other planets	p.60
3.4.1 Photosynthetic Active Radiation (PAR)	p.64
3.5 Biomarkers set in context	p.68
3.6 Red edge and Vegetation Red Edge (VRE)	p.72
4. Ancillary science: plants on other planets	p.79
4.1 Leaves	p.79
4.2 Leaves and radiation	p.80

4.3 Leaf venation	p.80
4.4 Leaf surface	p.81
4.5 Plants and gravity	p.81
4.6 Plants and pressure	p.81
4.7 Plants and temperature	p.81
4.8 Photosynthesis and plants colours	p.81
4.9 Alternative photosynthetic ways on alternative worlds	p.84
4.10 Plants and IR radiation: The Effect of Infrared Light on Plant Growth	p.84
4.10.1 Weak light	p.84
4.11 Expected colours of extrasolar plants	p.87
4.12 Planets orbiting multiple star planet systems	p.87
4.13 Detection	p.88
5. Radiative sources analysis	p.91
5.1 About M stars	p.91
5.2 Molecular features	p.94
5.3 Variability	p.97
5.4 Flares	p.97
5.5 CME	p.99
5.6 Starspots	p.100
6. Experiment project and management	p.101
6.1 Radiation sources	p.101
6.1.1 Stellar spectra analysis	p.101
6.1.2 Radiation devices analysis: lamps and LEDs	p.102
6.1.2.2. LEDs	p.106
6.2 Biological samples	p.109
6.2.1 Narrowing down the range	p.110

6.2.2 Organisms choice	p.112
6.2.3 Productivity simulations and estimate	p.115
6.2.3.1 Productivity estimates	p.116
6.3 Experiment planning	p.119
6.4 General estimate	p.120
6.4.1 Void pumps purchase estimate	p.120
6.4.2 O-rings purchase estimate	p.120
6.4.3 Hardware and irradiation tools purchase estimate	p.120
6.4.3.1 LEDs	p.120
6.4.4 Additive radiation sources	p.123
6.4.5 Gas purchase estimate	p.123
6.4.6 Incubator chamber estimate	p.123
7. Starlight simulator	p.125
7.1 Work Breakdown Structure and GANTT Diagram	p.131
7.2 Radiation source build-up	p.135
7.3 Simulations	p.136
7.4 Control software	p.137
7.5 Stellar simulator characterization	p.140
7.6 Other applications of the instrument	p.147
8. The experiment	p.149
8.1 Void pumps test	p.149
8.1.1 Preliminary tests	p.153
8.1.1.1 Test of cell n°1	p.155
8.1.1.2 Test of cell n°2	p.156
8.1.1.3 Test of cell n°3	p.156

8.1.1.4 Test of cell n°4	p.157
8.1.1.5 Test of cell n°5	p.159
8.1.1.6 Test of cell n°6	p.161
8.1.1.7 Intermediate procedures	p.163
8.1.1.8 Test of cell n°1	p.165
8.1.1.9 Test of cell n°2	p.167
8.1.1.10 Test of cell n°3	p.168
8.1.1.11 Test of cell n°4	p.170
8.1.1.12 Test of cell n°5	p.173
8.1.1.13 Test of cell n°6	p.176
8.1.1.14. Glass characterization	p.178
8.1.1.15: Conclusions	p.181
8.2 New cell design	p.182
8.3 Cell characterization	p.186
8.4 Bacteria preliminary tests	p.188
8.4.1 Determination of growth parameters	p.189
8.4.2 Reference O ₂ productivity tests with oxymeter	p.191
8.5 Irradiation of the samples with a stellar spectrum simulator and terrestrial pressure, temperature and gaseous mixture	p.192
8.5.1 Analysis of bacteria productivity and gas abundances in cell	p.197
8.6 Pigment reflectance tests	p.197
9. Conclusions	p.205
Appendix A: Publications and conference papers	p.207
Appendix B Software codes	p.209
Appendix C: Starlight simulator building drawings	p.239

Appendix D: Bacteria gas cell building drawings	p.243
Appendix E: ESIs datasets	p.251
Appendix F: Stellar simulations	p.261
APPENDIX G: PPFd conversion table	p.293
Bibliography	p.299

1. Introduction

The incredible number of extrasolar planets discovered so far (over 4826 planets among confirmed and Kepler candidates from the site exoplanet.org) unveils an incredible variety and variability. Most of these planets are very different from those of our Solar System in terms of masses and densities, as well as physical conditions.

In figure 1.1 can be seen the mass-radius diagram of different planet types.

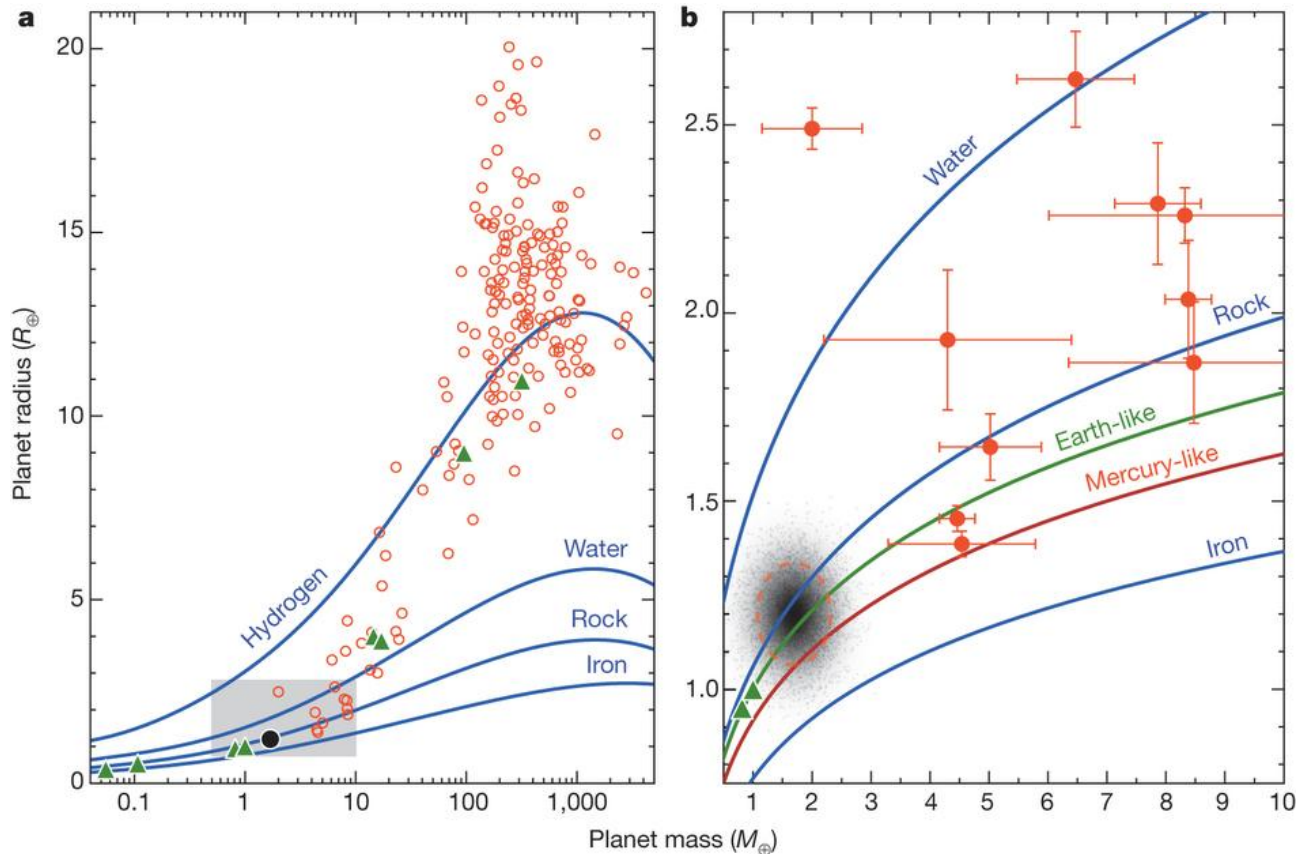


Figure 1.1: Extrasolar planets are denoted by red circles and Solar System planets are represented by green triangles. a) spans the full range of sizes and masses on logarithmic axes. The shaded grey rectangle denotes the range of parameters shown in b) on linear mass and radius axes. Kepler-78b is depicted as a black filled circle in a) and as a distribution of allowed masses and radii with a dotted red ellipse marking the 68% confidence region in b). Model mass–radius relationships for idealized planets consisting of pure hydrogen, water, rock (Mg_2SiO_4), and iron are shown as blue lines. Green and brown lines denote Earth-like composition (67% rock, 33% iron) and Mercury-like composition (40% rock, 60% iron). Exoplanet masses, radii and their associated errors are from the Exoplanet Orbit Database (<http://exoplanets.org>, 1 September 2013).

These new worlds can spread along a great range of combinations. There are gas giants, similar to Jupiter and Saturn with masses over $10 M_{\oplus}$. They are composed mainly of H and He with a possible rocky or metallic nucleus. Among them, the so called hot jupiters have orbital distances very close to their parent star and temperatures above 700°C . This planetary class is the most discovered and studied one (Knutson et al., 2014). Earths and Super earths are rocky exoplanets with mass ranging between 1 and $10 M_{\oplus}$ (Valencia et al., 2007). While the lower mass limit is obvious for historical reasons the upper limit is somewhat arbitrary. It is due to the physical argument that above $\sim 10 M_{\oplus}$, planets can retain Hydrogen and Helium in their atmospheres (Ida & Lin 2004). The Earths have radius $\leq 1.25 R_{\oplus}$ while super earths have radii ranging between the interval $[1.25, 2.0] R_{\oplus}$ (Borucki et al., 2011; Batalha et al., 2013). Since the discovery of GJ876d in the 2005 the existence of a set of super earths has been confirmed up to now. Some astronomers have been using the terms "water world" or "ocean planet" to describe another class of planets that have a proportion of water (solid or liquid) relative to the composition of the entire planet higher than 70% (Léger et

al., 1996). The oceans on such planets would be hundreds of kilometres deep, much deeper than the oceans of Earth. The immense pressures in the lower regions of these oceans could lead to the formation of a mantle of exotic forms of ice. This ice would not necessarily be as cold as conventional ice. If the planet is close enough to its star that the water reaches its boiling point, the water will become supercritical and lack a well-defined surface. Even on cooler water-dominated planets, the atmosphere can be much thicker than that of Earth, and composed largely of water vapour, producing a very strong greenhouse effect. Smaller ocean planets would have less dense atmospheres and lower gravity; thus, liquid could evaporate much more easily than on more massive ocean planets (Léger et al., 1996). Theoretically, such planets could have higher waves than their more massive counterparts due to their lower gravity. An important concern has been distinguishing between large planets with thick hydrogen-helium gas envelopes from worlds with similar densities due to a high water content (Adams et al, 2008). In addition, an ocean world's suitability for habitation by Earth-type life is limited if the planet is completely covered by liquid water at the surface, even more restricted if a pressurized, solid "ice" layer is located between the global ocean and the heavier elements and minerals of the lower rocky mantle.

Pulsar planets can be discovered through the time pulsation anomalies of the star. Before 1991 it was thought that any planets orbiting such stars would have been destroyed in the explosion of the supernova that created the pulsar star. This is why it is possible that these planets have been captured by these stars. Pulsar planets would be unlikely to harbour life as we know it, because the high levels of ionizing radiation emitted by the pulsar and the corresponding paucity of visible light (Wolszczan et al., 1994).

In this thesis we'll analyze the planetary conditions of Earth-like planets orbiting around the habitable zone (HZ) of stars fainter than our Sun. The study of super earths in HZ of stars cooler than the Sun will challenge the paradigm of the Earth-twin orbiting a Sun twin as the only possible cradle of life (Segura et al., 2005). In the past, starting by Huang (1959, 1960) and Dole (1964), astronomer have considered stars very different by the Sun not suitable for biology. The stars with larger masses aren't considered suitable for life because evolve too fast, and those with smaller masses because their luminosity is too faint. In the latter case (the M star case) the HZs are so close to the star that the planet results tidally locked to the host star (e.g. Kasting et al 1993) keeping always the same hemisphere facing the star. Haberle et al. (1996) with a one dimensional simple model and successively Joshi et al (1997) with a more complex 3-D model showed that the atmospheric heat transport could prevent the freeze out of the night hemisphere of the planet. All these considerations coupled with the realization that 75% or more of the stars are M type dwarfs (Henry, 2004) make them appealing stars to search for life.

2. Extrasolar planets characterization

The road towards the knowledge of extrasolar planets goes through different steps. The first is obviously the discovering of planetary systems around different kind of stars. Each star has its own characteristics and can form with high or low probability an environment able to host planets. Once we have a good panorama of planets the second step is characterizing them. This means understand their composition, their density and the atmospheric envelope, if present. This last step can be achieved with spectroscopic data combined with radiative-convective models and photochemical models that simulates the atmospheric layers and their interactions with the stellar radiation and the endogenous molecular sources. In particular is crucial to understand the link between the albedo of hazes and clouds and the planetary equilibrium and surface temperature. All these steps can help to draw a classification roadmap.

2.1 Discovery methods: Radial velocity, Transits, Direct imaging

Figure 2.1 shows a representation of all the detection methods for extrasolar planets searching, also called Perryman's tree (Perryman, 2000).

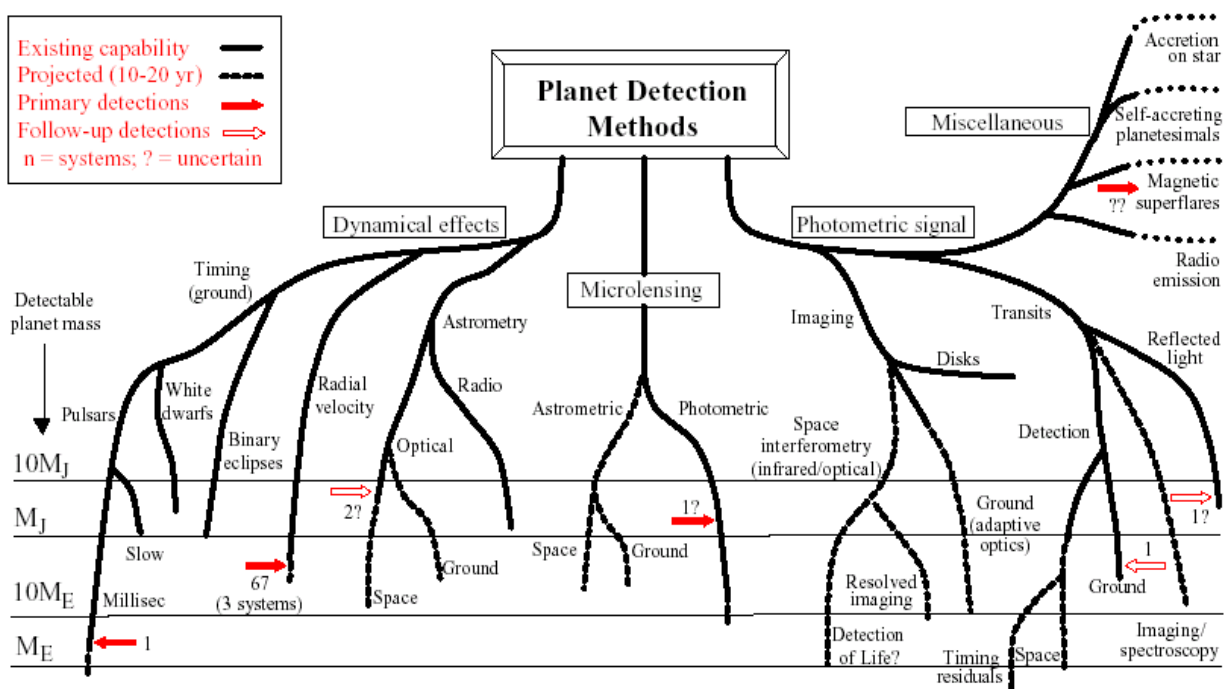


Figure 2.1: A representation of all detection methods for extrasolar planets searching (Perryman, 2000)

The most used techniques are radial velocity, direct imaging and the transit method, described later. Figure 2.2 shows some of the different indirect detection methods and the data acquirable with them.

Pulsar Timing	<i>Pulsars</i>	$M_p \sin i ; P, e, a, \omega, T_0$	<i>Indirect</i>
Radial Velocity	<i>Solar-Type stars / activity (AF, M, evolved, young...)</i>	$M_p \sin i ; P, e, a, \omega, T_0$	
μ -lensing	<i>crowded field / probability</i>	M_p, M_*, d, P, a	
Astrometry	<i>nearby stars</i>	$M_p, P, i, e, a, \omega, T_0$	
Transit (+RV) secondary	<i>crowded field / probability</i>	R_p, M_p, P, a, i, T_0 $T_{eff}, \log(g), Fe/H, Chem.$	<i>direct</i>
Direct Imaging	<i>young, nearby stars</i>	$L, \Delta_{proj}, (P, e, i, \omega, T_0)$ $T_{eff}, \log(g), Fe/H, Chem.$	

<http://exoplanet.eu/>

Figure 2.2: Discovery methods and data acquirable, where P ω are the period and the frequency of the orbit, T_0 is the orbital time, a is the semi-major axis of the orbit, $M_p \sin(i)$ the minimum mass of the planet, i is the inclination angle of the orbit, M_* the mass of the star and G is the universal gravitational constant equal to $6.67 \cdot 10^{-11} \frac{m^3}{Kg \cdot s^2}$, R_* and R_p are the stellar and planetary radii and T_{eff} is the effective temperature of the planet and e is the eccentricity of the orbit.

For the time being only two techniques among these can be used in order to probe the atmospheres of a planet: direct imaging and transits. Direct imaging can give information about masses, radii (from the luminosity and temperature data), temperature and chemical composition from the spectra and polarization. The direct detection of a planet is still very challenging due to its high contrast ratio with respect to the host star, which can reach values of 10^{-10} for an earth-like planet (see e. g. Lafrenière et al., 2007, Marois et al., 2008, Chauvin et al., 2010, Biller et al., 2013). For hot planets the flux doesn't depend on the separation from the star but only from the intrinsic emission while for warm and cold planets the flux depends from the reflected radiation and scales with the square distance from the star. Figure 2.3 shows an example of direct imaging of four planets (Marois et al. 2008)

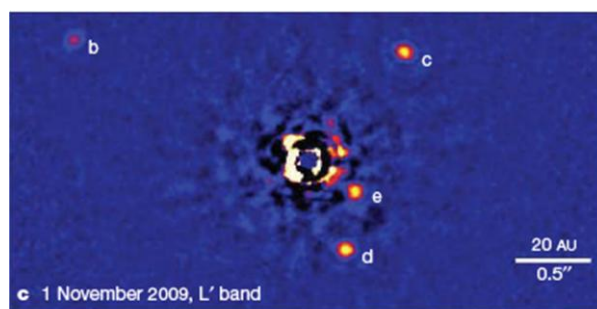


Figure 2.3: direct imaging of four planets around the star HR 8799

The radial velocity technique is based on the fact that the radial velocity of a star orbiting around the barycentre of a star-planet system varies in time depending on the quantity K given by:

$$K = \left(\frac{2\pi G}{P}\right)^{\frac{1}{3}} \frac{M_p \sin(i)}{(M_p + M_*)^{\frac{2}{3}} (1-e^2)^{\frac{1}{2}}} \quad (2.1)$$

where P is the orbital period of the planet, $M_p \sin(i)$ the minimum mass of the planet, i is the inclination angle of the orbit, M_* the mass of the star and G is the universal gravitational constant equal to $6.67 \cdot 10^{-11} \frac{m^3}{Kg \cdot s^2}$. It is easier to detect planets around low-mass stars for two reasons: first, these stars are more affected by gravitational tug from planets. The second reason is that low-mass main-sequence stars generally rotate relatively slowly. Fast rotation makes spectral-line data less clear because half of the star quickly rotates away from observer's viewpoint whereas the other half closes in. Detecting planets around more massive stars is easier if the star has left the main sequence because leaving the main sequence slows down the star's rotation. Sometimes Doppler spectrography produces false signals which is more common in multi-planet and multi-star systems. Magnetic field and certain types of stellar activity can also give false signals. When the host star has multiple planets, false signals can also arise from having insufficient data where multiple solutions can fit with gathered data as stars are not generally observed continuously. Some of the false signals can be eliminated by analyzing the stability of the planetary system, conducting photometry analysis on the host star and knowing its rotation period and stellar activity cycle periods. Planets with orbits highly inclined to the line of sight from Earth produce smaller wobbles, and are thus more difficult to detect. One of the advantages of radial velocity method is that eccentricity of the planet's orbit can be measured directly. One of the main disadvantages of the radial-velocity method is that it can only estimate a planet's minimum mass. The distribution of the inclination angle i depends on the true mass distribution of the planets (Stevens et al., 2013). However, when multiple planets are present in the system that orbit relatively close to each other and have sufficient mass, orbital stability analysis allows to constrain the maximum mass of the planets in question. The radial-velocity method can be used to confirm findings made by using the transit method. When both methods are used in combination, then the planet's true mass can be estimated. The detection of planets with the radial velocity method is usually possible only if the planet orbits around relatively bright star and if the planet reflects or emits a lot of light. Although radial-velocity of the star only gives a planet's minimum mass, if the planet's spectral lines can be distinguished from the star's spectral lines then the radial-velocity of the planet itself can be found and this gives the inclination of the planet's orbit. This allows measure planet's actual mass. This also rules out false positives and allows to gain information about the composition of the planet. The transits method is the strongest and most used one in order to find and characterize exoplanets. Studying the effects that the star undergo when one or more planets passes in front or behind it astronomers can infer several physical planetary data. Figure 2.4 shows the different phases of a transiting planet around its host star and the variation of the flux.

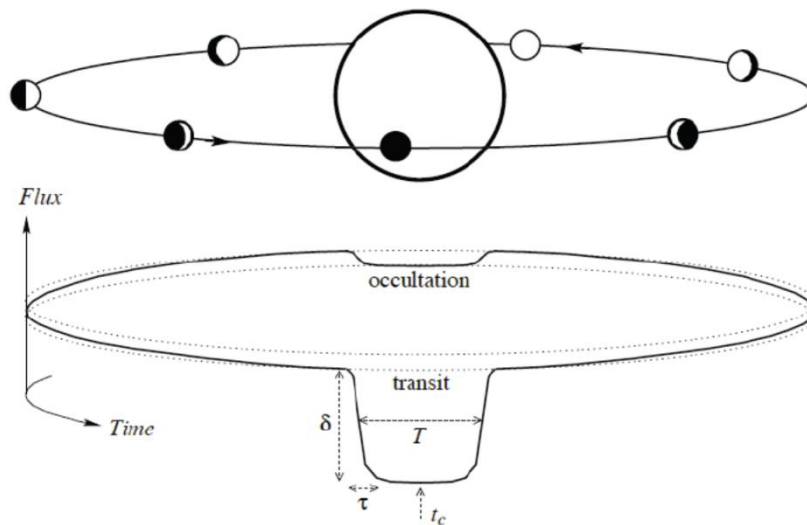


Figure 2.4: Different phases of a transiting planet around its host star and the variation of the flux (Winn, 2010).

Transits give important diagnostic on the probable modification of the atmosphere due to the history of the planet allowing transmission and emission spectroscopy. Transmission spectroscopy, possible only when the planet transits its host star along the line of sight, allows to infer the main opacity sources present in the high atmosphere of the planet (Tinetti et al. 2007). Complementary, emission spectroscopy (Charbonneau et al. 2005), observing the day hemisphere of the planet and exploiting its occultation during the secondary transit, gives evidence on the thermal structure of the planetary atmosphere and the emission/reflection properties of the planetary surface. In order to maximize the finding of habitable planets with transit search, a lot of surveys have been dedicated to search for earth and super earths size planets around M stars (e.g. Nutzman & Charbonneau, 2008). Due to a more favourable ratio between the radii, some small rocky companions have been discovered in the habitable zone (HZ) of these red and cold stars.

The data that can be acquired with this method are the radius ratio:

$$\frac{R_p}{R_*} \sim \sqrt{\delta} \quad (2.2)$$

the impact parameter b , defined as the projected distance between the planet and star centres during mid-transit, is, in unit of R_* (Seager et al., 2003):

$$b = 1 - \sqrt{\delta} \frac{T}{\tau} \quad (2.3)$$

the scaled stellar radius

$$\frac{R_*}{a} = \frac{\pi\sqrt{T\tau}}{\delta^{\frac{1}{4}}P} \left(\frac{1+e\sin(\omega)}{\sqrt{1-e^2}} \right) \quad (2.2)$$

the stellar mean density ρ_*

$$\rho_* = \frac{3P}{\pi^2 G} \left(\frac{\sqrt{\delta}}{T\tau} \right)^3 \left[\frac{1-e^2}{(1+e\sin(\omega))^2} \right]^{\frac{3}{2}} \quad (2.3)$$

and the planetary surface gravity g_p .

In figure 2.4 are summarized the data acquirable with the different detection methods where P ω are the period and the frequency of the orbit, T_0 is the orbital time, a is the semi-major axis of the orbit, the minimum mass of the planet, i is the inclination angle of the orbit, M_* the mass of the star and G is the universal gravitational constant equal to $6.67 \cdot 10^{-11} \frac{m^3}{Kg \cdot s^2}$, R_* and R_p are the stellar and planetary radii and T_{eff} is the effective temperature of the planet and e is the eccentricity of the orbit.

Finally in figure 2.5 can be seen the number of planets discovered over 25 years with different methods:

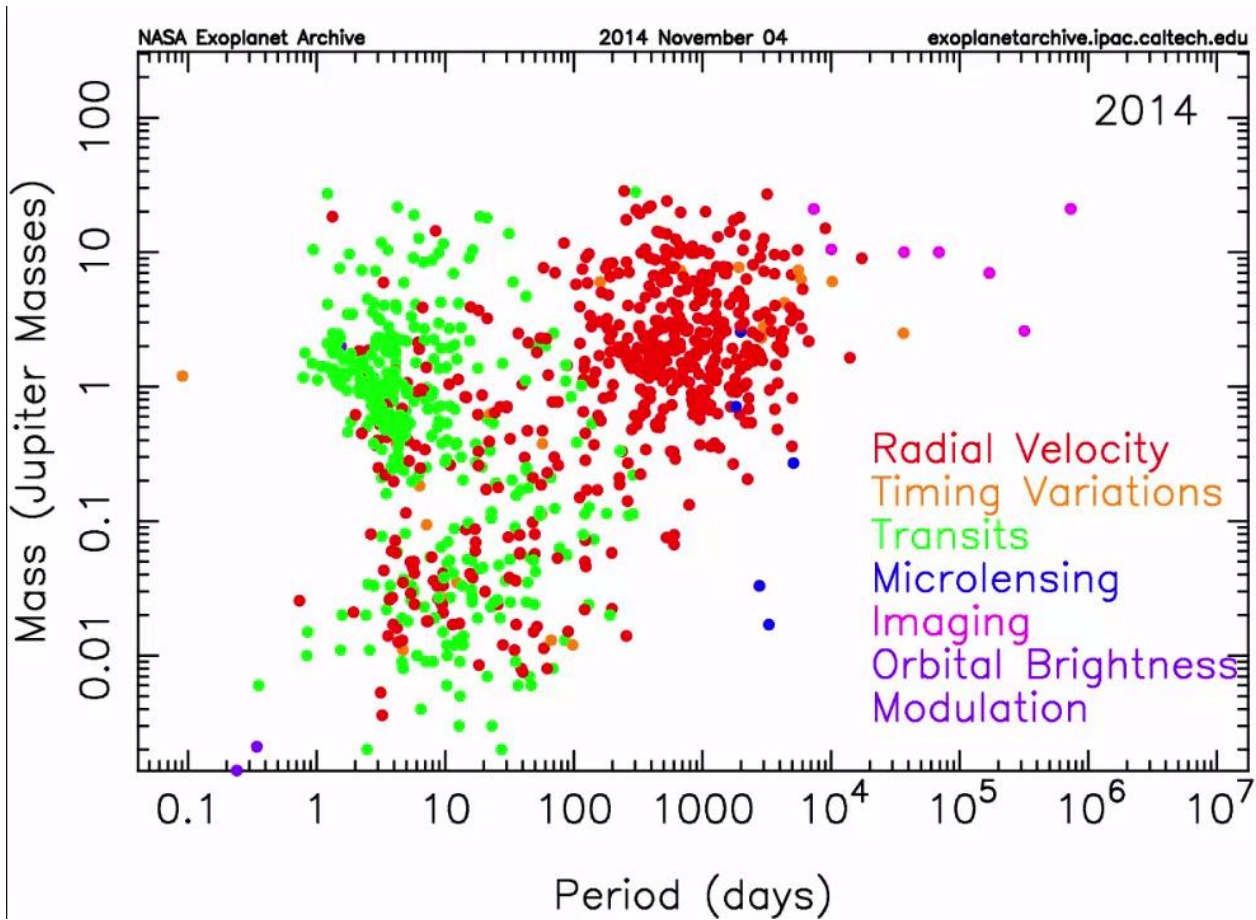


Figure 2.4: Number of exoplanets discovered with different methods.

2.2 Exoplanet characterization: past present and future ground and space missions

In order to discover and characterize exoplanets the world panorama offers a great variety of instruments and projects. A big distinction must be made between ground based and space instruments. Each one of them have pros and contras. Ground instruments can be readily repaired when damaged and all the devices can be close followed in order to ensure an optimal working. Of course, all ground based instruments are affected by atmospheric fluctuations and aberrations. This means to empower them with expensive and more and more sharp adaptive optics devices (as well as active optics ones) in order to correct the image deterioration. Space instruments have the advantage of being unaffected by this problem but require greater efforts in order to ensure a good working offset. Hereafter are described all the exoplanetary search and characterization projects, with a particular interest on the upcoming ones.

2.2.1 Ground based projects

Leonhard Euler Telescope, or Swiss 1.2-m Leonhard Euler Telescope, is a national 1.2-metre (3.9 ft) diameter aperture reflecting telescope of the Geneva Observatory at ESO's La Silla Observatory site in Chile. The telescope uses the **CORALIE** instrument to search for exoplanets. Its first discovery was a planet in orbit around Gliese 86 (from <http://exoplanets.ch/projects/euler/>). It was determined to be a 4MJ planet with an orbital period of 15.8 earth days. Since then, many other extra solar-system planets have been discovered or examined. The observatory is operated by the University of Geneva of Switzerland since the telescopes was finished in 1998. and was named after the Swiss mathematician Leonhard Paul Euler (1707–1783). The

Euler 1.2 and the Mercator Telescope were part of the Southern Sky extrasolar Planet search Programme which has discovered numerous extrasolar planets.

East-Asian Planet Search Network, (EAPSNET), is an international collaboration between Korea, China and Japan. Each facility, BOAO (Korea), Xinglong (China), and OAO (Japan), has a 2 m class telescope, a high dispersion echelle spectrograph, and an iodine absorption cell for precise RV measurements, looking for extrasolar planets (Izumiura, 2005).

The **European Extremely Large Telescope (E-ELT)** is a project of a ground-based extremely large telescope for the optical/near-infrared range, currently being built by the European Southern Observatory (ESO) on top of Cerro Armazones in the Atacama Desert of northern Chile. The design comprises a reflecting telescope with a 39.3m diameter segmented primary mirror, a 4.2-metre-diameter secondary mirror, and will be supported by adaptive optics and multiple instruments (Schilling, 2011). It is expected to allow astronomers to probe the earliest stages of the formation of planetary systems and to detect water and organic molecules in proto-planetary discs around stars in the making. It is endorsed with EPICS, an optical/NIR planet imager and spectrograph with extreme adaptive optics (Kasper et al., 2008).

The **New Mexico Exoplanet Spectroscopic Survey Instrument (NESSI)** is a ground-based instrument specifically designed to study the atmospheres of exoplanets (Withney, 2014). The instrument is the first purpose-built device for the analysis of exoplanet atmospheres, and is expected to have a powerful impact on the field of exoplanet characterization (Martin, 2014). The Principal Investigator is Michele Creech-Eakman at the New Mexico Institute of Mining and Technology, working with seven co-investigators. The NESSI instrument was mounted on the institute's 2.4 meter telescope at the Magdalena Ridge Observatory in Socorro County, New Mexico, USA. It is partly funded by NASA's Experimental Program to Stimulate Competitive Research, in partnership with the New Mexico Institute of Mining and Technology.^[1] The instrument is currently being calibrated and its first exoplanet observations are expected to begin in the summer of 2014. The novel technology is expected to achieve high definition readings by using algorithms to calibrate and compensate for time-variable telluric features and instrumental variability throughout an observation.

PARAS is a ground based extrasolar planet search device. Based at 1.2m telescope is located at Mt. Abu, India. The project is funded by Physical Research Laboratory, India. The spectrograph works at a resolution of 67000. With the help of simultaneous calibration technique, PARAS has achieved an RV accuracy of 1.3 m/s for bright sun like quiet stars. Thorium-Argon lamp is used for calibration. New calibration techniques are also being explored by the project team. PARAS can detect planet in the habitable zone around M type stars (Chakraborty et al., 2010).

The **Fiber-Optic Improved Next-Generation Doppler Search for Exo-Earths (FINDS Exo-Earths)** is a radial-velocity spectrograph developed by Debra Fischer. It is installed on the 3m telescope in Lick Observatory in Mount Hamilton. In operation since 2009. Is used to verify exoplanet candidates found by Kepler (from <http://www.planetary.org/explore/projects/exoplanets/finds.html>).

The **SOPHIE (Spectrographe pour l'Observation des Phénomènes des Intérieurs stellaires et des Exoplanètes) échelle spectrograph** is a high-resolution echelle spectrograph installed on the 1.93m reflector telescope at the Haute-Provence Observatory located in south-eastern France. The purpose of this instrument is asteroseismology and extrasolar planet detection by the radial velocity method. It builds upon and replaces the older ELODIE spectrograph. This instrument was made available for use by the general astronomical community October 2006 (Perruchot et al., 2008).

SPHERE or the Spectro-Polarimetric High-contrast Exoplanet Research instrument is the extreme adaptive optics system and coronagraphic facility at the VLT. Its primary science goal is imaging, low-resolution spectroscopic, and polarimetric characterization of extra-solar planetary systems at optical and near-infrared wavelengths. The instrument is equipped with 3 subsystems: ZIMPOL, IRDIS and IFS. ZIMPOL is a special purpose camera, that can both make very sharp images and measure polarisation in visible light and the near infrared (from 600 to 900 nanometres). Its role is to detect the reflected polarised light of gaseous planets orbiting very close to their host stars, and detect the scattered light from the dusty discs around young stars. It uses a unique trick to detect very faint objects around very bright stars. IRDIS is a camera working at near-infrared wavelengths, from 900nm to 2.3 microns, whose main goal is to image young self-luminous giant planets thanks to advanced observational strategies based on a technique called differential imaging. IFS is a near-infrared integral field spectrograph that can work simultaneously with IRDIS to provide a spectrum at each given location of the field of view. This enables astronomers to characterise the composition of the atmosphere of giant planets (from <https://www.eso.org/public/teles-instr/vlt/vlt-instr/sphere/>).

HIRES is the largest and most mechanically complex of the Keck's main instruments, the High Resolution Echelle Spectrometer breaks up incoming light into its component colours to measure the precise intensity of each of thousands of colour channels. Its spectral capabilities have resulted in many breakthrough discoveries, such as the detection of planets outside our solar system and direct evidence for a model of the Big Bang theory. This instrument has detected more extrasolar planets than any other in the world. The radial velocity precision is up to one meter per second (1.0 m/s). The instrument detection limit at 1 AU is 0.2 M_J (from <http://www.keckobservatory.org/about/instrumentation>).

The **Gemini Planet Imager (GPI)** is a high contrast imaging instrument that was built for the Gemini South Telescope in Chile (see <http://planetimager.org/>). The instrument achieves high contrast at small angular separations, allowing for the direct imaging and integral field spectroscopy of extrasolar planets around nearby stars. The collaboration involved in planning and building the Gemini Planet imager includes the American Museum of Natural History (AMNH), Dunlap Institute, Gemini Observatory, Herzberg Institute of Astrophysics (HIA), Jet Propulsion Laboratory, Lawrence Livermore National Lab (LLNL), Lowell Observatory, SETI Institute, The Space Telescope Science Institute (STSCI), the University of Montreal, University of California, Berkeley, University of California, Los Angeles (UCLA), University of California, Santa Cruz (UCSC), University of Georgia.

There are many exoplanet survey programs as the **Lick–Carnegie Exoplanet Survey (LCES)** that is a search for exoplanets using the Keck I optical telescope of the W. M. Keck Observatory in Hawaii. The survey is sponsored by NASA and the National Science Foundation. The survey comprises a decade of observations. The survey is led by Steven Vogt, professor of astronomy and astrophysics at University of California at Santa Cruz, and R. Paul Butler of the Carnegie Institution (Howard et al., 2010).

Another search program is the **Magellan Planet Search Program**. It is a ground based extrasolar planet search device which began gathering data in December 2002 (Minniti et al., 2009). It utilizes the MIKE echelle spectrograph mounted on the Magellan Telescopes which are twin, 6.5m Magellan II (Clay) telescope located within the Las Campanas Observatory in Chile. The program is surveying approximately 400 stars which ranges from F7 to M5 type stars. The stars included in the program has been chosen to minimize overlapping surveys with both Anglo-Australian Planet Search (AAT) and the KECK programs. Any star with larger jitters have been removed from the program specifically those that has 2 magnitudes above the main sequence when basing it from Hipparcos distances. The Magellan Planet Search Program has discovered 5 eccentric Jupiter-mass planets. Announcement was made in January 2010, regarding the discovery of the 5 long period extra-solar planets from Magellan velocity surveys. They were found orbiting G and K type dwarfs which are Jovian-mass planets in both long-period and eccentric orbits.

The MEarth Project is a United States NSF-funded, robotic observatory that is part of Fred Lawrence Whipple Observatory on Mt. Hopkins, Arizona, USA. The project monitors the brightness of thousands of red dwarf stars with the goal of finding transiting planets. As red dwarf stars are small, any transiting planet blocks larger portion of starlight than transits around Sun-like star. This allows smaller planets to be detected through ground-based observations. MEarth consists of eight RC Optical Systems 40 cm (16 in) f/9 Ritchey-Chrétien telescopes (on Paramount ME robotic mounts) paired with commercially available cameras with 2048 × 2048 Apogee U42 CCDs (FROM <https://www.cfa.harvard.edu/MEarth/gj1132b.html>).

WASP (Wide Angle Search for Planets) is an international academic organisation performing an ultra-wide angle search for transiting extrasolar planets with the aim of covering the entire sky down to ~13th magnitude. WASP consists of two robotic observatories; Super WASP-North at Roque de los Muchachos Observatory on the island of La Palma in the Canaries and WASP-South at the South African Astronomical Observatory, South Africa. Each observatory consists of an array of eight Canon 200 mm f1.8 lenses backed by high quality 2048 x 2048 science grade CCDs, the model used is the iKon-L manufactured by Andor Technology. The telescopes are mounted on an equatorial telescope mount built by Optical Mechanics, Inc.. The large field of view of the Canon lenses gives each observatory a massive sky coverage of 490 square degrees per pointing.

The **Trans-Atlantic Exoplanet Survey** or TrES, uses three 4-inch (10 cm) telescopes located at Lowell Observatory, Palomar Observatory, and the Canary Islands to locate exoplanets. It was made using the network of small, relatively inexpensive telescopes designed to look specifically for planets orbiting bright stars using the transit method. The array uses 4-inch Schmidt telescopes having CCD cameras and automated search routines. The survey was created by David Charbonneau of the Center for Astrophysics, Timothy Brown of the National Center for Atmospheric Research, and Edward Dunham of Lowell Observatory (Alonso et al., 2004).

The **XO Telescope** is a telescope located on the 3,054 m summit of Haleakala on Maui, Hawaii, formed by a pair of 200 mm telephoto lenses. It is used by the XO Project to detect extrasolar planets using the transit method. It is similar to the TrES survey telescope. The construction of the one-of-a-kind telescope cost \$60,000 for the hardware, and much more than that for the associated software.

ZIMPOL (Zurich IMaging POLarimeter)/CHEOPS (CHaracterizing Exo-planets by Opto-infrared Polarimetry and Spectroscopy) is a polarimetric imager being developed for the Very Large Telescope for the direct detection of extra-solar planets. The imager is operated by the European Southern Observatory on Cerro Paranal in the Atacama Desert of northern Chile.

2.2.2 Space missions

Past and current

Here will described some of the main space missions in the exoplanet finding and characterization panorama.

CoRoT (French: **CO**nvection **RO**tation et **Tr**ansits planétaires; English: **CO**nvection **RO**tation and planetary **Tr**ansits) is a space mission led by the French Space Agency (CNES) in conjunction with the European Space Agency (ESA) and other international partners. The mission's two objectives are to search for extrasolar planets with short orbital periods, particularly those of large terrestrial size, and to perform asteroseismology by measuring solar-like oscillations in stars (from <http://www.spaceref.com/news/viewpr.html?pid=21129>).

It was launched in 2006, atop a Soyuz 2.1b carrier rocket and reported first light on 18 January 2007 (Hellmans et al., 2007). CoRoT is the first spacecraft dedicated to the detection of transiting extrasolar planets, opening the way for more advanced probes such as Kepler as well as future missions such as TESS and PLATO. It detected its first extrasolar planet, COROT-1b, in May 2007 (from http://www.esa.int/Our_Activities/Space_Science/COROT/COROT_discovers_its_first_exoplanet_and_catches_scientists_by_surprise). Mission flight operations were originally scheduled to end 2.5 years from launch but operations were extended to 2013. CoRoT has been retired and would be decommissioned; lowered in orbit to allow it to burn up in the atmosphere (from http://www.spacedaily.com/reports/Retirement_for_planet-hunting_space_probe_999.html).

Kepler is a space observatory launched by NASA to discover Earth-like planets orbiting other stars (Koch et al., 2009). The spacecraft was launched on March 7, 2009. Designed to survey a portion of our region of the Milky Way to discover dozens of Earth-size extrasolar planets in or near the habitable zone and estimate how many of the billions of stars in our galaxy have such planets (Overbye, 2013, Overbye, 2015), Kepler's instrument is a photometer that continually monitors the brightness of over 145,000 main sequence stars in a fixed field of view. This data is transmitted to Earth, then analyzed to detect periodic dimming caused by extrasolar planets that cross in front of their host star. The Kepler primary mirror is 1.4 meters in diameter, the largest mirror located outside Earth. Manufactured by glass maker Corning using ultra-low expansion (ULE) glass, the mirror is specifically designed to have a mass only 14% that of a solid mirror of the same size orbit (from <http://www.spacedaily.com/news/extrasolar-03q.html>). In order to produce a space telescope system with sufficient sensitivity to detect relatively small planets, as they pass in front of stars, a very high reflectance coating on the primary mirror was required. Using ion assisted evaporation, Surface Optics Corp. applied a protective 9-layer silver coating to enhance reflection and a dielectric interference coating to minimize the formation of colour centres and atmospheric moisture absorption (Fulton et al., 2011).

Gaia is a space observatory of the European Space Agency (ESA) designed for astrometry (from http://www.esa.int/Our_Activities/Space_Science/Gaia). The mission aims to construct a 3D space catalogue of approximately 1 billion astronomical objects, mainly brighter than 20 G magnitudes, where G is the Gaia magnitude pass band between about 400 and 1000 nanometres light wavelengths. Additionally Gaia is expected to detect thousands to tens of thousands of Jupiter-sized planets beyond the Solar System, 500,000 quasars and tens of thousands of new asteroids and comets within the Solar System. The spacecraft will monitor each of its target stars about 70 times over a period of five years (from <http://www.cam.ac.uk/research/features/gaias-mission-solving-the-celestial-puzzle>). Gaia will create a precise three-dimensional map of astronomical objects throughout the Milky Way and map their motions, which encode the origin and subsequent evolution of the Milky Way. The spectro-photometric measurements will provide the detailed physical properties of all stars observed, characterizing their luminosity, effective temperature, gravity and elemental composition. This massive stellar census will provide the basic observational data to tackle a wide

range of important questions related to the origin, structure, and evolutionary history of our galaxy. The spacecraft currently operates in a Lissajous orbit around the Sun–Earth L_2 Lagrangian point.

Planned

CHEOPS (CHaracterising ExOPlanets Satellite) is a planned European space telescope for the study of the formation of extrasolar planets. Slated for launch in 2017, the mission aims to bring an optical Ritchey–Chrétien telescope with an aperture of 30 cm, mounted on a standard small satellite platform, into a sun-synchronous orbit of about 800 km altitude. For the planned mission duration of 3.5 years, CHEOPS is to examine transiting exoplanets on known bright and nearby host stars. Its main goal will be to accurately measure the radii of the exoplanets for which ground-based spectroscopic surveys have already provided mass estimates. Knowing both the mass and the size of the exoplanets will allow scientists to determine the planets' approximate composition, such as whether they are gaseous or rocky. Knowing where to look and at what time to observe makes CHEOPS the most efficient instrument to search for shallow transits and to determine accurate radii for planets in the super-Earth to Neptune mass range ($1-6 R_{\text{Earth}}$). CHEOPS will measure photometric signals with a precision limited by stellar photon noise of 150 ppm/min for a 9th magnitude star. This corresponds to the transit of an Earth-sized planet orbiting a star of $0.9 R_{\text{sun}}$ in 60 days detected with a $S/N_{\text{transit}} > 10$ (100 ppm transit depth). For example an Earth size transit toward a G star creates an 80 ppm depth. The spacecraft will provide 54W of continuous power for instrument operations and allow for at least 1Gbit/day downlink. Organized as a partnership between the European Space Agency (ESA) and the Swiss Space Office, CHEOPS was selected in October 2012 from among 26 proposals as the first S-class ("small") space mission in ESA's Science Programme. The project is to be led by the Center for Space and Habitability at the University of Bern, Switzerland, with contributions from other Swiss and European universities. After a competition phase, Airbus DS Spain was selected to be the spacecraft contractor.

The **Transiting Exoplanet Survey Satellite (TESS)** is a planned space telescope for NASA's Explorers program, designed to search for exoplanets using the transit method. The primary mission objective for TESS is to survey the brightest stars near the Earth for transiting exoplanets over a two-year period. The TESS project will use an array of wide-field cameras to perform an all-sky survey. It will scan nearby stars for exoplanets. With TESS, it will be possible to study the mass, size, density and orbit of a large cohort of small planets, including a sample of rocky worlds in the habitable zones of their host stars. TESS will provide prime targets for further characterization by the James Webb Space Telescope, as well as other large ground-based and space-based telescopes of the future. Previous sky surveys with ground-based telescopes have mainly picked out giant exoplanets. In contrast, TESS will examine a large number of small planets around the very brightest stars in the sky. TESS will record the nearest and brightest main sequence stars hosting transiting exoplanets, which will forever be the most favourable targets for detailed investigations. Led by the Massachusetts Institute of Technology with seed funding from Google, TESS was one of 11 proposals selected for NASA funding in September 2011, down from the original 42 submitted in February of that year. On April 5, 2013, it was announced that TESS, along with the Neutron Star Interior Composition Explorer (NICER), had been selected for launch in 2017 (from http://space.mit.edu/TESS/TESS/TESS_Overview.html).

The **James Webb Space Telescope (JWST)**, previously known as **Next Generation Space Telescope (NGST)**, is a space observatory which is under construction and its launch is scheduled in October 2018. The JWST will offer a very good resolution and sensitivity from long-wavelength visible to the mid-infrared (from <https://directory.eoportal.org/web/eoportal/satellite-missions/j/jwst>). It is the successor of the Hubble Space Telescope and the Spitzer Space Telescope. JWST's telescope is composed by a segmented 6.5-meter diameter primary mirror and will be located near the Earth–Sun L_2 point. A large sunshield will keep its mirror and four science instruments below 50 K ($-220\text{ }^\circ\text{C}$; $-370\text{ }^\circ\text{F}$) (Mather et al., 2006). JWST's capabilities can enable a broad range of investigations across the fields of astronomy and cosmology. One particular goal involves observing some of the most distant objects in the Universe, beyond the reach of current ground and space based instruments. This includes the very first stars, the epoch of re-ionization, and the formation of the first galaxies. Another goal is understanding the formation of stars and planets. This will include imaging molecular clouds and star-forming clusters, studying the debris disks around stars, direct imaging of planets, and spectroscopic examination of planetary transits. In gestation since 1996, the project represents an international collaboration of about 17 countries led by NASA, and with significant

contributions from the European Space Agency and the Canadian Space Agency. It is named after James E. Webb, the second administrator of NASA, who played an integral role in the Apollo program.

Planetary Transits and Oscillations of stars (PLATO) is a planned European Space Agency space observatory that will use a group of photometers to discover and characterize rocky extrasolar planets of all sizes around red dwarf stars, yellow dwarf stars like our Sun, and subgiant stars where water can exist in liquid state (Amos et al., 2014). The goal is to find planets like Earth, not just in terms of their size but in their potential for habitability (from <http://sci.esa.int/plato/42276-summary>). PLATO will search for planets around up to one million stars by using 34 separate small telescopes and cameras. The main objective of PLATO is to understand the conditions for planet formation and the emergence of life. To achieve this objective, the mission has these goals: 1) Discover and characterise a large number of close-by exoplanetary systems, with a precision in the determination of the planet mass up to 10%, of planet radius of up to 2%, and of stellar age up to 10%. 2) Detect Earth-sized planets in the habitable zone around solar-type stars. 3) Detect super-Earths in the habitable zone around solar-type stars. 4) Measure solar oscillations in the host stars of exoplanets. 5) Measure oscillations of classical pulsators.

The PLATO payload is based on a multi-telescope approach, involving a set of 32 "normal cameras" working at a readout cadence of 25 sec and monitoring stars fainter than $m_v = 8$ (apparent visual magnitude), plus two "fast cameras" working at a cadence of 2.5 sec, and observing stars in the magnitude range 4 to 8. The cameras are based on a fully dioptric telescope including 6 lenses; each camera has an 1100 deg² field, and a pupil diameter of 120 mm. Each camera is equipped with its own CCD focal plane array, consisting of 4 CCDs with 4510 x 4510 pixels. The 32 'normal cameras' are arranged in four groups of 8 cameras with their lines of sight offset by a 9.2° angle from the +ZPLM axis. This particular configuration allows surveying a total field of about 2250 deg² per pointing. The satellite will be rotated around the mean line of sight by 90° every 3 months, for a continuous survey of exactly the same region of the sky (Magrin et al., 2010). PLATO will differ from COROT and Kepler space telescopes in that it will study relatively bright stars (between magnitudes 4 and 8) making it easier to confirm extrasolar planets using follow-up radial velocity measurements. It will have a much larger field of view than the Kepler mission (which has 100 deg²) allowing PLATO to study a larger sample of stars. The satellite is planned to launch in 2024 from Guiana Space Centre with a Soyuz rocket to the Earth-Sun L2 Lagrangian point.

Among the proposed missions a pivotal role can be given to **ARIEL (Atmospheric Remote-sensing Infrared Exoplanet Large survey)**.

ARIEL is a 1m class telescope endorsed with a spectrograph with a bandwidth enclosed with 1.95 - 7.8 micron and spectral resolution ~200. It is a dedicated mission to investigate exoplanetary atmospheres, addressing the suitability of those planets for life and placing our Solar System in context. It would measure the atmospheric composition, temperature and albedo of a representative sample of known exoplanets, constrain models of their internal structure and improve our understanding of how planets form and evolve. It will orbit around the L2 Lagrange point, 1.5 million km from Earth in the anti-sunward direction (from http://ariel-spacemission.eu/press-releases/ariel_2015-07-16.html). ARIEL has born from the ashes of EChO. EChO, the Exoplanet Characterisation Observatory, was a mission concept specifically geared for investigation of exoplanetary atmospheres. EChO was supposed to probe the atmospheres of extrasolar planets combining three techniques, making use of planet transits, secondary eclipses, and planet phase-variations, which also could have been used for non-transiting planets. In the first case it would perform measurement of the upper part of the planetary atmosphere by means of the transmission spectroscopy technique (Erculiani et al., 2014).

2.3 Exoplanet atmospheres: key concepts

In this chapter will be explained several basic concepts for the study of the atmosphere. In particular will be treated the basis of exoplanet atmospheric models, the scale height, the definition of albedo with particular attention to geometric Albedo $A_{g(v)}$ and Bond Albedo A_B , the definition of effective temperature, equilibrium temperature and brightness temperature, the concept of Earth similarity index and a brief introduction to the analysis of the biosignatures.

2.3.1 The scale height

It is true that the light spectrum incident on the planet surface is the result of the parent star spectrum processed by the atmosphere through which it is transmitted, whatever it is gas or water.

The transmittance is usually a function of its ingredients, between which photosynthesis and biotic products are important ingredients

The atmosphere of a planet can be divided into a definite number of regions.

The lowest part of it is called troposphere, where the principal form of heat is the planetary surface and its convective fluxes transported through turbulent motions.

This is the cause of an adiabatic (convective) temperature distribution, whose gradient or adiabatic lapse rate is defined by $\frac{\partial T}{\partial z} = -\frac{g}{c_p}$, with g acceleration of gravity, c_p specific heat at constant pressure.

The upper limit of the troposphere is the tropopause, where the adiabatic lapse rate doesn't work anymore.

Above this height, heat distribution is governed by radiative processes and $\left|\frac{\partial T}{\partial z}\right| < -\frac{g}{c_p}$ or $\frac{\partial T}{\partial z} \sim 0$.

Above the tropopause there is the stratosphere, where the temperature increases constantly. On Earth the UV absorption caused by O_3 molecules provide a heating source until it reaches its maximum at the stratopause.

The temperature start decreasing in the mesosphere, the upper region, in which $\frac{\partial T}{\partial z} < 0$ and it reaches a minimum in the mesopause. In this region molecules provide a heat sink by radiating in the IR.

Further above, in the thermosphere, is absorbed the XUV radiation leading to an increase of $\frac{\partial T}{\partial z}$. Here convection at the termobase evolves in conduction at the upper limit of the thermosphere, leading to an isothermal region ($T=\text{constant}$).

In this region, because of the negligible collisions, the mean free path of the atmospheric species increase and light elements acquire an escape velocity such that they can go out from the atmosphere.

The outer region is called exosphere, where the exobase begins where the mean free path is equal to the local scale height defined as $H = \frac{kT_\infty}{mg}$, where μ_m is the molecular weight expressed in UMA, T_∞ the temperature at the exobase, g the gravitational acceleration (Scalo et al., 2007). If the atmosphere is H dominated, $\mu_m=2$ and hydrogen is high, but if there is very few hydrogen, $\mu_m=40$ and the atmosphere is thinner. The depth variation ΔD of spectral lines in transmission give useful informations on H:

$$\Delta D = \frac{HR_p}{R_*^2} \quad (2.6)$$

and

$$\mu_m = \frac{kT}{g} \frac{R_p}{\Delta DR_*^2} \quad (2.7)$$

where R_p and R_* are planet and star radii.

2.3.2 Exoplanet atmospheric models

All planetary atmospheres have an high level of complexity due to a large number of degrees of freedom, the interaction of various scales, and the fact that atmospheres tend to propagate many kind of waves. The key physical and dynamical processes at work on a terrestrial planet are finite and can be isolated. To first order, on most planets, the dynamical and physical processes that control the climate are (Figure 2.15) the radiative transfer of stellar and thermal radiation through gas and aerosols, the general circulation of the atmosphere forced by the large scale, radiatively induced temperature gradients, the vertical mixing and transport due to small scale turbulence and convection, the storage and conduction of heat in the subsurface, the phase changes of volatiles on the surface and in the atmosphere like clouds and aerosols and a big list of processes which are only relevant in particular cases, or which play a secondary role. These are photochemistry (producing aerosols, hazes or creating spatial inhomogeneities in the atmospheric composition), mineral dust

lifting, oceanic transport, molecular diffusion and conduction (at very low pressure) and others. The planetary characteristics and the composition of its atmosphere can generate a different palette of climates.

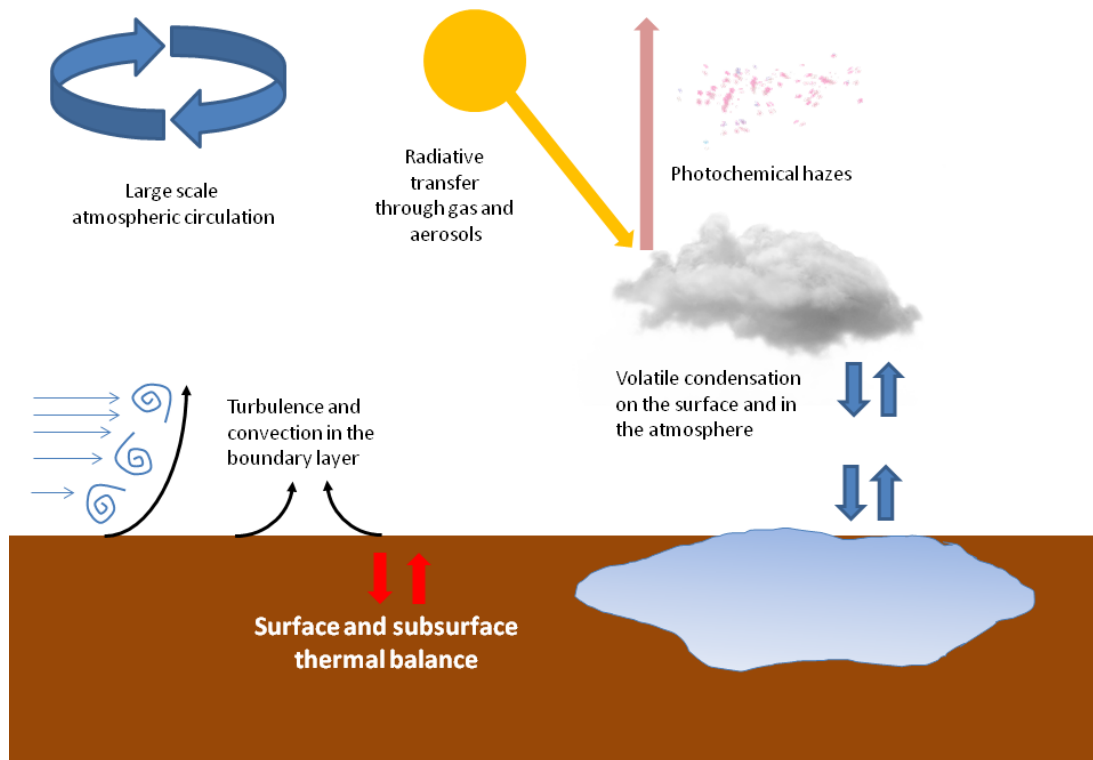


Figure 2.15: A scheme of the major factor that can determine the climate on a planet

Until recently, a majority of studies on terrestrial exoplanets had been performed with simple 1D steady-state radiative convective models. They can evaluate the global mean conditions on a given planet resulting from the radiative properties of its atmosphere and the insolation from its star, although they are often not sufficient to predict the actual state of a planet, and in particular represent the formation, distribution and radiative impact of clouds, or to simulate local conditions at a given time (Forget et al., 2013). 3D models are used to study the movement of great air masses to the poles and the night side energy transport by the sea and by the atmosphere. Basically a 3D model uses the Navier-Stokes equations to describe the fluid motions inside the atmosphere. More complete three dimensional numerical global climate models (“GCMs”) combine various components described above. For example, a 3D hydrodynamic “core”, and, for each grid point of the model, a radiative transfer solver, a parametrization of the turbulence and convection, a subsurface thermal model, a cloud model, and so on. Of course the error sources depend on processes which are non-linear or which depend on poorly understood physics.

Usually two types of fast climate tools are commonly employed in studies of planetary habitability: single atmospheric column calculations and energy balance models. Atmospheric column calculations treat in detail the physics of vertical energy transport, taking into account the influence of atmospheric composition on the radiative transfer (Kasting 1988, Koppapapu, 2014). This tool is usually used in the calculations of the habitable zone. Energy balance models (EBMs) calculate the zonal and seasonal energy budget of a planet using a heat diffusion formalism to describe the horizontal transport and simple analytical functions of the surface temperature to describe the vertical transport (North et al. 1981). This model explains the effect of variations of the rotational period, the eccentricity of the orbit and stellar insolation on the planetary climate. In zonal EBMs, the most simple EBMs model, the surface of the planet is divided into zones and these zones are delimited by latitude circles. The surface quantities of interest are averaged in each zone over one rotation period so as to can determine the spatial dependence by means of a single coordinate: the latitude φ . The time, t , represents the seasonal evolution during the orbital period. The thermal state is described by a single temperature, function of t and φ , $T = T(\varphi; t)$, that represents the surface conditions. By assuming that the heating and cooling rates are balanced in each zone, one obtains an energy balance equation:

$$C \frac{\partial T}{\partial t} - \frac{\partial}{\partial x} \left[D(1 - x^2) \frac{\partial T}{\partial x} \right] + I = S(1 - A) \quad (2.8)$$

with $x = \sin(\varphi)$ and all terms normalized per unit area. The first term represent the temporal evolution of each zone. C is the zonal heat capacity per unit area (North et al. 1981). The second term represents the amount of heat per unit time and unit area leaving each zone along the meridional direction. It is the diffusion term. D is a coefficient determined as

$$\Phi = -D \frac{\partial T}{\partial \varphi} \quad (2.9)$$

where $2\pi R^2 \Phi$ is the energy rate transport across a circle of constant latitude and R is the planetary radius (Pierrehumbert 2010). I is the thermal radiation outgoing from the zone or Outgoing Longwave Radiation (OLR). S is the incoming stellar radiation and A the planetary albedo at the top of the atmosphere. All the second part of the equation is the fraction of stellar photons that heat the surface of the zone. In classic EBMs the coefficients D , I and A are expressed in a very simplified form. D is often treated as a constant, because the meridional transport is influenced by planetary. The OLR and albedo are modelled as simple analytical functions, $I = I(T)$ and $A = A(T)$, while they should depend not only on T , but also on other physical/chemical quantities that influence the vertical transport. The ESTM features a dependence on surface pressure, p , gravitational acceleration, g , planet radius, R , rotation rate, Ω , surface albedo, A_S , stellar zenith distance, Z , atmospheric chemical composition, and mean radiative properties of the clouds. The atmospheric flux can be derived applying basic equations of fluid dynamics to the energy content of a parcel of atmospheric gas. The energy budget of the parcel is expressed in terms of the moist static energy (MSE) per unit mass, is

$$m = c_p T + L_v r_v + gz \quad (2.10)$$

where the terms $c_p T$, $L_v r_v$ and gz measure the sensible heat, the latent heat and the potential energy content of the parcel at height z , respectively. L_v is the latent heat of the phase transition between the vapor and the condensed phase; r_v the mass mixing ratio of the vapor over dry component and g is the surface gravity acceleration. The MSE and the velocity of the parcel are a function of time, t , longitude, ζ , latitude, φ , and height, z . The latitudinal transport is obtained by integrating the fluid equations in longitude and vertically, the height z being replaced by the pressure coordinate, $p = p(z)$.

$$\Phi(t, \varphi) = \frac{1}{R} \int_0^{2\pi} d\zeta \int_0^p v m \frac{dp'}{g} = \frac{p}{Rg} \overline{v m} \quad (2.11)$$

where p is the surface atmospheric pressure and v the meridional velocity component of the parcel. The second equality of this expression is valid for a shallow atmosphere, where g can be considered constant, as in the case of the Earth (Vladilo et al., 2015). Here, variability on time scales shorter than one planetary day are averaged out. For an ideal planet with constant insolation and null axis obliquity, we can neglect the seasonal dependence on t . For fast-rotating terrestrial-type planets, with latitudinal transport dominated by eddies in the baroclinic zone, a commonly adopted formalism consists in dividing the variables of interest into a mean component and a perturbation from the mean, that are the eddies. $v = \bar{v} + v'$ and $m = \bar{m} + m'$. So easy to show that $\overline{v m} = \bar{v} \bar{m} + \overline{v' m'}$. When the eddies dominate, $\overline{v m} \sim 0$ and

$$\Phi(t, \varphi) \approx \frac{p}{Rg} \overline{v' m'} \quad (2.12)$$

so

$$D = -\Phi \left(\frac{\partial T}{\partial \varphi} \right)^{-1} = \frac{p}{R^2 g} \left(\frac{\partial T}{\partial (R d\varphi)} \right)^{-1} \overline{v' m'} \quad (2.13)$$

and from the $m = c_p T + L_v r_v$ we have:

$$\overline{v' m'} = c_p \overline{v' T'} + L_v \overline{v' r'_v} \quad (2.14)$$

This way,

$$\overline{v'T'} = k_s |v'| |T'| \quad (2.15)$$

and

$$\overline{v'r'_v} = k_L |v'| |r'_v| \quad (2.16)$$

where k_s and k_L are the correlation coefficients.

In eddy diffusivity theories these perturbations can be written as a mixing length, l_{mix} , times the spatial gradient of the quantity. We consider the gradient along the meridional coordinate y and we write

$$|T'| = l_{mix} \frac{\partial T}{\partial y} \quad (2.17)$$

and

$$|r'_v| = l_{mix} \frac{\partial r_v}{\partial y} \quad (2.18)$$

with

$$r_v = \frac{\mu_v}{\mu_{dry}} \frac{p_v}{p_{dry}} = \frac{\mu_v}{\mu_{dry}} \frac{qp_v^*}{p_{dry}} \quad (2.19)$$

and where μ_v and p_v are the molecular weight and pressure of the vapor, μ_{dry} and p_{dry} the corresponding quantities of the dry air, q is the relative humidity and $p_v^* = p_v^*(T)$ is the saturation vapor pressure. If the relative humidity is constant,

$$\frac{\partial r_v}{\partial y} = \left(\frac{\partial r_v}{\partial T} \cdot \frac{\partial T}{\partial y} \right) = \frac{\mu_v}{\mu_{dry}} \frac{q}{p_{dry}} \frac{\partial p_v^*}{\partial T} \cdot \frac{\partial T}{\partial y} \quad (2.20)$$

and from 2.22 and 2.27 we have

$$\overline{v'm'} = -l_{mix} |v'| \frac{\partial T}{\partial y} \left(k_s c_p + k_L L_v \frac{\mu_v}{\mu_{dry}} \frac{q}{p_{dry}} \frac{\partial p_v^*}{\partial T} \right) \quad (2.21)$$

and

$$D \approx \frac{p}{R^2 g} l_{mix} |v'| \frac{\partial T}{\partial y} \left(k_s c_p + k_L L_v \frac{\mu_v}{\mu_{dry}} \frac{q}{p_{dry}} \frac{\partial p_v^*}{\partial T} \right) \quad (2.22)$$

Assuming an average dependence only on the length scale and the dissipation rate per unit mass, dimensional arguments yield the velocity scaling law

$$|v'| \propto (l_{mix} \eta \frac{T_w - T_c}{T_w} Q)^{\frac{1}{3}} \quad (2.23)$$

where η is an efficiency factor representing the fraction of the generated kinetic energy used by heat transporting eddies, T_w and T_c are the temperatures of the warm and cold regions and Q is the energy received by the atmosphere per unit time and unit mass.

So we can write that

$$l_{mix} = \sqrt{\frac{2|v'|}{2\left(\frac{\partial \Omega n(\varphi)}{\partial y}\right)}} \quad (2.24)$$

Finally, at the latitude φ_m of maximum energy,

$$l_{mix}|v'| = \left(\eta \frac{T_w - T_c}{T_w} Q\right)^{\frac{3}{5}} \frac{R}{\Omega \cos(\varphi_m)} \quad (2.25)$$

and inserting 2.33 in 2.30 we have

$$\frac{pk_s c_p \eta^{\frac{3}{5}}}{\Omega^{\frac{4}{5}} R^{\frac{6}{5}} \cos(\varphi_m)^{\frac{4}{5}}} \left(\frac{T_w - T_c}{T_w} Q\right)^{\frac{3}{5}} \left(1 + \frac{k_L L_v}{k_s c_p} \frac{\mu_v}{\mu_{dry}} \frac{q}{p_{dry}} \frac{\partial p_v^*}{\partial T}\right) = D_{dry}(1 + \Lambda) \quad (2.26)$$

where D_{dry} is the dry component of the atmospheric eddies transport and Λ is the ratio of the moist over dry components. Taking k_L , k_s , η and φ_m as constants we can calculate \mathcal{B}_{dry} , the dry term of the transport, as

$$\mathcal{B}_{dry} \propto \frac{c_p}{\Omega^{\frac{4}{5}} R^{\frac{6}{5}}} \left(\frac{p}{g}\right)^{\frac{2}{5}} \left[\frac{T_w - T_c}{T_w} S(1 - A)\right]^{\frac{3}{5}} \quad (2.27)$$

where $S(1 - A)$ is the absorbed stellar radiation $\left(\frac{W}{m^2}\right)$ averaged over one orbital period in the latitude range (φ_1, φ_2) and $\frac{p}{g}$ is the atmospheric columnar mass $\left(\frac{kg}{m^2}\right)$.

The ratio of the moist over dry components is

$$\mathcal{B}_{md} \propto \frac{Q(p_v^*(T_v) - p_v^*(T_c))}{p_{dry} c_p \mu_{dry} \delta T} \quad (2.28)$$

Finally, using 2.34, 2.35 and 2.36 for a generic terrestrial planet and for the Earth, indicated by the subscript \oplus , we obtain

$$\frac{D}{D_{\oplus}} = \zeta(\varphi, t) \frac{\mathcal{B}_{dry}}{\mathcal{B}_{dry}_{\oplus}} \left[\frac{1 + \Lambda_{\oplus} \left(\frac{\mathcal{B}_{md}}{\mathcal{B}_{md}_{\oplus}}\right)}{1 + \Lambda_{\oplus}} \right] \quad (2.29)$$

with $\zeta(\varphi, t) = c_0 + c_1 \cos(Z)$ and where Z is the stellar zenith distance and c_0 and c_1 general parameters. That's why the global pattern of atmospheric circulation is influenced, among other factors, by the seasonal variation of the zenith distance of the star. Without Hadley cell complication we have $\zeta(\varphi, t) = 1$.

ESTM should be applied to planets orbiting stars with spectral distributions not very different from the solar one. As already said, a planet orbiting around the HZ of an M star was thought to have an orbit so close that its rotation should have been tidally locked. This way, the dark side would become a sink for atmospheric condensates, making the planet uninhabitable. Though Haberle *et al.* (1994) used a simple one-dimensional energy balance model to show that an atmosphere of more than 0.1 bar of CO_2 would be stable, as atmospheric heat transport from the starlit side would compensate for radiative cooling on the dark side (Joshi *et al.*, 2003).

The Intermediate General Circulation Model (IGCM) is a three-dimensional global atmospheric circulation model that has physical parameterizations like those of a full general circulation model. This is the upgrade to the model described in Joshi *et al.*, (1997) and takes into account the presence of clouds and the evaporation, transport, and precipitation of water. There are 22 layers between the surface at 1 bar and the model top at the 0.001 bar level.

Joshi's 1997 model was a modified version of the so-called SGCM or simplified global circulation model (Joshi *et al.* 1995, James and Gray 1986). It was composed by two parts: an adiabatic or transport part and a diabatic or radiation and friction part. Here, variables are represented by spherical harmonics truncated at a specified wave number. The model employs the σ coordinate system in the vertical, where σ denotes

pressure/surface pressure. The adiabatic part solves the primitive equations of dynamical meteorology on the sphere (Hosantistellar and Simmons 1975, Holton 1992). In Joshi et al., (1997) is defined an advective time scale $t_d = \frac{\Delta L}{U}$ where ΔL is the day–night distance, and U is a typical atmospheric wind speed. The radiative relaxation time scale t_r of a planetary atmosphere is defined as:

$$t_r = \frac{c_p p_0}{\sigma g T_e^3} \quad (2.30)$$

where c_p is the specific heat of the gas, σ is the Stefan–Boltzmann constant, T_e is the effective emission temperature and p_0 is the surface pressure. The substellar–antistellar surface temperature difference ΔT_{DN} is the difference between t_d and t_r .

The radiative scheme in the model is the representation of solar heating at the surface given by

$$F = F_0 \cos(\varphi) \cos(\zeta) \quad (2.31)$$

for $-\frac{\pi}{2} \leq \zeta \leq \frac{\pi}{2}$ and $F=0$ elsewhere, handling the IR part of the radiation in grey approximation.

Exchanges of heat and momentum between the surface and atmosphere are:

$$\left(\frac{\partial T}{\partial t}\right)_{\text{heating from surface}} = \frac{g}{\rho_*} \frac{\partial H_s}{\partial \sigma} \quad (2.32)$$

where H_s is the sensible heat that, in stable conditions is

$$H_s = \rho_* c_{dh} |u| d\vartheta \quad (2.33)$$

and in unstable conditions is

$$H_s = \rho_* c_{dh} (|u| + \mathcal{K} \frac{\Delta T_{pt}^{\frac{1}{2}}}{T_{pt}}) \Delta T_{pt} \quad (2.34)$$

where ρ_* is the surface density, c_{dh} the drag coefficient for heat transfer, \mathcal{K} is the stability parameter and T_{pt} is the surface potential temperature that variates only with latitude.

The surface energy balance is balance between downwelling solar insolation F_D , upwelling IR radiation (black body radiation), downwelling IR radiation F_G (the greenhouse effect), and sensible heat fluxes between atmosphere and ground F_S .

$$\chi \left(\frac{\partial T_0}{\partial t}\right) = 1 - AF_D + F_G - F_S - \sigma T^4 + L \quad (2.35)$$

where A is the ground albedo, and L is the latent heat released by condensing CO_2 . χ is the thermal inertia of the ground. The condensation of CO_2 is modelled by not allowing the surface or atmosphere to fall below its frost point.

This is done by an energy conservation scheme that condensed sufficient CO_2 such that the amount of heat energy gained equalize the latent heat energy released by condensation.

The frost point of CO_2 is approximated by the relation

$$T_{cond} = 194.5 + 27.75P + 3P^2 \quad (2.36)$$

where P is in bars. If the CO_2 condense over a certain limit, the atmosphere collapse.

2.3.3 Albedo

The planetary albedo is a measure of its surface and/or atmosphere reflectivity. It is usually defined as the ratio of the light scattered by a planet to the light received by the planet.

Planetary albedo is an extremely important parameter because it can give us a measure of the amount of clouds a planet have in its atmosphere, or can be indicative of surface physical conditions (ice, rock or water).

2.3.3.1 The geometric Albedo $A_{g(\nu)}$

The geometric albedo $A_{g(\nu)}$ is the ratio between a planet's flux at zero phase angle (figure 2.16) to the flux from a Lambertian disk at the same distance and with the same cross section of the planet.

Choosing a spherical polar coordinate system with latitude θ and longitude ϕ , can be found that

$$A_{g(\nu)} = \frac{\int_{-\frac{\pi}{2}}^{\frac{\pi}{2}} \int_{-\frac{\pi}{2}}^{\frac{\pi}{2}} I_{s,scat}(\theta, \phi, \nu) \cos \theta d\theta d\phi}{\pi I_{inc}} \quad (2.37)$$

where $I_{s,scat}$ is the intensity of the scattered radiation flux at the planet's surface and I_{inc} is the incident uniform intensity.

2.3.3.2 The Bond Albedo A_B

The Bond Albedo is the ratio between the power reflected and incident on a planet integrated on the whole solid angle and wavelengths. By its definition $A_B < 1$.

Let's begin defining the spherical albedo A_S as the ratio of the scattered energy by the planet to the incident energy on the planet.

$$A_S = \frac{2I_{inc} \int_0^\pi \psi_\alpha(\nu) \sin \alpha d\alpha}{\pi I_{inc}} = \frac{2}{\pi} \int_0^\pi \psi_\alpha(\nu) \sin \alpha d\alpha \quad (2.38)$$

where $\psi_\alpha(\nu)$ is the fraction of scattered radiation in the direction of the observer as a function of the phase angle α (described in figure 2.16) and I_{inc} is the incident uniform intensity.

The Bond albedo is defined as:

$$A_B = \int_0^\infty A_S(\nu) d\nu = \frac{2}{\pi} \int_0^\infty \int_0^\pi \psi_\alpha(\nu) \sin \alpha d\alpha d\nu \quad (2.39)$$

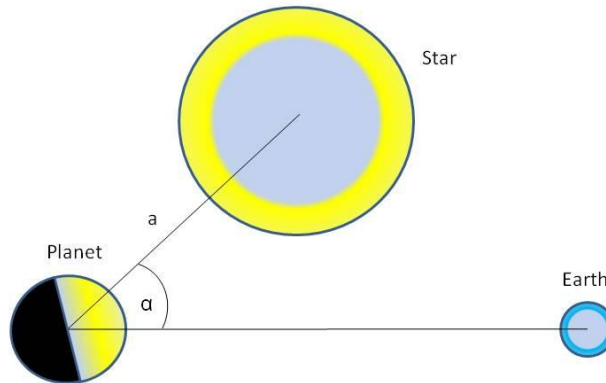


Figure 2.16: Schematization of the phase angle α .

As said before, albedo can give information on the planet superficial structure. Tinetti et al., (2006c) simulated the different albedo on Earth for different types of surface landscape (Figure 2.17).

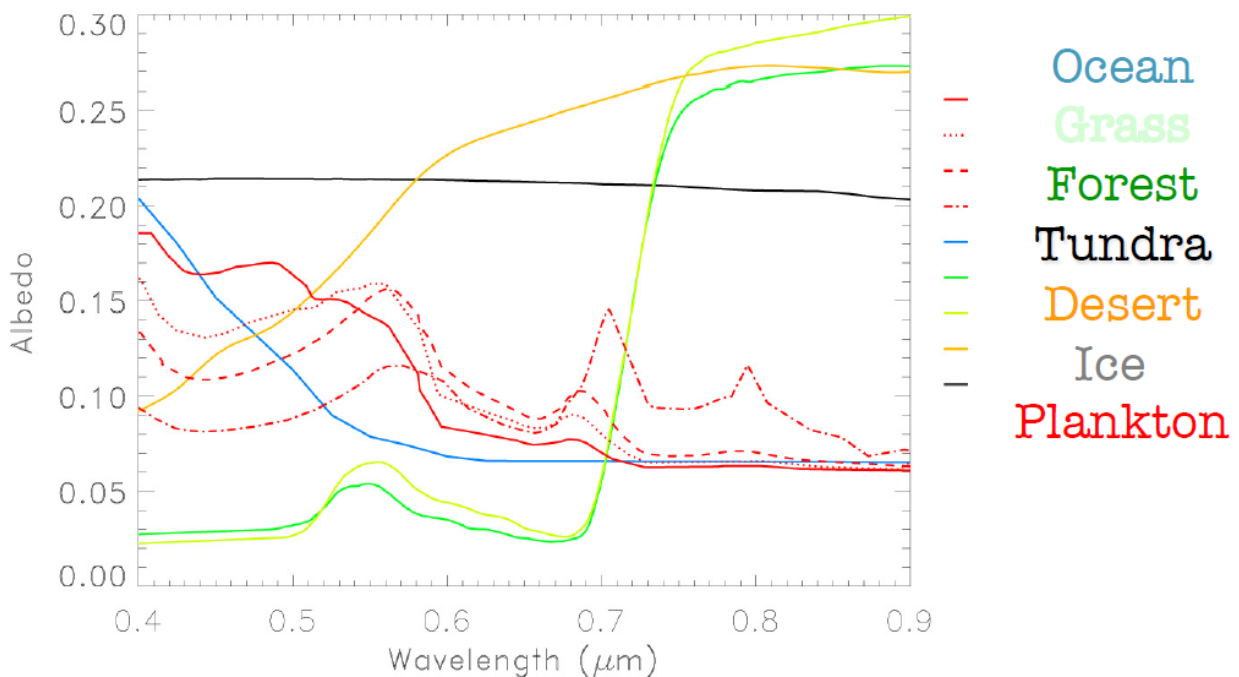


Figure 2.17 Different albedo on Earth as in Tinetti et al., (2006) for different types of surface landscape

2.3.4 The effective temperature

The effective temperature T_{eff} is usually used to describe the global temperature of a planet atmosphere. It is defined as the temperature of a black body of the same shape and flux and at the same distance of the planet.

Usually, T_{eff} is a measured quantity, taking the total flux of a planet, converting it to surface flux and finding the temperature of a black body with the same total flux. Using the definition of black body flux

$$F_s(T, \nu) = \pi B(\nu, T) = \pi \frac{2hc^2}{\lambda^5} \frac{1}{e^{k\lambda T} - 1} \quad (2.40)$$

and integrating the black body flux over all frequencies, assuming the surface flux to be uniform across the object's surface:

$$F_s = \int_0^{+\infty} F_s(\nu) d\nu = \pi \int_0^{+\infty} B(\nu, T) d\nu = \sigma T_{eff}^4 \quad (2.41)$$

with σ defined as $\sigma = \frac{2\pi^5 k^4}{15c^2 h^3} = 5.670 \cdot 10^{-8} J K^{-4} m^{-2} s^{-1}$ (with h Planck's constant, k Boltzmann's constant and c speed of light) a is the semi major axis of the planetary orbit and β is a proxy for day night redistribution (1 for full redistribution, 2 for no redistribution).

2.3.5 Equilibrium Temperature

The equilibrium temperature of a planet is defined as the theoretical temperature that the planet would be at when considered simply as if it were a black body being heated only by its parent star. In this model, the presence or absence of an atmosphere (and therefore any greenhouse effect) is not considered, and one treats the theoretical black body temperature as if it came from an idealized surface of the planet:

$$T_{eq} = \left[\frac{(1-A_B)L_*}{16p\sigma a^2 \beta} \right]^{\frac{1}{4}} = T_{eff} \left[\beta(1-A_B) \left(\frac{R^*}{2a} \right)^2 \right]^{\frac{1}{4}} \quad (2.42)$$

where T_{eff} is the effective temperature of the star, L_* is the stellar luminosity, R^* is the star radius in terms of solar radii, A_B is the Bond albedo, σ is the Stefan-Boltzmann constant. β is a correction factor born from the consideration that for exoplanets we can observe only one hemisphere at the time. If the absorbed stellar radiation is uniformly redistributed around the planet, $\beta = \frac{1}{4}$ and T_{eq} is the same of any hemispheric view of the planet. If we are not in this case, for example for slowly rotating or tidally locked planets, where the stellar energy is absorbed only by one hemisphere of the planet, $\beta = \frac{2}{3}$. In this case, T_{eq} of the day-side hemisphere is much hotter than in the uniform irradiation case.

It must be kept in mind that for planets with dense atmospheres T_{eq} do not indicate any physical temperature at the surface or in the atmosphere.

Venus, for example, has an Albedo of 0.75 and a $T_{eq} = 231 K$, but a mean surface temperature of 737 K.

The small atmosphere and consequent small greenhouse effect can make T_{eq} and surface temperature quite similar.

If a planet has an atmosphere and an equilibrium temperature above 270 K, two cases can take place. The first is that superficial temperature remain below the critical temperature of water but there is no liquid water on it other than no or little water vapour in the atmosphere. The second is that an atmosphere can have a certain amount of water vapour but a surface temperature that exceed 1400 K.

The planet could so re-irradiate the absorbed stellar energy in the visible and radio wavelengths through an optically IR-thick atmosphere

2.3.6 The Brightness Temperature

From the Earth is possible measure the flux \mathcal{F}_{\oplus} of exoplanets at different wavelengths where

$$\mathcal{F}_{\oplus} = \frac{R_p^2}{d_{\oplus}^2} \quad (2.43)$$

where d_{\oplus} is the distance of Earth from the planet and R_p is the radius of the planet.

As fluxes depend on the planet's distance from Earth they change from one planet to the other whereas the temperature of the atmosphere is distance independent, measured exoplanet fluxes are often stated as temperatures.

The brightness temperature $T_b(\nu)$ is defined as the temperature of a black body of the same shape and at the same distance as the planet with the same flux as the planet in a specified frequency range.

We can define:

$$T_b(\nu) = \left(\frac{F_s(\nu)}{\sigma}\right)^{\frac{1}{4}} = \left(\frac{\mathcal{F}_{\oplus}}{\sigma}\right)^{\frac{1}{4}} \left(\frac{d_{\oplus}^2}{R_p^2}\right)^{\frac{1}{4}} \quad (2.44)$$

While a black body radiator has a constant $T_b(\nu)$ planets with spectra that depart from black bodies have $T_b(\nu)$ that can vary widely with wavelength or frequency. $T_b(\nu)$ is the only temperature that we can currently measure for exoplanets because for $T_b(\nu)$ flux at only one frequency or wavelength need be observed.

2.4. Earth similarity index

The Earth Similarity Index (ESI), is a number between zero (no similarity) and one (identical to Earth) that provides a powerful tool for categorizing and extracting patterns from large and complex datasets. The ESI can be used to prioritize exoplanets observations, perform statistical assessments and develop planetary classifications. The basic ESI expression is

$$ESI = \prod_{i=1}^n \left(1 - \left|\frac{x_i - x_{i0}}{x_i + x_{i0}}\right|\right)^{\frac{w_i}{n}} \quad (2.45)$$

where x_i is a planetary property (i.e. surface temperature), x_{i0} is the corresponding terrestrial reference value (i.e. 288 K), w_i is a weight exponent, n is the number of planetary properties, and ESI is the similarity measure (Schulze-Makuch et al., 2011). The weighting exponents are used to adjust the sensitivity of the scale and equalize its meaning between different properties.

Earth-like planets have similar terrestrial composition and a temperate atmosphere. As a general rule, any planetary body with an ESI value over 0.8 can be considered an Earth-like planet. This means that the planet is rocky in composition (silicates) and has an atmosphere suitable for most terrestrial vegetation including complex life.

Planets with ESI values in the 0.6 to 0.8 range (i.e. Mars) might still be habitable too, but only by simple extremophilic life, because they are either too cold or too hot for life as we know it.

The parameters for the ESI equation for mean radius, bulk density, escape velocity, and surface temperature are shown in Table 2.1.

Planetary Property	Reference Value (Eu, Earth's Unit)	Weight Exponent
Mean Radius	1.0	0.57
Bulk Density	1.0 Eu	1.07
Escape velocity	1.0 Eu	0.70
Surface Temperature	288 K	5.58

Table 2.1: Parameters for the ESI equation for mean radius, bulk density, escape velocity, and surface temperature as in (Schulze-Makuch, 2011).

Calculations for solar and extrasolar planets are shown in Figure 2.18. They are also divided for convenience into an Interior ESI, based on the mean radius and bulk density, and a Surface ESI, based on the escape velocity and surface temperature. Both the interior and surface ESI are combined into a global ESI. A similar formulation can be constructed for other planetary bodies using different reference values (i.e. ocean-like planets) (Schulze-Makuch et al., 2011). One of the most practical applications of the ESI is in studies about the distribution and diversity of Earth-like planets (Figure 2.19).

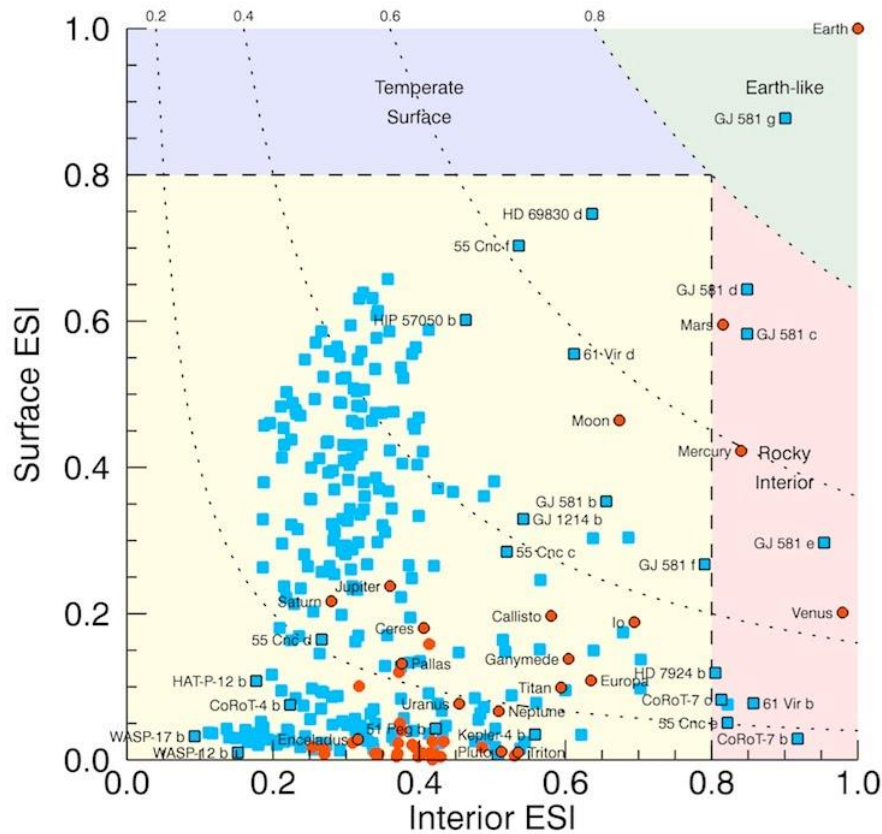


Figure 2.18: ESI for 47 Solar System bodies with radius greater than 100 km (orange) and 258 known extrasolar planets (blue). The ESI scale is differentiated between those rocky interior (light red area) and temperate surface (light blue area) planets. Only planets within these two categories can be considered Earth-like planets (light green area). The dotted lines represent constant ESI values. If confirmed, only Gliese 581 g is in the Earth-like category together with Earth (figure from <http://phl.upr.edu/projects/earth-similarity-index-esi>).

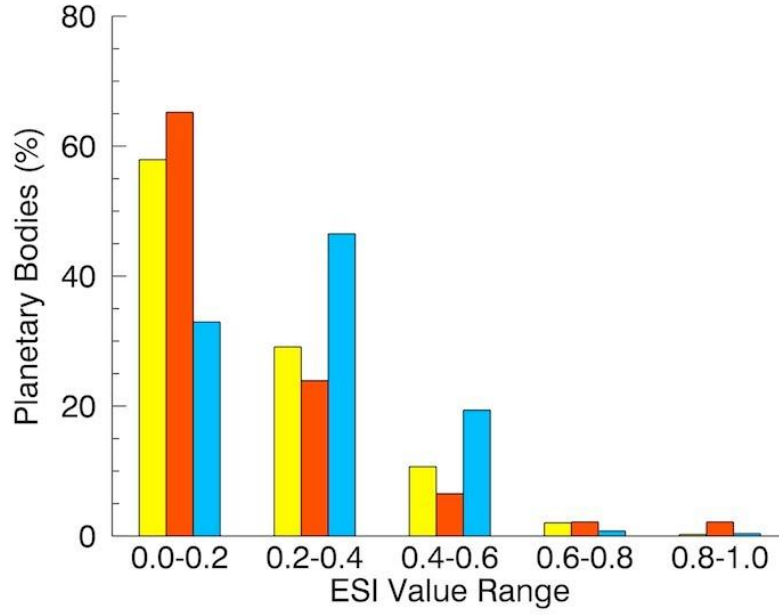


Figure 2.19: Distribution of ESI values based on a theoretical statistical prediction (yellow), for 47 Solar System bodies with radius greater than 100 km (orange), and 258 known extrasolar planets (blue). Our Solar System match the prediction but the bars for the known extrasolar planets show the bias of current observational techniques toward large planetary bodies (ESI values between 0.2 and 0.4). This type of analysis with the ESI can be used to predict the number of expected Earth-like planets within a sample of stars (figure from <http://phl.upr.edu/projects/earth-similarity-index-esi>).

In Appendix E can be seen a list of recently discovered exoplanets with the relative ESIs.

Here, ESI_{int} , ESI_{sur} , ESI_{grav} and ESI are the Earth Similarity Index for the internal composition of the planet, the surface and the gravity, and the total one. They are calculated like in Schulze-Makuch et al., (2011):

$$ESI = \sqrt{ESI_{int} \cdot ESI_{sur}} = \sqrt{ESI_r \cdot ESI_d \cdot ESI_v \cdot ESI_T} \quad (2.46)$$

where

$$ESI_r = \left(1 - \left| \frac{r-r_0}{r+r_0} \right| \right)^{0.57} \quad (2.47)$$

$$ESI_\rho = \left(1 - \left| \frac{\rho-\rho_0}{\rho+\rho_0} \right| \right)^{1.07} \quad (2.48)$$

$$ESI_v = \left(1 - \left| \frac{v-v_0}{v+v_0} \right| \right)^{0.70} \quad (2.49)$$

$$ESI_T = \left(1 - \left| \frac{T-T_0}{T+T_0} \right| \right)^{5.58} \quad (2.50)$$

and ESI_r , ESI_ρ , ESI_v , ESI_T are the ESI relative to radius, density, escape velocity and temperature.

In table 2.2 can be seen planets around relatively cool stars (with $T_{eff} < 4010$ K) and in table 2.3 can be seen the ESIs for the most recent Earth most similar and potential habitable planets discovered (from <http://phl.upr.edu/projects/earth-similarity-index-esi>).

Of this list only there are planets around stars with $T_{eff} < 4010$ K:

Planet	Mass (EU)	Radius (EU)	Density (EU)	g (EU)	V escape (EU)	A (AU)	T_{surf} (K)	T_{eq} (K)	ESI_{int}	ESI_{surf}	ESI_{grav}	T_s
GJ 581 g	3.100	1.36	1.22	1.67	1.51	0.15	278	248	0.901	0.877	0.889	3498
GJ 581 d	5.600	1.30	1.36	2.18	1.87	0.22	232	202	0.849	0.643	0.739	3498
GJ 581 c	5.600	1.60	1.36	2.18	1.87	0.07	380	350	0.849	0.583	0.703889	3498
GJ581 e	1.700	1.16	1.10	1.27	1.21	0.03	591	561	0.954	0.297	0.532889	3498
HIP 57050 b	94.71	6.64	0.32	2.15	3.78	0.16	250	220	0.464	0.602	0.528	3200
GJ 581b	15.60	3.14	0.51	1.59	2.23	0.04	499	469	0.656	0.353	0.481	3498
GJ 581 f	7.0	2.16	0.70	1.51	1.80	0.76	139	109	0.790	0.267	0.459	3498
GJ 1214 b	5.689	2.71	0.29	0.77	1.45	0.01	548	518	0.542	0.329	0.423	2730
GJ179b	260.6	10.12	0.25	2.55	5.08	2.41	89	59	0.375	0.084	0.177	3370

Table 2.2: planets around stars with $T_{eff} < 4010$ K (from <http://phl.upr.edu/projects/earth-similarity-index-esi>)

Name	Type	Mass (M_E)	Radius (R_E)	Flux (F_E)	T_{eq} (K)	Period (days)	Distance (ly)	ESI
001. Kepler-438 b	K-Warm Terran	4.0 - 1.3 - 0.6	1.1	1.38	276	35.2	473	0.88
002. Kepler-296 e	M-Warm Terran	12.5 - 3.3 - 1.4	1.5	1.22	267	34.1	1692	0.85
003. GJ 667C c	M-Warm Terran	3.8	1.1 - 1.5 - 2.0	0.88	247	28.1	24	0.84
004. Kepler-442 b	K-Warm Terran	8.2 - 2.3 - 1.0	1.3	0.70	233	112.3	1115	0.84
005. Kepler-62 e	K-Warm Superterran	18.7 - 4.5 - 1.9	1.6	1.10	261	122.4	1200	0.83
006. GJ 832 c	M-Warm Superterran	5.4	1.2 - 1.7 - 2.2	1.00	253	35.7	16	0.81
007. EPIC 201367065 d	M-Warm Superterran	14.1 - 3.7 - 1.5	1.5	1.51	282	44.6	147	0.80
008. Kepler-283 c	K-Warm Superterran	35.3 - 7.0 - 2.8	1.8	0.90	248	92.7	1741	0.79
009. tau Cet e	G-Warm Terran	4.3	1.1 - 1.6 - 2.0	1.51	282	168.1	12	0.78
010. GJ 180 c	M-Warm Superterran	6.4	1.3 - 1.8 - 2.3	0.79	239	24.3	38	0.77
011. GJ 667C f	M-Warm Terran	2.7	1.0 - 1.4 - 1.8	0.56	221	39.0	24	0.77
012. Kepler-440 b	K-Warm Superterran	41.2 - 7.7 - 3.1	1.9	1.43	273	101.1	851	0.75
013. GJ 180 b	M-Warm Superterran	8.3	1.3 - 1.9 - 2.4	1.23	268	17.4	38	0.75
014. GJ 163 c	M-Warm Superterran	7.3	1.3 - 1.8 - 2.4	1.40	277	25.6	49	0.75
015. HD 40307 g	K-Warm Superterran	7.1	1.3 - 1.8 - 2.3	0.68	227	197.8	42	0.74

016. EPIC 201912552 b	M-Warm Superterran	N/A - 16.5 - 6.0	2.2	0.94	251	32.9	111	0.73
017. Kepler-61 b	K-Warm Superterran	N/A - 13.8 - 5.2	2.2	1.27	267	59.9	1063	0.73
018. Kepler-443 b	K-Warm Superterran	N/A - 19.5 - 7.0	2.3	0.89	247	177.7	2540	0.71
019. Kepler-22 b	G-Warm Superterran	N/A - 20.4 - 7.2	2.4	1.11	261	289.9	619	0.71
020. GJ 422 b	M-Warm Superterran	9.9	1.4 - 2.0 -2.6	0.68	231	26.2	41	0.71
021. GJ 3293 c	M-Warm Superterran	8.6	1.4 - 1.9 -2.5	0.60	223	48.1	59	0.70
022. Kepler-298 d	K-Warm Superterran	N/A - 26.8 - 9.1	2.5	1.29	271	77.5	1545	0.68
023. Kapteyn b	M-Warm Terran	4.8	1.2 - 1.6 -2.1	0.43	205	48.6	13	0.67
024. Kepler-62 f	K-Warm Terran	10.2 - 2.8 - 1.2	1.4	0.39	201	267.3	1200	0.67
025. Kepler-174 d	K-Warm Superterran	N/A - 14.8 - 5.5	2.2	0.43	206	247.4	1174	0.61
026. Kepler-186 f	M-Warm Terran	4.7 - 1.5 - 0.6	1.2	0.29	188	129.9	561	0.61
027. GJ 667C e	M-Warm Terran	2.7	1.0 - 1.4 -1.8	0.30	189	62.2	24	0.60
028. Kepler-296 f	M-Warm Superterran	28.7 - 6.1 - 2.5	1.8	0.34	194	63.3	1692	0.60
029. GJ 682 c	M-Warm Superterran	8.7	1.4 - 1.9 -2.5	0.37	198	57.3	17	0.59
030. KOI-4427 b	K-Warm Superterran	38.5 - 7.4 - 3.0	1.8	0.24	179	147.7	782	0.52

Table 2.3: Earth most similar and potential habitable planets

(from: <https://sites.google.com/a/upr.edu/planetary-habitability-laboratory-upra/projects/habitable-exoplanets-catalog/data> (updated on 18/04/2013)). Here Name is the name of the exoplanet, a letter m after the name denotes an exomoon. pClass is the planetary class: [hot, warm, cold] mercurian, subterran, terran, superterran, jovian, neptunian. WS=Warm Superterran. hClass is the habitable class: hypopsychroplanet (O), psychroplanet (P), mesoplanet (M), thermoplanet (T), hyperthermoplanet (E), non-habitable (X). M is the mass in Earth units (EU), using most probable inclination (60°) or estimated from mass-radius relationships in many cases. R is the radius in Earth units (EU), estimated from mass-radius relationships in many cases. P is the orbital period in days (for exomoons is the exoplanet period). d is the distance from Earth in light years (lyr). Teq is the equilibrium temperature in kelvins (K) assuming an albedo of 0.3 in all cases. Ts is the mean surface temperature in kelvins (K) based on a similar terrestrial atmosphere to planet mass ratio and a greenhouse effect due to 1% CO₂ (assuming an albedo of 0.3 in all cases). ESI is the Earth Similarity Index, a measure of similarity to Earth (results are sorted by this number).

2.5 Biosignatures

One of the ultimate goals in the search for exoplanets is to find life outside of our solar system.

To determine if the planet's atmosphere contains any biosignatures, which are chemical species that may indicate the presence of life, telescopes first measure the spectra of light radiated and reflected from the target planet. These spectra are then analysed to identify specific peaks in the infrared and visible regions. In the infrared region for example, peaks can be seen which indicate molecules such as carbon dioxide, water, ozone, methane, ammonia and nitrous oxide. The second step is to attempt to determine whether life may be present. One method is to look for peaks that indicate molecules or compounds that should not be present naturally, or at least cannot remain in equilibrium in an atmosphere for long periods of time. Methane, nitrous oxide and ammonia are produced on Earth primarily by bacteria. Oxygen, and ozone, are produced by photosynthetic life and composes approximately 20% of Earth's atmosphere. Since these molecules are a by-product of life on earth, and are not produced abiotically in large quantities, they are considered to be biosignatures, or signs of life. Another reason why molecules such as oxygen and methane are considered to be reliable biosignatures is that even if they can be produced naturally in low quantities, they are unstable over long periods of time in the atmosphere; if these compounds are detected the atmosphere of an exoplanet, it is likely that there is a source continually producing them in high quantities, and the only such source currently known is life. In addition to the detection of molecules in the atmosphere, infrared measurements can also give clues about the planet's surface temperature, and whether or not it is capable of supporting liquid water. On Earth, there are a large number of chemical by-products produced by the many forms of life. But, only a small subset of these are classified as biosignatures. This is because biosignatures must first of all be gaseous, otherwise they could not be detected in transmission spectra. Of those gaseous by-products, those that are known to be produced naturally through geology or photochemistry must also be eliminated. Of the remaining chemicals, those that are soluble in water or easily broken down are less likely to be found. The final set of all remaining biosignature candidates are oxygen (O_2), ozone (O_3), and nitrous oxide (N_2O). Scientists also look for water (H_2O) and methane, however they can also be produced naturally and so are not considered strong biosignatures. Figure 2.20 shows an example of hierarchy of biosignature classification. In table 2.4 can be seen a summary of Earth's potential biosignatures and the pros and contras of their features (Seager et al., 2012).

Biosignature	Example	Pros	Contras
Inorganic gases	O_2 , O_3 , CH_4	Detectable in planetary spectra	Most are also produced abiotically
Organic gases without methane	DMS, isoprene and other foliar emissions	Many different compounds	Usually existing in very small concentrations
Solids	Banded iron formations, Sulphur	Stability, greater range of compounds	Requires localized sources difficult to detect
Photopigments	Chlorophyll	Fairly unique	Relatively complex in an evolutionary sense
Dissolved molecules	Ocean chemistry	Can sustain a great range of compounds; life lives in water	Dilute, relatively little partitioned into vapour phase

Table 2.4: Summary of Earth's potential biosignatures and the pros and contras of their features (Seager et al., 2012).

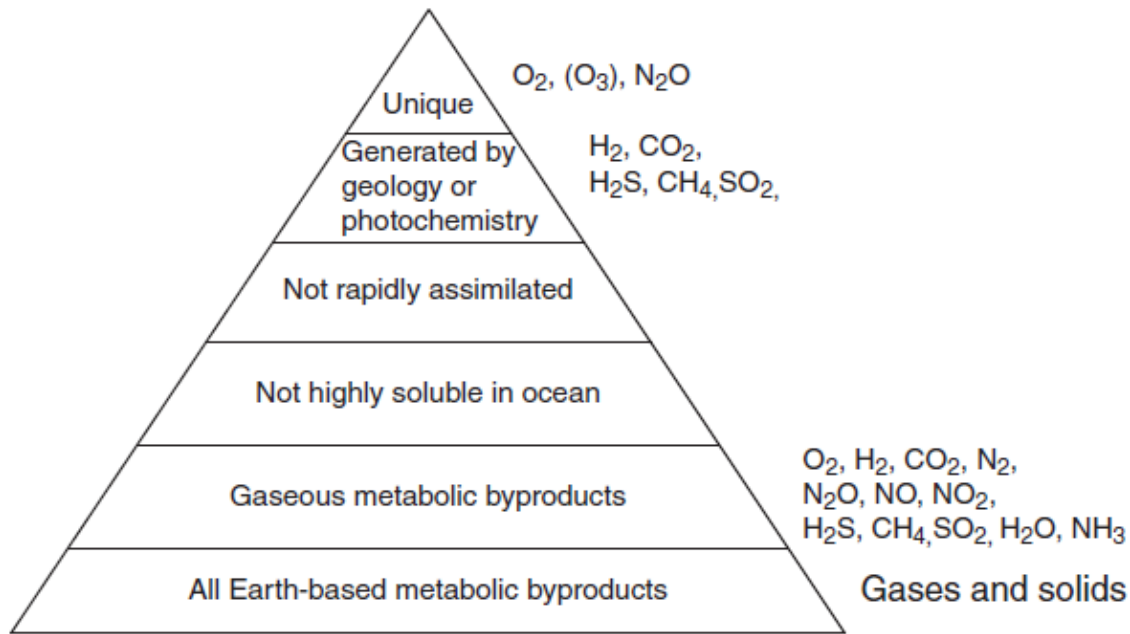


Figure 2.20: example of hierarchy of biosignature classification.

There are evidences that non photosynthetic pigments could be an alternative biosignatures source other than those generated by photosynthesis. In particular, this may be the case for highly productive chemosynthetic biospheres that have evolved pigmentation to survive in extreme environments, or for photosynthetic biospheres where the spectral reflectance is dominated by a non photosynthetic pigment (Schwieterman et al., 2015).

In chapter 3 and in particular 3.4 and 3.5 will be described in detail the potential biosignature and biomarker. In particular an extremely strong feature of chlorophyll denoted red edge, characterized by the dominant spectral signature of the green plants, that absorb between 0.4 and 0.7 μm but less in the green part of the spectrum while in the IR band reflect between 0.7 and 0.85 μm .

The atmosphere's effect on the observed colours is due primarily to Rayleigh scattering, which drives colours to bluer regions of color-color space, although absorption from water vapour and ozone also modifies the colours inferred from the surface alone. A planet dominated by even a single surface type could exhibit a variety of broadband colours depending on the overlying atmosphere's level of Rayleigh scattering and cloud cover (Schwieterman et al., 2015).

3. Habitable planets

Since many years astronomers have wondered if other planetary systems than ours could bear life forms.

This is a very interesting topic, but of course it is necessary to understand how a planet could be defined habitable and what characteristics should it have in order to host life. Dole, for example, in 1964, defined a habitable planet as one on which at least 10% of the surface had a mean temperature of between 0° and 30°C, with extremes -10° and 40°C. Of course these are the limits suitable for mankind. Other authors (Rasool and DeBergh, 1970, Hart, 1978, Kasting et al, 1988, Whitmire et al., 1991) have outlined the liquid water on the planet's surface as a stringent condition. Fogg (1992) has enclosed both the previous conditions in the term "biocompatible" to describe planets possessing liquid water and using the term "habitable" to describe only the ones suitable for human life. Lammer et al., (2009) studied the effects of the host star dependent radiation and particle fluxes on the evolution of atmospheres and initial water inventories, with particular attention to the geodynamical and geophysical environments which are necessary for planets where plate tectonics remain active over geological time scales and for planets which evolve to one-plate planets. Lammer developed a classification of four habitat types: class I habitats represent bodies on which stellar and geophysical conditions allow Earth-like planets to evolve so as to be capable to evolve a complex multi-cellular life forms. Class II habitats includes bodies on which life may evolve but due to stellar and geophysical conditions that are different from the class I habitats, the planets rather evolve toward Venus- or Mars-type worlds where complex life-forms may not develop. Class III habitats are planetary bodies where subsurface water oceans exist which interact directly with a silicate-rich core, while class IV habitats have liquid water layers between two ice layers, or liquids above ice (Lammer et al., 2009). Nowadays in determining the habitability potential of a body, studies focus on its bulk composition, orbital properties, atmosphere, and potential chemical interactions. Stellar characteristics of importance include mass and luminosity, stable variability, and high metallicity. Rocky, terrestrial-type planets and moons with the potential for Earth-like chemistry are a primary focus of astrobiological research, although more speculative habitability theories occasionally examine alternative biochemistries and other types of astronomical bodies.

3.1 The Habitable Zone (HZ)

The Habitable Zone (HZ) is a very discussed concept that gripped astronomers for a long time.

In fact, there are a great variety of definitions of it (Heath et al., 1999).

Here we define the HZ as that region around a star in which a planet with an atmosphere can sustain liquid water on its surface (Tarter et al., 2007), and it is a function of the stellar luminosity, the planet geology and energy balance the atmosphere and some critical stellar fluxes values.

The choice of liquid water is fundamental, because it represents the basic requirement for life on Earth and because extrasolar planets with life and water on it should be spectroscopically observable (Leger et al., 1993; Tinetti et al., 2005). Moreover, water is the best solvent in which life can emerge and evolve and is essential to maintain stable bio molecular and cellular structure (Des Marais et al., 2002). It has a large dipole moment, the capability to form hydrogen bonds, to orient hydrophobic-hydrophilic molecules and to stabilize macromolecules (Lammer et al., 2009).

The estimated width of the HZ around our sun has fluctuated over the last 50 years. Dole (1964) predicted that it should extend from 0.725 A.U. and 1.24 A.U., that is from close the orbit of Venus to halfway between Mars and Earth.

These extremes were calculated assuming optically thin atmospheres and fixed planetary albedo. In reality Earth's atmosphere is optically thick at most infrared wavelengths, giving rise to a greenhouse effect of about 33°C. Moreover Earth's albedo is not fixed but can change depending on soil and clouds conditions. The greenhouse effect increases with the planet's temperature because of increased water vapor while albedo is enhanced at cold surface temperatures by increased ice and snow cover (Kasting et al., 1993).

The Sun's HZ is affected by solar evolution. In fact as a star, it can increase its luminosity during its lifetime on the main sequence. Hart (1978) was the first to include the solar evolution in a model of planetary habitability concluding that Earth would have experienced a runaway greenhouse during its history had it formed inside 0.95 A.U. and would have encountered runaway glaciation if formed outside 1.01 A.U.

It can be defined the Continuously habitable zone (CHZ) as the zone that remains habitable around a star during a given period of time (Hart, 1978). The CHZ is enclosed in the previous described limits.

A binary system can host habitable planets too. For this complex variety there are two main configurations: p-type orbits and s-type orbits. In the first case the planet orbits both stars, in the second case the planet orbits only one of the two, and the other is quite distant.

The region in which stable orbits are possible for both these configurations have been studied by Holman and Wiegert, (1999), where mass, eccentricity, and star separation data for test particle simulations are used to form empirical expressions for the critical orbital distance of a planet in both p-type and s-type scenarios.

The equations for maximum and minimum distance for stable orbits are:

$$a_{p-type} = [1.6 + 4.12\mu - 5.09\mu^2]a \quad (3.1)$$

$$a_{s-type} = [0.464 - 0.38\mu]a \quad (3.2)$$

where a is the semi axis of the orbit and μ the mass ratio. The eccentricity has been assumed zero.

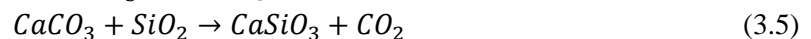
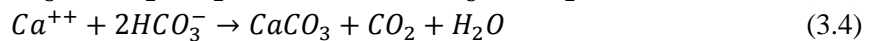
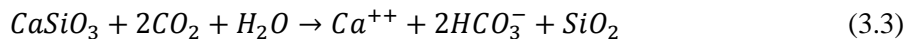
These equations represent some kind of minimum and maximum distances, corresponding to the first and the second binary configurations.

For the wide-binary cases, radiation from each star hits an area that totals half the planet's surface. These areas can be completely separate or overlap partially or completely. When there is no overlap, the entire planet is illuminated, half by one star and half by the other. Conversely, when there is complete overlap, only half the planet is illuminated and intercepts radiation from both stars. Knowing the orbital period allows the duration of these different radiation regimes to be estimated (O'Malley-James et al., 2012).

The HZ is embodied between two limits, an outer edge and an inner edge, that are the constraints at which the stellar insolation (SI) liquid lead to a no-more-stable water configuration on a planetary surface. Around M stars the HZ is closer respect to other stars like F, G or K ones because of the smaller; in fact it can be vary from 0.02 to 0.2 AU. Moreover, as the core composition have a small part in the changes of the emitted flux, and as a result of that, the habitable zone of M stars is the same for a long period of time. Thus, a planet in the HZ stays there for many Gyrs (Kasting et al. 1993).

The carbonate-silicate cycle, that plays a key role in stabilizing Earth's climate over long time scales, begins when atmospheric CO_2 dissolves in rainwater, forming carbonic acid, H_2CO_3 . Through a process termed "weathering", this weak acid dissolves silicate rocks on the continents, releasing Ca^{++} , Mg^{++} , HCO_3^- (bicarbonate), and SiO_2 (dissolved silica) into solution. The products of weathering make their way down to the oceans in streams and rivers. There, organisms such as the planktonic foraminifera that live in the surface ocean use them to make shells out of calcium carbonate ($CaCO_3$). When the organisms die, they fall down into the deep ocean, where most of the shells re-dissolve. Some of the calcium carbonate survives, however, and is buried in sediments on the seafloor. The seafloor spreads from the mid ocean ridges and, at some plate margins, is carried down subduction zones. The carbonate minerals recombine with SiO_2 , which by this time is the mineral quartz, to reform calcium and magnesium silicates and release gaseous CO_2 . This CO_2 is vented into the atmosphere through volcanoes, thereby completing the cycle.

The chemical process is:



Usually, ocean-covered tidally locked Earth has a mean albedo of 0.35, that is 20% higher (due to ice and clouds) than planets not tidally locked (Joshi, 2003). A higher albedo would move the inner edge of the HZ nearer the star (Kasting et al., 1993).

In Kasting et al, (1993) can be found a model in order to calculate the inner edge limits. Considering the incident solar flux F_S and the net outgoing infrared flux F_{IR} at the top of the atmosphere and assuming that the flux incident at the top of the atmosphere is equal to the present solar constant $S_0=1360 \frac{W}{m^2}$ he found that the planetary albedo was

$$A_p = 1 - \frac{4F_S}{S_0} \quad (3.6)$$

and the effective solar flux was found to be

$$S_{eff} = \frac{F_{IR}}{F_S} = \frac{S}{S_0} \quad (3.7)$$

normalized to maintain a given surface temperature.

In this equation can be seen that the net incoming solar radiation must equal the outgoing infrared.

He found F_{IR} to increase with surface temperature to $T_s=360$ K and levelling off at higher temperatures when the atmosphere became optically thick to all infrared wavelengths. F_{IR} increase occurs only at $T_s > 1400$ K where the surface begins to radiate in the visible. F_S increase is though proportional to the increase absorption of solar radiation by water vapor. It decreases then to a constant value at high surface temperatures because of the increased Rayleigh scattering. The planetary albedo behaves in the opposite way from F_S .

The limits can be calculated as:

$$d_{HZ} = 1 A.U. \left(\frac{L}{L_{\odot}} \right)^{\frac{1}{2}} \quad (3.8)$$

finally, it is important to remember that when the star loss mass, as can be found in Tarter et al., (2007), the planet has to move outward to conserve angular momentum and, because of the decreasing stellar luminosity, the habitable zone must decrease in size. Moreover he asserted that a star would have to lose about 25% of its mass for the planet to migrate from the inner edge to the outer edge of the HZ.

The albedo could be thought to influence the HZ boundaries, but it is not so important when determining the inner and outer boundaries.

In fact, the albedo of a habitable planet close to these edges would be fully determined by its atmospheric composition (including clouds) and the spectral distribution of the stellar radiation. In the NIR, the peak of M stars, the contribution of Rayleigh backscattering to the albedo becomes negligible and the strong absorption bands of H_2O (plus CO_2 and possibly CH_4 in the outer HZ) cause additional absorption of stellar radiation. For this reason, stellar luminosity isn't the only component determining the HZ limits (Selsis et al., 2008).

3.1.1 The inner edge (IHZ)

As said before, two can be the main requirements for habitability:

i) Liquid water must be present on the planet surface between the triple point of water, 273 K and the critical temperature of water, 647 K.

If fully vaporized, this water would produce a surface pressure higher than 220 bars that, with Earth gravity, would mean a 2.2 km deep water layer (Earth's one is 2.7 km) (Selsis et al., 2008).

ii) The planet has to be geologically active . If the planet has this peculiarity (maybe generating plate tectonics motions), it continuously out-gasses CO_2 . Without CO_2 in the atmosphere, the HZ would be 10 times narrower than is assumed. For example, in this situation, the Earth would be frozen (Selsis et al.,

2008). Moreover, when the mean surface temperature falls below 273 K CO_2 must accumulate in the atmosphere, a consequence of the carbonate-silicate cycle.

The inner edge is the limit beyond which the climate stabilization given by CO_2 fails and the stratosphere composition changes from being several orders of magnitude drier than the surface of the planet (like on the Earth), to being almost wet. At the same time there is the photo dissociation of H_2O and the H_2 production rate and its escape rate increase, until the time the planet's surface dries (Kasting and Pollack, 1993).

Two limits for the Inner Habitable Zone (IHZ) boundary can be calculated. The first one is the “moist greenhouse” (or water-loss) limit. According to Kopparapu et al., (2013), for a terrestrial planet orbiting a solar star this is encountered at a surface temperature of 340 K when solar effective flux is $S_{eff}=1.015$. At this limit, the water vapor content in the stratosphere increases dramatically, by more than an order of magnitude. The actual inner edge may be closer to the Sun if cloud feedback tends to cool the planet's surface, as expected. The orbital distance corresponding to the cloud-free water loss limit is 0.99 AU for an Earth like planet orbiting the Sun.

The runaway greenhouse effect occurs at distances at which the oceans evaporate entirely.

The limiting S_{eff} is 1.06, which corresponds to a distance of 0.97 AU (Kopparapu et al., 2013).

The water loss limit is difficult to extrapolate to other stars and terrestrial exoplanets (Selsis et al., 2008).

The third estimate for the HZ boundary can be obtained from radar observations of Venus by Magellan spacecraft, which suggest that liquid water has been absent from the surface of Venus for at least 1 Gyr (Solomon & Head 1991). The Sun at that time was ~92% of the present day luminosity, according to standard stellar evolutionary models (Baraffe et al. 1998; Bahcall et al. 2001). The current solar flux at Venus distance is 1.92 times that of Earth. Therefore, the solar flux received by Venus at that time was 1.76 times that of Earth. This empirical estimate of the IHZ edge corresponds to an orbital distance of 0.75 AU for the present day (Kopparapu et al., 2013).

On a habitable planet close to the inner boundary of the HZ, the IR opacity of the atmosphere is fully dominated by water vapour, and clouds do not contribute to warming the surface, as some types of clouds (high cirrus clouds) can do on Earth. But, on the other hand, clouds can significantly increase the planetary albedo and thereby reduce the greenhouse warming. In particular, thick clouds forming at high altitude, above the level where the incident radiation is backscattered or absorbed, can result in a very high albedo and can thus move the habitability limits closer to the star (Selsis et al., 2008).

1 D models can only give an approximation of cloud distribution and contribution, as for their own nature they have a tridimensional extension. It would be useful to use 3 D models to better understand how cloud formations can influence climate and the HZ.

3.1.2 The outer edge

As discussed in Kasting et al., (1993), the CO_2 amount in the Earth's atmosphere is controlled, on geological times, by several factors, and among all weathering, that depends itself on temperature.

If a planet freezes, the weathering ceases, and the amount of CO_2 rise in the atmosphere heating again the planet surface. This process can extend the limits of the HZ around the star.

The HZ outer limit, the outer edge, occurs when the SI is such that CO_2 condenses in the atmosphere, so that the weathering is irrelevant.

The outer edge has not been accurately determined yet because of the complex effects of clouds resulting from CO_2 condensation. If we consider a cloud-free CO_2 atmosphere with a water pressure fixed, the outer edge should lie at 1.67 AU for the present Sun, where a planet would have a CO_2 pressure of about 8 bar (Kasting 1991). For CO_2 pressures above 6 bar, the cooling caused by the albedo exceeds the warming caused by the IR opacity of the CO_2 column (Selsis et al., 2008).

CO_2 clouds, differently from H_2O droplets ones, are very transparent at visible wavelengths but efficiently scatter thermal radiation around 10 μm . This effect exceeds the cooling effect caused by the increasing of the albedo. As a consequence, CO_2 condensation increases the greenhouse warming.

Numerous geochemical and geological features indicate that 4 Gyrs ago, on the surface of Mars, were present liquid water. At that time, the Sun was 28% less luminous and its flux at Mars orbit was then equal to what is it today at a distance of 1.77 AU.

This fact suggest empirically that the outer edge in our solar system is located beyond this distance.

CO_2 is not the only greenhouse gas able to maintain habitable conditions at low stellar irradiation.

Even CH_4 or NH_3 can increase the greenhouse effect. Taking this as true, models can be made to find the correct gas mixture in order to maintain the mean surface temperature above 273 K. Gas species must be transparent in the visible but have to be in complex opaque in the mid-IR.

Moreover, life can be a strong component in the atmospheric balance with its by- and bio-products.

3.1.3 The effect of planetary properties on HZ

Surface pressure and habitability are intimately linked.

In fact, the former influence both the planet temperature and the extent of liquid water temperature interval available for habitability. It can be said that temperature can be affected by pressure variations in two ways. First of all, given an atmospheric composition, the infrared optical depth of the atmosphere increase with pressure. A rise of pressure (P) lead to a rise of the greenhouse effect and the temperature.

If the greenhouse effect dominates, an increase of P will always raise the temperature at a given semi-major axis a , at a given insulation $I = \frac{L_*}{4\pi a^2}$.

However, when the atmospheric column density of greenhouse gases is sufficiently low, pressure variations will not significantly affect the optical depth and temperature. This explains the absence of a temperature rise with increasing P in the regime of very low pressures. In this regime an increase of the pressure can lead a coolness of the planet.

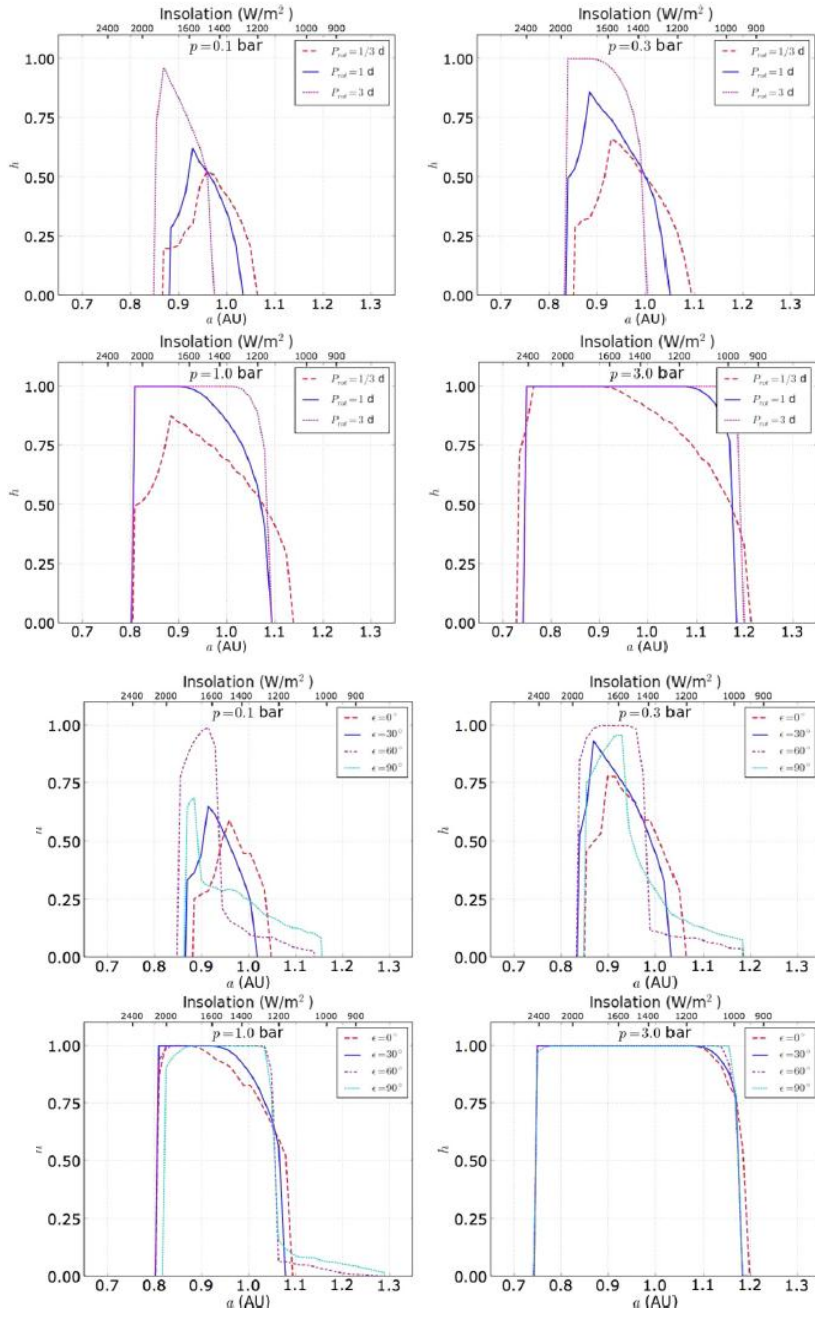
The location of the inner and outer edges of the HZ is related to the boiling and freezing points of water, respectively. The temperature of the boiling point increases with P, while that of the freezing point is basically constant.

As the pressure increases, neglecting any other factor, the inner edge of the HZ to approach the star while the outer edge, instead, moves away from the star as the pressure increases. This is due to the pressure–temperature effects described above: at high pressure the greenhouse effect becomes more important with increasing P and the planet can remain above the freezing point at increasing a . At the inner edge, the rise of the boiling point dominates over the pressure–temperature effects.

The second way with which pressure affect the HZ is its relation with the horizontal heat transport, that increases with pressure. For this reason, planets with high pressure have an uniform surface temperature as a result of the high diffusion.

As said before, other parameters like rotation period, axis obliquity, planet geography and surface albedo, in combination with surface pressure variations, can affect the habitability.

The main effects of varying planetary parameters can be summarized as follows. As illustrated in Vladilo et al., (2013), the results at low pressure are quite sensitive to variations of rotation period, axis obliquity, and ocean coverage (figure 3.2 a, b, c). Specifically, the habitability tends to increase with increasing rotation period, axis obliquity (up to 60°), and ocean coverage. At high pressure, the shape of the habitability curves becomes insensitive to variations of these parameters. The results are modestly influenced by variations of planetary parameters, even at low pressure. Variations of the latitudinal/seasonal gradient of the heat transport efficiency do not affect the properties of the HZ. Albedo variations tend to shift the habitability curves without affecting their shape. In figure 3.2 are illustrated the habitability curves as in Vladilo et al., (2013) for the semi-major axis, obliquity and ocean fraction.



(a)

(b)

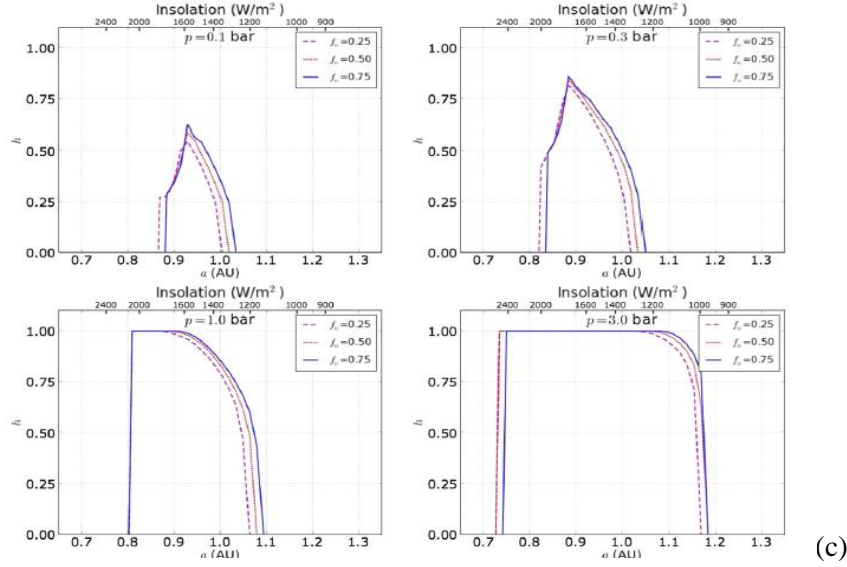


Figure 3.2: Fractional habitability, h , as a function of semi-major axis, a , for planets with rotation periods $P_{rot} = 1/3, 1,$ and 3 days (a), as a function of semi-major axis, a , for planets with axis obliquity $\epsilon = 0^\circ, 30^\circ, 60^\circ,$ and 90° (b) and as a function of semi-major axis, a , for planets with ocean fractions $f_0 = 0.25, 0.50,$ and 0.75 (c). Each panel shows the results obtained at a constant pressure P (Vladilo et al., 2013).

According to Vladilo et al., (2013) the habitability h is defined as

$$h = \frac{\int_{-\pi/2}^{\pi/2} d\varphi \int_0^P dt [H(\varphi, t) \cos\varphi]}{2P} \quad (3.9)$$

where P is the orbital period and $H(\varphi, t)$ is defined as:

$$H(\varphi, t) = \begin{cases} 1 & \text{if } T_{ice}(P) \leq T(\varphi, t) \leq T_{vapor}(P) \\ 0 & \text{otherwise} \end{cases} \quad (3.10)$$

and $T_{ice}(P)$ and $T_{vapor}(P)$ are the melting and boiling points of water at pressure P (Lide, 1997).

3.1.4 Gravity and the HZ

As the water column determines the IR opacity of the atmosphere, a higher gravity is expected to shift the inner edge of the HZ closer to the star (Kaltenegger et al., 2011). However, IR opacity is not the only parameter to be affected by the gravity. For a given value of surface temperatures, gravity also influences the lapse rate and the albedo produced by the water column. When treated self-consistently, these effects tend to compensate for each other, thus weakening the overall influence of gravity (Selsis et al., 2008). Radiative-convective simulations of a planet with a surface gravity of $2.5 g$ were carried out by Kasting et al. (1993), who found an inner edge only 3% closer.

In figure 3.3 can be seen a schematic representation of the HZ taken by Ramirez R. for different distances and insulations (Kasting et al., 2014).

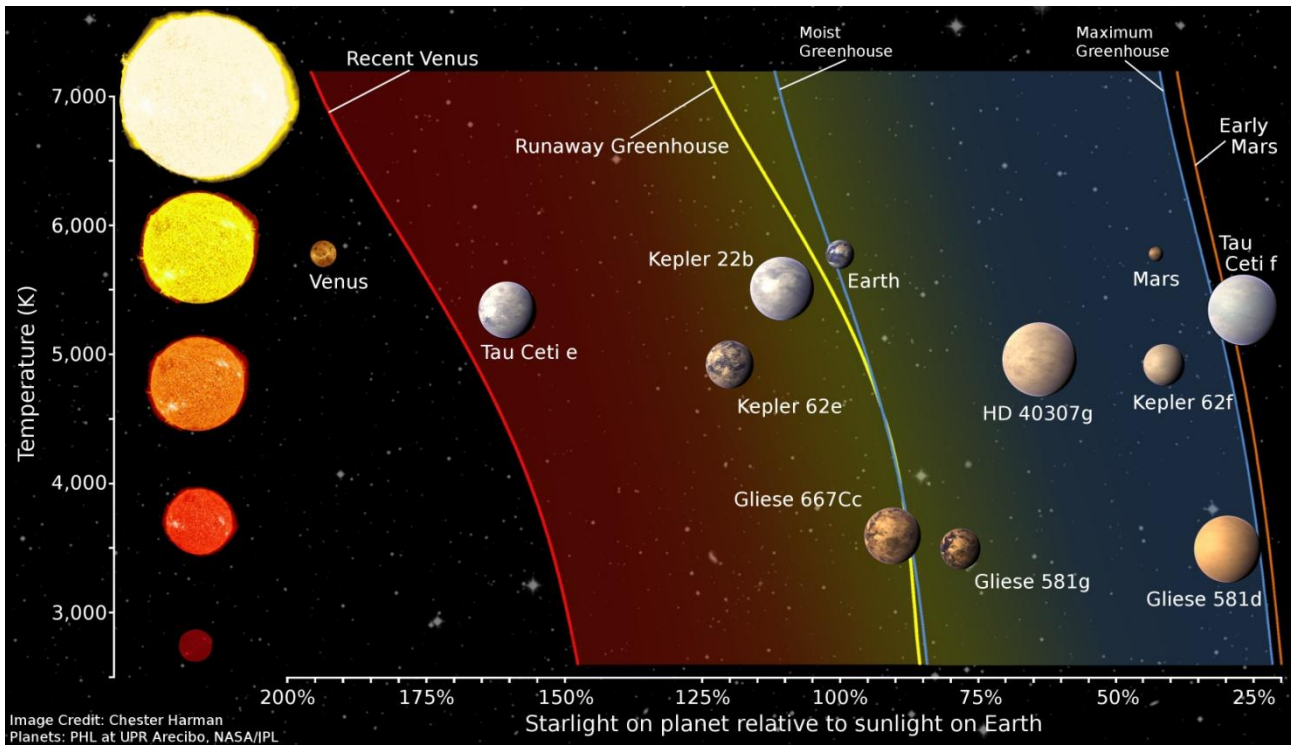


Figure 3.3: A schematic representation of the HZ taken by Ramirez R. for different planets, distances and insulations (Kasting et al., 2014).

As already said in chapter 3.1, the geophysical conditions of a synchronous rotating planet plays an important role in determining whether it is habitable or not. In fact a higher gravity on rocky planets can aid the development of a plate tectonic system. On planets with plate tectonics, the drift of plates through the colder zones near the terminator would extinguish Earth-type arboreal forms while drifts onto the dark side would extinguish a wide variety of organisms. Contrarily, one-plate planets with long-term geologic activity history can have persistent habitability regions. Volcanic regions can be constantly replenished by young material or recycled volatiles than can generate surface heat and consequently heat fluxes. Moreover, geologic activity sometimes is necessary to provide greenhouse gases to the atmosphere (Tarter et al., 2007). In Heath et al., (1999) it's underlined that an ice layer formed on the surface of the sea wouldn't mean the freezing of the whole sea at its base, because geothermal heat from the interior of the planet would prevent it. This can demonstrate that a liquid water environments can exist even in presence of low insulation and in absence of a massive greenhouse layer (Bada et al., 1994). This can be the key to understand the hydrological cycle of ice on oceans of synchronous rotating planets. A snow deposit on a thick ice layer on the sea is balanced by a melting at its base. This, coupled with the deep basin communications between dark and lit hemispheres is the base of hydrological cycle. In addition to planetary radius, the other primary control on the depth of the mantle is the relative amount of metallic iron in the planet. For example, the Earth's metallic core comprises ~55% of the planet's radius compared with ~75% inferred for Mercury (e.g., Lodders and Fegley, 1998). Therefore, bulk composition and internal structure of 1-10 Earth-mass planets (e.g., Valencia et al. 2006) will also affect the truncation of terrestrial planet habitability. Water affects the melting and the deformations of silicates that are constituents of mantle and crust of terrestrial planets and can affect the strength of geological activity like on Venus (Kaula, 1995; Mackwell et al., 1998). Geodynamical regimes of geologically active Earth-sized planets subject to substantial tidal torque remain to be investigated. It is universally known that small bodies develop very quickly a stable thick lithosphere within the first 100 Myr (Nelson, 2004). This implies small convection cells and weaker heat flows from the surface of the planet. If there were plate tectonics on all terrestrial bodies, it seems likely that it stopped very early on small bodies, at least about 3.5 Gyr ago. On Earth the first signs of life are detectable at the time of

Late Heavy Bombardment (LHB) time (Schopf, 2004). Earth developed a stronger tectonic system that eroded almost the 80% of its craters. Plate tectonics with water provides black smokers, the first environments of life. It regulates the atmospheric composition by the cycling of volatiles, including CO_2 and the surface temperature and habitability. On the rear of the medal, planetary activity is an incentive to evolve. On the present Earth sedimentation removes about 0.2 G tonnes of reduced C each year out of 100 G tonnes of primary productivity (Raven and Falkowski 1999). The net removal of Fe_2O_3 from the crust permits the reaction $2FeO + H_2O \rightarrow Fe_2O_3 + H_2$ to proceed, with O_2 removal from the atmosphere by reaction with H_2 . Accumulation of Fe_2O_3 at the surface limits H_2 production, allowing O_2 to accumulate. Furthermore, H_2 escape following biogenic H_2 production and photolysis of biogenic CH_4 could have caused irreversible oxidation of early Earth (Sleep, 2001; Catling *et al.* 2001, Hoehler *et al.* 2001). Landscape and environments changes, and life conditions change as well, and this imply a development and a modification of organisms adaptability. So, on an active planet, evolution can proceed at a faster rate. Plate tectonics in Earth-like planets can generate an intrinsic magnetic dynamo which can protect the atmosphere from solar wind erosion and cosmic rays. (Khodachenko *et al.*, 2007). The critical ingredients for planetary dynamo action are, other than a sufficient volume of electrically conducting fluid, an energy source to drive motions in the fluid and net organization of the flow field (Roberts and Glatzmaier, 2000; Aurnou, 2004). Numerical studies of planetary dynamo propose the following scaling law for planetary magnetic dipole moment (Olson and Christensen, 2006; Christensen and Aubert, 2006):

$$\Phi_M = (Q_B D_{DR})^{\frac{1}{3}} R_C^3 \quad (3.11)$$

where Φ_M is the magnetic dipole moment, Q_B is the buoyancy flux, D_{DR} is the thickness of the dynamo generation region, and R_C is the radius of the planet's core.

Water is useful in tectonic subduction too, because it lubricate and allows the plated to slide one each other (Regenauer-Lieb *et al.* 2001; Solomatov 2004).

Moreover water makes the lithosphere deformable enough for subduction of the crust to occur and reduces the activation energy for creeping and the solidus temperature of the mantle rock, enhancing the cooling of the interior and the efficiency of volcanic activity.

The tectonic plates subduction is useful because it maintains crust thin. If the crust is too thick the lithosphere comprising the crust will be too buoyant to be subducted.

In figure 3.1 are shown the connections between plate tectonics, mantle cooling and magnetic Earth-type dynamos. In the upper panel are shown active geodynamic conditions due to plate tectonics, while in the lower panel shows how inefficient cooling processes lead to a one-plate mantle with weak or absent magnetic protection (Lammer *et al.*, 2009). Because the solidification of the inner core is thought to be the energy source for the present day terrestrial magnetic field, and smaller bodies thermally evolve more rapidly than larger bodies, one can conclude that the terrestrial planets today are in three different magnetic phases, where Venus is most likely in a predynamo phase, not having cooled to the point of core solidification (Russel, 1993). The Earth is in a dynamo phase and Mars is in a post-dynamo phase.

Maintaining an intrinsic magnetic moment would have been problematic following the loss of water.

Moreover, the generation of planetary magnetic moments is based on convective motion in the planetary core. As a requirement for convection to occur, the Coriolis force must have a large effect on the flow. This condition, however, is easily satisfied, even for slow rotators like Venus (Stevenson 1983, 2003).

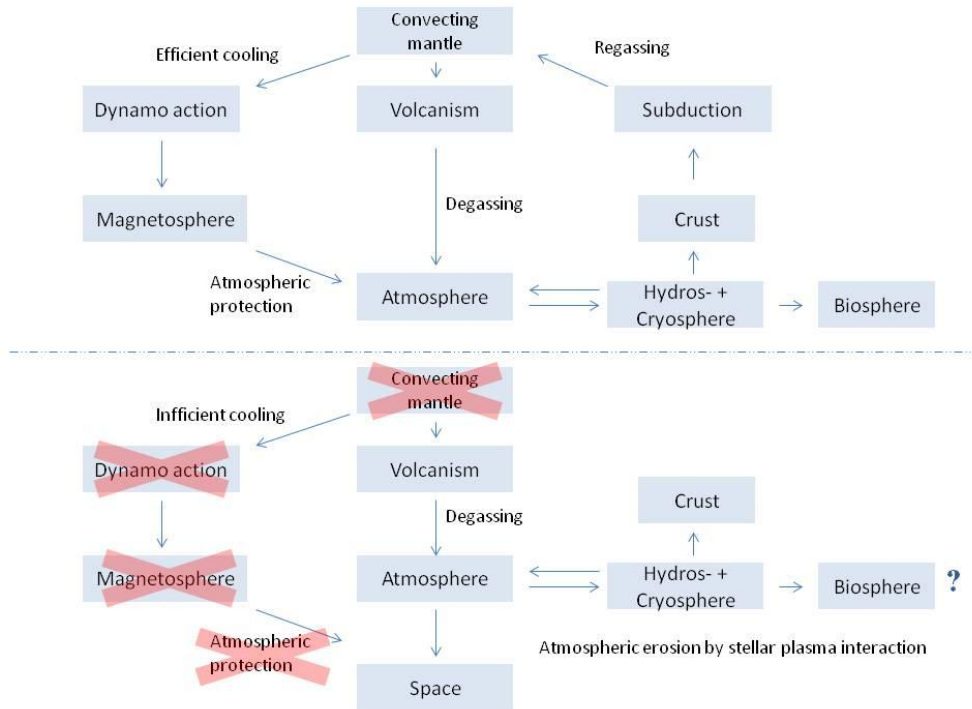


Figure 3.1: Connection between plate tectonics, mantle cooling and magnetic Earth-type dynamos. In the lower panel shows how inefficient cooling processes lead to a one-plate mantle with weak or absent magnetic protection (Lammer et al., 2009).

In conclusion, planets smaller than Earth lose early their ability to form plate tectonics, while water rich Earth-sized ones can maintain it for a longer period of time.

For super-earth plate velocities should be faster and orogenesis heavier. This results in higher mountains and more volcanic activity. Moreover, on these planets, the crust is slightly thinner.

As a result, plate velocities increases linearly with planetary mass (Valencia, 2007).

Cain et al., (1995) and Léger et al., (2004), based on the formulas given in Grießmeier et al., (2005) found that the magnetic moment depends on the planetary mass, as shown in figure 3.2:

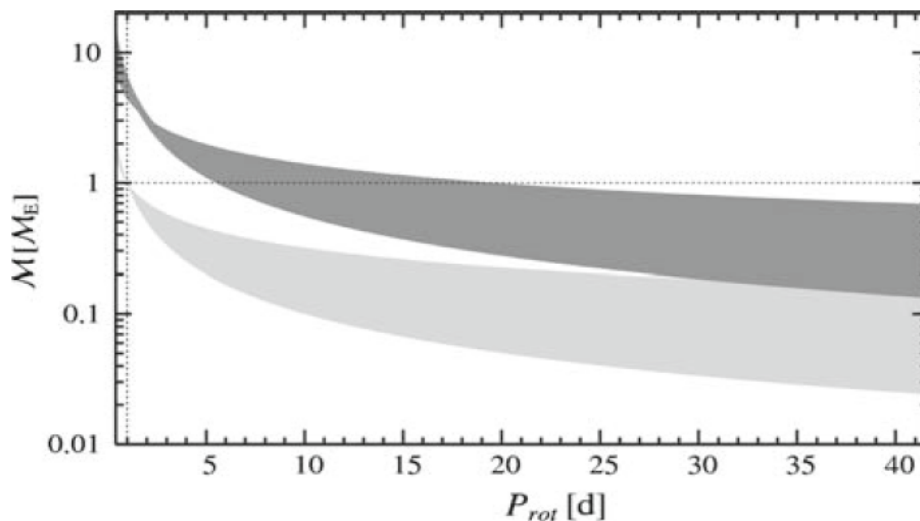


Figure 3.2: Planetary magnetic dipole moments as a function of rotation period and planetary mass. Light grey: Earth-like planets. Dark grey: Super-Earths with 6 Earth masses and 1.63 Earth radii (Léger et al., 2004). Dotted line: Earth current values.

Tidally locked planets have rotation periods equal to their orbital period (rotation periods 10–100 times larger than for the Earth), and are likely to have a much lower magnetic moment than the Earth. Large

terrestrial planets of 6 Earth masses are likely to have a magnetic moment approximately a factor of 5 higher than Earth-like planets (Lammer et al., 2009).

3.1.5 Habitable limits calculation

The first attempt to calculate the HZ limits is described in chapter 3.1.1.

The HZ limits can be calculated with the formula $d_{HZ} = 1 \text{ A.U.} \cdot \left(\frac{L}{S_{eff}}\right)^{\frac{1}{2}}$ where S_{eff} is the effective flux.

In his analysis, Mendez Torres, (2011) has been considered a conservative HZ bounded by a "recent Venus" model for the inner edge and an "early Mars" model for the outer edge (Underwood et al., 2003; Selsis et al. 2007). The inner r_i and outer r_o boundaries of the HZ in AU units are given by: $a_i=2.7619e-5$, $b_i=3.8095e-9$, $a_o=1.3786e-4$, $b_o=1.4286e-9$, $T_* = T_{eff} - 5780$, $R_{is}=0.72$, $R_{os}=1.77$.

$$D_{in} = [(R_{is} - a_i \cdot T_* - b_i \cdot T_*^2)] \cdot [(L)]^{0.5} \text{ A.U.} \quad (3.12)$$

$$D_{out} = [(R_{os} - a_o \cdot T_* - b_o \cdot T_*^2)] \cdot [(L)]^{0.5} \text{ A.U.} \quad (3.13)$$

Habitable exoplanets are those that their mean distance from the star fall between this boundary. The habitable zones distance (HZD) is therefore given as

$$HZD = \frac{2r - r_o - r_i}{r_o - r_i} \quad (3.14)$$

where r is the distance of the exoplanet from the star in AU units and HZD in HZU units. These units are very practical because they mean the same thing independently of the stellar system under consideration. HZD values between -1 and +1 HZU always correspond to planets within the HZ.

The results of the HZ (D_{in} and D_{out}) for different spectral types are collected in table 3.0. The temperature data have been taken from Gray & Corbally, *Stellar Spectral Classification*, Princeton University Press, (2009), appendix B, with interpolated magnitude values. The quantity $\frac{L}{L_{\odot}}$ have been calculated with the formula:

$$\frac{L}{L_{\odot}} = e^{\frac{4.77 - M}{2.5}} \quad (3.15)$$

where M is the absolute magnitude of the star and the distances have been calculated with equation 3.17 and collected in table 3.0.

T_{eff}	$\frac{L}{L_{\odot}}$	Spectral type	Recent Venus (AU)	Runaway Greenhouse (AU)	Moist Greenhouse (AU)	Maximum Greenhouse (AU)	Early Mars (AU)
7250	2.3821418	F0	1.101678	1.383113	1.457707	2.375883	2.470723
7120	2.1989940	F1	1.061782	1.336438	1.404919	2.296883	2.388572
7000	2.0299273	F2	1.023422	1.2914313	1.354161	2.220915	2.309575
6750	1.9503327	F3	1.010758	1.282777	1.337406	2.210007	2.298237
6659	1.8003840	F4	0.974045	1.238898	1.288829	2.136196	2.221483
6550	1.7297900	F5	0,958343	1,222194	1,268052	2,109795	2,19403
6395	1.5341861	F6	0,907581	1,161938	1,200886	2,009573	2,089812
6250	1.4740298	F7	0,89446	1,149306	1,183525	1,991846	2,071381

T_{eff}	$\frac{L}{L_{\odot}}$	Spectral type	Recent Venus (AU)	Runaway Greenhouse (AU)	Moist Greenhouse (AU)	Maximum Greenhouse (AU)	Early Mars (AU)
6170	1.3607010	F8	0,862033	1,109851	1,140619	1,925918	2,002823
5900	1.1595129	G0	0,857569	1,111366	1,134713	1,938267	2,015674
5800	1.1140477	G1	0,822269	1,068094	1,088005	1,866824	1,941381
5750	1.0283957	G2	0,751432	0,977184	0,994275	1,709881	1,778172
5686	0.9493288	G3	0,687088	0,894776	0,909137	1,568065	1,630694
5644	0.9121051	G4	0,657279	0,856733	0,869694	1,502953	1,562983
5620	0.8419792	G5	0,600027	0,782508	0,79394	1,373572	1,428435
5592	0.8089646	G6	0,57367	0,748576	0,759065	1,314954	1,367476
5496	0.7467685	G7	0,525223	0,686697	0,694962	1,209355	1,257662
5430	0.7174873	G8	0,502917	0,658374	0,665447	1,161627	1,208029
5280	0.6363541	K0	0.61086311	0.80184676	0.80827914	1.4211349	1.4779071
5110	0.5874289	K1	0.59083439	0.77762669	0.78177799	1.3858752	1.4412438
4940	0.5422652	K2	0.57136426	0.75366694	0.75601593	1.3512840	1.4052757
4700	0.4265609	K3	0.51122704	0.67589207	0.67644422	1.2231030	1.2719798
4538	0.3492385	K4	0.46519073	0.61563328	0.61553027	1.1215463	1.1663688
4400	0.2747207	K5	0.41448367	0.54879142	0.54843600	1.0057513	1.0459493
4275	0.2535992	K6	0.39981687	0.52945706	0.52902941	0.97574027	1.0147415
4130	0.2249223	K7	0.37818728	0.50075246	0.50040978	0.92898748	0.96612299
3900	0.2076295	K8	0.36570491	0.48383622	0.48389368	0.90736817	0.94364409
3760	0.1699926	M0	0.33209858	0.43902630	0.43942662	0.82886418	0.86200406
3625	0.1391782	M1	0.30147470	0.39817264	0.39890584	0.75662899	0.78688288
3490	0.0971013	M2	0.25258005	0.33324901	0.33420947	0.63738055	0.66286803
3355	0.0650889	M3	0.20738310	0.27331873	0.27440578	0.52614246	0.54718317
3220	0.0386967	M4	0.16032739	0.21107381	0.21214256	0.40892638	0.42528060
3085	0.0204044	M5	0.11671036	0.15349741	0.15442930	0.29926100	0.31123012
2950	0.0107591	M6	0.084946390	0.11162684	0.11239977	0.21898180	0.22774064
2815	0.0048343	M7	0.057066497	0.074944409	0.075509562	0.14791548	0.15383214
2680	0.0020052	M8	0.036830032	0.048354243	0.048732992	0.096002743	0.099843104

Table 3.0: Results of the HZ (D_{in} and D_{out}) for different spectral types. The lightened cells underline M stars. In the table are collected the stars luminosities in solar units too.

In Kopparapu et al., (2013) has been developed a new HZ approach. Here, the parameter S_{eff} is directly calculated from the climate model and is dependent on the type of star considered. The relationships between HZ stellar fluxes (S_{eff}) reaching the top of the atmosphere of an Earth-like planet and stellar effective temperatures (T_{eff}) applicable in the range $2600\text{ K} < T_{eff} < 7200\text{ K}$ is:

$$S_{eff} = S_{eff \odot} + aT_* + bT_*^2 + cT_*^3 + dT_*^4 \quad (3.16)$$

Here, S_{eff} provides a better metric for habitability than does T_{eq} , because T_{eq} involves an assumption about Bond's albedo A_B , [usually 0.3, or 0.29 for Earth (Selsis et al., 2008)] that is generally not valid. This value of A_B is good for present Earth around our Sun, but for a planet around a late M-star, A_B can vary from 0.01 near the inner edge to 0.1 at the outer edge (figure 3.4), depending on its location. Similarly, A_B for an F-star can range in between 0.38 – 0.51 for the inner and outer edge, respectively. This changes the corresponding T_{eq} , and so a uniform criterion for HZ boundaries based on T_{eq} cannot be determined. The corresponding habitable zone distance is (Kopparapu et al., 2013).

$$d = \left(\frac{L}{S_{eff \odot}} \right)^{0.5} \quad (3.17)$$

Eccentric planetary orbits increase the annually averaged irradiation from the primary star by a factor $1/(1 - e^2)^{\frac{1}{2}}$ (Borucky et al., 2013), where e is the orbital eccentricity. The coefficients a , b , c and d and $S_{eff \odot}$ are calculated for different distances such as Recent Venus (rv), Runaway greenhouse (rg), Moist greenhouse (mg), Maximum greenhouse (maxg) and Early Mars (em) and collected in Table 3.1.

Quantity	Recent Venus	Runaway Greenhouse	Moist greenhouse	Maximum greenhouse	Early Mars
$S_{eff \odot}$	1.7753	1.0512	1.0140	0.3438	0.3179
a	1.4316×10^{-4}	1.3242×10^{-4}	8.1774×10^{-5}	5.8942×10^{-5}	5.4513×10^{-5}
b	2.9875×10^{-9}	1.5418×10^{-8}	1.7063×10^{-9}	1.6558×10^{-9}	1.5313×10^{-9}
c	-7.5702×10^{-12}	-7.9895×10^{-12}	-4.3241×10^{-12}	-3.0045×10^{-12}	-2.7786×10^{-12}
d	-1.1635×10^{-15}	-1.8328×10^{-15}	-6.6462×10^{-16}	-5.2983×10^{-16}	-4.8997×10^{-16}

Table 3.1: Coefficients a , b , c and d and $S_{eff \odot}$ calculated for different distances such as Recent Venus (rv), Runaway greenhouse (rg), Moist greenhouse (mg), Maximum greenhouse (maxg) and Early Mars (em).

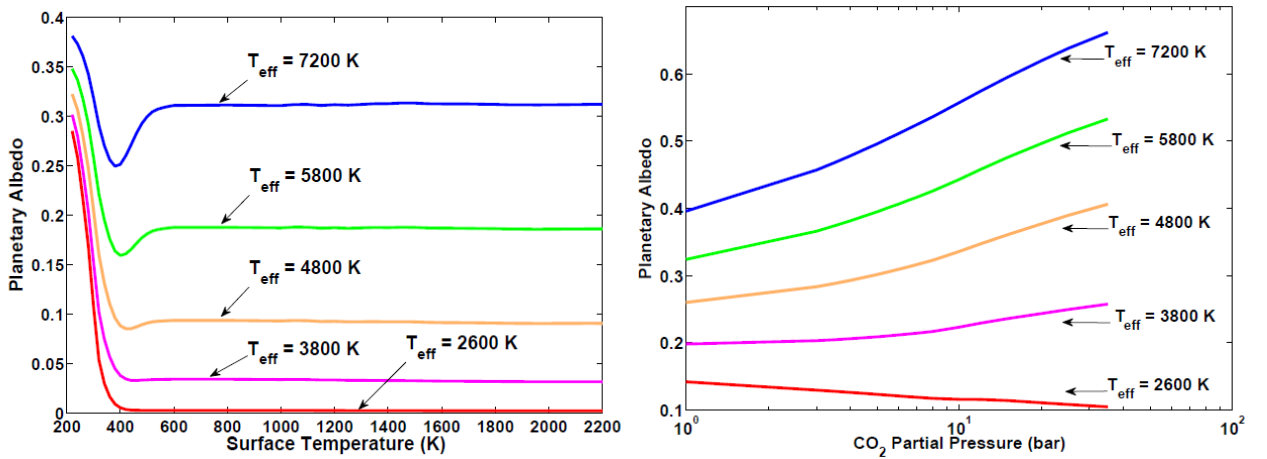


Figure 3.4: Various Bond's albedo for different temperature stars regarding the inner edge (a) and the outer edge (b).

The coefficients a , b , c and d and $S_{eff \odot}$ are calculated for different distances such as Recent Venus (rv), Runaway greenhouse (rg), Moist greenhouse (mg), Maximum greenhouse (maxg) and Early Mars (em) and collected in Table 3.1.

Quantity	Recent Venus	Runaway Greenhouse	Moist greenhouse	Maximum greenhouse	Early Mars
$S_{eff \odot}$	1.7753	1.0512	1.0140	0.3438	0.3179
a	1.4316×10^{-4}	1.3242×10^{-4}	8.1774×10^{-5}	5.8942×10^{-5}	5.4513×10^{-5}
b	2.9875×10^{-9}	1.5418×10^{-8}	1.7063×10^{-9}	1.6558×10^{-9}	1.5313×10^{-9}
c	-7.5702×10^{-12}	-7.9895×10^{-12}	-4.3241×10^{-12}	-3.0045×10^{-12}	-2.7786×10^{-12}
d	-1.1635×10^{-15}	-1.8328×10^{-15}	-6.6462×10^{-16}	-5.2983×10^{-16}	-4.8997×10^{-16}

Table 3.1: Coefficients a, b, c and d and $S_{eff \odot}$ calculated for different distances such as Recent Venus (rv), Runaway greenhouse (rg), Moist greenhouse (mg), Maximum greenhouse (maxg) and Early Mars (em).

In the next tables (Table 3.2) are shown comparisons between Earth-size planet transiting around sample F, G, K and M stars for what concerns mass, radius, T_{eff} , luminosity (a), distance limits (b), flux limits (c), equilibrium temperatures (d) expected periods (e), transit probabilities (f) and maximum transit durations (g) for the five distances of the HZ.

(a) Star Type	Name	Mass (SU)	Radius (SU)	T_{eff} (K)	Luminosity (SU)
F	Ups And A	1.310	1.383	6213	2.554
G	Sun	1.000	1.000	5780	1.000
K	HD 40307	0.740	0.839	4977	0.387
M	Gliese 581	0.310	0.299	3498	0.012

(b) Star Type	Inner Edge			Outer Edge	
	Recent Venus	Runaway Greenhouse	Moist Greenhouse	Maximum Greenhouse	Early Mars
F	1.18	1.53	1.56	2.60	2.84
G	0.75	0.98	0.99	1.69	1.84
K	0.48	0.64	0.64	1.13	1.23
M	0.09	0.12	0.12	0.22	0.24

(c) Star Type	Inner Edge			Outer Edge	
	Recent Venus	Runaway Greenhouse	Moist Greenhouse	Maximum Greenhouse	Early Mars
F	1.8383	1.0945	1.0500	0.3765	0.3163
G	1.7763	1.0385	1.0146	0.3507	0.2946
K	1.6668	0.9511	0.9521	0.3053	0.2565
M	1.5252	0.8736	0.8712	0.2451	0.2060

(d) Star Type	Inner Edge			Outer Edge	
	Recent Venus	Runaway Greenhouse	Moist Greenhouse	Maximum Greenhouse	Early Mars
F	296	260	257	199	191
G	294	257	255	196	187
K	289	251	251	189	181
M	283	246	246	179	171

(e) Star Type	Inner Edge			Outer Edge	
	Recent Venus	Runaway Greenhouse	Moist Greenhouse	Maximum Greenhouse	Early Mars
F	408	602	621	1341	1529
G	237	355	361	801	913
K	142	216	216	507	578
M	17	26	26	68	77

(f) Star Type	Inner Edge			Outer Edge	
	Recent Venus	Runaway Greenhouse	Moist Greenhouse	Maximum Greenhouse	Early Mars
F	0.55	0.42	0.41	0.25	0.23
G	0.62	0.47	0.47	0.28	0.25
K	0.81	0.61	0.61	0.35	0.32
M	1.57	1.19	1.19	0.63	0.58

(g) Star Type	Inner Edge			Outer Edge	
	Recent Venus	Runaway Greenhouse	Moist Greenhouse	Maximum Greenhouse	Early Mars
F	17.2	19.5	19.7	25.5	26.6
G	11.4	13.0	13.1	17.0	17.8
K	8.9	10.2	10.2	13.6	14.2
M	2.1	2.5	2.5	3.4	3.5

Table 3.2: (a) Stellar properties of representative main-sequence stars. An Earth-size planet transiting around these F, G, K, or M-stars should have a full transit depth of 43, 83, 119, and 939 ppm, respectively. (b) Distance limits (AU) for the Habitable Zone of main-sequence stars. (c) Stellar flux limits (Solar Units) for the Habitable Zone of main-sequence stars. (d) Expected equilibrium temperatures (K) for a planet within the Habitable Zone limits of main-sequence stars (assuming a 0.3 bond albedo). (e) Expected periods (days) for a planet within the Habitable Zone limits of main-sequence stars. (f) Expected transit probabilities (%) for a planet within the Habitable Zone limits of main-sequence stars. (g) Expected maximum transit durations (hours) for an Earth-size planet within the Habitable Zone limits of main-sequence stars. SU = solar units, stellar. Data from exoplanets.org.

3.1.6 The galactic HZ

The galactic habitable zone is the region of a galaxy in which life is most likely to develop. More specifically, the concept of a galactic habitable zone incorporates various factors, such as metallicity and the rate of major catastrophes such as supernovae, in order to calculate which regions of the galaxy are more likely to form terrestrial planets, initially develop simple life, and provide a stable environment for this life to evolve and advance. For the Milky Way this region is commonly believed to be an annulus with a radius of about 10 kilo parsecs. It is centred close to the Galactic Centre and lacks hard boundaries.

In figure 3.5 is represented a scheme of our galaxy, its HZ and the position of the Sun.

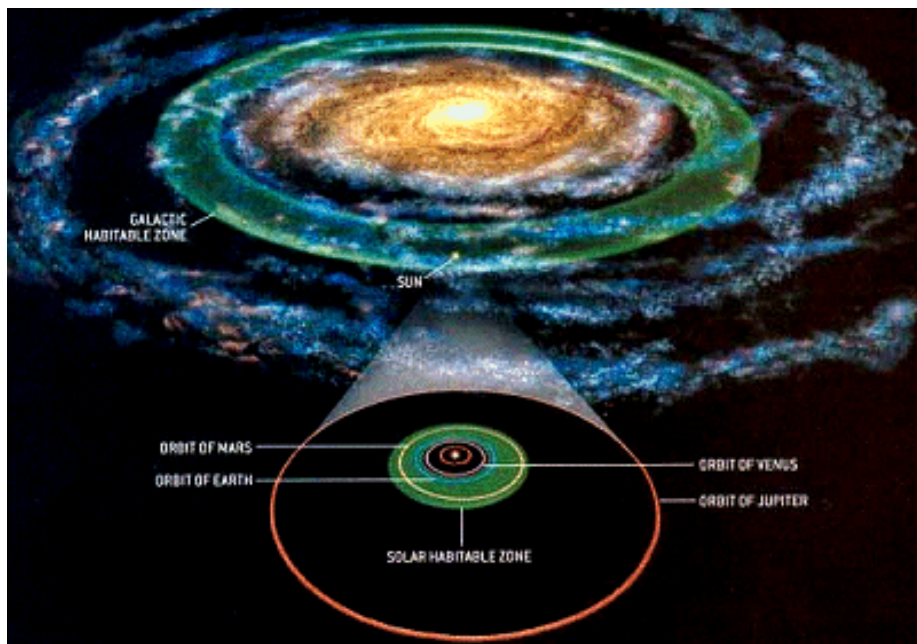


Figure 3.5: Scheme of our galaxy, its HZ and the position of the Sun

3.2 Life on other planets: the basis

A melody becomes such not with a melting pot of notes in a straggling way, but placing them in an ordinate pattern. It is not written, not coded, but simply sounds like it is right.

Life is a wonderful crossing point between several factors that must join in a precise way to generate it.

Life, as any open thermodynamic system needs to separate internal processes from the external world. In biological life forms it is represented by a membrane.

Life needs a solvent, a bunch of chemical elements like C, H, N, O, P and S, and relative small differences of free energy (Ball, 2004; Benner et al., 2004) too. The two solvents that can act as the basis for life are water and ammonia. For the purposes of this study we'll concentrate on water and carbon line forms.

Energy is usually transduced within organisms using electrical gradients across membranes or by oxidation of organic molecules to generate energy-rich molecules (typically containing phosphate) and organic electron pair carriers (often involving sulphur) that can drive the synthesis of essential bio molecules.

Such energy transduction processes frequently involve the use of transition metals, which makes their presence in trace amounts necessary (Tarter et al., 2007).

To replicate a life form needs a way of passing information to subsequent generations. This is achieved by the genetic material in the form of nucleic acids. Schematically, life needs:

- 1) a membrane
- 2) proteins, lipids and other macromolecular structures
- 3) an information carrier

3.2.1 Lipids, proteins and other requirements

On Earth, the first essential group of chemical elements for life are the lipids, or fatty acids, as said, the constituents of the cell membranes.

The driving force that induce the formation of these proto-cells is simply the increase in entropy when hydrophobic molecules stick together in aqueous surroundings. This cause a freeing of water molecules that would otherwise be oriented on the surface of the hydrophobic molecules. Since water is the medium on Earth which facilitated the origin of life, we can assume that the formation of micelles and vesicles acted as the outside boundary for the first proto-cells. Compartmentization may have occurred in this way from diverse starting materials (carboxylic acids, PAHs, lipids, etc.) (Lammer et al., 2009).

Proteins and amino acids compounds are a fundamental requirement for life. Amino acids have a unique property: the chirality. This feature tells us that they can present left handed (L-enantiomer) and right-handed (D-enantiomer), even if these last ones are rare and used only in cell receptors and in some enzymes.

There is, however, a certain consensus that the collection of those 20 amino acids found in all life forms is not entirely by chance, but rather that the best option for each chemical function is chosen (Weber and Miller 1981).

The backbone of DNA is composed by sugars, while the nucleobases, attached to it, encode the information.

DNA structure consists of a chain of alternating molecules of the 5-carbon sugar deoxyribose and phosphoric acid. The pairs of sugar and phosphate molecules are called a nucleotide.

In DNA there are four different types of nucleotides depending on which nucleobases (adenine, guanine, cytosine, thymine) is attached to the sugar and the information in the DNA are encoded by the sequence those nucleotides form (Lammer et al., 2009).

DNA in cellular evolution may have been preceded by RNA (Gilbert, 1986), a molecule made of another sugar, the 5-carbon sugar ribose. The chemical difference between these two sugar molecules is only one hydroxyl-group more in ribose but RNA is capable of catalyzing its own copy (while DNA is not) and making proteins (Lincoln and Joyce, 2009); by his side, DNA has information stored in it more stable and better shielded.

In early biological evolution RNA had a chief role, but it might have been preceded by an even earlier form of molecule, the Peptide Nucleic Acid (PNA), not based on sugars an phosphoric acid, but on diamino acids, that have been found on meteorites (Meierhenrich et al., 2004).

But how much time takes a living organism to form?

Indeed it is a difficult question, because there are not certain answers, but given the concentrations of the building chemical essentials blocks for life, is necessary to quantify the mass of organic material needed for a given volume of water, that can range from small shallow puddle to oceans (Lammer et al., 2009).

On earth, the first microfossils found formed about 3.5 Gyr ago (Schopf and Packer, 1987) and, because the Large Heavy Bombardment (LHB) occurred 3.8 Gyr ago, life had about 300 Myr to evolve and leave behind a fossil.

3.2.2 Adaptability of the organisms to hostile environments

Evolution isn't a random process, as at first look might seem. Evolution, citing Luca Signorile, is a short-sighted clockmaker. Evolution has a guideline, an aim, that is life preservation as long as possible, and adaptation is the key word. Adaptation is the strategy. A long term time strategy that can operate through mutation.

On Earth even the greediest and inhospitable environments have been colonized, which adapted to live in his own and probably unique ecological niche. On Earth, life can prosperate when environmental pH span between less than 1 and over 12, pressure ranges between less than 1 and more than 500 bars, salinity from zero to saturation (saline lakes) and temperature ranges from 233 to 380 K.

In particular, the temperature tolerance of higher plants on Earth is narrower than the limits 233-380 K fixed for the microorganisms. For example, sclerophyll trees and shrubs can bear temperatures from 268-271 K to 323-333 K. Other authors found that arctic ice shelf cyanobacteria and arctic snow algae have a lower temperature limit at 257.45 K (Gorton *et al.*, 2001; Mueller *et al.*, 2005) and a higher limit at 348.15 K (Miller *et al.*, 1998).

Other methanogenic bacteria seem to tolerate temperatures down to 77.15 K (Junge *et al.*, 2006).

In table 3.3 can be summarized the limits for life as we know it described in Cockell, (1999).

Parameter	Boundary conditions
Temperature (K)	<273-386
Surface pressure (Mpa)	>100
Acidity (pH)	<12
Atmospheric composition	Pure CO_2 can be tolerated by some organisms. High N_2 will not prevent life.
Water availability	Liquid H_2O should be present, but some halophilic organisms live in high (4-5 M) NaCl

Table 3.3: Limits for life as we know it

Extremophyles have evolved a bouquet of enzymes, called "extremozymes", that can ease vital processes in forbidding environments.

Photosynthetic bacteria and some algae are able to inhabit what on Earth are considered extreme or stressful environments. Cyanobacteria for example, are observed to form crusts on dry, hot sand dunes in deserts (Karnieli *et al.*, 1999) and are also found in extreme cold in snow and ice (Mueller *et al.*, 2005), as snow algae (Gorton *et al.*, 2001). Both desert crusts and marine water are highly saline environments, and marine microbial mats are inhabited by a range of anoxygenic photosynthesis bacteria and cyanobacteria (Decker *et al.*, 2005). In table 3.4 is shown a summary of different physical and geochemical conditions in which extremophyles can live.

Environmental parameter	Class	Growth conditions	Environment/Source	Remotely detectable observable	Example organism
High temperature	Hyperthermophile	> 80° C	Submarine hydrothermal vents	Water	<i>Pyrolobus fumarii</i> , Strain 121
	Thermophile	60-80° C	Hot spring		<i>Synechococcus lividis</i> , <i>Sulfolobus</i> sp.
Low temperature	Psychrophile	< 15° C	Ice, snow	Ice, snow	<i>Psychrobacter</i> , <i>Methanogenium</i> sp.
High pH	Alkaliphile	pH>9	Soda lakes	Salt	<i>Bacillus firmus</i> OF4, <i>Haloanaerobium alcaliphilum</i>
Low pH	Acidophile	pH<5	Acid mine drainage, volcanic springs	Acid mine drainage	<i>Picrophilus oshmae/torridus</i> , <i>Stygiolobus azoricus</i>
High pressure	Piezophile	High pressure	Deep ocean (Mariana Trench)	Water	<i>M. kandler</i> , <i>Pyrococcus</i> sp., <i>Colwellia</i> sp.
Radiation	-	Tolerates high levels of radiation	Sunlight and high UV radiation	Sand, rocks	<i>Deinococcus radiodurans</i> , <i>Thermococcus gammatolerans</i>
Salinity	Halophile	2-5 M NaCl	Salt lakes, salt mines	Salt	<i>Halobacteriaceae</i> , <i>Dunaliella salina</i> , <i>Halanaerobacter</i> sp.
Dessiccation	Xerophile	Anhydrobiotic	Desert, rock surfaces	Sand, rocks	<i>Artemia salina</i> , <i>Deinococcus</i> sp., <i>Lichens</i> , <i>Methanosarcina barkeri</i>
Rock dwelling	Endolith	Resident in rocks	Upper subsurface to deep subterranean	Rocks	<i>Lichens</i> , <i>Cyanobacteria</i> , <i>Desulfovibrio cavernae</i>

Table 3.4: Classification of extremophiles. Remotely detectable observable denotes the surface reflection signatures that can be observed remotely for the extreme environments (Hegde and Kaltenecker, 2013).

3.2.2.1 Temperature

Some microbes, called hyper-thermophiles, can live above 100° C, sometimes in the hydrothermal vents, undersea rock chimneys through which erupts superheated mineral-rich fluid as hot as 350° C.

The most heat-resistant of these microbes is *Pyrolobus fumari*. It reproduces best in an environment of about 105° C, can multiply in temperatures of up to 113° C and it stops growing at temperatures below 90° C.

On the contrary, no microbial eukarya can tolerate long term exposures to temperatures higher than 60° C. These kind of microorganisms on Earth would likely to be found wherever liquid water existed.

Current understanding suggests the limit will be about 150 degrees C. Above this temperature, probably no life-forms could prevent dissolution of the chemical bonds that maintain the integrity of DNA and other essential molecules (Madigan and Marrs, 1997). According with Dartnell, (2011), chlorophyll is only stable up to 75 °C, so photosynthesis does not take place in hyperthermophile environments. In table 3.5 can be seen a list of hyperthermophilic organisms, their enzymes, their optimal temperature (T_{opt}), optimal pH (pH_{opt}), stability and references found in Gomes and Steiner, (2004).

Hyperthermophiles	Thermophilic enzymes	$T_{opt}/^{\circ}C$	pH_{opt}	Stability
Bacteria <i>Bacillus, Clostridia, Fervidobacterium pennavorans, Rhodothermus marinus, Rhodothermus obamensis, Thermus caldophilus, Thermoanaerobacter sp., Thermoplasma acidophilum, Thermotoga maritima, Thermotoga neapolitana, Picrophilus oshimae, Picrophilus torridus</i> Archaea <i>Desulfurococcus mucosus, Pyrococcus furiosus, Pyrococcus woesei, Pyrodictium abyssi, Staphylothermus marinus, Sulfolobus solfataricus, Thermococcus hydrothermalis, Thermococcus litoralis, Thermococcus celer, Thermococcus profundus, Thermococcus aggregans</i>	Cellulase Amylase Pullulanase I Pullulanase II α -Glucosidase β -Glucosidase Glucoamylase Xylanase Mannanase Pectinase Chitinase Protease Lipase Esterase Phytase			
<i>Alicyclobacillus acidocaldarius</i>	Endoglucanase (CelB)	80	4.0	Stable at pH=1-7 retains 60% activity after 1h at 80°C
Environmental DNA	β -Xylanase	100		Stable at 90°C
<i>Methanococcus jannaschii</i>	α -Amylase	120		Stable against denaturants
<i>Pyrobaculum calidifontis</i>	Carboxylesterase	90		1/2 life: 2h at 100°C
<i>Pyrococcus furiosus</i>	Chitinase a and b	90-95		NA
<i>Pyrodictium abyssi</i>	Xylanase	105		1/2 life: 100 min at 105°C
<i>Rhodothermus marinus</i>	Amylase Pullulanase α -L-Arabinofuranosidase β -Mannanase	85 80 85 85		1/2 life: 3h at 85°C 30 min at 85°C 8.3h at 85°C 45.3h at 85°C
<i>Sulfolobus solfataricus</i>	Xylanase	100		1/2 life: 47 min at 90°C
<i>Sulfolobus solfataricus</i>	α -Glucosidase	120		Highly thermostable (whole cells used)
<i>Sulfolobus solfataricus</i>	Trehalosyl transglucoylase	75		Stable at pH=4.5-11.0 after 2h at 80°C
<i>Sulfolobus shibatae</i>	α -Glucosidase	98		Retained 67% activity after 5h at 80°C
<i>Thermococcus litoralis</i>	L-Aminoacylase	85		1/2 life: 25h at 70°C, 1.7h at 85°C
<i>Ralstonia sp. A-471</i>	Chitinase	70		NA
<i>Thermococcus chitonophagus</i>	Chitinase	70		1/2 life: 1h at 120°C
<i>Thermoplasma acidophilum</i> <i>Picrophilus torridus</i> <i>Picrophilus oshimae</i>	Glucoamylases	90 90 90		1/2 life: 24h at 90°C for <i>Picrophilus torridus</i> and <i>Thermoplasma acidophilum</i> , 20h for <i>Picrophilus oshimae</i>

Table 3.5: A list of hyperthermophilic organisms, their enzymes, their optimal temperature (T_{opt}), optimal pH (pH_{opt}), stability and references found in Gomes and Steiner, (2004). NA= not available.

Psychrophyles are life forms that prefers cold environments, like microbial communities that populate Antarctic sea ice-ocean water, frozen for much of the year. These communities include photosynthetic eukarya, notably algae and diatoms, as well as a variety of bacteria. *Polaromonas vacuolata* for example, lives in optimal conditions between 4° C and 12° C.

In table 3.6 can be seen a list of psychrophiles organisms, their cold-active enzymes, their optimal temperature (T_{opt}), optimal pH (pH_{opt}), stability and references found in Gomes and Steiner, (2004).

Psychrophiles/psychrotolerant	Cold-active anzymes	$T_{opt}/^{\circ}C$	pH_{opt}	Stability
<i>Acinetobacter sp.</i> strain n°6	Novel esterase Lipase	50 20	7.8 7.0	lost 75% activity AT 40°c in 30 min 1/2 life: 30 min at 50°c
<i>Arthrobacter sp.</i> C2-2	β-Galactosidase	40	7.5	1/2 life: 8 min at 50°C, stable after 4h at 40°C
<i>Arthrobacter s.</i> strain TAD20	Chitinases	NA	NA	NA
<i>Bacillus, Clostridium,</i> <i>Actinomycetes, Cytophaga-</i> <i>Flexibacter-Bacteroides</i>	α-Amylase β-Galactosidase	NA	NA	NA
<i>Pedobacter cryoconitis sp.nov</i>	Oxydase, catalase, protease, amylase, β- Galactosidase, β- Glucosidase, β- Lactamase	NA	NA	NA
<i>Clostridium</i> strain PXYL1	Filter paper cellulase Ednocellulase Xylanase	20 20 20	5.0-6.0 5.0-6.0 5.0-6.0	1/2 life: 30 min at 40°C for xylanase, CMCase and FPase
<i>Cystofilobasidium larimarini</i> <i>Cystofilobasidium capitatum</i> <i>Cryptococcus macerans</i> <i>Cryptococcus aquaticus</i>	Polygalacturonase Polygalacturonase Polygalacturonase Polygalacturonase	40 40 50 50	5.0 5.0 4.0 4.0	The enzymes were very unstable at 30- 40°C
<i>Cryptococcus adeliae</i>	Xylanase	45-50	5.0-5.0	1/2 life: 78 min at 35°C
<i>Cryptococcus cylindricus</i> <i>Mrakia frigida</i> <i>Cystofilobasidium capitatum</i>	Pectinase	NA	NA	NA
<i>Flavobacterium psychrophilum</i>	Metalloprotease	24	6.5	Lost all activity after 5 min at 40°C
<i>Pseudoalteromonas haloplanktis</i>	Cellulase	NA	NA	NA
<i>Pseudoalteromonas haloplanktis</i>	Xylanase (family 8)	25	5.3-8.0	Mp 52.6°C 1/2 life: 1.9 min at 55°C
<i>Psychrobacter sp.</i> Ant300	Esterase	5-25	7.0-9.0	16 min at 40°C
<i>Psychrobacter okhotskensis sp.</i> <i>nov</i>	Lipase	NA	NA	NA
<i>Penicillium chrysogenum</i>	Edno-arabinanase	30-40	6.0-7.0	Stabel up to 30°C
<i>Pseudomonas</i> strain DY-A	Alkaline protease	40	10.0	NA
<i>Bacillus spp.</i>	Subtilisin	40-45	10.5-11.0	Thermolabile

Table 3.6: List of psychrophiles organisms, their cold-active enzymes, their optimal temperature (T_{opt}), optimal pH (pH_{opt}), stability and references found in Gomes and Steiner, (2004). NA= not available.

3.2.2.2 pH

Other organisms prefer acid or basic conditions (acidophiles or alkaliphiles).

Acidophiles can live in habitats with pH below five and acidophiles prefer habitats with pH greater than nine.

As a joke of destiny, acidophiles cannot tolerate great acidities inside their cells because it would destroy their DNA: cell wall has the task to isolate the inner part from the outer part of the organism.

Alkaliphiles live in soils laden with carbonate and in so-called soda lakes, such as those found in Egypt, the Rift Valley of Africa and the western U.S. Alkaliphiles, like acidophiles, maintain neutrality in their interior, and their extremozymes are located on or near the cell surface and in external secretions.

In table 3.7 can be seen a list of thermoalkaliphiles and alkaliphiles organisms, their enzymes, their optimal temperature (T_{opt}), optimal pH (pH_{opt}), stability and references found in Gomes and Steiner, (2004).

Thermoalkaliphiles/alkaliphiles	Thermoalkaliphilic/alkaliphilic enzymes	$T_{opt}/^{\circ}C$	pH_{opt}	Stability
<i>Alkalimonas amylolytica</i>	Amylase	NA	NA	NA
<i>Streptomyces sp.</i>	Endocellulase	50	8.0	Retained 95% activity at opt. temp. and pH for 30 min
<i>Bacillus firmus</i>	Xylanases (xyn10A and xyn11A)	70	5.0-9.5	Retained ca. 70% activity after 16h at 62°C
<i>Bacillus halodurans strains</i>	Amylase, pullulanase	55-65	10.0	NA
<i>Bacillus subtilis</i>	α -Amylase	52-55	9.0	Lost 60% activity after 10 min at 95°C
<i>Bacillus</i> isolate KSM-K38	α -Amylase	55-60	8.0-9.0	Highly resistant to chelating reagents and chemical oxidants
<i>Nesterenkonia sp.</i> AL-20	Alkaline protease	$T_m = 74^{\circ}C$	10.0	HIGHLY STABLE AGAINST H_2O_2 and sequestering agents
<i>Bacillus pumilus</i>	Alkaline protease	50-60	11.5	NA
<i>Arthrobacter ramosus</i>	Alkaline protease	65	11.0	Both enzymes are stable at 30-65°C and pH=7-12
<i>Bacillus alcalophilus</i>	Alkaline protease		10.0	
<i>Nocardiopsis sp.</i>	Alkaline protease Keratinase	70-75	11.0-11.5	Stable below 60°C for 10 min and pH=8.0
<i>Pseudomonas sp.</i> LBA34 <i>Halomonas sp.</i> LBBB1	Lipase	NA	NA	NA
<i>Bacillus sp.</i>	Azoreductase	80	8.0-9.0	NA
<i>Bacillus sp.</i>	Catalase-peroxydase	60	8.0	1/2 life: 20h at pH=9 and 60°C
<i>Thermus brockianus</i>	Catalase	90	8.0	1/2 life: 3h at 90°C, 330h at 80°C
<i>Bacillus alcalophilus</i>	Pectate lyase	45	9.0-10.0	NA
<i>Thermomonospora (actinomycete)</i>	Endocellulase	50	5.0	Stable at pH=7-10 1/2 life: 3h at 70°C

Table 3.7: List of thermoalkaliphiles and alkaliphiles organisms, their enzymes, their optimal temperature (T_{opt}), optimal pH (pH_{opt}), stability and references found in Gomes and Steiner, (2004). NA= not available.

3.2.2.3 Pressure

High pressure compresses the packing of lipids in cellular membranes, and so restricts membrane fluidity, giving a similar outcome to low temperatures. Many organisms respond to this by increasing the proportion of unsaturated fatty acids in the composition of their membranes. On the other hand, high pressure causes a shift in the equilibrium of chemical reactions that involve a change in volume in the consumption or production of gases. Thus, biochemical reactions that produce an increase in volume are inhibited by high-pressure environments and piezophilic organisms must adapt to this. Natural high-pressure environments on the Earth include deep lakes and seas, or the subsurface.

Pressure increases at a rate of 10.5 kPa per metre depth in water (hydrostatic pressure), while lithostatic pressure increases at over twice the rate, 22.6 kPa per metre beneath the Earth's surface. The greatest pressure in the Earth's oceans is at the bottom of the Mariana Trench, at just over 11 km depth, corresponding to ~110 MPa water pressure. (Marion et al., 2003). This abundance of life is due to the fact that fish and mammals, once dead, fall down in the deepness of ocean and form a big layer of nutrients to suit life (Guld et al., 2013). On the other hand, as pressures drop very low, towards vacuum, water sublimates and organisms become desiccated. Different exposure experiments on space missions have found that organisms, particularly those in a dormant or spore state, are able to survive the vacuum and consequent desiccation of the space environment, provided they receive adequate shielding from solar ultraviolet radiation. Indeed, freeze-drying or lyophilisation, is a standard laboratory procedure for preserving microbial samples for storage (Dartnell, 2011).

3.2.2.4 Irradiation

Irradiation is the key for the photosynthetic process to start. As we have seen, there are a lot of organisms that are able to live in the oddest and most harsh environments of the world and in most of these cases the light of the sun struggles to reach these organisms. Anyway, some of them, thanks to their adaptative strategies and of course, thanks to evolution, have lowered the irradiance limit in order to benefit of even the smallest number of photons available.

In fact it has been estimated by Raven (1984) that the theoretical unicellular light limit is 0.1 μmol of photons/ m^2/s (or 6×10^{16} photons/ m^2/s).

For the upper limit of photon flux density, Wolstencroft and Raven (2002) summarized the literature and found a theoretical tolerance for land plants against photo damage at 6–9 mmol of photons/ m^2/s over the PAR band (or $3.6\text{--}5.4 \times 10^{21}$ photons/ m^2/s), which is well above Earth's typical flux of 2 mmol photons/ m^2/s (1.2×10^{21} photons/ m^2/s). For Earth-like planets in general, they conjectured a theoretical upper limit for land organisms to be 10 mmol of photons/ m^2/s (6×10^{21} photons/ m^2/s). Since aquatic organisms are shielded under water, they could exist for even higher surface photon flux densities (Kiang et al., 2007a). The photon flux density impacting on a planet can be found by

$$PPFD = \frac{1}{4} \frac{L_*}{4\pi d^2} \frac{\lambda_{max}}{hc} \frac{1 \times 10^6}{N_A} \quad (3.18)$$

where L_* is the luminosity associated with the star, λ_{max} is the maximum photon flux obtained with Wien's law in its photon basis, d is the mean distance between the planet and star, and the $\frac{1 \times 10^6}{N_A}$ term (N_A is the Avogadro constant) ensures that the flux density is counted in μmol of photons (McDonald, 2003; Puxley et al., 2008). It can be useful to remember that surface fluxes needed to produce biogenic observed mixing ratios in Earth's present atmosphere are: -1.31×10^{12} g of H_2/yr , 9.54×10^{14} g of CH_4/yr , 1.32×10^{13} g of $\text{N}_2\text{O}/\text{yr}$, 2.35×10^{15} g of CO/yr , and 7.29×10^{12} g of $\frac{\text{CH}_3\text{Cl}}{\text{yr}}$. The negative sign on the H_2 flux indicates that the calculated flux is downward (Segura et al., 2005). With sufficient nutrients, and hence sufficient pigment per unit area to absorb almost all of the incident photons, the lower limit on photon flux density at which gross photosynthesis can occur is set by unavoidable back reactions and, for almost 100% photon absorption and a two photons per electron mechanism, it is some 20 nmol of photon $\text{m}^{-2}\text{s}^{-1}$ (Raven *et al.* 2000).

3.2.2.5 UV damages

Many terrestrial organisms are sensible to UVA and UVB variations, a consequence of the solar light radiation environment. Many of them evolved a bunch of pathways to protect themselves from UV radiation, so more simply, by cellular damages. For example free radicals produced in the cytoplasm or replication errors can be strategies to repair cells, but UV specific hints have been developed too, such as photo reactivation repair of dimer formation by UV using visible radiation or bypass polymerases, that specifically allow the replication of UV-induced lesions.

On early Earth without a thick ozone shield, only a few of present organisms could survive, even if even in that case, various types of protection, including oceanic minerals, pigmentation, or atmospheric sulfur molecules and hazes could have prevented some of them by death (see Cleaves and Miller, 1998; Cockell, 2002).

The great bafflement about exoplanet habitability of M star planets regards the periodically short term fluctuations of the radiation environment.

Indeed the region of stellar spectrum between 0.20 and 0.30 μm is relevant for atmospheric chemistry and for life regarding biologically radiation doses (Scalo et al., 2007). However, while U-band (0.331-0.339 μm) in astronomy coincides with UVA band, there are few information about UVB and UVC (<0.29 μm) bands.

Besides DNA damage, UV light also affects membranes such as the photosynthetic thylakoids and cell boundaries, degrades proteins, lipids, and chromophores, interferes with photosynthesis, cell division, and development, and affects many biochemical processes including nitrogen fixation and energy production [Harm (1980) and Jagger (1985); Scalo et al., 2007)]. UV damage to plants has been observed at doses of 15-16 kJ/day (Kakani et al., 2003). The most relevant question is whether the short-term fluctuations in M star planet environments should lead to accelerated evolution powered by the fluctuation time scales, or to the inability of genetic systems to keep up with the changing environment, noting that "accelerated evolution" refers to extinction as well as fixation of rare alleles or development of complex phenotypes. An answer will require a multiple-gene model with positive and negative epistasis, as well as multiple competing beneficial mutations (clonal interference); this problem can be treated as a stochastically driven gene network (Scalo et al., 2007). In Segura et al., (2005) a study of how a terrestrial planet orbiting around M dwarves could evolve

and what differences between Earth could arise has been carried out, and the results show that UV doses are $10^{-2} - 10^{-3}$ times of those of the Earth. The maximum Earth's surface UV rate is $1.8 - 2.8 \times 10^{-18}$ photons/m²/s over the UVB band at the Equator at noon under cloudless conditions or averages globally 0-12 KJ /m²/s (2.1×10^{-18} photons/m²/s). Moreover, during the time interval between flares, in M stars planet terrestrial organisms would be exposed less 0.35-0.50 μ m damage than for the Earth.

For terrestrial organisms on a planet with a thick ozone layer, even if most of the damage radiation occurs in the UVB (0.28-0.315 μ m), a not negligible fraction of damage comes from UVA (0.315-0.40 μ m) and from the visible part of the stellar spectrum. This last range is associated to oxidative damage. Michelet et al., (2003) underlined how the inclusion of UVA radiation can lower the sensitivity of UV radiation damage to ozone column. In Table 3.8 can be seen the relation between Ozone column Depth and UV dose rates for DNA damage relative to present Earth for planets orbiting M stars.

Parent star	O ₃ column depth (cm ⁻²)	UV dose rate	
		No atmosphere	Present Earth-like atmosphere
Sun	8.4×10^{18}	7.1×10^3	1.00
AD Leo	4.4×10^{18}	7.3×10^1	1.4×10^{-2}
$T_{eff}=3100$ K	1.2×10^{18}	1.2	6.0×10^{-2}
$T_{eff}=3400$ K	2.4×10^{18}	1.3×10^1	8.5×10^{-2}
$T_{eff}=3650$ K	3.2×10^{18}	3.9×10^1	9.8×10^{-2}

Table 3.8: Ozone column Depth and UV dose rates for DNA damage relative to present Earth for planets orbiting M stars

Photosynthetic organisms on planets around active M stars with high UV flares (the UV can also come from the chromosphere during no flare activity) could have adaptations to survive flare disturbances; some of these adaptations have been observed in Earth organisms (e.g., protective pigments, regenerative capacity, life cycles timed to avoid disturbances). There will be little need to protect against UV radiation from quiescent stars (Kiang et al., 2007b). On Earth, when PAR is unavailable for an extended period of time, most photosynthetic organisms can survive by using major macromolecular pools as shown for the cyanobacterium *Phormidium autumnale*, which is able to survive for at least three weeks in continuous darkness without using any external organic matter (Montechario and Giordano, 2006; Montechario et al., 2006).

3.2.2.6 Salinity

Another group of extremophiles prefer very intense saline environments.

Some saline environments are also extremely alkaline because weathering of sodium carbonate and certain other salts can release ions that produce alkalinity. Microbes in those environments are adapted to both high alkalinity and high salinity. These organisms produce large amounts of an internal solute to avoid cell dehydration.

In fact, normal bacteria cytoplasm should have large concentration of salt to live in these environments.

For instance, an archaean known as *Halobacterium salinarum* concentrates potassium chloride in its interior.

In table 3.9 can be seen list of Halophile organisms, their halophilic enzymes, their optimal temperature (T_{opt}), optimal pH (pH_{opt}), stability and references found in Gomes and Steiner, (2004).

In figure 3.6 is shown the survival envelope of terrestrial life. The graph illustrates in green the limits of terrestrial organisms. On the axes are shown salinity, temperature and pH

Halophiles	Halophilic enzymes	$T_{opt}/^{\circ}C$	pH_{opt}	Stability
<i>Halothermothrix orenii</i>	α -Amylase	65	7.5	Tolerates up to 25% NaCl, T_{opt} at 5% NaCl
<i>Bacillus dipsosauri</i>	α -Amylase	60	6.5	Stable up to 60°C
<i>Halobacillus</i> sp. strain MA-2	Amylase	50	7.5-8.5	Maximum stable at 5% NaCl
<i>Haloferax mediterranei</i>	α -Amylase	50-60	7-8	Stable at 2-4 M NaCl Optimum 3 M NaCl
<i>Halophilic bacterium, CL8</i>	Xylanase 1	60	6.0	Stable 7 min at 60°C Stable 192 min at 60°C (T_{opt} at 4 M NaCl)
	Xylanase 2	65	6.0	
<i>Halorhabdus utahensis</i>	β -Xylanase	55,70	NA	Optimum activity at 5-15% NaCl Optimum activity at 5% NaCl
	β -Xylosidase	65	NA	
<i>Pseudoalteromonas</i> sp. strain CP76	Protease	55	8.5	Tolerates 0-4 M NaCl Optimum activity at 7.5% NaCl

Table 3.9: List of Halophile organisms, their halophilic enzymes, their optimal temperature (T_{opt}), optimal pH (pH_{opt}), stability and references found in Gomes and Steiner, (2004).

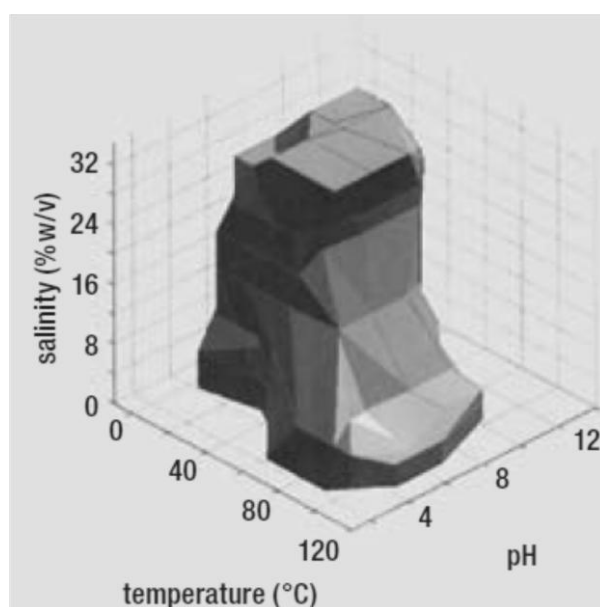


Figure 3.6: The survival envelope of terrestrial life. On the axes are shown salinity, temperature and pH (courtesy of Julian Wimpenny).

3.2.2.7 Dessiccation

Dessiccation is the capacity to resist in scarce water conditions. An example organism studied for this thesis is *Chroococcidiopsis*. Xerophiles grow with very little water like in sand deserts, ice deserts and salt flats like the Atacama Desert in Chile. In plants, xeromorphism is the ability to form spines to conserve water and survive to long desiccation periods, during which their metabolic activity may effectively shut down. Plants with such morphological and physiological adaptations are called *xeromorphic*. It seems that UV resistance would be linked to desiccation as a consequence of this process (Mattimore and Battista, 1996; Battista, 1997; Ferreira et al., 1999).

3.2.2.8 Rock dwelling

Endoliths live inside rocks like sandstone that protect the organisms by attenuating the UV radiation whilst allowing the photosynthetically active radiation (PAR) through its upper translucent surface (Southam et al., 2007), thereby allowing for photosynthetic metabolism. This phenomenon is often described as “cryptic

photosynthesis” due to the effective shielding of any specific reflection signature that could indicate the biota by the overlaying rock surface in the reflection spectrum. Rocks protect the organisms residing within against low temperatures, UV radiation and severe desiccation (Cockell et al., 2009; Canganella and Wiegel, 2011). Endolithic communities are also found in complete darkness whereby they receive their energy by reducing sulfate and iron among other metals found in the host rock (Cavicchioli, 2002).

3.2.2.9 Nutrients

Nutrients are another limitation factor to productivity of the organisms. N is fixed by enzymatic processes. In particular, this process is carried out in the oceans, by diazotrophic bacteria, also said "sea sand", that transform N_2 in NO_3^- or NH_4^+ and make it available for phytoplankton metabolism by an enzyme called nitrogenase, that is composed by iron and sulphur agglomerates (Coelho, 2009). The presence of other minerals like P, K, S, Mg, Fe or Mn are the ones required for the production of pigments and enzymes. As Chls are tetrapyrroles with four nitrogens around a magnesium atom, it is evident that N is the first photosynthetic limitant. Moreover, the components of photosynthetic apparatus have high nitrogen content too (Raven, 1984). In aquatic and marine environments nutrient availability is provided by atmospheric depositions from land-surface runoff of organic compounds.

Other minerals are instead baneful for some organisms, like picoeukaryotes and some varieties of cyanobacteria like *Synechococcus* (Paytan et al., 2009).

Phosphorus, an essential mineral for DNA, ATP, and phospholipids of cell membranes, becomes available from weathering of the mineral apatite but then, over time, complexes with Al, Fe, and Mn (at low pH) or with Ca (at high pH), such that it becomes unavailable (Kiang et al., 2007a).

There are examples among photosynthetic algal flagellates on Earth in which oxygenic photosynthesis coexists with the capacity to ingest smaller organisms (phagotrophy) as a means, complementary to photosynthesis, of obtaining organic carbon (and other nutrients); such mixotrophy is common among marine flagellates (Gasol et al., 2008; Raven et al., 2009). Figure 3.7 shows some of representative samples of extremophyles.

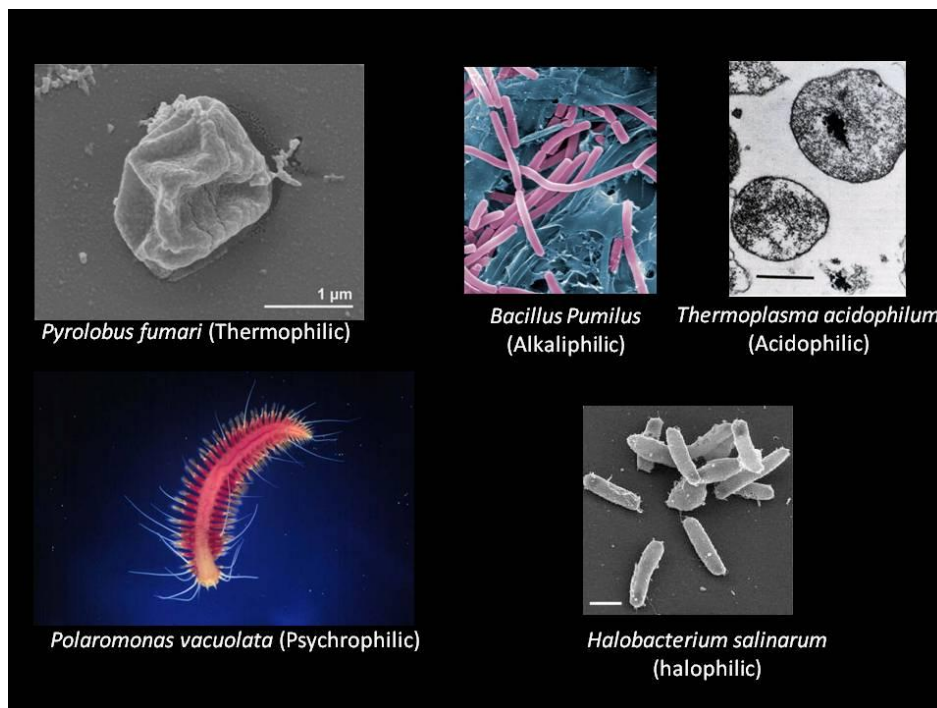


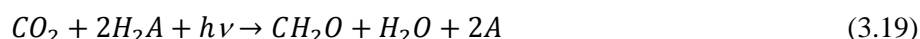
Figure 3.7: Some of representative samples of extremophyles.

3.2.2.10 Gravity

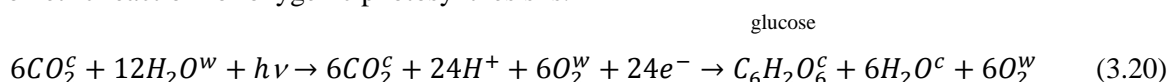
Gravity is another parameter to keep under control. The larger an organism, the more sensitive it is to gravitational forces. The bodies of multicellular organisms, such as humans, start to collapse and turn to mush under the force of just a few g. Deguchi et al., 2011 was able to replicate hypergravity on Earth using a machine called an ultracentrifuge. They used some bacteria as *Escherichia coli* to test life conditions in increasingly intense gravity conditions. When they spun *Escherichia coli* up to the equivalent of 7,500 g (7,500 times the force of Earth gravity), they didn't find variations as it grew and reproduced just fine. The bacteria clumped together into pellets as the gravity increased, but their forced closeness didn't seem to deter growth: all four species multiplied normally under thousands to tens of thousands of times Earth's gravity. The experiment was expanded, exposing four other microbe species to hypergravity for up to 140 hours. They found that another bacterium, *Paracoccus denitrificans*, can also reproduce at about the limit threshold of 403,627 g, though its proliferation, like that of *E. coli*, is stunted in such extreme conditions. *Paracoccus denitrificans* and *Escherichia coli* were the hypergravity-tolerance champs, but all five examined species could reproduce to some extent up to about 20,000 g.

3.3 Photosynthesis: model and description (oxygenic vs non anoxygenic)

As said, photosynthesis is a process that can convert light energy to electrochemical energy. The reduction of CO_2 is a consequence of electron transport along biochemical pathways. The basic photosynthetic process is:



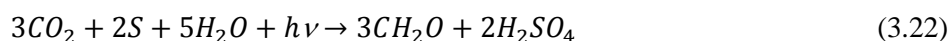
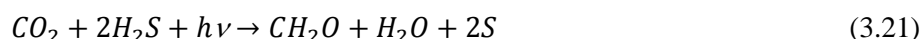
where $2H_2A$ is a reducing substrate like H_2O or H_2S and $h\nu$ is the energy per photon. Oxygenic photosynthesis is a particular case in which the reductant is water. The stoichiometric reaction for oxygenic photosynthesis is:



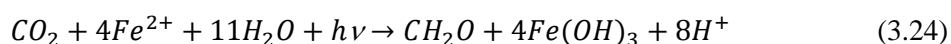
where the superscript c and w denotes the oxygen from carbon dioxide and from water.

The main requirement for photosynthesis is that 479.1 kJ mol^{-1} of energy be stored to allow the process. Four photons are required for each O_2 produced and four ones are used to reduce two molecules of $NADP^+$ that can be used to reduce one CO_2 . Within six cycles six carbons are obtained to produce glucose. The energy input by these eight photons is 1387.2 kJ mol^{-1} , if 0.68 μm is used in PS II or 1,339.0 V if 0.73 μm . The efficiency of energy input for typical plant photosynthesis is 479.1/(1339.0 to 1387.0), or almost 35%. In typical conditions the efficiency is closer to 27% (Blankenship, 2002). On extrasolar lands this efficiency may sensibly variate. The efficiency of photosynthesis is instead influenced by the amount of photons involved (Kiang et al., 2007b). Other photons may be used in the process because some can product unsuccessful reactions or for ATP production .

Anoxygenic photosynthesis can use reductants other than water. For example they can be H_2S , H_2 or Fe^{2+} . In the first case, elemental sulphur is produced and then sulfate:



If the reductant is H_2 (Vignais et al., 1985) or Fe^{2+} (Ehrenreich and Widdel, 1994; Jiao et al., 2005), the reactions are these:



Oxygenic photosynthesis on Earth is limited to photosystems that operate at 400–730 nm, but anoxygenic photosynthesis occurs at wavelengths as long as 1,015–1,020 nm (Trissl, 1993; Scheer, 2003). Among the phototrophic bacteria, only cyanobacteria are oxygenic.

3.3.1 Pigments, metabolism and environmental limits: photosynthetic organisms evolution

One theory about the origin of photosynthesis is that it began as a casual adaptation of primitive pigments for infrared thermotaxis of chemolithotrophic bacteria in hydrothermal ocean vents, possibly 3.8 Gyrs ago in the Archean (Nisbet *et al.*, 1995). Thus, with these organisms being less dependent on the heat of the hydrothermal vents, their habitats gradually expanded to shallower waters where solar light could be utilized (Nisbet and Fowler, 1999; Des Marais, 2000).

Another theory says that oxygenic photosynthesis may have been the first to provide an ozone shield and UV screening proteins led to the transfer of excitation energy to the porphyrin (Mulkidjanian and Junge, 1997). Moreover, the evolution of oceans may have been the first step in the evolution of chlorophyll (see Kiang *et al.*, 2007a and references therein).

Protocyanobacteria early in the Archean may have utilized $Fe(OH)^+$ as a reductant (Olson, 2006) or bicarbonate (Dismukes *et al.*, 2001). Since oxygen damages bacteriochlorophylls, it seems to be possible that the first photosynthesizers were green sulphur anoxygenic bacteria and purple bacteria, and successively oxygenic photosynthesis took place (in the early Proterozoic) with cyanobacteria.

Plastids, the photosynthetic organelle, in algae, are the result of an endosymbiosis between cyanobacteria and early protists. Red algae appeared on Earth 1.2 Gyr ago, while green eukaryotic ones appeared not before 750 Myr ago. As the sun had a stronger emissivity than today they needed to evolve a method to shield themselves from UV. That's why the first photosynthesizers developed under water. This let them to take a long time to modify the climate of the planet, producing O_2 that can build O_3 . This is the era of oxygenic photosynthesis became the most diffuse and dominating.

Land plants began their story facing the world about 460 Myr ago and reaching a peak in the Devonian about 360 Myr ago (Bambach, 1999; Carroll, 2001; Igamberdiev and Lea, 2006).

The first ones were the Bryophytes, mosses and liverworts. Flowering plants came on Earth as an upgrade of green plants, 144 Myr ago. Crassulacean acid metabolism (CAM) photosynthesis, which arose 70–55 Myr ago and C4 photosynthesis (25–30 Myr ago) are expedients to improve the energetic storage. Here, CO_2 is stored in an intermediate at night to be used during the day.

Finally, it is useful to underline the fact that not all photosynthesizers are autotrophs (fix CO_2), but many of the bacteria are heterotrophs that utilize organic carbon, though some may use both inorganic and organic carbon. The halobacteria do not perform actual photosynthesis, in that no electron transfer is performed, but their pigment bacteriorhodopsin drives a proton pump for heterotrophic assimilation of organic carbon (Kiang *et al.*, 2007b).

3.3.2 Light harvesting

The photon flux density, and not the spectral energy flux is the main parameter for photosynthesis.

Photosynthetic organisms have a bouquet of photosystems that regulate light absorption and transformation.

These are the outer antenna complex that has the task to transfer light energy to the core antenna.

Both form the light harvesting complex (LHC).

The core antenna is part of the RC complex too, where light energy is converted to chemical energy (Ke, 2001). In plants and in all oxygenic photosynthetic organisms light utilization has two stages. The first consists in the electron extraction from water by means of Photosystem II (PS II) to restart the next step. The absorption peak of PS II is at 680 nm. The second step is the reduction of the electron carrier $NADP^+$ used in the Calvin-Benson cycle and for the synthesis of ATP. Its peak is at 700 nm.

These steps compose the Z-scheme. The redox potential is the Gibbs free energy change of a reaction calculated by the Nernst equation. This gives a measure of the propensity of an oxidation–reduction reaction to proceed spontaneously in one direction (Kiang et al, 2007a).

All oxygenic photosynthesizers use both PS I and PS II and water as reductant, while anoxygenic photosynthesizers use only one of them. In figure 3.8 are shown the electron transport pathways of photosynthesis, the midpoint redox potential and the RC excited states for purple and green bacteria and oxygenic photosynthesizers.

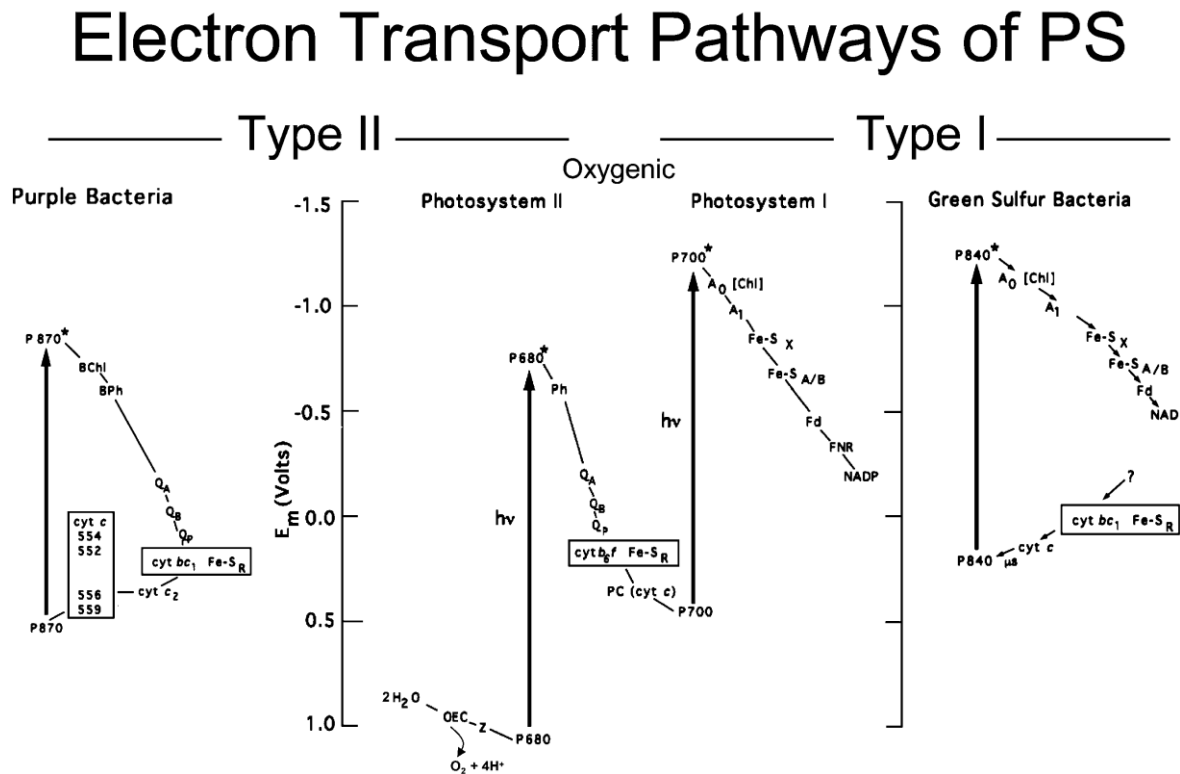


Figure 3.8: Electron transport pathways of photosynthesis, midpoint redox potential and RC excited states for purple and green bacteria and oxygenic photosynthesizers.

PAR represent the active radiation boundaries between which photosynthesis can be able to operate.

Other living organisms, such as green bacteria, purple bacteria and heliobacteria, can exploit solar light in slightly extended spectral regions or in ecological niches, such as the near-infrared. These bacteria live in environments such as the bottom of stagnant ponds, sediment and ocean depths. Because of their pigments, they form colorful mats of green, red and purple.

Purple bacteria have absorbance peak in the 1.013-1.025 μm range which use bacteriochlorophylls b like *Blastochloris viridis* or *Rhodospseudomonas viridis* (that absorbs at 0.96 μm) and other bacteriochlorophylls in the range 0.7-0.9 μm (Scheer, 2003). They don't use water as H donor, and then don't release oxygen as byproduct.

Other bacteria that can photosynthesize in the IR are the genus *Colobrium* ones, with an absorbance peak in their pigments of 0.84 μm or *Rhodospirillum Rubrum* and *Rhodospirillum Capsulata* that absorb respectively at 0.87 μm (Heath et al., 1999).

The bounds of the shorter PAR band could be set at 0.400–0.730 μm to acknowledge the ability of *Acaryochloris marina* to utilize the longer wavelengths (Chen et al., 2005). At <http://vplapps.astro.washington.edu/pigments> can be found a database of absorbance spectra for the most common pigments used by photosynthetic organisms.

Plants, instead, photosynthesize in red light, and keep advantage from the Emerson effect. PAR for plants is 0.40-0.70 μm . In fact, plants utilize only Chl a, Chl b, and carotenoids but have developed more complex mechanisms to acquire CO_2 and retain water.

The Emerson effect led to the conclusion that in the photosynthetic process would operate two pigment complexes capable to absorb different radiation wavelength, and, from there, to the discovery of PSII.

Theoretically photosynthetic range can extend to 1.4-1.5 μm with the utilization of low-energy photons if three or four of them are used instead of the usual two (Kiang et al., 2007b).

Theoretically is the right word, because at some long wavelengths the photons can't provide electronic useful states and induce only vibrational and no electronic transitions.

It has been estimated that for a four photons per electron mechanism the lower limit is 20 $\text{nmol photon m}^{-2}\text{s}^{-1}$ (Raven et al. 2000).

Though it is hard to set limits extremes, we can assert that an upper limit to radiation energy is 1.1 μm , because radiation less energetic is all thermal and cannot be measured with optical sensors.

On the other hand, wavelengths below 0.28 μm are not considered photosynthetically active not only for planets with an ozone shield orbiting G stars, but even for F, K, and a few M star ones (Kiang et al., 2007b).

It has been observed that the lowest observed light compensation points are $\sim 3 \mu\text{mol of photons m}^{-2}\text{s}^{-1}$ (0.7 W/m^2 , $1.8 \times 10^{18} \text{ photons m}^{-2}\text{s}^{-1}$) of PAR for green plants (Nobel, 1999) and $\sim 0.01 \mu\text{mol of photons m}^{-2}\text{s}^{-1}$ for red macro-algae [$6 \times 10^{15} \text{ photons m}^{-2}\text{s}^{-1}$ (Littler et al., 1986)]. Overmann et al. (1992) observed a brown sulfur bacterium, living at $\sim 80 \text{ m}$ depth in the Black Sea, that is adapted to an available irradiance of $0.003\text{--}0.01 \mu\text{mol of photons m}^{-2}\text{s}^{-1}$ ($1.8\text{--}6.0 \times 10^{15} \text{ photons m}^{-2}\text{s}^{-1}$) (additional characterization by Manske et al., 2005). As previously said, the theoretical unicellular light limit has been estimated by Raven (1984) to be $\sim 0.1 \mu\text{mol of photons m}^{-2}\text{s}^{-1}$ ($6 \times 10^{16} \text{ photons m}^{-2}\text{s}^{-1}$), and as this is higher than that observed, additional efficiency strategies for survival at low light must be more a possibility than current understanding allows (Kiang et al. 2007a).

3.3.3 Photosynthetic pigments

Photosynthetic pigments are divided in three groups called chromophores: the Chls, carotenoids and phycobilines. All photosynthetic organisms have carotenoids. Chl a is found in all photosynthetic organisms except some photosynthetic bacteria; Chl b is found in higher plants and green algae; accessory pigment β carotene is found in all photosynthetic organisms except photosynthetic bacteria; phycoerythrin and phycocyanin (phycobilines) are found in red algae and cyanobacteria respectively. Allophycocyanin is an accessory pigment to absorb orange light.

The Chls can be found in the core antennae and light harvesting antennae (Grimm et al., 2006). The funnelling of energy from the LHCs in all eukaryotes is achieved through a rather remarkable process known as resonance excitation transfer in which a pigment is excited by light at a particular wavelength, and the subsequent de-excitation of the pigment, rather than resulting in a loss of energy to heat or fluorescence, leads to the excitation of another pigment whose energy level overlaps. A series of such excitations and de-excitations creates an "energy cascade" toward longer wavelengths.

The chlorophyll pigment itself comes in different forms with absorption maxima at different wavelengths. For example, photosynthetic bacteria (both aerobic and anaerobic) have bacteriochlorophylls (Bchl) pigments. Cyanobacteria that have Chl a and phycocyanin can be found in lakes and ponds and often form a dense surface layer, absorbing a large amount of blue and red light. In all oxygenic eukaryotes, Chl a occurs in the core antenna and has a chief role as primary donor in the RC while other Chls, Chl b, c and d, provide light harvesting roles. Chl d, recently discovered in cyanobacteria (Miyashita et al., 1996; Miller et al., 2005, Mielke et al., 2011), may replace Chl-a in the RCs in some cyanobacteria that live in environments with little visible light (Chen et al., 2005; Larkum and Kühl, 2005). Recently Chl f has been discovered which is able to capture light energy in the infrared spectrum. Chlorophyll f has an absorption peak of 706 nm while Chl d has its major peak absorbance in the NIR at 720 nm (Manning and Strain, 1943; Larkum and Kühl, 2005), and thus oxygenic photosynthesis is being performed in the NIR (Kiang et al, 2007a). Chl f was discovered from ground up stromatolites, colonies of rock forming shallow water bacteria which have been reef building since way before corals. It is possible that some endosymbiotic bacteria that use Chlorophyll f could be living inside corals. Purple photosynthetic bacteria (Bchl a or b) and green photosynthetic bacteria (major

pigment is Bchl c, d, or e) grow best in anaerobic conditions in deep water. At these depth, the previously cyanobacteria-absorbed blue and red light is not available. The bacteriochlorophylls pigments allow the purple and green bacteria to take advantage of their ecological niche in deep water by absorption of longer wavelength light. In addition, Bchl a and b have absorption maxima at shorter wavelengths than Chl a, taking advantage of the deep water where shorter wavelength light can penetrate water farther (Seager et al., 2005). Carotenoids work in the blue and green part of the spectrum and helps organisms to protect themselves against photooxidative stresses, high temperatures, the presence of certain pigments and the presence of O₂, that can be toxic to photosynthetic organisms. Phycobilines, can be found in cyanobacteria and red algae, and work in the green and yellow spectral regions.

The red pigment lycopene is found in vegetables. Some red algae are in fact nearly black, so that increases their photosynthetic efficiency. Brown algae have the pigment fucoxanthin in addition to chlorophyll to widen their absorption range. These red and brown algae grow to depths around 270 meters where the light is less than 1% of surface light.

Another photosynthetic cycle using a dedicated pigment has been evolved: this pigment is rhodopsin. Bacteriorhodopsin (a type of rhodopsin) occurs in halobacteria (Oesterheld & Stoeckenius 1971) found in highly salty environments, for example in the Dead Sea. Proteorhodopsin is found in marine bacterioplankton that are widespread in the surface ocean (Beja et al. 2001). The rhodopsin photosynthetic system is chemically fundamentally different from the chlorophyll photosynthetic system.

In figure 3.9 can be seen the absorption spectra of the principal photosynthetic pigments, while in figure 3.10 is illustrated the solar spectral photon flux densities at the top of the Earth's atmosphere, at the Earth's surface, at 5 cm depth in pure water, and at 10 cm depth of water with an arbitrary concentration of brown algae and bacteria pigment absorbance spectra.

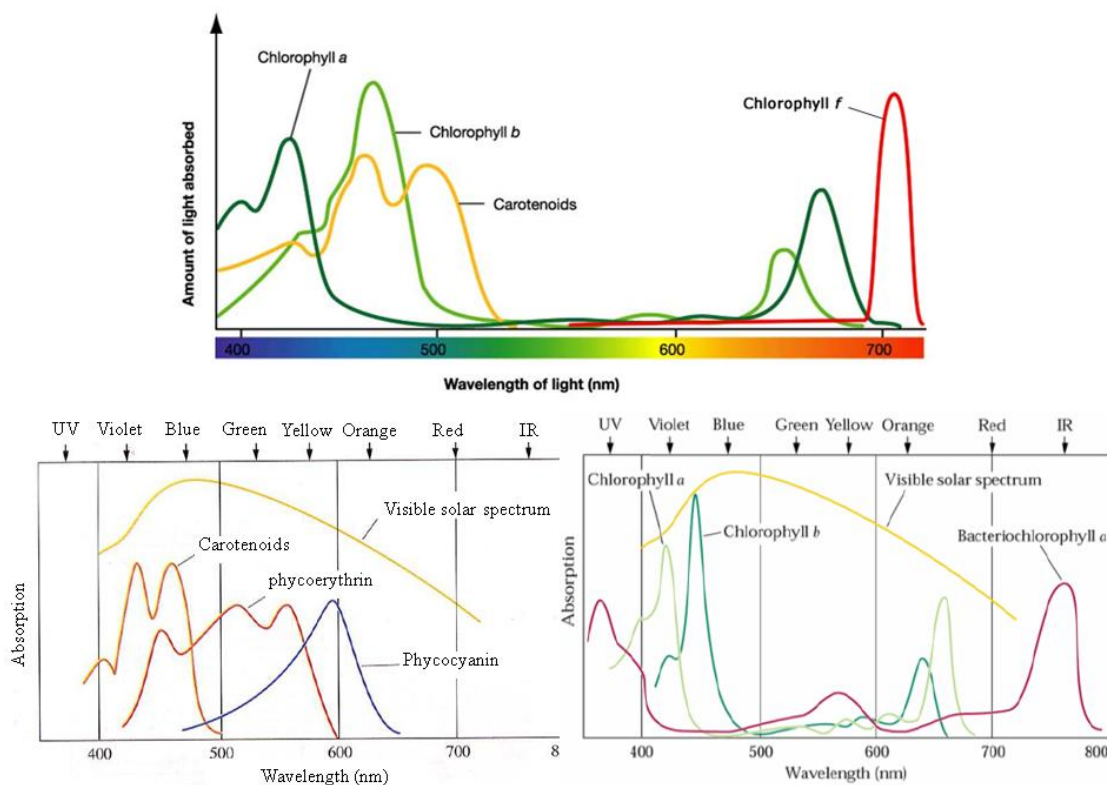


Figure 3.9: The absorption spectra of the principal photosynthetic pigments: Chl a, Chl a, Carotenoids, Chl f, Phycoerythrin, phycocyanin and bacteriochlorophylls.

In table 3.10 are shown the main function of the biological pigments and examples of organisms that uses them.

Function	Pigment type	Example pigments	Example organism	References
Photosynthesis	Chlorophylls, bacteriochlorophylls	Chls a, b; Bchls a,c,g	<i>Cyanobacteria</i> , <i>anoxygenic phototrophs</i>	Hohmann-Marriott and Blankenship, 2012; Clayton, 1966
Other light capture, other phototrophy	Some rhodopsins, some carotenoids	Xanthorhodopsin, bacteriorhodopsin	<i>Salinbacter ruber</i> , <i>Halobacterium salinarum</i>	Boichenko et al., 2006; Oren, 2013; Grote and O'Malley, 2011
Sunscreen	cyclized β -ketoacid	Scytonemin	<i>Cyanobacteria</i>	Proteau et al., 1993
Antioxidant	Carotenoids	Bacterioruberin, deinoxanthin	<i>Halobacterium salinarum</i> , <i>Deinococcus radiodurans</i>	Lemee et al., 1997; Saito et al., 1997; Shahmohammadi et al., 1998
Protection against temperature extremes	Tyrosine derivative	Melanin	<i>Cryptococcus neoformans</i>	Dadachova et al., 2007; Liu and Nizet, 2009
Acquisition of nutrients such as iron	Siderophore	Pyoverdine	<i>Pseudomonas putida</i>	Meyer, 2000
Regulation of growth (cytotoxicity)	Prodiginine	Prodigiosin	<i>Serratia marcescens</i>	Bennett and Bentley, 2000; Hejazi and Falkiner, 1997
Protection against competition or grazing (antimicrobial)	Indole derivative	Violacein	<i>Janthinobacterium lividum</i>	Kimmel and Maier, 1969; Schloss et al., 2010; Dura'n et al., 2007
Signaling other organisms	Carotenoids, anthocyanins, betalains	Cryptoxanthin	<i>Narcissus pseudonarcissus</i>	Tanaka et al., 2008; Chittka and Raine, 2006; Valadon and Mummery, 1968
Bioluminescence	Luciferin	Dinoflagellate Luciferase	<i>Dinoflagellates</i>	Haddock et al., 2010

Table 3.10: Main functions of the biological pigments and examples of organisms that uses them.

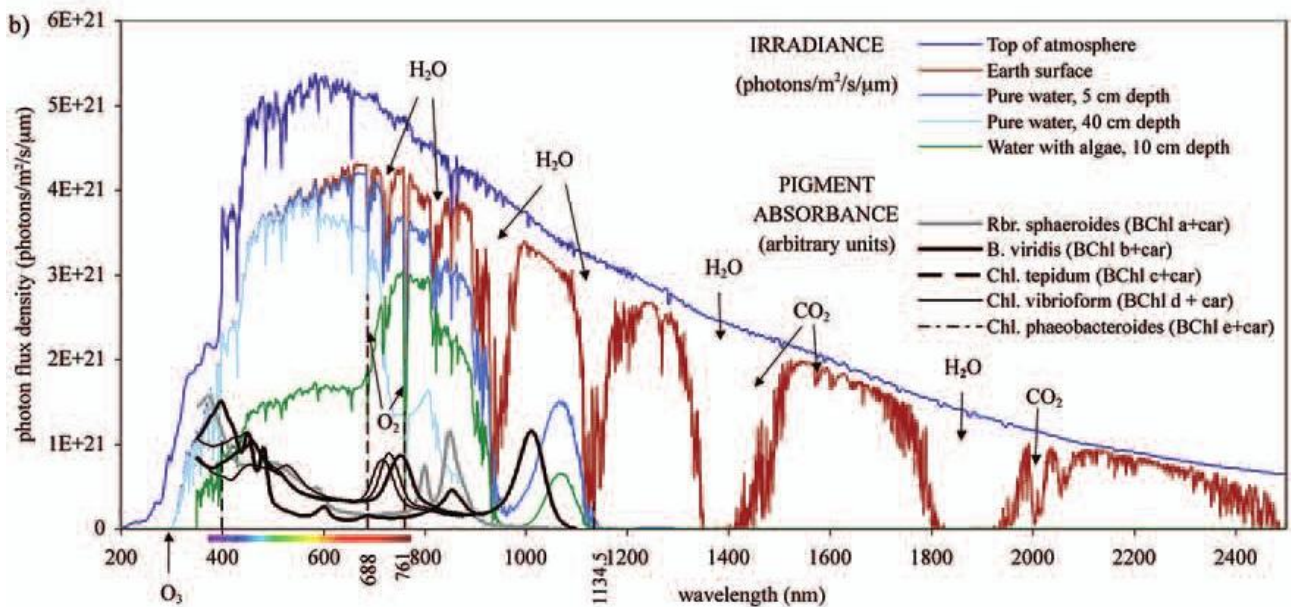


Figure 3.10: Representation of the solar spectral photon flux densities at the top of the Earth's atmosphere, at the Earth's surface, at 5 cm depth in pure water, and at 10 cm depth of water with an arbitrary concentration of brown algae; algae and bacteria pigment absorbance spectra.

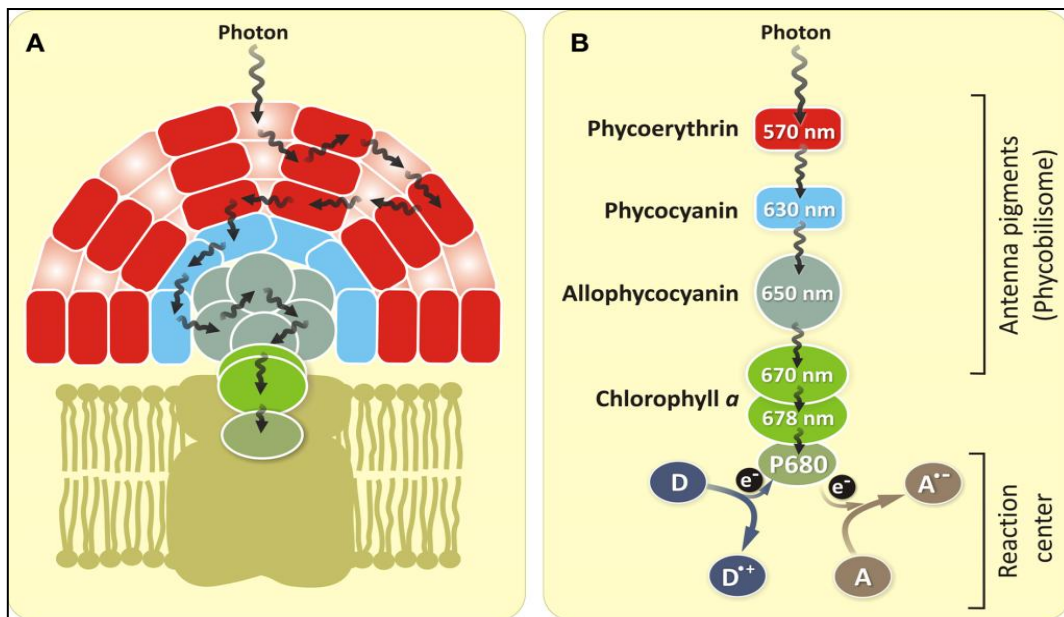


Figure 3.11: Representation of the photonic path in the photosynthetic apparatus

3.4 Oxygenic and anoxygenic photosynthesis on other planets

Life can go on and proliferate in a great variety of ecological niches from extreme habitats to more comfortable ones, like crystal rocks that can shield life from UV radiation.

Among all photolithoautotrophic photosynthetic organisms are the most useful for our purposes because they primary producers that harvest light energy to fix CO_2 .

The big question associated to planets that can bear liquid water and orbiting low temperature M stars is whether is provided enough flux in the wavelength region useful to make photosynthesis.

On earth the primary production of photosynthesis is oxygen.

Wolstencroft and Raven (2002) asserted that oxygenic photosynthesis on other planets is possible, even in different radiation conditions and with different flux densities.

Moreover, Heath et al., (1999) studied the temperature distribution and the radiation zones suitable for Earth-like plants photosynthesis on the surface of tidally locked M star planets and found some regions that could be favorable.

In Tarter et al., (2007) can be found a limit for M star "forest habitability" between 283 and 323 K.

The cold and hot limits of CO_2 uptake of plants on Earth have been found to be 268-273 K and 318-323 K while the temperature ranges at which CO_2 uptake is 50% are 288-293 K and 313-318 K.

Oxygenic photosynthesis on an extrasolar planet can be possible with a broader spectrum other than visible one. On M star planets, even though a small part of the spectrum is in the visible band, this type of photosynthesis can still be present and operate though with smaller productivity (Kiang et al., 2007b).

Anoxygenic photosynthesis is the oldest form of photosynthesis. Unlike the oxygenic one, it can produce a different bouquet of elements in the atmosphere.

Unlike Earth's modern-day ecosystem, global anoxic ecosystems may drive an atmosphere toward equilibrium. For example, in the anoxic Archean biospheres considered by Kharecha et al. (2005), methanogens and acetogens combine H_2 and CO with CO_2 and H_2O to produce CH_4 .

The biosignature potential of S-bearing gases was reviewed by Pilcher (2003), who focused on gases with bonds between methyl groups ($-CH_3$) and sulfur: methanethiol (CH_3SH , also known as methyl mercaptan), dimethyl sulphide (CH_3SCH_3 or DMS), and dimethyl disulfide ($CH_3S_2CH_3$ or DMDS). More recently, Vance et al. (2011) suggested that CH_3SH could be used as an in situ signature for life on Mars. On modern Earth, the production of these species is dominated by biota, but they are rapidly destroyed by photolysis and by reaction with hydroxyl (OH) radicals (Kettle et al., 2001), and do not build up to concentrations detectable across interstellar distances (Domagal-Goldman et al., 2011). Other biogenic gases are COS, CS_2 and

hydrogen sulphide (H₂S). For this last one, though it is another S-bearing gas produced by biota, large quantities of this species enter the atmosphere via volcanism. Thus, it is not considered as a biosignature.

The modern-day organic sulphur-composed molecules fluxes, predominantly biological in source, are as follows (in units of molecules cm⁻²s⁻¹): 0 for DMDS, 4.2 x 10⁹ for DMS, 0 for CH₃S, 8.3x10⁸ for CH₃SH, 1.4 x 10⁷ for CS₂, 1.4 x 10⁷ for OCS, and 0 for CS (Kettle et al., 2001). DMDS, CH₃S and CS have zero biological production but produced photochemically from other organic sulphur-producer species.

Global productivity by anaerobic organisms make it difficult to detect because the magnitude of gases produced is small (Canfield et al., 2006), but if there is enough biomass they can be revealed.

Most sulphur species are produced via methylation of (addition of methyl groups to) CH₃SH or dehydrogenation of (removal of H atoms from) CH₃SH, or both. The main modern-day global source of CH₃SH is the degradation of methionine, an amino acid that contains a terminal methio group (-SCH₃), from eukaryotes (Domagal-Goldman et al., 2011).

Anaerobic metabolism have difficulty in sustaining pluricellular organisms and so it is difficult to have enough biomass to produce detectable marks (Caitling et al., 2005).

While it may be possible to detect sulphuric acid biosignatures, there would be the risk of false-positive results (Domagal-Goldman et al., 2011).

Nevertheless there is evidence of anaerobic worms that live with sulfur cycles in deep water depths.

The sulfates instead, are provided by aerobic microbial symbionts (Woyke et al., 2006).

The direct production of CH₃SH for metabolic purposes could lead to higher Sorg fluxes. *Methanosarcina acetivorans*, a methanogen, can produce CH₃SH via the metabolic reaction 3CO +H₂S +H₂O/ CH₃SH + 2CO₂ (Moran et al., 2008).

On Earth, all N₂O production is by anaerobic activities of denitrifying bacteria (Lammer et al., 2009).

Organic sulphur-composed molecules absorb in the 8-12 μm window, which can be used to discern surface temperatures because on modern Earth is the most transparent to IR radiation emitted from the surface.

An increase in greenhouse gases though would increase opacity in this region, decreasing the effectiveness with which the surface temperature can be ascertained.

For anoxic atmospheres, it is important to be able to detect Sorg absorption features at wavelengths shortward of the window region.

Absorption by DMS and DMDS between 6 and 9 μm provides an extra constraint on the abundance of these gases. Similarly, the C₂H₆ feature could be used in conjunction with photochemical models to further constrain the Sorg flux rates. A comprehensive characterization of an anoxic atmosphere could therefore be achieved with spectra from 6 to 13 μm (and preferably down to 5 μm and out to 20 μm to help constrain water abundances) at a spectral resolution of at least 20 and a S/N greater than 15.

These baseline parameters are consistent with the current requirement goals for the TPF-I and ARIEL mission concept (Domagal-Goldman et al., 2011).

Though oxygenic photosynthesis is the most favorite and the most likely to be successful on other planets, even the anoxygenic one can be revealed using the right tools.

Anoxygenic photosynthesis could be the dominant form of photosynthesis, if there were abundant non-H₂O electron donors (Kiang et al., 2007b).

M star spectra starts at about 400 nm and peak at about 991 nm in NIR. Normally photosystems can only use photons whose energy exceeds a threshold value of approximately 1.8 eV (700 nm). Longer wavelengths are not even absorbed by chlorophylls and other photosynthetic antenna pigments. (Antal et al. 2012)

Although, as said, oxygenic photosynthesis on Earth is limited to photosystems that operate at 400–730 nm, anoxygenic photosynthesis can occur at wavelengths as long as 1,015–1,020 nm (Trissl, 1993; Scheer, 2003 in Kiang et al., (2007a, b). So, more or less every photosynthetic bacteria or algae could use an M class star spectrum to activate photosynthesis. The main constraint is their light requirements.

Moreover a process called photon up-conversion (PUC) can turn NIR radiation into a useful radiation for photosynthesis. Especially concerning cyanobacteria growing in endolithic habitats (is means that they grow inside rocks), changes in insulation would not influence the occurrence of photosynthesis as they are already adapted to low light conditions on Earth. Chasmoendolithic cyanobacteria (like *Chroococcidiopsis*) are exposed to irradiance ranging from 0.3 to 1400 μmol of photons m⁻² s⁻¹ so would not be impaired by a low light condition of a M class star. In figure 3.12 is represented a picture of *Chroococcidiopsis spp.*

O_2 production in *Chroococcidiopsis* (evolution – uptake) was recorded to be around 40 fmol/cell/h in normal growth condition ($20 \mu\text{mol}$ of photons $\text{m}^{-2} \text{s}^{-1}$). Taking as approximation a typical bacterial cell mass around 1pg this would lead to $\sim 40 \text{ mmol/g/h}$. *Chroococcidiopsis* normal growth condition of $20 \mu\text{mol}$ of photons $\text{m}^{-2} \text{s}^{-1}$ corresponds to 4.84 W m^{-2} at 494 nm.

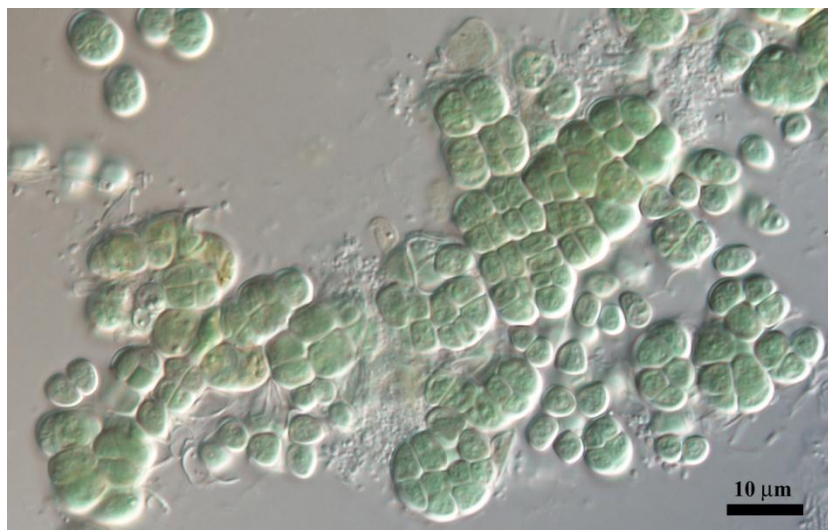


Figure 3.12: A colony of *Chroococcidiopsis* spp.

As already said, the presence of a red edge, or any surface biological signature, depends upon the photosynthetic organisms growing on the planetary surface influencing reflected light. In many environments, microbial phototrophs are hidden beneath substrates, but they remain sufficiently close to the surface to collect light for photosynthesis (Cockell and Raven, 2004). This phenomenon (which can be called "cryptic photosynthesis") is particularly common in extreme environments where organisms may escape detrimental conditions on the surface, such as desiccation and UV radiation, within shielded micro-habitats. This phenomenon raises the possibility of a 'false-negative' detection of life if the alteration of surface reflection spectra, including the red edge, is used as a criterion for habitability, i.e., an atmospheric spectral signature of photosynthesis – oxygen or ozone – indicates habitability but no surface reflected signature is found. Raven (1995) provides estimates for many microbial non-cryptic biota, e.g. $1248 \text{ g O}_2/\text{m}^2/\text{y}$ for a mat of filamentous cyanobacteria, $4577 \text{ O}_2/\text{m}^2/\text{y}$ for epilithic green algae with a CO_2 pump, $4993 \text{ O}_2/\text{m}^2/\text{y}$ for liverworts with intercellular gas spaces. The open ocean is estimated to produce about $475 \text{ g O}_2/\text{m}^2/\text{y}$ (Whittaker, 1975, Field et al., 1998, del Giorgio and Williams 2005). Some workers have attempted to estimate the annual productivity of communities taking into account nanoclimate data acquired in the field. The mean net photosynthetic uptake of Antarctic cryptoendoliths is estimated to be $606 \text{ mg C/m}^2/\text{y}$ (Friedmann et al., 1993). Assuming a classic stoichiometric production of O_2 for CO_2 taken up in photosynthesis, this is equivalent to the production of $2.2 \text{ g O}_2/\text{m}^2/\text{y}$. If these communities covered the entire planetary surface then their annual O_2 output could be $\sim 1.1 \times 10^{15} \text{ g/y}$. The quantity of oxygen in the atmosphere today is $\sim 1.5 \times 10^{18} \text{ kg}$. Therefore, in theory these communities could produce the total quantity of O_2 found in the present atmosphere in about 1.3 Myr. Not all organic carbon is buried to cause net O_2 atmospheric accumulation. If 0.1% of the net carbon taken up by the endoliths is eventually buried as is assumed for deep sea sediments (Hedges, 2002), then it would take approximately 1.3 Gyr to accumulate today's oxygen concentration. However, generating this concentration is not required to produce a detectable oxygen biosignature. Kaltenecker et al. calculate that the lowest concentration of oxygen that could be detected in a planetary atmosphere is 10^{-3} PAL (Present Atmospheric Level) for a resolution of 70 in the visible and 25 in the mid IR (Kaltenecker et al. 2007). Thus, oxygen accumulation to detectable levels could occur much more rapidly. In figure 3.13 are shown the results of Cockell et al., (2009) for cryptic photosynthesis simulations.

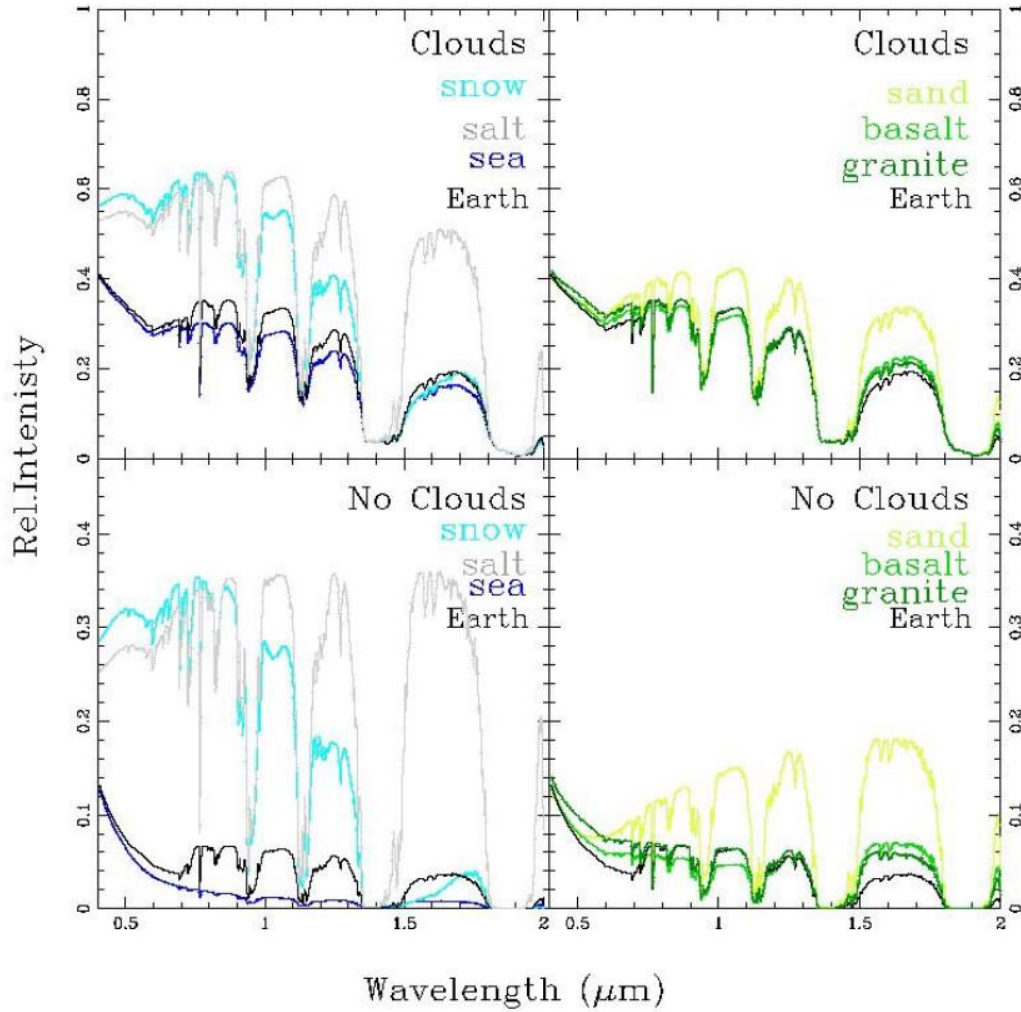


Figure 3.13. Calculated reflection spectra from 0.4 to 2 μm (the visible to near-IR region) for different cryptic photosynthesis habitats (left: snow, salt, sea) (right: sand, basalt, granite) compared to present-day Earth with clouds (case b, upper panel) and with no clouds (case a, lower panel) for a disk averaged view Cockell et al., (2009). We assume here that the surface area covered by vegetation on current Earth is replaced by the habitat of the chosen cryptic biota. Substrates represent typical habitats for different cryptic biota (see Table 6.29).

In order to understand the conversion between PPF_D[W m⁻²] to PPF_D[mol of photons m⁻² s⁻¹] it is necessary to know the energy of a photon. It is defined as:

$$E' = hv = \frac{hc}{\lambda} \left[\frac{\text{J}}{\text{photons}} \right] \quad (3.25)$$

with $h=6.626 \times 10^{-34}$ Js and $c= 299792458$ m/s.

The energy of a mole of photons is

$$E_{\text{mol photons}} = N_A hv = N_A \frac{hc}{\lambda} \left[\frac{\text{J}}{\text{mol of photons}} \right] \quad (3.26)$$

and

$$\frac{1}{E_{\text{mol photons}}} = \frac{1}{N_A hv} = \frac{\lambda}{N_A hc} \left[\frac{\text{mol of photons}}{\text{J}} \right] \quad (3.27)$$

The photon density flux (PPFD) in unities of [mol of photons m⁻² s⁻¹] is given by:

$$\text{PPFD}[\text{mol of photons m}^{-2}\text{s}^{-1}] = \frac{10^6}{E_{\text{mol photons}}} \text{PPFD}[\text{W m}^{-2}] = \frac{\lambda}{N_A h c} \text{PPFD}[\text{W m}^{-2}] \quad (3.28)$$

and vice versa

$$\text{PPFD}[\text{W m}^{-2}] = \frac{N_A h c 10^{-6}}{\lambda} \text{PPFD}[\text{mol of photons m}^{-2}\text{s}^{-1}] \quad (3.29)$$

The conversion factors depend on the wavelength and have been calculated in APPENDIX G. In table 3.11 can be seen the global time averaged PPFDs and the O₂ and CO₂ flux from Net Primary Production (NPP) for a 26% ice-free land and 71% ocean for planets around other stars as in Kiang et al., (2007b). We can define Gross primary production (GPP) the rate at which an ecosystem's producers capture and store a given amount of chemical energy as biomass in a given length of time. Part of this fixed energy is used by primary producers for cellular respiration and maintenance of existing tissues, while the remaining fixed energy is referred to as net primary production (NPP). As the M star planets' photon flux in the 0.4-1.1 μm band is more than twice that the Earth's PPFD can be concluded that M stars can host land-based plants (Kiang et al., 2007b). The NPP is than the rate at which all the plants in an ecosystem produce net useful chemical energy. Therefore, photosynthetic organisms during the flaring stage of M star planets should be able to survive even with visible light, though their productivity would be limited to less than 14% of Earth's with smaller flares and less than 4% with very active M stars like AD Leo with daily large flares (Kiang et al., 2007b). The theoretical photosynthetic production limit of 0.1x10⁻⁶ mol of photons m⁻²s⁻¹ corresponds to 0.024 Wm² at a typical wavelength of 494 nm. In table 3.11 are collected the fluxes of photosynthetically productive photons at the inner edge of the HZ of different spectral types.

Spectral type	G2	M0	M1	M2	M3	M4	M5	M6	M7	M8
Blackbody <i>T_{eff}</i> (K)	5860	3850	3720	3580	3470	3370	3240	3050	2940	2640
<i>λ_{max}</i> (nm)	494.37	752.47	778.76	809.22	834.87	859.64	894.14	949.84	985.37	1097.35

Table 3.11: Integrated fluxes of photosynthetically productive photons at the inner edge of the HZ of different spectral types.

From the previous table (Table 3.11) can seen the temperatures, *T_{eff}* and black body peak wavelengths of M-type stars, compared with sun.

Thanks to this table and APPENDIX F it is possible to calculate the irradiance for different type of stars.

From Table 3.12 can be seen that the integrated fluxes of photosynthetically productive photons at the inner edge of the HZ of a planet orbiting a G2V and M0 star are respectively 14.4x10²⁰ photons m⁻²s⁻¹ and 4.63x10²⁰ photons m⁻²s⁻¹ that can be expressed in W m⁻² and their value is respectively 579.03 W m⁻² and 122.23 W m⁻², as in Wolstencroft and Raven (2002).

The irradiation value for an M0 star is 4.74 times smaller than that for a G2V star.

3.4.1 Photosynthetic Active Radiation (PAR)

Because of these constraints is useful to introduce the concept of Photosynthetic Active Radiation (PAR).

PAR is the spectral region inside which organisms are photosynthetically active. On M star planets can be lower than the average terrestrial value ever by an order of magnitude (Heath et al., 1999). Nevertheless this could not represent a problem because several marine organisms on Earth evolved to use only 5x10⁻⁴ times the average flux received at the Earth's surface, like sulfur bacteria that embed a large antenna complex, the chlorosome, that permit to use only small fractions of light intensities (McKay, 2000). In these regions radiation is dominated by red or IR radiation.

Heath et al., (1999) estimates that PAR arriving on a planet from a *T_{eff}* = 4000 K star at solar Earth insulation radius is about 1/3 and the window of photic radiation (PZWR) is 1/4 of that incident on Earth.

For a *T_{eff}* = 2800 K star these are respectively 1/12 and 1/20 (Heath et al., 1999).

Zhang et al., (2004) estimated the Earth's average annual 0.4-0.7 μm photosynthetic photon flux density per surface area as 3.1×10^{20} photons $\text{m}^{-2} \text{s}^{-1}$, for clear sky conditions and 2.4×10^{20} photons $\text{m}^{-2} \text{s}^{-1}$, including clouds (with a General Circulation Model and with satellite and ground data).

As can be seen clouds operate a 24 % reduction of surface visible radiation.

The upper limit of photon flux density at which photosynthesis can occur on Earth is set by the availability of non-photon resources used in constructing and using the photosynthetic apparatus and by the occurrence of photo damage at high photon flux densities (Wolstencroft and Raven, 2002 and references therein). In fact, some plants on Earth could grow at a photon flux density of 6000–9000 $\mu\text{mol photon m}^{-2} \text{s}^{-1}$, despite the maximum natural photon flux density (400–700 nm) on Earth being 2000 $\mu\text{mol photon m}^{-2} \text{s}^{-1}$. It has been suggested that photosynthetic primary production can occur on land on an ELP with 10,000 $\mu\text{mol photon m}^{-2} \text{s}^{-1}$; aquatic habitats permit the screening of supra-optimal irradiance by water, provided the water is deep enough (Falkowski and Raven 1997).

On Earth, gross primary productivity (GPP)—GPP is defined by biogeochemists as the gross amount of carbon fixed excluding respiration (on land ranges from 90 to 120 Pg-C/year, Cramer, 1999) for an ice-free land area of $1.32 \times 10^{14} \text{ km}^2$ (about 26% of the Earth's surface). Ocean productivity is approximately the same, but spread over 71% of the Earth's surface. Ocean productivity, in fact, is the main contributor to atmospheric oxygen through carbon burial. The annual surface incident PAR (400–700 nm) of 2.6×10^{20} photons/ m^2/s gives then an average quantum yield of just 0.006 fixed CO_2 per incident PAR photon for land and 0.002 for the ocean (Kiang et al., 2007b).

Moreover, for M0V parent stars Wolstencroft and Raven (2002) suggested that, because of the longer wavelength of radiation from these stars, it is possible that a three-or four-photon mechanism might bring the photosynthetic rate closer to that on the present Earth, even granted that absorption by atmospheric CO_2 and H_2O vapor diminishes the potential for (especially land surface) photosynthesis at very long wavelengths.

In Table 3.12 are shown the surface photon flux densities for cloudless planets (a) at solar noon and (b) illuminated face average for different stars as in Kiang et al., (2007b).

	Photon flux density ($\times 10^{20}$ photon/ m^2/s)									
	F2V (1 PAL) (Sun/Earth)	G2V (1 PAL)	K2V (1 PAL)	M1V (1 PAL)	M4.5V (1 PAL)	M5V		M5V Under water ($\text{O}_2 \times 10^{-5}$)		
						($\text{O}_2 \times 10^{-5}$)	1 PAL	5 cm	100 cm	
a. Solar noon										
UVB 280–315 nm	0.049	0.018	0.015	0.001	0.000	0.000	0.000	—	—	—
UVA 315–400 nm	2.319	0.871	0.588	0.095	0.021	0.016	0.016	—	—	—
PAR										
400–700 nm	16.4	11.0	11.5	6.1	1.8	1.5	1.5	1.4	1.1	
400–1,100 nm	29.8	23.8	26.3	23.2	16.1	17.3	16.9	9.9	1.5	
400–1,400 nm	34.0	28.6	32.1	29.3	23.7	25.7	24.9	10.2	1.5	
400–1,800 nm	37.9	33.7	38.9	36.4	34.2	35.3	34.3	10.2	1.5	
400–2,500 nm	40.5	36.9	43.3	40.2	40.0	40.1	38.4	10.2	1.5	
Peak photon flux	450.8	668.5	666.6	753.5	1,045.1	1,042.8	1,042.8	1,073.2	1,073.2	
Wavelength range (nm)	451.0	685.5	667.8	754.3	1,045.9	1,043.6	1,043.6	1,075.7	1,075.7	
b. Illuminated face average										
UVB 280–315 nm	0.006	0.017	0.003	0.000	0.000	0.000	0.000	—	—	—
UVA 315–400 nm	0.940	0.518	0.241	0.040	0.009	0.007	0.007	—	—	—
PAR										
400–700 nm	7.5	6.3	5.4	2.9	0.9	0.7	0.7	0.7	0.5	
400–1,100 nm	13.8	12.4	12.3	10.8	7.4	7.8	7.8	4.7	0.7	
400–1,400 nm	15.6	14.2	14.8	13.2	10.6	11.0	11.0	4.8	0.7	
400–1,800 nm	17.4	16.4	17.9	16.2	15.0	15.0	15.0	4.8	0.7	
400–2,500 nm	18.5	17.6	19.8	17.7	17.3	16.5	16.5	4.8	0.7	

In b, average fluxes are approximated by the photon flux at a solar zenith angle of 60° from vertical.

Table 3.12: Surface photon flux densities for cloudless planets (a) at solar noon and (b) illuminated face average for different stars.

In Figure 3.12 is shown the flux of photons absorbed by land plants at the surface of a cloud-free ELP orbiting at the inner edge of the habitable zone for different parent stars: F0V (1.85 AU), G0V (1.02 AU), G2V (0.95 AU), K0V (0.67 AU), and M0V (0.25 AU). The dependence of photosynthesis on photon flux rather than energy flux and the decreasing atmospheric attenuation with increasing wavelength provides a bias in favour of cooler stars.

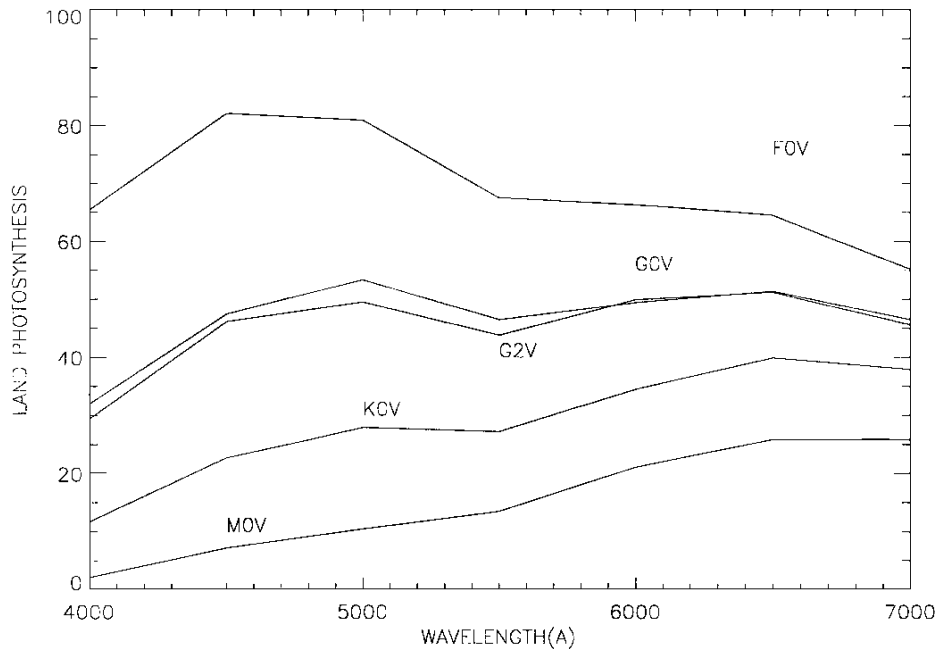


Figure 3.14: Flux of photons absorbed by land plants at the surface of a cloud-free ELP orbiting at the inner edge of the habitable zone for different parent stars: F0V (1.85 AU), G0V (1.02 AU), G2V (0.95 AU), K0V (0.67 AU), and M0V (0.25 AU) (units of 10^{17} photons $m^{-2}s^{-1} nm^{-1}$).

The flux of photons observed by marine algae at 10 m depth and shown in figure 3.15 has been calculated assuming deep ocean seawater transmission, which varies from 97% at the blue peak of chlorophyll (450 nm) to 0.3% at the red peak (about 700 nm).

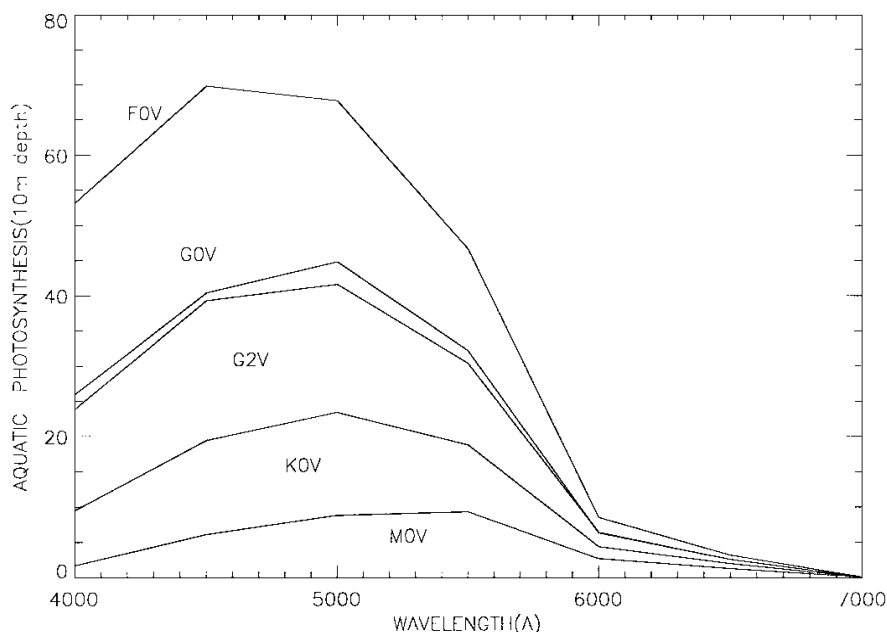


Figure 3.15: Flux of photons absorbed by algae (units of 10^{17} photons $m^{-2}s^{-1} nm^{-1}$) at 10 m ocean depth on a cloud-free planet (direct light from the parent star only) for a planet at the inner edge of the star's habitable zone for five types of main-sequence star.

In table 3.13 are shown the integrated fluxes of photosynthetically productive photons at the inner edge of the HZ of different spectral types as in Wolstencroft and Raven (2002).

Spectral type	Stellar temperature	Inner edge of HZ (AU)	Absorbed photon flux ($\frac{10^{20} \text{ photons}}{m^2 s}$)
F0V	7200	1.85	21.2
G0V	6030	1.02	14.4
G2V	5860	0.95	14.0
K0V	5250	0.67	8.89
M0V	3850	0.25	4.63 (14.4 for a photosynthesis using 3 instead of 2 photons)

Table 3.13: Integrated fluxes of photosynthetically productive photons at the inner edge of the HZ of different spectral types.

According to the above table, a M0V class star has a flux of photosynthetically active photons of 4.63×10^{20} photons $m^{-2} s^{-1}$ which is less than 1 order of magnitude lower than our Sun (G2V). For the ocean the analogous is (Table 3.14):

Spectral type	Inner hedge of HZ (distance, AU)	Absorbed photon flux ($10^{20} \text{ photons } m^2 s^{-1}$)
F0V	1.85	11.4
G0V	1.02	7.2
G2V	0.95	6.8
K0V	0.67	3.8
M0V	0.25	1.5

Table 3.14: Integrated Flux of Photosynthetically Productive Photons at the Inner Edge of the Habitable Zone at 10 m Ocean Depth in the ELP Ocean (Cloud-Free Planet)

Wolstencroft and Raven (2002) discussed the problem of the clouds. The net flux of photons arriving at any given location of the Earth's surface comprises the direct sunlight after transmission through the atmosphere and the diffuse component scattered in the atmosphere (Fleagle and Businger 1963). Both of these components depend on the cloud cover at this location. To estimate the global PAR flux, G , integrated over the planet we need to be able to assess the global cloud cover, which varies with time of year and latitude, as does the type, vertical extent, and opacity of "cloud," and how the diffuse and direct components differ at clear and cloudy sky sites. This information comes from both satellite studies and surface observations from meteorological stations but is not well determined.

The dependence of the flux, Q , of diffuse plus direct solar radiation at surface stations on the cloud cover has been examined by a number of authors, and these studies have been discussed by Coulson (1975). Probably the most useful relation is Ångström's formula (1924)

$$Q = Q(\text{clear}) [k + (1 - k)(n/N)] \quad (3.30)$$

where Q is the flux of diffuse plus direct solar radiation measured on a horizontal surface during a day when n/N is the fraction of the day with bright sunshine, and $Q(\text{clear})$ is the value on a cloudless day ($n/N = 1$); k is a constant that depends on the type of cloud and varies from about 0.25 for stratus cloud to 0.82 for cirrus (Haurwitz 1948).

To deduce the flux of PAR radiation received at the surface of an ELP it is useful to estimate the cloud cover factor $G/G(\text{clear})$. For the Earth we can use of the global version of the previous equation:

$$Q/Q(\text{clear}) = k + (1 - k)(n/N) \rightarrow G/G(\text{clear}) = (1 - f) + kf \quad (3.31)$$

where f is the fraction of global cloud cover. The fraction of the day with bright sunshine, n/N , transforms to the fraction of the planet with no cloud, $(1 - f)$, for which $n/N = 1$ and hence $G/G(\text{clear}) = 1$; and the cloudy fraction of the day, for which $n/N = 0$, transforms to the cloudy fraction of the planet and hence $G/G(\text{clear}) = k$. For simplicity we assume either all clear or all overcast (stratus: $k = 0.25$) conditions: hence

$$G/G(\text{clear}) = 1 - f + 0.25f = 1 - 0.75f \quad (3.32)$$

In table 3.15 can be seen the components of photon flux (in units of $10^{17} \text{photons m}^{-2} \text{s}^{-1} \text{nm}^{-1}$) at the surface of a cloud-free planet at the distance of 1 AU from its parent star and with an Earth-like atmosphere as in Wolstencroft and Raven, (2002).

λ (nm)	A0V	F0V	G0V	G2V	K0V	M0V
350	693	73.0	12.2	16.6	-	-
400	2520	236	35.0	27.9	5.51	0.138
450	2440	299	52.5	44.4	10.9	0.480
500	2240	298	59.7	48.1	13.4	0.703
550	1960	296	62.1	50.7	15.6	1.08
600	1630	264	59.8	52.3	18.0	1.53
650*	1460	245	59.4	51.3	19.9	1.80
700*	1320	231	59.0	50.2	20.7	1.97
800	1120	212	58.5	45.9	21.3	2.23
1000	854	169	49.8	36.4	19.1	2.78

Table 3.15: Components of photon flux at the surface of a cloud-free planet at the distance of 1 AU from its parent star and with an Earth-like atmosphere (*= Interpolated data). (units of $10^{17} \text{photons m}^{-2} \text{s}^{-1} \text{nm}^{-1}$)

3.5 Biomarkers set in context

Biomarkers, as the word says, are defined as biotic signatures that can be detected in the atmospheres of other planets.

Understanding how photosynthesis can evolve in atmospheres different from Earth's one can give a helping hand to better set the future mission targets and to interpret the data.

Photosynthetic organisms can produce gases, like O_2 (or O_3 from its photolysis), and nitric oxides like N_2O , NO_x , CH_3Cl or COS from the breakdown of organic matter.

All these molecules can modify exoplanet's atmospheres in time and can be detected from Earth. O_2 can be produced even abiotically through photolysis and the effects of carbon burial and hydrogen escape. Though, its simultaneous presence with other reduced gases can be explained only with biotic processes that maintain chemical disequilibrium (Kiang et al., 2007b).

Detectability of photosynthetic processes depends as already said on biotic productivity, which depends on several factors, like availability of resources (water, light, minerals, electron donors, nutrients and so on).

As O_2 and O_3 and CH_4 molecules are used as biomarkers, it is crucial to understand the ability of organisms to use photosynthesis on M star planets.

A detectable concentration of O_2 and/or O_3 in combination with reduced gases like CH_4 is a strong signature of biologic activity (Lammer et a., 2009).

The spectrum of the Earth has exhibited a strong infrared signature of O_3 at $9.6 \mu\text{m}$ for more than 2 Gyrs and a strong visible signature of O_2 at $0.76 \mu\text{m}$ for a period of time between 2 and 0.8 Gyrs (depending on the required depth of the band for detection and also the evolution of the O_2 level) (Kaltenegger and Selsis 2007). Is it also true that anaerobic processes developed on Earth in the first phases of its evolution between the first 1-2 Gyr of its life (Scalo et al., 2007).

N_2O is another strong biomarker detectable at 17 μm and 7.8 μm . On Earth it is hard to detect at low resolution because it has a low concentration (3 ppmv) and falls off rapidly in the stratosphere.

There are other molecules that could, under some circumstances, act as excellent biomarkers, for example, the manufactured chloro-fluorocarbons (CCl_2F_2 and CCl_3F) in our current atmosphere in the thermal infrared waveband, but their abundances are too low to be observed spectroscopically at low resolution (Segura et al. 2005). Water vapour is a signature of planet habitability. It can be seen in the visible and IR bands. In the visible-IR band (0.5-1 μm) the regions that show absorption features of this molecule are at 0.7, 0.8 and 0.9 μm , while other bands are at 1.1, 1.7 and 1.9 μm . In the MIR water can be detected between 5 μm and 8 μm and from 17 μm to 50 μm . CH_4 absorbs in the wavelength between 6 and 7 μm .

A big deal is not to let terracentrism lead our thoughts and try to think as an M star planet organism.

In fact, processes that are common on earth may not be so common on other planets due to different environment, geological and atmospheric conditions as well as different irradiation features.

Organisms on an M star would face a fewer deficit in of photons at wavelengths less than 0.50-0.60 μm , increasingly bigger with the decreasing wavelength down to 0.100 μm . This assertion is not valid during the irradiation of flares.

Photosynthesis due to “typical” plants such as the oleander (*Nerium oleander*) would generate O_2 molecules globally at the photosynthetic rate, $p(\lambda)$, in units of O_2 molecules/s, where

$$p(\text{land}) = 1.25 \times (1/8) \times hBq_1 \times (G/G(\text{clear})) \times T_1 \times F_{abs} \quad (3.33)$$

and where the factor 1.25 allows for the diffuse sky radiation; (1/8) accounts for the number of absorbed photons needed to generate one molecule of O_2 ; B is the cross-sectional area of the solid planet, h is the fraction of the Earth where surface photosynthesis as opposed to aquatic photosynthesis takes place; q_1 is the effective fraction of that surface covered in such plants (allowing for the density of plants and nutrient availability); $G/G(\text{clear})$ allows for cloud cover; T_1 is an atmospheric transmission factor that takes account of the air mass; and F_{abs} , is proportional to the flux of photons absorbed by the plant pigments.

In Table 3.16 can be seen the direct Component of Flux of Photons Absorbed by Land Plants at the Surface of a Cloud-Free Planet for Unit Air Mass for an extrasolar planet 1 AU from Its Parent Star.

$\lambda(\text{nm})$	A0V	F0V	G0V	G2V	K0V	M0V
400	2394	224	33.3	26.5	5.23	0.131
450	2294	281	49.4	41.7	10.2	0.451
500	1083	277	55.5	44.7	12.5	0.654
550	1529	231	48.4	39.5	12.2	0.842
600	1402	227	51.4	45.0	15.5	1.316
650	1314	221	53.5	46.2	17.9	1.620
700	1082	189	48.4	41.2	17.0	1.615

Table 3.16: direct Component of Flux of Photons Absorbed by Land Plants at the Surface of a Cloud-Free Planet for Unit Air Mass for an extrasolar planet 1 AU from Its Parent Star.

On a tidally locked planet with zero orbital obliquity in stellar radiation no seasonal or diurnal variations in the insulation are expected and photosynthesis reaction centers are supposed to be all oriented in the same direction (Heath et al., 1999).

In a tidally locked planet, the sub stellar point (SP) for a given SI would be warmer than if the stellar radiation would be distributed evenly in longitude. This would produce an inner edge at a lower SI than G stars.

It has been said that ocean-covered tidally locked Earth has a mean albedo of 0.35, that is 20% higher than planets not tidally locked (Joshi, 2003).

Another negative effect of the synchronous rotation is that as the insulation conditions are the same, there are permanent light and dark regions and there is no sunfleck precession for hypothetical forests.

Photosynthesis can theoretically proceed in low energy conditions. In fact a study of Wolstencroft and Raven (2002) underlines how a photosystem could use 12 rather than 8 photons per O_2 in a PAR range of 0.6-1.05

μm , while Heath et al., (1999) extended the PAR range to 1.46 μm with an upper limit of 2.1 μm (Scalo et al., 2007).

In Kiang et al., (2007b) is asserted that for M stars PAR bands in the NIR are restricted to a 1.04 μm three photosystem upper wavelength limit for the energy required for PSI and PSII, a 1.10 μm upper wavelength thermal limit and transmittance windows where there is the most available radiation.

Photosynthetic organisms suffer a severe drop in photosynthetic skills for $\lambda > 680 \text{ nm}$, better said "red drop".

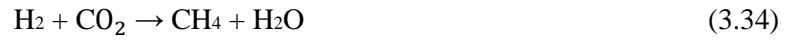
In other words a sharp decrease in quantum yield (the number of oxygen molecules released per light quanta absorbed) at wavelengths greater than this value takes place in the red part of the spectrum.

Then, the reflectance has a plateau at 720-760 nm.

Seager et al., (2013) have developed a new method for linking biosignature gas detectability to biomass estimates, including atmospheric photochemistry and biological thermodynamics.

They identify three types of biosignatures: Type I biosignature gases are generated as by-product gases from microbial energy extraction. The biomass model derived from these gases is based on thermodynamics.

Type I biosignature gas discussed for exoplanets is CH_4 produced from methanogenesis via the reaction



Typical Type I biosignature gases produced by Earth-based microbes are H_2 , CO_2 , N_2 , N_2O , NO , NO_2 , H_2S , SO_2 and H_2O .

The biomass estimate Σ_B expressed in gm^{-2} is a complicate equation:

$$\Sigma_B = \left\{ \Delta G_0 + RT \ln \left[\frac{[A]^n [B]^m}{[X]^o [Y]^p} \frac{F_{source}}{Ae^{-\frac{E_A}{RT}}} \right] \right\} \quad (3.35)$$

where ΔG_0 is the "standard free energy", the free energy available when all the reactants are in their standard state, 1 molar concentration (for solutes) or 1 atmosphere pressure (for gases).

Q_i is the stoichiometric balance of the equation



The biosignature gas source flux F_{source} (in units of $\text{mol mol}^{-2} \text{s}^{-1}$) describes the surface flux emitted as the metabolic byproduct.

The minimal maintenance energy rate, P_{me} , in units of $\text{kJ g}^{-1} \text{s}^{-1}$, is the minimal amount of energy an organism needs per unit time to survive in an active state (for example a state in which the organism is ready to grow).

$$P_{me} = Ae^{-\frac{E_A}{RT}} \quad (3.37)$$

Here $E_A = 6.94 \times 10^4 \text{ J mol}^{-1}$ is the activation energy, $R = 8.314 \text{ J mol}^{-1} \text{K}^{-1}$ is the universal gas constant, and T in units of K is the temperature. The constant A is $3.9 \times 10^7 \text{ kJ g}^{-1} \text{s}^{-1}$ for aerobic growth and $2.2 \times 10^7 \text{ kJ g}^{-1} \text{s}^{-1}$ for anaerobic growth (Tijhuis et al. 1993) (here per g refers to per g of wet weight of the organism).

P_{me} is even the minimal energy needed for a bacterial cell to keep going under conditions under which it is capable of growth, is measured during growth, and is extrapolated to growth = 0.

Type II biosignature gases are instead the by-products of the metabolic reactions for biomass building.

This processes require energy. Though, for Type II biosignature gases there is no useful biomass model because once the biomass is built a Type II biosignature gas is no longer generated.

On Earth photosynthesis captures carbon for biomass building comes from this reaction



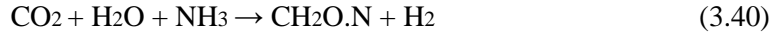
where CH_2O represents sugars.

For the process of building biomass in an oxidized environment, where carbon is tied up as carbonates or CO_2 , living organisms have to generate a highly oxidized by-product in order to reduce CO_2 to biomass.

The most plausible oxidized species is molecular oxygen itself.

Other potential oxidized Type II biosignature gases include volatiles that are oxidized forms of nitrogen (nitrogen oxides) or halogens (molecular halogens, halogen oxides or halates, all other common elements that could form volatile chemicals are completely oxidized in the Earth's surface environment.

Moreover, on a planet with a reduced atmosphere, these reactions take place:



And because H₂ is the by-product gas, (already abundant in an H-rich atmosphere), there are no useful Type II by-product candidate biosignature gases.

Finally, Type III biosignature gases are produced by life but they are not by-products of their central chemical functions. These gases appear to be special to particular species or groups of organisms, and require energy for their production. Moreover, they are not linked to the local chemistry and thermodynamics, and this biomass model is an estimate based on field fluxes and lab culture production rates.

There are a wide range of Type III biosignatures including sulphur compounds [DMS, OCS, CS₂ (Domagal-Goldman et al. 2011)]; hydrocarbons; halogenated compounds [CH₃Cl (Segura et al. 2005), CH₃Br] and a variety of volatile organic carbon chemicals (VOCs including isoprene and terpenoids).

These products are sometimes called the products of secondary metabolism (Seager et al. 2012).

These gases are unlikely to be made geologically in substantial amounts, and so are unlikely to be present in the absence of life. In general, the more complicated a molecule is (i.e., the more atoms it has) and the further from fully oxidized or reduced the molecule is, the less are produced by geological sources as compared to more simple molecules.

Type III biosignatures are not directly tied to the environment and therefore could be produced by life on any exoplanet.

The biomass surface density can be calculated by taking the biosignature gas source flux F_{source} (in units of $\text{mol m}^{-2}\text{s}^{-1}$) divided by the mean gas production rate in the lab R_{lab} (in units of $\text{mol g}^{-1}\text{s}^{-1}$):

$$\Sigma_B = \frac{F_{source}}{R_{lab}} \quad (3.41)$$

The source flux is measured in the field (F_{field}) but assumed or calculated for exoplanet biosignature gas detectability models (and called F_{source}).

The source flux is described by

$$F_{source} = \int_z L[A] + \Phi_{dep} = \int_z K_{AB}[A][B] + nv_d \quad (3.42)$$

where L is the loss rate and [A] is the steady state gas concentration.

[B] is the steady state gas concentration of the second reactant and K_{AB} is the second order reaction rate in units of $\text{m}^3\text{molecule}^{-1}\text{s}^{-1}$.

Φ_{dep} is the deposition flux, or the deposition velocity at the planetary surface, where n is the number density (in units of molecules m^{-3}) at the surface of the species under consideration, and v_d is the dry deposition velocity (in units of ms^{-1}).

If the loss rate is due to photochemical dissociation of species,

$$L[A] = J(A) = \int_\lambda q_\lambda I_\lambda e^{-\tau_\lambda} \sigma_\lambda[A] d\lambda \quad (3.43)$$

where J is the photo dissociation loss rate, q_λ is the quantum yield, I_λ is the stellar intensity, $e^{-\tau_\lambda}$ is the attenuation by optical depth τ_λ , $\sigma_\lambda[A]$ is the photodissociation cross section of the species A, and is λ wavelength.

3.6 Red edge and Vegetation Red Edge (VRE)

Among the other life detection methods must be cited the Vegetation Red Edge (VRE) one.

VRE is a surface feature of terrestrial plants that is characterized by the dominant spectral signature of the green plants, that absorb between 0.4 and 0.7 μm but less in the green part of the spectrum while in the IR band reflect between 0.7 and 0.85 μm .

This phenomenon, called "red edge", or vegetation red edge (VRE) cause an apparent discrepancy between the visible and IR spectral band (Tucker, 1976; Grant, 1987).

The dominant color of photosynthetic organisms on other planets can be different because of various reasons. The first is that, as the spectral fluxes are different, the peak of absorbance is different itself and take advantage of the available light. The second reason is that evolution could have led phycobilin-tipe pigments occurring in surface photosyntheticizers. Anyroad, the color could be the same because of the nature of energy funneling from the bluest, most energetic wavelengths to the redder wavelengths in the reaction centers (Kiang et al., 2007b).

Red edge could be detectable in combination with other gases like O_2 or O_3 (Seager et al., 2005).

Wolstencroft and Raven (2002) also asserted that photosynthetic pigments may have evolved adapting to different stellar types, possibly using more photons for carbon fixed, so that the "red edge" may not be red.

As detectability depends on the photosyntheticizers cover and density on the planet, Tinetti et al., (2006b) also found that vegetation must cover at least 20% of the planet's cloud free surface to be detectable, while in Tinetti et al., (2006c) simulated an extrasolar vegetation reflectance spectrum for planets orbiting around M stars by shifting the Earth reflectance spectrum so as the red edge is in the NIR.

In figure 3.16 are represented the spectral reflectance's of different taxa on Earth and in particular for (a) land-based vascular plants, (b) aquatic vascular plants, (c) mosses, (d) lichens, (e) algae, and (f) different layers of a microbial mat in an alpine lake. It is evident that all photosyntheticizers have a red edge, except purple bacteria that have a strong absorbance in the NIR. The purple bacteria are *Chromatium* species, anoxygenic photolithoautotrophs with BChl a or BChl b, and engage in sulphide reduction. By comparison, hematite and (live) human skin show some similarities to the photosynthetic organism spectra in that they have a colour in the visible and high reflectance at longer wavelengths, but which are very different from those of the red edge features (Kiang et al., 2007a and references therein).

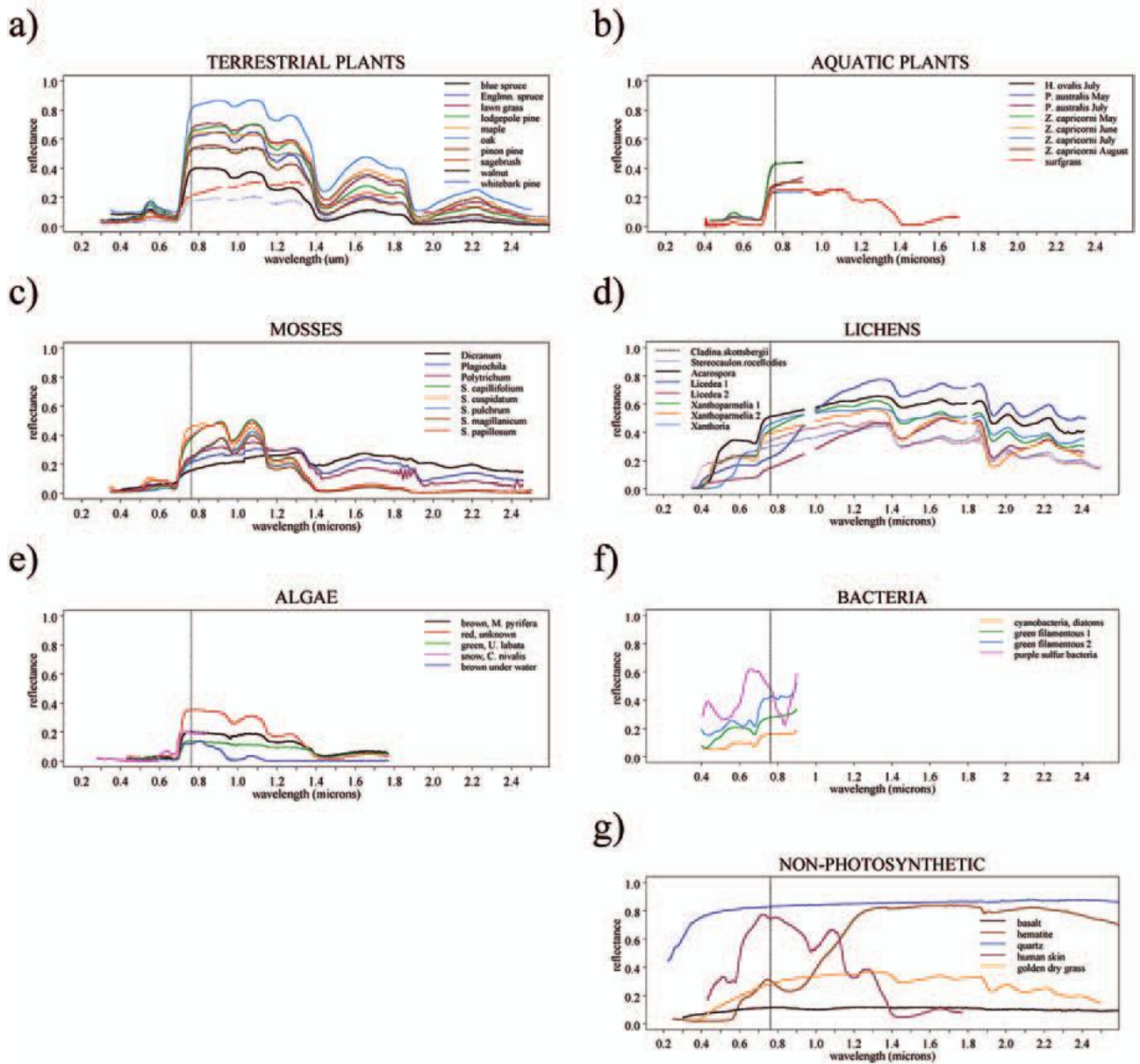


figure 3.16: Reflectance spectra on Earth for (a) land-based vascular plants, (b) aquatic vascular plants, (c) mosses, (d) lichens, (e) algae, and (f) different layers of a microbial mat in an alpine lake (Kiang et al., 2007a and references therein)

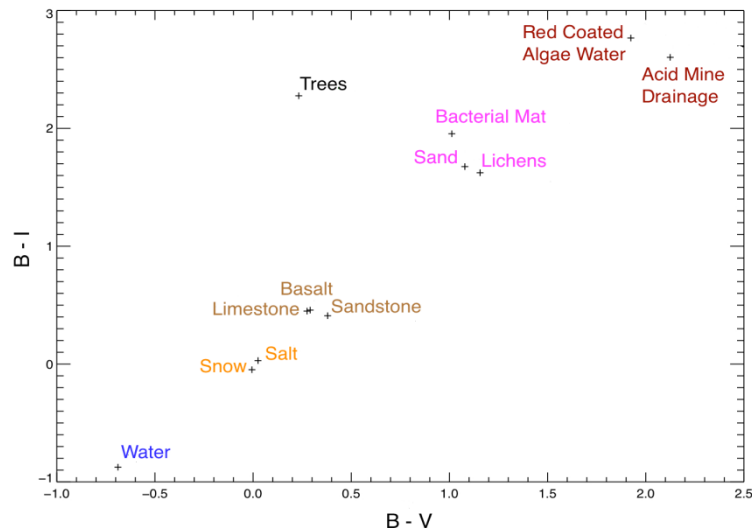


Figure 3.17: Color-color diagram based on observed reflection spectra of characteristic surfaces that support extremophiles on Earth as well as bacterial mat, lichens and trees using conventional Johnson-Cousins BVI filters.

In figure 3.18 are linked the habitats to some species that live inside them. The plot indicates as to where the different classes of extremophiles fall, distinguishing an environment that is aerobic (3.18a) and anaerobic (3.18b). The VRE surface albedo is shown in for reference. Note that the data points for photosynthesis-based organisms have been removed from the anaerobic plot, as they are aerobic in nature (Hegde and Kaltenecker., 2013). In 3.18c are shown the data point represented in blue denotes the position of Present-day Earth: it is modelled by assigning 70% of the planetary surface as ocean, 2% as coast, and 28% as land. The land fraction consists of 60% vegetation, 9% granite, 9% basalt, 15% snow and 7% sand.

It can be seen that the addition of water surface fraction from 10% to 90%, moves the position of the planet in the color-color diagram along a diagonal.

The albedo and therefore the position in a color-color diagram of vegetation or any chlorophyll-bearing photosynthetic organism on an extrasolar rocky planet depend on the radiation received from the host star. For example, the chlorophyll signature for planets around hot stars, may have a “blue-edge” to reflect some of the high energy radiation in order to prevent the leaves from overheating (Kiang et al., 2007b).

Plants on these kind of planets may have developed high superficial concentrations of or foliar waxes and hairs anthocyanins to protect themselves from high energetic photons .

Chlorophyll signature for planets orbiting cooler stars, may appear black due to the total absorption of energy in the entire visible waveband such that plants gain as much available light as possible for photosynthetic metabolism (O’Malley-James et al., 2012). Therefore, the positions of trees, microbial mats and lichens in figure 6.22 are only valid for an Earth-analogue planet orbiting around a Sun-like star and should be taken as guides. The albedo of vegetation and chlorophyll-bearing organisms for non-Sunlike stars requires further studies (Hegde and Kaltenecker., 2013).

In figure 3.19 are some examples of how could appear plants and leaves on F star planets (left column), M star planets (central column) compared with similar species on Earth (right column).

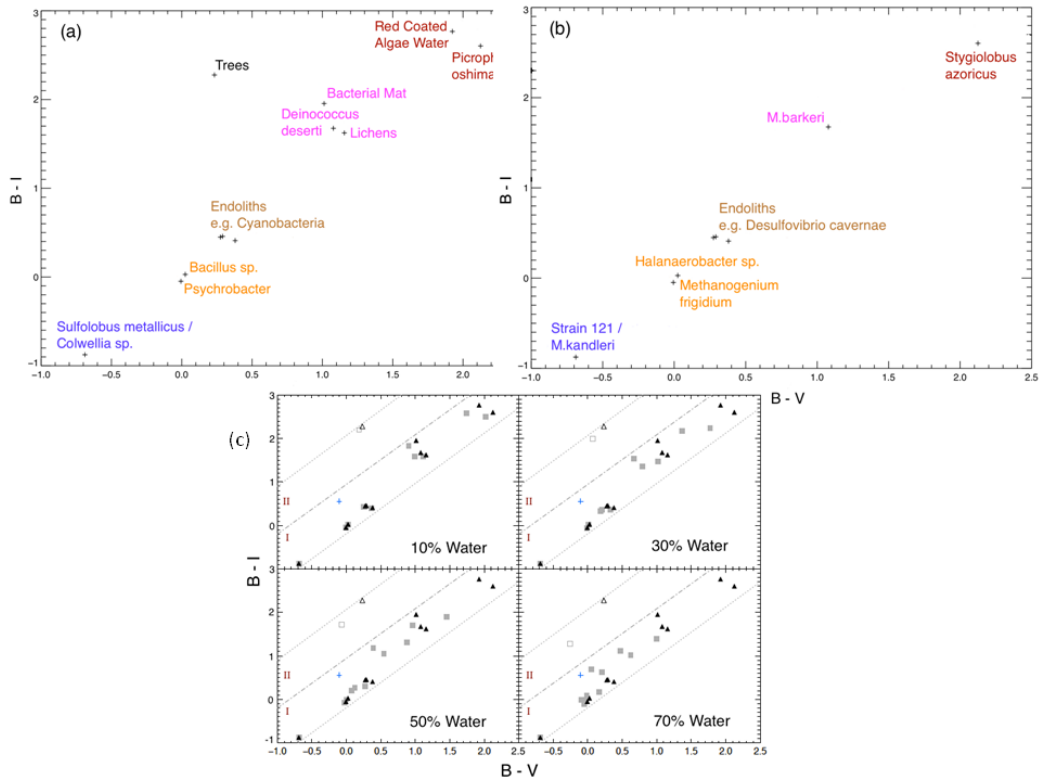


Figure 3.18: Color-color diagram based on observed reflection spectra of characteristic surfaces that support extremophiles as well as bacterial mat and lichens in (a) an aerobic atmosphere (top) and (b) an anaerobic atmosphere (bottom). In (c) filled triangles represent a planet completely covered by a particular surface. Filled squares denote the case when the planet is (a) 90%, (b) 70%, (c) 50% and (d) 30% covered by a particular surface with the rest being liquid water. Trees are shown as non-filled triangles (complete coverage) and squares as reference to other VRE studies. Blue data point represents Present-day Earth. Region I defines the area of extreme Earth surfaces, region II includes surface vegetation for nonextreme forms of life (Hegde and Kaltenecker., 2013).



Figure 3.19: Some examples of how could appear plants and leaves on F star planets (left column), M star planets (central column) compared with similar species on Earth (right column).

From several environments on Earth it is outstanding that, even in the presence of photosynthetic primary producers, the dominant reflectance biosignature comes from biologically produced pigments developed to provide functions other than light capture for photosynthesis. Halophilic archaea such as *Halobacterium salinarum* for example, or bacteria such as *Salinbacter ruber* dominate the spectral reflectance of hypersaline lakes and saltern crystallizer ponds with their nonphotosynthetic pigments (DasSarma, 2006; Oren, 2009, 2013). It is an example the northern portion of the Great Salt Lake, Utah, USA. Its pink coloration is visible in photographs from the International Space Station as well as Owens Lake in California, USA, and the saltern crystallizer ponds of San Francisco, USA.

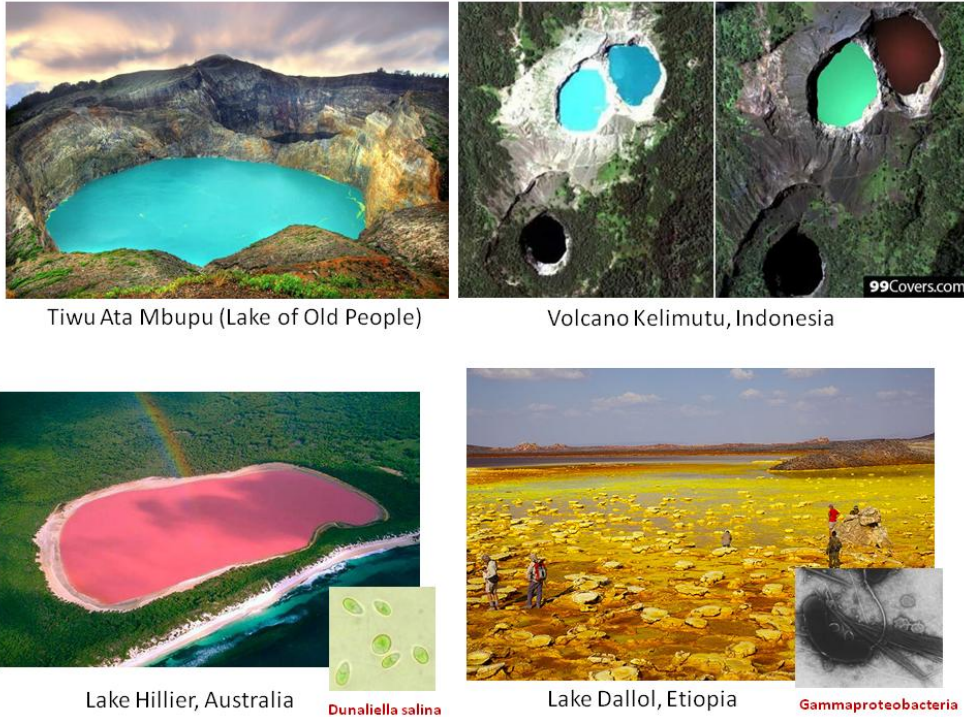
Other environments where pigmented halophiles dominate the spectral reflectance are Lake Hillier in Australia, Lake Retba in Senegal and the Sivash in Ukraine/Russia. Halophilic organisms contain carotenoids such as bacterioruberin, resulting in red, pink, or orange coloration to water above threshold salinities.

Although the photosynthetic primary producers in hypersaline environments are often green algae like *Dunaliella salina*, which also contain carotenoid pigments, it has been found in Oren et al. (1992) and Oren and Dubinsky (1994) that the visible coloration of these lakes is dominated by the halophilic archaea and bacteria and that the cause is the even distribution of pigments in the archaeal cells, which provides them with more surface area per volume and allows them to effectively shade the more concentrated pigments in the *Dunaliella* cells (Oren et al., 1992). Another example where nonphotosynthetic pigments dominate the reflectance spectra are extremophiles and chemotrophic thermophiles at the edges of hot springs, where temperatures can exceed the 73°C temperature limit for photosynthesis (Meeks and Castenholz, 1971). Thermophiles such as *Thermus aquaticus* (Brock and Freeze, 1969), developed such a pigmentation in order to adapt at to oxidative stress and are the responsables of the inner ring of yellow in the Grand Prismatic Spring in Yellowstone National Park, USA. Pigmented thermophilic chemotrophs, and carotenoid-bearing cyanobacteria, are the organisms forming the visible colour gradient across the spring (Dartnell, 2011). The visible red and pink coloration of snow called “Watermelon snow” are caused by the green algae *Chlamydomonas nivalis* (Painter et al., 2001; Williams et al., 2003). This organism thrives at high altitudes and polar regions during the summer using astaxanthin, a red carotenoid pigment, to protect it from UV radiation and to warm the cell by absorbing more incident solar radiation than the surrounding snow.

Moreover many types of vegetation can alter their spectral features seasonally changing colour. This is another case where nonphotosynthetic pigments that can dominate the visible reflectance spectrum. In fact, the red and orange autumn coloration of leaves is due to carotenoid pigments that are unmasked as chlorophyll degrades, while red pigmentation is due to anthocyanin, a pH-dependent pigment that is produced de novo in autumn foliage, perhaps to provide photo protection (Archetti et al., 2009).

In figure 3.20 and 3.21 are shown some examples lakes where the reflectance spectra is altered by biotic processes.

Nonphotosynthetic pigments can serve a variety of functions, typically helping the organism adapt to stressors in the environment. These compounds can be used for photo protection (Proteau et al., 1993; Williams et al., 2003; Solovchenko and Merzlyak, 2008; Archetti et al., 2009) and as quenching agents for protection against free radicals (Saito et al., 1994, 1997). Desiccation- and ionizing radiation-resistant organisms such as *Deinococcus radiodurans* and *Rubrobacter radiotolerans* contain carotenoids that are antioxidants (Saito et al., 1994; Cox and Battista, 2005; Tian et al., 2008). Some pigments serve as bio control mechanisms to slow growth as resources are exhausted (Venil and Lakshmanaperumalsamy, 2009) or to facilitate interactions between bacterial cells in colonies or aggregates through a phenomenon known as “quorum sensing” (McClellan et al., 1997; Williams et al., 2007). “Siderophore” pigments are used as Fe^{3+} bonding agents in iron-limited conditions (Meyer, 2000). Plants and animals use pigments in signalling to other organisms (Chittka and Raine, 2006), (pigments used in flowers for attracting pollinators). These examples show that the spectral properties of many biological pigments are not strictly dependent from the light environment. While some nonphotosynthetic pigments are adapted to be sensitive to small portions of the electromagnetic spectrum, such as UV-screening pigments, others are hosted by organisms in zero light conditions (Kimura et al., 2003). Moreover, organisms with nonphotosynthetic pigments are not necessarily closely related genetically to photosynthetic species, and the phylogenetic diversity of pigment-producing species in general is much broader than that of photosynthetic species (Klassen, 2010).



Tiwu Ata Mbupu (Lake of Old People)

Volcano Kelimutu, Indonesia

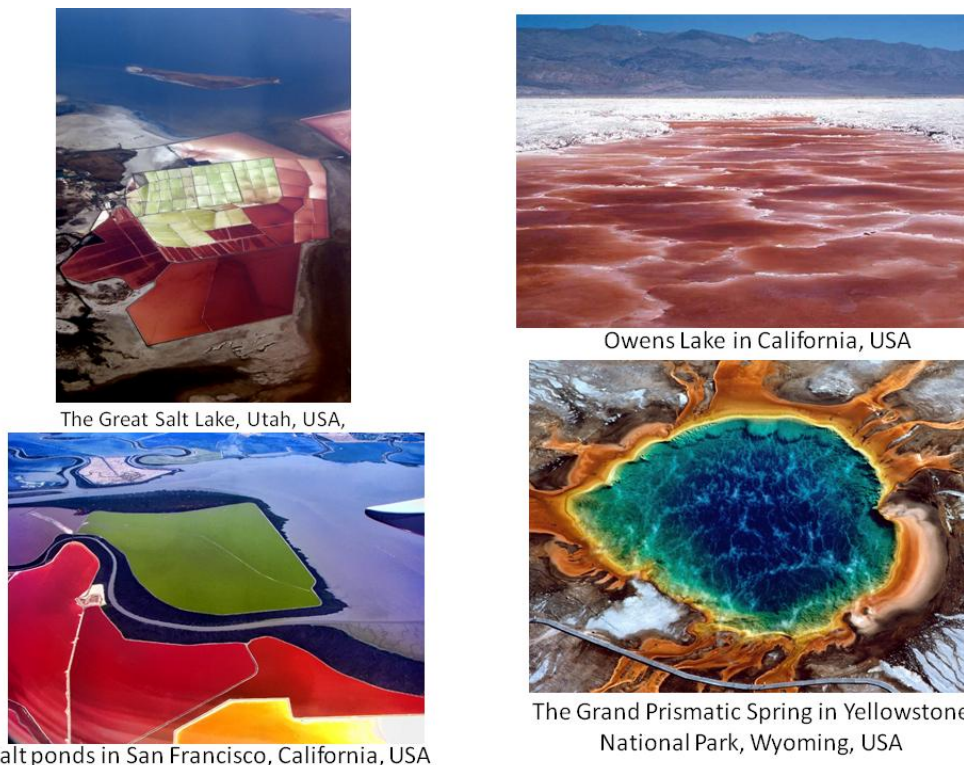
Lake Hillier, Australia

Dunaliella salina

Lake Dallol, Ethiopia

Gammaproteobacteria

Figure 3.20: These are some examples lakes where the reflectance spectra is altered by biotic processes, like in the Tiwu Ata Mbupu in Ende Regency, Flores Island, Indonesia, Vulcano Kelimutu in Indonesia, Lake Hillier in Australia or Dallol Lake in Ethiopia. In these two cases we can see the bacteria responsible of the colour alterations: *Dunaliella salina* in the first, *Gammaproteobacteria* in the second.



The Great Salt Lake, Utah, USA,

Owens Lake in California, USA

Salt ponds in San Francisco, California, USA

The Grand Prismatic Spring in Yellowstone National Park, Wyoming, USA

Figure 3.21: Macroscopic surfaces where carotenoid-type pigments dominate the spectral reflectance. (a) The Great Salt Lake, Utah, USA. The Great Salt Lake is approximately 120 km long, 45 km wide, and 4.9m deep on average. Owens Lake in California, USA. Owens Lake is 28 km long, 16 km wide, and 0.9m deep on average. Salt ponds in San Francisco, California. The Grand Prismatic Spring in Yellowstone National Park, Wyoming, USA. The spring is 90m long by 80m wide and approximately 50m deep.

4. Ancillary science: plants on other planets

Finding photosynthetic life on other planets implies a number of questions to be answered: which stars shall we target, given there are so many out there? Will we be able to measure the reflectance spectra of the planetary surfaces? What wavelength range and resolution do the new telescopes need in order to do this? Our understanding of photosynthesis will be key to designing these missions and interpreting their data? Starting from these questions we try to understand the features that complex photosynthetic organisms could show on other planets. In particular this ancillary study aims to understand what kind of plants could grow on M star planets. Plants descends from green algae emerged onto land about two billion years after oxygen had begun accumulating in the atmosphere. Then their complexity began to differentiate them into a great variety of species, from mosses to liverworts on the ground, to tall land plants. Under abiotic stress and in response to environmental changes plants can alter their physiology, morphology and development processes. These properties can allow plants to settle in a great widespread bouquet of environmental niches and habitat types. Because different conditions of irradiation, pH, water availability can occur as well as mechanical stress conditions, plant on Earth have evolved to adapt and, in some cases, to use them in a productive way. For example, conifer trees have conical shape to capture light efficiently at high latitudes with low sun angles and shade-adapted plants contains anthocyanin to screen themselves from the excesses of light. On other planets orbiting other stars physiology and morphology of plants could be different to face different environmental constraints.

4.1 Leaves

Leaves are an important part of a plant, because they play a chief role in its growth and metabolic processes. Leaf morphology can be altered by the allometric expansion and phenotypic plasticity can occur to produce a great variety of leaf traits, driven by environmental conditions. In figure 4.1 is shown a representative scheme of a typical leaf and its parts.

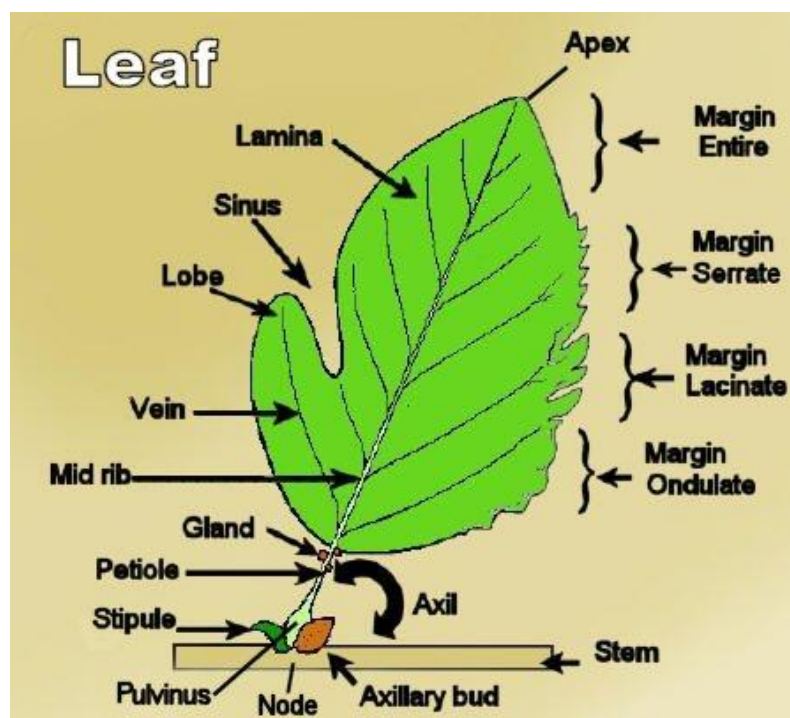


Figure 4.1: A representative scheme of a typical leaf and its parts.

Though, recent studies in plant traits have found that some relationships between specific leaf traits are globally repeated despite large variations in the values of the traits across individual species with very diverse phylogenetic, biogeographical and environmental affinities (Shiplot et al., 2006; Wright et al., 2004).

There are many types of leaves in nature, from blades to needles. Differences in leaf size can significantly alter whole-lamina- and whole-leaf-integrated chemical and structural characteristics and thereby modify general scaling relationships between plant structure, chemistry and function (Niinemets et al., 2007).

Studies have suggested that palmate- and parallel-veined leaves are hydraulically and mechanically more efficient than pinnate-veined leaves due to a more uniform distribution of major veins in parallel/palmate-veined leaves (Sack et al., 2003) while the minor veins, the less support and the more sensitive responses to environmental variations the leaves have. Xu et al., (2009) found that leaf size shrinks with scarce water and light availability while the more water supply requires a bigger evaporative surface for gaseous exchange.

However, leaf size may also decline due to overall resources limitation in stressful environments, making the construction of large leaves with extensive vascular and cell-wall fractions overly expensive (Niinemets et al., 2007). Compound leaves may act as highly dissected leaves to improve heat transfer efficiency in a plant by allowing better air exchange over the leaf surface (Gurevitch et al., 1990).

Specific leaf area (SLA) is an integration of leaf area and dry mass. It has been shown that SLA is negatively correlated with leaf lifespan and positively correlated with mass-based nitrogen content, photosynthetic capacity, transpiration rate and respiration rate (Wright et al., 2004; Reich et al., 1997).

Moreover, Higher dry mass per area in drought-stress leaves also enables the prolongation of the leaf lifespan to compensate for fewer units and lower activity of the photosynthetic apparatus. Sun and shade environments are likely to be selected for different leaf constitutions, that is, differing investment in structural and symplastic components (Lusk et al., 2007).

Finally, in xeric environments, the leaves became narrower. This is thought to be an adaptation trick reduce the transpiration by reducing the size of the boundary layer.

4.2 Leaves and radiation

Leaves are the primary plant tool to acquire light and transform it into energy. Though, not all the wavelengths are useful for the plant and some of them, indeed, are harmful. It has been found that the intensity of visible and UV light is positively correlated with cuticle thickness and integration of protective flavonoid compounds in the cuticle. In fact, plants grown in high light generally have thick leaves caused by extra layers of palisade mesophyll or longer palisade cells to protect them from high-light damage (Davi et al., 2008).

However, the production of leaves with a more symplastic component should be advantageous in the shade by reducing both construction and maintenance costs (Lusk et al., 2007).

On the other hand, Xu et al., (2009) found that in low light available conditions, both the leaf elongation and the lamina areas located close to the leaf apex increased. This an important feature because it is the proof that leaves can optimize their shape to maximize light and reduce self shading (Takenaka et al., 2001).

Xeromorphic features, the progressive transformation of the leaves into stings, can serve, among the other things, to protect the plant from excessive light and so, son leaves will display an increased xeromorphism in comparison to shade leaves (Xu et al., 2009).

Due to the economics of light interception and biomechanical requirements, increases in leaf size are often bound to enhanced biomass investment in the petiole (Niinemets et al., 2006). The elongation of petioles will achieve optimal leaf display to deal with the denseness of the canopy, but it may not be the major way to reduce self-shading, as the plants face a trade-off between the need for increasing interception areas and support structures. Increasing the investment in petioles needs to synthesize more xylogens, and longer petioles will lead the leaf to bend (Pickup et al., 2005).

4.3 Leaf venation

Leaf venation have physiological and hydraulic implications other than a role in the light utilization efficiency. from biomechanical considerations, large leaves needs a bigger support structure to keep them together. So a stronger midrib is required (Niinemets et al., 2007).

An increase of the distance between the midrib and the margins would mean a larger network of veins to carry resources to and from the cells. Xu et al., (2009) found a weak increased trend of vein density under drought stress to avoid leaf dehydration while larger paths imply slower metabolic processes and a slower photosynthesis (Price et al., 2007). Moreover, strong positive correlations have been observed between vein density and leaf hydraulic

conductance (Sack et al., 2006). Relatively broader and thinner leaves in the low light available condition show higher vein density to prevent leaf margins drooping when the centroid is far away from the leaf base and increase the overall bending moment.

4.4 Leaf surface

In high radiation conditions plants can modify the structure of the leaves to face this condition. Evolution has endowed leaves with hairs to enhance superficial albedo, or waxes to protect them from drying and absorb UV radiation, harmful for them.

Moreover, leaf thickness is bigger in high irradiation environments. This can increase PAR cross section. A study of Heber et al., (2000) shows that strong illumination can cause photo-damage in the dried leaves, but not in the dry moss and dry lichens. So these biota can be evolved in such way to face environmental stresses. In fact, less water means more compact cells. This cause an increase in the NIR reflectance spectrum.

4.5 Plants and gravity

While the light condition is the most important environmental factor, another important environmental factor for plant growth is gravity. The direction of shoot elongation is affected by gravity. However, the responses of plant organs to gravity have been extensively studied only for roots and shoots. Whether leaves react to gravity has yet to be determined, although the behaviour of the leaves of wild plants suggests that their graviresponses differ from those of shoots or roots. The graviresponse of leaf expansion in *Arabidopsis* was investigated by altering the direction of potted seedlings and it was found that the expansion of rosette leaves depended on the direction of the shoots in main. In other words, the rosette leaves of *Arabidopsis* simply bend in the direction opposite the shoot axis, independent of gravity (Kozuka, T., Mano, E. and Tsukaya, H., unpublished data). However, some climber type species, such as *Oxalis spp.* and *Pueraria lobata*, clearly show gravitropism of the leaf petiole (Kozuka, T. and Tsukaya, H., unpublished observations) and even *Arabidopsis* shows a graviresponse under certain environmental conditions (Mano, E., Kozuka, T. and Tsukaya, H., unpublished data). Further analysis of the gravitropism of leaves is required to understand how leaf expansion is adjusted in natural environments (Tsukaya, 2005).

4.6 Plants and pressure

Pressure can influence plants' growth rate. It has been found that up to 101 kPa growth proceed without problems, but under this value growth rate become slower. Under 25 kPa the plant dies for the lack of gaseous exchanges.

4.7 Plants and temperature

The temperature can affect the plant growth, as previously described in chapter 3. In particular we can set some habitability limits for some kind of plants. Usually, plants can live and use CO₂ at temperatures between 268-273 K and 318-323 K at 100% of their productivity and at 50% at temperatures between 288-293 K and 313-318 K. Sclerophyll trees and shrubs can live at temperatures between 268-271 K and 323-333 K.

Cold and dry environments foster conifers, while humid and temperate environments broadleaf plants while Bryophyte species (like *Physcomitrella patens*) growing in areas in which temperatures fall below zero in winter are likely to have tolerance to freezing stress (Minami et al., 2004). Hot and dry environments foster succulents with low surface-volume ratio.

4.8 Photosynthesis and plants colours

On Earth, plants use the 400-700 nm part of the solar radiation to operate photosynthesis. As Earth's spectrum has a peak in the blue-green region, plants has evolved to operate in that photosynthetic range. The colours of plants are given by photosynthetic pigments that operate inside the leaf cells. As known, Earth's vegetation has a bump in the green region of the reflectivity spectrum.

This is due to lower absorbance of green light by chlorophyll (Chl). Plants have an absorbance peak between 700 and 850 nm, in the NIR, and it is called “red edge”. This phenomenon is due to refraction between leaf mesophyll cell walls and air spaces in the leaf (Kiang et al., 2007).

There is also an effect known as the red drop, whereby photosynthesis is impaired when plants are illuminated *only* with radiation of $> 6,800 \text{ \AA}$. However, they can benefit from the Emerson effect (Emerson *et al.*, 1957), whereby the efficiency of photosynthesis at around $7,000 \text{ \AA}$ is boosted if a shorter red wavelength, such as $< 6,500 \text{ \AA}$, is present and the combined level of photosynthetic efficiency is greater than that expected from the sum for both wavelengths taken separately (Tarter et al., 2007).

But why Earth's plants are mostly green?

The answer is up described, but it hasn't still understood why photosynthetic evolution has led to a refusal of green light, that is quite energetic and useful for metabolic processes.

This seems to be an error in the evolutionary process if we wouldn't know that photosynthetic processes are led by the energy per photon and by the number of photons in the light, and do not depend on the total amount of light energy.

Blue photons has more energy than red ones and the red photons are the most numerous.

So, green light is not enough energetic nor enough in number to be useful.

Though, blue light is not used efficiently by plants on Earth because, when chlorophyll absorbs a photon of blue light, an electron is promoted to an unstable upper excited singlet state that decays within a mere 10^{12} s . This means that both blue light photons and less energetic red light photons produce the first excited singlet as the starting point for energy transfer (Nobel, 1974).

As already said, the basic photosynthetic process, which fixes one carbon atom (obtained from carbon dioxide, CO_2) into a simple sugar molecule, requires a minimum of eight photons. It takes one photon to split an oxygen-hydrogen bond in water (H_2O) and thereby to obtain an electron for biochemical reactions. A total of four such bonds must be broken to create an oxygen molecule (O_2). Each of those photons is matched by at least one additional photon for a second type of reaction to form the sugar. Each photon must have a minimum amount of energy to drive the reactions (Kiang et al., 2008).

In the photosynthetic process pigments operate as an array of antennas each tuned to pick out photons of particular wavelengths. Chlorophyll preferentially absorbs red and blue light while carotenoid pigments (which produce the reds and yellows of fall foliage) pick up a slightly different shade of blue. All this energy gets funnelled to a special chlorophyll molecule at a chemical reaction centre, which splits water and releases oxygen. Funnelling process is an evolutive masterpiece.

To use blue photons, that are too energetic, the antenna pigments work in concert to convert these high energetic sources into less energetic ones.

The process begins when a blue photon hits a blue-absorbing pigment and energizes one of the electrons in the molecule. When that electron drops back down to its original state, it releases this energy, but because of energy losses to heat and vibrations, it releases less energy than it absorbed.

The array of pigments can also convert cyan, green or yellow to red. The reaction centre, as the receiving end of the cascade, adapts to absorb the lowest-energy available photons. (Kiang et al., 2008).

In figure 4.2 can be seen a schematization of this process.

The upper limit of photon flux density at which photosynthesis can occur on Earth is set by the availability of non-photon resources used in constructing and using the photosynthetic apparatus and by the occurrence of photo-damage at high photon flux densities (Wolstencroft and Raven, 2002 and references therein). These data suggest that some plants on Earth could grow at a photon flux density of $6000\text{--}9000 \mu\text{mol photon } m^{-2} s^{-1}$, despite the maximum natural photon flux density (400–700 nm) on Earth being $2000 \mu\text{mol photon } m^{-2} s^{-1}$. It has been suggested that photosynthetic primary production can occur on land on an Earth like planet with $10,000 \mu\text{mol photon } m^{-2} s^{-1}$; aquatic habitats permit the screening of supra-optimal irradiance by water, provided the water is deep enough (Falkowski and Raven 1997).

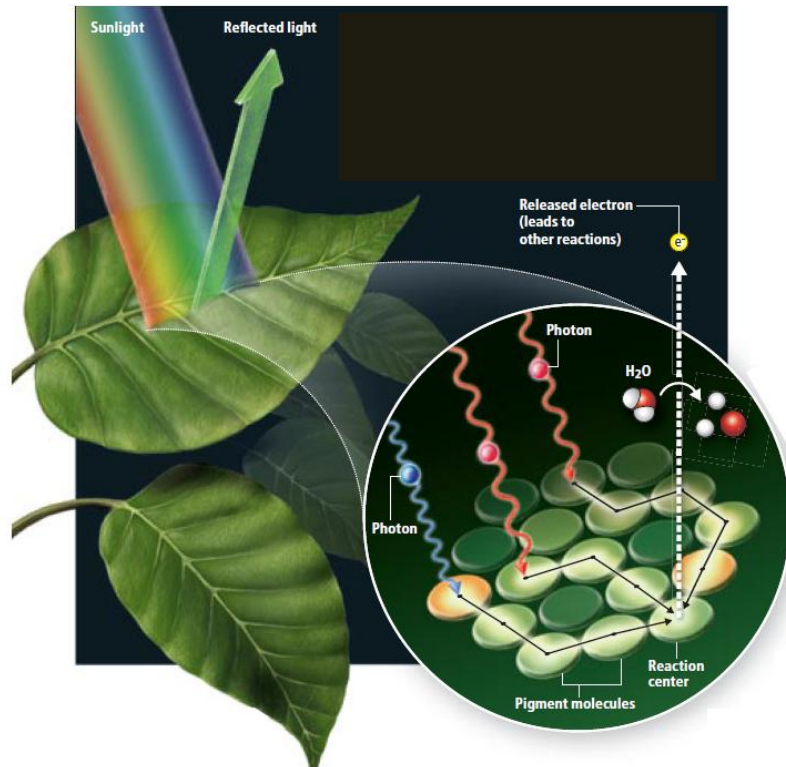


Figure 4.2: Schematization of the funnelling process

Under water less energy is available because of the absorbing power of the sea. That's why there is a stratification of photosynthesizing life forms at different depths, according to their mix of pigments. In fact, low water life forms have pigments that absorb the light colors left over by the layers above (Kiang, 2008). In figure 4.3 are represented some plant species that adapted to environmental conditions evolving a black, blue and gray pigmentation.



Figure 4.3: A small sample of plant species that adapted to environmental conditions evolving a black, blue and gray pigmentation.

4.9 Alternative photosynthetic ways on alternative worlds

On other planets, the photosynthetic driving parameter is the light spectrum available at the planet's surface and this depends mainly on the parent star.

Only certain types are long-lived enough to allow for complex life to evolve. These are, in order from hottest to coolest, F, G, K and M stars. Our sun is a G star. F stars are larger, burn brighter and bluer, and take a couple of billion years to use up their fuel. K and M stars are smaller, dimmer, redder and longer-lived.

A planet in the HZ of an F or K star would receive almost the same visible radiation quantity as Earth and could easily support oxygenic photosynthesis. In this case, the pigment colour of the leaves would only be shifted within the visible band (400–700 nm, with limited photosynthesis at wavelengths up to 1.1 μm). M star represent a different case. They emit much less visible radiation than Sun, with a spectral peak in the IR. On a tidally locked planet with zero orbital obliquity in stellar radiation no seasonal or diurnal variations in the insolation are expected and photosynthetic reaction centers are supposed to be all oriented in the same direction (Heath et al., 1999). About the topic of whether a three- or four-photon mechanism might have evolved on Earth like planets orbiting the cooler K or M stars we note that the achieved rate of photosynthesis could be as little as two-thirds or half that for the terrestrial two photon mechanism. An example is an M0V star planet for which the assumed range of PAR is 600–1050 nm and with a three-photon mechanism of photosynthesis. We assume that the pigments absorb the fraction of photons tabulated in Table 3 but at wavelengths of 600 nm (0.95), 675 nm (0.94), etc. The integrated flux between 600 and 1050 nm PAR yields 14.4 instead of 4.63 for the two-photon mechanisms.

4.10 Plants and IR radiation: The Effect of Infrared Light on Plant Growth

Recent studies demonstrated that infrared radiation encourages plants to flower and can also affect how plants grow.

According to Texas A&M University, plants grown indoors may grow well under fluorescent lights, but will not bloom until appropriate levels of infrared radiation have been introduced.

Increased infrared waves can affect the speed at which plant stems grow too. A short exposure to far infrared light should increase the space between nodes when the exposure occur at the end of an eight-hour light period. Exposing the plant to ordinary red light this effect would be reversed. A combination of far red and red light produced the longest internodes. Plants grown in light that is too red may seem spindly and long-stemmed (Vince-Pure, 1977). Moreover, infrared waves can also be used to measure the growth of plants. According to Applied Spectroscopy Reviews, infrared micro-spectroscopy may be used to study plant development. Scientists using this technique inject the plants with a radioactive substance, then analyze their cellular development using infrared cameras. The radioactive substance emits infrared waves, which can be picked up by the camera. From this information, scientists can determine what is going on inside the plant.

4.10.1 Weak light

When plants are exposed to weak light, some of them show a shade-avoidance syndrome.

It consists in an elongation of the petiole and a decrease of the leaf blade area.

This reaction to weak light is a typical example of leaf plasticity, that can help plants to survive even in not ideal conditions.

A specific transport protein (PIN3) enables the accumulation of the plant hormone auxin, which plays an important role during this adaptation process, in the outer cell layers of the plants, thus enhancing the growth process. In figure 4.5 is shown this effect taken on a plant in different light conditions.

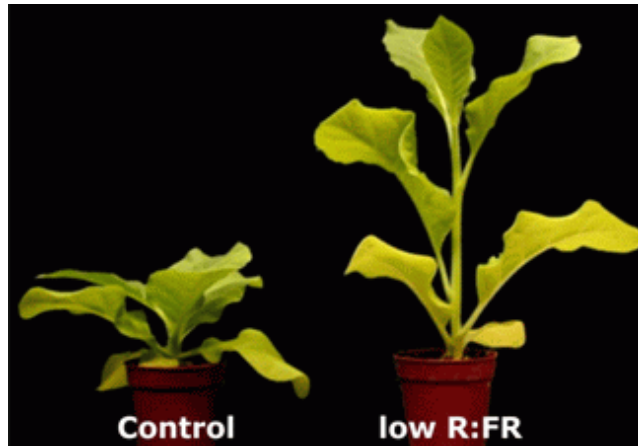


Figure 4.5: Weak light reaction (right) compared to normal light growth (left).

In comparison with control plants, which grow in the sun, plants growing in the shade of other foliage are characterized by hyponasty, extended leaf stalks and increased shoot growth. Taken together, these processes are referred to as shade avoidance reaction or shade avoidance syndrome. They are initiated by a change in the fraction of far red in favour of red light, for example by a low far-red to red ratio.

In figure 4.6 is shown another example of shade-avoiding syndrome, the variation of palisade cells and of the number of palisade layers.

In many species, light intensity affects the number of layers of palisade cells as well as the shape of the palisade cells. In *Arabidopsis* under low light conditions (standard culture conditions for *Arabidopsis* in a culture room: *ca.* $60 \mu\text{moles m}^{-2}\text{s}^{-1}$ in photosynthetically active photon flux density), palisade cells are round and develop into one layer. In contrast, under high light conditions ($> 200 \mu\text{moles m}^{-2}\text{s}^{-1}$ in photosynthetically active photon flux density), palisade cells develop into two or three layers and are columnar as a result of polarized growth in the leaf thickness direction (Tsukaya 2005).



Figure 4.6: The light-dependent control of leaf shape and architecture. (A) Under dark conditions (right), leaf blades remain smaller and leaf petioles elongate more than under light conditions (left; i.e., shade-avoidance syndrome). Photo: Courtesy of Mr. T. Kozuka, Graduate University for Advanced Studies, Japan. Bar, 5 mm. (B) High light conditions produce sun leaves (bottom) that differ from the shade leaves (top), which develop under low light conditions, in terms of the shape of the palisade cells and the number of palisade layers. Photo: Courtesy of Dr. S. Yano, Okazaki Institutes for Integrated Bioscience, Japan. Bar, 100 μ m.

In figure 4.7 are shown the effects of gravitropism on a plant growth.



figure 4.7: gravitropism can affect leaves

Though, an experiment made by Paul et al., 2010 tested the growth of plants in absence of gravity. The scientists ran their experiment on *Arabidopsis* plants—a go-to species for plant biologists. The control group was germinated and grown at the Kennedy Space Center (A), while the comparative group was housed on the International Space Station (B). For 15 days, researchers took pictures of the plants at six-hour intervals and compared them. Their results surprised even them: the plants in space exhibited the same growth patterns as those on Earth.

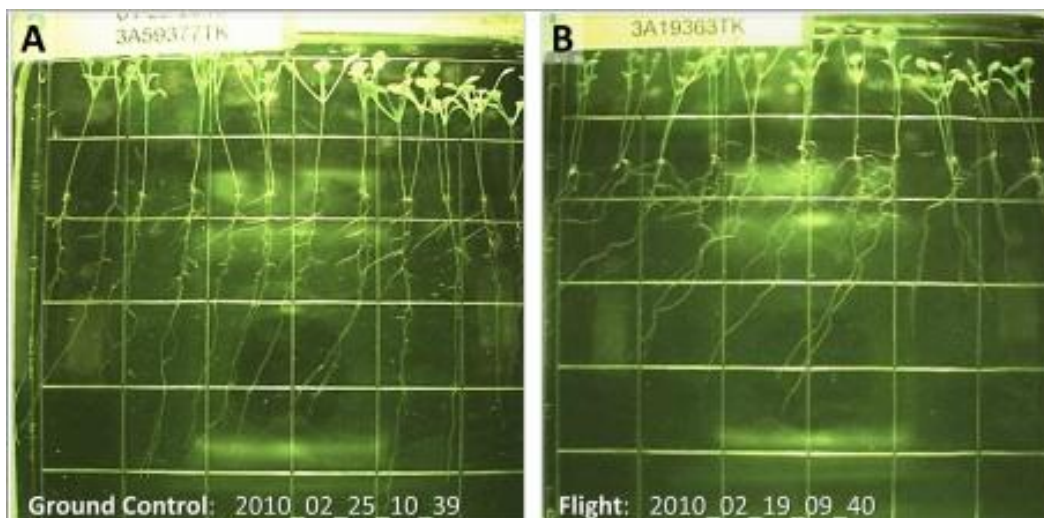


Figure 4.8: Growth patterns in different gravity conditions.

4.11 Expected colours of extrasolar plants

As illustrated in Kiang, (2008), the photons reaching the surface of planets around F stars tend to be blue, with a peak at 451 nm. For K stars, the peak is in the red at 667 nm, nearly the same as on Earth. Moreover, ozone plays a strong role, making the F starlight bluer than it otherwise would be and the K starlight redder. So, the useful radiation for photosynthesis would be in the visible range, as on Earth. Thus, plants on both F- and K-star planets could have colors like those on Earth but with small variations. For F stars, for example, the flood of energetic blue photons is so intense that plants might need to reflect it using a screening pigment similar to anthocyanin, giving them a blue tint. Alternatively, plants might need to harvest only the blue, discarding the lower-quality green through red light. That would produce a distinctive blue edge in the spectrum of reflected light, which would stand out to telescope observers. A planet around a quiescent M star would receive about half the energy that Earth receives from our sun. Although that is plenty for living things to harvest—about 60 times more than the minimum needed for shade-adapted Earth plants—most of the photons are near-infrared. Evolution might favour a greater variety of photosynthetic pigments to pick out the full range of visible and infrared light. With little light reflected, plants might even look black to our eyes Kiang, (2008). In figure 4.9 is shown a simulation of red edge limits for Earth vegetation compared with M star planet's edge of the reflectance spectrum (Tinetti et al., 2006).

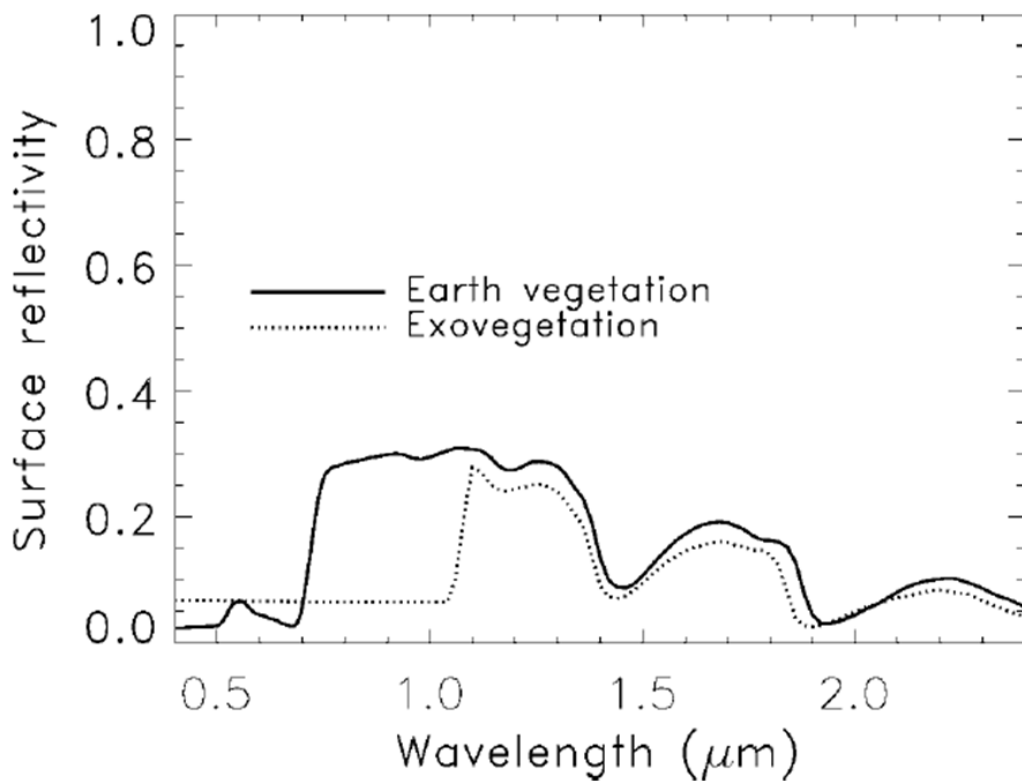


Figure 4.9: Simulation of red edge limits for Earth vegetation compared with M star planet's edge of the reflectance spectrum (Tinetti et al., 2006).

4.12 Planets orbiting multiple star planet systems

Up to now, we have considered planets orbiting a single star.

We have already said that a photosynthesizers on a mono-star planet evolved pigments tuned on the radiation of this star.

But what would happen if a planet would orbit around a multiple star planet systems, for example a two or three star system?

The answer is not trivial, especially with binary or ternary systems with very different types of stars.

If the stars are close together, a planet could orbit both stars as if they were a single star or if the stars are further apart, a planet could orbit one of the two stars. In figure 4.10 are shown the two cases.

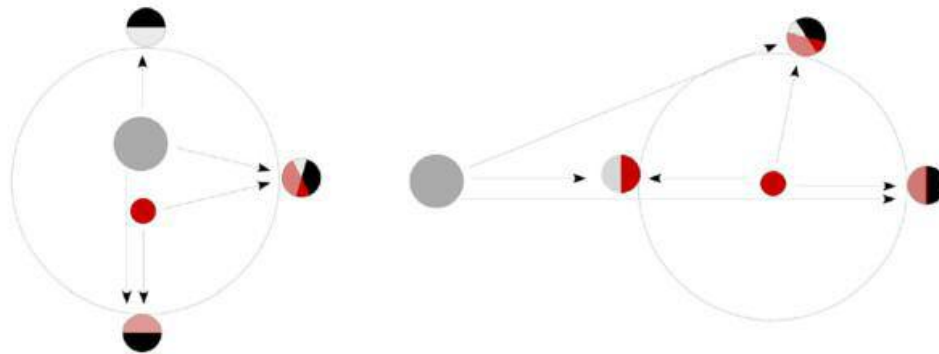


Figure 4.10: Two cases of binary orbiting planets are possible: if the stars are close together, a planet could orbit both stars as if they were a single star or if the stars are further apart, a planet could orbit one of the two stars.

Systems composed of M and G stars are the most probable because approximately 57% of G stars are found in multiple systems and, though only 25-30% of M stars are found in multiple systems, there are so many M stars in the galaxy that 25-30% is still a very large number.

The simulations suggest that planets in multi-star systems may host exotic forms of the more familiar plants we see on Earth. A planet orbiting close to an M star with a more distant G star companion would have a photosynthetic light regime dominated by infrared radiation. In such infrared-dominated radiation environments, vegetation may have more photosynthetic pigments in order to make use of a fuller range of wavelengths, giving them a darker appearance.

At the distance of 1 AU a G star would overwhelm an M star and so, the radiation used by photosynthesizers would be mainly the G star one. The case for photosynthetic organisms adapted to use both forms of radiation is harder to make. It would be complicated and expensive in terms of energetic investments to house both of these systems in a single organism.

For a wide binary M-G star scenarios things are different. In this case, the primary star's radiation always has a greater magnitude than that of the distant secondary star; however, there are periods where a portion of the planet would be illuminated only by light from the less photosynthetically favourable secondary star. When the G star is the planet-hosting star, the M star is too distant to make any useful contribution to a habitable planet's photosynthetically active radiation. However, if the M star hosts a planet, some organisms may evolve to exploit the low photon flux density from the distant G star, as G-star-only illumination can persist in some regions on the planet's surface for a significant portion of its orbit.

This situation could lead to a differentiation of the organisms, with different species living in the same habitat and adapted to use one form of radiation or the other radiation from different stars at different times in the planet's orbit, perhaps entering a dormant state when the necessary radiation conditions are absent.

4.13 Detection

Tinetti calculated that for land plants to show up in spectra taken with the upcoming telescopes, at least 20 % of the surface must be a land both covered in vegetation and free of clouds. On the other hand, oceanic photosynthesis releases more oxygen to the atmosphere. Therefore, the more prominent the pigment biosignature, the weaker the oxygen biosignature, and vice versa. On Earth, we have been able to determine that the signature of chlorophyll is unique to plants, which is why we can detect plants and ocean phytoplankton with satellites. We will have to figure out unique signatures of vegetation for other planets.

In figure 4.11 is shown a map of terrestrial chlorophyll as seen by NASA SeaWiFS satellite

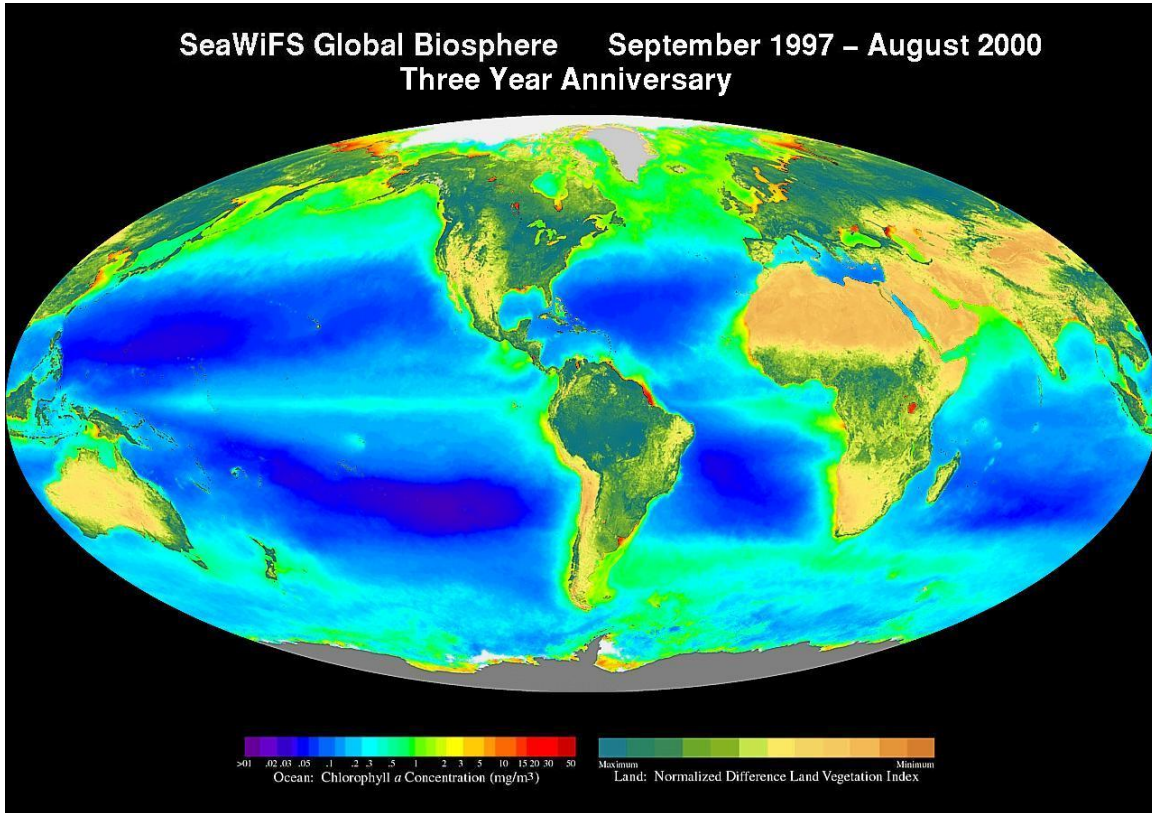


Figure 4.11: NASA SeaWiFS, Average type *a* chlorophyll from September 1997 to August 2000

Reflectance spectra have been taken on Earth to understand the spectral signatures from other planets. Plants grow and thrive through photosynthesis, a process that converts sunlight into energy. During photosynthesis, plants emit what is called fluorescence – light invisible to the naked eye but detectable by satellites orbiting hundreds of miles above Earth. NASA scientists have now established a method to turn this satellite data into global maps of the subtle phenomenon in more detail than ever before.

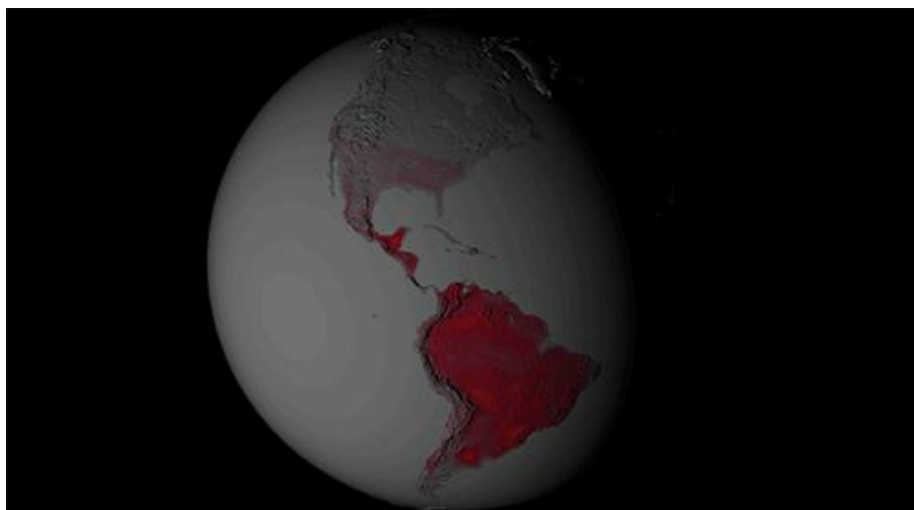


Figure 4.12: Plants fluorescence. Credit: NASA's Goddard Space Flight Center

5. Radiative sources analysis

Hereafter we will describe in detail the sources of radiation that will be used in the experiment, mainly M stars. In particular a brief overview with the main characteristics will be made, in particular starting from the motivations that led us to choose these stars for the experiment. Then, the age limits (between 50 Gyr for the most massive ones to several billions years) makes them good parent stars for planets enough old for life to have developed in. The fact, as described in chapter 5.1, that the peak of the energy distribution is at around $1 \mu\text{m}$ was the constraint that drove the choice of the bacteria. Stellar variability could be important because it can influence the suitability for life (chapter 5.3) and the same can be said for (chapter 5.4). In fact the smallest flares detectable are about 10^{28} erg of energy, while the highest ones have energies in the order of $10^{34} - 10^{37}$ ergs. Though, as described in chapter 3.4, photosynthetic organisms during the flaring stage of M star planets should be able to survive even with visible light, though their productivity would be limited to less than 14% of Earth's with smaller flares and less than 4% with very active M stars like AD Leo with daily large flares (Kiang et al., 2007b). Moreover, the maximum Earth's surface UV rate is $1.8 - 2.8 \times 10^{-18}$ photons/m²/s over the UVB band at the Equator at noon under cloudless conditions or averages globally 0-12 KJ /m²/s (2.1×10^{-18} photons/m²/s). Then, during the time interval between flares, in M stars planet terrestrial organisms would be exposed less 0.35-0.50 μm damage than for the Earth. The effects of planetary atmospheric erosion in the HZ due to CME events is described in chapter 5.5 while in chapter 5.6 are described the effects of starspots.

5.1 About M stars

The first step to understand how a coupled planet-star system may harbor life and have the basis to try to reproduce foreign environments in laboratory is to understand very well the main source of radiation, that is, the parent star.

M stars represent almost 75% of the stars and about a half of the stellar mass in our Galaxy.

This could be a good starting point as statistical data on a so big number of stars can give hope of planetary habitable systems. This idea is supported by the evidence that M stars can host planets.

To date, with all exoplanets found (available at <http://exoplanets.org>) we know that this is true.

In fact, protoplanetary disks around M stars are as common as other solar-type stars, and around half of all objects at ages of a few Myr possessing such disks (*e.g.*, Haisch et al., 2001; Liu et al., 2004; Sicilia-Aguilar et al., 2005; Lada et al., 2006). Older debris disks around M stars are far rare, but this paucity may be due to the limited sensitivity of previous surveys (Tarter et al., 2007).

The lowest mass exoplanets orbiting main sequence stars are M star planets, with masses between 5.5 and $7.5 M_{\oplus}$ (Rivera et al., 2005).

The peak of the energy distribution of the M dwarves is located at around $1 \mu\text{m}$, in the NIR, while in most of the brown dwarves the flux is located in the portion of spectrum between 1 and $10 \mu\text{m}$. By comparison, the radiation from F, G, and K stars peaks in the visible part of the spectrum ($0.5 \mu\text{m}$). In figure 5.1 can be seen the UV spectra of M stars compared with that of the Sun.

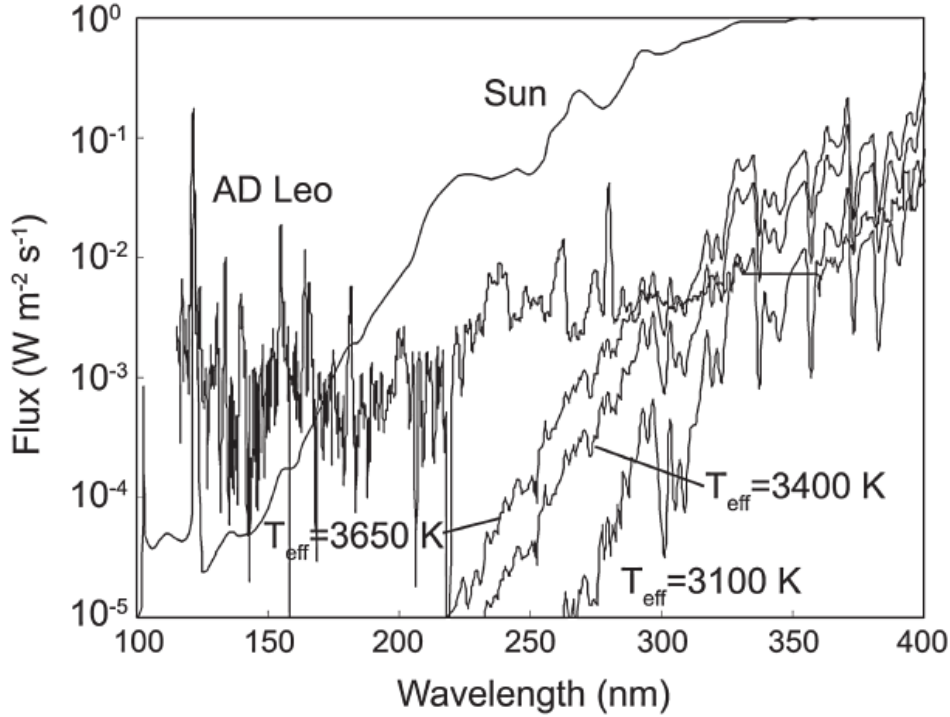


Figure 5.1: In this spectra, the curves are normalized at the distance that a planet like Earth should have to maintain a surface mean temperature of 288 K. The spectrum of AD Leo is a composite of International Ultraviolet Explorer observations during non-flaring. The stars identified by their effective temperature are model photospheres from the BaSeL website (<http://www.astro.mat.uc.pt/BaSeL/>). The most quiescent M dwarfs, because of the absence of chromospheric emissions, give a lower limit to the blue and UV emission (Tarter et al., 2007).

M dwarves, even in the solar neighborhood, do not form a homogeneous sample with the same metallicity and age, but span up to ± 0.5 - 1.0 dex around the solar metallicity and 10^3 years in age (Burrows & Liebert, 1993; Allard et al., 1997). Moreover, the masses of M stars span a range between 0.6 to $0.08 M_{\odot}$.

Upper and lower limits are given by the calculations based on the M0 stars YYGem and the brown dwarves limits (Delfosse et al., 2000). In table 5.1 can be seen some data about M stars, like radius, their effective temperature T_{eff} , orbital radius in A.U. and the distance from the parent star at which total energy contained in insolation would be equal to present solar insolation $I(e)$ on Earth, that is $1360 \times 10^6 \text{ ergs/cm}^2/\text{s}$ (Heath et al., 1999). In Figure 5.2 can be seen a relation between mass and luminosity for star masses lower than that of the sun, base on the calculations of Hillenbrand and White (2004).

A polynomial to fit the data is given by the equation

$$\log L = 4.1 (\log M)^3 + 8.16 (\log M)^2 + 7.11 \log M + 0.065 \quad (5.1)$$

with L stellar luminosity and M stellar mass, both in solar units [Hillenbrand and White (2004)].

It can be seen that even the most luminous M0 stars are at least 10 times less luminous than the Sun.

Spectral type	G2	M0	M1	M2	M3	M4	M5	M6	M7	M8
Radius/Solar radius	1.00	0.62	0.58	0.53	0.45	0.39	0.33	0.26	0.18	0.12
Blackbody T_{eff} (K)	5860	3850	3720	3580	3470	3370	3240	3050	2940	2640
Ie orbital radius (AU)	1.00	0.26	0.23	0.19	0.15	0.12	0.10	0.07	0.04	0.02
Ia orbital radius (stellar radii)	214	56	48	41	33	27	21	14	9	5
λ_{max} (nm)	494.37	752.47	778.76	809.22	834.87	859.64	894.14	949.84	985.37	1097.35

Table 5.1: Data about M stars, like radius, their effective temperature T_{eff} , orbital radius in A.U. and the distance from the parent star at which total energy contained in insolation would be equal to present solar insolation $I(e)$ on Earth, that is $1360 \times 10^6 \text{ ergs/cm}^2/\text{s}$ (Heath et al., 1999). From these data, with the Wien's law is possible to calculate the peak of emission. Lower mass objects become degenerate before they can reach the H ignition temperature and fade continuously cooling down their temperature, while the least massive M9 stars ($M=0.08 M_{\odot}$) can burn hydrogen and are able to maintain the same luminosity for at least 100 billion years.

M0V star produces only 1.9% of the light in the visual band as the Sun, but 16% of the light in the IR K band. Corresponding values for an M9V star are 0.00014% at V and 0.13% at K. Thus, the balance of radiation relative to our Sun is very different for M dwarfs, which produce relatively more IR radiation than visible.

For a complete analysis of stars there is need of several other parameters like sub-photospheric and photospheric convection, line radiative transfer, level populations of some species, opacities or other data.

Because of the high outer opacities and low temperatures, the interior opacities are supposed to be high and these stars can easily move luminosity outward by convection rather than radiation throughout the bulk.

This make the whole star available as nuclear fuel (Tarter et al., 2007).

As M stars have lower luminosities than the Sun, they have longer hydrogen burning lifetimes that can range between 50 Gyr for the most massive ones to several billions years for the least massive.

It is well known that red stars emit fainter and fainter fractions of their energy in the blue, visible and UV part of the spectrum, going to later type, but the difference is due not only to the temperature dependence of the Planck spectrum, but even by the mass and by absorption features. In fact, the visible and IR spectral regions are dominated by molecular absorption bands, and the shorter wavelengths are controlled by chromospheric and coronal activity. Even during periods of non activity active M stars present nearly flat UV continua resulting by the presence of their chromosphere. The T_{eff} range of these stars spans between 3800 K for M0 stars to 2500 K for M9 ones. For comparison, T_{eff} of our Sun is 5780 K. The radii for M stars though are available for only a small number of double line eclipse binaries or by interferometry, but the radius scales approximately with the mass (Scalo et al., 2007). Indeed, stellar luminosity is the main parameter that can influence the planetary conditions. In fact this can influence planet's greenhouse effect and their clouds.

Without the chromosphere, the photosphere alone of an M star would emit a fraction of total luminosity in the $0.25 \mu\text{m}$ region that is between 10^3 and 10^8 times less than that of the Sun, but active M stars have relevant chromospheric emissions in the $0.20\text{-}0.30 \mu\text{m}$ region with a flux one order of magnitude less than that of the Sun even for strong flares like AD Leo (Segura et al., 2005). M stars were in the past considered not probable systems able to harbor life because most of the planets close enough to them and capable to handle liquid water on their surface are expected to be tidally locked (Dole, 1964). This environmental conditions were supposed to induce a freezing in the dark side of the planet and harsh flare whippings in the

lightened side. Here the surface pressure is controlled by a thin balance between the latent heat of condensation and radiative cooling on the dark side. This pressure would be far below the triple point of water and then it wouldn't allow habitability (Tarter et al., 2007).

All the same, Joshi et al., (1997) and Joshi (2003) demonstrated that planetary atmospheres as thin as 0.1 bar could be sustained by wind circulation between the light and dark sides, with tolerable wind speed of 10-20 m/s, where atmospheres as thick as 1-2 bars could sustain liquid water on the surface (Scalo et al., 2007).

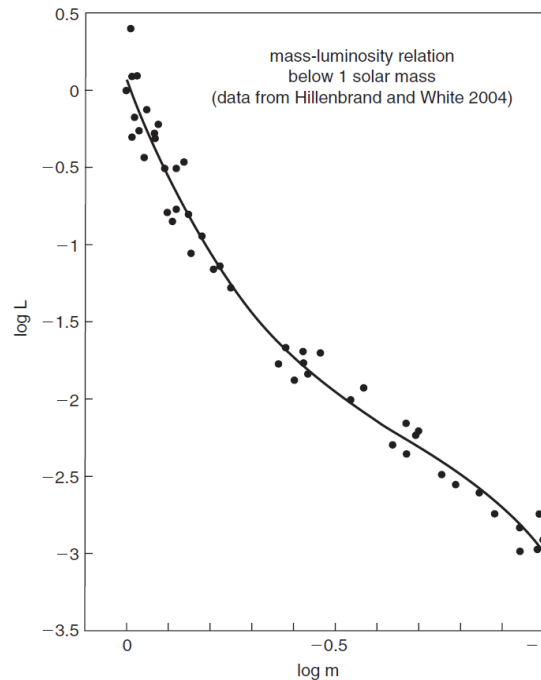


Figure 5.2: Mass-Luminosity for main sequence stars with masses lower or equal to the sun's mass (Delfosse, 2000).

5.2 Molecular features

In M stars the dense forest of absorption lines can lower the total energy flux, leading to an overall spectrum that is quite dissimilar from a black body one (Heath et al., 1999). Moreover, line blanketing reduces emitted radiation and must be balanced by continuum stellar warming at other wavelengths (Scalo et al., 2007).

The surface pressures of M stars are again higher than for the solar-type stars, despite the lower mass.

Due to their low surface temperatures and high pressures, the atmosphere can support atoms and molecules, making the IR portion of the spectrum dominated by absorption lines (Tarter et al., 2007).

Molecular bands are the most important cause of absorption in M dwarves spectra.

Several studies such as those of Sauval & Tatum (1984), Rossi et al., (1985), Irwin (1987, 1988), Cherchneff & Barker (1992), Neale & Tennyson (1995), and Sharp & Huebner (1990) have provided partition functions for most molecules inside M stars atmospheres.

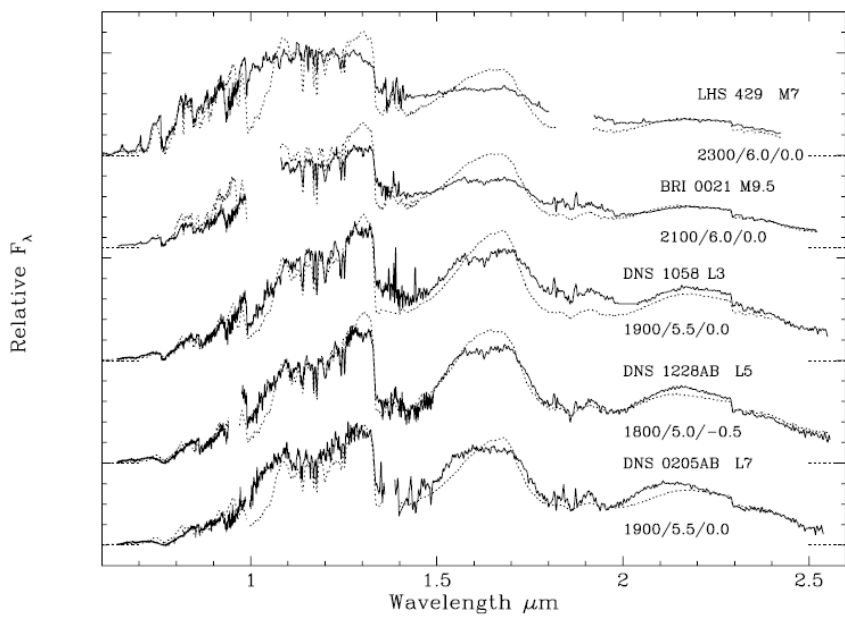
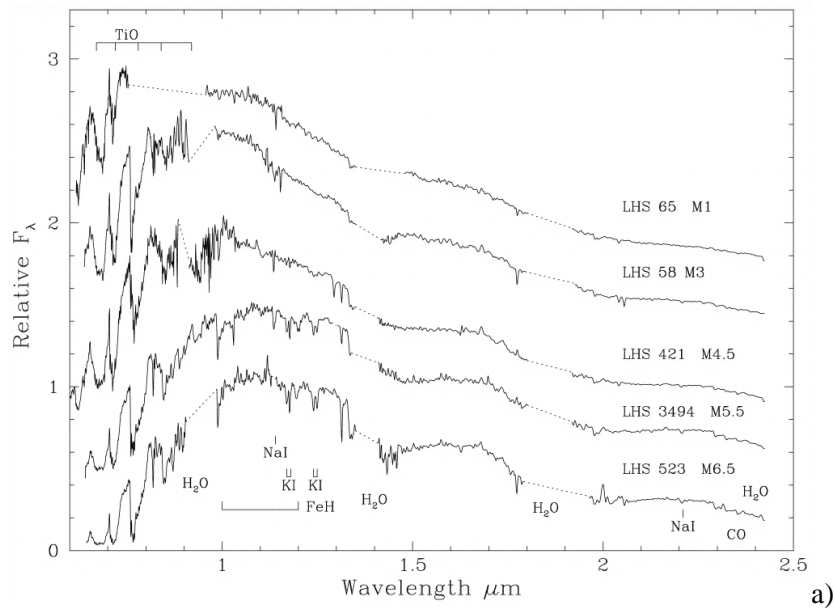
In M stars' atmospheres, most of the hydrogen is in the form of H_2 and H_2O . These molecules, together with carbon CO compounds, sign the IR part of the spectrum. Oxygen can be found again in molecules like TiO (that absorb between 459 nm and 625 nm) or VO, that because of the high absorbance properties, dominate the absorption visible spectrum. The strengths of TiO bands define the spectral optical distribution of late K to M stars in the 0.4-1.2 μm band and with the VO bands it is the principal indicator of the T_{eff} (Allard et al., 1997). These last two molecules dominate the absorption spectrum of M stars in the optical band and absorb a significant part of the stellar flux bluewards of the peak of the spectrum of M0-M2 stars. Late M stars atmospheres are covered by a warm blanket of steam (Scalo et al., 2007).

With their extremely low intrinsic faintness ($10^{-2} - 10^{-5} L_{\text{sun}}$), in particular in the V bandpass, the spectral classification of the nearby stars aiming toward a complete census of the luminosity function is still in progress (Reid, 1994, Kirkpatrick & Beichman, 1995, Liebert et al., 1995, Reid et al., 1995a).

The first complete work aimed to the knowledge of the effective temperature scale of low luminosity stars can be found in Boeshaar et al. (1976), in the visual channel (0.44-0.68 μm), with the identification of CaOH lines at 0.54-0.556 μm as temperature indicators of later than M3.5 stars or the introduction of VO and TiO bands to classify late M5 stars (Henry et al., 1994, Kirkpatrick et al., 1995, Martín et al., 1996).

Boeshaar's classifications soon were extended beyond even the limits of the classical Morgan & Keenan spectral sequence, i.e. to types M9.5-M10, by Kirkpatrick et al., (1995) in the optical to near-infrared regime (0.65–1.5 μm) and by Davidge & Boeshaar (1993), Jones et al., (1994), and Leggett et al (1996) in the near infrared (1.1–2.5 μm).

In Figure 5.3a, 5.3b, 5.3c and 5.3d can be seen the spectral features of M dwarves and brown dwarves as described in Allard et al., (1997) and Leggett et al., (2001).



b)

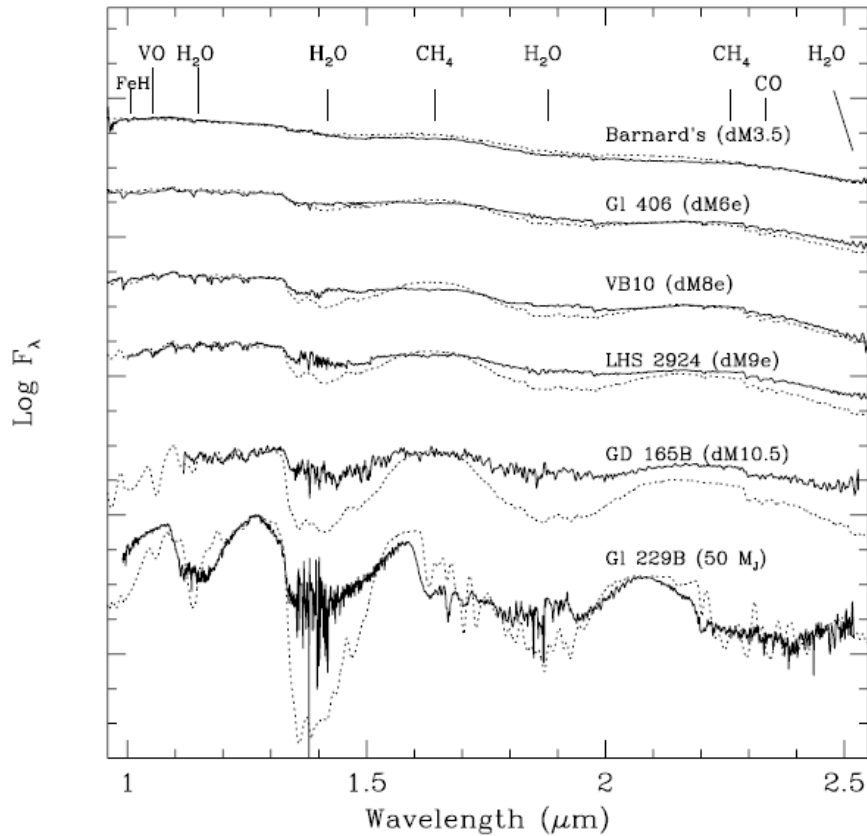
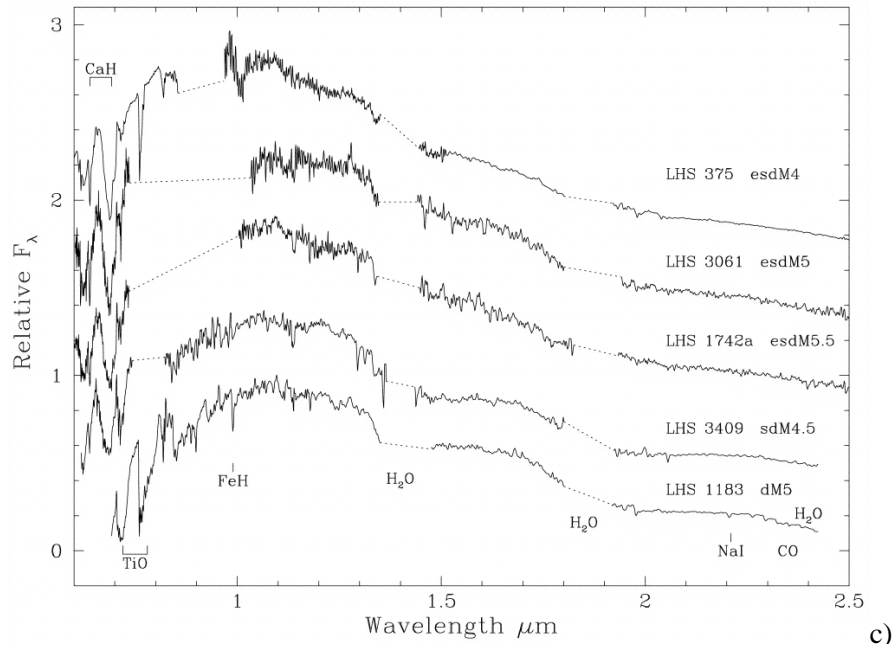


Figure 5.3: (a) Spectral sequence for M dwarfs where the spectra normalized to the flux at 1.2 μm (Leggett et al., 2001), (b) Spectral sequence for late M to L dwarfs where the spectra are normalized to the flux at 1.2 μm ; horizontal dotted lines indicate zero flux levels (Leggett et al., 2000). (c) Spectral sequence for M subdwarfs where the spectra are normalized to the flux at 1.2 μm (Leggett et al., 2000) and (d) NIR spectral sequence of M stars and brown dwarves. The full lines represent the data obtained by Jones et al., (1994) and Geballe et al., (1996), while the dotted lines show OS models with T_{eff} =3400, 3000, 2700, 2600, 2000 and 1000 K. The smaller is the mass, the stronger are the absorption features of water vapor (d) (Allard and Hauschildt, 2000).

Reaching the hydrogen burning limit for M10.5 stars with effective temperature $T_{eff}=2000$ K, the TiO bands disappear from the optical spectral distribution, leaving only the VO bands (Davis, 1994; Kirkpatrick et al., 1995), CaH, CaOH and FeH bands.

As the effective temperature drops into the brown dwarf regime, methane (CH_4) features begin to appear (Tsuji et al., 1995, Allard et al., 1996, Marley et al., 1996), and corundum (Al_2O_3), perovskite (CaTiO_3), iron, enstatite (MgSiO_3), and forsterite (Mg_2SiO_4) clouds may form, enhancing the carbon-oxygen abundance ratio and hardly modifying the thermal structure and opacity of the photosphere (Sharp & Huebner 1990, Fegley & Lodders 1996). From the ground, one of the difficulties in determining the quality of model spectra is due to telluric absorption water bands that filter the light over most of the IR range. Surely, beyond $2.5 \mu\text{m}$, the Earth's atmosphere is nearly opaque and red dwarfs and exoplanet must be observed with infrared space-based facilities such as the HST, NICMOS, ISO, SIRTf, NGST, and Kepler and ARIEL missions. NASA's Kepler mission or CoRoT by ESA can, by the analysis of transits, to discover terrestrial exoplanets. Other instruments are optimized to acquire exoplanetary spectra with coronagraphic or interferometric techniques.

5.3 Variability

Stellar variability could be an important feature to keep under control because it can influence the chemistry of the planets that orbit around as well as their suitability for life.

The luminosities of M stars, once it reaches the main sequence, can be stable on a very long time scale with negligible brightening. It is known that lifetimes for these stars can be $10^{11} - 10^{13}$ years (Laughlin et al., 1997).

The mass loss rate would be destabilizing in term of habitability especially when stellar masses are small because of the large fractional mass change.

As inferred by several measures radio, lack of x-ray halos and Ly α modeling of M star atmospheres mass loss rates are thought to be two orders of magnitude smaller that of the Sun, and then too small to be significant on a timescale of 10^{10} years (Scalo et al., 2007). This seems to be a relation between the mass loss rate and the magnetic activity. In fact a drop in mass loss rate would be the consequence of an high active star (Wood et al., 2005).

This could be due to the formation of large polar spots which may signal the magnetic field reconfiguration into a strong dipole that inhibits the wind, even if Barnes & Cameron (2001) pointed out that polar spots are not so frequent on late, rapidly rotating or active M stars.

Star with masses lower than $0.2 M_{\odot}$ could take 0.3-1 Gyr to reach the main sequence (Burrows et al., 2001) during which time the luminosity can decrease ever of a factor of two. A planet close to the star would have to suffer a temperature lowering from 800 to 1000 K. This phenomenon could be dangerous for the planet because of the risk to loose its atmosphere. This might delay the formation of life on this planet or box it up under the planet's surface. Anyway, though the above assertions are the results of simplified models, it seems that there is no evidence for the mass loss rate to be so high to preclude biological activity on M stars.

5.4 Flares

On short timescales, because of their strong magnetic activity (that begins to cease after 0.55 Gyr depending on the mass of the star), M stars can undergo a period of extreme intermittent variability that manifests under the form of periodic flares, that can enhance the visible, UV, X-ray and radio regions of the stellar spectrum, with a mean interval from hours to weeks.

It is useful to remember that the energy of the flares is dependent on their strength as E^{-p} where E is the energy and p the period (Audard et al., 2000).

The problem in characterizing flares is that when flares occur in several wavelength regions, the emission is not synchronized in time because of transport effects and the amplitudes may not be correlated (Scalo et al.,

2007). It is shown that magnetic indicators like X-ray and H α emission reach a peak around spectral type M6-M7 and decline for later types (Reid et al., 2002; West et al., 2004; Scalo et al., 2007).

As solar-mass stars are thought to have activity decay time scales of 1–3 Gyrs, habitable planets around M stars may be subjected to intense stellar activity for either shorter or longer times than a planet around a solar-type star. This also indicates that, for the stars that are accessible to planet search and biosignature characterization programs and are of early spectral types, the fraction of active stars is very small.

Statistics of flares energies are only well known for soft X-ray and visible band, but in the wavelength region where they can make potential damages to terrestrial type of biota and operate atmospheric photolysis (0.2–0.3 μm) data are still fragmentary.

The smallest flares detectable release about 10^{28} erg of energy, while the most active M stars (dMe) can have flares with energies in the order of $10^{34} - 10^{37}$ ergs (Hawley and Pattersen, 1991; Liebert et al., 1999). Simultaneous X-ray and UV monitoring of flares in five dMe stars using XMM-Newton by Mitra-Kraev showed that there is a slight correlation between X-ray and UV peak fluxes, with a steeper relation for total energies. As UV flares have fluxes one order of magnitude smaller than X-ray flares, these last radiation can be used to monitor UV flares (Mitra-Kraev et al., 2005).

It is important to keep in mind that strong UV fluxes occur only during flares, but absolute chromospheric emission in the 0.2–0.3 μm band for planets in the Habitable Zone is at least one order of magnitude lower than for the Earth. It must be kept in mind that non active M stars exhibits almost no UV flux short ward 250 nm (Segura et al., 2005).

Optical flares are important since UVB flares can operate an intermittent heating of planetary atmospheres and U band light (0.335 μm) can affect biological activity even if it doesn't influence atmospheric photochemistry.

The Palomar/Michigan State University sample suggests that the magnetic activity of M0–M3 stars is bimodal, with most exhibiting no H α emission, some strong H α emission, but with few emissions at intermediate levels. The Sloan sample shows the fraction of dMe stars peaks at 75% of M8 stars with almost 50% between M5 and L0; the somewhat lower fraction of dM3 stars is probably due to the higher fraction of older stars in this high galactic latitude survey (Tarter et al., 2007).

Planets near these stars have the atmosphere constantly out of the equilibrium and a surface whose blue, UV and for thin atmospheres, X-ray luminosity is enhanced 2–100 times.

Barnes (2005) predicted that the (re)coupling of the convective and radiative zones by a magnetic field generated at the interface is required for spin-down, and that the time to reach this state increases with decreasing mass, with fully convective stars never generating the field needed for rotational breaking.

It is indeed known that late type stars spin down monotonically with their age because of angular momentum loss, following a power law $P_{rot} = t^{-\frac{1}{2}}$ (Soderblom, 1982).

Qualitatively, the evolution of luminosity for a late-type star (L_{bol} is nearly constant) has a flat plateau from its arrival at the main sequence up to a certain age (end of saturation phase) and then decreases monotonically with age (Scalo et al., 2007).

A fit to the data gives the relation:

$$L_X = 2.5 \times 10^{28} [t(\text{in Gyrs})]^{1.72} \text{ erg s}^{-1} \quad (5.2)$$

In Figure 5.4 can be seen the evolution in time of late star luminosity L_X normalized with L_{bol} to cope with different types of stars, including solar types and M star types.

Results indicate that M-type stars have scaled XUV irradiances that are 10–100 times higher than the solar type stars of the same age. This XUV radiation could result in heating of the upper atmospheres and evaporation of the planetary atmosphere and water inventory (Lammer et al., 2007). Using the fraction of active stars found by West et al. (2004) at each M subtype, and assuming a constant star formation rate over the age of the galactic disk (10 Gyr), the characteristic time for activity decline and associated decrease in flare activity increases from about 0.2 Gyr to 7 Gyr as stellar mass ranges from 0.5 to 0.1 M_{\odot} .

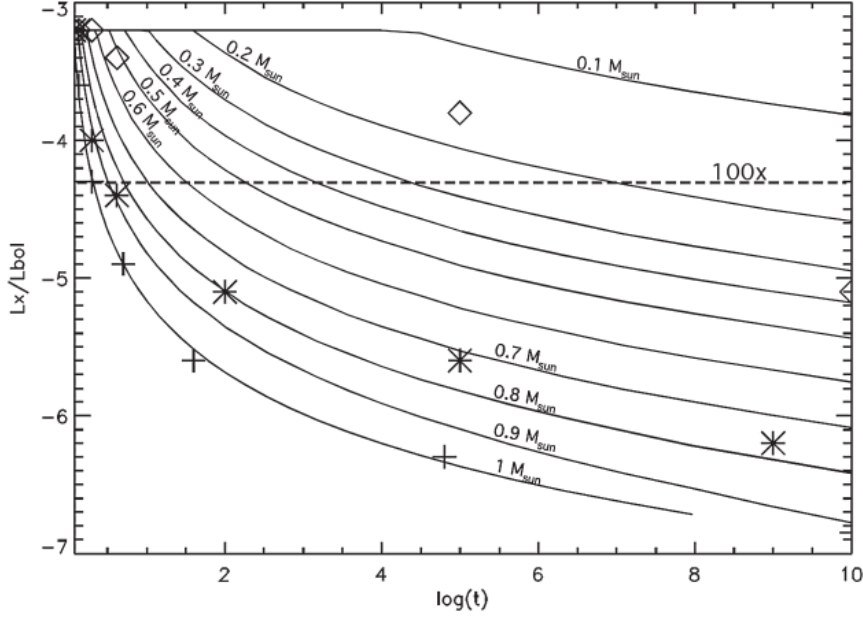


Figure 5.4: In reality, $\frac{L_X}{L_{bol}}$ depends on the age for stars with masses less than $1 M_{\odot}$. Symbols represent stars from the Sun in Time program for solar-like stars and for M stars. In this case, each star begins its life in a saturated plateau phase whose lifetime increases with decreasing mass (Barnes, 2005).

5.5 CME

The powerful flares happening on magnetically active, late-type stars are supposed to be accompanied by strong Coronal Mass Ejection (CME) events. These ones are burst of stellar wind and magnetic fields rising above the stellar corona. CME activity can be found under the form of absorption features in the UV range during the impulsive phase of strong flare events. Some examples where there strong ejections have been found are M stars like EV Lac (Ambruster *et al.*, 1986), AD Leo (Houdebine *et al.*, 1990, 1993a,b, 1996), and AU Microscopii (Cully *et al.*, 1994). The results of Cully *et al.* (1994) lead to the conclusion that CMEs on those stars might be much stronger than solar events.

Moreover, Khodachenko *et al.* (2007) showed that expected magnetospheres of tidally locked weakly magnetized Earth-like exoplanets are strongly affected by the incoming CME plasma flow. He provided a power law of CME density (n_{ejecta}) with the distance to the star. It is composed by two parts: $n_{ejecta}^{min}(d) = 4.88 \left(\frac{d}{d_0}\right)^{-\frac{2}{3}}$ and $n_{ejecta}^{max}(d) = 7.10 \left(\frac{d}{d_0}\right)^{-3}$ with $d_0 = 1$ AU and d in AU.

Together with high X-ray and EUV emissions, the CME effects should lead to an expanded thermosphere–exosphere regions and strong atmospheric erosion.

At large distances (<0.3 AU), the CME plasma density is determined by the density measurements of magnetic clouds (Lammer *et al.*, 2009).

The expected strengths and frequencies of flare and CME events on M stars, along with the evidence that activity and age are strongly correlated, with decay postponed for perhaps 0.1–1 Gyr in early-type M stars, indicate that a major threat to habitability for M star planets is loss of atmosphere (Scalo *et al.*, 2007).

Planets with a small magnetic moment also have a small magnetosphere.

For a small magnetic moment or a strong enough plasma flow, the magnetosphere is so small that its boundary surface (the magnetopause) is located below the outermost layers of the planetary atmosphere (Khodachenko *et al.* 2007b; Lammer *et al.* 2007). The results shown in Figure 5.5 indicate that one can expect many planets within the HZ of dwarf stars with Venus- or Mars-like stellar plasma-atmosphere interactions.

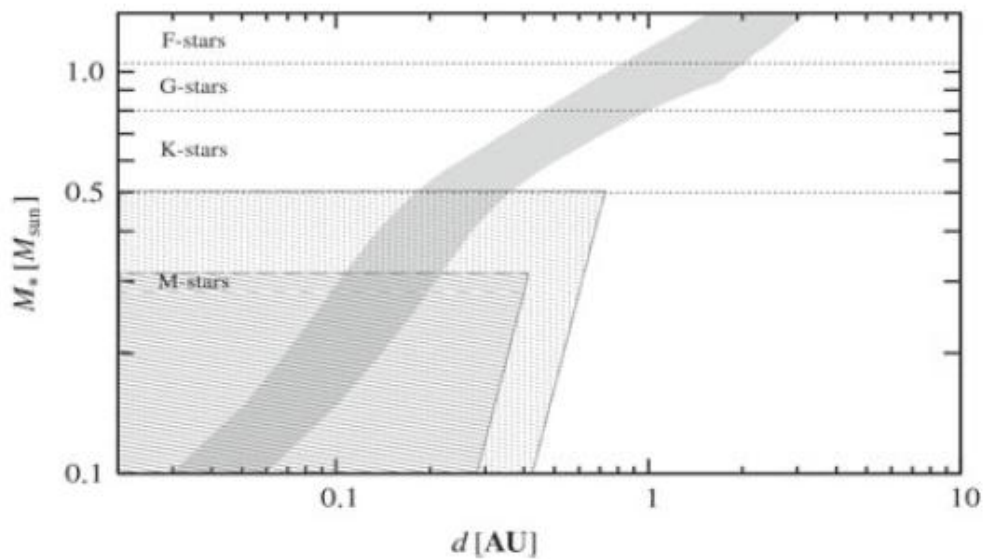


Figure 5.5: Regions where the magnetosphere lies close to the planetary surface. Grey area: Liquid water HZ; Dotted area: region where the magnetopause can be compressed to altitudes <1,000 km above the planetary surface by strong stellar CMEs for an Earth-like planet. *Darker dotted area* same for a super-Earth with 6 times the mass of the Earth and 1.63 times its radius (Léger et al. 2004).

5.6 Starspots

Another example of short term variability is represented by spots, dark regions on the stellar photosphere. They can reduce the stellar flux less than few percent for field M stars (Messina et al., 2003).

However in extreme case spots on M stars could reduce the flux up to 40% for a few months dropping the temperature by 30 K (Joshi et al., 1997). Nevertheless, an atmosphere with a surface pressure of 1 bar would not freeze out even in this extreme cases (Tarter et al., 2007).

Even if it is a large temperature excursion, on Earth some organisms have adapted to suffer similar variations. It is already suspected that photospheric spot activity is not correlated with soft X- ray coronal luminosity for M stars as it is for F, G, and K stars (Messina *et al.*, 2003), with a large range in maximum spot amplitudes at a given high coronal activity (Scalo et al., 2007).

6. Experiment project and management

Hereafter will be described the whole project. In chapter 6.1 will be described the stars, from blackbody curves to the simulated ones and an overview of the different kind of radiation sources available on the market. Then there will be an analysis of reliability of a starlight simulator and a discussion on whether it would be the best solution a time variable or fix illumination device. The realization and construction of the radiation source will be better described in chapter 7. The technical design and realization of the reaction cell where bacteria will be lodged is well described in chapter 8.2. In chapter 6.2 will be described all the biological samples that can match with the exoplanetary conditions and a first creaming off of the best ones. In this chapter will be described the pigments that can allow bacteria to do photosynthesis and the radiation intensity suitable for them to live and operate metabolic processes. Then there will be a section describing the tests for oxygen productivity (described in chapter 8.4.2) to understand how much of it will be expected inside the environmental chamber and the method to detect its concentration (chapter 6.2.3.1). Chapter 6.3 will deal with the planning of the experiment. Finally, in chapter 6.4 there will be an overview of the costs of the project, starting from the vacuum pumps for the preliminary tests, going through the hardware and led prices as well as the gas tanks and the incubator build-up costs.

6.1 Radiation sources

Radiation is the key topic for the experiment. An accurate study of the illumination process and devices available is crucial to have the whole overview of the problem. As already said, the goal is to build a starlight simulator that is capable to reproduce the irradiation of different spectral class stars, mainly F, G, K and M. To understand how build a starlight simulator it must to be understood what kind of sources are available on the market and how their action spectra cover the useful bandwidth.

6.1.1 Stellar spectra analysis

For the led fitting have been used the simulations of four different main sequence stellar types: F, G, K and M and inside these categories 9 stars for each type have been analyzed, from the coldest to the hottest. The temperatures of these stars are illustrated in table 3.1. All the spectra have been realized with a 0.1 nm accuracy and defined over a wavelength range between 340 nm and 1060 nm. In figures 6.1, 6.2, 6.3 and 6.4 can be seen the cited spectra of the stars (Baraffe et al., 2015).

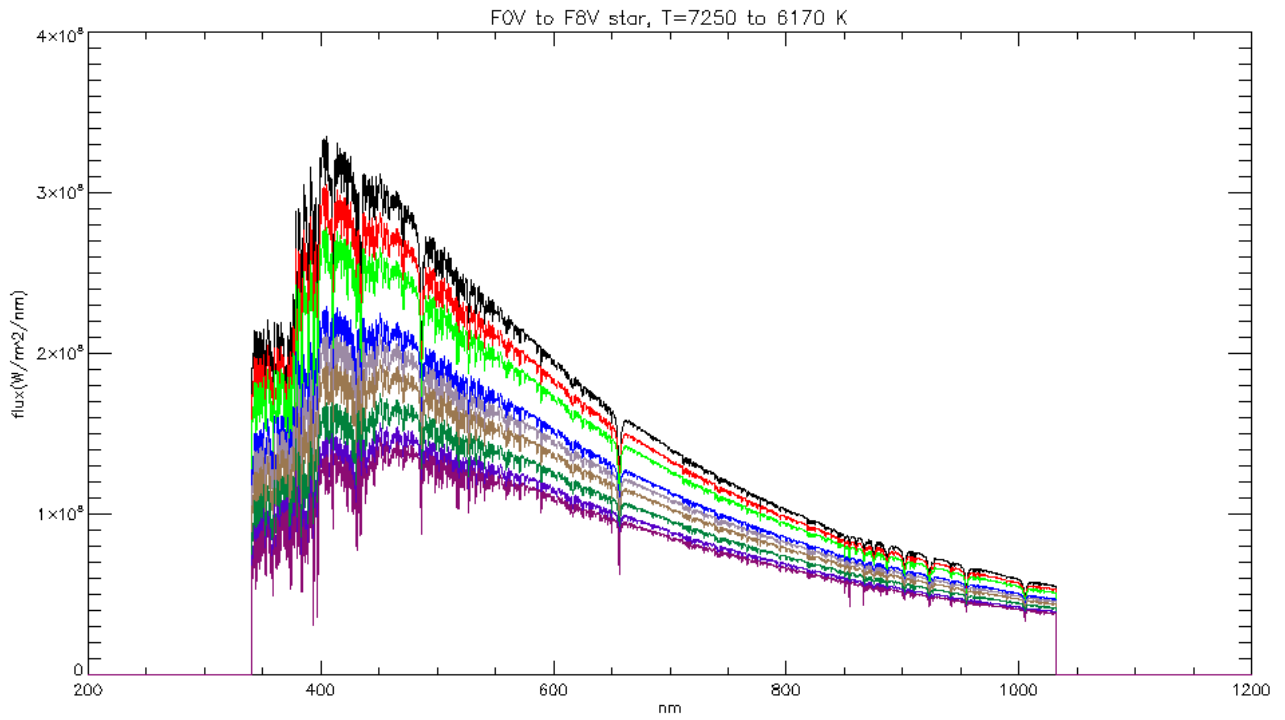


Figure 6.1: Simulated spectra ranging from F0V to F8V stars, temperatures from 7250K and 6120K.

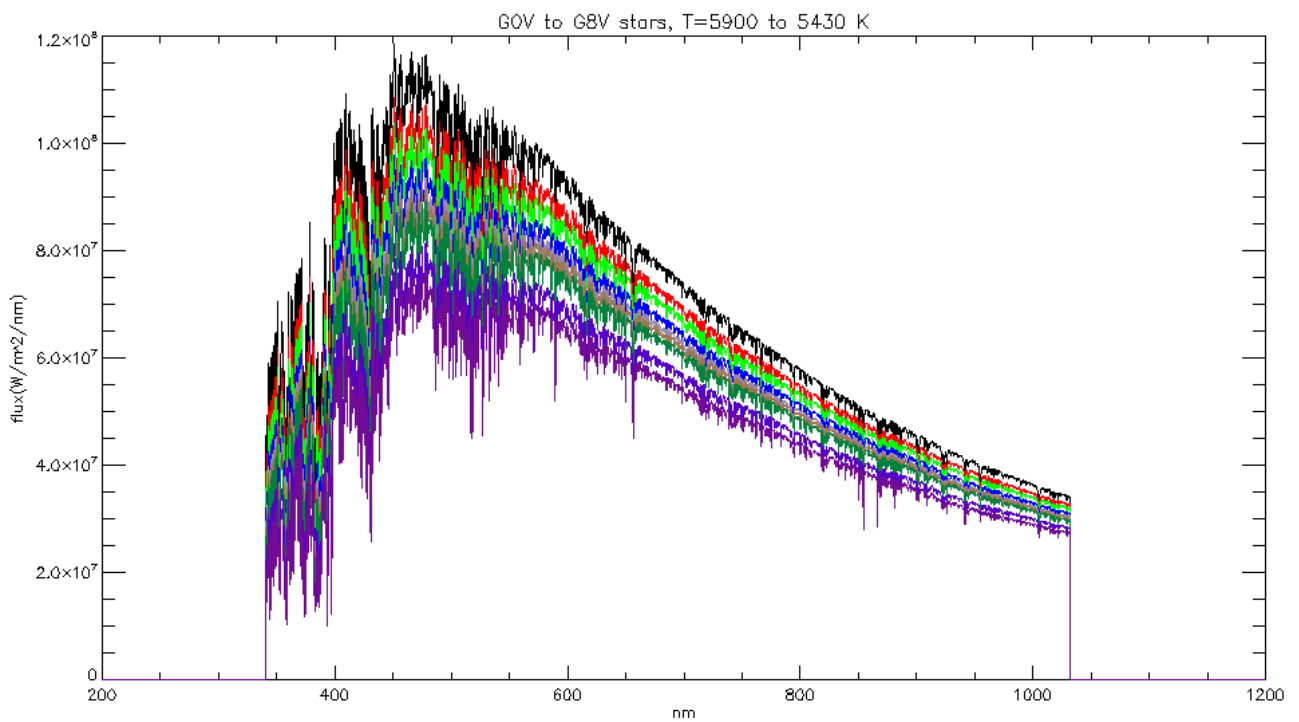


Figure 6.2: Simulated spectra ranging from G0V to G8V stars, temperatures from 5900K and 5430K.

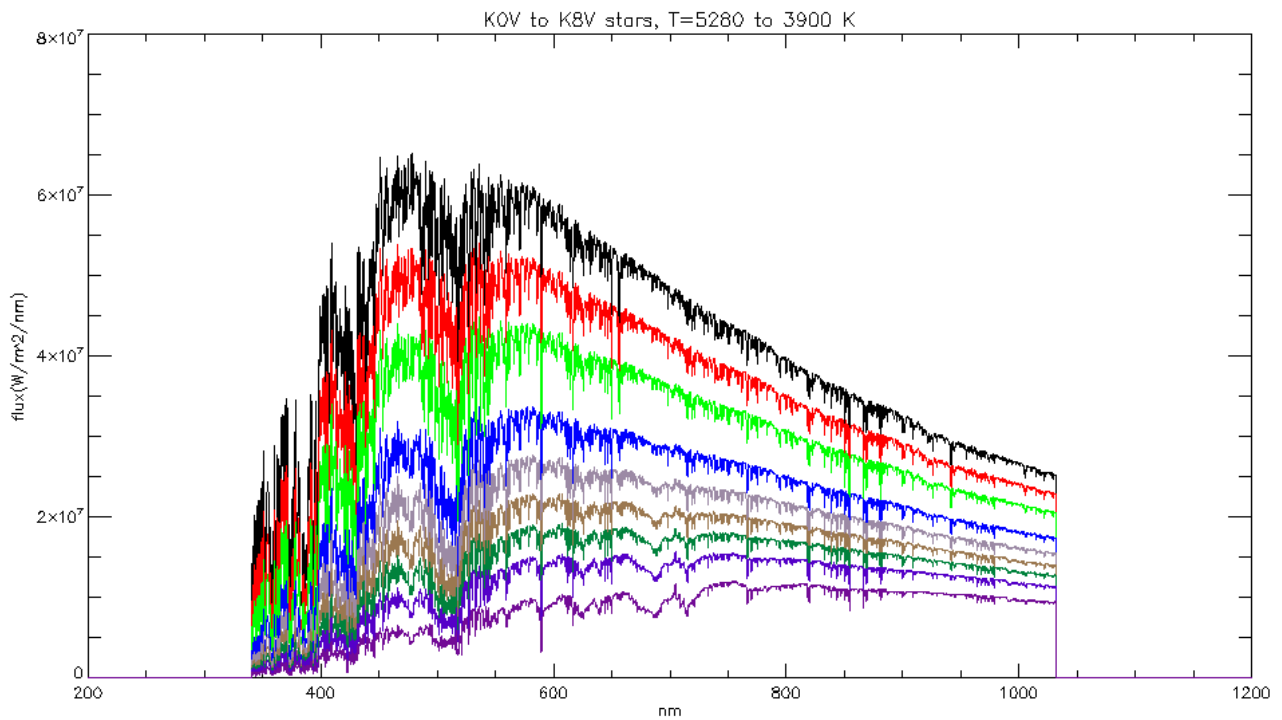


Figure 6.3: Simulated spectra ranging from K0V to K8V stars, temperatures from 5280K and 3900K.

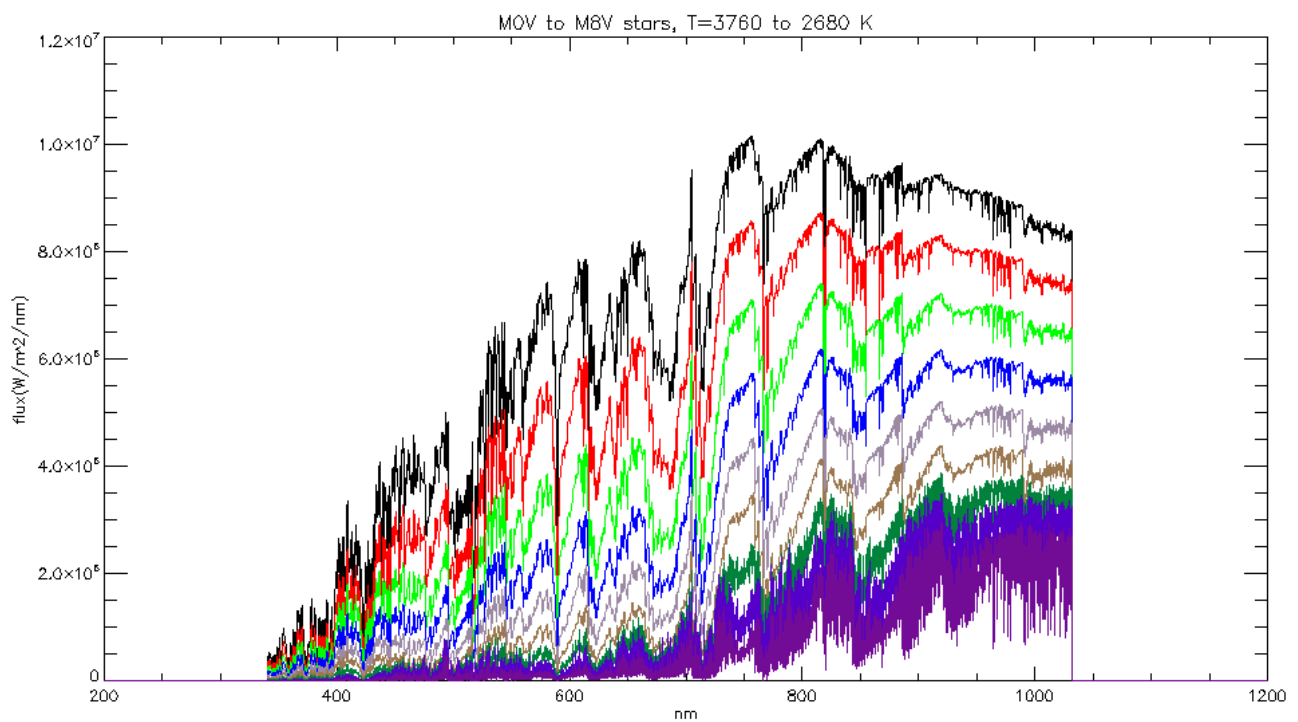


Figure 6.4: Simulated spectra ranging from M0V to M8V stars, temperatures from 3760K and 2680K.

6.1.2 Radiation devices analysis: lamps and LEDs

In order to build a new concept illuminator, the first starting point is the chosen of the radiative source. Lamps are the most common radiation sources on the marketplace. They are broadband devices with an emission spectrum that can cover different wavelengths.

In figure 6.5 are shown different blackbody radiation spectra at different temperatures, corresponding to F, G, K and M stars with superimposed the radiative spectrum of the most common lamps available: Tungsten-Halogen, Mercury, Xenon and Metal-Halide. In figure 6.6 are shown the blackbody radiation spectra at different temperatures, corresponding to F, G, K and M stars with superimposed the absorption spectra of some of the principal photosynthetic pigments As can be seen, the Tungsten-Halogen and the Xenon ones are the only capable to emit in the NIR bandwidth (the peak of M type stars).

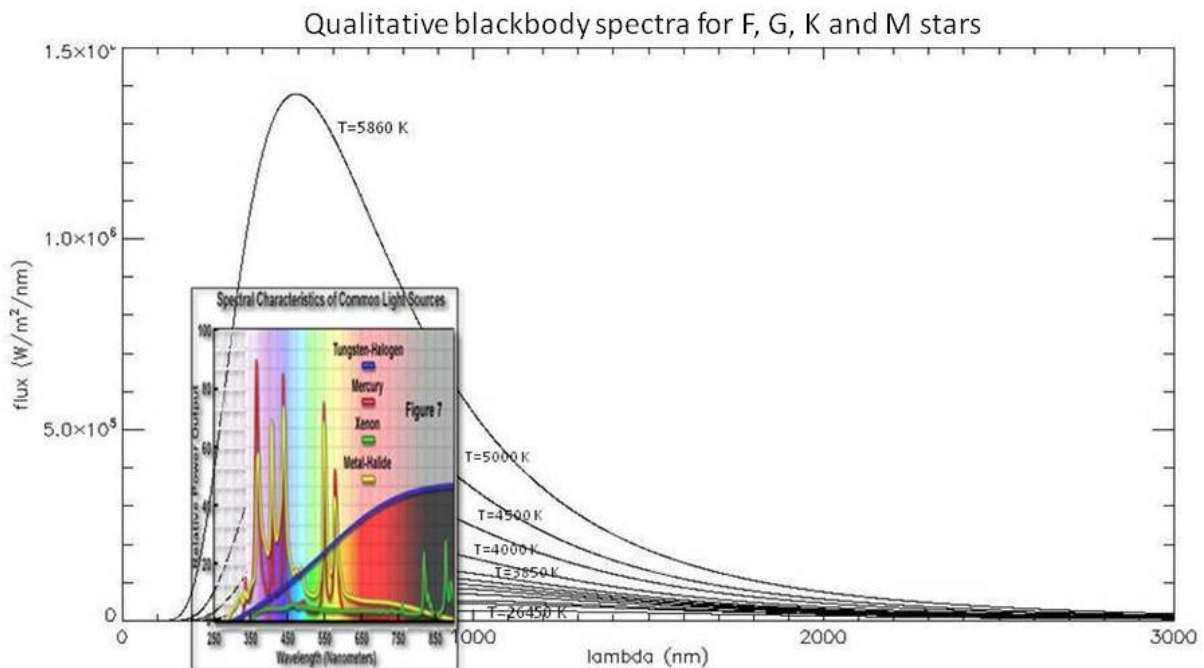


Figure 6.5: Different blackbody radiation spectra at different temperatures, corresponding to F, G, K and M stars with superimposed the radiative spectrum of the most common lamps available: Tungsten-Halogen, Mercury, Xenon and Metal-Halide.

The portion we want to focus on is the photosynthetic active region of several bacteria, that is the region of the spectrum where an organism is capable to metabolize light in order to produce energy for its life.

Adopting broader extremes, we have a lower limit of 280 nm, under which no photosynthetic process is possible, while the higher limit is defined by the ability of the photosynthetic bacteria to absorb the radiation.

In figure 6.6 are shown the different radiation spectra for F, G, K and M stars and the absorption spectra of some of the principal photosynthetic pigments used by photosynthetic bacteria (b).

For the first part of the experiment, the first step of this research, we would need to reproduce the solar spectrum at the surface of the Earth and for this purpose each kind of these lamps could be useful.

An evaluated choice was a Xenon Arc lamp, in particular the ORIEL 6258 300 Watt Ozone Free one used in Galletta et al., 2007, shown in figure 6.7 while in figure 6.8 is shown its spectrum.

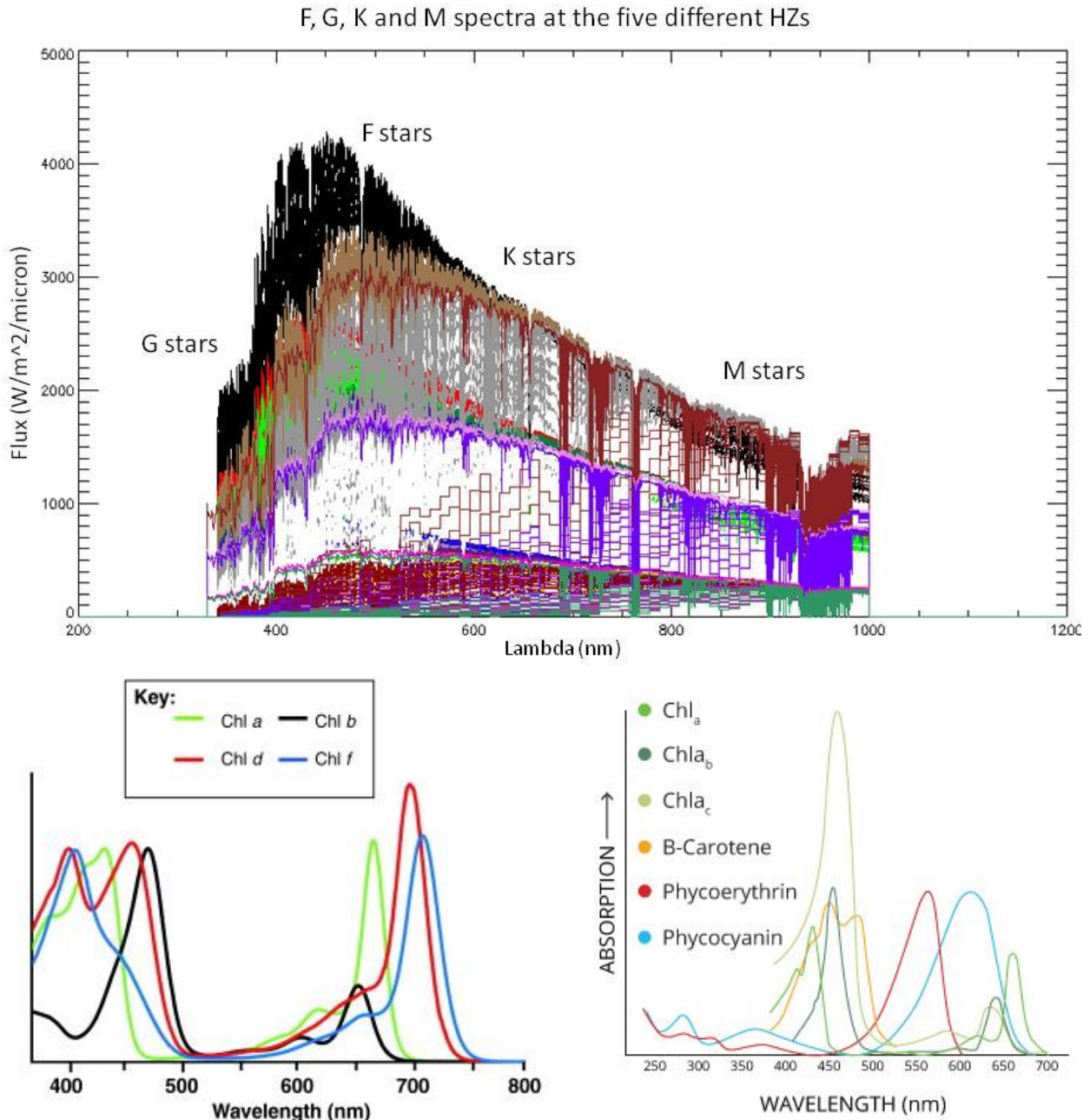


Figure 6.6: different radiation spectra for F, G, K and M stars and the absorption spectra of some of the principal photosynthetic pigments used by photosynthetic bacteria (b). Images from (<http://www.fondriest.com/environmental-measurements/> and Chen et al., (2011))

The advantage of lamps is their high luminosity and broad bandwidth, but their disadvantage is the stillness of the spectrum and the impossibility to change it in real time. Moreover, because several bacteria used for this work are sensible to NIR light and live in ecological niches, the total radiance power of this lamp could be even more than some organisms could bear.



Figure 6.7: Image of ORIEL 6258 300 Watt Ozone Free Xenon Arc lamp

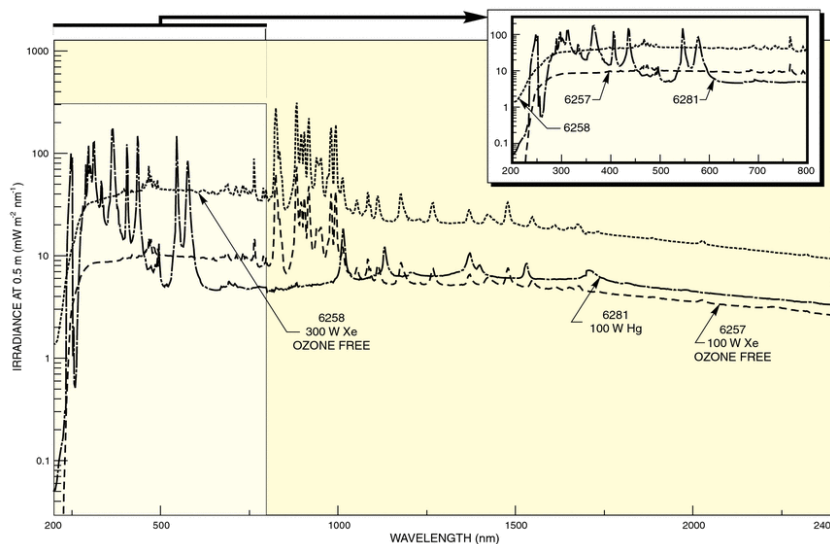


Figure 6.8: Spectrum of the ORIEL 6258 300 Watt Ozone Free Xenon Arc lamp

6.1.2.2. LEDs

The LED consists of a chip of semiconducting material doped with impurities to create a p-n junction. As in other diodes, current flows easily from the p-side, or anode, to the n-side, or cathode, but not in the reverse direction. Charge-carriers—electrons and holes—flow into the junction from electrodes with different voltages. When an electron meets a hole, it falls into a lower energy level and releases energy in the form of a photon. The wavelength of the light emitted, and thus its colour, depends on the band gap energy of the materials forming the p-n junction. In silicon or germanium diodes, the electrons and holes recombine by a non-radiative transition, which produces no optical emission, because these are indirect band gap materials. The materials used for the LED have a direct band gap with energies corresponding to near-infrared, visible, or near-ultraviolet light. Conventional LEDs are made from a variety of inorganic semiconductor materials. Table 6.1 shows the available colours with wavelength range, voltage drop and material (from http://www.oksolar.com/led/led_color_chart.htm).

Color	Wavelength (nm)	Material
	940	GaAIAs/GaAs -- Gallium Aluminum Arsenide/Gallium Arsenide
	880	GaAIAs/GaAs -- Gallium Aluminum Arsenide/Gallium Arsenide
	850	GaAIAs/GaAs -- Gallium Aluminum Arsenide/Gallium Aluminum Arsenide
	660	GaAIAs/GaAs -- Gallium Aluminum Arsenide/Gallium Aluminum Arsenide
	635	GaAsP/GaP - Gallium Arsenic Phosphide / Gallium Phosphide
	633	InGaAIP - Indium Gallium Aluminum Phosphide
	620	InGaAIP - Indium Gallium Aluminum Phosphide
	612	InGaAIP - Indium Gallium Aluminum Phosphide
	605	GaAsP/GaP - Gallium Arsenic Phosphide / Gallium Phosphide
	595	InGaAIP - Indium Gallium Aluminum Phosphide
	592	InGaAIP - Indium Gallium Aluminum Phosphide
	585	GaAsP/GaP - Gallium Arsenic Phosphide / Gallium Phosphide
	4500K	SiC/GaN -- Silicon Carbide/Gallium Nitride
	6500K	SiC/GaN -- Silicon Carbide/Gallium Nitride
	8000K	SiC/GaN - Silicon Carbide / Gallium Nitride
	574	InGaAIP - Indium Gallium Aluminum Phosphide
	570	InGaAIP - Indium Gallium Aluminum Phosphide

Color	Wavelength (nm)	Material
Red	565	GaP/GaP - Gallium Phosphide/Gallium Phosphide
Orange	560	InGaAlP - Indium Gallium Aluminum Phosphide
Yellow	555	GaP/GaP - Gallium Phosphide/ Gallium Phosphide
Green	525	SiC/GaN - Silicon Carbide / Gallium Nitride
Cyan	505	SiC/GaN - Silicon Carbide / Gallium Nitride
Blue	470	SiC/GaN - Silicon Carbide / Gallium Nitride
Violet	430	SiC/GaN - Silicon Carbide / Gallium Nitride

Table 6.1: available colours with wavelength range, voltage drop and material ()

LEDs have a lot of advantages for this research. The first is the efficiency. LEDs emit more light per watt than incandescent light bulbs. The efficiency of LED lighting fixtures is not affected by shape and size, unlike fluorescent light bulbs or tubes. Moreover, LEDs can emit light of an intended colour without using any colour filters as traditional lighting methods need. This is more efficient and can lower initial costs. LEDs can be very small, sometimes smaller than 2 mm². LEDs light up very quickly [a typical red indicator LED will achieve full brightness in under a microsecond (Avago Technologies Inc., 2010)]. LEDs can have a relatively long useful life. One report estimates 35,000 to 50,000 hours of useful life, though time to complete failure may be longer. They have reduced maintenance costs from this extended lifetime, rather than energy savings. Being solid-state components, are difficult to damage with external shock, unlike fluorescent and incandescent bulbs, which are fragile. The solid package of the LED can be designed to focus its light. Incandescent and fluorescent sources often require an external reflector to collect light and direct it in a usable manner. For larger LED packages total internal reflection (TIR) lenses are often used to the same effect. However, when large quantities of light is needed many light sources are usually deployed, which are difficult to focus or collimate towards the same target. The disadvantages are the temperature dependence: LED performance largely depends on the ambient temperature of the operating environment: over-driving a LED in high ambient temperatures may result in overheating the LED package, eventually leading to device failure. An adequate heat sink is needed to maintain long life. Another drawback is the light quality: most cool-white LEDs have spectra that differ significantly from a black body radiator like the sun or an incandescent light. Single LEDs do not approximate a point source of light giving a spherical light distribution, but rather a lambertian distribution. So LEDs are difficult to apply to uses needing a spherical light field, however different fields of light can be manipulated by the application of different optics or "lenses". LEDs cannot provide divergence below a few degrees. In contrast, lasers can emit beams with divergences of 0.2 degrees or less (Hecht, 2002). For our purpose, one of the best feature of LEDs is that it is possible to switch it on or off driving it by a pc. This is a great advantage respect to lamp illumination, that have a fix spectrum, because an array of LEDs could be used to match the desired part of the spectrum lightening them in sequence. High-power LEDs (figure 6.9) are an alternative to overcome this problem, especially at high wavelengths.



Figure 6.9: High-power light-emitting diodes attached to an LED star base (Luxeon, Lumileds)

High-power LEDs (HPLEDs) or high-output LEDs (HO-LEDs) can be driven at currents from hundreds of mA to more than an ampere, compared with the tens of mA for other LEDs. Some can emit over a thousand lumens. LED power densities up to 300 W/cm^2 have been achieved (Poensgen et al., 2013). Since overheating is destructive, the HPLEDs must be mounted on a heat sink to allow for heat dissipation. Some well-known HPLEDs in this category are the Nichia 19 series, Lumileds Rebel Led, Osram Opto Semiconductors Golden Dragon, and Cree X-lamp. As of September 2009, some HPLEDs manufactured by Cree Inc. now exceed 105 lm/W (e.g. the XLamp XP-G LED chip emitting Cool White light) and are being sold in lamps intended to replace incandescent, halogen, and even fluorescent lights, as LEDs grow more cost competitive. The efficacy of this type of HPLED is typically 40 lm/W (Leds magazine, 2006). A large number of LED elements in series may be able to operate directly from line voltage. The best choice, taking account of all radiative sources is to build a radiation source capable to adapt to different situations and to mimic different stellar types. The concept is twofold: dynamism and simplicity. Standard lamps can give us a good spectral range but they have the drawback that they aren't modular at low orders. That's important when it is necessary to simulate different absorption lines. For this point the intuition of LEDs is crucial. LEDs have the advantage of the modularity and can well fit with our purposes. Different LEDs channels can allow low order simulations and dynamism because they can be driven by a PC. They are simple too, and cheap, and can be modulated in different arrays so as to replace only the broken ones in case of failure. In chapter 7 will be described in detail the road that led us to the realization of our starlight simulator, starting from the idea up to the real hardware make-of.

6.2 Biological samples

Biological samples are another key point for the experiment. The idea behind the choice of these samples is twofold. We'll use both photosynthetic organisms that have photosynthetic pigments capable to use NIR light like Chld and Chlf and organisms that usually don't have these photopigments but can modify their photosynthetic apparatus in order to adapt to different light conditions, and in particular to NIR light conditions. In Gan et al., (2015) is well described the occurrence of Far-Red Light Photo-acclimation (FaRLiP) in diverse cyanobacteria. Organisms performing FaRLiP contain a conserved set of 17 genes encoding paralogous subunits of the three major photosynthetic complexes. Far-red light photo-acclimation leads to substantial remodelling of the photosynthetic apparatus and other changes in cellular metabolism through extensive changes in transcription. Far-red light photo-acclimation appears to be controlled by a red/far-red photoreceptor, RfpA, as well as two response regulators (RfpB and RfpC), one of which is a DNA-binding protein. The remodelled photosynthetic complexes, including novel phycobiliproteins, absorb light above 700 nm and enable cells to grow in far-red light. A much simpler acclimation response, low-light photo-acclimation (LoLiP), occurs in some cyanobacteria that contain the *apcD4-apcB3-isiX* cluster, which allows cells to grow under low light conditions (Gan and Bryant, 2015). The advantage of this approach is that we can choose bacteria all over the phylogenetic tree, according to the temperature, salinity, acidity and pressure of the planet under study. To extend the experiment to different biota we will perform measurements even with algae and mosses.

6.2.1 Narrowing down the range

In order to perform our experiment we considered both model and atypical photosynthetic organisms. Between the model ones the moss *Physcomitrella patens*, the green microalga *Chlamydomonas reinhardtii* the cyanobacterium *Synechococcus* and *Chroococcidiopsis thermalis* PCC 7203 have been chosen. All of them are characterized by the presence of chlorophylls (chlorophyll a and b) with an in vivo absorption major peak in the Red (around 680 nm). We also selected a series of other peculiar photosynthetic microorganisms able to extend their in vivo absorption to the NIR (around 710 nm), due to particular rearrangement of the chlorophyll a in their photosystems or to the presence of other chlorophyll forms (chlorophyll d and f). To this second group of organisms belong the cyanobacteria *Acaryochloris marina*, *Halomicronema hongdechloris* and *Chlorogloeopsis fritschii*. The microalga *Ostreobium* sp. is capable to organize its photosynthetic apparatus to photosynthesize in far red light. *Physcomitrella patens* is an early colonist moss that can grow on exposed mud and earth around the edges of pools of water. *P. patens* has a disjunct distribution (separated from each other geographically) in temperate parts of the world, with the exception of South America. They contain Chl a and b.

Chlamydomonas species are widely distributed worldwide in soil and fresh water. *Chlamydomonas reinhardtii* is a single-cell green alga about 10 micrometers in diameter. It has an “eyespot” that senses light and the organism is able to swim due to the presence of two flagella.

Chlamydomonas reinhardtii is an especially well studied biological model organism, partly due to its ease of culturing and the ability to manipulate its genetics. When illuminated, *C. reinhardtii* can grow photoautotrophically, but it can also grow in the dark if supplied with organic carbon. They contain Chl a and b.

Synechococcus sp. is a unicellular (3-4 μ of diameter), euryhaline cyanobacterium. It is a model organism for studies of cyanobacterial metabolism. It exhibits an exceptional tolerance of high-light irradiation and shows very rapid growth. The habitats from which this and closely related strains were isolated are subject to changes in several environmental factors, including light, nutrient supply, temperature, and salinity. It contains Chla.

Chroococcidiopsis sp. 7203 is one of the most primitive cyanobacteria (blue-green algae) known. It is a photosynthetic, coccoidal bacteria. The ability of *Chroococcidiopsis* to resist desiccation in arid environments is due in part to the fact that it colonizes the underside of translucent rocks. The underside of these rocks provides enough condensed moisture for growth while the rock's translucent nature allows just enough light to reach the organism for photosynthesis to occur.

Halomicronema hongdechloris is the first reported filamentous cyanobacterium containing Chl f together With Chl a (Chen et al., 2012). It was isolated from a stromatolite cyanobacterial community. The extremely slow growth rate of *H. hongdechloris* has hindered research on this newly isolated cyanobacterium and the investigation of chlorophyll f-photosynthesis. Chlf is Reported to be a “red-light-induced” chlorophyll with increased amount when *H. hongdechloris* is cultured under far-red-light (Chen et al., 2012)

Acaryochloris marina is a cyanobacterium containing Chlorophyll d, instead of Chlorophyll a allowing it to utilize far-red light, at 710 nm wavelength.

It is a species living in symbiosis with invertebrate marine organisms.

It was first discovered in 1993 from coastal isolates of coral in the Republic of Palau in the west Pacific Ocean.

Scientists including NASA's Nancy Kiang have proposed that the existence of *Acaryochloris marina* suggests that organisms that use Chlorophyll d, rather than Chlorophyll a, may be able to perform oxygenic photosynthesis on exoplanets orbiting red dwarf stars (which emit much less light than the Sun). Because approximately 70 percent of the stars in the Milky Way galaxy are red dwarfs, the existence of *Acaryochloris marina* implies that oxygenic photosynthesis may be occurring on far more exoplanets than astrobiologists initially thought possible (Kiang et al., 2007a).

Chlorogloeopsis fritschii is a terrestrial cyanobacterium that can grow in hot springs.

In 2014 the production of chlorophyll f and chlorophyll d in the cyanobacterium *Chlorogloeopsis fritschii* cultured under near-infrared and natural light conditions was reported.

In the laboratory, the ratio of chlorophyll f to chlorophyll a changed from 1:15 under near-infrared, to an undetectable level of chlorophyll f under artificial white light.

C. fritschii produced chlorophyll f and chlorophyll d when cultured under natural light to a high culture density in a 20 L bubble column photobioreactor.

In figure 6.10 are shown different images of these biotypes.

Cyanobacterium aponinum strain PCC 10605 is a fresh water cyanobacterium of the Chroococcales gender. It absorbs large quantities of CO₂ and produce O₂.

Ostreobium sp. is a green alga.

The plants consists of endozoic (endolithic) branched siphonous filaments 1-160 µm in diameter. Filaments are straight and sparsely branched or forming irregular, tangled networks. They form cylindrical portions and/or with inflated regions. Chloroplasts are small, spherical or polyhedral to reticulate with no presence of pyrenoids. Cell walls are thin and undifferentiated to thick and lamellose. Their reproduction is by quadriflagellate zoospores known only *Ostreobium quekettii*. *Ostreobium marine* is widely distributed in tropical to temperate areas, growing primarily in calcified substrata including corals, calcified red algae and old mollusk shells. *Ostreobium* is among the deepest growing macroalgae in both temperate and tropical regions. Physiological studies on in situ photosynthesis by *Ostreobium* confirm low levels of light requirements and an ability to utilize near infra-red light greater than other green algae. A modified photosystem I reaction centre was hypothesized to account for this.

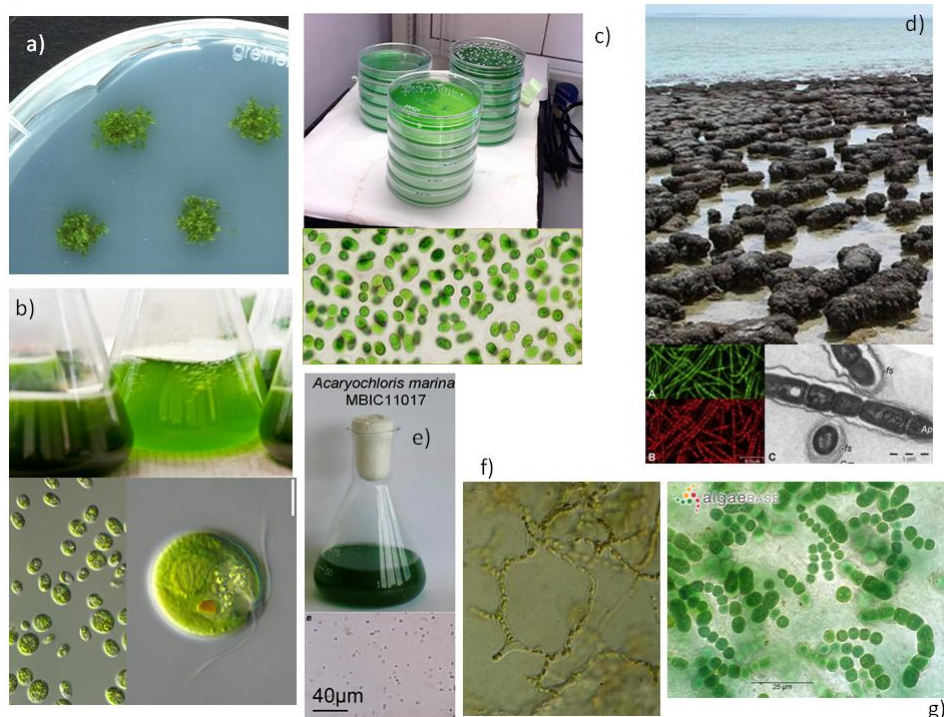


Figure 6.10: In figure we can see samples of (a) "Physcomitrella growing on agar plates" by Sabisteb - Anja Martin from the Ralf_Reski lab., (b) *Chlamydomonas reinhardtii*, (c) *Synechococcus sp.* , (d) *Halomicronema hongdechloris* (Chen et al., 2012), (e) *Acaryochloris marina*, (f) *Ostreobium quekettii* and (g) *Chlorogloeopsis fritschii*

6.2.2 Organisms choice

The bacteria that have been chosen for this research are *Chroococcidiopsis Thermalis* strain PCC 7203, *Chlorogloeopsis fritschii* PCC 6912, *Synechococcus sp.* PCC 7335 and *Cyanobacterium aponinum strain PCC 10605* as well as the moss *Physcomitrella patens*. In particular *Chlorogloeopsis fritschii* has been chosen because it owes the capability of modify its photosynthetic apparatus, if grown in NIR light, to develop Chls that can metabolize such wavelengths and use them to produce energy. *Cyanobacterium aponinum* has been chosen because it is a model and well known organisms like *Synechococcus sp.* PCC 7335. *Chroococcidiopsis Thermalis* has been chosen for its ability to resist to desiccation and *Physcomitrella patens* because it is not a bacterium but a moss. It is important to understand the behavior of organisms that are the direct link from aquatic and land plants and know their adaptability to different environments. Hereafter will be described the final part of the research of the best substrates for the bacteria to live in. In particular, as many of them are not well known yet, a great research work have been done to find the most suitable culture terrains.

The best substrate for *Chroococcidiopsis Thermalis* strain PCC 7203 is composed by:

5 ml/L of NaNO₃ Sodium nitrate (150 g for 500 ml of H₂O)

5 ml/L of K₂HPO₄ potassium hydrogen phosphate (3,05 g for 500 ml of H₂O)

5 ml/L of MgSO₄ *7H₂O magnesium sulphate heptahydrate (7,5 gr in 500 ml di H₂O)

5 ml/L of CaCl₂ *2H₂O Calcium chloride dihydrate (3,6 gr in 500 ml di H₂O)

5 ml/L of AS00005 Solution of Citric acid monohydrate +Iron (III) ammonium citrate (0,06 + 0,06 g for 50 ml of H₂O)

5 ml/L of AS00006 EDTA (0,1 g for 500 ml of H₂O)

10 ml/L of Na₂CO₃ sodium carbonate (2 g for 500 ml of H₂O)

10 ml/L of AS00008 Micro-nutrients solution

959 ml of H₂O distilled water (up to a volume of 1000ml)

This solution have been put into an autoclave at 120°C for 20m ad then added with Blue Green medium (BG11) 0,02% carbonic anhydrase activity (CAA).

Here, AS00005, AS00006 EDTA and AS00008 are described as follow:

AS00005 is citric acid monohydrate + Iron (III) ammonium citrate:

0,06 g of C₆H_{5+4y}Fe_xN_yO₇ Iron (III) ammonium citrate

0,06 g of C₆H₈O₇ *H₂O Citric acid monohydrate

H₂O distilled water (up to a volume of 50 ml)

Each quantity has been weighted and dissolved separately in 15 ml of sterile water and then mixed together reaching the final volume.

Then the solution has been preserved for 10 days without light.

AS00006 EDTA is composed this way:

0,1 g of C₁₀H₁₆N₂O₈ EDTA (Ethylenediaminetetraacetic acid)

H₂O distilled water (up to a volume of 500ml)

Preservable for 3 months at 4°C

AS00008 micronutrient solutions is composed this way:

H₃BO₃ boric acid (1,43 g for 500 ml of H₂O)

MnCl *4H₂O manganese chloride tetrahydrate (0,905 g for 500 ml of H₂O)

ZnSO₄ *7H₂O zinc sulfate heptahydrate (0,111 g for 500 ml of H₂O)

NaMoO₄ *2H₂O sodium molybdate dihydrate (0,1572 g for 500 ml of H₂O)

CuSO₄ *5H₂O Copper sulphate (II) pentahydrated (0,0395 g for 500 ml of H₂O)

Co(NO₃)₂ *6H₂O cobaltous nitrate hexahydrate (0,0247 g for 500 ml of H₂O)

Each component has been dissolved in a small volume of sterile water (< 41,6 ml for each so as not to run over 500 ml of H₂O) and then mixed in the order they have been described.

sodium molybdate dihydrate (NaMoO₄ *2H₂O) can be replaced with sodium molybdate pentahydrated (NaMoO₄ *5H₂O) weighting 0,195 g for 500 ml.

Preservable for 2 years at a 4°C.

The solution for *Cyanobacterium aponinum* strain PCC 10605 and *Chlorogloeopsis fritschii* PCC 6912 is:

5 ml/L of AS00050 solution of *sodium hydrogen carbonate* (25,2 g for 300 ml of H₂O)

5 ml/L of K₂HPO₄ *potassium hydrogen phosphate* (3,05 g for 500 ml of H₂O)

5 ml/L of MgSO₄*7H₂O *magnesium sulphate eptahydrate* (7,5 g for 500 ml of H₂O)

5 ml/L of CaCl₂*2H₂O *Calcium chloride dihydrate* (3,6 g for 500 ml of H₂O)

5 ml/L of AS00005 *Citric acid monohydrate solution* + *Iron (III) ammonium citrate* (0,06 + 0,06 g for 50 ml of H₂O)

5 ml/L of AS00006 *ETDA* (0,1 g for 500 ml of H₂O)

10 ml/L of Na₂CO₃ *Sodium carbonate* (2 g for 500 ml of H₂O)

1 ml/L of AS00008 *Micro-nutrients solution*

964 ml of H₂O *distilled water* (up to a volume of 1000ml)

This solution have been put into an autoclave at 120°C for 20m

AS00005 is *citric acid monohydrate* + *Iron (III) ammonium citrate*:

0,06 g of C₆H_{5+4y}Fe_xN_yO₇ *Iron (III) ammonium citrate*

0,06 g of C₆H₈O₇*H₂O *Citric acid monohydrate*

H₂O *distilled water* (up to a volume of 50 ml)

Each quantity has been weighted and dissolved separately in 15 ml of sterile water and then mixed together reaching the final volume.

Then the solution has been preserved for 10 days without light.

AS00006 *EDTA* is composed this way:

0,1 g of C₁₀H₁₆N₂O₈ *EDTA (Ethylenediaminetetraacetic acid)*

H₂O *distilled water* (up to a volume of 500ml)

Preservable for 3 months at 4°C

AS00008 *micronutrient solutions* is composed this way:

H₃BO₃ *boric acid* (1,43 g for 500 ml of H₂O)

MnCl*4H₂O *manganese chloride tetrahydrate* (0,905 g for 500 ml of H₂O)

ZnSO₄*7H₂O *zinc sulfate eptahydrate* (0,111 g for 500 ml of H₂O)

NaMoO₄*2H₂O *sodium molybdate dihydrate* (0,1572 g for 500 ml of H₂O)

CuSO₄*5H₂O *Copper sulphate (II) pentahydrated* (0,0395 g for 500 ml of H₂O)

Co(NO₃)₂*6H₂O *cobaltous nitrate exahydrate* (0,0247 g for 500 ml of H₂O)

Each component has been dissolved in a small volume of sterile water (< 41,6 ml for each so as not to run over 500 ml of H₂O) and then mixed in the order they have been described.

sodium molybdate dihydrate (NaMoO₄*2H₂O) can be replaced with *sodium molybdate pentahydrated* (NaMoO₄*5H₂O) weighting 0,195 g for 500 ml.

Preservable for 2 years at a 4°C.

AS00050 *Sodium hydrogen carbonate solution*:

25,2 g of NamcoO₃ *Idrogenocarbonato di sodio*

distilled H₂O (up to a volume of 300ml)

This solution have been put into an autoclave at 120°C for 20m

The substrate for *Synechococcus sp.* PCC 7335 is, for 1L of substrate:

900 ml of *Chroococcidiopsis thermalis* PCC7203 substrate (without CAA) + 100 ml of *Turks Island Salts 4X*.

This solution have been put into an autoclave at 120°C for 20m

Chroococcidiopsis thermalis PCC7203 substrate (without CAA) is such composed:

5 ml/L of NaNO₃ *Sodium nitrate* (150 g for 500 ml of H₂O)

5 ml/L of K₂HPO₄ *potassium hydrogen phosphate* (3,05 g for 500 ml of H₂O)

5 ml/L of MgSO₄*7H₂O *magnesium sulphate heptahydrate* (7,5 gr in 500 ml di H₂O)

5 ml/L of CaCl₂*2H₂O *Calcium chloride dihydrate* (3,6 gr in 500 ml di H₂O)

5 ml/L of AS00005 Solution of *Citric acid monohydrate* +Iron (III) ammonium citrate (0,06 + 0,06 g for 50 ml of H₂O)
5 ml/L of AS00006 EDTA (0,1 g for 500 ml of H₂O)
10 ml/L of Na₂CO₃ sodium carbonate (2 g for 500 ml of H₂O)
10 ml/L of AS00008 Micro-nutrients solution
959 ml of H₂O distilled water (up to a volume of 1000ml)

AS00005 is *citric acid monohydrate* + Iron (III) ammonium citrate:

0,06 g of C₆H_{5+4y}Fe_xN_yO₇ Iron (III) ammonium citrate

0,06 g of C₆H₈O₇ *H₂O *Citric acid monohydrate*

H₂O distilled water (up to a volume of 50 ml)

Each quantity has been weighted and dissolved separately in 15 ml of sterile water and then mixed together reaching the final volume.

Then the solution has been preserved for 10 days without light.

AS00006 EDTA is composed this way:

0,1 g of C₁₀H₁₆N₂O₈ EDTA (*Ethylenediaminetetraacetic acid*)

H₂O distilled water (up to a volume of 500ml)

Preservable for 3 months at 4°C

AS00008 micronutrient solutions is composed this way:

H₃BO₃ boric acid (1,43 g for 500 ml of H₂O)

MnCl *4H₂O manganese chloride *tetrahydrate* (0,905 g for 500 ml of H₂O)

ZnSO₄ *7H₂O *zinc sulfate eptahydrate* (0,111 g for 500 ml of H₂O)

NaMoO₄ *2H₂O *sodium molybdate dihydrate* (0,1572 g for 500 ml of H₂O)

CuSO₄ *5H₂O *Copper sulphate (II) pentahydrated* (0,0395 g for 500 ml of H₂O)

Co(NO₃)₂ *6H₂O *cobaltous nitrate exahydrate* (0,0247 g for 500 ml of H₂O)

Each component has been dissolved in a small volume of sterile water (< 41,6 ml for each so as not to run over 500 ml of H₂O) and then mixed in the order they have been described.

sodium molybdate dihydrate (NaMoO₄ *2H₂O) can be replaced with *sodium molybdate pentahydrated* (NaMoO₄*5H₂O) weighting 0,195 g for 500 ml.

Preservable for 2 years at a 4°C.

Turks Island Salts (for 1 L):

112 g of NaCl Sodium chloride to be dissolved in 450 ml of H₂O

2,68 g of HCl potassium chloride to be dissolved in 50 ml of H₂O

22 g of MgCl₂*6H₂O Magnesium chloride hexahydrate to be dissolved in 100 ml of H₂O

27,7 g of MgSO₄*7H₂O Magnesium sulphate eptahydrate to be dissolved in 150 ml of H₂O

5,8 g of CaCl₂*2H₂O Calcium chloride dehydrated to be dissolved in 100 ml of H₂O

H₂O distilled water (up to a volume of 1000ml)

Solutions have been mixed in the order they have been described.

This solution have been put into an autoclave at 120°C for 20m and can be preserved up to 6 months at room temperature.

In figure 6.11 can be seen the chosen bacteria cultures



figure 6.11: Cultures of *Chroococidiopsis Thermalis* strain PCC 7203, *Chlorogloeopsis fritschii* PCC 6912, *Synechococcus sp.* PCC 7335 and *Cyanobacterium aponinum* strain PCC 10605

6.2.3 Productivity simulations and estimates

The O_2 production QO_2 in time can be calculated:

$$QO_2(\lambda, t) = g_t \zeta(\lambda, t) = g_0 [n_0 2^{\frac{t}{t_D}} - n'(t)] \zeta(\lambda, t) \quad (6.1)$$

where $\zeta(\lambda, t)$ is the O_2 production in [mol O_2 /g/h].

Pretending that $n'(t)=0$ and that $g_0 = 1g$, O_2 production, an implementation of this theoretical measurements is to use the Gompertz's law (M. H. Zwietering et al., 1990) in order to simulate the growth curve of *Acaryochloris marina* considering a doubling time μ_e of 43.68 h and 26.16 h respectively, if irradiated with VIS or NIR light.

$$\frac{n}{n_0} = A e^{-e^{-\frac{\mu_e}{A}(\lambda-t)+1}} \quad (6.2)$$

It has been found in Behrendt et al, (2012) that t_D is 1.82 days between 400 and 700 nm and 1.09 at 720 nm. So, O_2 production is $1.272 \cdot 10^{-6}$ mol O_2 /mg Chld/h in the NIR and $1.128 \cdot 10^{-6}$ mol O_2 /mg Chld/h. Considering that Chld concentrations are 0.017 pg/cell in the NIR bandwidth and 0.007 pg/cell in the visible bandwidth, it can be found $\zeta(\lambda, t)$ to be $2.6 \cdot 10^{-14}$ mol O_2 /cell/h and $7.89 \cdot 10^{-15}$ respectively. For an irradiation of 7.27 W/m² in the Visible (considering a mean wavelength is 494 nm as before) and 4.99 W/m², it can be found the results in figure 6.12.

In this last plot i considered a constant O_2 production of 1.128 micromoles O_2 /mg Chld/h for bacteria grown in blue light and 1.272 micromol O_2 /mg Chld/h for bacteria grown in NIR light (Lars Behrendt et al., 2013).

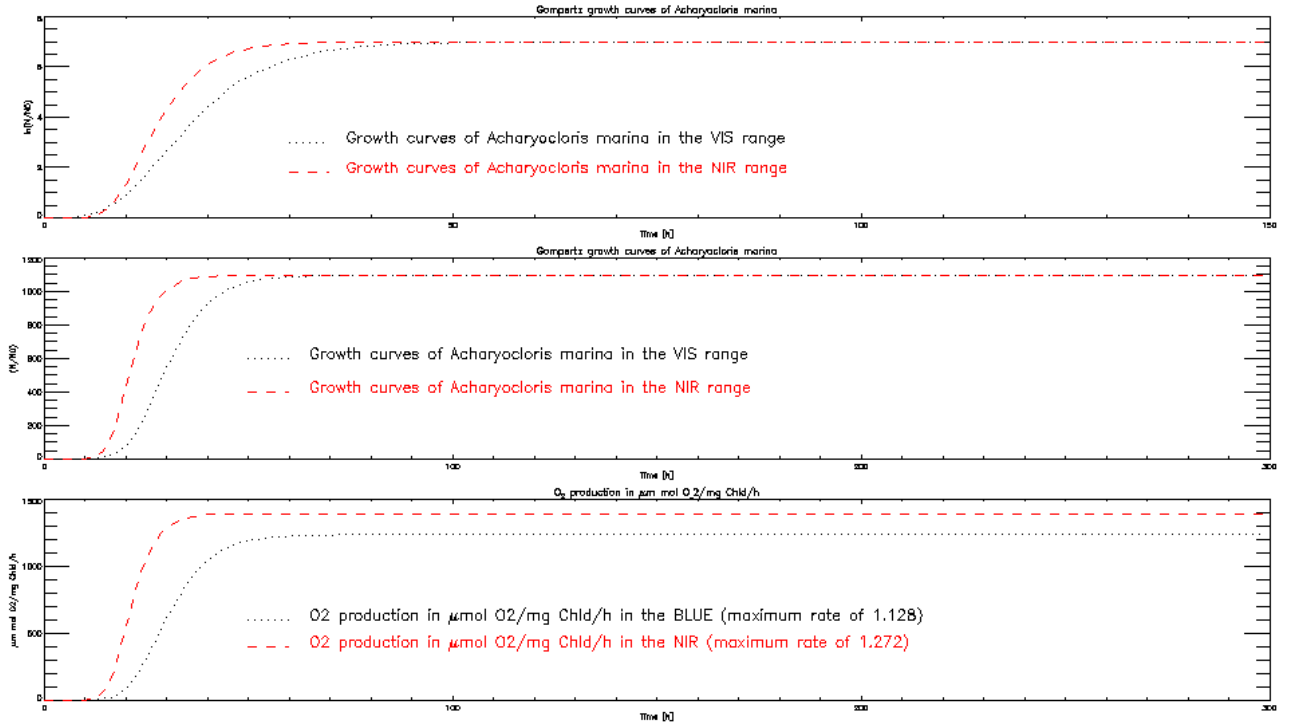


Figure 6.12: Growth curved of *Acharyochloris marina* in different light growth conditions. $QO_2(\lambda, t)$ is the same as in equation 6.60 but with the difference that the growth factor n is given by the Gompertz law. For *Chlorogloeopsis fritschii* the mean O_2 production is about $300 \mu\text{mol } O_2 / \text{mg Chl/h}$.

6.2.3.1 Productivity estimates

The measurements of the bacteria gaseous production, in the advanced phase of the experiment, will be made in a stainless steel (described in chapter 8.2) with two 1/8" stainless steel nozzles for the atmosphere fluxing. Four wedged optical windows opening on the lateral surface will be used to test the gas concentration inside the closed cell by means of a TDLAS (Tunable Diode Laser Absorption Spectroscopy) system and two channels will be used, one for oxygen and one for carbon dioxide. On the top of the cell a 125x6.5 mm BOROFLOAT uncoated window from Edmund Optics is placed to collect the light coming from the stellar simulator (described in chapter 7). In order to understand what expect from the measurements and understand if the gas concentration inside the cell is or not detectable with the TDLAS system i made an analysis of gaseous volumes and bacteria productivity. I considered the volume V_c of the cell and the number of moles of gas inside it.

$$V_c = h\pi r^2 = (57\text{mm}) * \pi * (52.5\text{mm})^2 = 493313.6\text{mm}^3 = 0.493\text{dm}^3 = 0.4933\text{l} \quad (6.3)$$

The total number of moles would be

$$n = \frac{PV_c}{RT} \quad (6.4)$$

and it depends on the temperature T and pressure P .

Using $P=1\text{ atm}$ and $T=30^\circ\text{C}=303.15\text{ K}$, the number of moles become:

$$n = \frac{1\text{ [atm]} * 0.493313625\text{ [l]}}{0,08205784\text{ [l} * \frac{\text{atm}}{\text{k} * \text{mol}}] * 303.15\text{ [k]}} = 0.019841098\text{ mol} \quad (6.5)$$

If the gas composition is 15% of CO₂ and 85% of N₂, then, if all CO₂ is turned into O₂ by bacteria with a mean O₂ production $P_{O_2} = 300 \frac{\mu\text{mol } O_2}{\text{mg Chl} \cdot \text{h}} = 300 * 10^{-6} \frac{\text{mol } O_2}{\text{mg Chl} \cdot \text{h}}$, then we can have an estimate of the time t involved in the process.

$$t = \frac{0.15 * n}{P_{O_2}} [\text{h} * \text{mg Chl}] = \frac{0.0029761647 [\text{mol } O_2]}{300 * 10^{-6} \frac{[\text{mol } O_2]}{[\text{mg Chl} \cdot \text{h}]}} = 9.9205490 [\text{h} * \text{mg Chl}] \quad (6.6)$$

This time depends on the solution quantity and on the concentration expressed in $\frac{\text{mg}}{\text{ml}}$ of chlorophyll. The next tables show the time used by bacteria in order to transform the CO₂ into O₂ in different concentration and gaseous mixture conditions. In table 6.2 can be seen the estimate of the CO₂ into O₂ evolution in the cell at different Chl concentrations. This is the case of *Cyanobacterium Aponinum* and *Chroococciopsis*. *Chlorogloeopsis fritschii* has a mean O₂ production P_{O_2} of $100 \frac{\mu\text{mol } O_2}{\text{mg Chl} \cdot \text{h}} = 100 * 10^{-6} \frac{\text{mol } O_2}{\text{mg Chl} \cdot \text{h}}$.

Then considering that the mean Chl concentration in the samples is $0.35 \frac{\text{mg}}{\text{ml}}$ we can infer a time of 3.47 h for *Cyanobacterium Aponinum* and *Chroococciopsis* and a time of 1.16 h for *Chlorogloeopsis fritschii*.

Cell volume (l)	% CO ₂	% N ₂	mol CO ₂	mol N ₂	Total mols	solution (ml)	concentration (mg/ml)	Time for each mgChl (h*mgChl)	time (h)
0,49356385	15	85	0,00297616	0,016864933	0,019841098	10	0,1	9,920549	9,920549
0,49356385	14	86	0,00277775	0,017063344	0,019841098	10	0,1	9,259179067	9,25917907
0,49356385	13	87	0,00257934	0,017261755	0,019841098	10	0,1	8,597809133	8,59780913
0,49356385	12	88	0,00238093	0,017460166	0,019841098	10	0,1	7,9364392	7,9364392
0,49356385	11	89	0,00218252	0,017658577	0,019841098	10	0,1	7,275069267	7,27506927
0,49356385	10	90	0,00198411	0,017856988	0,019841098	10	0,1	6,613699333	6,61369933
0,49356385	9	91	0,00178570	0,018055399	0,019841098	10	0,1	5,9523294	5,9523294
0,49356385	8	92	0,00158729	0,01825381	0,019841098	10	0,1	5,290959467	5,29095947
0,49356385	7	93	0,00138888	0,018452221	0,019841098	10	0,1	4,629589533	4,62958953
0,49356385	6	94	0,00119047	0,018650632	0,019841098	10	0,1	3,9682196	3,9682196
0,49356385	5	95	0,00099205	0,018849043	0,019841098	10	0,1	3,306849667	3,30684967
0,49356385	4	96	0,00079364	0,019047454	0,019841098	10	0,1	2,645479733	2,64547973
0,49356385	3	97	0,00059523	0,019245865	0,019841098	10	0,1	1,9841098	1,9841098
0,49356385	2	98	0,00039682	0,019444276	0,019841098	10	0,1	1,322739867	1,32273987
0,49356385	1	99	0,00019841	0,019642687	0,019841098	10	0,1	0,661369933	0,66136993
0,49356385	15	85	0,00297616	0,016864933	0,019841098	10	0,2	9,920549	4,9602745
0,49356385	14	86	0,00277775	0,017063344	0,019841098	10	0,2	9,259179067	4,62958953
0,49356385	13	87	0,00257934	0,017261755	0,019841098	10	0,2	8,597809133	4,29890457
0,49356385	12	88	0,00238093	0,017460166	0,019841098	10	0,2	7,9364392	3,9682196
0,49356385	11	89	0,00218252	0,017658577	0,019841098	10	0,2	7,275069267	3,63753463
0,49356385	10	90	0,00198411	0,017856988	0,019841098	10	0,2	6,613699333	3,30684967

Cell volume (l)	% CO ₂	% N ₂	mol CO ₂	mol N ₂	Total mols	solution (ml)	concentration (mg/ml)	Time for each mgChl (h*mgChl)	time (h)
0,49356385	9	91	0,00178570	0,018055399	0,019841098	10	0,2	5,9523294	2,9761647
0,49356385	8	92	0,00158729	0,01825381	0,019841098	10	0,2	5,290959467	2,64547973
0,49356385	7	93	0,00138888	0,018452221	0,019841098	10	0,2	4,629589533	2,31479477
0,49356385	6	94	0,00119047	0,018650632	0,019841098	10	0,2	3,9682196	1,9841098
0,49356385	5	95	0,00099205	0,018849043	0,019841098	10	0,2	3,306849667	1,65342483
0,49356385	4	96	0,00079364	0,019047454	0,019841098	10	0,2	2,645479733	1,32273987
0,49356385	3	97	0,00059523	0,019245865	0,019841098	10	0,2	1,9841098	0,9920549
0,49356385	2	98	0,00039682	0,019444276	0,019841098	10	0,2	1,322739867	0,66136993
0,49356385	1	99	0,00019841	0,019642687	0,019841098	10	0,2	0,661369933	0,33068497
0,49356385	15	85	0,00297616	0,016864933	0,019841098	10	0,3	9,920549	3,30684967
0,49356385	14	86	0,00277775	0,017063344	0,019841098	10	0,3	9,259179067	3,08639302
0,49356385	13	87	0,00257934	0,017261755	0,019841098	10	0,3	8,597809133	2,86593638
0,49356385	12	88	0,00238093	0,017460166	0,019841098	10	0,3	7,9364392	2,64547973
0,49356385	11	89	0,00218252	0,017658577	0,019841098	10	0,3	7,275069267	2,42502309
0,49356385	10	90	0,00198411	0,017856988	0,019841098	10	0,3	6,613699333	2,20456644
0,49356385	9	91	0,00178570	0,018055399	0,019841098	10	0,3	5,9523294	1,9841098
0,49356385	8	92	0,00158729	0,01825381	0,019841098	10	0,3	5,290959467	1,76365316
0,49356385	7	93	0,00138888	0,018452221	0,019841098	10	0,3	4,629589533	1,54319651
0,49356385	6	94	0,00119047	0,018650632	0,019841098	10	0,3	3,9682196	1,32273987
0,49356385	5	95	0,00099205	0,018849043	0,019841098	10	0,3	3,306849667	1,10228322
0,49356385	4	96	0,00079364	0,019047454	0,019841098	10	0,3	2,645479733	0,88182658
0,49356385	3	97	0,00059523	0,019245865	0,019841098	10	0,3	1,9841098	0,66136993
0,49356385	2	98	0,00039682	0,019444276	0,019841098	10	0,3	1,322739867	0,44091329
0,49356385	1	99	0,00019841	0,019642687	0,019841098	10	0,3	0,661369933	0,22045664
0,49356385	15	85	0,00297616	0,016864933	0,019841098	10	0,4	9,920549	2,48013725
0,49356385	14	86	0,00277775	0,017063344	0,019841098	10	0,4	9,259179067	2,31479477
0,49356385	13	87	0,00257934	0,017261755	0,019841098	10	0,4	8,597809133	2,14945228
0,49356385	12	88	0,00238093	0,017460166	0,019841098	10	0,4	7,9364392	1,9841098
0,49356385	11	89	0,00218252	0,017658577	0,019841098	10	0,4	7,275069267	1,81876732
0,49356385	10	90	0,00198411	0,017856988	0,019841098	10	0,4	6,613699333	1,65342483
0,49356385	9	91	0,00178570	0,018055399	0,019841098	10	0,4	5,9523294	1,48808235
0,49356385	8	92	0,00158729	0,01825381	0,019841098	10	0,4	5,290959467	1,32273987

Cell volume (l)	% CO ₂	% N ₂	mol CO ₂	mol N ₂	Total mols	solution (ml)	concentration (mg/ml)	Time for each mgChl (h*mgChl)	time (h)
0,49356385	7	93	0,001388 88	0,0184522 21	0,0198410 98	10	0,4	4,629589533	1,15739738
0,49356385	6	94	0,001190 47	0,0186506 32	0,0198410 98	10	0,4	3,9682196	0,9920549
0,49356385	5	95	0,000992 05	0,0188490 43	0,0198410 98	10	0,4	3,306849667	0,82671242
0,49356385	4	96	0,000793 64	0,0190474 54	0,0198410 98	10	0,4	2,645479733	0,66136993
0,49356385	3	97	0,000595 23	0,0192458 65	0,0198410 98	10	0,4	1,9841098	0,49602745
0,49356385	2	98	0,000396 82	0,0194442 76	0,0198410 98	10	0,4	1,322739867	0,33068497
0,49356385	1	99	0,000198 41	0,0196426 87	0,0198410 98	10	0,4	0,661369933	0,16534248
0,49356385	15	85	0,002976 16	0,0168649 33	0,0198410 98	10	0,5	9,920549	1,9841098
0,49356385	14	86	0,002777 75	0,0170633 44	0,0198410 98	10	0,5	9,259179067	1,85183581
0,49356385	13	87	0,002579 34	0,0172617 55	0,0198410 98	10	0,5	8,597809133	1,71956183
0,49356385	12	88	0,002380 93	0,0174601 66	0,0198410 98	10	0,5	7,9364392	1,58728784
0,49356385	11	89	0,002182 52	0,0176585 77	0,0198410 98	10	0,5	7,275069267	1,45501385
0,49356385	10	90	0,001984 11	0,0178569 88	0,0198410 98	10	0,5	6,613699333	1,32273987
0,49356385	9	91	0,001785 70	0,0180553 99	0,0198410 98	10	0,5	5,9523294	1,19046588
0,49356385	8	92	0,001587 29	0,0182538 1	0,0198410 98	10	0,5	5,290959467	1,05819189
0,49356385	7	93	0,001388 88	0,0184522 21	0,0198410 98	10	0,5	4,629589533	0,92591791
0,49356385	6	94	0,001190 47	0,0186506 32	0,0198410 98	10	0,5	3,9682196	0,79364392
0,49356385	5	95	0,000992 05	0,0188490 43	0,0198410 98	10	0,5	3,306849667	0,66136993
0,49356385	4	96	0,000793 64	0,0190474 54	0,0198410 98	10	0,5	2,645479733	0,52909595
0,49356385	3	97	0,000595 23	0,0192458 65	0,0198410 98	10	0,5	1,9841098	0,39682196
0,49356385	2	98	0,000396 82	0,0194442 76	0,0198410 98	10	0,5	1,322739867	0,26454797
0,49356385	1	99	0,000198 41	0,0196426 87	0,0198410 98	10	0,5	0,661369933	0,13227399

Table 6.2: estimate of the CO₂ into O₂ evolution in the cell at different Chl concentrations.

6.3 Experiment planning

The experiment is divided in several parts. The part zero that consists in the ideation and construction of the hardware. In this part i designed and realized both the stainless steel cell that will host the bacteria, well described in chapter 8.2 and tested both the oxygen and carbon dioxide detection limits and the thermal control system. Then a starlight LED simulator has been realized (described in chapter 7), tested in flux and calibrated at the distances where bacteria would have to be located. An IDL routine has been created to fit the spectral distributions with the 25 LED channels and a java software has been created in order to drive the LEDs and turn them on at the desired intensity. Once completed the hardware starts the bacteria measurements. The first part consists of three steps. In the first step, called the fiduciary experiment, measurements of photosynthetic bio-products taken in terrestrial conditions, both in white light and in NIR light (730 nm). Here will be tested the amount of O₂ produced by the organisms at first in air, and then will be used an atmosphere of 15% CO₂ and 85% N. Oxymeter productivity tests will be made to have a

reference for the measurements. Bacteria will be lodged for the first measurements in a Erlenmeyer flask and then in an environment chamber. The temperature is kept around 303 K, a temperature suitable for oxygenic photosynthetic bacteria. The irradiation will simulate an M star spectrum at the surface of the planet. Later on we will be able to change even the gas mixture inside the cells, keeping the irradiation source as in the previous step. The gas composition will come by theoretical simulation of super earths atmospheres. Measurements of bacteric vitality will be made by means of a PAM imaging system, that measure the fluorescence of the bacteria in order to know their vitality.

6.4 General estimate

Hereafter will be a brief description of the costs of the hardware, starting from the void pump purchase going through the O-rings one, then analyzing the LEDs and the building of the radiation source, going ahead with the gas mixture and the stainless steel cell components.

6.4.1 Void pumps purchase estimate

In table 6.3 are shown the total costs of the void pump

COMPANY	ITEM DESCRIPTION	QUANTITY	TOTAL (EURO)
Agilent Technologies Italia S.p.A.	EX9699359	1	1268.48

Table 6.3: Total costs of the void pump.

6.4.2 O-rings purchase estimate

In table 6.4 are shown the total costs of the O-rings used for the first preliminary measurements of the cells.

COMPANY	ITEM DESCRIPTION	QUANTITY	TOTAL (EURO)
Trasmissioni Industriali SAS	OR 12.37 x 2.62	20	8.4
	OR 47.62 x 3.53	20	31.5
	OR 49.20 x 3.53	20	32.2
	OR 69.85 x 3.53	20	50.4
TOTAL			122.5

Table 6.4: In this table are shown the total costs of the O-rings used for the first preliminary measurements of the cells.

6.4.3 Hardware and irradiation tools purchase estimate

Hereafter will be described the total amount of money used to buy the hardware and irradiation tools

6.4.3.1 LEDs

In table 6.5 are shown the total costs of the preliminary LEDs

COMPANY	ITEM DESCRIPTION	QUANTITY	TOTAL (EURO)
DIGI-KEY	Philips Lumileds 997-LXZ26570	3	6.33
MOUSER	Philips Lumileds 997-LXZ230905	3	6.33
FARNELL	LED Engin 897-LZ100U600	3	127.53
MOUSER	Philips Lumileds 997-LHUV-0380-0200	3	65.82
MOUSER	Philips Lumileds997-LHUV-0400-0500	3	81.27
MOUSER	Philips Lumileds 997-LHUV-0420-0650	3	81.27
MOUSER	997-LXZ1PR01	3	6.99
MOUSER	997-LXZ1PR01 997-LXZ1PB01	3	7.38
MOUSER	997-LXZ1PR01 997-LXZ1PE01	3	7.38
MOUSER	997-LXZ1PR01 997-LXZ1PM01	3	7.38
MOUSER	997-LXZ1PR01 997-LXZ1PX01	3	11.28
MOUSER	997-LXZ1PR01 997-LXZ1PL01	3	7.38
MOUSER	997-LXZ1PR01 997-LXZ1PD01	3	7.38
MOUSER	997-LXZ1PR01 997-LXZ1PA01	3	7.38
MOUSER	997-LXZ1PR01 897-LZ100R300	3	20.61
ROITHNER	Osram 720-SFH4715	3	21.09
ROITHNER	Osram 720-SFH4725S	3	26.4
RS	LED OSLON LB CRBP-HXJX-47-1	5	6.28
ROITHNER	LED SMB1N-700	3	29.28
ROITHNER	LED SMB1N-810D-02	3	35.25
ROITHNER	LED SMB1N-880	3	36.61
ROITHNER	LED SMB1N-760D	36	343.08
TOTAL			949.7

Table 6.5: Total costs of the LEDs used for the first preliminary measurements of radiation.

In table 6.6 are shown the costs for the stellar simulator building and design.

COMPANY	ITEM DESCRIPTION	QUANTITY	TOTAL (€)
LightCube SrL	3D system and feasibility study	1	600
	Master and electrical board project of DALI DRIVER	1	500
	DC/DC converters of DALI constant current (one channel)	32	640
	PCB on FR4 realization	1	376
	Connectors and other electro-mechanical materials	1	300
	Power supply 54 Volt 320 Watt	1	240
	DALI RS232 Controller	1	310
	LED welding	320	480
	Heath dissipative system	1	320
	System developing, realization and testing of intermediate prototypes	1	1700
	Light mixer and other mechanical parts	1	400
	Assembly, testing and final thermal/optical characterization	1	800
	Helicoids	1	300
	Design of MCPCB boards, gerber file generation, Board build-up, LED assembly for prototype, electrical test, Characterization with integrating sphere	1	2500

COMPANY	ITEM DESCRIPTION	QUANTITY	TOTAL (€)
FARNELL	LZ1-00U600	5	212,55
MOUSER	LHUV-0380-0200	15	329,1
MOUSER	LHUV-0400-0500	10	270,9
MOUSER	LHUV-0420-0650	10	270,9
MOUSER	LXZ1-PR01	10	23,3
MOUSER	LXZ1-PB01	10	24,6
RS	CRBP-HXJX-47-1	7	8,792
MOUSER	LXZ1-PE01	25	61,5
MOUSER	LXZ1-PM01	10	24,6
MOUSER	LXZ1-PX01	45	110,7
MOUSER	LXZ1-PL01	20	49,2
MOUSER	LXZ1-PD01	10	24,6
DIGI-KEY	Philips Lumileds 997-LXZ2-2280-5	14	32,76
MOUSER	LXZ1-PA01	10	24,6
ROITHNER	SMB1N-680	14	149,66
ROITHNER	SMB1N-700	10	97,6
ROITHNER	SMB1N-720D	11	75,57
MOUSER	LZ1-00R300	8	76,24
ROITHNER	SMB1N-760D	6	62,64
ROITHNER	SMB1N-780N	8	94
ROITHNER	SMB1N-810D-02	8	77,68
ROITHNER	SMB1N-830D	15	149,7
MOUSER	SFH 4715S	6	42,18
ROITHNER	SMB1N-880	16	192,3733
MOUSER	SFH 4725S	9	79,2

Table 6.6: Total costs for the stellar simulator realization

COMPANY	ITEM DESCRIPTION	QUANTITY	TOTAL EURO)
Ghifer via LightCube	Metallic material for main structure	1	268.203
RS components	Guide rails and metallic material	4	768,44
TOTAL			1264.70

Table 6.7: Total costs for the main structure

COMPANY	ITEM DESCRIPTION	QUANTITY	TOTAL (EURO)
GHT Photonics srl	Spectrometer Ocean Optics STS-VIS	1	1149
	Optical fiber QP400-025-UV-VIS	1	235
	Cosine corrector CC-3-UV-T	1	150
TOTAL			1534

Table 6.8: Total costs for the loop spectrometer

In table 6.9 can be seen the costs of the helicoils and of the mandrels used for the copper plate on which have been tightened the wafers with LEDs

COMPANY	ITEM DESCRIPTION	QUANTITY	TOTAL (EURO)
Tecnimetal SrL	2CT10-M2F	1	193.5
	M2 FR TANGLESS MANDREL XEX+CIL		
	2TNM2X.4C-4	100	27.85
	M2x0.4x4(2D) FR TANGLESS		
	MA3279-240		
	2CT10-M2.5F	1	151.2
	M2.5 FR TANGLESS MANDREL		
	HEX+CIL		
	2TNM2.5X.45C-5	100	18.38
	M2.5X0.45X5(2d) FR TANGLESS		
	NA0276M2A-20		
	SHIPMENT	1	10
TOTAL			400.93

Table 6.9 costs of the helicoils and of the mandrels used for the copper plate on which have been tightened the wafers with LEDs

6.4.4 Additive radiation sources

In table 6.10 are shown the costs of the two additional light sources for oxymetric measurements

COMPANY	ITEM DESCRIPTION	QUANTITY	TOTAL (EURO)
LightCube SrL	30V-3A power supply	1	90
	5 LED Osram 730nm radiation source	1	70
	Ø 16 mm 730nm Osram LED radiation source	1	30
	Mechanical system for the Ø 16 mm radiation source	1	20
	Projectation and realization costs		150
TOTAL			360

Table 6.10: Costs of the two additional light sources for oxymetric measurements

6.4.5 Gas purchase estimate

In table 5.10 are shown the costs of the gas mixture purchasing

COMPANY	ITEM DESCRIPTION	QUANTITY	TOTAL (EURO)
SIAD S.p.a.	Gas mixture	1	190.0
	RSD2S 400/-1+3 N2		302.0
	MIXIN UNI4409 valve	1	
TOTAL			492.0

Table 6.11: costs of the gas mixture purchasing

6.4.6 Incubator chamber estimate

The costs for the incubator chamber are resumed in table 6.12

COMPANY	ITEM DESCRIPTION	QUANTITY	TOTAL (EURO)
Cinquepascal S.r.l	STAINLESS STEEL CELL	1	990
	SHIPMENT	1	25
Edmund Optics Ltd	WINDOW 125x6.5 THK BOROFLOAT	1	38.95
SOCIMA SRL.	SMKFGH0604-01S INOX FITTINGS	4	43.01
	Ø6 1/8" KFG2H604-01S STRAIGHT		
	INOX FITTINGS Ø6 1/8" KFG2L0604-01S	4	68.61
	CURVE		
dB electronic instruments srl	SM1L10	4	51.32
	SM1 Lens Tube. 1" Thread Depth		
	One Retaining Ring Included		
	PS810-B	4	152.28
	Ø1" Round Wedge Prism. 2° Beam		
	Deviation, AR Coating: 650 - 1050 nm		
	CP02/M	4	57.6
	SM1-Threaded 30 mm Cage Plate		
	0.35" Thick, 2 Retaining Rings, Metric		
2LO master bond polimery system	EP42HT-2LO EPOXY	1	830
INAF-Oapd	mechanical structure	1	1000
TOTAL			3256.77

Table 6.12: costs for the incubator chamber

7. Starlight simulator

The Star Light Simulator is composed of a multiple LED matrix cooled by means of a fan cooling technology. In order to generate a dynamical spectrum we evaluated different kind of radiation sources, but LEDs have been chosen instead of lamps because they are cheap, very small and dynamic. This last feature can allow a non-static characteristic of this novel radiation source, that can be tuned by a PC and a dedicated software in order to match the desired radiative spectrum, limited to a precision of 24 nm. This limit is driven by the wavelength range and by the number of channels that we have used. The wavelength intervals (365nm-940nm) overlap the limits of photosynthetic pigment absorption range (280-850 nm) present inside the most common photosynthetic bacteria. The reason why we chose a higher outer limit is that M stars have the emission peak at about 1000 nm and we want to study the effects of low-light radiation on bacteric vitality. The path that drove the concept was the idea of modularity. This idea led us to think a multi-plate system shaped in the form of annuli, with mosaic of circuit boards arranged in a pie-chart shape, on the surface of which have been welded the LEDs. Up to now no such devices have been developed. The only three studies of feasibility of LED radiation sources for biological aims are described in Moreno, (2007), Phillips, (2012) and Fryc et al., (2005). In the first article a tunable lamp is described that uses both LEDs and incandescent or fluorescent sources. Phillips describes the construction of another tunable light source that has the ability to mimic the spectral output of the sun in the photosynthetic active radiation range (400 – 700 nm). Our device is capable to extend the wavelength range from 365 nm to 940 nm and has the ability to reproduce not only the solar spectrum but even other star's spectra. The infrared component is very important, especially when studying photosynthesis. In fact this part of the radiative spectrum influences heavily the metabolic processes, leading to changes in the whole apparatus. Fryc designed a spectrally tunable source capable to have a capability of reproducing any visible spectral distribution, with a 380-780 nm interval and a 35 LEDs palette, mimicking various light sources in the visible region by feedback control of the radiant power emitted by individual LEDs. The first step to build a starlight simulator is the choice of LEDs. For our purpose, we definitively isolated a set of 25 different wavelength. This choice has been forced even by the costs of extended wavelength limits and the availability of the market. In Table 7.1 are listed all the LEDs chosen in order to span as close as possible all the possible wavelengths of the spectrum we want to reproduce.

Modularity is a successful idea because in case of LED damage it allows to remove only the plate where the problem is. Moreover dividing the tool in plates can allow future implementations, such as to reproduce other spectral types of stars just changing some kind of LEDs without building a new lamp *ex-novo*. In figure 7.1 and 7.2 is shown the concept design of the radiative system made with solid works.

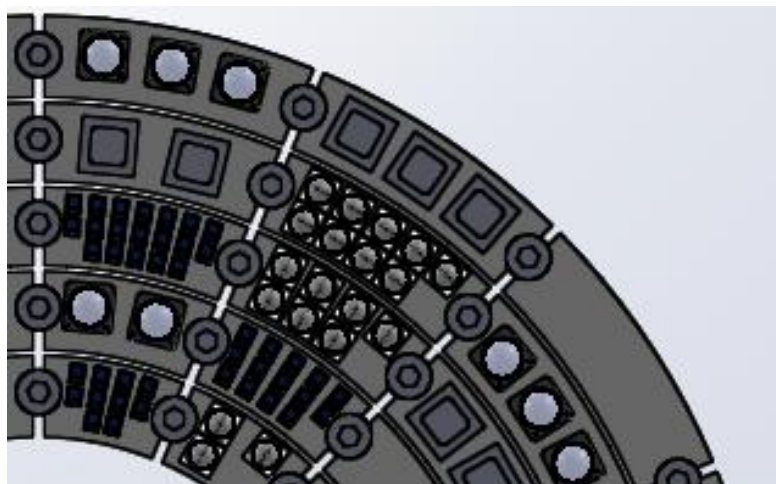


Figure 7.1: Main radiative system

LED CODE	Peak wavelength (nm) from datasheet
Luxeon LZ1-00U600	365
Luxeon LHUV-0380-0200	380-385
Luxeon LHUV-0400-0500	400-405
Luxeon LHUV-0420-0650	420-425
Luxeon LXZ1-PR01	447,5
Luxeon LXZ1-PB01	470
Olson LB CRBP-HXJX-47-1	485
Luxeon LXZ1-PE01	505
Luxeon LXZ1-PM01	530
Luxeon LXZ1-PX01	567,5
Luxeon LXZ1-PL01	590
Luxeon LXZ1-PD01	627
Philips Lumileds 997-LXZ1-2280-5	(2200K)
Luxeon LXZ1-PA01	655
Roithner SMB1N-680	680
Roithner smb1n-700	700
Roithner SMB1N-720D	720
Luxeon LZ1-00R300	740
Roithner SMB1N-760D	760
Roithner SMB1N-780N	780
Roithner SMB1N-810D-02	810
Roithner SMB1N-830D	830
Osram SFH 4715(S)	850-870
Roithner SMB1N-880	880
Oslon SFH 4725S	940

Table 7.1: List of LEDs chosen and peak wavelength

LEDs have an intrinsic light exit angle. Assembling them in an array on over 300 pieces means at least to make a good effort in order to uniform the fluxes. Our purpose for this task was to use a silver plated 130 mm diameter cylinder with a 98% reflectivity that embrace as a glove the outer face of the source. The layout of the mesh-up coil is shown in figure 7.2.

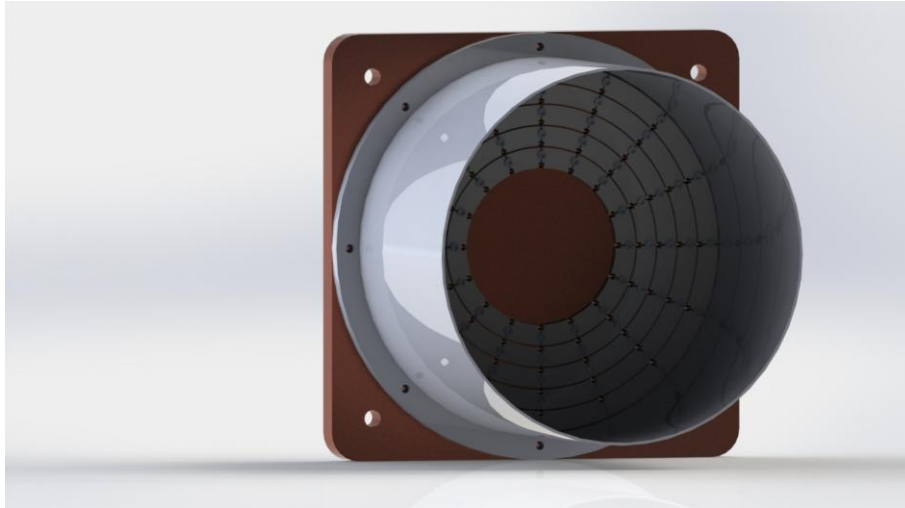


Figure 7.2: Reflective cylinder assembled with the main radiative system.

In figure 7.3 is shown a sample of the plates and in figure 7.4 can be seen the probe LEDs welded on the first plates.

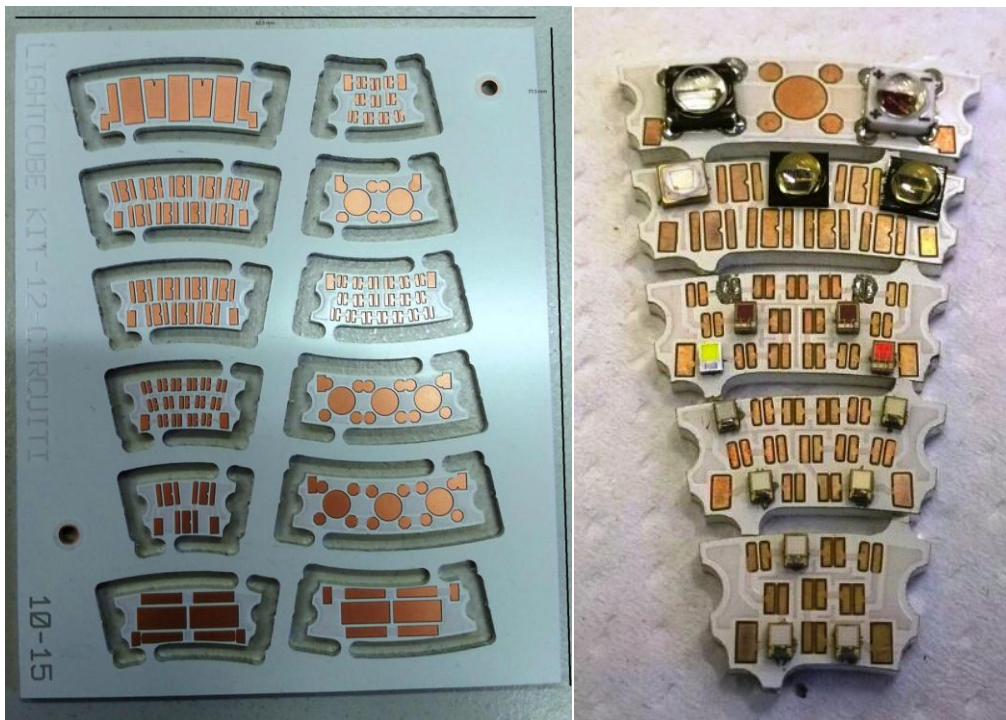


Figure 7.3 and 7.4: a prototype of the plates and in figure 2.8 can be seen the probe LEDs welded on the first plates

In the back of the stellar simulator is fixed a copper plate that is used to join the main body with the cooling system. This is important because the maximum calculated power emanated from the radiation source is 106.22 W while the thermal power is 434.05 W and it is crucial to dissipate it to avoid damages and overheating. This goal has been achieved using a cooling aggregate 0.06K/W 12V 6W from Thermo Electric Devices. Its dimensions are 200 x 135 x 98mm (figure 7.5). The noise produced by the whole dissipation system is 77 ± 2 db, 43 ± 2 db over environmental noise. The cooling is led to the Copper Plate (figure 7.6) by means of fittings.



Figure 7.5: Cooling aggregate 0.06K/W 12V 6W from Thermo Electric Devices used for the LED heat dissipation

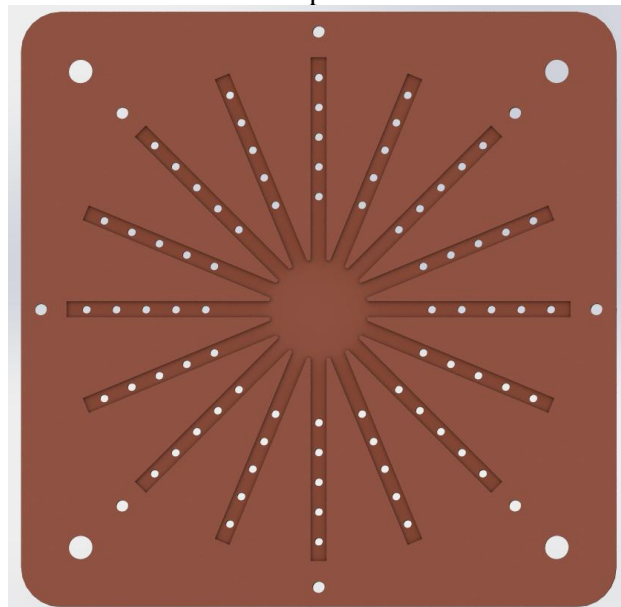


Figure 7.6: copper plate design

In figure 7.7 can be seen the realization process of the copper plate and the first LEDs welded.

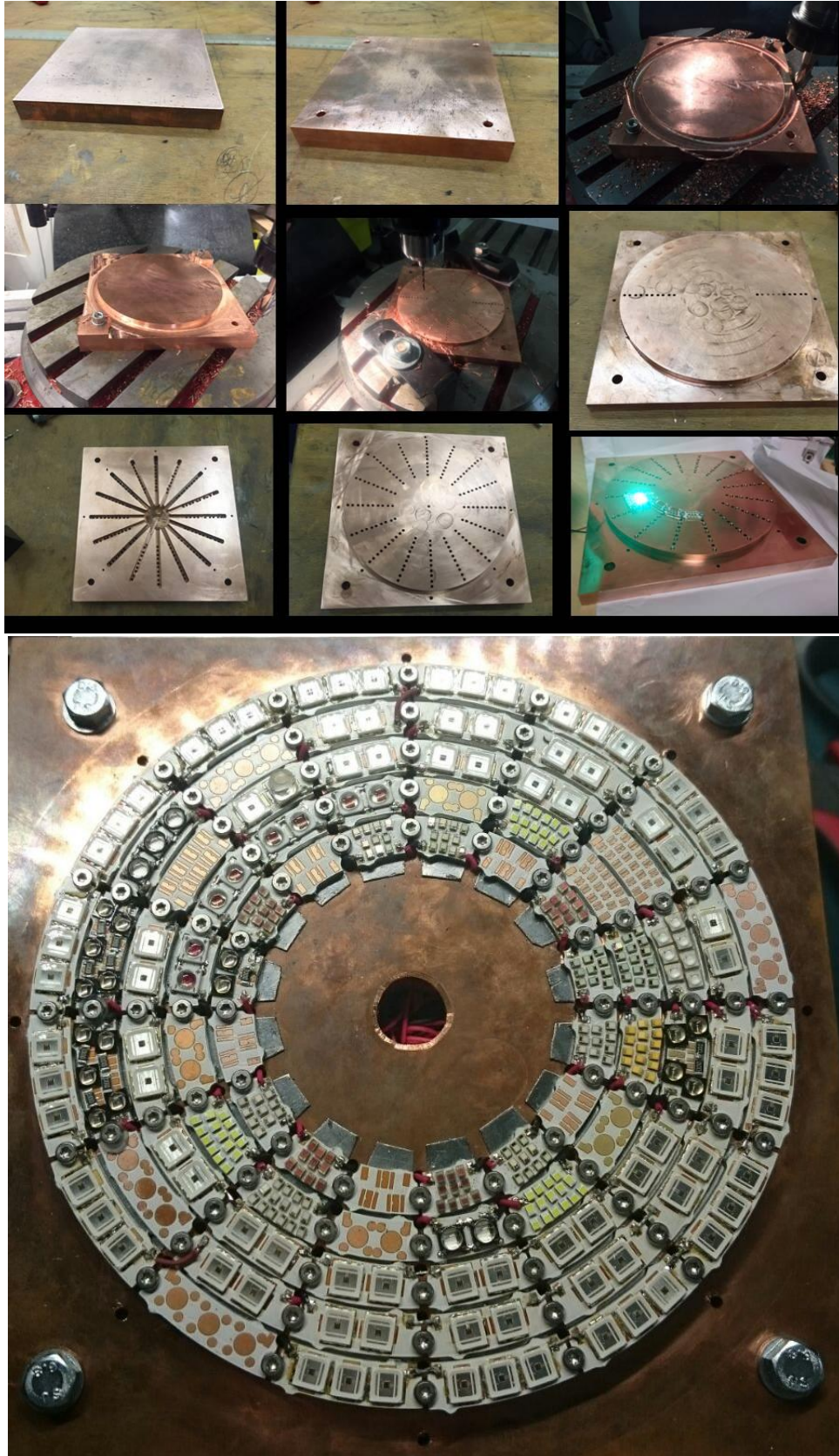


figure 7.7a,b: realization process of the copper plate and the first LEDs welded.

In order to allow a PC to control the radiation source e.g. raising or lowering the intensity of each LED and to set their luminosity, we chose a 15 channels expandable up to 63 DALI RS232 channel multiplier from Tridonic Labs and buck led drivers, illustrated in Figure 7.8:

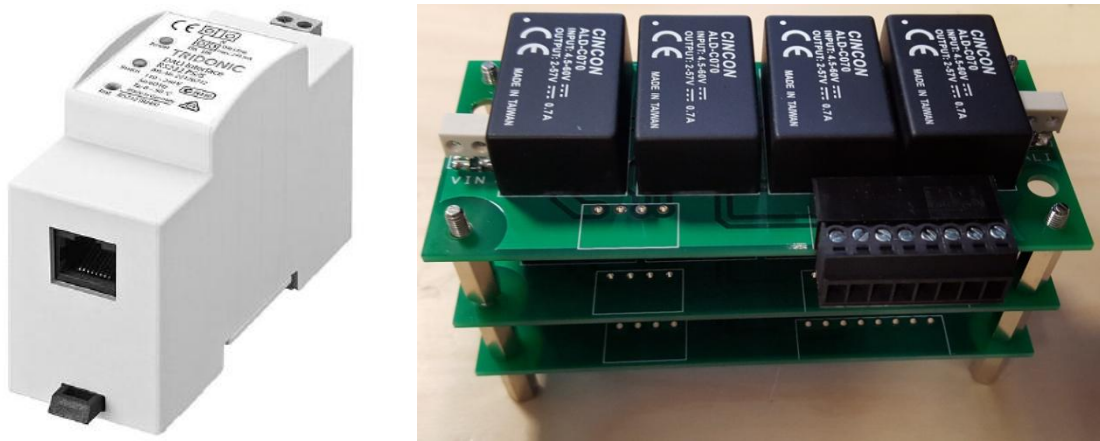


Figure 7.8: DALI USB channel multiplier from Tridonic Labs and buck led drivers.

Each channel can host a maximum of 45 V, that is about 15 LEDs, considering that each led have to be driven at 3 V. The power is granted to the LEDs by a HLG-320H-54A from Mean Well LED power supply. In order to monitor the LEDs' work an STS-VIS spectrograph from Ocean Optics with cosine corrector has been used. This spectrograph has a spectral range falling between 380 and 900 nm, an integration time varying from 1 ms and 10 s and a SNR of 2000:1. It has a dedicated diffraction grating with 600 rows/mm and a linear CMOS ELIS1024 with 1024 elements. Spectra have been collected by means of a 250 mm optical fiber QP400-025-UV-VIS from Ocean Optics and a cosine corrector designed to collect radiation from approximately a 180° field of view, thus eliminating light collection interface problems inherent to other sampling devices. In figure 7.9 can be seen a picture of the spectrometer. With a recent update we have bought a Flame VIS-NIR 190-1100 nm range spectrometer from Ocean Optics. This has the advantage to cover the 822-940 nm range where the STS-VIS is blind.



Figure 7.9: STS-VIS spectrograph from Ocean Optics

The building drawings are collected in Appendix C.

7.1 Work Breakdown Structure and GANTT diagram

The WBS of this work goes through 5 work packages (WP). In Table 7.2 are resumed the main packages of the experiment.

Work Package	Task
WP1	Simulations
WP 1.1	Choice of the LEDs
WP 1.1.1	Order of the probe LEDs
WP 1.1.2	Welding of the probe LEDs
WP 1.1.3	Collection of the probe LEDs spectra
WP 1.2	Development of the star spectrum fitting algorithm
WP 1.3	Simulations with black bodies
WP 1.4	Simulations with real or simulated spectra
WP 2	Design of the instrument
WP 2.1	Design of the mother boards
WP 2.2	Design of the LED's arrangement
WP 2.3	Design of the cooling system
WP 2.4	Design of the light mesh-up collector
WP 3	Mechanics and electrical components realization
WP 3.1	Realization of the mother boards
WP 3.2	Welding of the LEDs on the mother boards
WP 3.3	Installation of the cooling system
WP 3.4	Realization of the light mesh-up collector
WP 3.5	Assembly of the instrument
WP 3.6	Interface the instrument with the PC
WP 4	Software development
WP 5	MAIT- Manufacturing, Assembly and Integration Tests
WP 5.1	Functionality tests
WP 5.1.1	On/Off tests
WP 5.1.2	Dissipation tests
WP 5.1.3	PC connection working tests
WP 5.1.4	Single channel tests
WP 5.2	Characterization tests
WP 5.2.1	Spectra acquisition
WP 5.2.2	Comparison with simulations
WP 5.2.3	Loop stability tests with spectrometer

Table 7.2: Main packages of the experiment.

WP1. SIMULATIONS

The first WP deals with the preliminary operations introductory to our work, in particular the ones described in WP1.2, WP1.3 and WP 1.4.

WP1.1 CHOICE OF THE LEDs

We started with the choice of the LEDs, searching on the market the widest palette available in order to span the 280-840 nm range of photosynthetic productivity

WP1.1.1 ORDER OF THE PROBE LEDs

Order the probe LEDs, one of each type in order to cover the broadest part of the stellar spectrum.

WP1.1.2 WELDING OF THE PROBE LEDs

Welding the probe LEDs to the mother boards

WP1.1.3 COLLECTION OF THE PROBE LEDs SPECTRA

Radiation tests in order to verify if the data sheet spectrum of the LED is compatible with the real spectrum. For simplicity all the LEDs are driven at the current of 700mAh, even if data are collected even at 500 mAh up to 1000 mAh.

WP1.2 GENERATION OF THE STAR SPECTRUM FITTING ALGORITHM

Generation of an IDL program in order to fit with the sum of all the LEDs a desired star.

WP1.3 SIMULATIONS WITH BLACK BODIES

At first the simulations have been performed trying to fit black bodies.

WP1.4 SIMULATIONS WITH REAL SPECTRA

Later for the simulations used real or simulated stars in order to improve the sensibility of our instrument.

WP2. DESIGN OF THE INSTRUMENT

In this WP is developed the whole design of the instrument and its components.

WP2.1 DESIGN OF THE MOTHER BOARDS

Design of the mother boards on which the LEDs have been welded

WP2.2 DESIGN OF LEDs ARRANGEMENT

The design of the LED arrangement is crucial in order to uniform the beam and to equalize and balance the radiation.

WP2.3 DESIGN OF THE COOLING SYSTEM

In order to cool the device a cooling system have been designed capable of carrying away the watt produced by the opto-electronic system.

WP2.4 DESIGN OF THE LIGHT MESH-UP COLLECTOR

This WP deals with the design of the mesh-up collector, a reflecting aluminium cylinder with reflection coefficient of 98% capable of uniform the beam.

WP3. MECHANICS AND ELECTRICAL COMPONENTS REALIZATION

In this WP have been realized the mechanic and electrical parts of the instrument.

WP3.1 REALIZATION OF THE MOTHER BOARDS

Realization of the mother boards on which LEDs are welded and connected.

WP3.2 WELDING OF LEDS ON THE MOTHER BOARDS

Welding the LEDs on the mother boards and wired together with the electrical bulk.

WP3.3 INSTALLATION OF THE COOLING SYSTEM

Installation of the cooling system in order to dissipate the energy produced. It is connected with the copper plate.

WP3.4 REALIZATION OF THE LIGHT MESH-UP COLLECTOR

Realization of the 98% reflecting silver coated mesh-up collector

WP3.5 ASSEMBLY OF THE INSTRUMENT

Assembly of the various parts of the instrument

WP3.6 INTERFACE THE INSTRUMENT WITH PC

Interfacing with the PC by means of a DALI USB device

WP4. SOFTWARE DEVELOPEMENT

The software development helps us to drive the device from the PC and the task required from the software is twofold. In fact it has to allow the regulation of the single channels corresponding to LEDs at different wavelengths and to fit the star spectrum with a suitable LED combination and communicate it to the device in order to enlighten only the LEDs required.

WP5. MAIT- MANUFACTURING, ASSEMBLY AND INTEGRATION TESTS

In this WP we made all the tests in order to confirm the correct functionality of the instrument

WP5.1 FUNCTIONALITY TESTS

The tests have been twofold. Functionality tests and characterization tests. In the functionality tests we made all the operations in order to validate the mechanical working of the instrument

WP 5.1.1 ON/OFF TESTS

The first test has been the On/Off test

WP 5.1.2 DISSIPATION TESTS

Then we analyzed the dissipation in order to understand if the previsions were correct and to set the cooling device working rate

WP 5.1.3 PC CONNECTION WORKING TESTS

Here we tested the connections with the PC

WP 5.1.4 SINGLE CHANNEL TESTS

Each channel has been tested in order to check its working goodness.

WP 5.2 CHARACTERIZATION TESTS

The second tests has been dealt with the characterization of the spectra and their matching with the previsions

WP 5.2.1 SPECTRA ACQUISITIONS

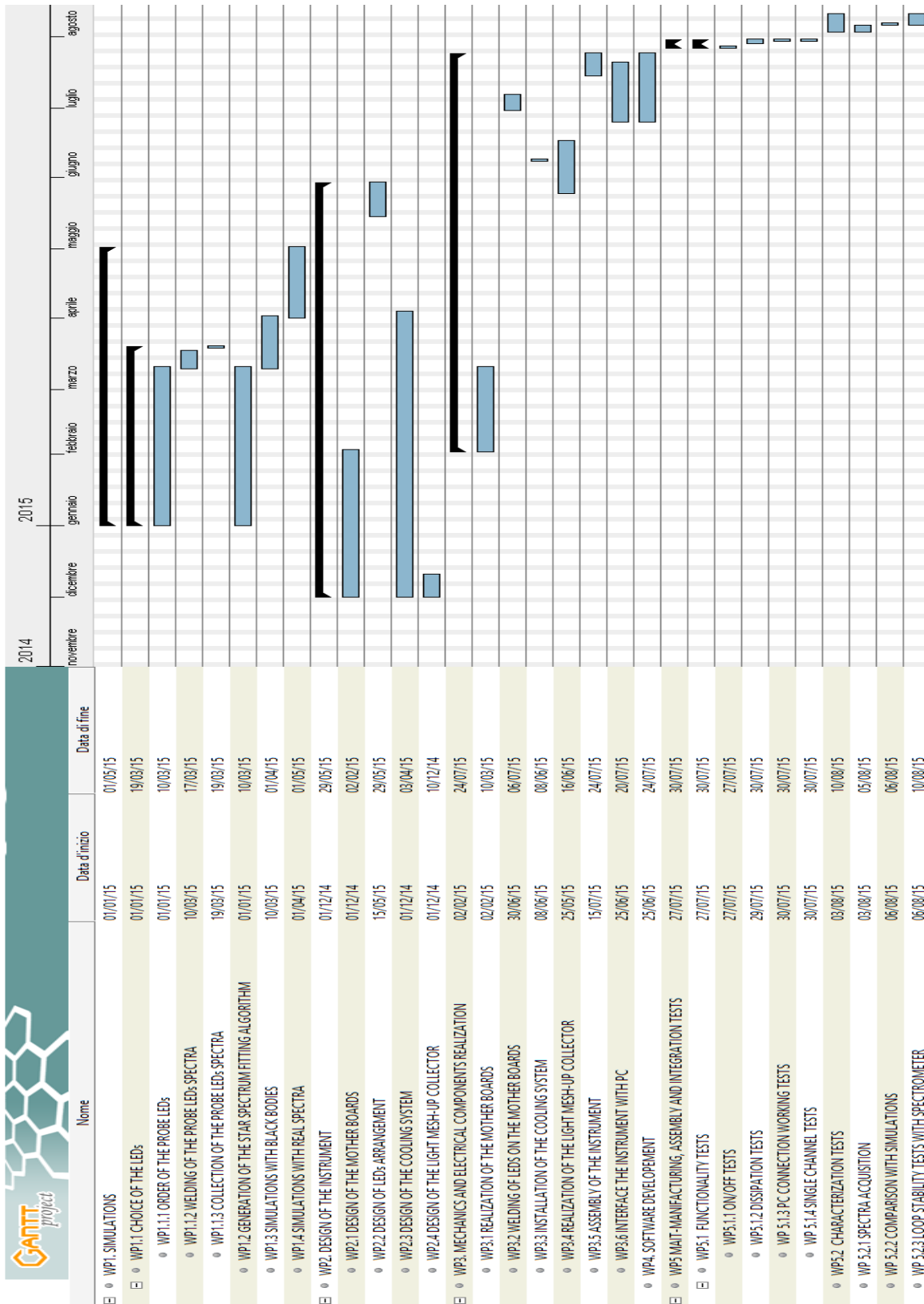
Here some spectra have been collected in order to tune the simulation software with the real data

WP 5.2.2 COMPARISON WITH SIMULATIONS

Here tests have been done acquiring the total radiant spectrum of the LEDs and comparing it with the simulated one.

WP 5.2.3 LOOP STABILITY TESTS WITH SPECTROMETER

Finally loop stability has been tested with a spectrometer in order to understand how to best reproduce a given spectrum and to maintain it in time.



7.2 Radiation source build-up

Here can be seen the preliminary tests like the measurements of probe LEDs peaks with an integrating sphere and comparison with the data sheet values. As can be seen in table 7.3 and figures 7.10 and 7.11 there are a few but acceptable differences.

LED CODE	Real peak wavelength (nm)	Peak wavelength (nm) from datasheet
Luxeon LZ1-00U600	368±4%	365±2
Luxeon LHUV-0380-0200	390±4%	380-385±2
Luxeon LHUV-0400-0500	404±4%	400-405±2
Luxeon LHUV-0420-0650	424±4%	420-425±2
Luxeon LXZ1-PR01	450±4%	447,5±2
Luxeon LXZ1-PB01	476±4%	470±2
Olson LB CRBP-HXJX-47-1	469±4%	485±2
Luxeon LXZ1-PE01	499±4%	505±2
Luxeon LXZ1-PM01	520±4%	530±2
Luxeon LXZ1-PX01	548±4%	567,5±2
Luxeon LXZ1-PL01	604±4%	590±2
Luxeon LXZ1-PD01	634±4%	627±2
Philips Lumileds 997-LXZ1-2280-5	605±4%	(2200K) ±2
Luxeon LXZ1-PA01	665±4%	655±2
Roithner SMB1N-680	689±4%	680±2
Roithner smb1n-700	708±4%	700±2
Roithner SMB1N-720D	727±4%	720±2
Luxeon LZ1-00R300	738±4%	740±2
Roithner SMB1N-760D	763±4%	760±2
Roithner SMB1N-780N	777±4%	780±2
Roithner SMB1N-810D-02	8,07±4%	810±2
Roithner SMB1N-830D	834±4%	830±2
Osram SFH 4715(S)	871±4%	850-870±2
Roithner SMB1N-880	889±4%	880±2
Oslon SFH 4725S	972±4%	940±2

Table 7.3: Measurements of probe LEDs peaks and the comparison with the data sheet ones

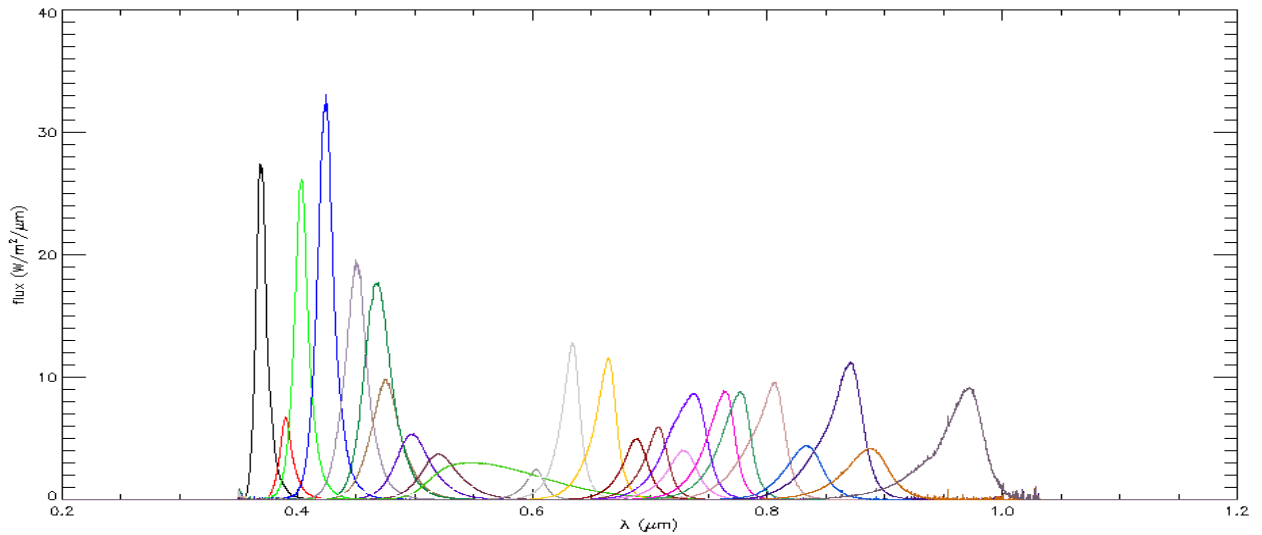


Figure 7.10 Complete LED palette driven at 700 mAh.

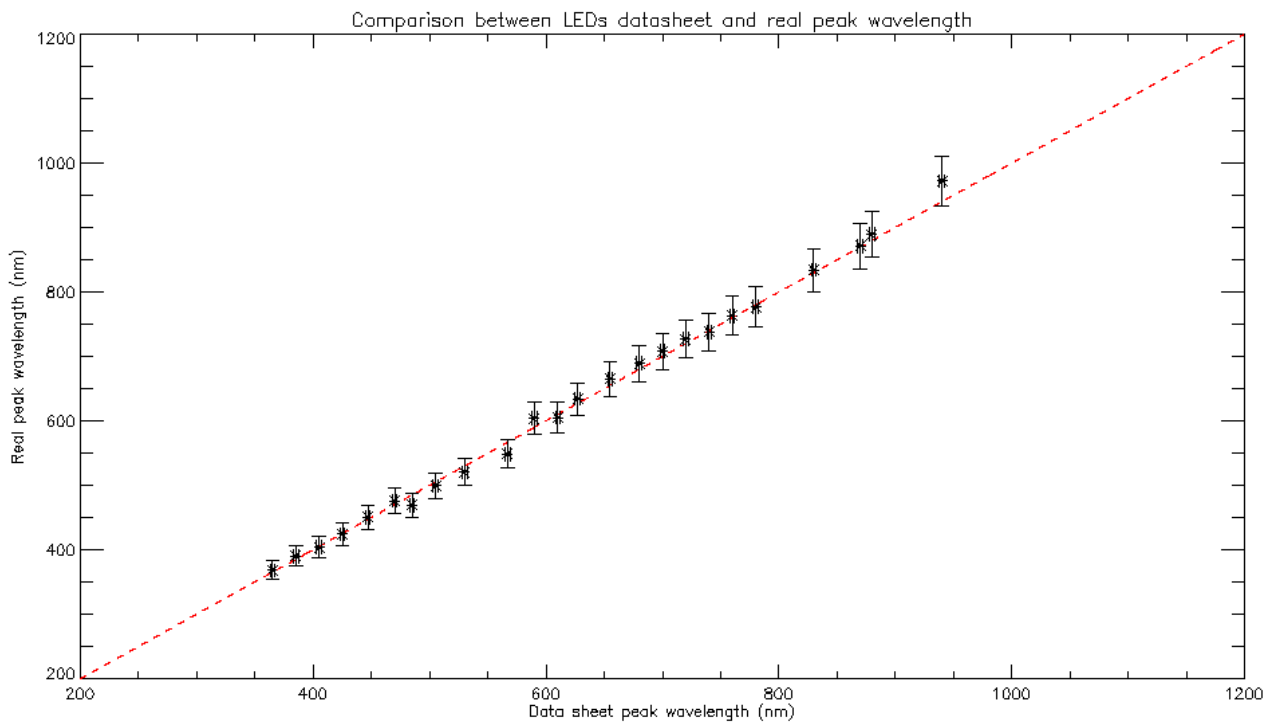


Figure 7.11. Linearity of the LEDs.

7.3 Simulations

In order to understand what could be the correct number of LEDs to use in order to match the highest number of stellar spectra we performed simulations using an IDL routine. Such routine has the task to fit, by means a χ^2 function, all the curve, real or simulated, with a LED combination that is the sum of all the LEDs, each of which multiplied by a constant. The routine reads the stellar fluxes we want to reproduce, calculate the habitable zone for the desired star and scales the flux with respect to that distance. Then it reads the spectra of the LED's palette, shape them in order to avoid noise errors and, once isolated the LED's peaks uses the "regress" function to find the best coefficients suitable for the stellar spectrum's fit. The fit can be twofold: we can fit the shape of the spectrum or the integral of it. Biologically speaking the fit of the shape is

the most correct. Then the routine defines the best fit as the sum of all the LEDs spectra singularly multiplied by each coefficient. The coefficients gives the total amount of power that have used for each LED channel. Then at the end it has been provided as output a plot of the best fit and a text document with the fit coefficients. We started from the black bodies, calculated from the black body formula:

$$B(\lambda, T) = \frac{2\pi h \nu^3}{c^2} \frac{1}{e^{\frac{h\nu}{kT}} - 1} \frac{\nu}{\lambda} * 10^{-6} \quad (7.1)$$

with

$$h=6.626*10^{-34} \text{ [Js]}, c=299792458.0 \left[\frac{m}{s}\right], k=1.3806488*10^{-23} \text{ [J/K]}, \nu = \frac{c}{\lambda}; [s^{-1}].$$

The stellar radius have been obtained using the formula

$$R_* = \sqrt{\frac{L}{4\pi\sigma T_{eff}^4}} \quad (7.2)$$

with $\sigma=5.67037321*10^{-8} \left[\frac{W}{m^2K^4}\right]$, $L = \frac{L}{L_{\odot}} * 3.846*10^{26} [W]$ e T_{eff}^4 in $[K^4]$ and $\frac{L}{L_{\odot}} = e^{\frac{4.77-M}{2.5}}$, M absolute magnitude, as described in chapter 1.

The black body functions have been shifted at the habitable distances d described in Table 3.1 multiplying $B(\lambda, T)$ by a factor $\frac{R_*^2}{d^2}$.

The simulations made for four different star classes, F, G, K and M, with parameters described in Table 3.1 are shown if Appendix F.

7.4 Control software

The system is composed by a Laptop which controls a LED box and a Spectrometer. The LED Box is composed by 25 array of LEDs, each one corresponding to one wavelength. Each array channel is composed by a maximum of 15 identical LEDs. We decided to drive them through an ALD Buck Led Driver by Cincon Electronics. The reason is that this component is multichannel, DALI compatible and dimmable, so we can easily specify the needed intensity of the entire channel. A DALI RS232 PS/S interface is needed to connect the laptop to the LED box through serial port. The light produced by the LED Box is analyzed by the STS spectrometer by Ocean Optics, which is connected via USB to the laptop and via optical fiber to the LED box. In figure 7.12 and 7.13 are illustrated the schemes of the hardware setup and the software duties. The main control process hosted in the laptop is a JAVA application, mainly for two reasons: we want to have a platform independent control system and the spectrometer interface provided by Ocean Optics (the Omni Driver package) is written in Java. The control process user requirements are summarized here below.

1. It has to read two input parameters: the spectral type T and distance D of the star to be reproduced;
2. It has to compute the synthetic spectrum S , function of T and D .
3. It can load an already provided spectrum S from a library file;
4. It has to compute the intensity $I(n)$ to be sent to the Led Box to reproduce the spectrum $S(T,D)$: for each channel n the intensity $I(n)$ is the same for all the LEDs in that channel;
5. It has to send the appropriate command to the LED Box in order to: to switch on, switch off, dimmer the channels;
6. It has to send the appropriate command to the Spectrometer in order to: setup the exposure (set the integration time, enable/disable the electric dark correction), start the exposure, read the measured spectrum M ;
7. It has to compare the measured spectra M with the spectra S fed to the LED Box;

8. It has to compute a correction $C(n)$ to adjust the output intensity $I(n)$ in order to reproduce the expected spectra S ; this procedure can be applied on a loop till $C(n)$ is below a given threshold.
9. It has to provide a GUI to choose the spectral type and the distance of the star to be reproduced, or eventually load the spectrum from library file, display the read spectrum, enable/disable the control loop, dimmer the intensity of each channel

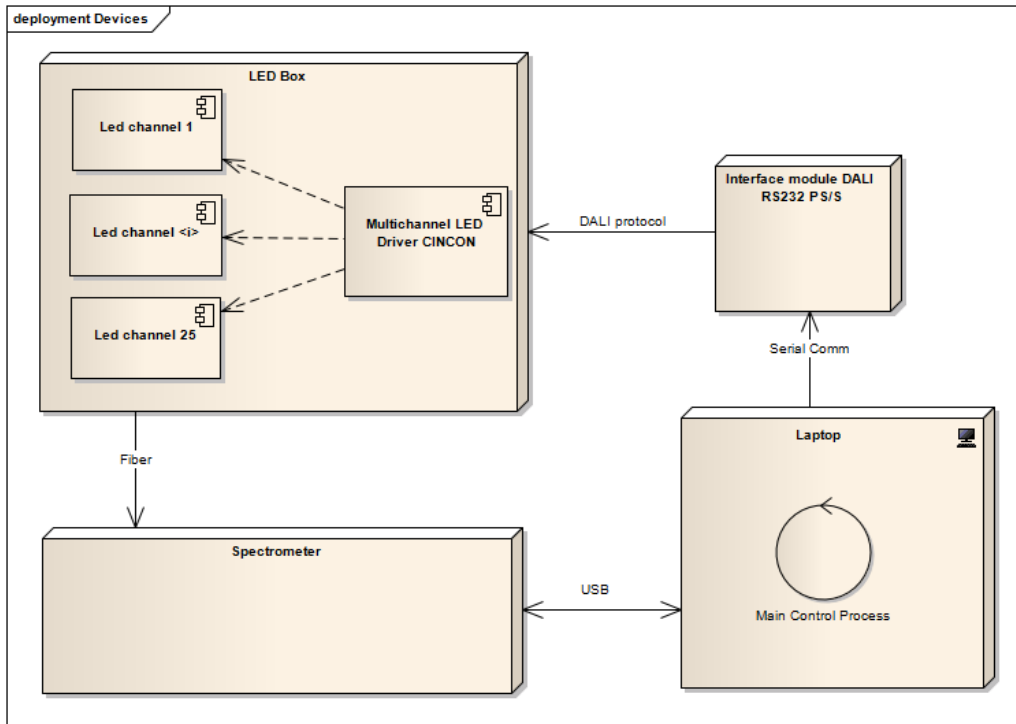


Figure 7.12: Scheme of the hardware setup

Points 2,3,4 (shown as “Compute Led Intensity” in figure 7.13 and 8 (shown as “Control Loop”) are developed, for the time being, in IDL by Exelis language.

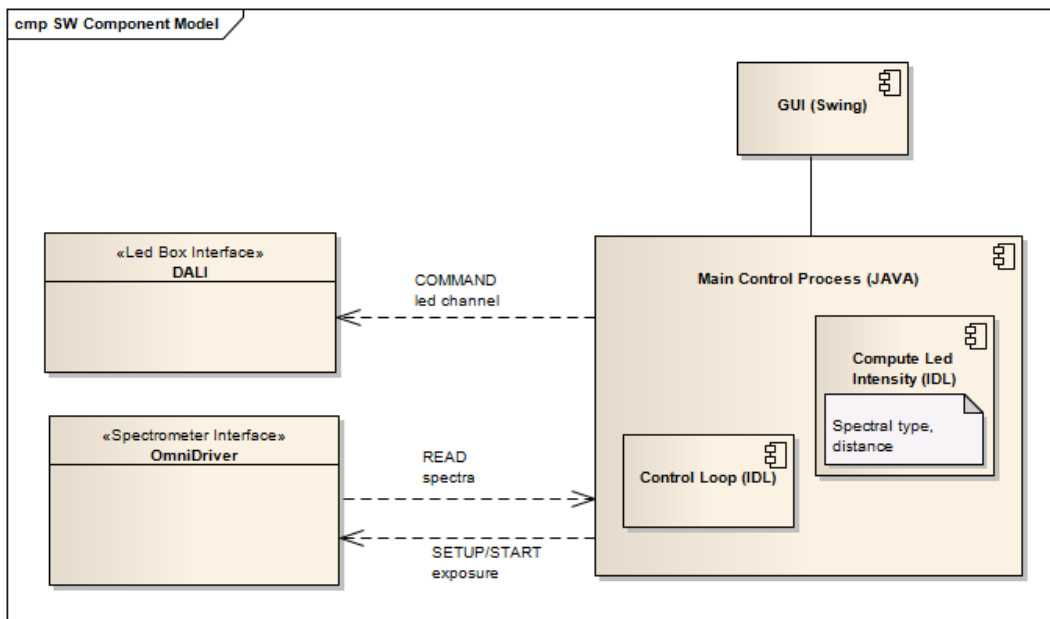


Figure 7.13: Scheme of the software duty cycle

In figure 7.14 can be seen the flow chart of the routine. The power of this code is that it is capable to fit each spectrum we provide and give as output the correct percentage of flux to attribute to each channel in order to best fit it

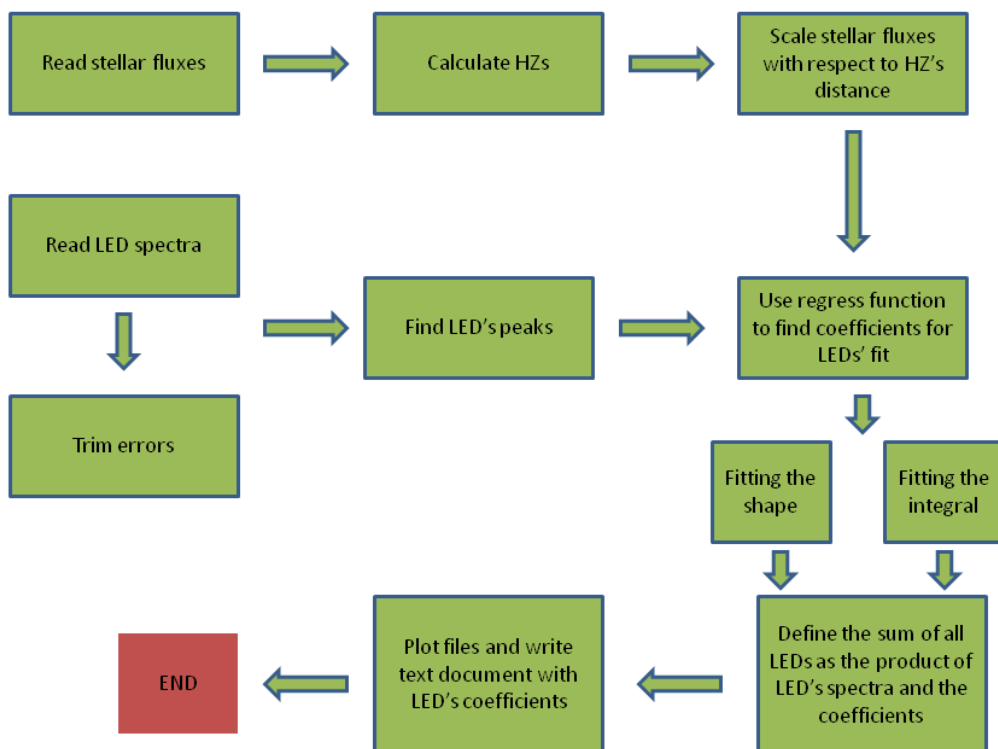


Figure 7.14: Flow chart of the simulation code.

Figure 7.15 shows a screenshot of the main program console. On the left side are placed the on/off buttons and the intensity settings of the single channels. The % column displays the percentage of channel operative. The correction column works only when the flag "loop" is on and displays the correction applied to each single channel. In the loop mode, the software load the fitted spectrum and turn the LEDs on as in the open loop mode. Then it compares the real spectrum (blue) with the ideal one (red) and raise or lower the intensity of the LEDs in order to reproduce the best real fit of it. The integration time is used to set the time the spectrometer uses to collect radiation. The button LIGHT OFF is used to turn off all the channels and the "dark" correction, made by means of a flag on/off makes the dark correction for the spectrometer.

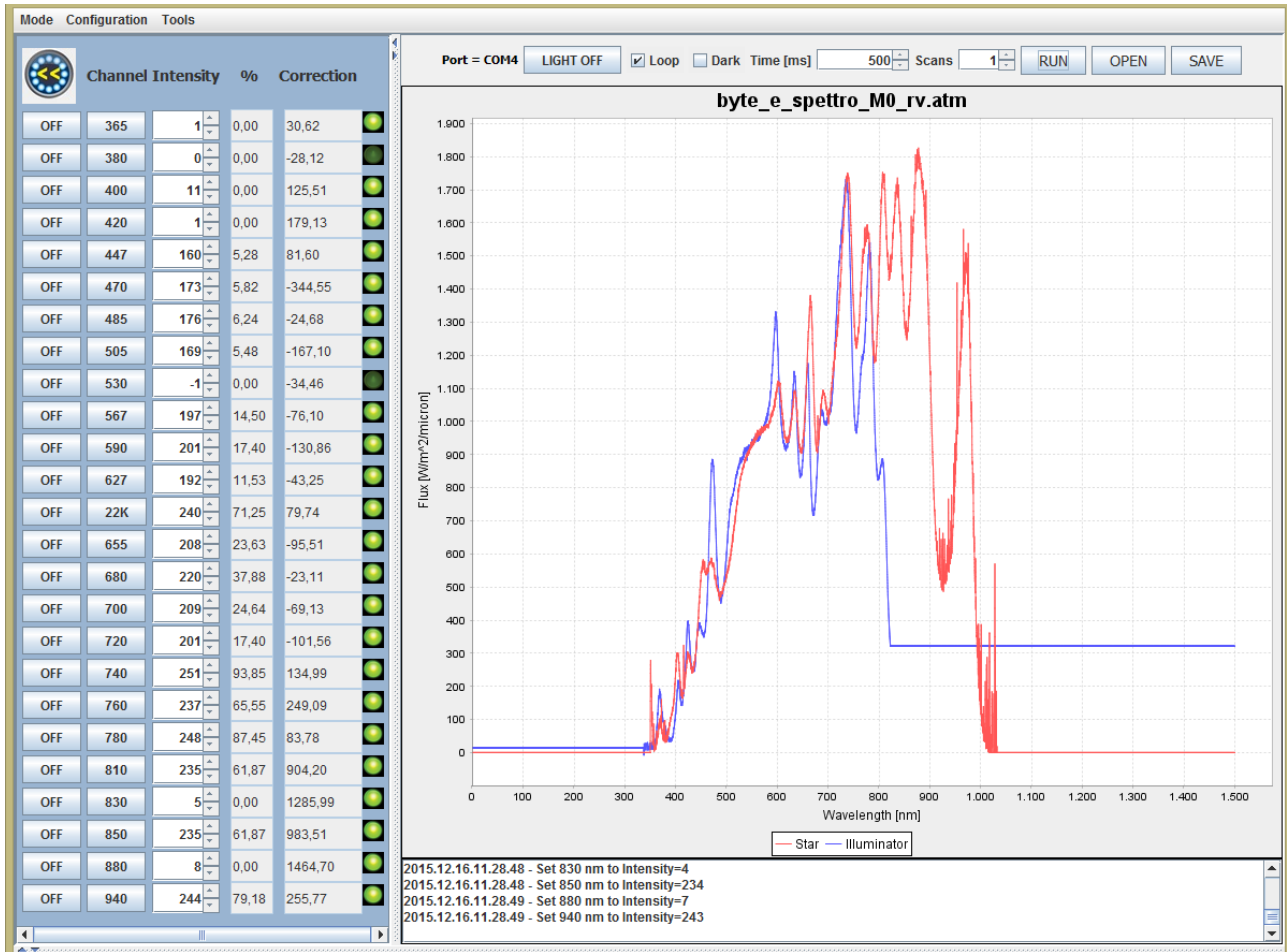


Figure 7.15 screenshot of the main program page.

7.5 Stellar simulator characterization

In order to characterize the stellar simulator, some tests have been performed. The first test has the aim to understand the relation that rules the dilution of the flux with the distance. For this task a set of measurements have been taken with all LEDs lightened at 16.63% of the maximum power, starting with the optical fiber of the spectrometer placed at 10 cm from the radiation source. This is a topic distance because at that distance the bacteria will be placed at the bottom of the incubator. One measurement has been taken for each distance above 10 cm, up to 25 cm, with intervals of 1 cm. Moreover, a zero measurement has been taken with the optical fiber attached to the diffusive glass at the end of the silver plated mixing coil (figure 7.16). In table 7.4 and figure 7.17 and figure 7.18 (a,b) are collected the results of the integrated flux dilution with distance, the total flux evolution and the plot of the integrated and normalized flux dilution with distance. Thanks to this we did manage in finding the relation that rules this phenomenon:

$$F_{\text{source}} = 1478.14894 - 127.37929 * d + 3.32587 * d^2 + 0.01817 * d^3 - 0.00133 * d^4 \quad (7.3)$$

where $\Delta d = \pm 0.5$ cm and $\Delta F_{\text{source}} = \pm 73.908$ W/m².

The same data have then been normalized at the maximum value (figure 7.19, table 7.5) and then the empirical power relation have been found:

$$F_{\text{norm}} = 1.0 - 0.086174868 * d + 0.0022500236 * d^2 + 1.2292401 * 10^{-5} * d^3 - 8.997740110^{-7} * d^4 \quad (7.4)$$

where $\Delta d = \pm 0.5$ cm and $\Delta F_{\text{source}} = \pm 0.05$ W/m².

This second form of the equation is useful in order to extrapolate a 0-100 % dilution coefficient in order to scale the flux at different distances. As can be seen, even though the quadratic term is positive, the linear term lower the curve more than the previous term. The fit was made up to the fourth grade in order to put in evidence the not perfect square law fit even though these terms are negligible. In fact, the terms $0.01817*d^3$ and $-0.00133*d^4$ derive from the not optimal isotropic distribution of the LEDs on the matrix and from a not perfect uniformity of the flux. The second bouquet of data have been taken in order to understand the absorption of the combined effect of the diffusive system and of the glass of the incubator. The data have been collected enlightening one by one each channel at its maximum power and taking 25 measurements for all the 25 wavelength channels. These data have been compared with the flux of the same LEDs taken with the integrating sphere, scaled according to the relation of flux dilution and multiplied both with the number of LEDs welded for each channel and the area of the radiation mesh-up coil. This last one is πR_{coil}^2 where R_{coil} is 6.5 cm. In figure 7.19 can be seen the plot of the processed spectra of each channel, taken with the integrating sphere (black) and the real spectra of each channel (red). In figure 7.20 and in table 7.5 are collected the ratios (Led Correction Factor) between the integrating sphere integrated flux data with respect to the real integrated flux data taken with the radiation source. As can be seen, the mean ratio is 0.55, which means that the optics places between the LEDs and the optical fiber absorb almost 45% of the light. The first point and the last four points on the plot, corresponding to the 365nm, 850nm, 880nm and 940 nm don't follow the mean value of the ratio (0.55) because the spectrometer is sensible from 359 nm (and 365 nm is near the inner limit) up to 822 nm and so the data collected are not complete.

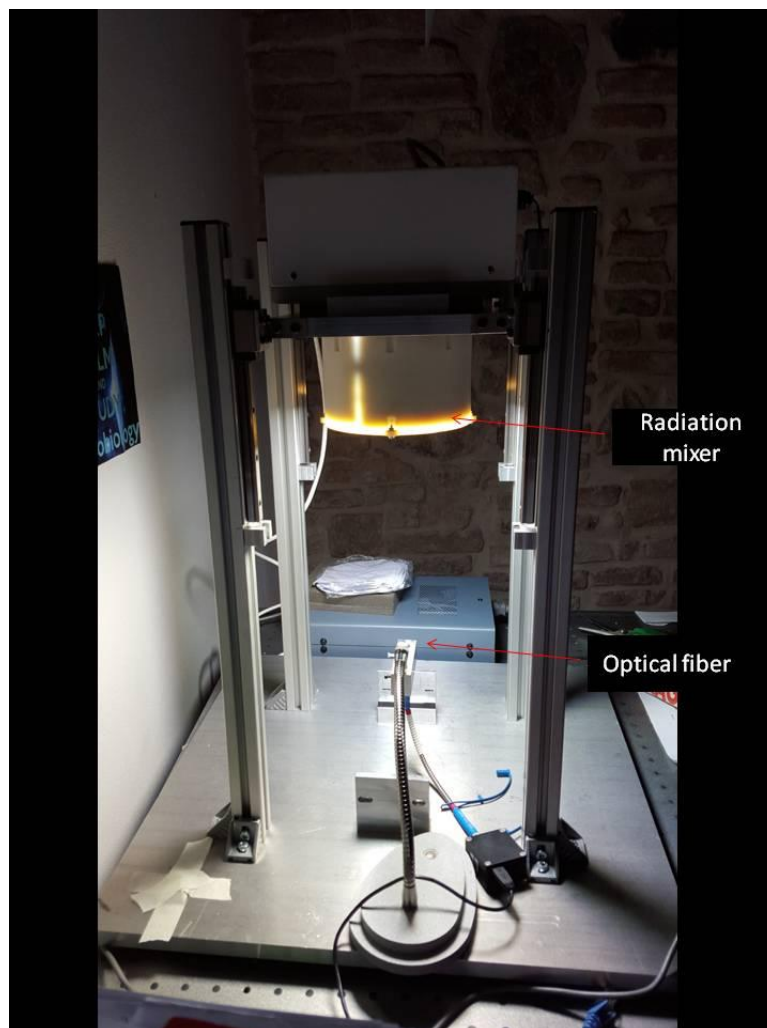


Figure 7.16: Layout of the test measurements

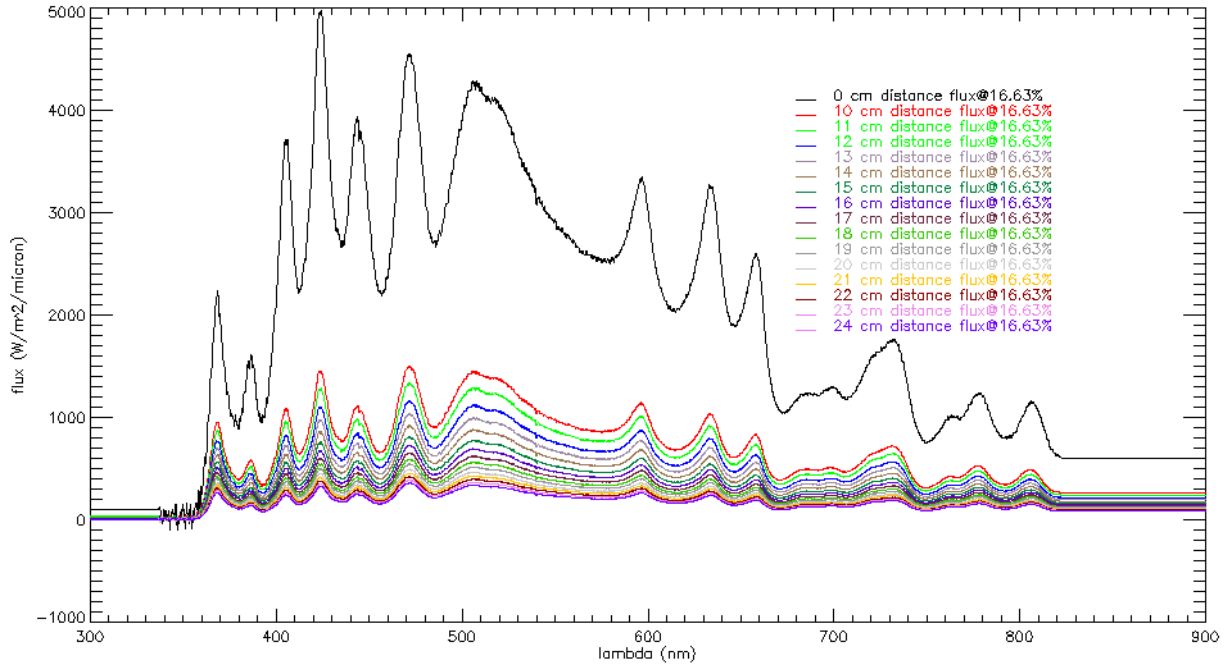


Figure 7.17: Measurements of flux scaling with the distance

Distance (cm)	flux (W/m ²)	Normalized flux (1=100%)
0±0.5	1478.155±73.908	1±0.05
10±0.5	537.947±73.908	0.363±0.05
11±0.5	491.800±73.908	0.332±0.05
12±0.5	430.166±73.908	0.291±0.05
13±0.5	385.268±73.908	0.260±0.05
14±0.5	344.705±73.908	0.233±0.05
15±0.5	309.643±73.908	0.209±0.05
16±0.5	277.240±73.908	0.187±0.05
17±0.5	248.797±73.908	0.168±0.05
18±0.5	236.359±73.908	0.160±0.05
19±0.5	210.720±73.908	0.142±0.05
20±0.5	190.976±73.908	0.129±0.05
21±0.5	179.918±73.908	0.122±0.05
22±0.5	165.890±73.908	0.112±0.05
23±0.5	157.173±73.908	0.106±0.05
24±0.5	147.129±73.908	0.099±0.05

Table 7.4: Integrated flux scaling with distance and normalized flux

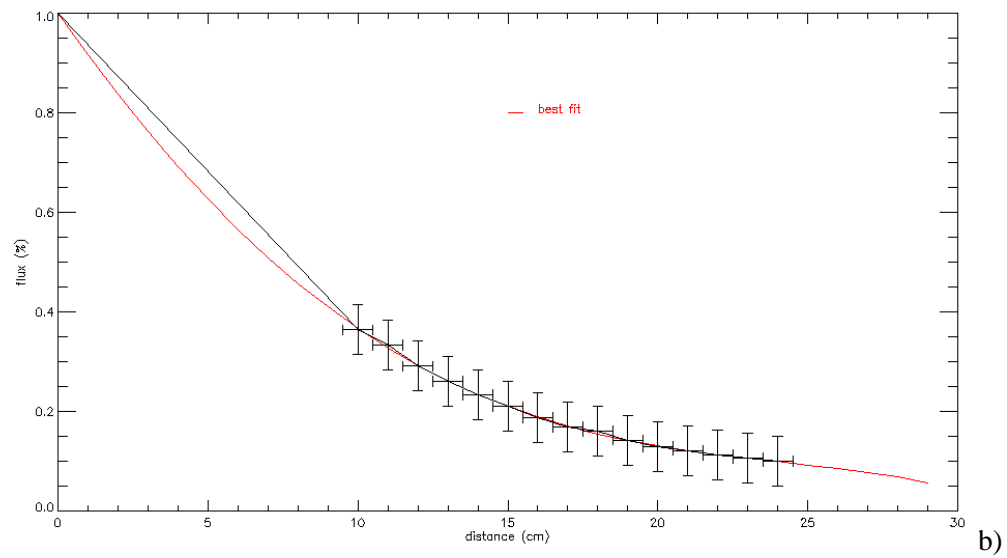
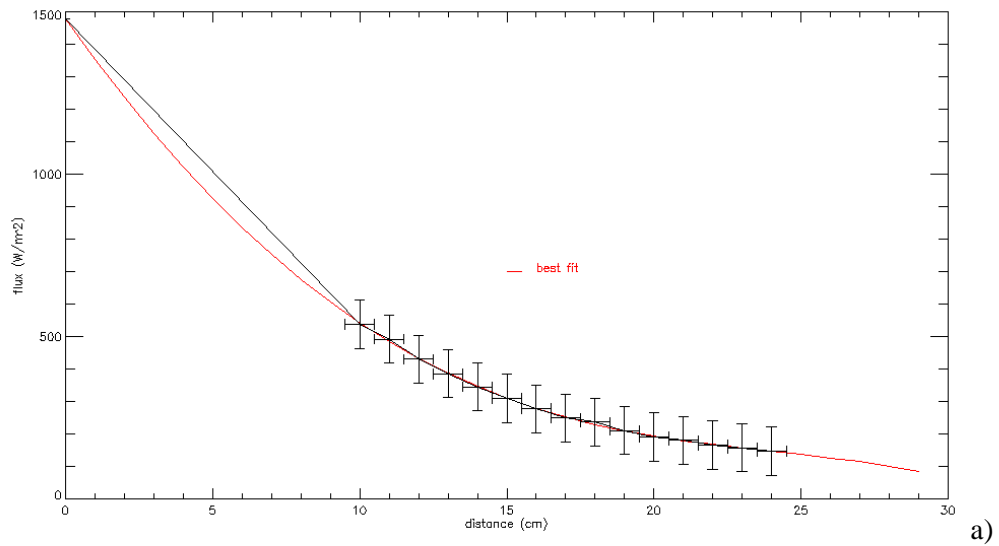


Figure 7.18: Evolution of the integrated (a) and normalized (b) flux dilution with distance. Here 1 is equal to 100%

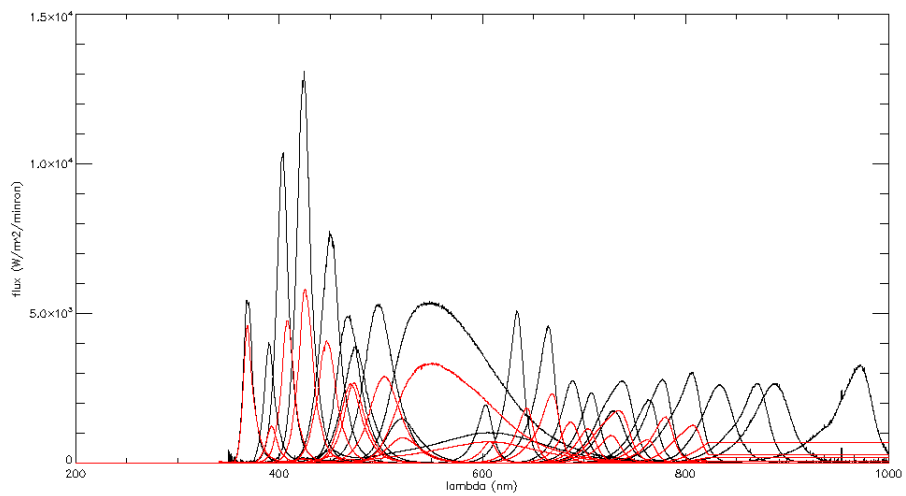


Figure 7.19: Plot of the processed spectra of each channel taken with the integrating sphere (black) and the real spectra of each channel (red).

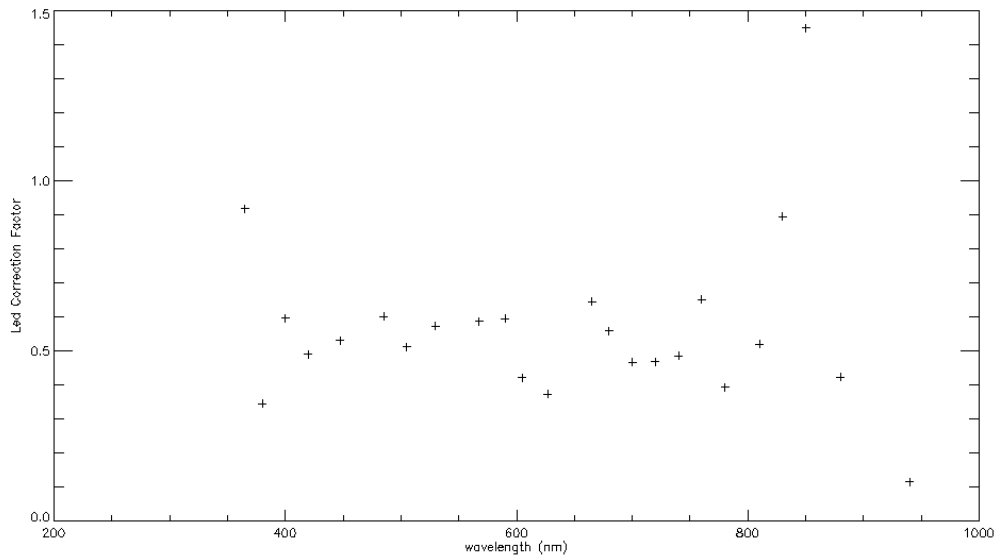


Figure 7.20: Plot of the ratio named Led Correction Factor between the integrating sphere integrated flux data with respect to the real integrated flux data.

Peak wavelength (nm) from datasheet	LCF
365±2	0,91800966
380-385±2	0,34465102
400-405±2	0,59544908
420-425±2	0,49060877
447,5±2	0,53026662
470±2	0,60118495
485±2	0,51217251
505±2	0,57260527
530±2	0,58620316
567,5±2	0,59412648
590±2	0,37200444
627±2	0,42108478
(2200K) ±2	0,64459006
655±2	0,55912445
680±2	0,46674277
700±2	0,46843271
720±2	0,48564362
740±2	0,65055179
760±2	0,39245436
780±2	0,52026033
810±2	0,89392847
830±2	1,4490509
850-870±2	0,42327055
880±2	0,11530063
940±2	0,007771708

Table 7.5: Ratio, named Led Correction Factor, between the integrating sphere integrated flux data with respect to the real integrated flux data.

In figure 7.21 can be seen the spectra of the stellar simulator taken all around the exit plate, within a radius of 6.5 cm and at a distance of 10 cm from the glass, enlightening all the single channels at 25.69% of the maximum power. As can be seen, the uniformity spans between 100% and 22.4%. Figure 7.23 shows the values of the integrated spectrum illustrated in figure 7.22 across the 13 cm diameter circumference around the centre. The data shown in figure 7.22 are collected in table 7.6.

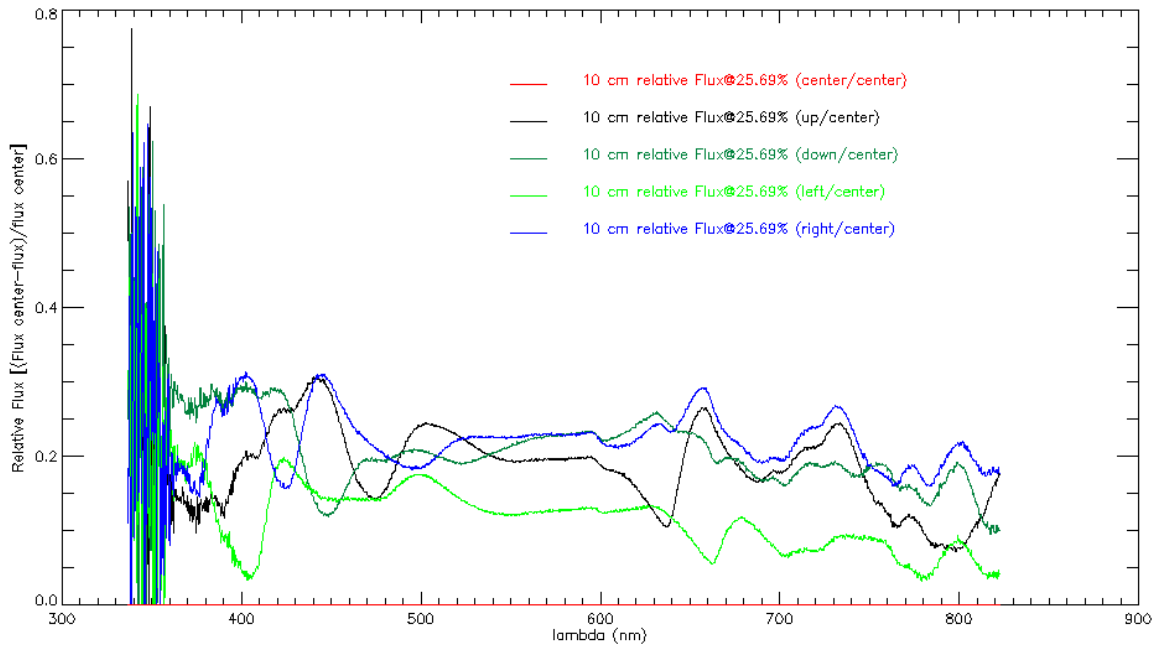


Figure 7.21: Spectra taken across a 6.5 cm diameter circumference around the centre

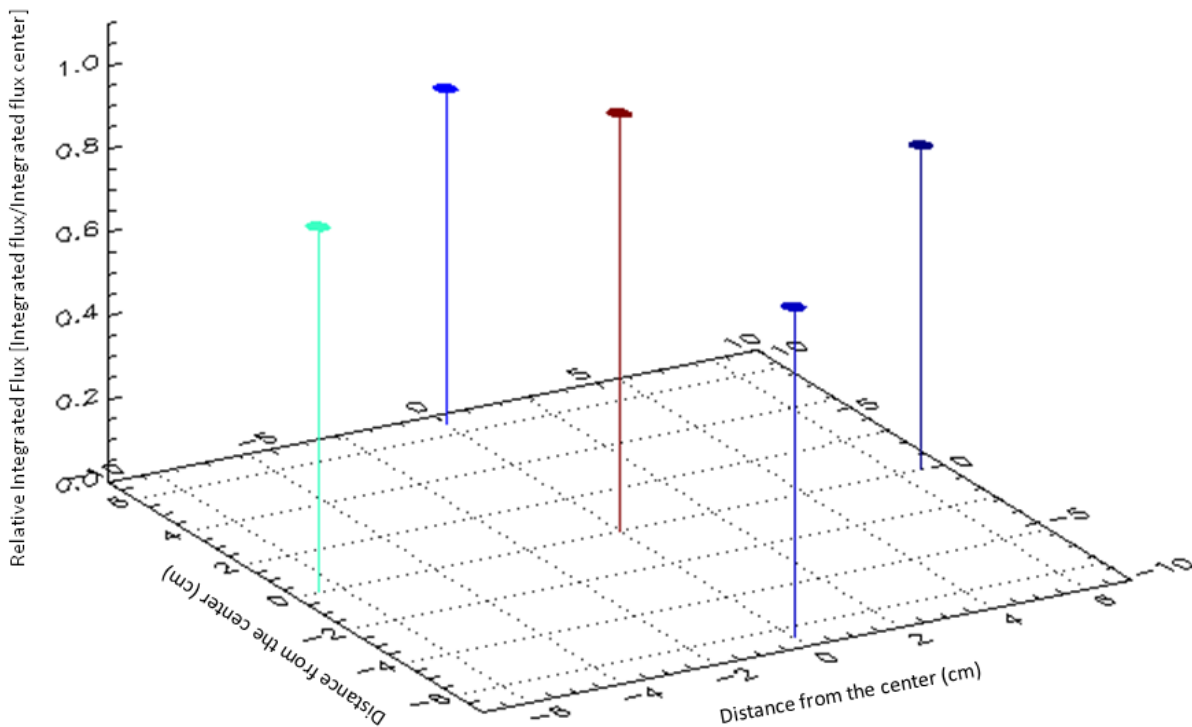


Figure 7.22: Uniformity of the integrated spectrum across a 6.5 cm diameter circumference around the centre

Position along x (cm)	Position along y (cm)	Relative integrated flux (Integrated flux/ Integrated flux centre)
0.0	6.5	0.804
0.0	-6.5	0.792
-6.5	0.0	0.875
6.5	0.0	0.776
0.0	0.0	1.000

Table 7.6: Uniformity of the integrated spectrum across a 6.5 cm diameter circumference around the centre

In order to calibrate the flux measurements with the final position of the optical fiber, as the centre of the incubator is in a different position with respect to the fiber itself, i generated two transfer functions that normalize the acquired spectrum with the spectrometer to the position where the bacteria have been lodged. The first function is obtained considering the bacteria at a distance of 10 cm from the centre of the exit glass, the second function have been generated taking into account that for the first part of the experiment the bacteria will be kept at a distance of 23 cm, not in the incubator cell but in a flask. In figure 7.23 can be seen a plot of the transfer functions made for the 10 cm distance and for the 23 cm one.

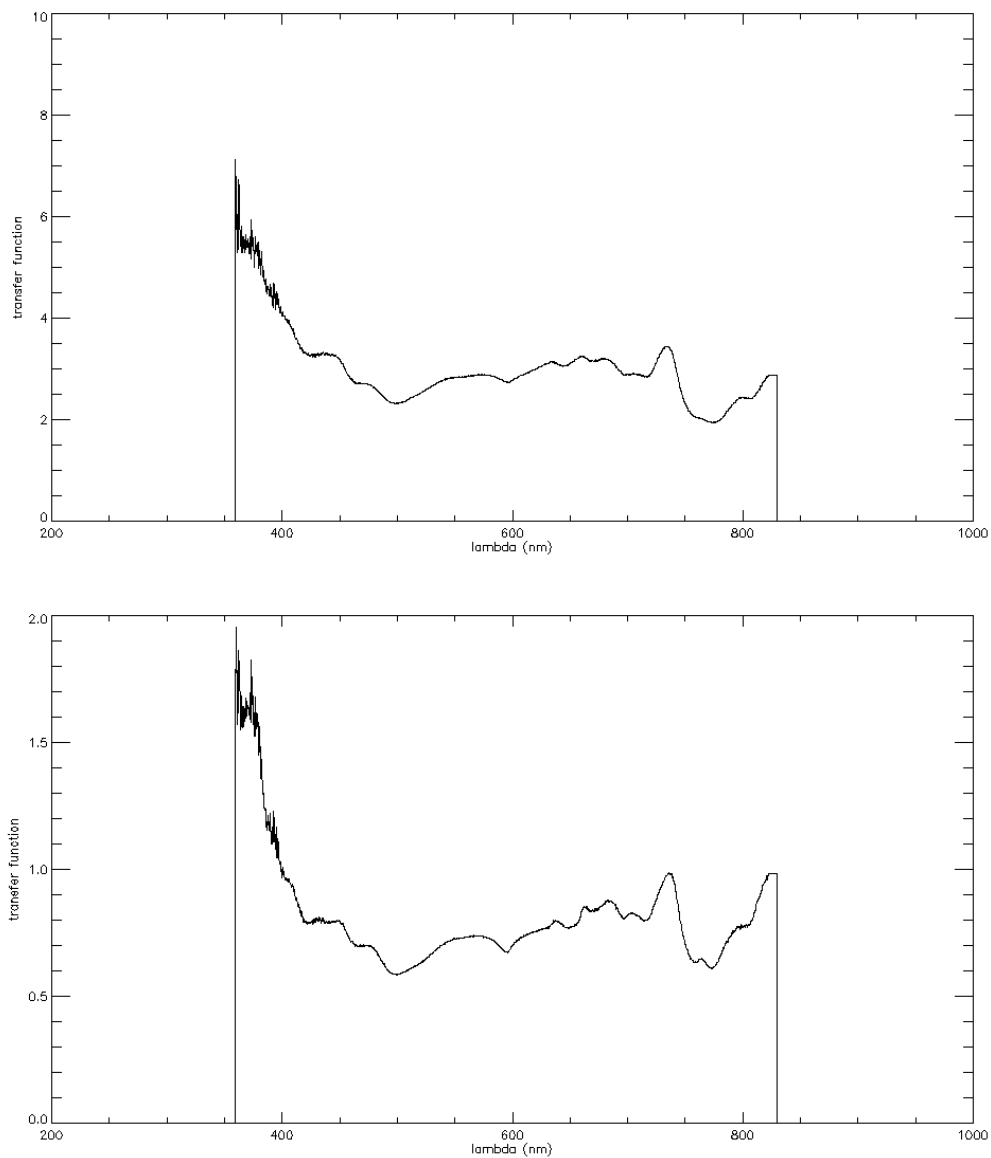


Figure 7.23: Plots of the transfer function for measurements made with the cell and with the 23 cm flask

Finally have been done measurements of the spectrum used to irradiate the bacteria and has been compared it with the simulated one. As can be seen in figure 7.24 the simulated spectrum (black) is almost the same as the real one (red).

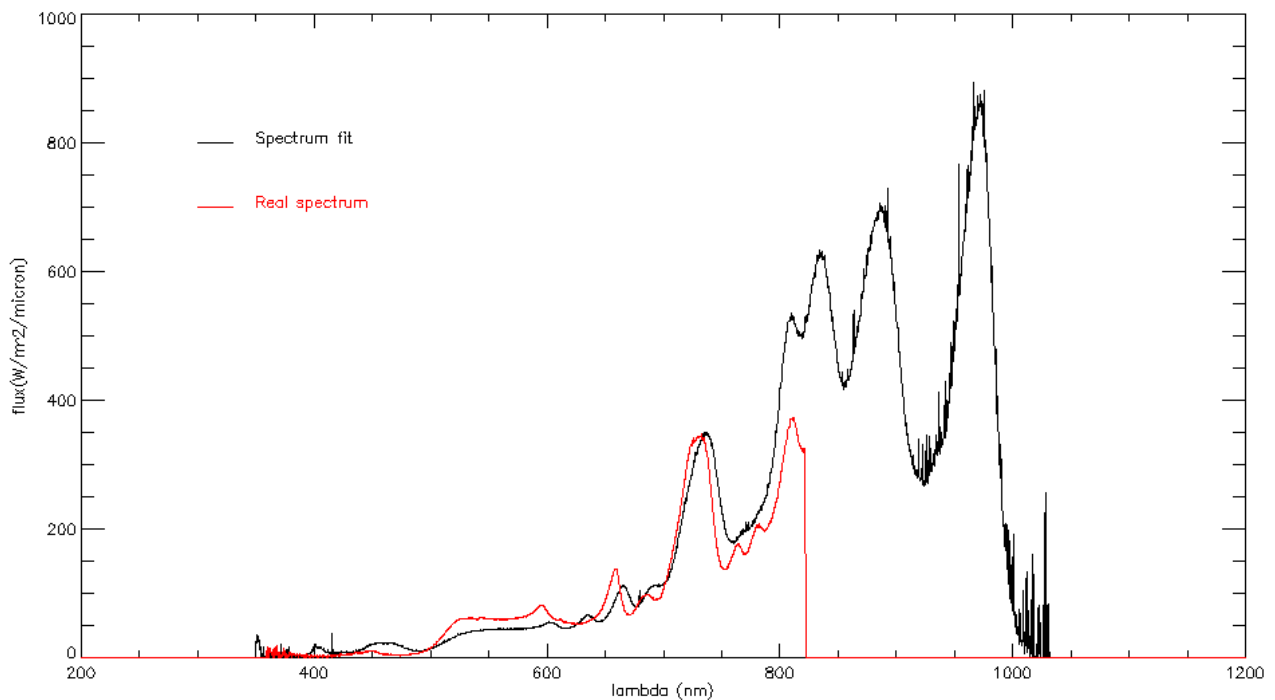


Figure 7.24: Spectrum used to irradiate the bacteria

7.6 Other applications of the instrument

The astronomical aim of the proposed device is not the only purpose of it, but several other applications are possible. For example, it could be used in the field of photo-bioreactors as a reference test bench for the choice of the wavelength to be used in order to maximize the production rate of the bacteria. Another field of application is microscopy. In fact it can be used as a dynamic light source to irradiate samples at different wavelengths and to study their features at different wavelengths without changing the source. Moreover the yeasts growth research could be a good field of application, because these organisms need precise wavelengths to evolve. Even the trap state transistors quantification and identification can be studied irradiating the electronic devices with NIR light. Finally, a pioneering study has linked the evolution of magnetic metallorganic structures with the cell behavior. Our device will help to better understand the link of these structures with the wavelength radiation.

8. The experiment

8.1 Void pumps test

In the first beginning part of the experiment we have tried to use the 6 aluminium cells that were available in the laboratory. These cells had a 250 cm^3 capacity.

A test cell, shown in figure 8.1 (a, b), has been connected to a vacuum pump through a pipe to make the void inside it and reach a value of 10^{-3} bar. Through a tube with a T-valve, it is connected with a pressure sensor (Leybold Vakuum CERAVAC CTR90).

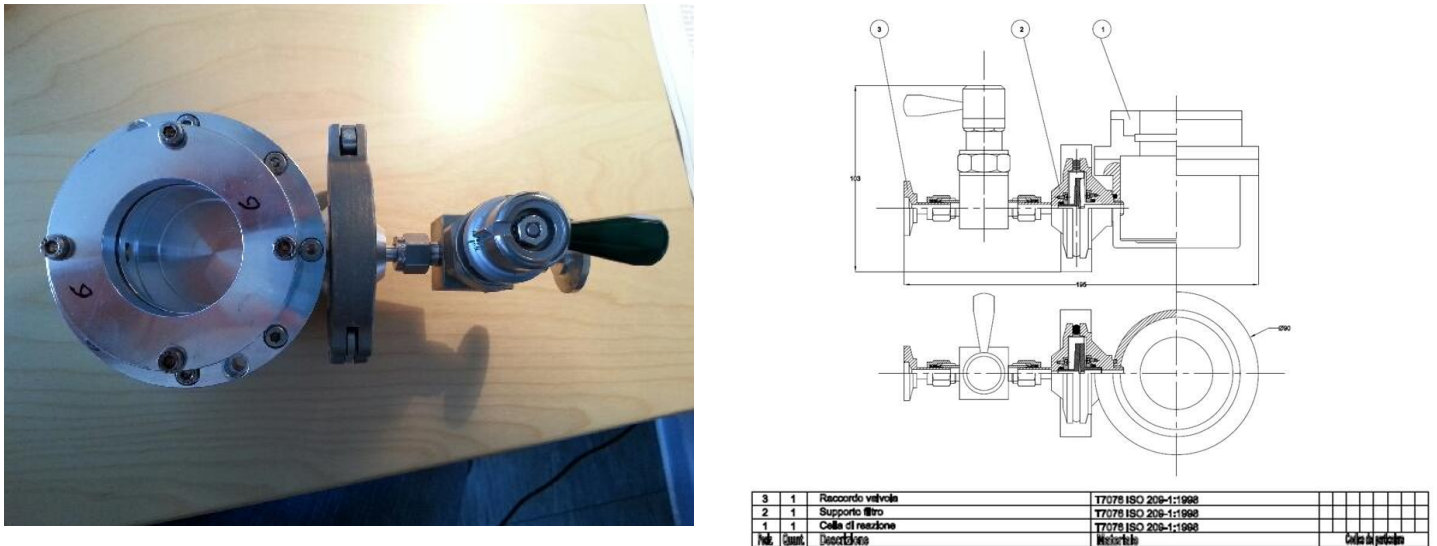


Figure 8.1: A picture of the cell (a) and the technical scheme of it (b)

In Figure 8.2 can be seen the vacuum pump and the Turbo molecular pump used in the experiment. Once this pressure has reached the desired value, the cell has been isolated by means of a stop valve. The cell has been let in this pressure condition for a discrete lapse of time, ranging from 5 days to few hours. Then, internal pressure of the cell has been measured at regular time intervals. What has been expected is a pressure increase with time. These measurements are important because can give useful information on pressure stability of the cells and can help us to keep the internal pressure constant and avoid gas loss during the experiment.

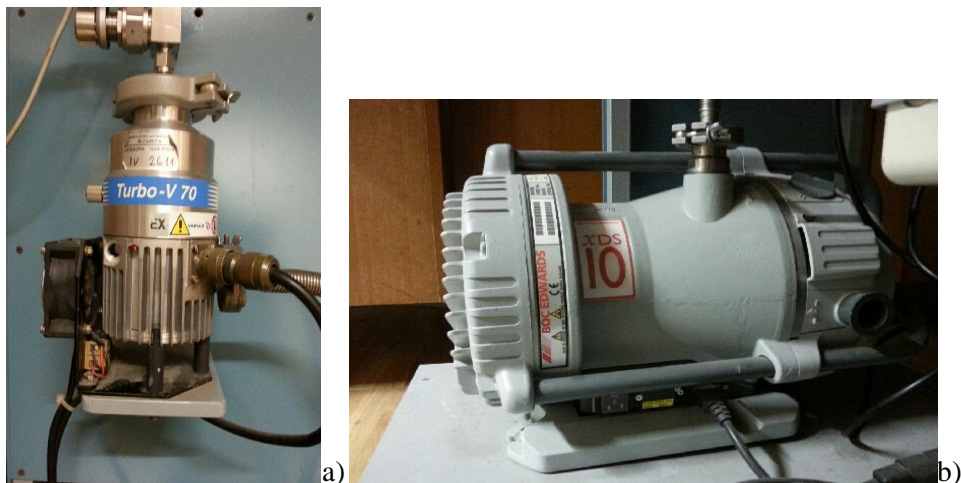


Figure 8.2: A picture of the vacuum pump (a) and the turbo molecular pump (b).

In particular we can calculate the time constant of the cell.

A void system is made up of four components: a void chamber, a void pump, a pressure tester and a complex of pipes and valves used in combination with void gaskets.

When a system is subjected to a continuous pumping is called a dynamic void system, while if the system is sealed after the evacuation is called a static void system.

The main sources of gas flux are due to gas loss inside the cells, gas penetrated by diffusion, gas evaporation from the cell inside and steams.

Of all the molecules that impact on the wall of a void chamber, only a fraction remains attached to it.

We can say that these molecules are adsorbed and are trapped in a quantum well produced by the other molecules. If these molecules join with the gas ones inside the chamber they increase the thickness and form the phenomenon of condensation. There may occur a physical phase change from gaseous to liquid.

Finally, if the molecules penetrate inside the porosities of the cell and remain trapped inside the pores they can be said to be absorbed. Only a few gases diffuse inside the walls of chambers, like H and He.

The main parameters of the cells are their volume V , inside which can be included N molecules of gas at temperature T and pressure P . As said before, the cell is connected to a vacuum pump by means of a pipe. At zero time t_0 there are N molecules inside the cell at pressure P . After a small amount of time dt inside the cell will be N' molecules at a pressure P' . From the gas equation we have:

$$PV=NKT \quad (8.1)$$

$$P'V=N'KT \quad (8.2)$$

and by difference

$$(P'-P)V=(N'-N)KT \quad (8.3)$$

If the difference of P and N is small we can write:

$$-dP \cdot V = -dN \cdot KT \quad (8.4)$$

In ideal conditions, the number of molecules that goes through the pipe is equal to that which go out from the cell. So $dN_A = -dN$ and:

$$-\frac{dP}{dt} \cdot V = -\frac{dN_A}{dt} \cdot KT \quad (8.5)$$

and

$$-\frac{dP}{dt} \cdot V = -\frac{dN_A}{dt} \cdot KT \quad (8.6)$$

calling $Q_A = \frac{dN_A}{dt} \cdot KT$ the carrying capacity, we can write:

$$Q_A = \frac{dP}{dt} \cdot V \quad (8.7)$$

With analogous passages can be defined the volumetric carrying capacity as $\Sigma = \frac{dV}{dt}$. From the perfect gas law we have:

$$dV = \frac{1}{P} \cdot dN_A KT \quad (8.8)$$

and then:

$$\frac{dV}{dt} = \frac{1}{P} \cdot \frac{dN_A}{dt} KT \quad (8.9)$$

and then

$$P\Sigma = \frac{dN_A}{dt} KT = Q_A \quad (8.10)$$

So, without gas losses we can write:

$$P\Sigma = -\frac{dP}{dt} \cdot V \quad (8.11)$$

and so:

$$dt\Sigma = -V\frac{dP}{P} \quad (8.12)$$

This can be considered as a first order system.

$$\int_{P_0}^P \frac{dP'}{P'} = \int_{t_0}^t -\frac{1}{V}\Sigma dt' \quad (8.13)$$

and then

$$\ln\left(\frac{P}{P_0}\right) = -\frac{1}{V}\Sigma(t - t_0) = -\frac{1}{\tau}(t - t_0) \quad (8.14)$$

The pressure results:

$$P = P_0 e^{-\frac{t}{\tau}} \quad (8.15)$$

When the cell is closed the gas begins to flow from the gaps. Let's consider the equation of the pressure evolution as:

$$P_{in} - P(t) = \tau \frac{dP}{dt} \quad (8.16)$$

where P_{in} is the input pressure and $P(t)$ the output pressure. Recall that the Laplace transform is defined as:

$$L[g(t)] = G(s) = \int_0^{\infty} g(t) e^{-st} dt \quad (8.17)$$

and that the inverse Laplace transform is:

$$L^{-1}[G(s)] = g(t) = \frac{1}{2\pi j} \int_{c-j\infty}^{c+j\infty} G(s)e^{st} ds \quad (8.18)$$

with c the abscissa of convergence, $g(t)$ the output variable and $G(s)$ the analogous of $g(t)$ in the phase space. Applying equation 2.16 to 2.15 we have that the transfer function is, for an input on width P_0 :

$$P(s) = H(s)P_{in} = \frac{P_0}{s(\tau s + 1)} \quad (8.19)$$

where $H(s)$ is the transfer function. Making the inverse Laplace transform we have that:

$$g_{out}(t) = P(t) = L^{-1} \left[\frac{P_0}{\tau s \left(1 + \frac{1}{\tau}\right)} \right] = P_0 \left(1 - e^{-\frac{t}{\tau}}\right) \quad (8.20)$$

The pressure in the cell follows then the law 2.20, keeping in mind that usually P_0 is different from $P(t=0)$, and we have to introduce a constant k that is equal to $P_0 - P(t=0)$:

$$P(t) = P_0 \left(1 - \frac{k}{P_0} e^{-\frac{t}{\tau}}\right) \quad (8.21)$$

$$P_0 - P(t) = k e^{-\frac{t}{\tau}} \quad (8.22)$$

where $P(t)$ is the pressure, P_0 is the zero pressure, and t is the increasing time. Solving for t we have:

$$P_0 \left(1 - \frac{P(t)}{P_0}\right) = k e^{-\frac{t}{\tau}} \quad (8.23)$$

$$\frac{P_0}{k} \left(1 - \frac{P(t)}{P_0}\right) = e^{-\frac{t}{\tau}} \quad (8.24)$$

$$\ln \left[\frac{P_0}{k} \left(1 - \frac{P(t)}{P_0}\right) \right] = -\frac{t}{\tau} \quad (8.25)$$

$$-\ln \left[\frac{P_0}{k} \left(1 - \frac{P(t)}{P_0}\right) \right] = \frac{1}{\tau} t \quad (8.26)$$

$$\ln \left[\frac{k}{P_0 - P(t)} \right] = \frac{1}{\tau} t \quad (8.27)$$

that is a linear relation with angular coefficient $\frac{1}{\tau}$. From the 2.27 can be found τ :

$$\tau = \frac{t}{\ln \left[\frac{k}{P_0 - P(t)} \right]} \quad (8.28)$$

The error $\Delta\tau$ associated to τ can be found from the following formula:

$$\Delta\tau = \sqrt{\left(\frac{\partial\tau}{\partial t} \Delta t\right)^2 + \left(\frac{\partial\tau}{\partial k} \Delta k\right)^2 + \left(\frac{\partial\tau}{\partial P_0} \Delta P_0\right)^2 + \left(\frac{\partial\tau}{\partial P(t)} \Delta P(t)\right)^2} \quad (8.29)$$

where $\Delta t = \frac{1}{120} h = 0.00833 h$. Δk is found from the definition of k that is:

$$k = P_0 - P(t=0) \quad (8.30)$$

and

$$\Delta k = \sqrt{\left(\frac{\partial k}{\partial P_0} \Delta P_0\right)^2 + \left(\frac{\partial k}{\partial P(t)} \Delta P(t)\right)^2} \quad (8.31)$$

$$\Delta P_0 = \Delta P = 0.005 \text{ mbar.}$$

$$\frac{\partial \tau}{\partial t} = \frac{\ln\left[\frac{k}{P_0 - P(t)}\right] - t\left[\frac{P_0 - P(t)}{k}\right](-1)\frac{\partial P(t)}{\partial t}}{\left(\ln\left[\frac{k}{P_0 - P(t)}\right]\right)^2} \quad (8.32)$$

$$\frac{\partial \tau}{\partial t} = \frac{\left[\frac{t}{\tau}\right] + k e^{-\frac{t}{\tau}} e^{-\frac{t}{\tau}}}{t^2} \tau^2 = \frac{t}{\tau} [k e^{-2\frac{t}{\tau+1}}] \quad (8.33)$$

$$\left(\frac{\partial \tau}{\partial t} \Delta t\right)^2 = \Delta t^2 \frac{\tau^2}{t^2} [1 + k^2 e^{-4\frac{t}{\tau}} + 2k e^{-2\frac{t}{\tau}}] \quad (8.34)$$

$$\left(\frac{\partial \tau}{\partial k} \Delta k\right)^2 = \Delta k^2 \frac{t^2 \left\{ \frac{P_0 - P(t)}{k [P_0 - P(t)]^2} \left[\frac{1}{P_0 - P(t)} - k e^{-\frac{t}{\tau}} \right] \right\}^2}{t^4} \tau^2 \quad (8.35)$$

$$\left(\frac{\partial \tau}{\partial k} \Delta k\right)^2 = \Delta k^2 \frac{\left[\frac{e^{-\frac{t}{\tau}}}{k} - k e^{-\frac{t}{\tau}}\right]^2}{k^4 e^{-2\frac{t}{\tau} t^2}} \tau^4 = \Delta k^2 \frac{\left[\frac{2t}{k^2} + k^2 e^{-\frac{2t}{\tau}} - 2\right]}{k^4 e^{-2\frac{t}{\tau} t^2}} \tau^4 \quad (8.36)$$

$$\frac{\partial \tau}{\partial P_0} = -t \frac{P_0 - P(t)}{k} \left[-\frac{k}{[P_0 - P(t)]^2} \right] \tau^2 = \frac{\tau^2}{t} \frac{1}{k} e^{\frac{t}{\tau}} \quad (8.37)$$

$$\left(\frac{\partial \tau}{\partial P_0} \Delta P_0\right)^2 = \frac{\tau^4}{t^2} \frac{1}{k^2} e^{\frac{2t}{\tau}} \Delta P_0^2 \quad (8.38)$$

$$\frac{\partial \tau}{\partial P(t)} = -t \frac{P_0 - P(t)}{k} \left[\frac{k}{[P_0 - P(t)]^2} \right] \tau^2 = -\frac{\tau^2}{t} \frac{1}{k} e^{\frac{t}{\tau}} \quad (8.39)$$

$$\left(\frac{\partial \tau}{\partial P(t)} \Delta P(t)\right)^2 = \frac{\tau^4}{t^2} \frac{1}{k^2} e^{\frac{2t}{\tau}} \Delta P^2 \quad (8.40)$$

$$\Delta \tau = \sqrt{\Delta t^2 \frac{\tau^2}{t^2} \left[1 + k^2 e^{-4\frac{t}{\tau}} + 2k e^{-2\frac{t}{\tau}} \right] + \Delta k^2 \frac{\left[\frac{2t}{k^2} + k^2 e^{-\frac{2t}{\tau}} - 2 \right]}{k^4 e^{-2\frac{t}{\tau} t^2}} \tau^4 + \frac{\tau^4}{t^2} \frac{1}{k^2} e^{\frac{2t}{\tau}} (\Delta P_0^2 + \Delta P^2)} \quad (8.41)$$

8.1.1 Preliminary tests

At the first beginning it has been done a preliminary test to verify the quality of the vacuum V-70 pump. Cell 4 has been connected to the void pump and has been created vacuum inside it.

To understand the minimum vacuum pressure at which the pump could operate we measured vacuum values at different times read with a Leybold Vakuum Single-Channel Vacuum Gauge Controller . Zero pressure hasn't been controlled. The results are the ones shown in Table 8.1.

Pressure (mbar)	Time (h)	Day	Zero pressure (mbar)
4.17	12.30	15/05/2013	
2.93	14.30		
2.23	16.30		
2.07	18.30		
	20.30		
	22.30		
	00.30	16/05/2013	
	02.30		
	04.30		
	06.30		
	08.30		
1.54	09.00		
1.43	10.00		
1.38	12.00		
1.29	14.00		
1.25	16.00		

Table 8.1: Vacuum pressure of the V-70 pump with time increasing

The trend of void pressure has been plotted in Figure 8.3.

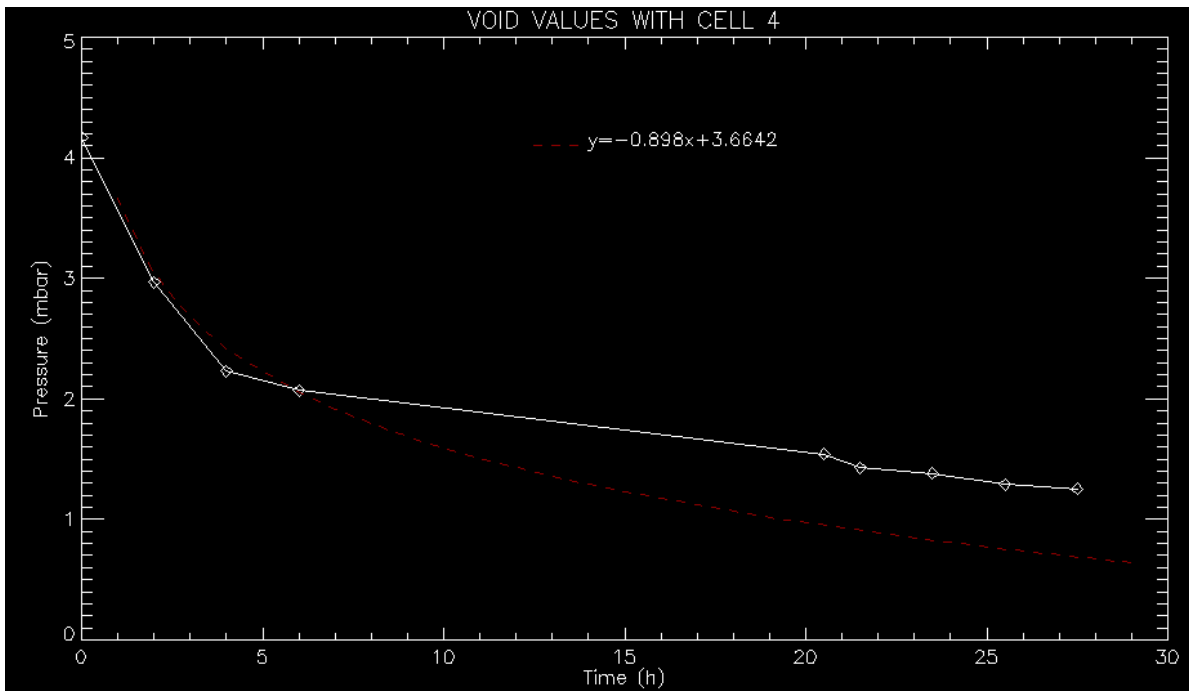


Figure 8.3: Plot of the vacuum pressure of the V-70 pump with time increasing

As can be seen, void values can't go below 1 mbar. Changing the cell the values were almost identical. Anyway, this threshold could have been due to vacuum pump malfunction or a pressure tester malfunction.

To remove residuals, cells have been disassembled one by one and cleaned with isopropyl alcohol. While making this operation, a fractiousness in the glass of cell number 1 near the O-ring. So, the glass have been replaced with another one. Cells have been analyzed with isopropyl alcohol to try to individuate gas losses making the void inside them and see if alcohol frosted near the losses, but no evident losses have been found. After this operation all cells have been tested.

8.1.1.1 Test of cell n°1

In the following table 8.2 and plot are summarized the vacuum pressure measurements of cell number 1

Pressure (mbar)	Time (h)	Day	Zero pressure (mbar)
1.54	09.55	05/06/2013	1016.3
15.81	10.00		
273.85	11.05		
589.76	12.55		
740.43	14.10		

Table 8.2: Vacuum pressure measurements of cell number 1

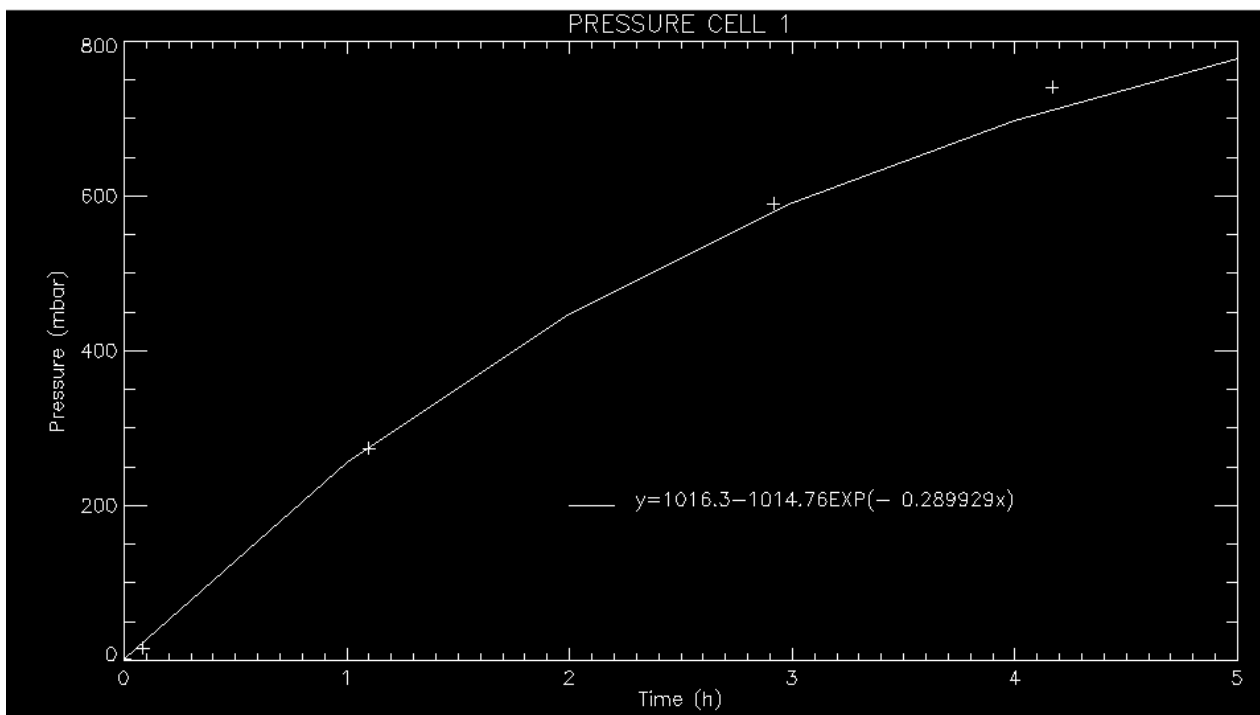
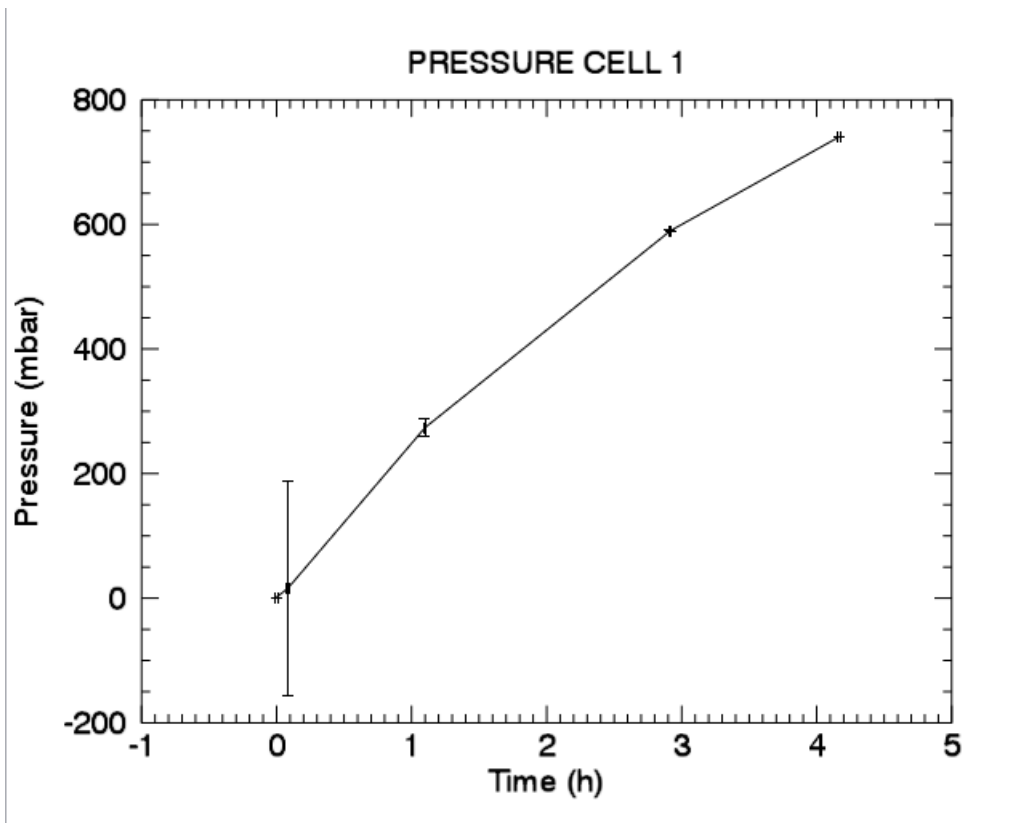


Figure 8.4: Vacuum pressure measurements plot of cell number 1 and error bars

As can be seen, the cell number 1 has very strong losses.



8.1.1.2 Test of cell n°2

In the first configuration, with two T-valves closing the air passage from the pump to the measurement tester, no data have been collected for cell number 2.

8.1.1.3 Test of cell n°3

In the following table 8.3 and plot are summarized the vacuum pressure measurements of cell number 3

Pressure (mbar)	Time (h)	Day	Zero pressure (mbar)
1.62	17.15	06/06/2013	1015
101.3	18.15		
1017	19.15		

Table 8.3: Vacuum pressure measurements of cell number 3

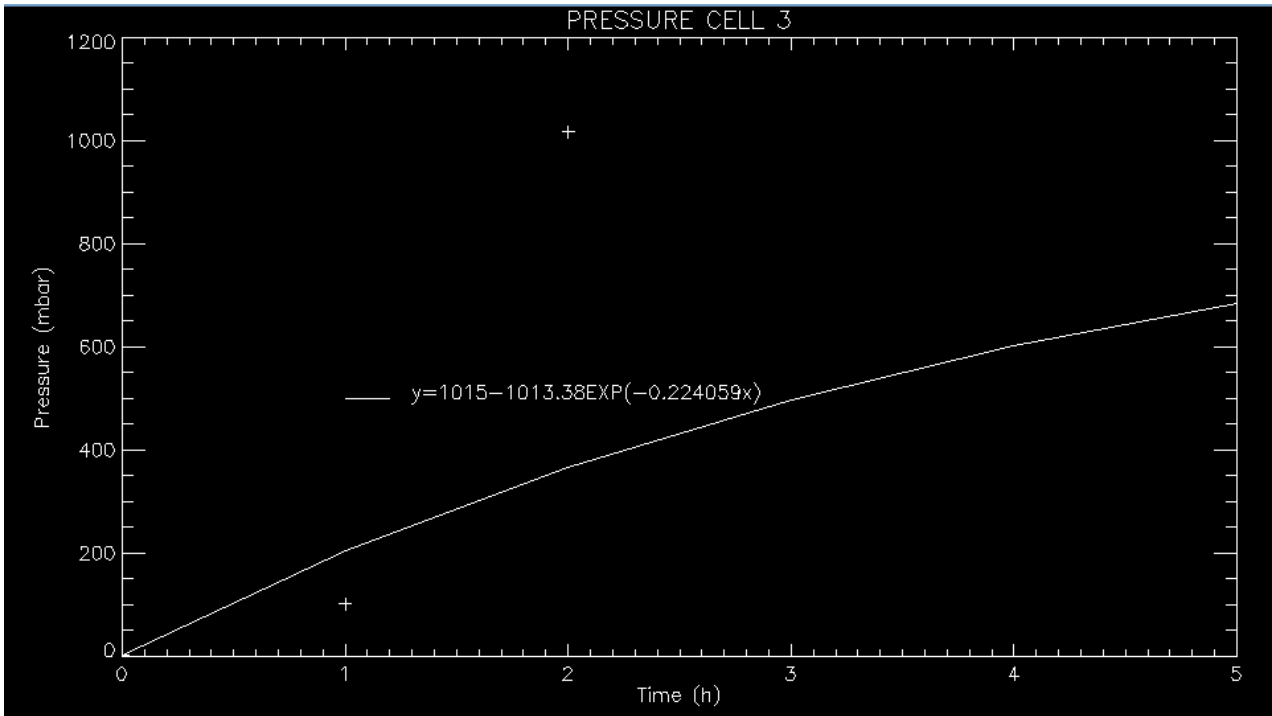
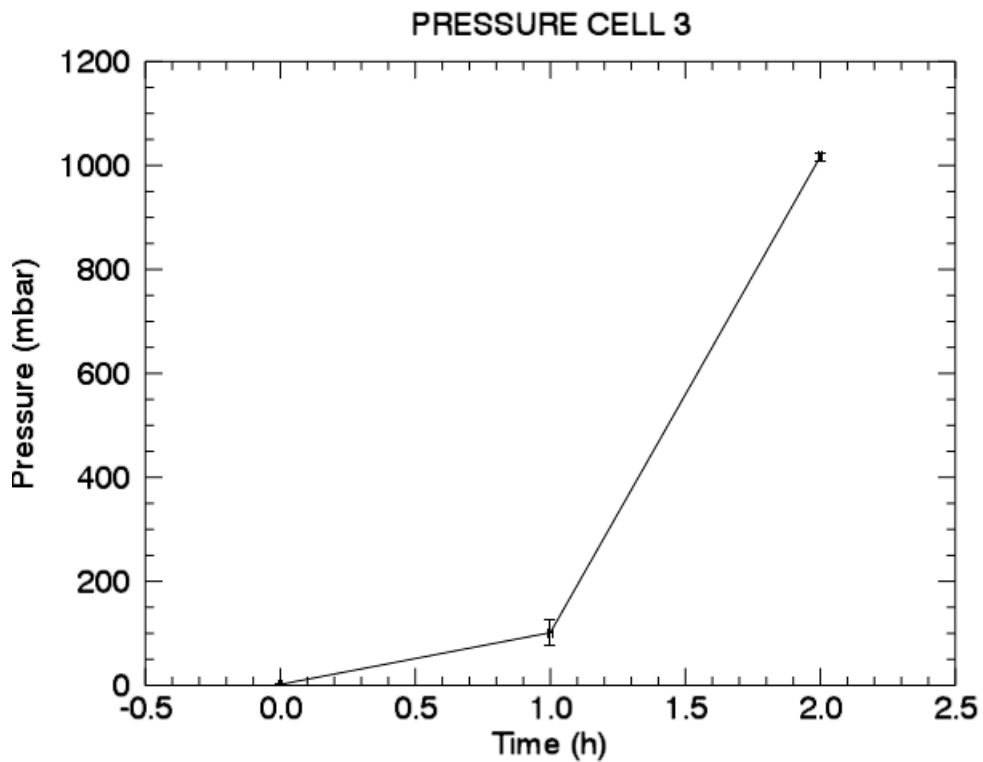


Figure 8.5: Vacuum pressure measurements plot of cell number 3 and error bars

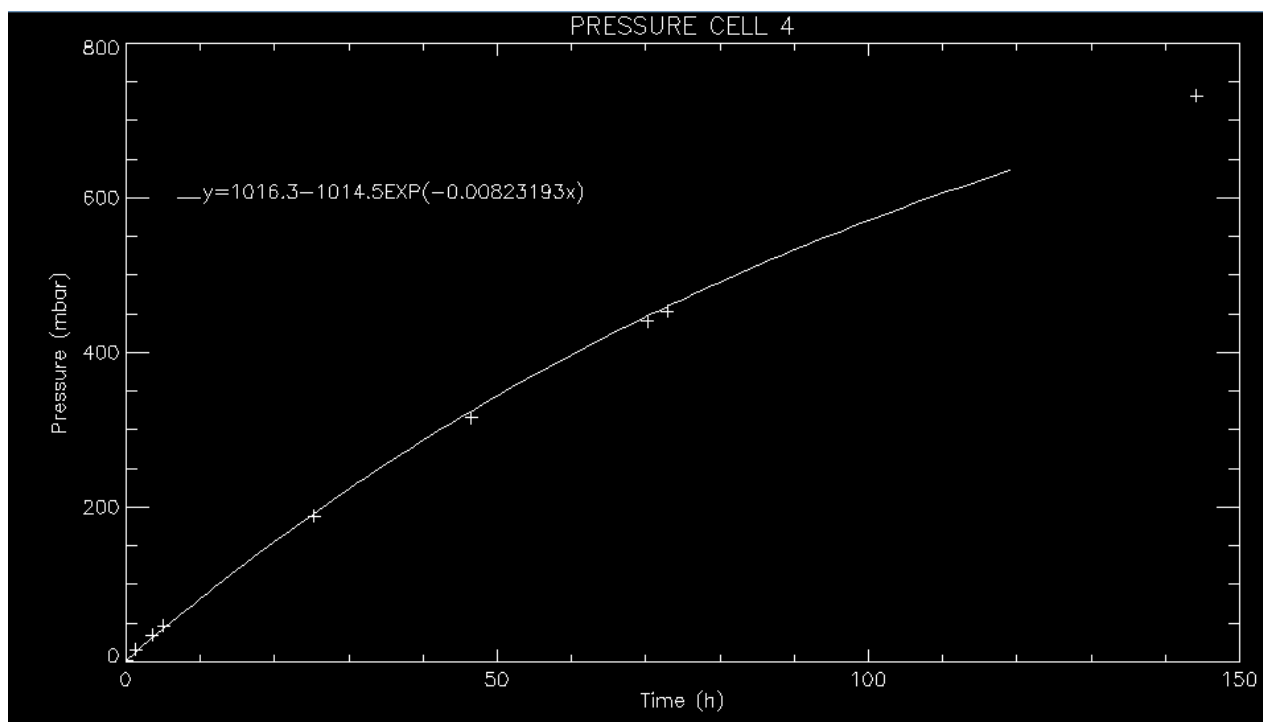


8.1.1.4 Test of cell n°4

In the following table 8.4 and plot are summarized the vacuum pressure measurements of cell number 4

Pressure (mbar)	Time (h)	Day	Zero pressure (mbar)
1.8	10.30	18/06/2013	1016.3
15.53	11.50		
34.73	14.00		
46.29	15.30		
188.5	11.50	19/06/2013	
315.7	09.00	20/06/2013	
440.23	08.45	21/06/2013	
453.22	11.25		
732.38	14.10	24/06/2013	

Table 8.4: Vacuum pressure measurements of cell number 4



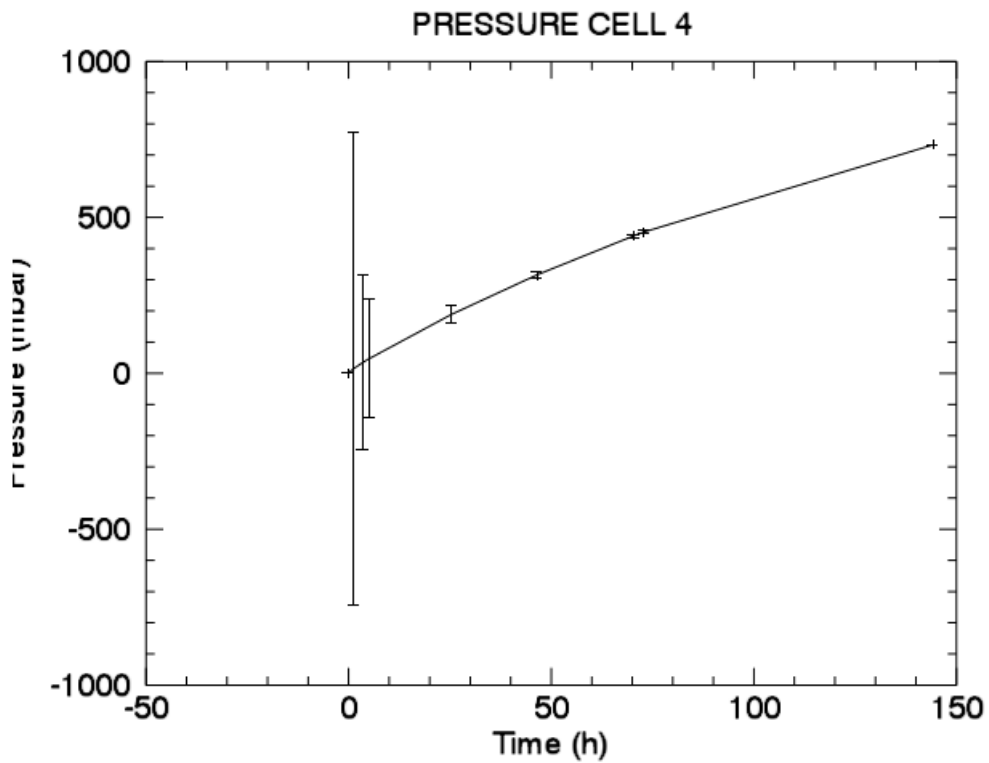


Figure 8.6: Vacuum pressure measurements plot of cell number 4 and error bars

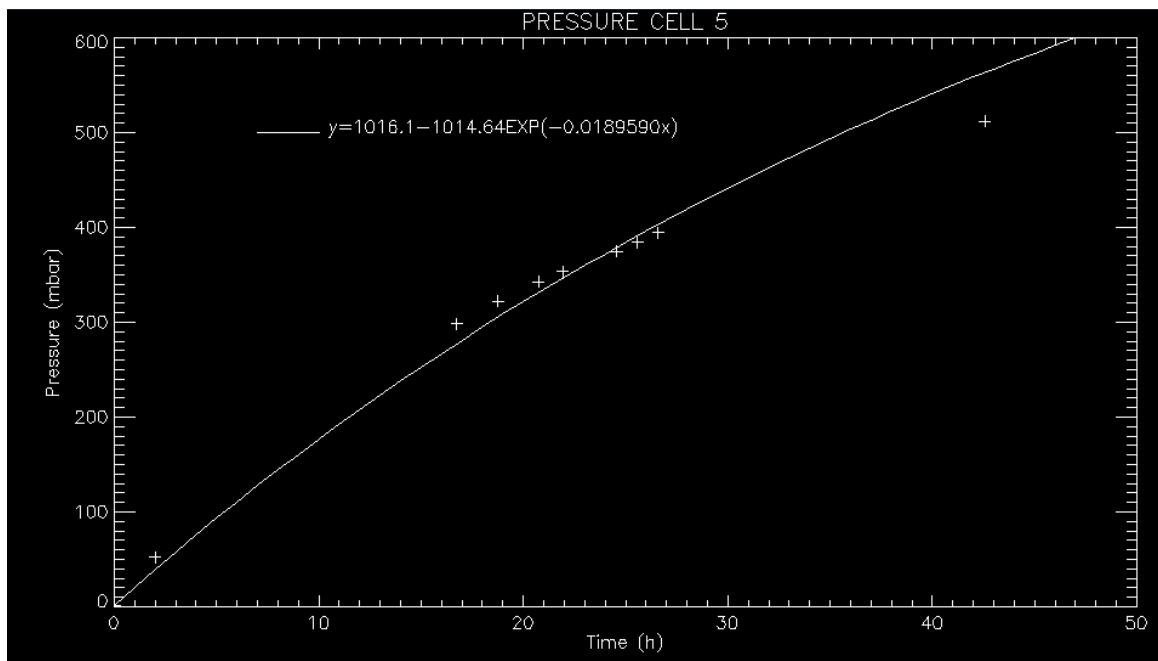
8.1.1.5 Test of cell n°5

The results of the test of cell number 5 are shown in the sequent tables 8.5 and relative plots.

Pressure (mbar)	time (h)	Day	Zero pressure (mbar)
1.46	16.30	03/06/2013	1016,1
52.02	18.30		
	20.30		
	22.30		
	00.30	04/06/2013	
	02.30		
	04.30		
	06.30		
298.09	09.15		
322.15	11.15		
342.36	13.05		

Pressure (mbar)	time (h)	Day	Zero pressure (mbar)
353.84	14.15		
374.42	16.15		
384.4	17.15		
394.41	18.15		
	20.15		
	22.15		
	00.15		
	02.15		
	04.15		
	06.15		
	08.15		
511.93	09.45	05/06/2013	

Table 8.5: Vacuum pressure measurements of cell number 5



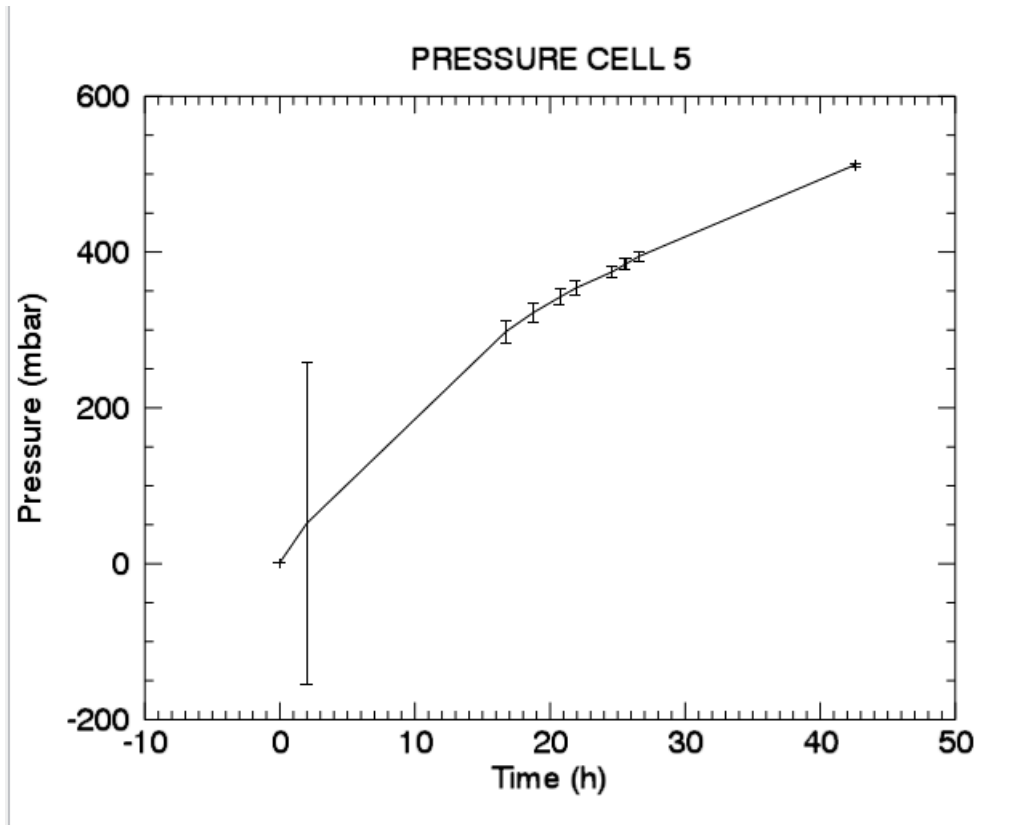


Figure 5.7: Vacuum pressure measurements plot of cell number 5 and error bars

8.1.1.6 Test of cell n°6

In the following table 8.6 and plot are summarized the vacuum pressure measurements of cell number 6.

Pressure (mbar)	Time (h)	Day	Zero pressure (mbar)
2.15	14.30	14/06/2013	1019.9
291.44	16.40		
446.23	18.00		
1020.8	10.00	17/06/2013	

Table 8.6: Vacuum pressure measurements of cell number 6

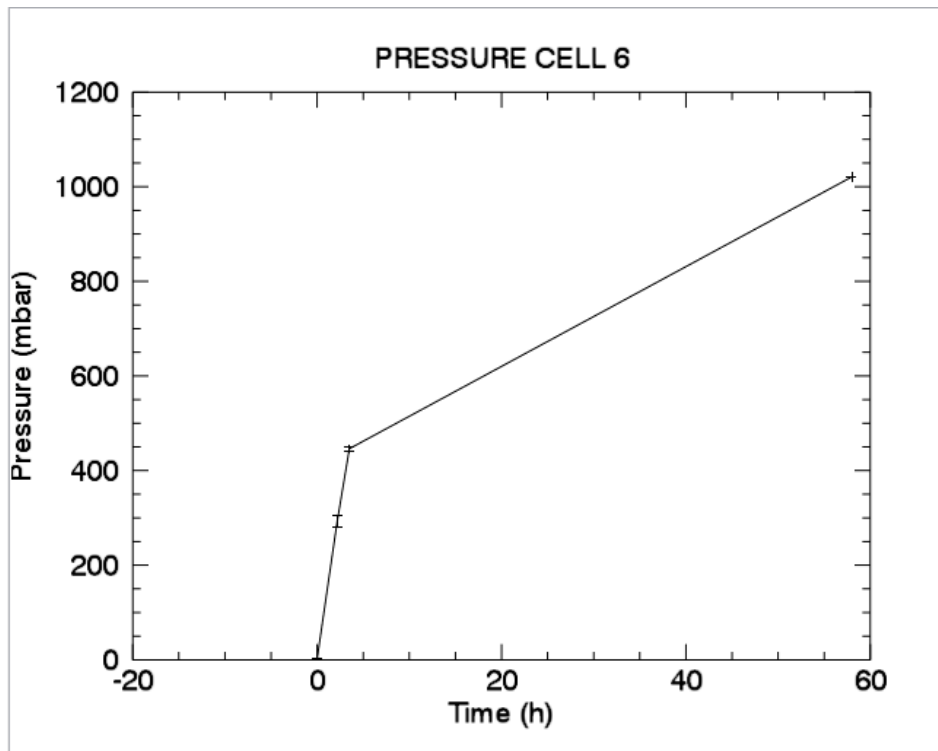
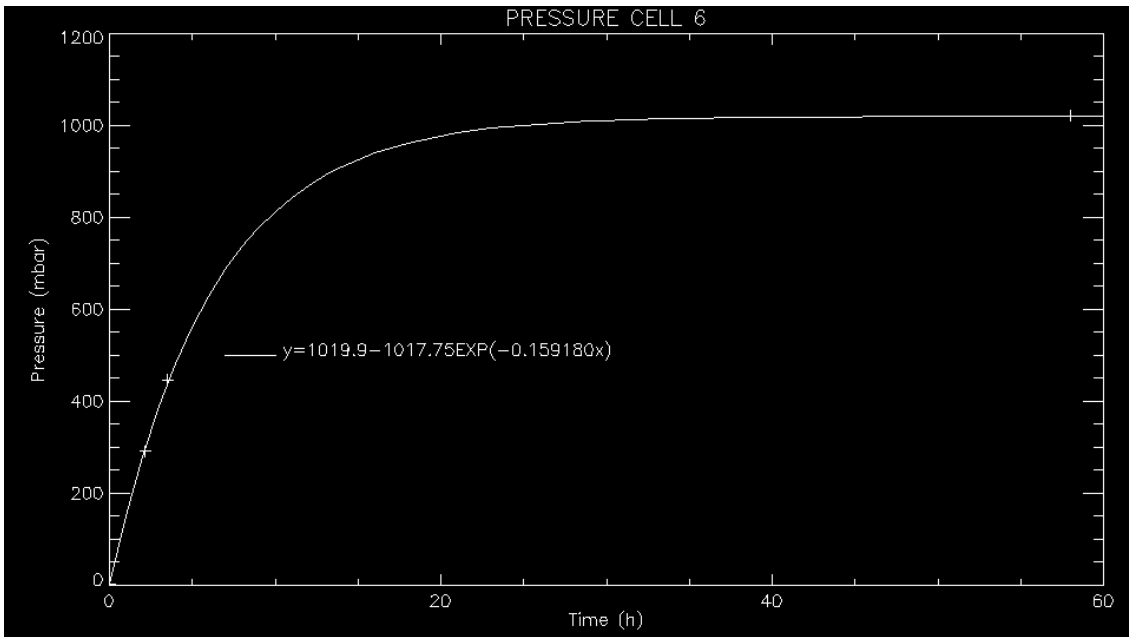


Figure 8.8: Vacuum pressure measurements plot of cell number 6 and error bars

A cumulative plot shows the overall pressure trend for all the six cells. For cell 2 data have been collected with a shorter pipe length. It can be seen that the best cells are in order: the number 4, the number 5, the number 6, the number 1, the number 2 and the number 3.

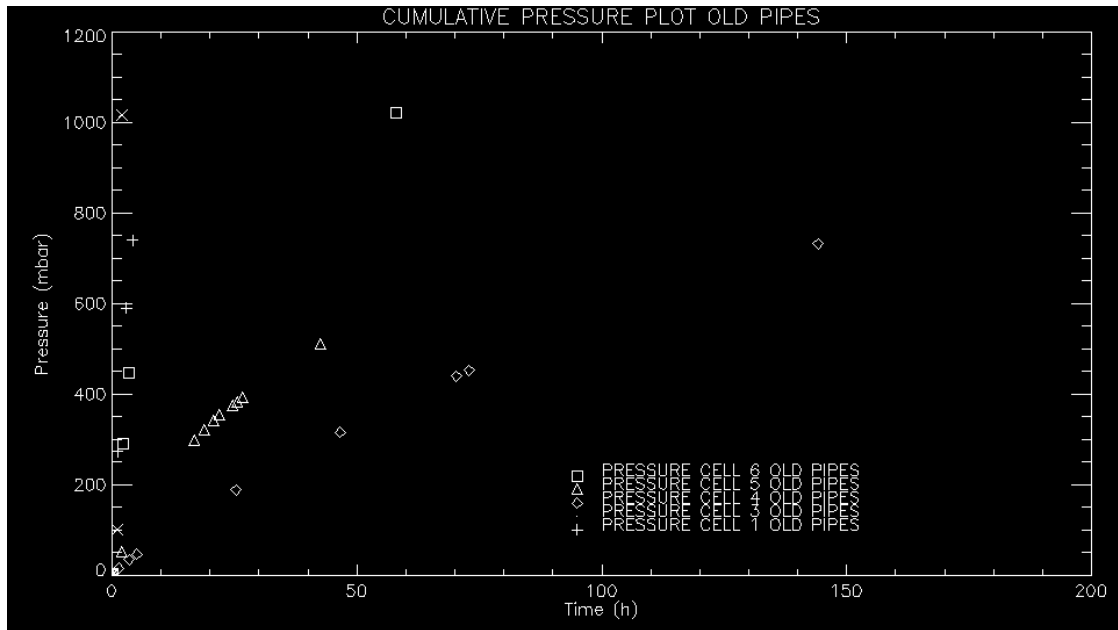


Figure 8.9: Cumulative vacuum pressure measurements plot of all cells

8.1.1.7 Intermediate procedures

After the previous measurements, it has though been found that the vacuum pump had a loss because of an open valve used to dehumidify it. This valve has been closed. At this time has been performed a tube test to be sure that the collector's pipes didn't have losses. The values are shown in Table 8.7 and in Figure 8.10

Pressure (mbar)	Time (h)	Day	Zero pressure (mbar)
1.55	14.40	05/06/2013	1105
7.32	16.40		
10.64	18.40		
	20.40		
	22.40		
	00.40		
	02.40		
	04.40		
	06.40		
	08.40		
29.6	10.40	06/06/2013	
32.6	12.40		

Table 8.7: Vacuum pressure measurements of collector pipes

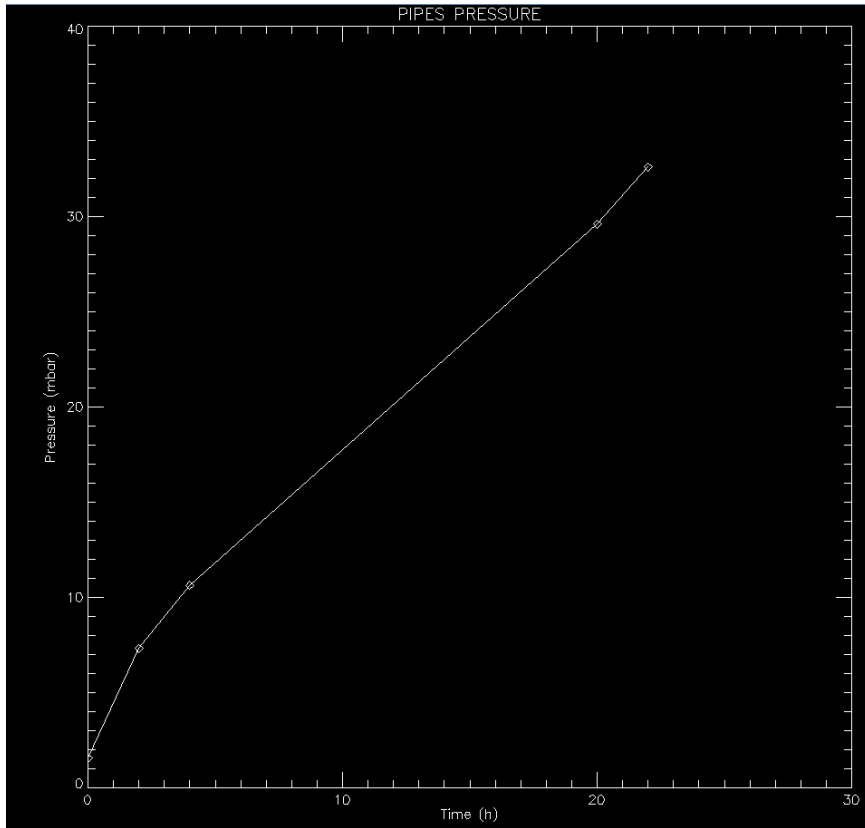


Figure 8.10: Vacuum pressure plot of collectors pipes

As can be seen the trend is linear. Moreover, pipe loss represents about 10% of the overall pressure loss of the cells. To try to increase vacuum pressure shortening the path, a part of the pipes has been removed. Moreover, to avoid valve losses it has been changed one valve replaced with one used for the cells. In Figure 8.11 can be seen the new pipe configuration

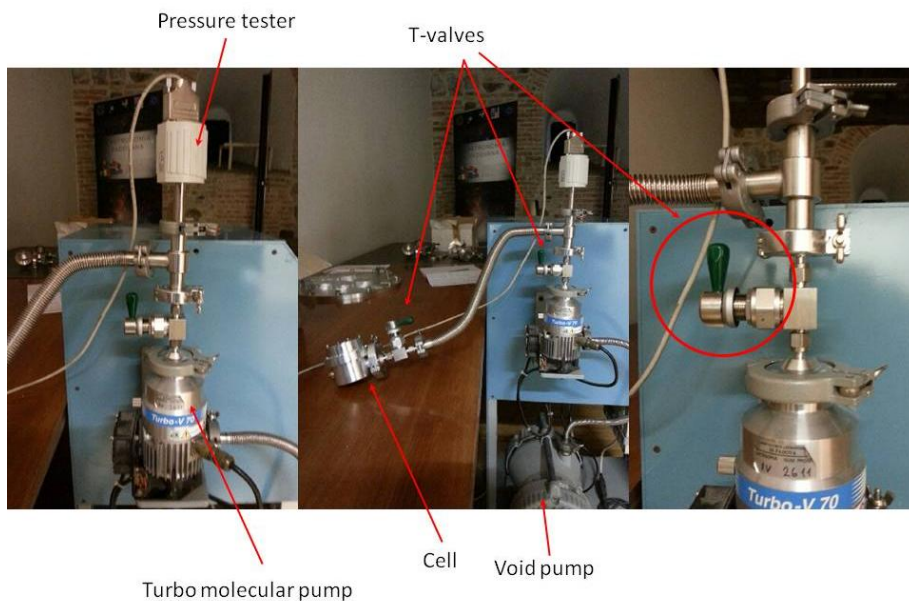


Figure 8.11: New pipe configuration

Then, all measurements have been collected. The results can be seen in the following tables and figures.

8.1.1.8 Test of cell n°1

In the following table 8.8 and plot are collected the vacuum pressure measurements of cell 1 with the new pipe configuration

Pressure (mbar)	Time	Day	Zero pressure (mbar)
1.69	09.30	03/07/2013	1015.1
182.4	10.30		
327.91	11.30		
479.29	12.30		
691.8	14.35		
777.95	15.40		
831.88	16.35		

Table 8.8: Vacuum pressure measurements of cell 1 with the new pipe configuration

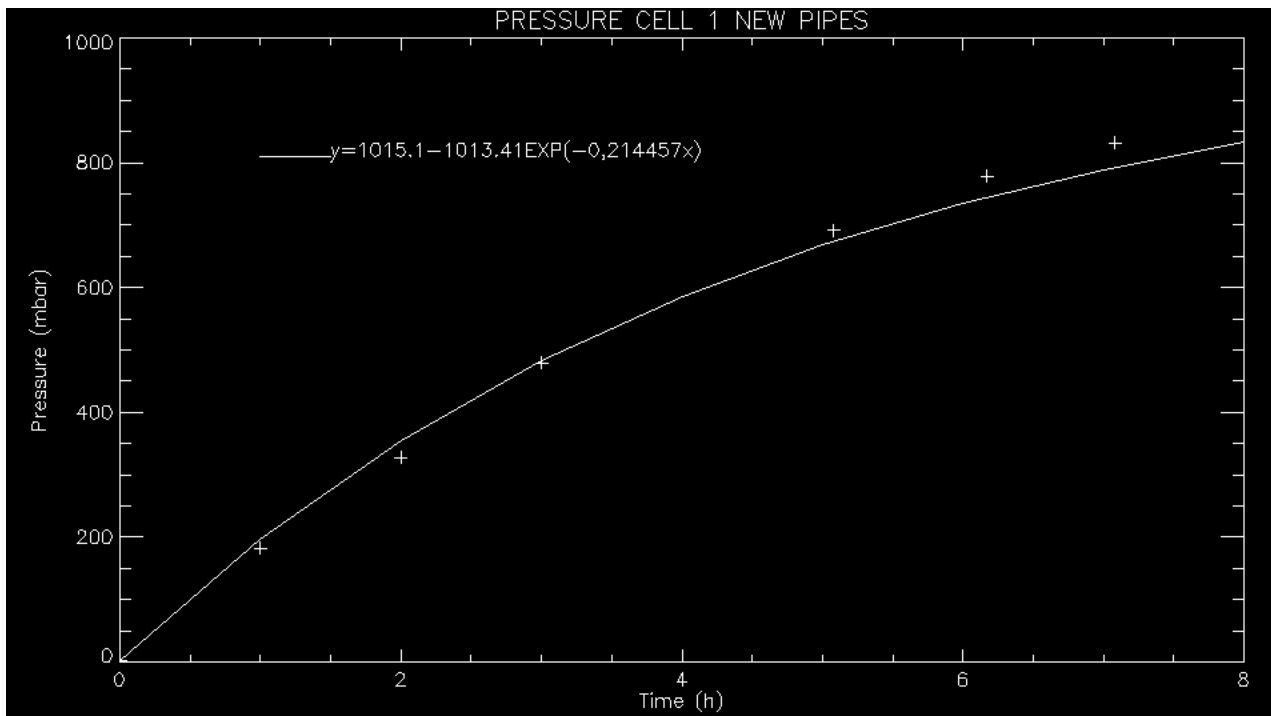


Figure 8.12: Vacuum pressure measurements plot of cell 1 with the new pipe configuration and error bars

The difference between the previous measurements and the new ones are shown in Figure 8.13.

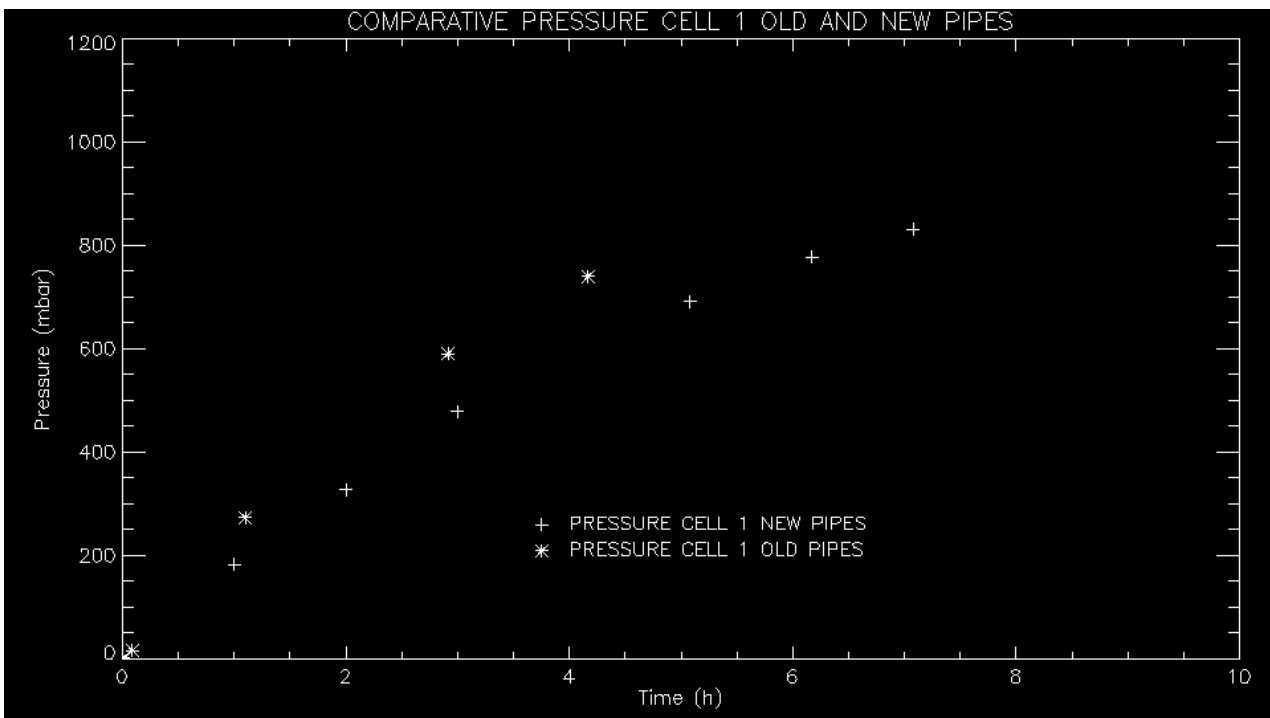
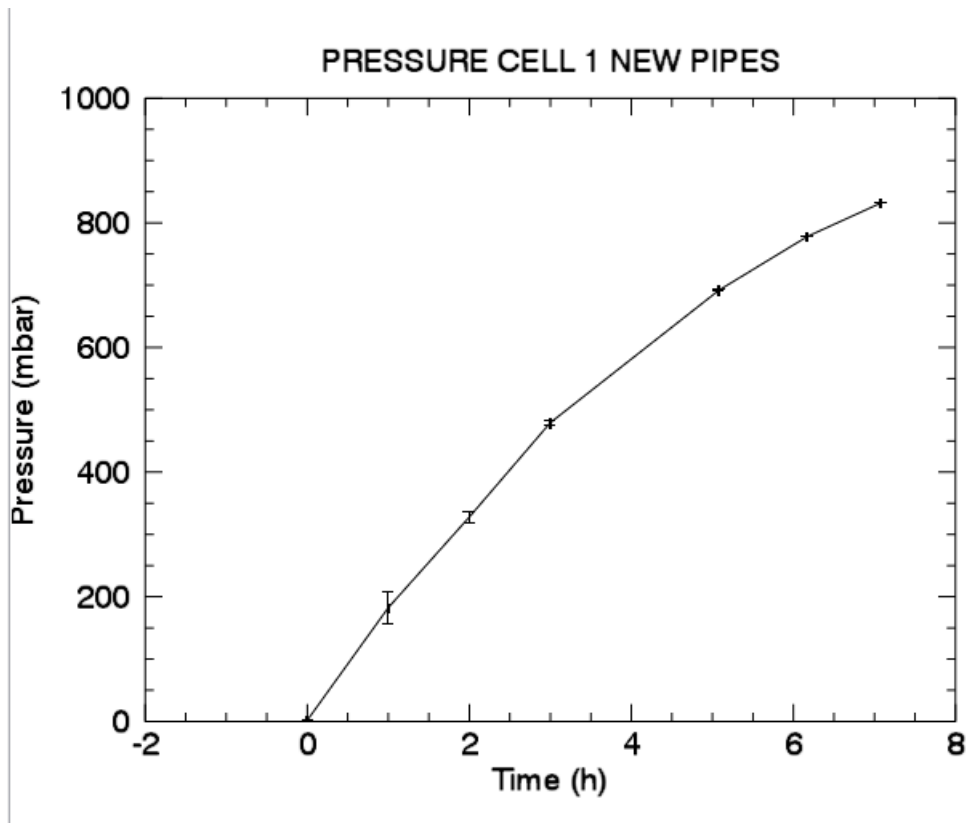


Figure 8.13: Vacuum pressure measurements plot of cell 1 in the old and new pipe configuration

As can be seen for all the cells there have been an increase of air-tight.

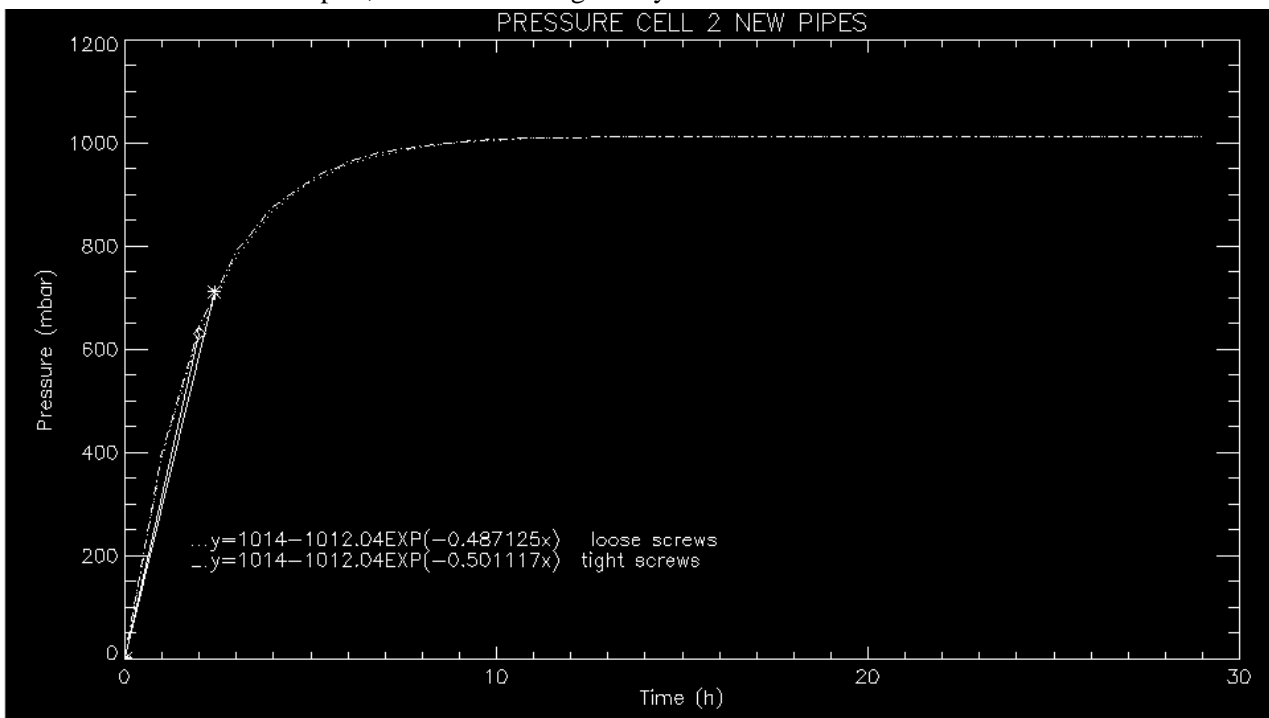
8.1.1.9 Test of cell n°2

In the following table 8.9 and plot are collected the vacuum pressure measurements of cell 2 with the new pipe configuration

Pressure (mbar)	Time (h)	Day	Zero pressure (mbar)	
1.96	10.10	28/06/2013	1014	Loose screws
631.98	12.00			
1.96	12.00			Tight screws
712.6	14.25			

Table 8.9: Vacuum pressure measurements of cell 2 with the new pipe configuration

Two measurements have been kept for cell 2 to test is loose screws could influence the tightness of the cell, but as can be seen from the plot, it affect its air-tight only for a 12.8 %.



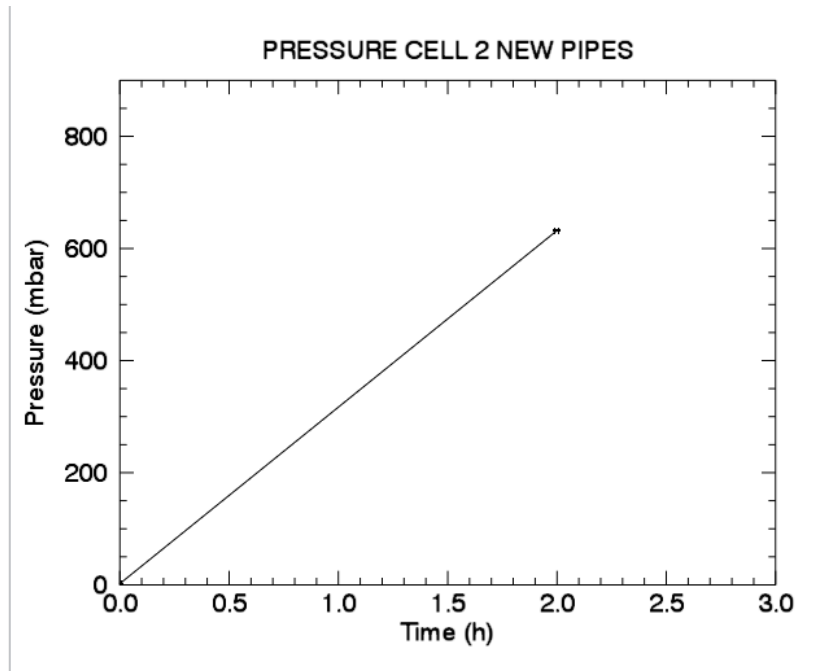


Figure 8.14: Vacuum pressure measurements plot of cell 2 with the new pipe configuration and error bars

8.1.1.10 Test of cell n°3

In the following table 8.10 and plot are collected the vacuum pressure measurements of cell 3 with the new pipe configuration. It clearly shows a very steep trend. So measurements every 5 minutes has been taken to control the trend. In Table 8.11 and in Figure 8.15 can be seen the results of the second pressure test with cell number 3. In Figure 8.16 are shown the comparative measurements before and after the pipe change.

Pressure (mbar)	Time (h)	Day	Zero pressure (mbar)
3.46	09.20	08/07/2013	1023.2
1023.2	10.15		

Table 8.10: Vacuum pressure measurements of cell 3 with the new pipe configuration

Pressure (mbar)	Time (h)	Day	Zero pressure (mbar)
3.39	10.30	08/07/2013	1023.2
97.46	10.35		
346.7	10.40		
707.89	10.45		
1000.9	10.50		
1023	10.55		

Table 8.11: Vacuum pressure measurements of cell 3 with the new pipe configuration every 5 minutes

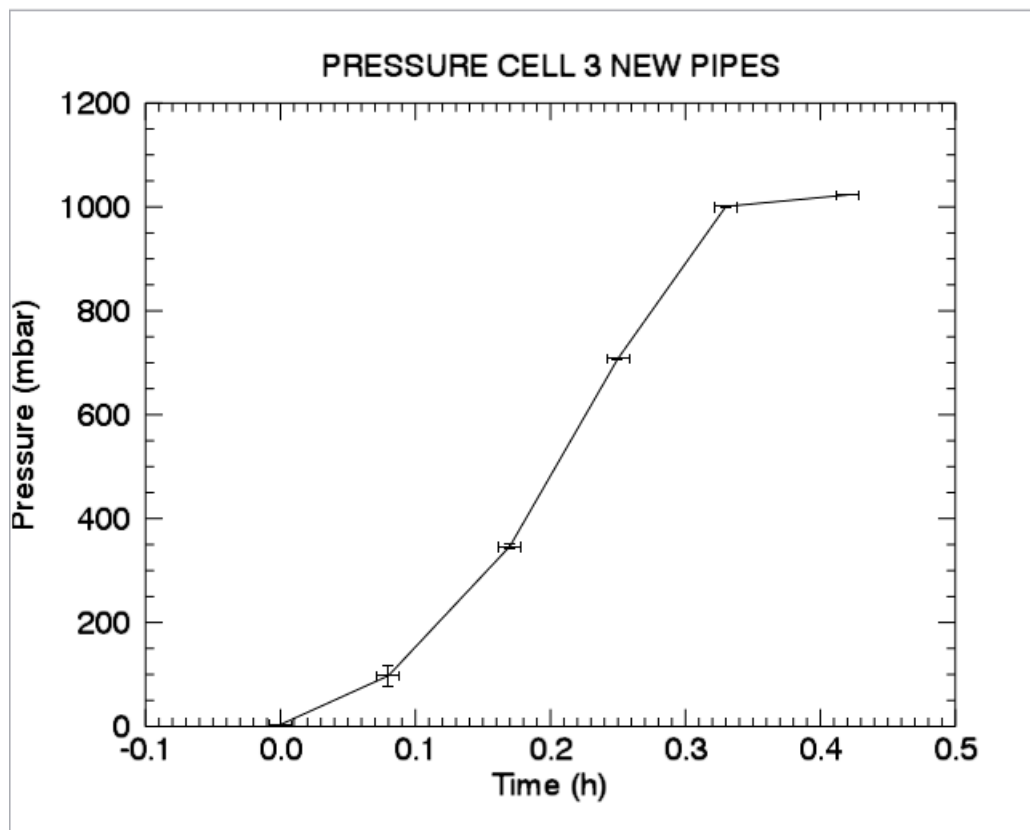
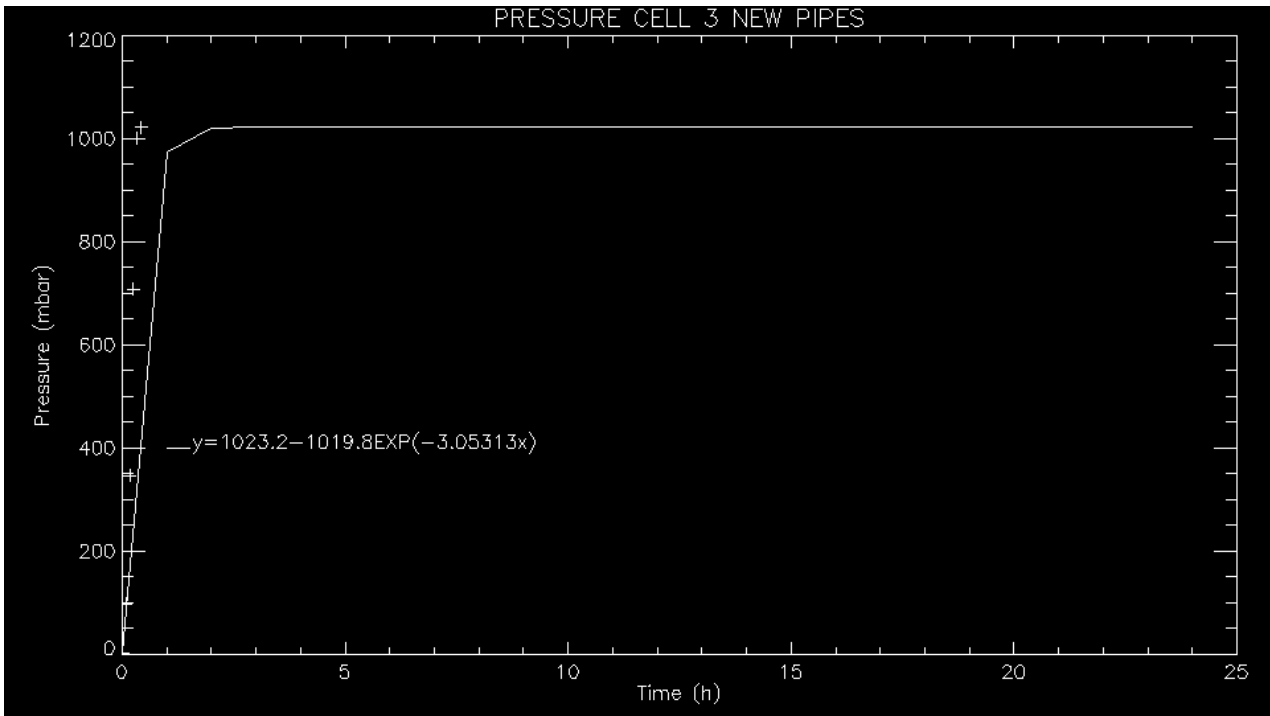


Figure 8.15: Vacuum pressure measurements plot of cell 3 with the new pipe configuration and error bars

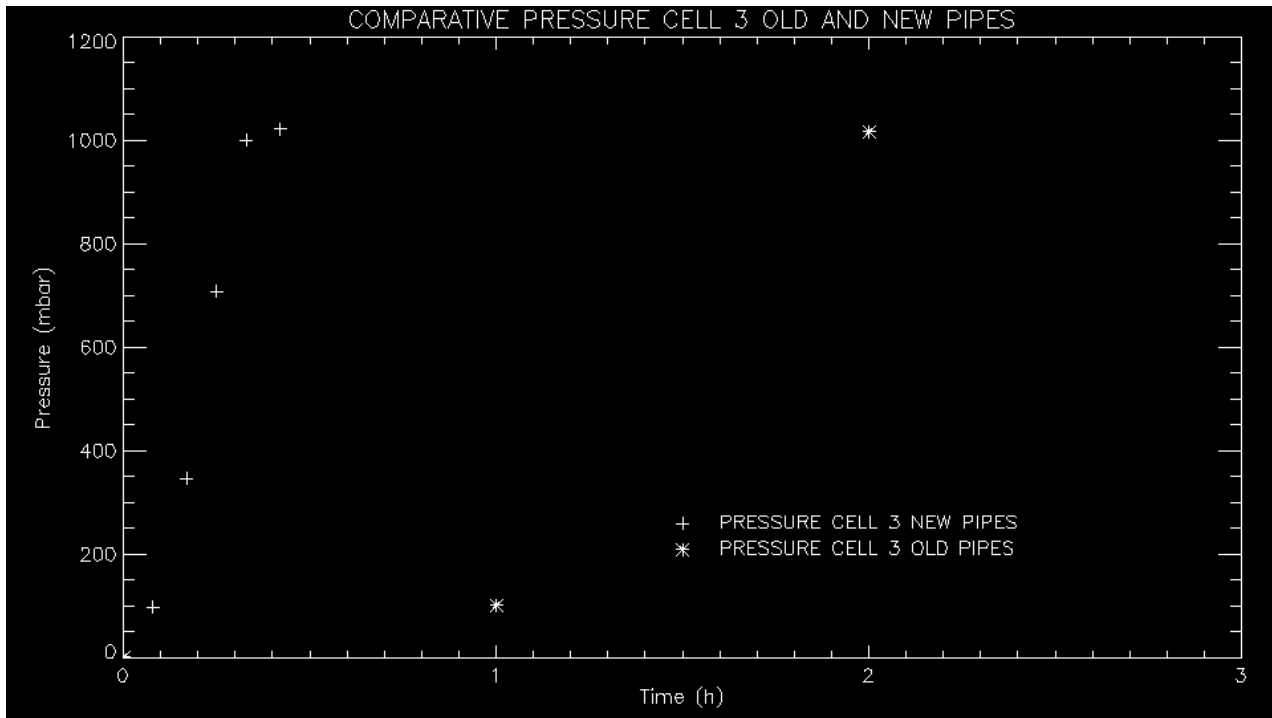


Figure 8.16: Vacuum pressure measurements plot of cell 3 in the old and new pipe configuration

From this plot it is clear that the steepness has increased in the new configuration.

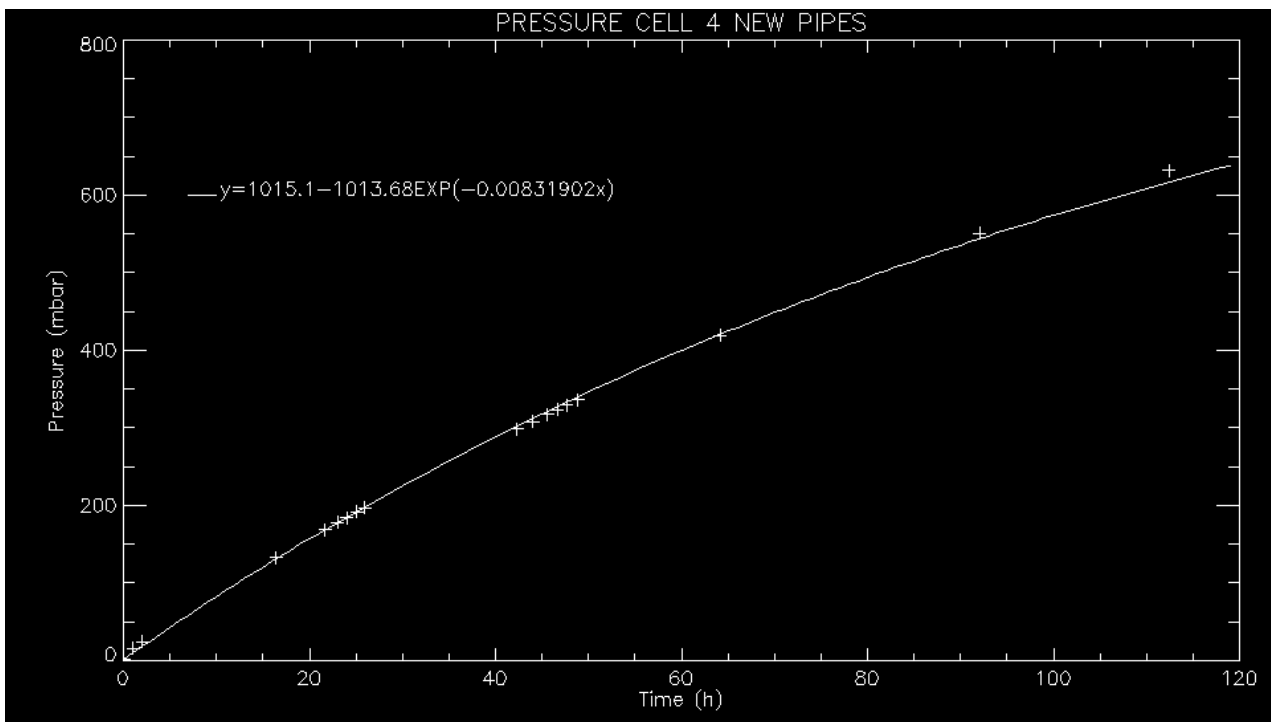
8.1.1.11 Test of cell n°4

In the following table 8.12 and plot are collected the vacuum pressure measurements of cell 4 with the new pipe configuration.

Pressure (mbar)	Time	Day	Zero pressure (mbar)
1.42	16.40	03/07/2013	1015.1
15.6	17.40		
24.56	18.40		
133.26	09.05	04/07/2013	
168.87	14.20		
177.84	15.40		
184.39	16.40		
191.75	17.45		
196.68	18.35		
298.41	11.00	05/07/2013	
307.81	12.40		

Pressure (mbar)	Time	Day	Zero pressure (mbar)
317.52	14.15		
323.74	15.20		
329.39	16.20		
336.05	17.30		
418.88	08.50	06/07/2013	
551.08	12.45	07/07/2013	
631.79	09.05	08/07/2013	

Table 8.12: Vacuum pressure measurements of cell 4 with the new pipe configuration



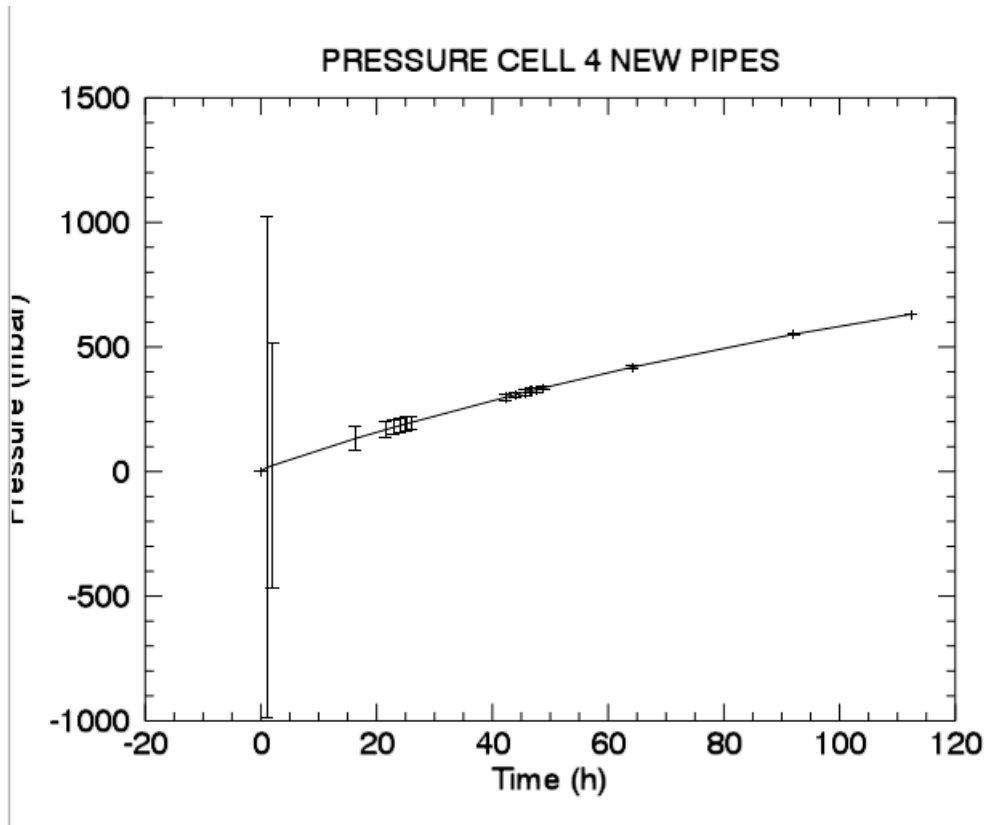


Figure 8.17: Vacuum pressure measurements plot of cell 4 with the new pipe configuration and error bars

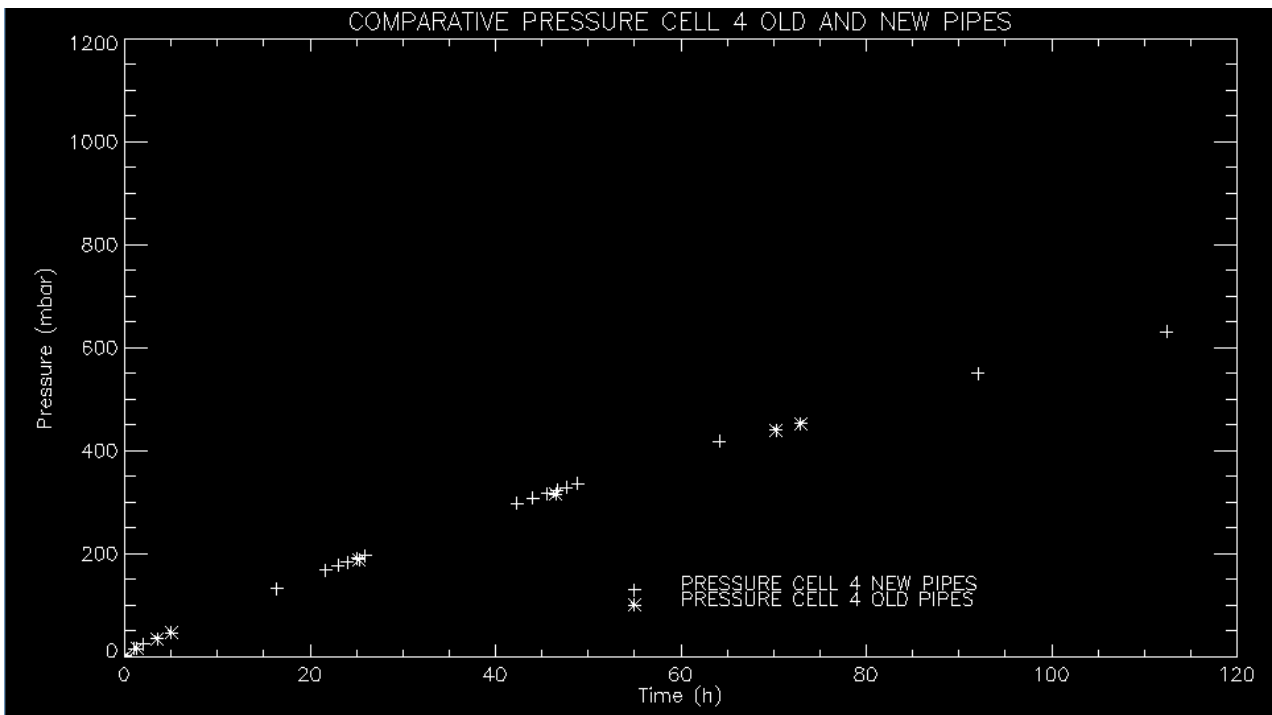


Figure 8.18: Vacuum pressure measurements plot of cell 4 in the old and new pipe configuration

As can be seen, no substantial differences can be seen from the previous measurements. In the following plot can be seen another way to show the results of cell 4 putting in evidence the time constant, described by the line steepness.

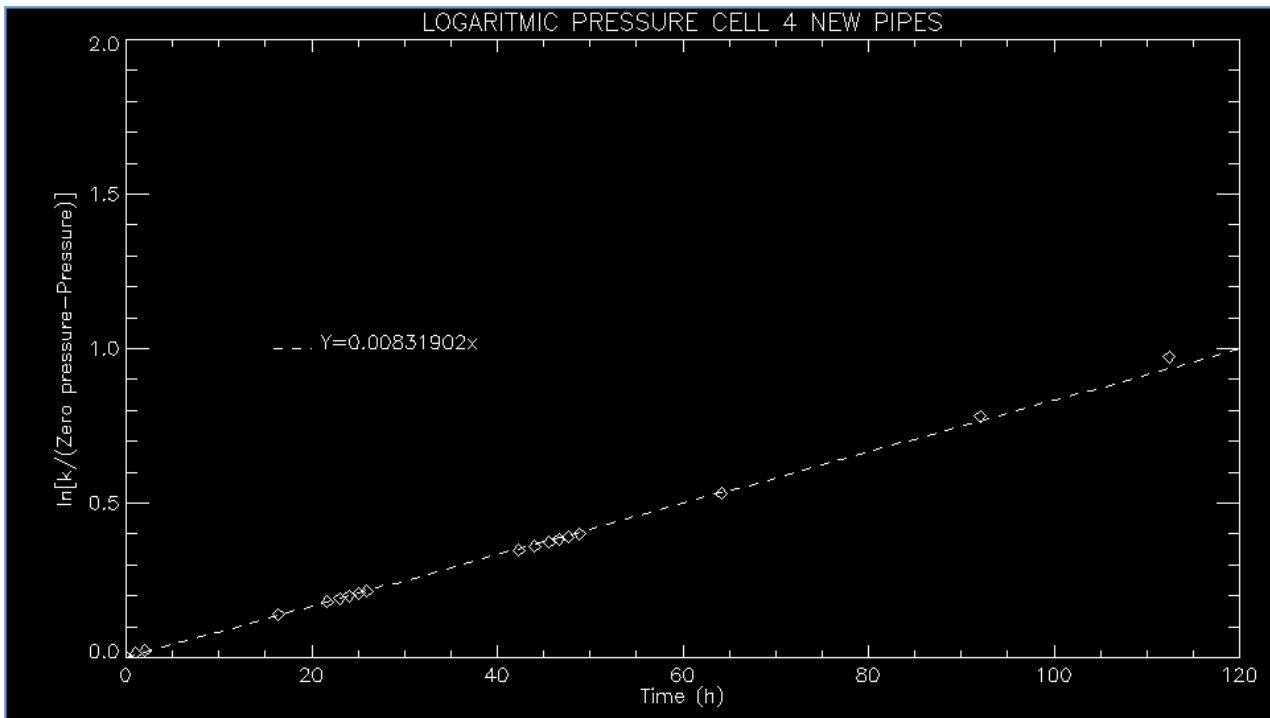


Figure 8.19: Logarithmic vacuum pressure measurements plot of cell 4 with the new pipe configuration

As can be seen, the time constant τ is 120.21 h.

8.1.1.12 Test of cell n°5

In the following table 8.13 and plot are collected the vacuum pressure measurements of cell 5 with the new pipe configuration.

Pressure (mbar)	Time (h)	Day	Zero pressure (mbar)
1.38	12.15	25/06/2013	1014
17,6	13.45		
153.48	09.00	26/06/2013	
166.76	11.00		
173.66	12.00		
188.26	14.00		
300.78	09.00	27/06/2013	
308.83	10.20		
327.72	13.20		
348.38	17.10		
435.7	09.00	28/06/2013	

Table 8.13: Vacuum pressure measurements of cell 5 with the new pipe configuration

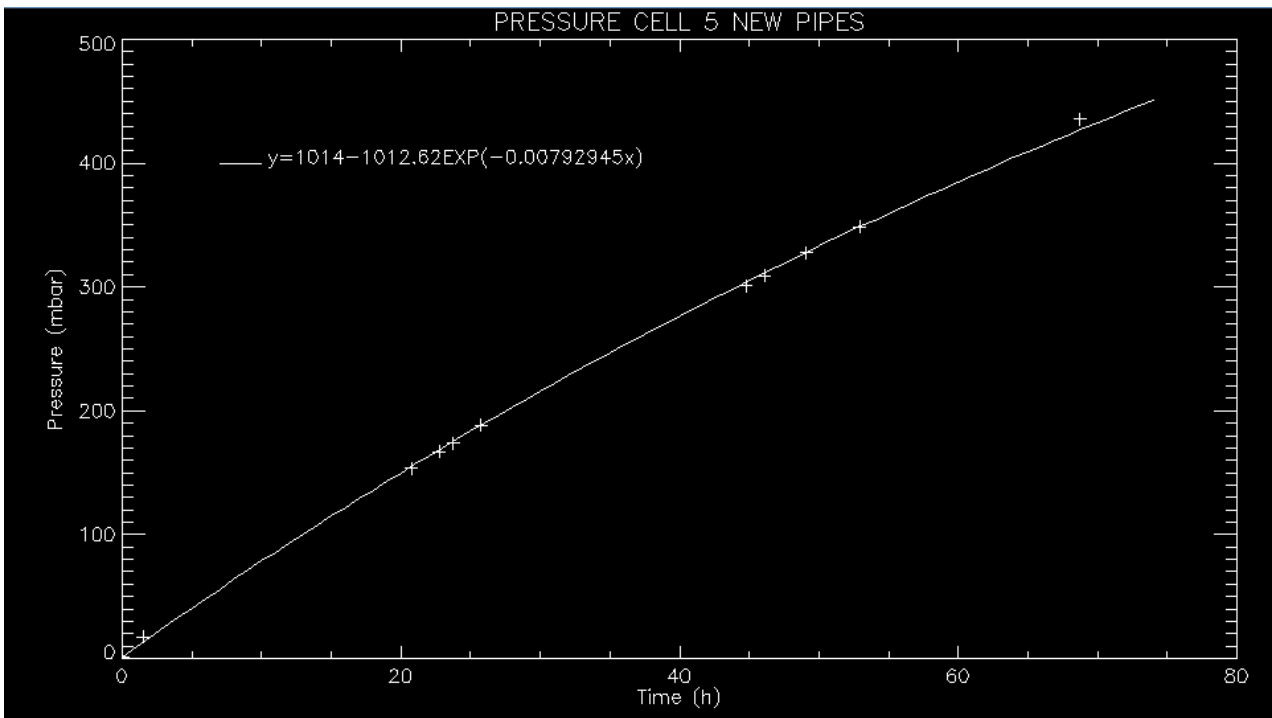
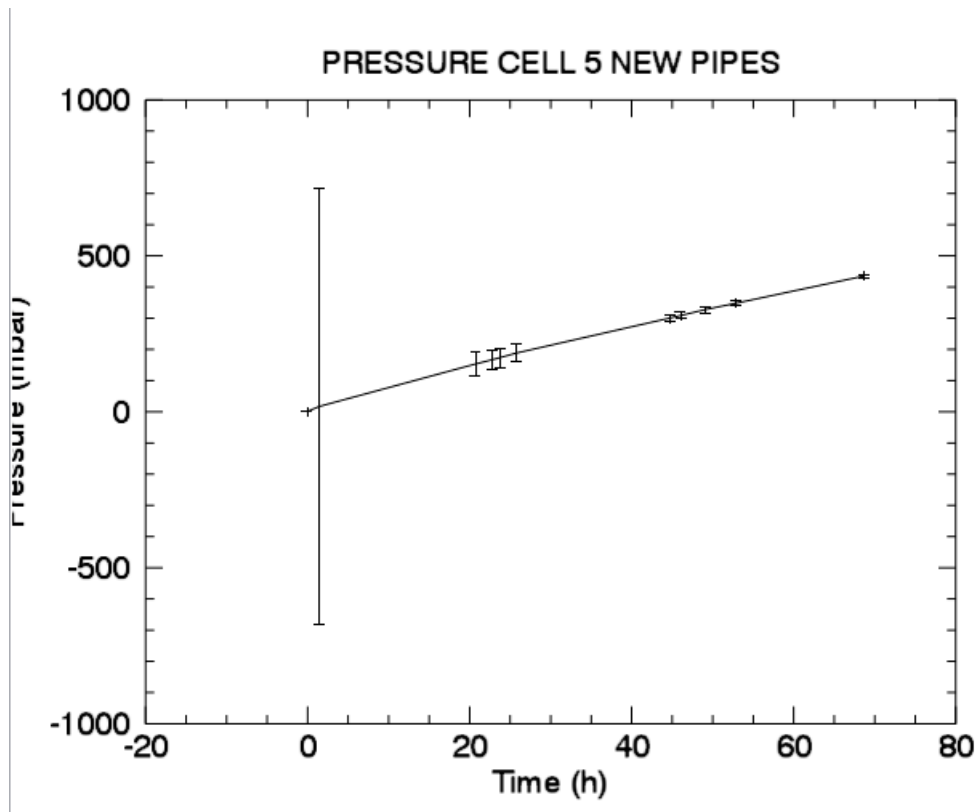


Figure 8.20: Vacuum pressure measurements plot of cell 5 with the new pipe configuration and error bars

The difference between the previous measurements and the new ones are shown in Figure 8.21.



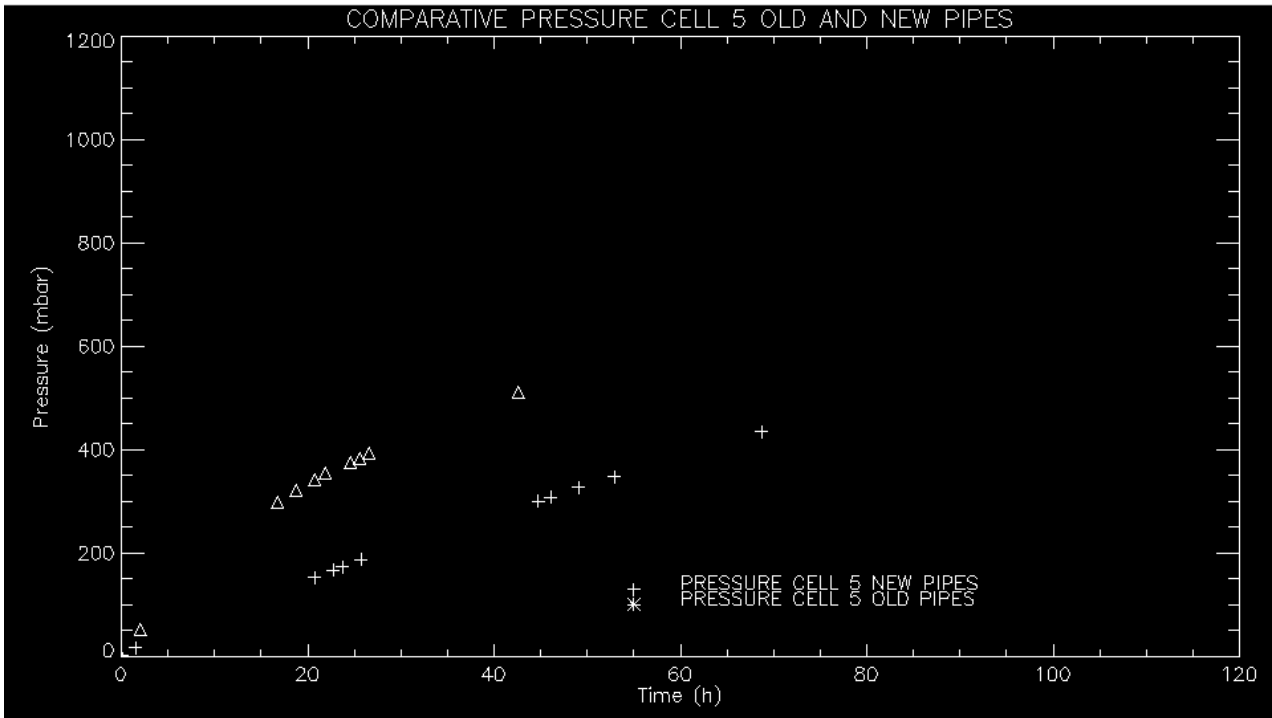


Figure 8.21: Vacuum pressure measurements plot of cell 5 in the old and new pipe configuration

In the following plot can be seen another way to show the results of cell 4 putting in evidence the time constant, described by the line steepness.

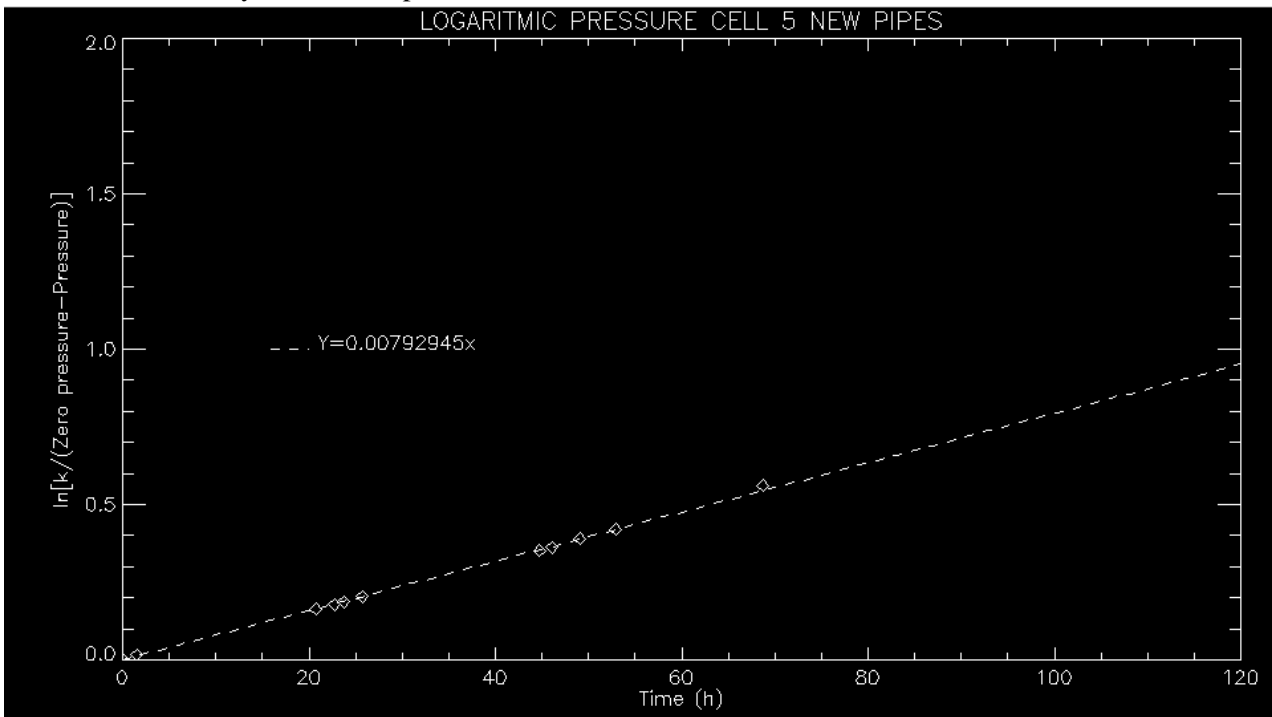


Figure 8.22: Logarithmic vacuum pressure measurements plot of cell 5 with the new pipe configuration

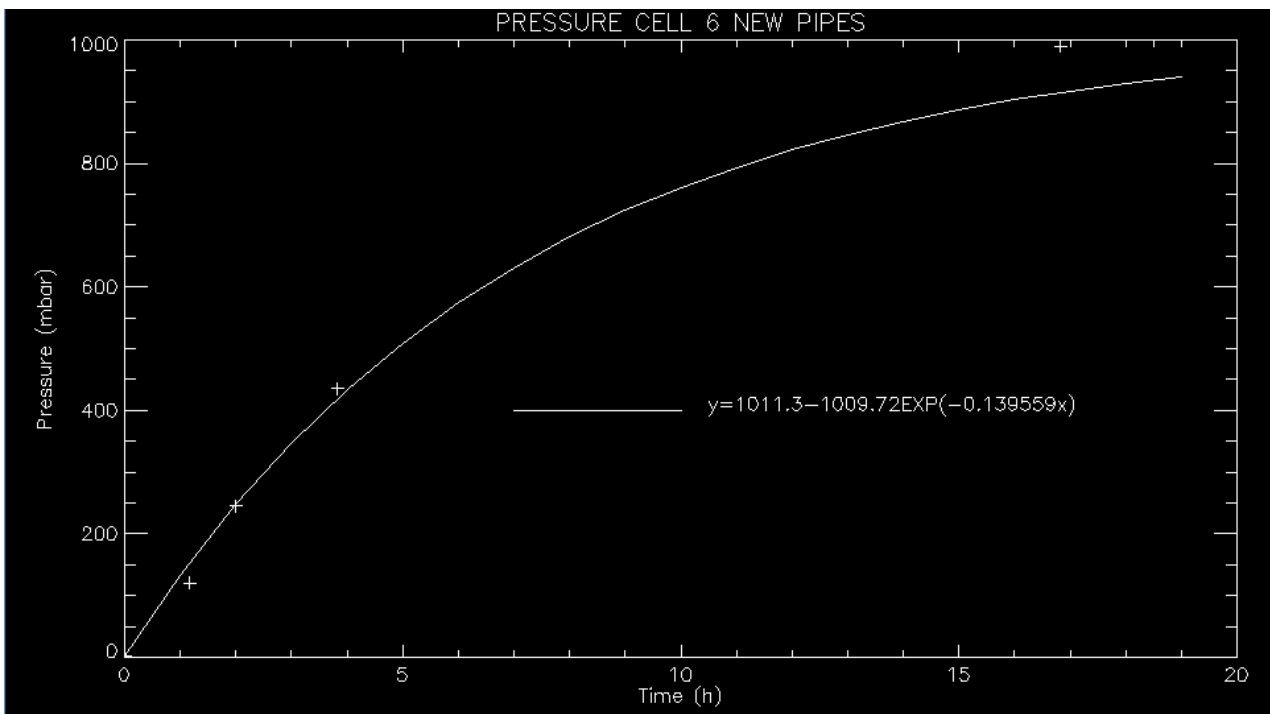
As can be seen, the time constant τ is 126.11 h.

8.1.1.13 Test of cell n°6

In the following table 8.14 and plot are collected the vacuum pressure measurements of cell 6 with the new pipe configuration.

Pressure (mbar)	Time (h)	Day	Zero pressure (mbar)
1.58	14.40	24/06/2013	1011.3
119.9	15.50		
245.6	16.40		
435.2	18.30		
989.85	09.30	25/06/2013	
999.9	11.10	27/06/2013	

Table 8.14: Vacuum pressure measurements of cell 6 with the new pipe configuration



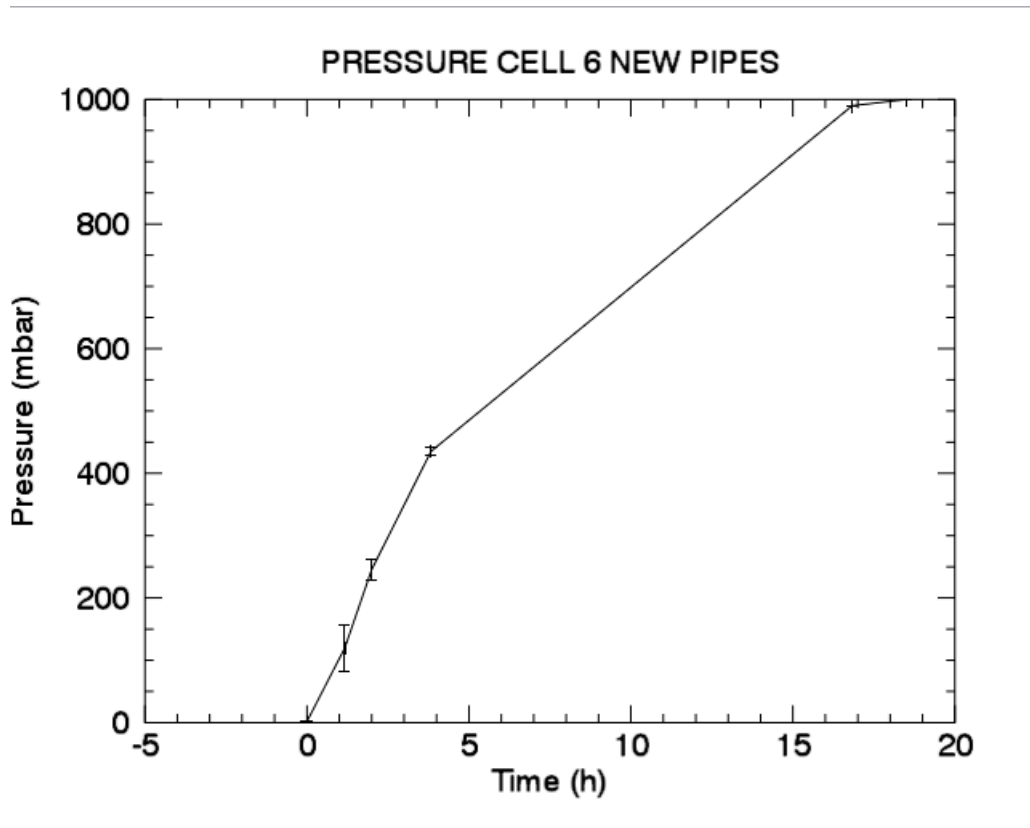


Figure 8.23: Vacuum pressure measurements plot of cell 6 with the new pipe configuration and error bars

The difference between the previous measurements and the new ones are shown in Figure 8.24:

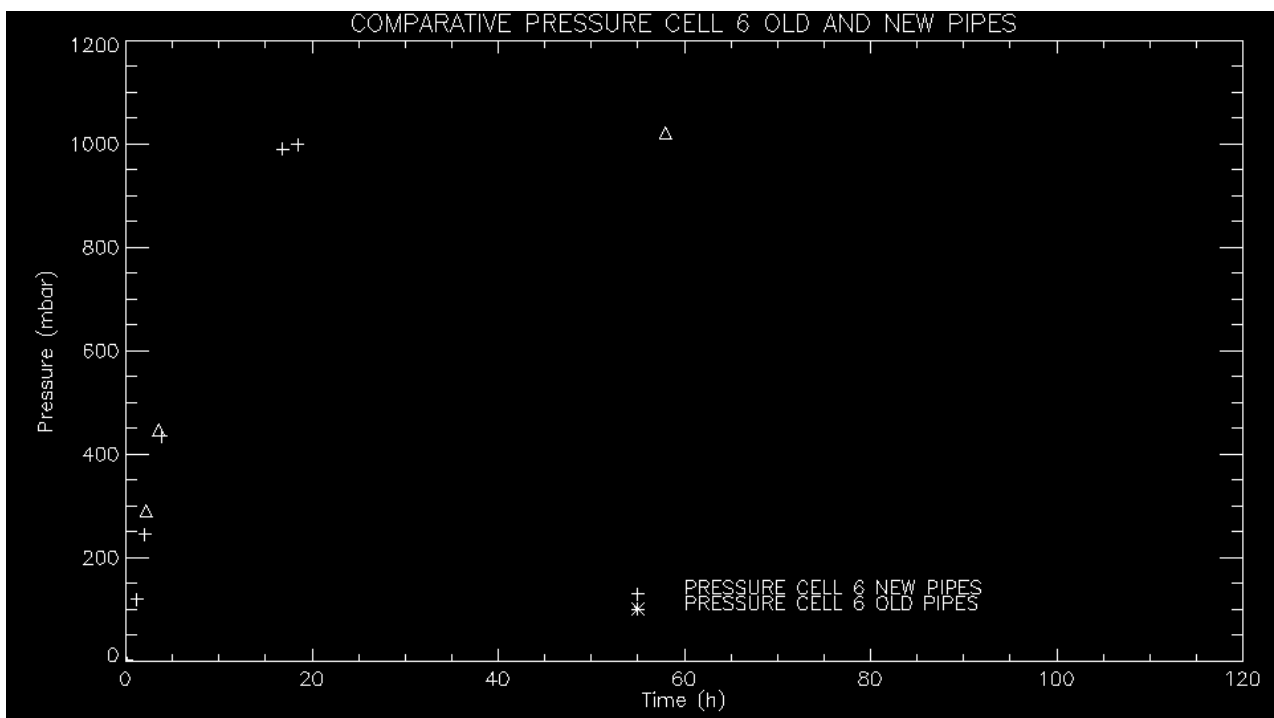


Figure 8.24: Vacuum pressure measurements plot of cell 6 in the old and new pipe configuration

Finally, in Figure 8.25 can be seen the cumulative plot of all the cells.

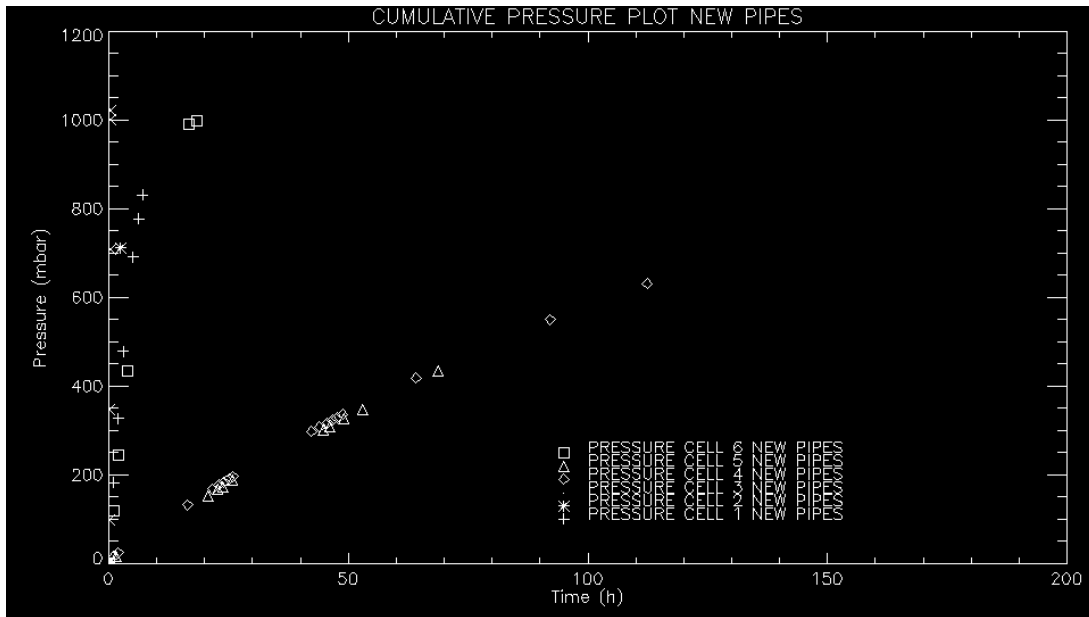


Figure 8.25: Cumulative vacuum pressure measurements plot of all cells with new pipes

This plot shows how cell 5 and cell 6 can be comparable from the air-tightness point of view, while cell 6 is in the middle. Cells 1, 2 and 3 are quite comparables.

8.1.1.14. Glass characterization

The suprasil glass characterization is an important part of the experiment to understand which component of the spectrum can be transmitted from it and can impact onto the biological samples. The measurements have been carried out by means of a spectrometer. The resulting plots are shown.

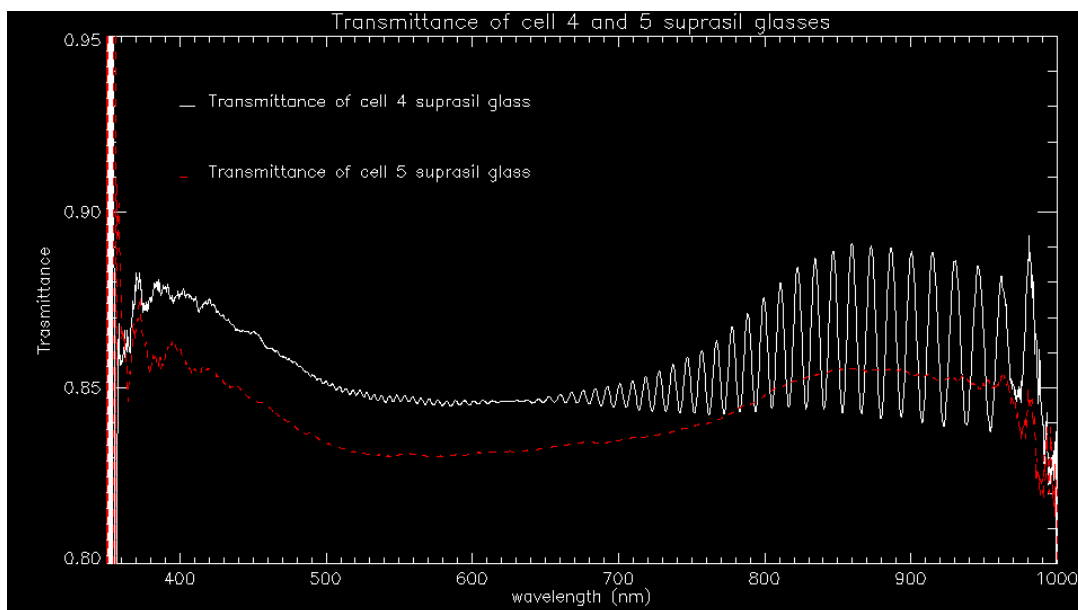


Figure 8.26: Cumulative Transmittance of cell 4 and 5 suprasil glasses

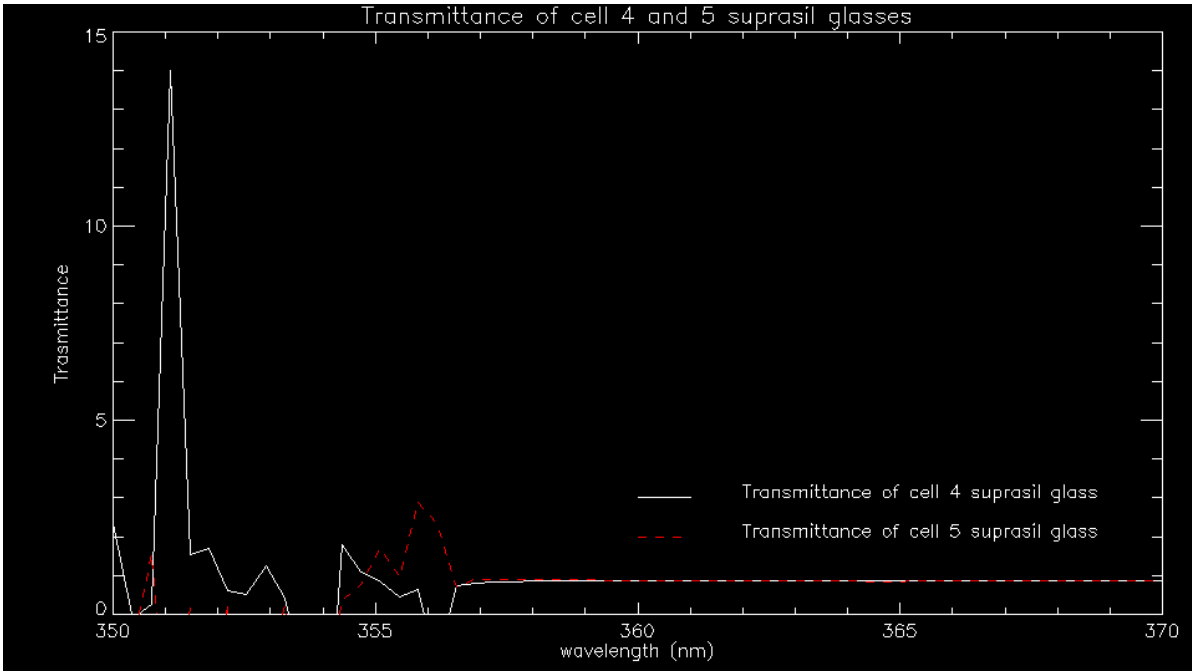


Figure 8.27: Cumulative Transmittance of cell 4 and 5 suprasil glasses in the range 350-370 nm

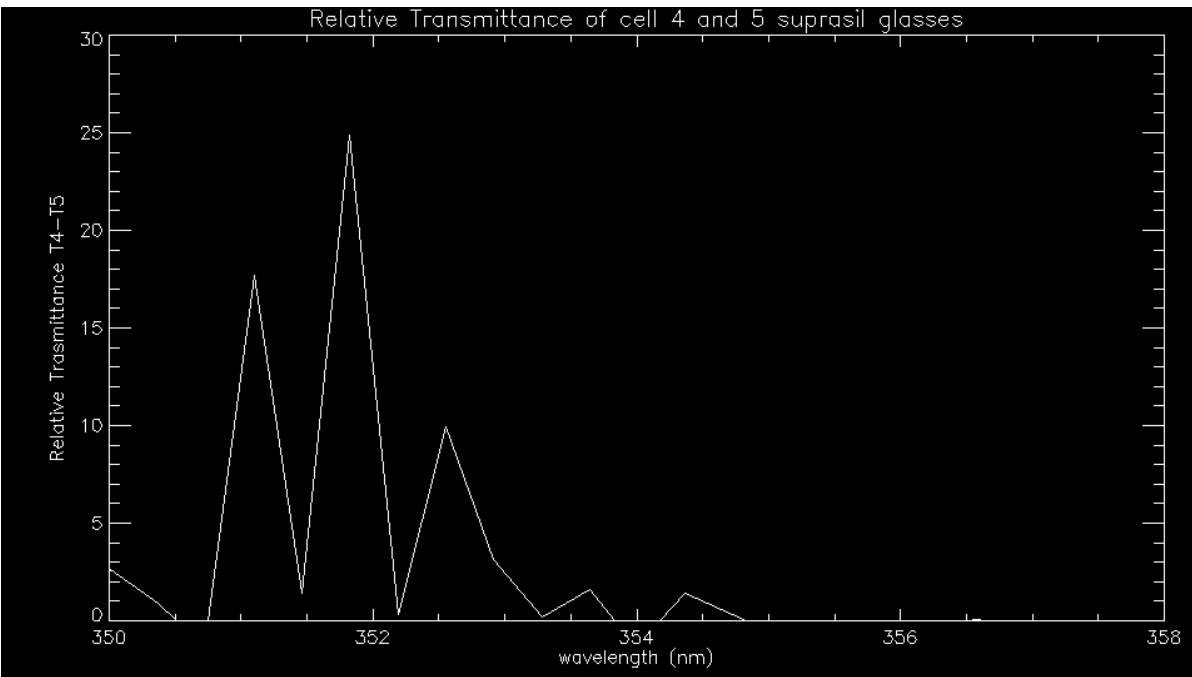


Figure 8.28: Relative Transmittance T4-T5 of cell 4 and 5 suprasil glasses in the range 350-358 nm

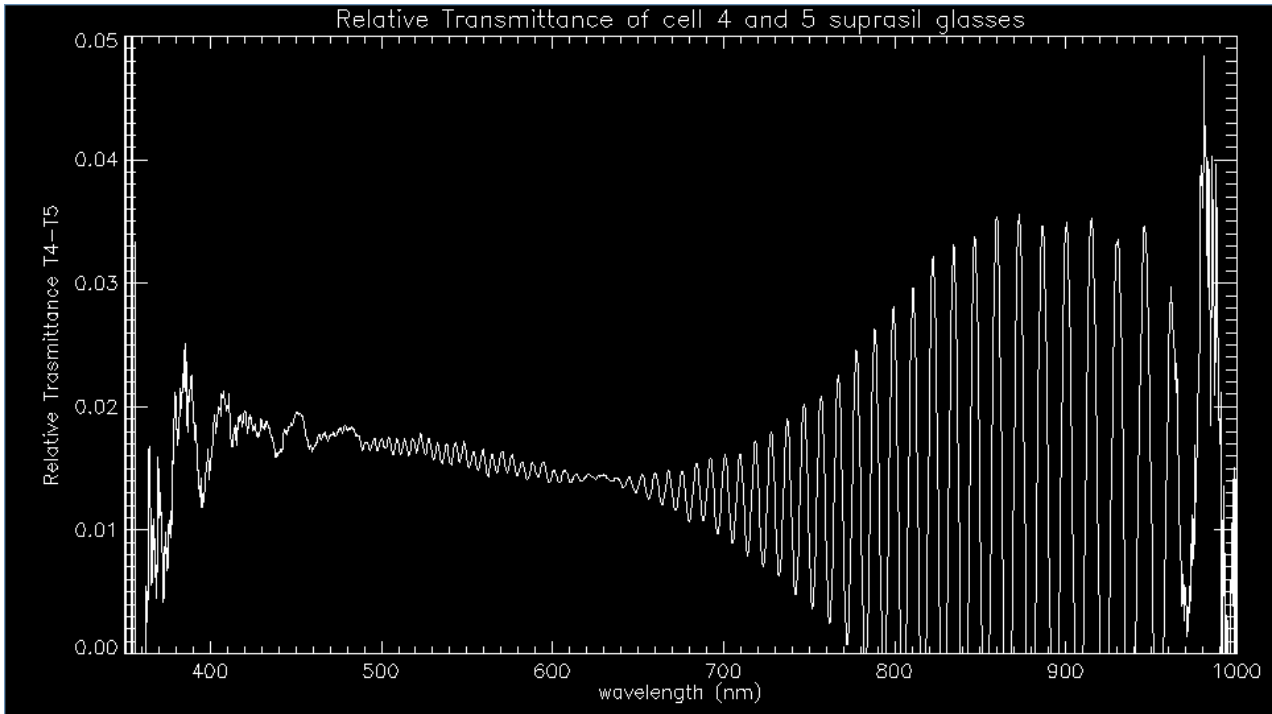


Figure 8.29: Relative Transmittance T4-T5 of cell 4 and 5 suprasil glasses in the range 350-1000 nm

If a light beam with the intensity I_0 that falls onto a glass plate having a thickness d , at the entrance surface part of the beam is reflected. Therefore after that the intensity of the beam is $I_1 = I_0(1-R)$ with R being the reflectivity. Inside the glass the light beam is attenuated according to the exponential function. At the exit surface the beam intensity is

$$I_i = I_1 e^{-\chi d} \quad (8.42)$$

where χ is the absorption constant. At the exit surface another reflection occurs. The transmitted beam has the intensity $I = I_i(1-R)$. These formulas give the following relation

$$I = I_0(1 - R^2)e^{-\chi d} \quad (8.43)$$

The beam reflected at the exit surface returns to the entrance surface and is divided into a transmitted and a reflected part. With multiple reflections taken into account, the transmittance of the glass plate is:

$$\tau = \frac{I}{I_0} = P \tau_i = \frac{2n}{n^2+1} \tau_i \quad (8.44)$$

with

$$\tau_i = \frac{I_i}{I_0} \text{ internal transmittance} \quad (8.45)$$

and

$$P = \frac{2n}{n^2+1} = (1 - R^2) \quad (8.46)$$

P is called the “reflection factor” and has been derived from Fresnel’s formula which describes the relation between the reflectivity R and the refractive index n. Taking the refractive index range of optical glass from 1.4 to 2.1 the reflection factor P ranges from 0.92 to 0.75. For suprasil the average value of n is 1.46, P is 0.93 and R is 0.26. From Figure 8.26 the average transmittance is 0.93 ± 0.61 for glass 4 and 0.82 ± 3.42 for glass 5. So, the mean value of transmittance for the glass is 0.88 ± 0.082 , according with the literature. The mean value of τ_i is 0.94 ± 0.088 . From the 2.42 can be found 0.062 ± 0.088 , even this inside the literature ranges.

8.1.1.15 Conclusions

All measurements of void tightness have been done for all the six cells.

Cells number 1 and 5 show an appreciable increase in tightness measurements, while cells 4 and 6 doesn't show appreciable mutations. Only cell 3 shows an evident worsening.

As can be seen from the comparison of Figure 8.25 with Figure 9, the overall trend of air tightness has remained the same, except for cell number 5.

In particular has been found that cell1 has $\tau=4.66$ h, cell 2 has $\tau=1.996$ h, cell 3 has $\tau=0.33$ h, cell 4 and 5 have almost the same time constant equal to 120.21 h and 126.11 h and cell 6 has $\tau=7.17$ h.

Q_i , the loss rate, can be calculated and is $\frac{P_0}{\tau}V$ where V is the cell volume, that is $250 \text{ cm}^3=0.25 \text{ dm}^3=0.25 \text{ l}$.

The error associated to Q_i can be found from the following formula:

$$\Delta Q_i = \sqrt{\left(\frac{\partial Q_i}{\partial P} \Delta P\right)^2 + \left(\frac{\partial Q_i}{\partial V} \Delta V\right)^2 + \left(\frac{\partial Q_i}{\partial \tau} \Delta \tau\right)^2} \quad (8.47)$$

$$\Delta Q_i = \sqrt{\left(\frac{V}{\tau} \Delta P_0\right)^2 + \left(\frac{P_0}{\tau} \Delta V\right)^2 + \left(\frac{P_0 V}{\tau^2} \Delta \tau\right)^2} = \frac{1}{\tau} \sqrt{V^2 \Delta P_0^2 + P_0^2 \Delta V^2 + \frac{P_0^2 V^2}{\tau^2} \Delta \tau^2} \quad (8.48)$$

The last term of 2.42 for $P(t)=P_0$ is negligible.

For cell 1 Q_i is $54.42 \pm 1.09 \text{ mbar l h}^{-1}$ for cell 2 it is $127.03 \pm 2.54 \text{ mbar l h}^{-1}$, for cell 3 it is $780.99 \pm 15.62 \text{ mbar l h}^{-1}$, for cell 4 it is equal to $2.11 \pm 0.042 \text{ mbar l h}^{-1}$, for cell 5 it is equal to $2.01 \pm 0.040 \text{ mbar l h}^{-1}$ and for cell 6 it is $35.28 \pm 0.70 \text{ mbar l h}^{-1}$.

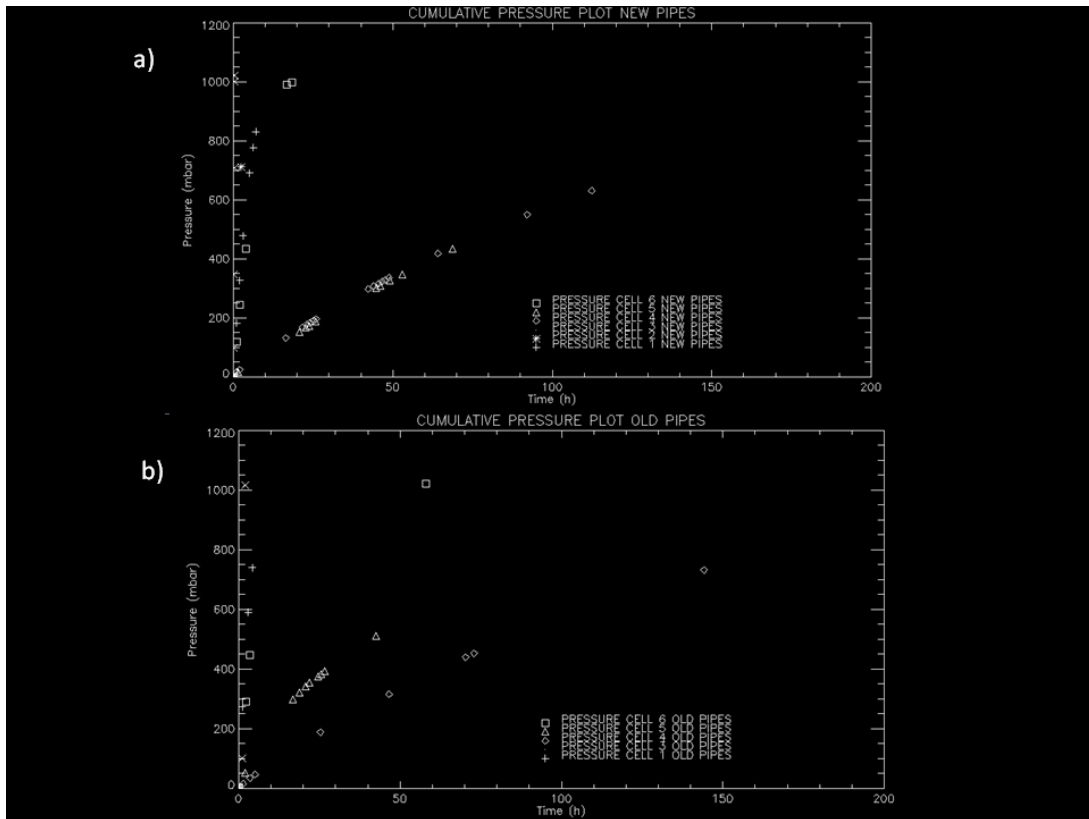


Figure 8.30: Cumulative vacuum pressure measurements plot of all cells with old (a) and new (b) pipes

8.2 New cell design

As all the previous measurements gave us an unsatisfying result we chose to project and realize a new one, bigger and made of stainless steel. This new cell has two 1/8" stainless steel nozzles (figure 8.31) that is used to flux the gas inside it and fill the cell with the desired gas mixture. Four wedged optical windows opens on the lateral surface. Two windows are 1" Round Wedge Prisms, with 2° Beam Deviation, and AR Coating: 650 - 1050 nm from Thorlabs. The other two windows are 1" Round Wedge Prisms, with 2° Beam Deviation without Coating (Figure 8.32). The windows needs to test the gas concentration inside the closed cell by means of a TDLAS (Tunable Diode Laser Absorption Spectroscopy) system and two channels is used, one for oxygen and one for carbon dioxide. Lasers are attached to the cell with two SM1-Threaded 30 mm Cage Plates, with a 0.35" thickness and two SM1 Lens Tubes, 1" Thread Depth (Figure 8.33 and 8.34). On the top of the cell a 125x6.5 mm BOROFLOAT uncoated window from Edmund Optics is placed to collect the light from the stellar simulator. In figure 8.35 can be seen the transmission given from the datasheet.

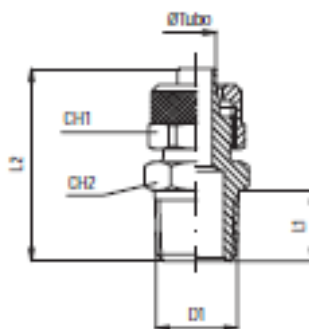


Figure 8.31: 1/8" stainless steel nozzle for the gas fluxing inside the cell

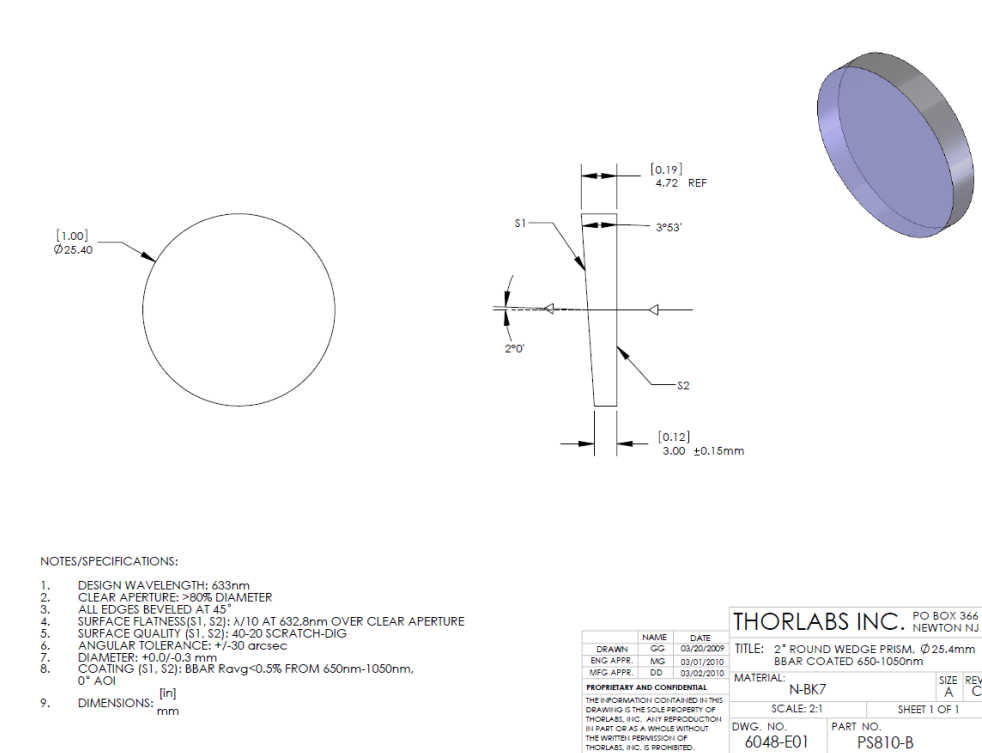


Figure 8.32: 1" Round Wedge Prism windows, with 2° Beam Deviation

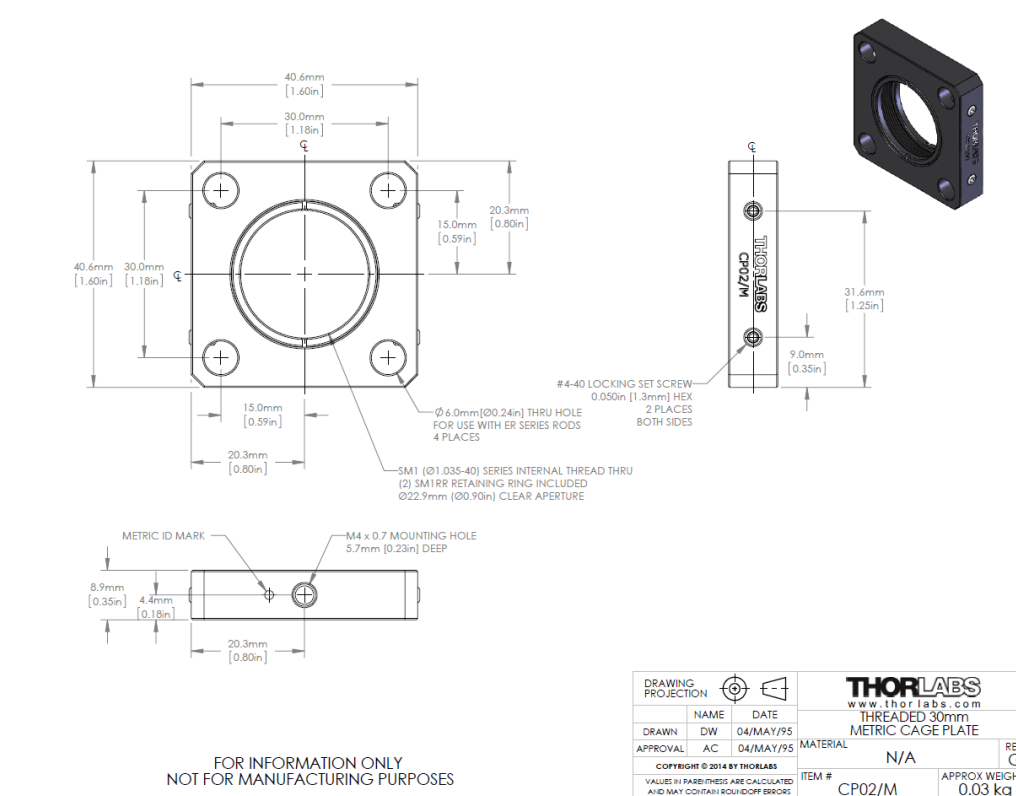


Figure 8.33: SM1-Threaded 30 mm Cage Plates, with a 0.35"thickness

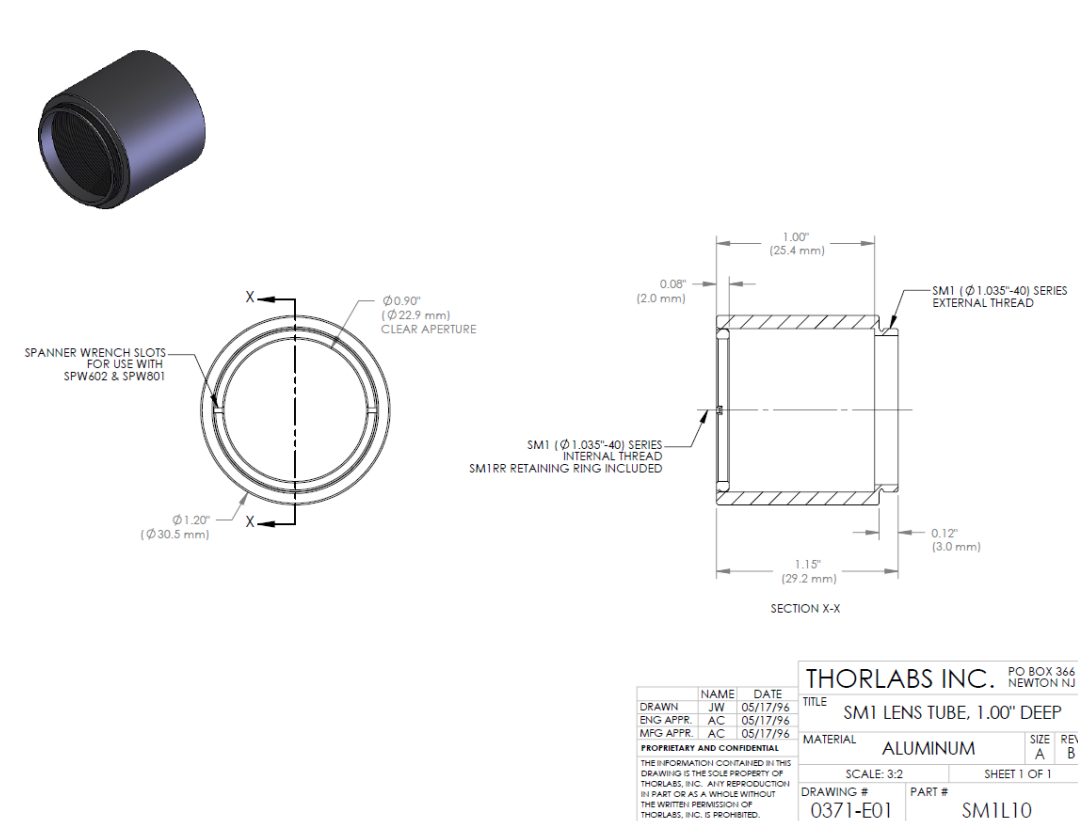


Figure 8.34: SM1 Lens Tubes, 1" Thread Depth

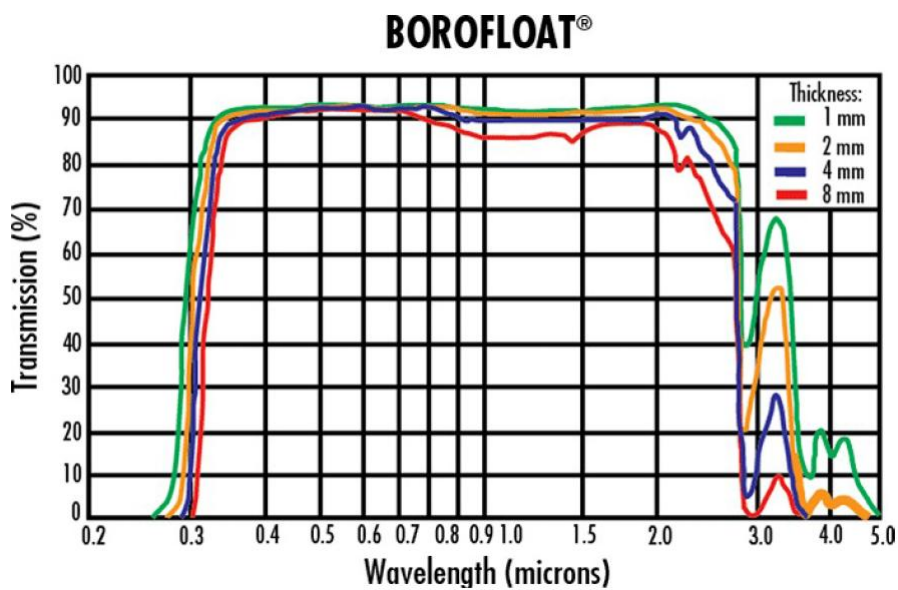


Figure 8.35: Transmission of different thickness 125 mm BOROFLOAT uncoated windows from Edmund Optics

In figure 8.36 is shown a 3D rendering made with the software SOLIDWORKS while in figure 8.37 can be seen the realized cell.

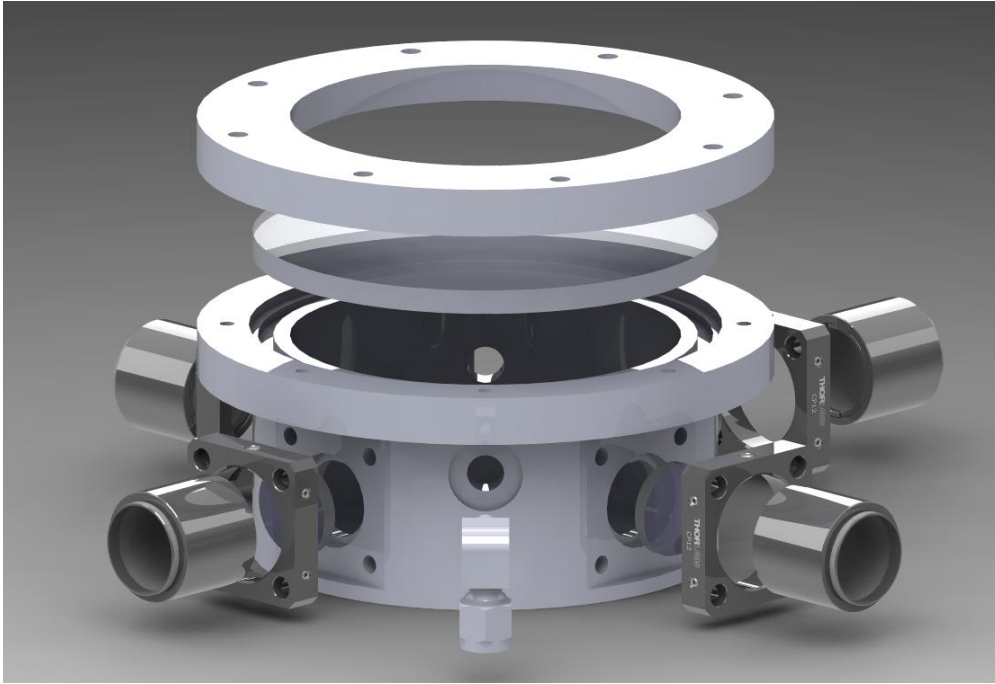


Figure 8.36: 3D rendering of the cell made with the software SOLIDWORKS

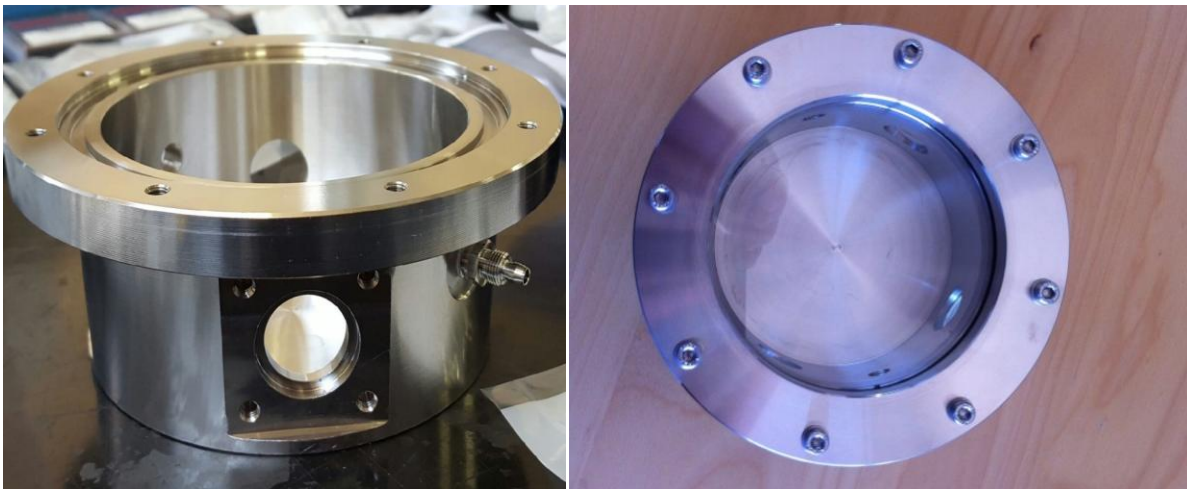


Figure 8.37: Realization of the stainless steel

The building drawings are collected in Appendix D. In order to raise and lower the temperature four peltier cells TEC1-12704 working at 60 W has been mounted on the bottom of the cell (figure 8.38) and suspended by means of a round aluminium plate of the same diameter of the cell lower part. The temperature is driven by means of a TEC controller 7-15V 0-8A. The heat dissipation system is a cooling aggregate 0.06K/W 12V 6W from Thermo Electric Devices. Its dimensions are 200 x 135 x 98mm.

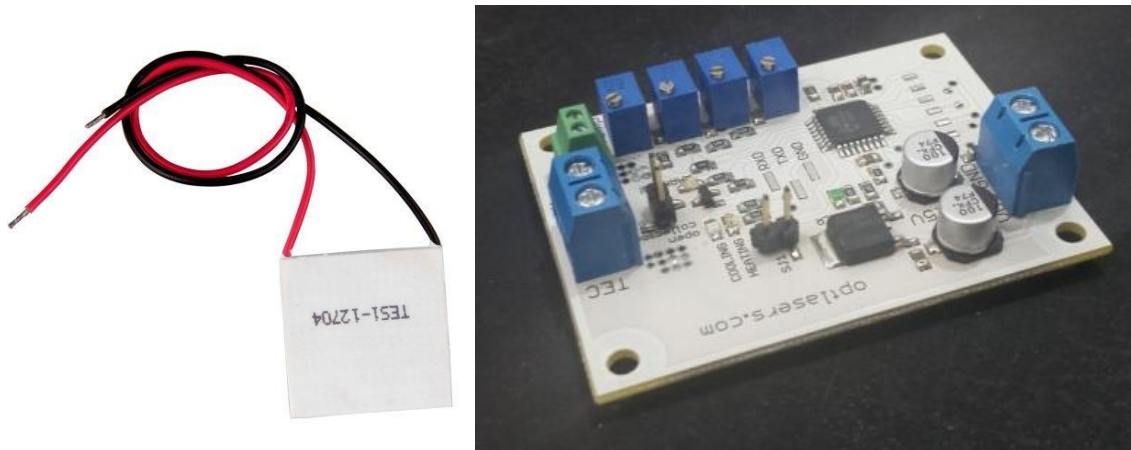


Figure 8.38: Peltier cell TEC1-12704 working at 60 W and TEC controller 7-15V 0-8A

8.3 Cell characterization

In order to characterize the cell two measurements have been done. The first measurement aims to understand the behavior of the temperature inside the cell. This task been done placing a thermistor inside it and another under its bottom, in the middle of the four Peltier cells. A set of data has been taken (Table 8.13). In figure 8.39 can be seen the plot of the data.

Inner cell temperature (°C)	Peltier temperature (°C)	Room temperature (°C)
4.0±1.0d	14.5±0.1	23.0±1.0d
9.0±1.0d	17.2±0.1	23.0±1.0d
13.0±1.0d	18.8±0.1	23.0±1.0d
16.0±1.0d	20.5±0.1	23.0±1.0d
19.0±1.0d	22.2±0.1	23.0±1.0d
23.0±1.0d	24.0±0.1	23.0±1.0d
25.0±1.0d	26.0±0.1	23.0±1.0d
28.0±1.0d	27.9±0.1	23.0±1.0d
30.0±1.0d	29.9±0.1	23.0±1.0d
32.0±1.0d	31.6±0.1	23.0±1.0d
34.0±1.0d	33.6±0.1	23.0±1.0d
36.0±1.0d	35.4±0.1	23.0±1.0d
38.0±1.0d	37.2±0.1	23.0±1.0d
40.0±1.0d	39.0±0.1	23.0±1.0d

Table 8.13: Temperature linearity data inside the cell, outside the cell and room temperature

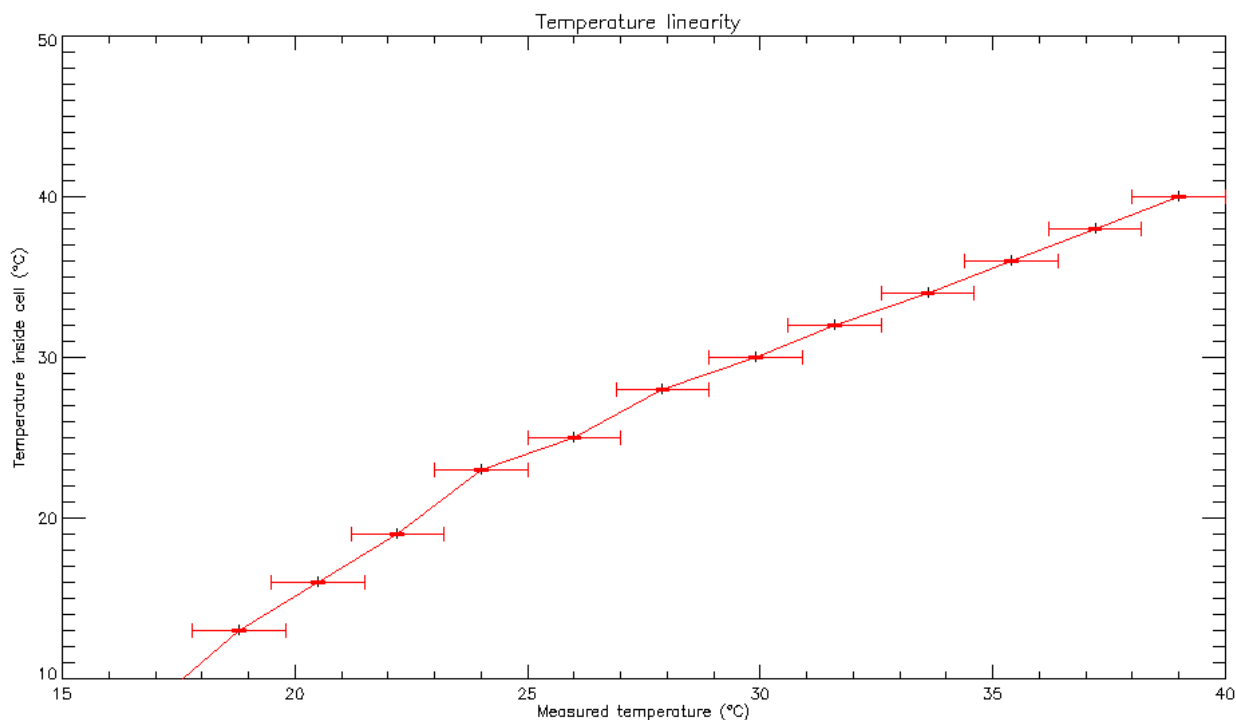
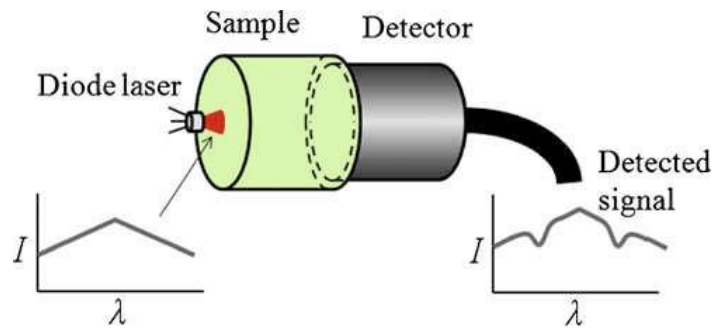


Figure 8.39: Temperature linearity inside and outside the cell

The fit is given by the equation $I_T = \text{Intercept} + B1 \cdot M_T + B2 \cdot M_T^2 + B3 \cdot M_T^3 + B4 \cdot M_T^4 + B5 \cdot M_T^5$ where Intercept=102,96011, B1=-24,90641, B2=2,15331, B3= -0,0816, B4= 0,00146 and B5=-1,00954x10⁻⁵ and where I_T and M_T are the inside and the measured temperatures.

As can be seen, starting from 28°C, the linearity begins to follow the same trend. The measurements of gas concentrations inside the cells are done with a Tunable Diode Laser Absorption Spectroscopy setup (TDLAS) and is based on absorption energy following Beer's law. This measurement method provides a Vertical Cavity Surface Emitting laser (VCSEL) source shot through the cell environment and to a photodiode diode laser tuned to a particular narrow emission band. The source wave number is selected in order to match a single absorption line on a molecule of interest and the laser emission is scanned several times across the whole spectral width of the absorption feature. Usually, the line width of the laser emission is much smaller than the molecular absorption line width allowing the instrument to be selective among components of a gas mixture and have no interferences from other gases, especially at low pressure (the absorption lines are narrower). The sensitivity of the analyzer is dependent on the absorption strength of the line chosen and on the absorption path length (Bowling et al., 2003). Many gases of biological interest can be sensed in this way, for example HF (detection limit 0.2 ppm.m), H₂S (detection limit 20.0 ppm.m), NH₃ (detection limit 5.0 ppm.m), H₂O (detection limit 1.0 ppm.m), CH₄ (detection limit 1.0 ppm.m), HCl (detection limit 0.15 ppm.m), HCN (detection limit 1.0 ppm.m), CO (detection limit 40.0 ppm.m), CO₂ (detection limit 40.0 ppm.m), NO (detection limit 30.0 ppm.m), NO₇ (detection limit 0.2 ppm.m), O₂ (detection limit 50.0 ppm.m). A Wavelength Modulation Spectroscopy scheme has been used to improve detection of weak absorptions from the low concentrations obtained. The measurement setup is based on a PC with a DAQ card for synchronous modulation and demodulation of the WMS waveforms as well as for fitting the absorption signals. In figure 8.40 is shown a scheme of its working. In figure 8.41 can be seen the arrangement of the gas measurement system on the cell. The laser used to detect the gases inside the cell are a 760 nm laser from ULM Photonics for O₂ and a 2004 nm laser from Vertilas for CO₂. The detectors used in this configuration are a Si 5.6x5.6 mm square Hamamatsu photodiode for O₂ and a round 1 mm radius InGaAs photodiode from Teledyne Judson Technologies.



Nomenclature: I – Intensity (a.u.), λ – Wavelength (nm)

Figure 8.40 Working scheme of the gas detector.

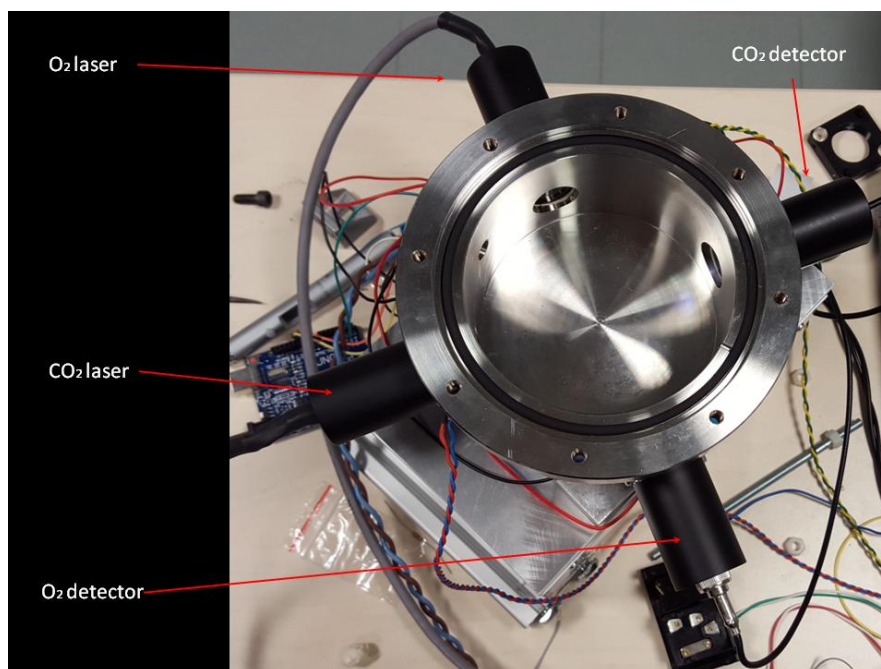


Figure 8.41: Gas sensors and detectors attached to the cell

The second tests have been done in order to understand the detection limits for O_2 and CO_2 . We filled the cell with a 84.3% N_2 and 15.7% CO_2 gas mixture and revealed an O_2 concentration of 1.45×10^{-4} with a sigma 1.79×10^{-5} as well a CO_2 concentration of 0.0498 with a sigma 7.057×10^{-4} . The same data for the air are an O_2 concentration of 4.23×10^{-4} with a sigma 1.44×10^{-5} and a CO_2 concentration of 5.72×10^{-4} with a sigma 3.12×10^{-5} . The results are 1% for O_2 and 54 ppm for CO_2 .

8.4 Bacteria preliminary tests

In this section will be treated the tests operated with bacteria in order to tune the experimental procedures and to characterize the organisms suitable to achieve the project goals. In particular for the chosen organisms (*Cyanobacterium aponinum* and *Chlorogloeopsis fritschii*) we defined the best medium, light and temperature for growth and we then determined the growth rate and the growth curve shape. This step is crucial for identifying the linear part of the diagram corresponding to the exponential growth phase: the proper moment to determine the maximum O_2 and to detect the organism responses to the switch from visible or to M star light. We also tuned the procedures for the organism's in vivo light absorption, transmission and reflectance spectra analyses as well as for the absorption spectra and pigment

concentrations determination of their lipophilic extracts. In particular we tested different photosynthetic microorganisms, such as a green alga (*Chlamydomonas reinhardtii*), an high light (*Synechococcus* PCC 7002) and a low light (*Chroococcus* sp.) adapted cyanobacteria. The biological analyses were performed at the Photosynthesis and Plant Biotechnology Laboratories, Department of Biology, University of Padova, under the supervision of Dr. Nicoletta La Rocca and with the help of graduating student Caterina Pozzer.

8.4.1 Determination of growth parameters

For the different types of cyanobacteria (*Cyanobacterium aponinum* and *Chlorogloeopsis fritschii*) have been performed some vitality tests at different temperatures and light exposure in controlled growth chambers (figure 8.42).

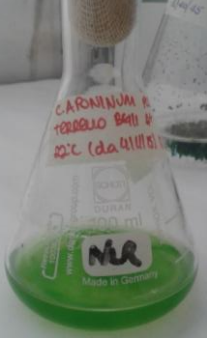
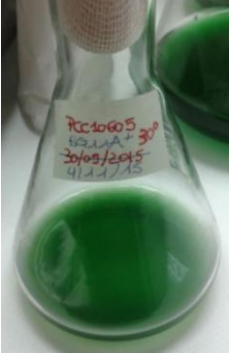


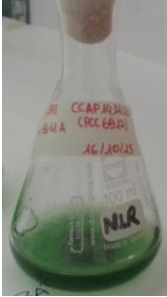
PCC 10605 (<i>Cyanobacterium aponinum</i>)		
Temperature: 22°C	Temperature: 30°C	
		
Radiation dose: 30-35 $\mu\text{mol photons/m}^2/\text{s}$	Radiation dose: 20-27 $\mu\text{mol photons/m}^2/\text{s}$	
CCAP 1411/1A (PCC 6912) (<i>Chlorogloeopsis fritschii</i>)		
Temperature: 16°C	Temperature: 30°C	Temperature: 22°C
		
Radiation: 10 $\mu\text{mol photons/m}^2/\text{s}$	Radiation: 22-25 $\mu\text{mol photons/m}^2/\text{s}$	Radiation: 25-27 $\mu\text{mol photons/m}^2/\text{s}$

Figure 8.42: Examples of different cultures grown at different temperatures and radiation doses

From these preliminary observations the best temperature and light intensity for growth experiments were identified to be 30°C and 20 $\mu\text{mol photons/m}^2/\text{s}$. For the bacteria *Cyanobacterium aponinum* and *Chlorogloeopsis fritschii* grown at 30°C in 20 $\mu\text{mol photons/m}^2/\text{s}$ radiation conditions taken for 24 days have been done some transmissivity measurements at 750 nm, also said Optical Density 750 (OD₇₅₀). These measurements give an estimate of the growth process in time (figure 8.43 and 8.44) The analyses were repeated for 4 independent experiments. For the bacteria *Cyanobacterium Aponinum* and *Chlorogloeopsis fritschii* grown at 30°C in 20 $\mu\text{mol photons/m}^2/\text{s}$ radiation conditions taken for 24 days have been done some

transmissivity measurements at 750 nm, also said Optical Density 750 (OD₇₅₀). These measurements give an estimate of the growth process in time (figure 8.43 and 8.44).

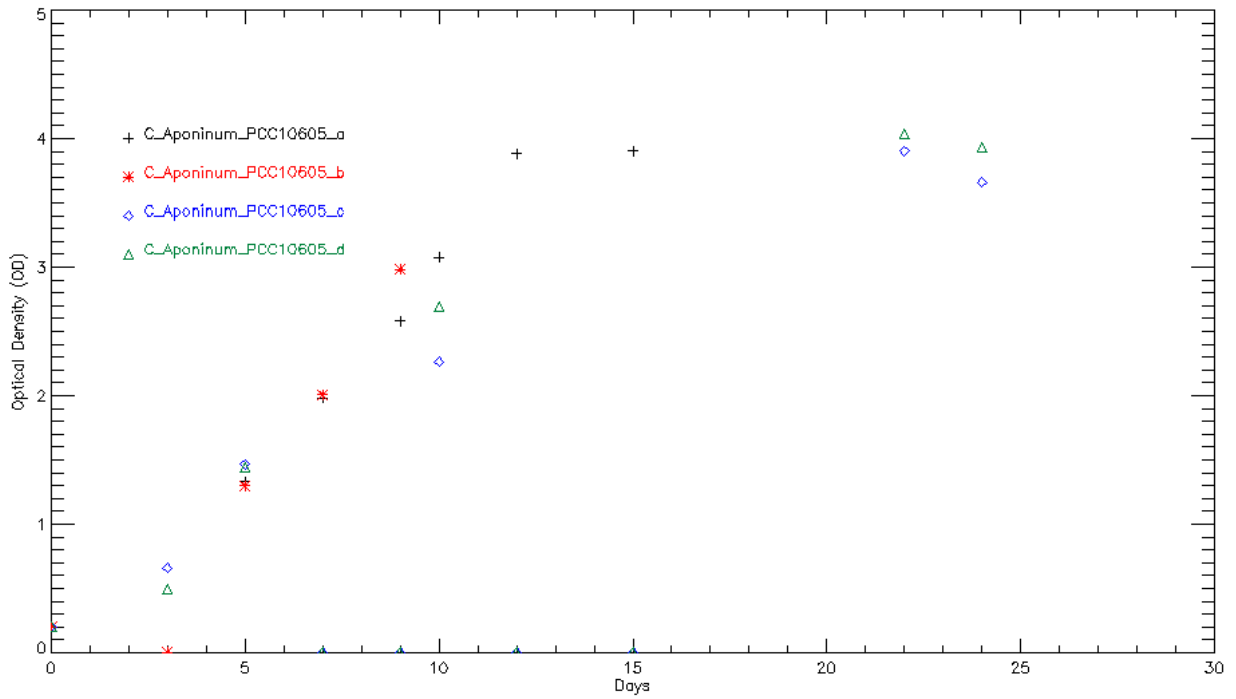


Figure 8.43: Growth curves of *Cyanobacterium aponinum* grown at 30°C and 20 $\mu\text{mol photons/m}^2/\text{s}$ for 24 days

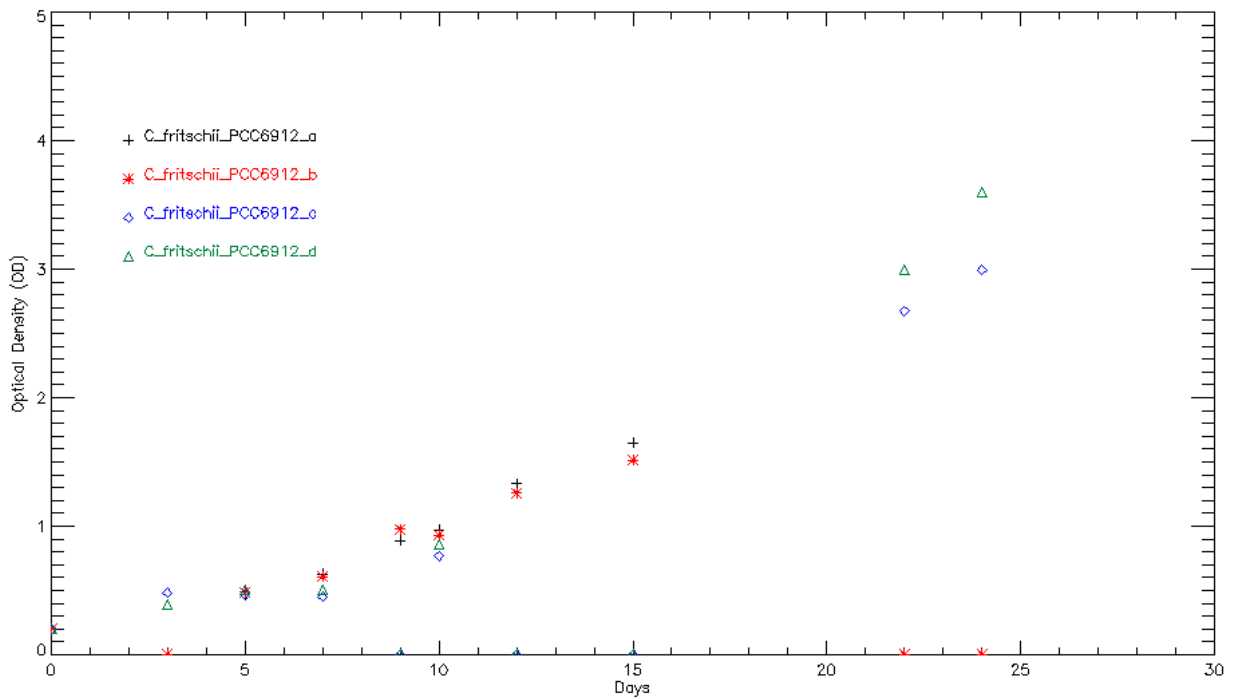


Figure 8.44: Growth curves of *Chlorogloeopsis fritschii* grown at 20 $\mu\text{mol photons/m}^2/\text{s}$ and 30°C for 24 days.

As can be shown all the curves follow the rules of growth: initial lag phase, exponential phase and stationary phase. In figure 8.43 can be seen the descending part of the curve.

8.4.2 Reference O₂ productivity tests with oxymeter

The preliminary tests for O₂ productivity have been made with a chlorolab 2 System from Hansatech instruments. This system provides the ability to automate the acquisition of oxygen evolution/uptake rate over a user-defined light intensity. The system comprises the OxyLab control unit, an S1 Clark type electrode disc, a DW2/2 liquid-phase electrode chamber, a standard white led source with a colour temperature 4100K and QRT PAR/temperature sensor for light source calibration (Figure 8.45).

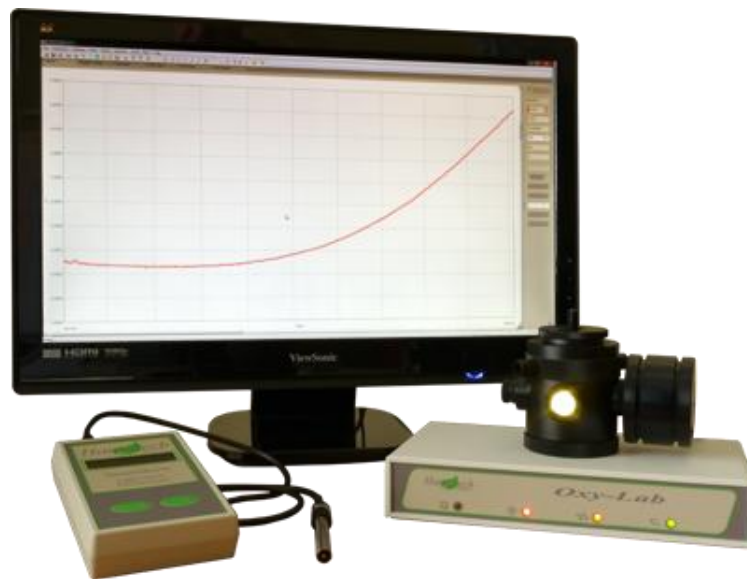


Figure 8.45: Chlorolab 2 System from Hansatech instruments

The procedure used to take oxygen measurements with the oxymeter are described hereafter:

- 1) Turn the thermostat and the oxymeter on
- 2) Clean the sample dish from residuals with a pipette using H₂O Millipore
- 3) In order to calibrate the oxymeter some steps have to be done:
 - 3a) Put in the sample holder a known volume of distilled H₂O Millipore (2 ml), the same that will be used for the samples, stabilized in oxygen and environmental temperature
 - 3b) Turn the sample shaker on
 - 3c) Turn the oxymeter on until the stability has been reached
 - 3d) Use the calibrate function and the liquid function of the software to set the reference values. The water reference has to be set in the “air saturated water” mode
 - 3e) Set the temperature at 30°C at environment pressure

- 3f) After having reached the maximum value of the oxygen saturation blow N inside the sample and, once reached the plateau of the saturation curve set the minimum value.
- 3g) Take the offset measurement
- 3h) Use the "self calibration" mode to complete the calibration and then use the "new calibration" mode to begin the measurements
- 3h) Remove the water from the sample holder
- 4) Place the sample to be tested in the oxymeter and close the lateral cap. The samples have to be previously quantified as regard to the number of cell or chlorophyll weight
- 5) Control that the sample shaker is on
- 6) Acquire the first reference oxygen data (nmol/ml)
- 7) Turn all the lights off and take a sample measurements of cell respiration
- 8) Measure the negative slope of the curve that trace the respiration as a function of time in nmol/ml/sec
- 9) Turn again the light on and add a label on the curve in order to mark the light-on event
- 10) After the oxygen evolution stabilization measure the maximum slope of the curve during the photosynthetic process. This value is positive and measured in nmol/ml/sec
- 11) Turn the oxymeter off and save the data
- 12) Clean again the sample dish from residuals with a pipette using H₂O Millipore

The first data of oxygen evolution have been taken in white light conditions for cultures grown for 6 days, thus in exponential growth phase, at 30°C and 20 $\mu\text{mol photons/m}^2/\text{s}$ in controlled climatic chamber Erlenmeyer flasks. The results for *Chlorogloeopsis fritschii*, taken from two different samples, have highlighted a mean O₂ production of $224.45 \frac{\mu\text{mol O}_2}{\text{mg Chl}\cdot\text{h}}$. Results for *Cyanobacterium aponinum* have shown the total O₂ production of $174.41 \frac{\mu\text{mol O}_2}{\text{mg Chl}\cdot\text{h}}$. In tables 8.14 and 8.15 are reported the measurements of oxygen evolution.

1 <i>Chlorogloeopsis fritschii</i>	206.761 $\mu\text{mol O}_2/\text{mg Chl/h}$
2 <i>Chlorogloeopsis fritschii</i>	242.138 $\mu\text{mol O}_2/\text{mg Chl/h}$

Table 8.14: Oxygen evolution for two different samples of *Chlorogloeopsis fritschii*

1 <i>Cyanobacterium Aponinum</i>	156.465 $\mu\text{mol O}_2/\text{mg Chl/h}$
2 <i>Cyanobacterium Aponinum</i>	192.358 $\mu\text{mol O}_2/\text{mg Chl/h}$

Table 8.15: Oxygen evolution for two different samples of *Cyanobacterium aponinum*

8.5 Irradiation of the samples with a stellar spectrum simulator and terrestrial pressure, temperature and gaseous mixture

During the second phase of the experiment eight samples have been used. Two samples of *Cyanobacterium aponinum* grown at 20 $\mu\text{mol photons/m}^2/\text{s}$ in white light for 6 days and then at 100 $\mu\text{mol photons/m}^2/\text{s}$ for the residual 3 days in white light. Two samples of *Chlorogloeopsis fritschii* grown at 20 $\mu\text{mol photons/m}^2/\text{s}$ for 6 days in white light and then at 100 $\mu\text{mol photons/m}^2/\text{s}$ for the residual 3 days in white light. Two samples of *Cyanobacterium Aponinum* have been grown at 20 $\mu\text{mol photons/m}^2/\text{s}$ for 6 days in white light

and then at 100 $\mu\text{mol photons/m}^2/\text{s}$ for the residual 3 days using the radiation spectrum of an M7 type star. Two samples of *Chlorogloeopsis fritschii* grown at 20 $\mu\text{mol photons/m}^2/\text{s}$ for 6 days in white light and then at 100 $\mu\text{mol photons/m}^2/\text{s}$ for the residual 3 days using the radiation spectrum of an M7 type star. The choice to use white light at 20 $\mu\text{mol photons/m}^2/\text{s}$ for the first 6 days and then a radiation dose of 100 $\mu\text{mol photons/m}^2/\text{s}$ for the next 3 days was made in order to compare the same initial common growth conditions with the different radiation conditions for the next 3 days, but keeping the number of photons the same: 100 $\mu\text{mol photons/m}^2/\text{s}$ in white light in one case and 100 $\mu\text{mol photons/m}^2/\text{s}$ of M7 light in the second case. In figure 8.48 are shown the fit of the M7 star produced as the output of the IDL routine (black) and the real spectrum at 23 cm distance from the centre of the radiation coil (red). The temperature has been kept at 30°C for the samples not exposed to M7 light and at a temperature oscillating from 35°C to 38°C for the samples exposed to M7 light. This has been due to the over-heating of the lamp. The radiation source has been driven by a PC used to control the LEDs via USB port while the spectrometer was collecting in real time the outgoing radiation. Figure 8.49 a and b shows the set-up of the experiment.

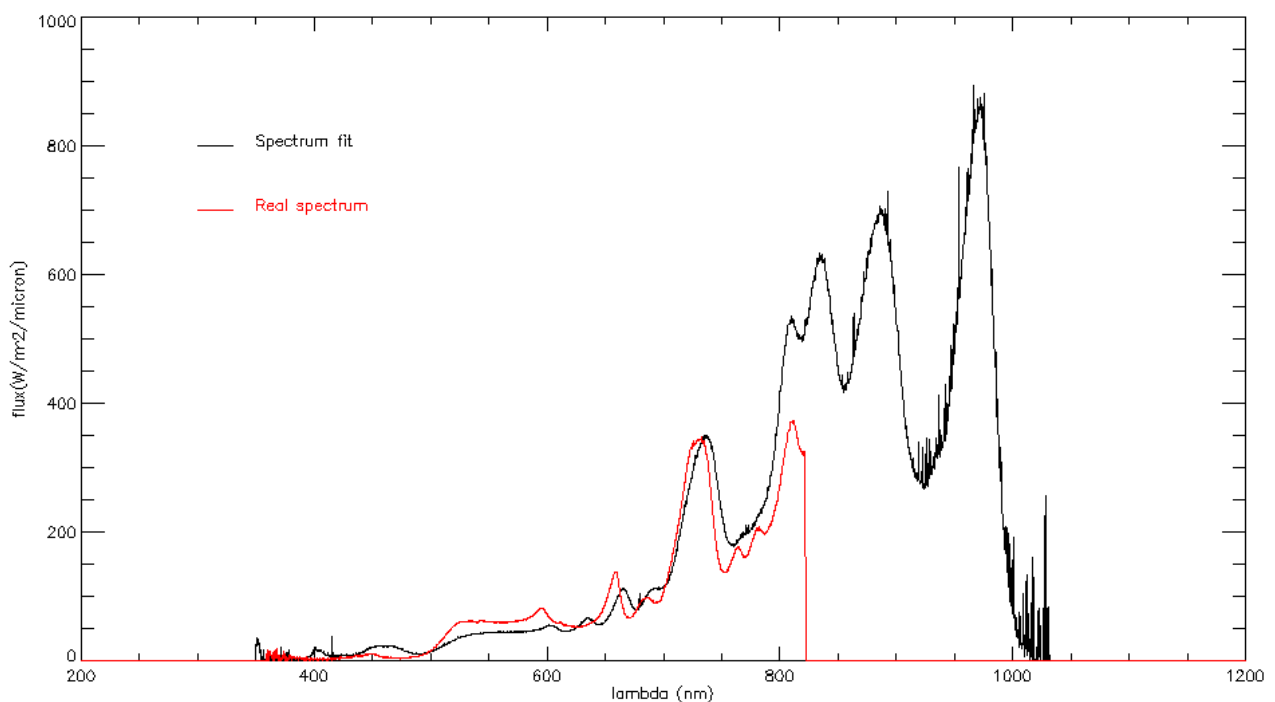


Figure 8.46: Spectrum used to irradiate the bacteria

During the exposure at different time (0h, 24h, 48h, 72h) the samples changed their colour, as can be well seen in figure 8.48. In particular, while *Chlorogloeopsis fritschii* has a good response to different light and continue growing even in M7 radiation conditions, *Cyanobacterium Aponinum* slightly suffer the new radiation. This feature can be well seen for the sample 2. The final chromatic evolution is resumed in figure 8.49.

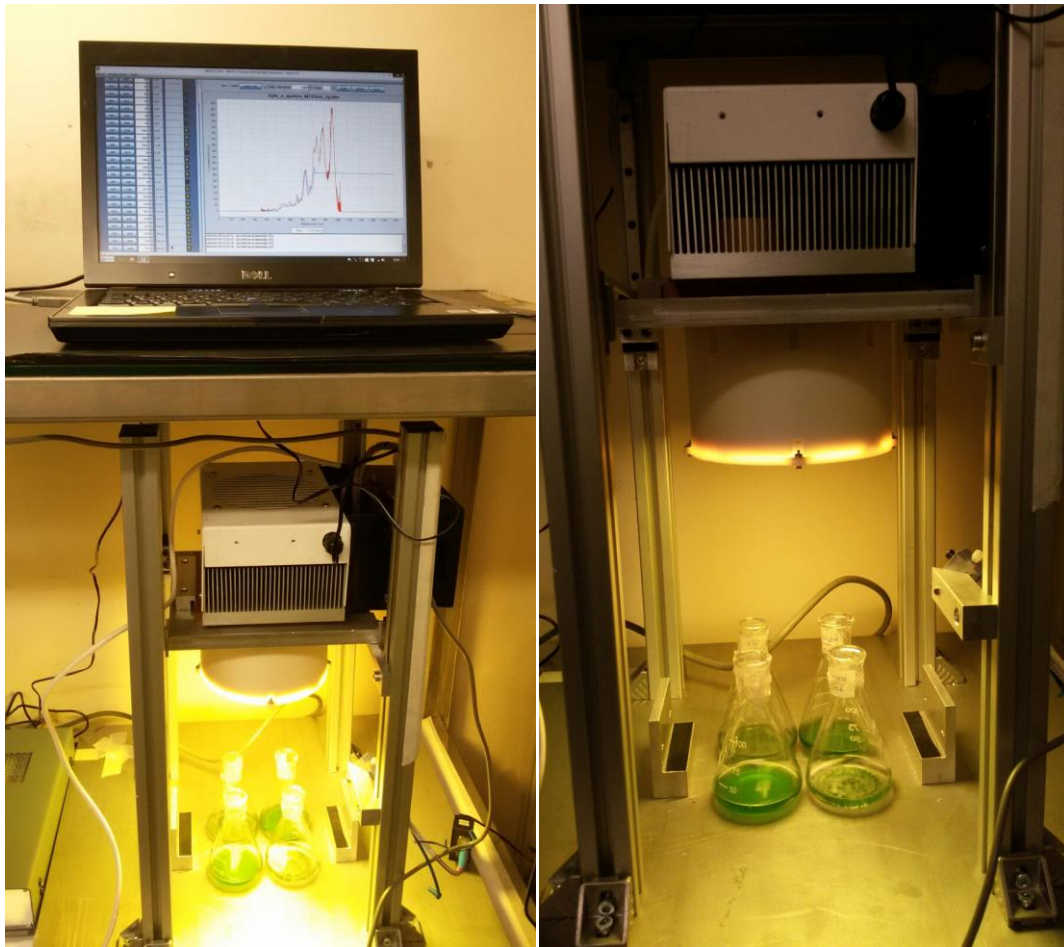


Figure 8.47: Set-up of the experiment

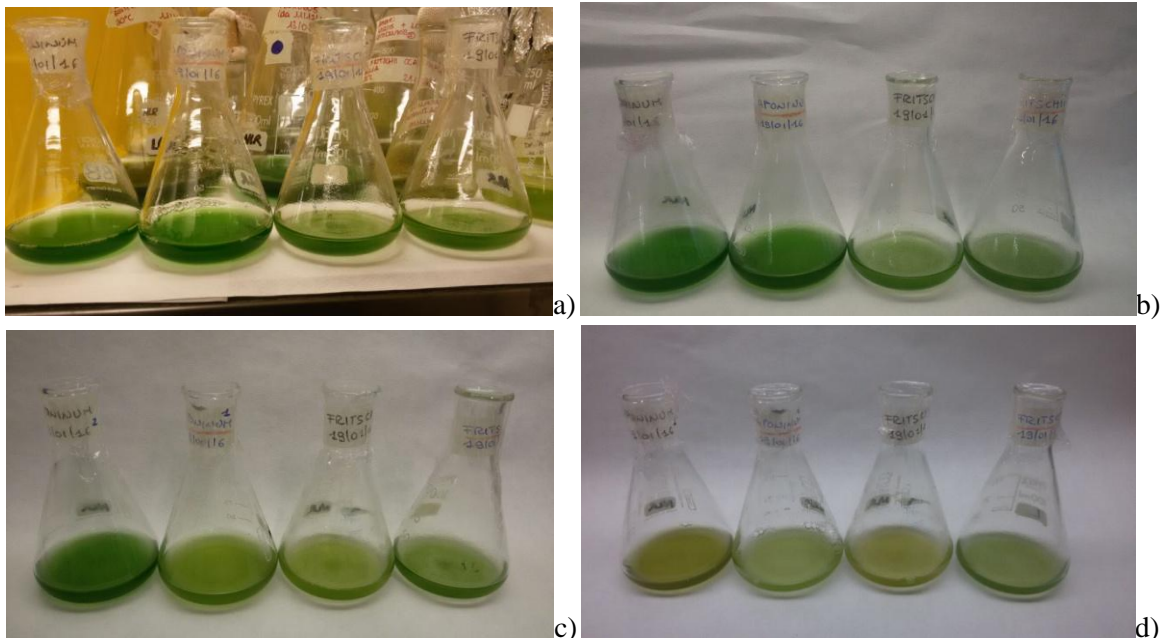


Figure 8.50: Four samples, two of *Cyanobacterium aponinum* and two of *Chlorogloeopsis fritschii*. Among them, two have been irradiated with the starlight simulator (the ones with red line label) and two irradiated with white light, at different time (0h (a), 24h (b), 48h (c) and 72h (d)). All of them are grown at 30°C in 20 $\mu\text{mol photons/m}^2/\text{s}$ irradiation conditions for 6 days and 100 $\mu\text{mol photons/m}^2/\text{s}$ irradiation conditions for the next days.

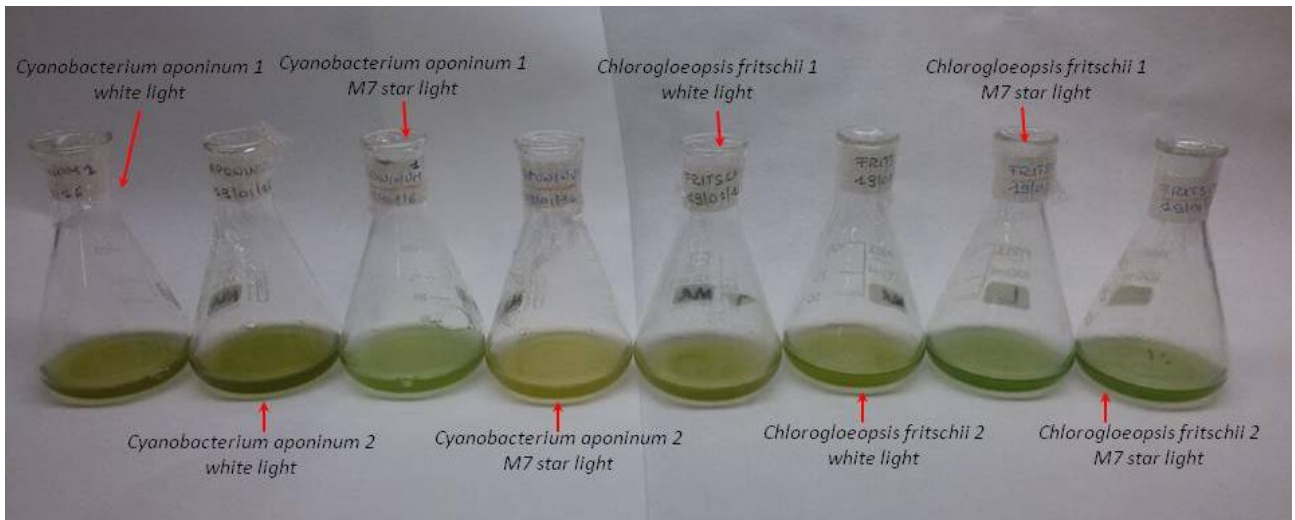


Figure 8.49: All-in-one visual representation of the final chromatic responses of all the 8 samples after 72h.

During the exposure to different light sources, growth curves have been taken. These data are collected in figure 8.50, 8.51 and 8.52.

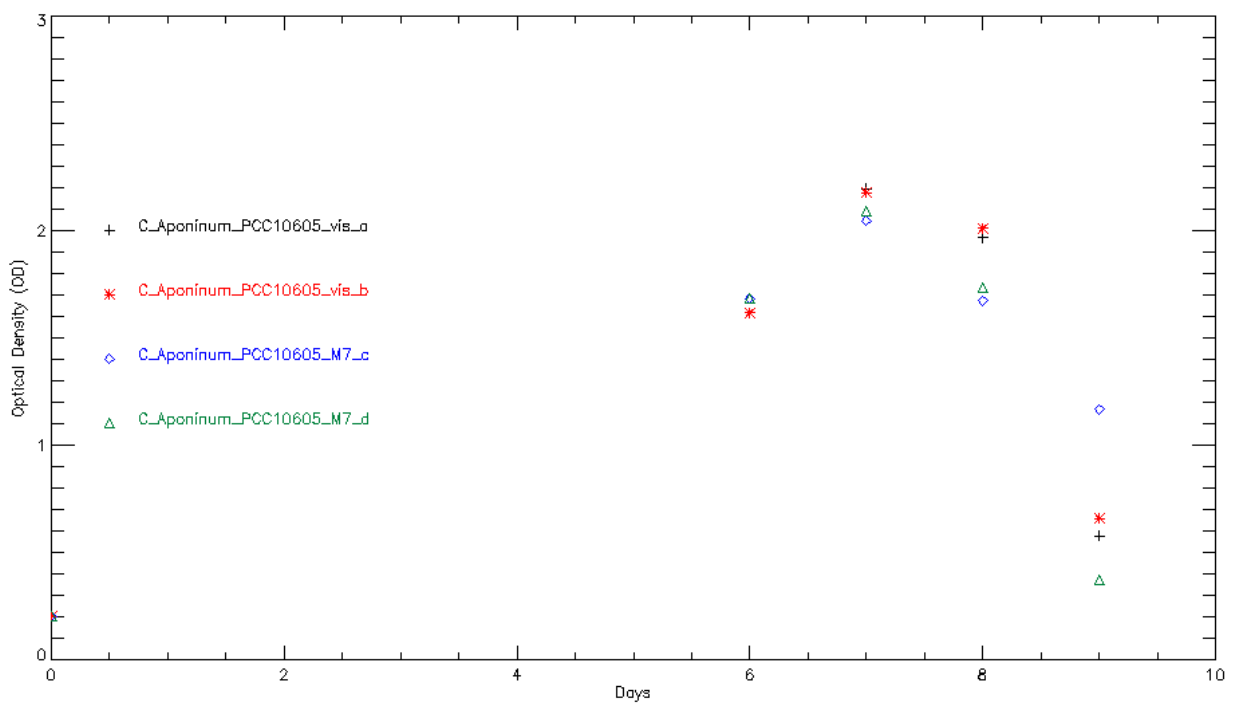


Figure 8.50: Growth curves of *Cyanobacterium Aponinum* both in visible and M7 light conditions.

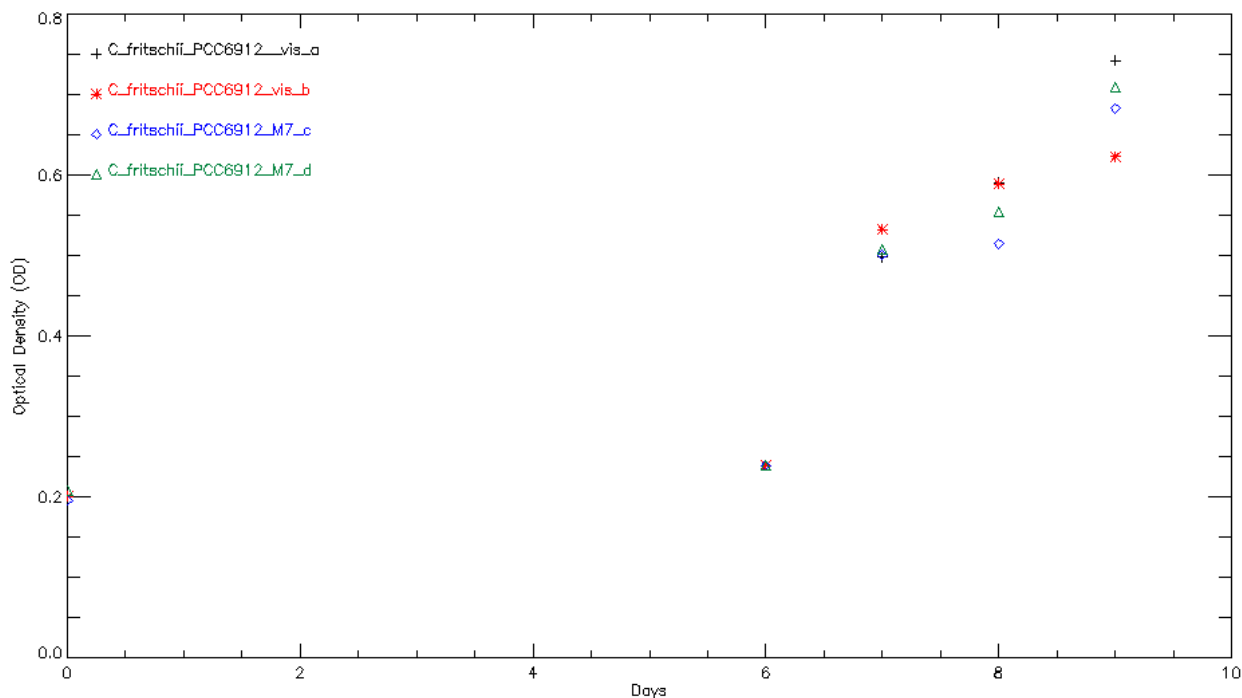


Figure 8.51: Growth curves of *Chlorogloeopsis fritschii* both in visible and M7 light conditions.

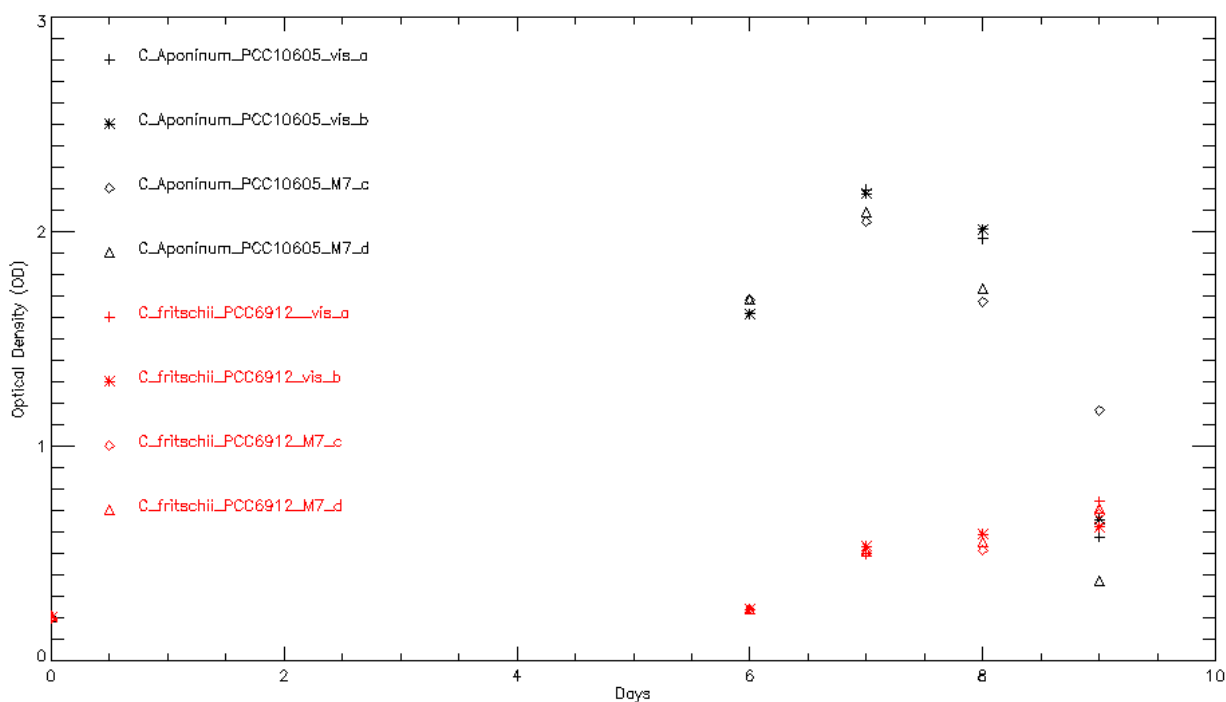


Figure 8.52: Growth curves of *Chlorogloeopsis fritschii* and *Cyanobacterium Aponinum* both in visible and M7 light.

From the analysis of the curves we infer that *Cyanobacterium Aponinum* has a quicker growth respect to *Chlorogloeopsis fritschii* which, on the other hand, has a longer lag phase. After the 6 days of 20 $\mu\text{mol photons/m}^2/\text{s}$ irradiation common for all the samples, samples have been irradiated with 100 $\mu\text{mol photons/m}^2/\text{s}$. We noticed a steep increase in the growth of *Cyanobacterium Aponinum* leading the samples to a descending phase in less than 2 days while *Chlorogloeopsis fritschii* continues its growth even with the

increase of the number of photons. Finally, even though a small delay in the optical density is appreciable for both *Chlorogloeopsis fritschii* and *Cyanobacterium Aponinum* under M7 light with respect to the samples under white light.

8.5.1 Analysis of bacteria productivity and gas abundances in cells

After the growth curves the analysis of oxygen production have been done for all the 8 samples except for *Chlorogloeopsis fritschii* 1 (due to a technical problem), after 48 hours of light exposition to the different radiations. In table 8.16 are reported the Chla concentration [Chla]mg/ml and the O₂ productivity in μmol O₂/mg Chla/h for the 8 samples examined.

Sample	[Chla]mg/ml	Total μmol O ₂ /mg Chla/h	Net evolution O ₂ /mgChl/h
<i>Cyanobacterium Aponinum</i> 1 Vis 48h	0.0053	47.479	23.0097
<i>Cyanobacterium Aponinum</i> 2 Vis 48h	0.0066	40.409	22.3289
<i>Cyanobacterium Aponinum</i> 1 M7 48h	0.0035	70.525	-29.2421
<i>Cyanobacterium Aponinum</i> 2 M7 48h	0.0042	3.311	-25.4770
<i>Chlorogloeopsis fritschii</i> 1 Vis 48h	-	-	-
<i>Chlorogloeopsis fritschii</i> 2 Vis 48h	0.0051	79.572	50.3176
<i>Chlorogloeopsis fritschii</i> 1 M7 48h	0.0053	89.716	65.8067
<i>Chlorogloeopsis fritschii</i> 2 M7 48h	0.0056	70.497	48.0808

Table 8.16: Analysis of oxygen production and Chla concentration for all the 8 samples except for *Chlorogloeopsis fritschii* 1, after 48 hours of light exposition to the different radiations.

Here are compared the total production of O₂ with the net O₂ production (O₂ evolved by photosynthesis – O₂ consumed by respiration). As can be seen, the oxymetric analysis reflect the chromatic response. In fact the oxygen production decreases for both *Cyanobacterium aponinum* and *Chlorogloeopsis fritschii* if compared with data recorded for the same samples after 6 days at 20μmol photons/m²/s and reported in Table 8.14 and 8.15. However the data show the ability of *Chlorogloeopsis fritschii* to have a net oxygen evolution also when exposed to M7 star light while this value is negative for *Cyanobacterium aponinum*. This is due to the fact that *Cyanobacterium aponinum* uses a lot of oxygen for cellular respiration and so, the net evolution is negative. The data well correlate with growth observations reported in figure 8.54. Moreover, the sample *Cyanobacterium aponinum* 2 shows a pale green colour, that means a poor oxygen productivity and scarce vitality. This feature could be not directly connected to the light but can be due to many unknown factors as the impact on the sample of slight changes of culture pH, temperature and a difference in radiation spectrum. This last assertion is made taking into account that the spectrum used to irradiate the bacteria was optimized for the centre of the simulator and the samples have been places at 6.5 cm from it and we have to take into account that the uniformity vary according to figure 8.22 in chapter 8. Finally, we have to point out that these are only really preliminary results and that all the experiments have to be repeated to have statistically evaluable.

8.6 Pigment reflectance tests

In order to start the red edge preliminary tests and to understand the reflectance properties of the absorption pigments we chose three bacteria, different from those used for the experiment: *Synechococcus* PCC 7002, *Chroococcus* sp. and *Chlamydomonas reinhardtii*. These bacteria were chosen for their known properties so as to have a first reference. In order to do this task, we suspended them in a salty solution. At first we isolated the solid part of the samples. In order to do this 1.5 ml of each solution were put in a test tube and centrifuged at a velocity of 14115 spin/minute for 3 minutes. Once the supernatant was separated from the

cells, it was picked away by means of a micropipette. Then, the solid part were diluted with dimethylformamide (DMF), an organic solvent (CH₃)₂NC(O)H and detached from the bottom of the test tubes by means of a laboratory shaker in green light conditions. The samples have then been put into a fridge a 4°C for 24 hours covered with aluminium. This helps pigments not to be damaged by the artificial light. Then the absorbance of the pigments have been collected by means of a spectrophotometer. In figure 8.53 and 8.54 are shown the absorbances of *Synechococcus* PCC 7002, *Chroococcus* sp. and *Chlamydomonas reinhardtii*.

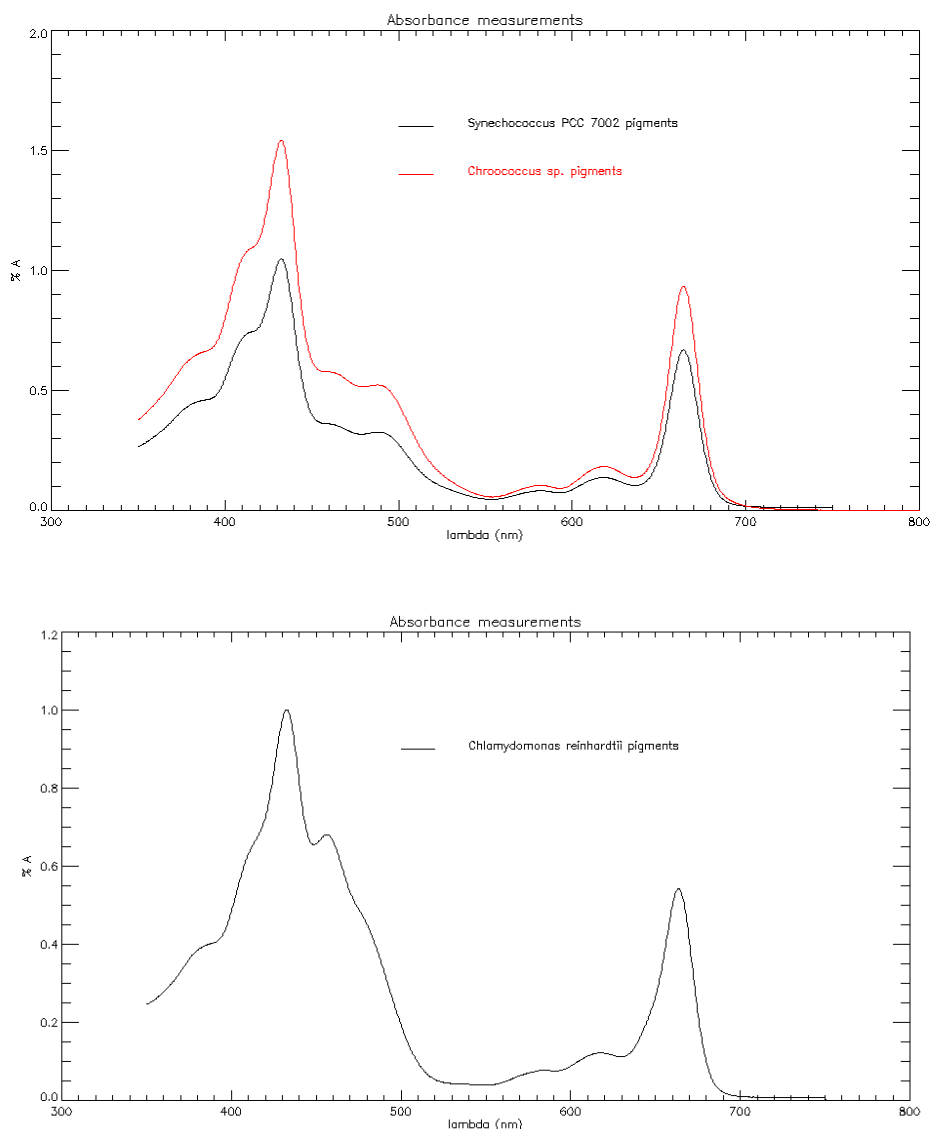


Figure 8.53 and 8.54: Absorbances of *Synechococcus* PCC 7002, *Chroococcus* sp. and *Chlamydomonas reinhardtii*.

In the second part of the experiment have been collected the transmission spectra if three different bacteria with the instrument Cary 5000 version 1.12. The first set of measurements have been collected directly in order to measure the total transmission at different concentrations (figures 8.55 and 8.56), the second set with a integrating sphere in order to measure even the scattered component with the same concentrations (figures 8.57 and 8.58).

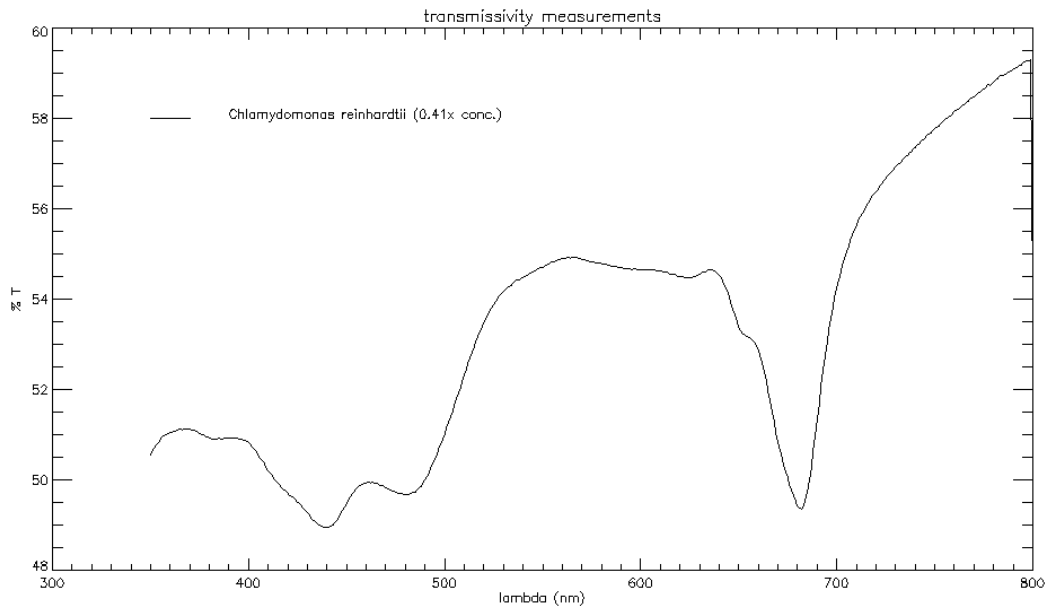
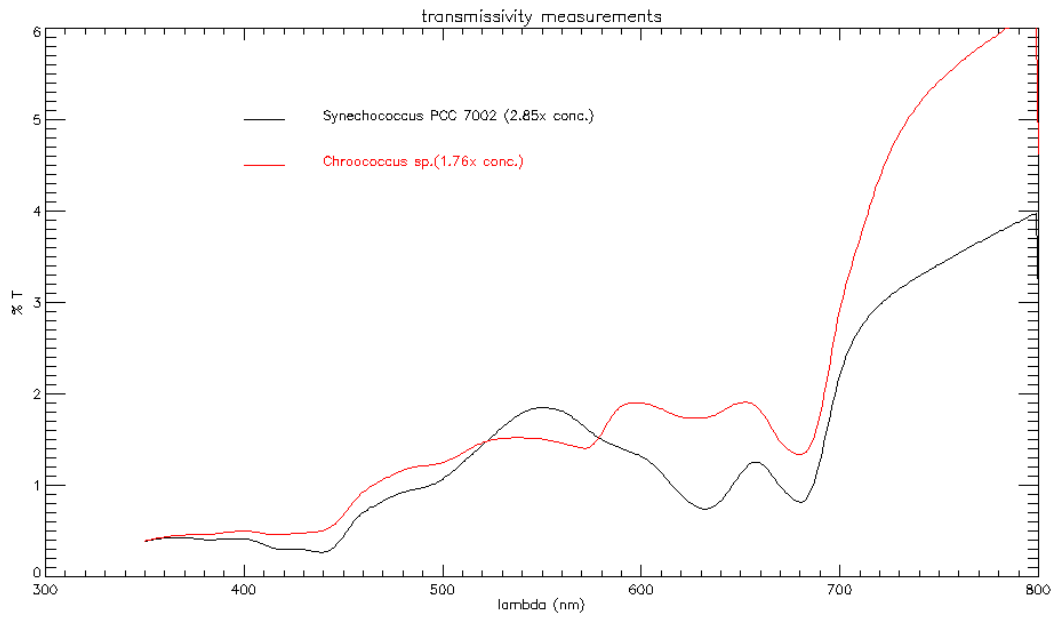


Figure 8.55 and 8.56: Measurements of Transmissivity of *Synechococcus* PCC 7002, *Chroococcus* sp. and *Chlamydomonas reinhardtii* without the integrating sphere

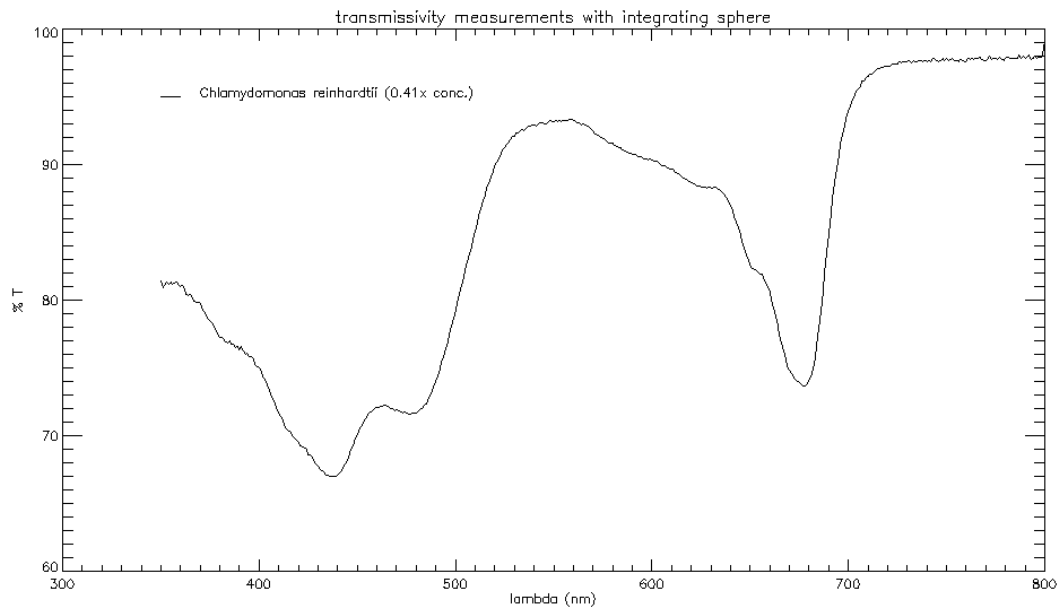
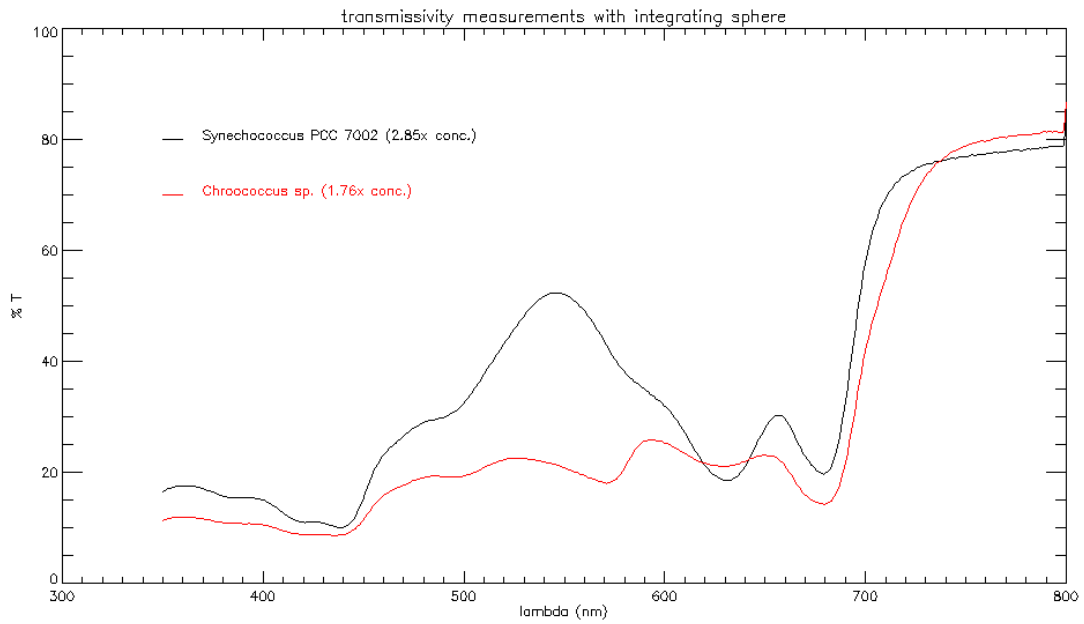


Figure 8.57 and 8.58: Measurements of Transmissivity of *Synechococcus* PCC 7002, *Chroococcus* sp. and *Chlamydomonas reinhardtii* with the integrating sphere

Taking the difference to 100% of transmissivity data in figures 8.48 and 8.49 we can calculate the absorbance in vivo (figures 8.59 and 8.60) and compare them with the pigment absorbance (figures 8.61 and 8.62).

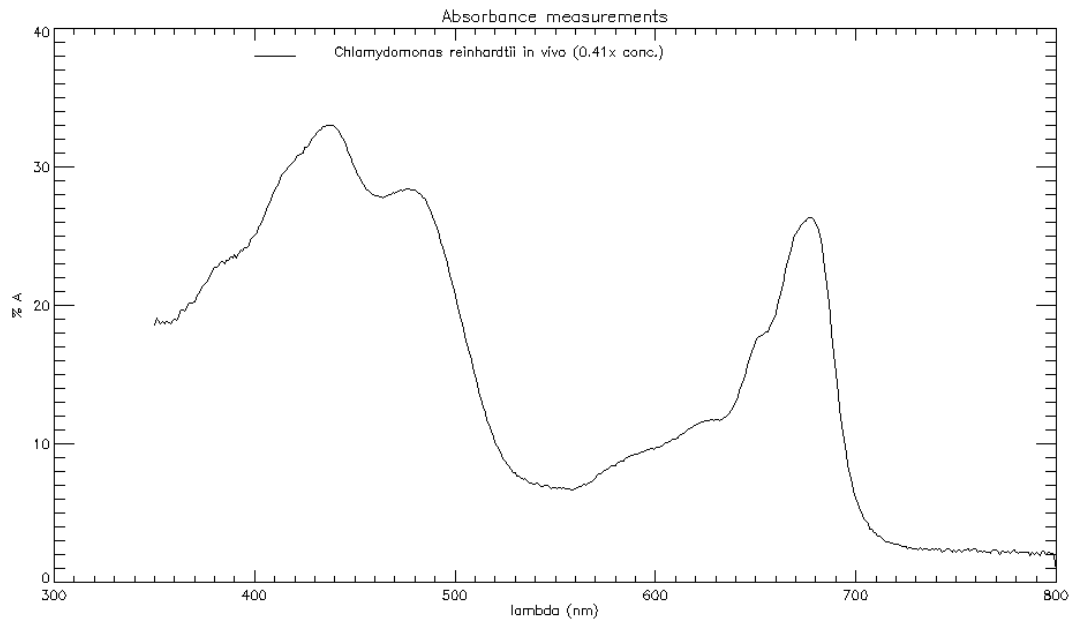
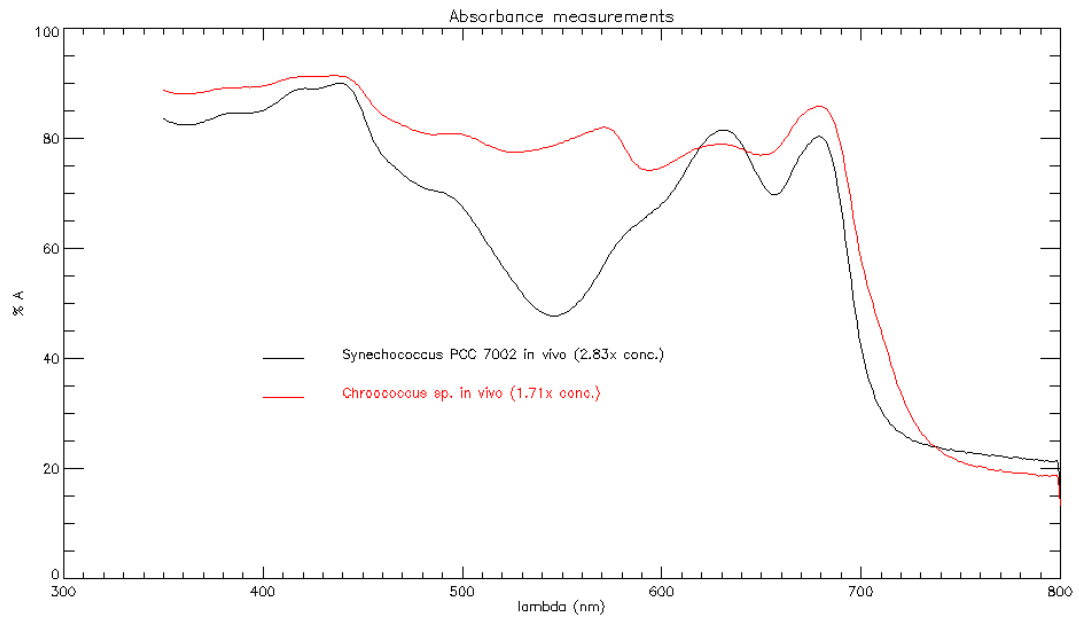


Figure 8.59 and 8.60: Measurements of Absorbance in vivo of *Synechococcus* PCC 7002, *Chroococcus* sp. and *Chlamydomonas reinhardtii*

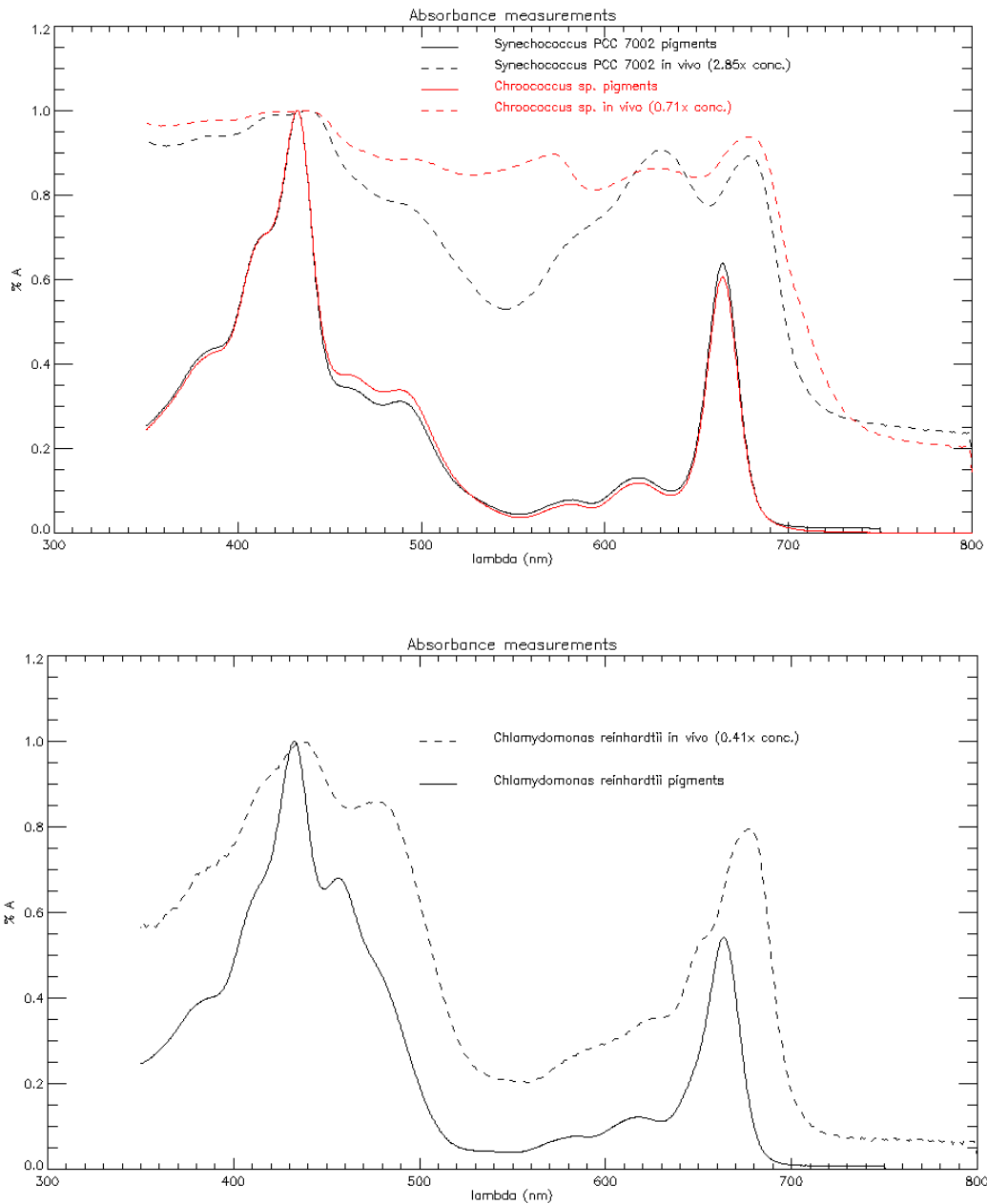


Figure 8.61 and 8.62: Measurements of compared Absorbance of *Synechococcus PCC 7002*, *Chroococcus sp.* and *Chlamydomonas reinhardtii* cells

These data have been normalized with respect to their highest value in order to be comparable. The dataset in vivo are different from the pigments data because in vivo there are several interactions of pigments and proteins that can modify the absorbance spectrum. Moreover in the dimethylformamide treated data, are shown only lipid soluble pigments while in the in vivo data are shown even the hydro soluble ones. Subtracting the spectra made with the integrating sphere from the ones taken without it we can have a measurement of scattering (figure 8.63 and 8.64).

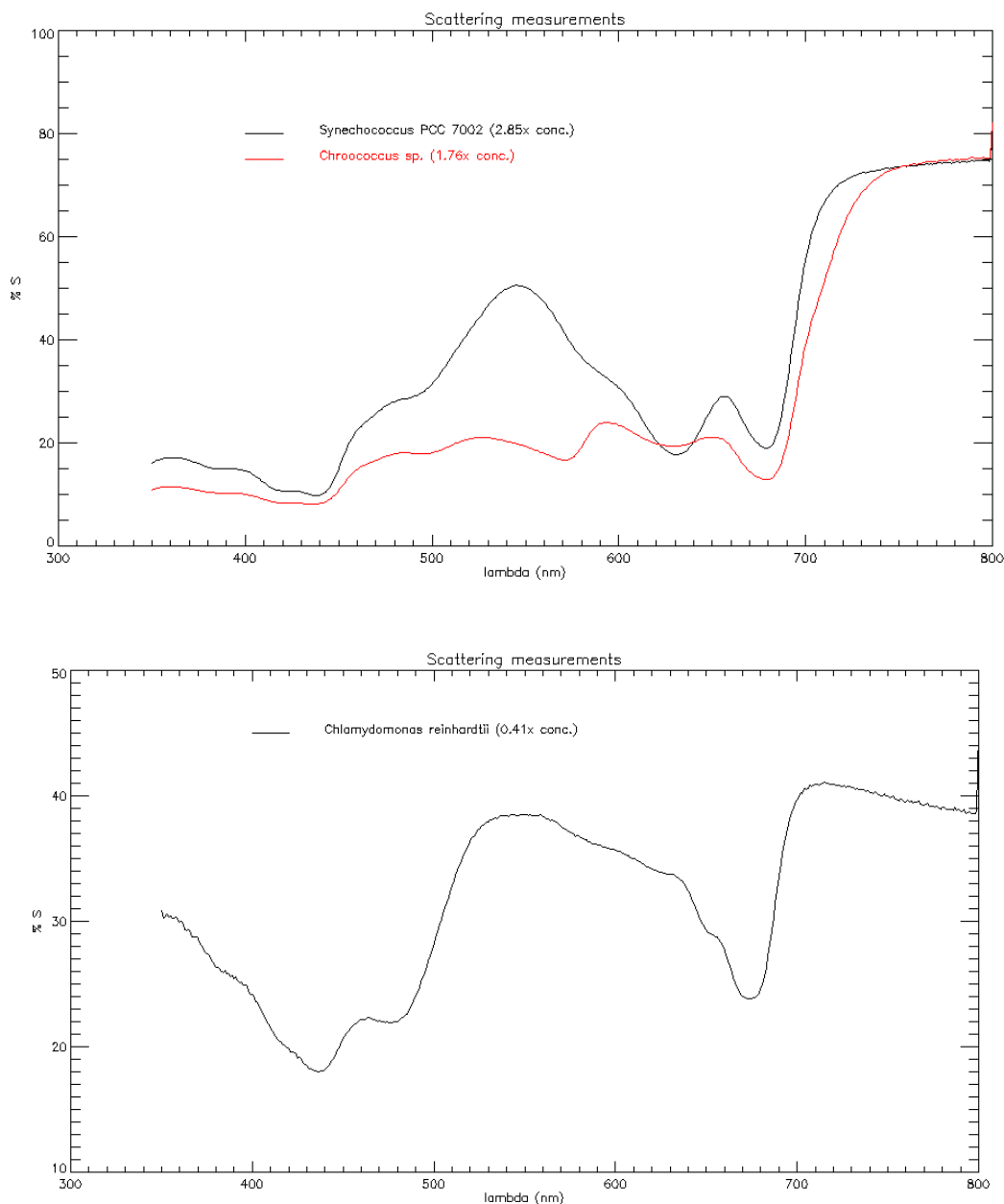


Figure 8.63 and 8.64: Measurements of scattering of *Synechococcus* PCC 7002, *Chroococcus sp.* and *Chlamydomonas reinhardtii* cells

In order to provide a useful tool to understand NIR light oxygen productivity and the FaRLiP properties of unknown organisms a novel kind of radiation sources have been developed instead of the white LED one. The first is composed by a combination of five OSLOM SSL80 730 nm SMD LEDs mounted on a paraboloidal frame (figure 8.65) while the second is a single OSLOM SSL80 730 nm SMD LED enclosed in a 16 mm diameter bulk. This way we are able to insert it in the chamber (figure 8.66). Samples have been irradiated with the same light before the oxymetric measurements. In this configuration, the radiation source has been placed on the top of the samples and the beam has been distributed on the dish.

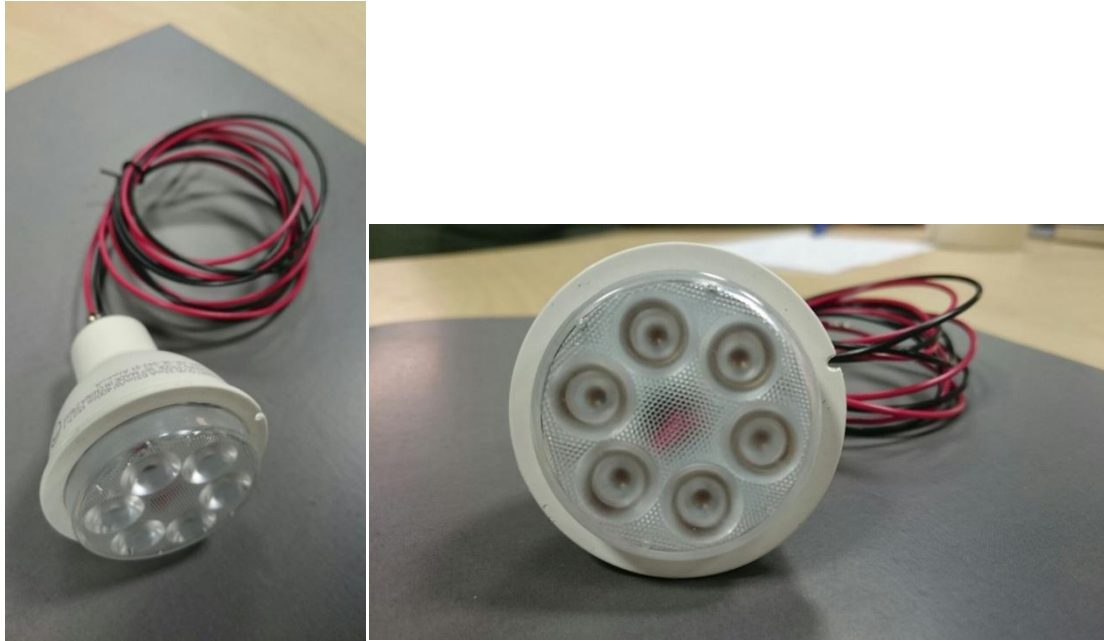


Figure 8.65: Paraboloidal radiation source to grow bacteria



Figure 8.66: Single 16 mm diameter radiation source for oxymetric measurements

9. Conclusions

In order to understand how photosynthetic life can handle different radiation doses, and to understand how the presence of photosynthetic organisms, if grown there, would affect the atmospheric composition of an Earth-like exoplanet in the habitable zone of M an star we started to think about a novel and pioneering radiation source, a sort of starlight simulator. The concept behind this is to endow this source with dynamical features, and this is the reason why we preferred the use of LEDs instead of lamps. Our simulator is composed by an array of 25 different channels with different kind of LEDs. The wavelength intervals chosen for this stellar simulator, that is enclosed between 365nm and 940nm, overlap the limits of photosynthetic pigment absorption range 280-850 nm present inside the most common photosynthetic bacteria. The idea of modularity led us to think a multi-plate LED system shaped in the form of annuli, with mosaic of circuit boards arranged in a pie-chart shape. This simulator is capable to reproduce the spectra of main sequence F, G, K and M stars as well as the most common commercial lamps within its wavelength intervals. The control system is composed by a Laptop which controls a LED box and an STS-VIS spectrograph from Ocean Optics with cosine corrector. The first system generate the best fit of the input spectrum and give informations to the simulator on how to reproduce it. The spectrometer has the task to control the goodness of the fit and, by means of a closed loop system, to adjust it tuning the LED's power in real time. The stellar simulator has been subjected to several tests. The power emanated from the radiation source has been estimated to be 106.22 W while the thermal power has been calculated to be 434.05 W. The stellar simulator has been characterized in flux, analyzing the radiation at different distances from the device, from the exit of the source up to 25 cm. Then uniformity measurements have been done, analyzing the flux on a distance of 6.5 cm from the centre. Finally, I calculated the absorption of the optics of the radiation source analyzing the spectra coming out from the stellar simulator and compared it with respect to the spectrum of the single LEDs. In order to lodge the bacteria a new concept incubator has been built, composed of a stainless steel cell and our wedged optical windows that opens on the lateral surface. Two windows are 1" Round Wedge Prisms, with 2° Beam Deviation, and AR Coating: 650 - 1050 nm from Thorlabs. The other two windows are 1" Round Wedge Prisms, with 2° Beam Deviation without Coating. The windows were projected to test the gas concentration inside the closed cell by means of a TDLAS (Tunable Diode Laser Absorption Spectroscopy) system and the channels used are two: one for oxygen and one for carbon dioxide. The cell has been characterized in void and oxygen and carbon dioxide detecting limits. We filled the cell with a 84.3% N and 15.7% CO₂ gas mixture and revealed an O₂ concentration of 1.45×10^{-4} with a sigma 1.79×10^{-5} as well a CO₂ concentration of 0.0498 with a sigma 7.057×10^{-4} . The same data for the air are an O₂ concentration of 4.23×10^{-4} with a sigma 1.44×10^{-5} and a CO₂ concentration of 5.72×10^{-4} with a sigma 3.12×10^{-5} . The results are 1% for O₂ and 54 ppm for CO₂. The bacteria incubator has been tested even from the thermal point of view. Once thoroughly tested the hardware we tried to find, among all the photosynthetic bacteria, the best. The two bacteria chosen for this task were *Chlorogloeopsis fritschii* and *Cyanobacterium aponinum*. The first is known to be able to change its photosynthetic apparatus to cope with new radiation conditions. In particular is capable to generate chlorophyll d and f if exposed to NIR light (720 nm). This feature is called FarLip acclimation. The second bacterium is a well known bacterium but no one has ever tried to understand if it has the same capability. Efforts have been done in order to find the best culture medium and the best growth conditions of temperature and pH. Bacteria have been grown in white light conditions at for 24 days at 20 $\mu\text{mol photons/m}^2/\text{s}$ and at 30°C in order to understand the growth times and the behaviour in optimal conditions. The growth curves have evidenced a quicker growth of *Cyanobacterium aponinum* with respect to *Chlorogloeopsis fritschii* that in comparison have a longer lag phase time. After that, a new growth experiment have been performed by growing both cyanobacteria species at 30°C and 20 $\mu\text{mol photons/m}^2/\text{s}$ and oxymetric measurements have been done after 6 days from the culture start, thus during their exponential growth phases. The results for *Chlorogloeopsis fritschii*, taken from two different samples and grown in white light conditions have highlighted a mean O₂ production of

$224.45 \frac{\mu\text{mol O}_2}{\text{mg Chl} \cdot \text{h}}$ while results for *Cyanobacterium aponinum* have shown the total O₂ production of $174.41 \frac{\mu\text{mol O}_2}{\text{mg Chl} \cdot \text{h}}$. Then, for the main part of the experiment, eight samples have been used. Two samples of *Cyanobacterium aponinum* have been grown at 20 μmol photons/m²/s in white light for 6 days and then at 100 μmol photons/m²/s for the residual 3 days in white light. Two samples of *Chlorogloeopsis fritschii* have been grown at 20 μmol photons/m²/s for 6 days in white light and then at 100 μmol photons/m²/s for the residual 3 days in white light. Two samples of *Cyanobacterium aponinum* have been grown at 20 μmol photons/m²/s for 6 days in white light and then at 100 μmol photons/m²/s for the residual 3 days using the radiation spectrum of an M7 type star. Two samples of *Chlorogloeopsis fritschii* have been grown at 20 μmol photons/m²/s for 6 days in white light and then at 100 μmol photons/m²/s for the residual 3 days using the radiation spectrum of an M7 type star. The choice to use white light at 20 μmol photons/m²/s for the first 6 days and then a radiation dose of 100 μmol photons/m²/s for the next 3 days was made in order to compare the same initial common growth conditions with the different radiation conditions for the next 3 days, but keeping the number of photons the same: 100 μmol photons/m²/s in white light in one case and 100 μmol photons/m²/s of M7 light in the second case. During this part of the experiment bacteria irradiated with the M7 radiation have been put under the stellar simulator and let grow, while a spectrometer was monitoring the correct input spectrum to remain constant. The temperature has been kept at 30°C for the samples not exposed to M7 light and at a temperature oscillating from 35°C to 38°C for the samples exposed to M7 light. The higher environmental temperature under the stellar simulator has been due to the over-heating of the LEDs. During the 3 days of different exposure measurements of optical density have been done in order to collect data about the different growth curves. Moreover, O₂ production have been calculated for each sample. A mean O₂ production of $80.1065 \frac{\mu\text{mol O}_2}{\text{mg Chl} \cdot \text{h}}$ has been found for *Chlorogloeopsis fritschii* grown for 48 h in M7 radiation conditions with respect to samples grown in white light conditions (both at 100 μmol photons/m²/s) that were $79.572 \frac{\mu\text{mol O}_2}{\text{mg Chl} \cdot \text{h}}$. The same measurements for *Cyanobacterium aponinum* give $70.525 \frac{\mu\text{mol O}_2}{\text{mg Chl} \cdot \text{h}}$ and $43.944 \frac{\mu\text{mol O}_2}{\text{mg Chl} \cdot \text{h}}$. These data compared with the growth curves in different light conditions shows that while *Chlorogloeopsis fritschii* is able to respond very well to the change from white light to M7 light, and continue to grow even at in different light conditions, confirming our hypothesis that cyanobacteria with FarLip properties could also exploit M-star light), *Cyanobacterium aponinum* suffers the new type of radiation and increase its cellular respiration decreasing the total oxygen production, as can be well seen in table 8.16 comparing net and total oxygen production. Finally, a chromatic response have been done, in order to understand if the colour would reflect the vitality of the bacteria. For the future experiments the bacteria will be lodged inside the environmental chamber in order to modulate even the gaseous mixture and temperature. Moreover, this radiation source, improved and sharpened could be useful to build a database of organisms capable to resist in different planetary conditions. Another proposal for future works is to understand if the feature of the "red edge" and pigmentation could be influenced by the extended undergoing to a radiation spectrum different from the Sun's one. This can be done growing organisms in different light conditions and studying the different reflectance spectra of the pigments developed and present inside them. Other than these two bacteria other photosynthetizers could be used, in particular the moss *Physcomitrella patens* that is the direct link between aquatic and land plants. Using these data we will give new light to the understanding of the "colors" that photosynthetic organisms could show and how these feature can impact on the biomarker panorama. Finally, chirality of organisms could be detected inside the reflectance spectra of the samples and compared with the absence of this feature in non-photosynthetic organisms.

APPENDIX A: Publications and conference papers

R.Claudi; M.S.Erculiani, E.Giro, M. D'alessandro, G.Galletta, D.Billi, E.Pace, G.Piccioni, A.Ciaravella "ATMOSPHERES IN A TEST TUBE", EPSC 2013, London:

R. Claudi, M.S.Erculiani , "ATMOSPHERE IN A TEST TUBE", EChO ITALIAN SCIENCE GROUP MEETING, PALERMO, 2013

Erculiani, Marco S.; Claudi, Riccardo U.; Giro, Enrico; Galletta, Giuseppe; D'Alessandro, Maurizio; Farisato, Giancarlo; Lessio, Luigi; Micela, Giuseppina; Billi, Daniela , "Interpreting EChO's future data: biological laboratory estimates under M star's planetary surface conditions", Proceedings of the SPIE, Volume 9143, id. 914355 12 pp. (2014)

Claudi,R., Benatti, S., Bonavita, M, Erculiani, M.,S., Garrido Rubio, A., Corvino, E., Maggio, A., Poretti, E., Micela, G., Gratton, R. , Pagano I. & the GAPS board, "SEARCH FOR SPECTRAL FEATURES IN TRANSITING PLANETS WITH THE GAPS PROJECT", 'Search for life beyond the Solar System - Exoplanets, Biosignatures & Instruments', Tucson, 2014, R.

Erculiani, M. S.; Claudi, R. U.; Lessio, L.; Farisato, G.; Giro, E.; Cocola, L.; Billi, D.; D'alessandro, M.; Pace, E.; Schierano, D.; Benatti, S.; Bonavita, M.; Galletta, G., "Laboratory investigation on super-Earths atmospheres", European Planetary Science Congress 2014, EPSC Abstracts, Vol. 9, id. EPSC2014-691

Schierano,D.,Baqué, M., Billi, D. Pace, E., Cestelli Guidi, M., Claudi, R., Verseux, C., Erculiani, M.S., "Biosignature Characterization: from Lab to Space" 40th COSPAR Scientific Assembly, Moscow, Russia; 08/2014

Claudi, R.U., Erculiani, M.S., Micela, G., D'Alessandro, M., Galletta, G., Giro, E., Adriani, A., Altieri, F., Bellucci, G., Billi,D.,Gilli,G., Giuranna, M., Grassi, D., Leto, G., Pace, E., Palumbo, M.E., Piccioni, G., Scuderi, S., Strazzulla, G., Turrini,D., "Preparing EChO space mission: laboratory simulation of planetary atmospheres", Proceedings of the SPIE, Volume 9143, id. 91432U 11 pp. (2014)

Claudi, R.; Erculiani, M. S.; Galletta, G.; Billi, D.; Pace, E.; Schierano, D.; Giro, E.; D'Alessandro, M., : "Simulating super earth atmospheres in the laboratory", International Journal of Astrobiology, Volume 15, Issue 1, pp. 35-44

Erculiani, M.S., Claudi, R., Cocola, L., Giro, E., La Rocca, N., Morosinotto, T., Poletto, L., Billi D., Barbisan, .D, Bonato, M., D'Alessandro, M., Galletta, G., Meneghini, M., Trivellin, N., Pace, E., Cestelli Guidi, M., Schierano, D., Micela,G., "Atmospheres in a test tube: state of the art at the Astronomical Observatory of Padova", XII Congresso Nazionale di Scienze Planetarie, Bormio, Italy; 02/2015

Claudi, R., Pace, E., Ciaravella, A., Micela, G., Piccioni, G., Billi,D., Cestelli Guidi,M., Cocola,L., Erculiani,M.S.,Fedel, M., Galletta, G., Giro,E., La Rocca, N., Morosinotto, T., Poletto,L., Schierano,D., Stefani,S., "ATMOSPHERE IN A TEST TUBE", The Astrobiology Science Conference 2015 (AbSciCon2015), Chicago, Illinois; 06/2015

Claudi, R., Pace, E., Erculiani,M.S., Ciaravella,A., Galletta,G., LaRocca, N., Micela, G., Morosinotto,T., Piccioni, G., Billi,D., "Atmosphere in a test tube", Pathways 2015: Pathways Towards Habitable Planets, Bern; 07/2015

Erculiani,M.S., Claudi, R., Barbisan, D., Giro E., Bonato M., Cocola L., Farisato G., Meneghini M., Poletto L., Salasnich B., Trivellin N., "A tunable integrated system to simulate colder stellar radiation", Proc. SPIE 9626, Optical Systems Design 2015: Optical Design and Engineering VI, 96262D (September 23, 2015); doi:10.1117/12.2189053

APPENDIX B: Software codes

Hereafter will be attached the program mono.pro that need to calculate the best fit of the spectrum by means of the 25 LED palette.

```
; *****
; *****

pro stellegi0

openw, outfile0, 'G0rv.txt', /get_lun ;Open the file to put results in
openw, outfile1, 'G0rg.txt', /get_lun ;Open the file to put results in
openw, outfile2, 'G0mg.txt', /get_lun ;Open the file to put results in
openw, outfile3, 'G0maxg.txt', /get_lun ;Open the file to put results in
openw, outfile4, 'G0em.txt', /get_lun ;Open the file to put results in

n_classi=1 ; Spectral classes considered

tipo_spett=strarr(n_classi)
Teff=dblarr(n_classi) ;Effective temperature
Lum=dblarr(n_classi) ;Luminosity
Magass=dblarr(n_classi); Magnitude

tipo_spett[0]="g0"
Teff[0]=5900.0d
magass[0]=4.4d
Lum[0]=10.0d^(((4.7-magass[0])/2.5d))

READCOL, '5900.txt', lambda, G0, FORMAT='d,d'

zerolambda=where(lambda LT 3.4060570e-007, nzerolambda)
if (nzerolambda ge 1) then G0(zerolambda)=0.0D

zerolambda=where(lambda gT 1.0323100e-006, nzerolambda)
if (nzerolambda ge 1) then G0(zerolambda)=0.0D

; *****
; *****
; *****HABITABLE DISTANCES DETERMINATION (Kopparapu et al.,
2014) *****

; recent venus

Seff_s0=1.7753d
a0=1.4316d*10.0d^(-4.0d)
b0=2.9875d*10.0d^(-9.0d)
c0=-7.5702d*10.0d^(-12.0d)
d0=-1.1635d*10.0d^(-15.0d)

; *****
; to calculate the 5 topic distances use n_black_body=1 and these coefficients

; runaway greenhouse

Seff_s1=[1.0512d]
a1=[1.3242d*10.0d^(-4.0d)]
b1=[1.5418d*10.0d^(-8.0d)]
c1=[-7.9895d*10.0d^(-12.0d)]
d1=[-1.8328d*10.0d^(-15.0d)]

; moist greenhouse
;
Seff_s2=[1.0140d]
a2=[8.1774d*10.0d^(-5.0d)]
b2=[1.7063d*10.0d^(-9.0d)]
c2=[-4.3241d*10.0d^(-12.0d)]
d2=[-6.6462d*10.0d^(-16.0d)]
```

```

;maximum greenhouse

Seff_s3=[0.3438d]
a3=[5.8942d*10.0d^(-5.0d)]
b3=[1.6558d*10.0d^(-9.0d)]
c3=[-3.0045d*10.0d^(-12.0d)]
d3=[-5.2983d*10.0d^(-16.0d)]

;early mars

Seff_s4=[0.3179d]
a4=[5.4513d*10.0d^(-5.0d)]
b4=[1.5313d*10.0d^(-9.0d)]
c4=[-2.7786d*10.0d^(-12.0d)]
d4=[-4.8997d*10.0d^(-16.0d)]
;*****

Ts=Teff-5780.0d ;[K]
Lsol=1.0d ;[solar luminosities]
n=0

Seff0=Seff_s0+a0*Ts+b0*Ts^(2.0d)+c0*Ts^(3.0d)+d0*Ts^(4.0d) ;calculate Seff
Seff1=Seff_s1+a1*Ts+b1*Ts^(2.0d)+c1*Ts^(3.0d)+d1*Ts^(4.0d) ;calculate Seff
Seff2=Seff_s2+a2*Ts+b2*Ts^(2.0d)+c2*Ts^(3.0d)+d2*Ts^(4.0d) ;calculate Seff
Seff3=Seff_s3+a3*Ts+b3*Ts^(2.0d)+c3*Ts^(3.0d)+d3*Ts^(4.0d) ;calculate Seff
Seff4=Seff_s4+a4*Ts+b4*Ts^(2.0d)+c4*Ts^(3.0d)+d4*Ts^(4.0d) ;calculate Seff

Dist0=((Lum/Lsol)/Seff0)^0.5d ;[AU]
Dist1=((Lum/Lsol)/Seff1)^0.5d ;[AU]
Dist2=((Lum/Lsol)/Seff2)^0.5d ;[AU]
Dist3=((Lum/Lsol)/Seff3)^0.5d ;[AU]
Dist4=((Lum/Lsol)/Seff4)^0.5d ;[AU]

;*****
***
;*****constants*****
h=6.6262e-34 ; [J*s] Planck's constant
c=299792458.0d ;[m/s] speed of light
k=1.3806488d*10.0d^(-23.0d) ; [J/K] Boltzmann's constant
sigma=5.67037321d*(10.0d^(-8.0d)) ; W*m^-2*K^-4 Stefan-Boltzmann's constant

;*****define lambda*****

val_min=10.0d^(-50.0d)
val_max=10.0d*10.0d^(-6.0d)
n_elem=100000.0d
lambda=val_min + findgen(n_elem)*((val_max-val_min)/(n_elem - 1.0d)) ;[m]
nu=c/lambda; s^-1

;****multiply the spectrum with a the transmission of the atmosphere*****

readcol, 'spettroatminlambdametrilr.txt', lambda, trasmissione, format='d,d' ; read the
atmospheric transmittance spectrum

costspetro=trasmissione ;define a constant
;*****
;*****define the spectral radiation*****

BG0_nu=G0*costspetro ;multiply the spectrum with a the transmission of the atmosphere

;**find the stellar fluxes*****
F_s0=BG0_nu ;stellar fluxes of stars going out from them [W/m^2/mincron]

;*****define the stellar luminosities in [W]*****

Lumwatt0=Lum[0]*3.846d*(10.0d^(26.0d));[W] ;evaluate the stellar luminosity in W

```

```

;*****
;****calculate the stellar radia*****

R_S_0=sqrt(Lumwatt0/(4.0d*pi*sigma*(Teff[0]^4.0d)); [m]
R_S_1=695800000.0d ; [m]

;**calculate the stellar fluxes at the 5 different habitability distances*****
;**for all the stellar classes*****

F_out_atmG0rv=((R_s_0/(dist0[0]*149597870691.0d))^2.0d)*F_s0; flux at Recent Venus
distance [W/m^2/mincron]
F_out_atmG0rg=((R_s_0/(Dist1[0]*149597870691.0d))^2.0d)*F_s0; flux at Runaway Greenhouse
distance [W/m^2/mincron]
F_out_atmG0mg=((R_s_0/(Dist2[0]*149597870691.0d))^2.0d)*F_s0; flux at Moist Greenhouse
distance [W/m^2/mincron]
F_out_atmG0maxg=((R_s_0/(Dist3[0]*149597870691.0d))^2.0d)*F_s0; flux at MAXimum
Greenhouse distance [W/m^2/mincron]
F_out_atmG0em=((R_s_0/(Dist4[0]*149597870691.0d))^2.0d)*F_s0; flux at Early Mard distance
[W/m^2/mincron]

F_black_body_matrix0=DBLARR(n_elements(F_out_atmG0rv),1)
F_black_body_matrix1=DBLARR(n_elements(F_out_atmG0rg),1)
F_black_body_matrix2=DBLARR(n_elements(F_out_atmG0mg),1)
F_black_body_matrix3=DBLARR(n_elements(F_out_atmG0maxg),1)
F_black_body_matrix4=DBLARR(n_elements(F_out_atmG0em),1)

F_black_body_matrix0=F_out_atmG0rv
F_black_body_matrix1=F_out_atmG0rg ;enable if using n_black_body=2
F_black_body_matrix2=F_out_atmG0mg ;enable if using n_black_body=3
F_black_body_matrix3=F_out_atmG0maxg ;enable if using n_black_body=4
F_black_body_matrix4=F_out_atmG0em ;enable if using n_black_body=5

;*****
;***define the scaling factor LEDs should be divided for*****

area=(13.0/2.0d)*0.01d
distanzacm=10.0d
ymax=1478.14894d
areacella=(!pi*area^(2.0d))/((1478.14894d -127.37929d*distanzacm
+3.32587d*distanzacm^(2.0d) + 0.01817d*distanzacm^(3.0d) -0.00133d*distanzacm^(4.0d
))/ymax)

;*****LEDS*****
*

LCF0=0.91800966d ;Led Correction Factor, is the utile LED radiation available (0.1=10%,
0.2=20% etc...)
LCF1=0.34465102d
LCF2=0.59544908d
LCF3=0.49060877d
LCF4=0.53026662d
LCF5=0.60118495d
LCF6=0.51217251d
LCF7=0.57260527d
LCF8=0.58620316d
LCF9=0.59412648d
LCF10=0.37200444d
LCF11=0.42108478d
LCF12=0.64459006d
LCF13= 0.55912445d
LCF14=0.46674277d
LCF15=0.46843271d
LCF16=0.48564362d
LCF17=0.65055179d
LCF18=0.39245436d
LCF19=0.52026033d
LCF20=0.89392847d

```

```
LCF21=0.55337871d
LCF22=0.55337871d
LCF23=0.55337871d
LCF24=0.55337871d
```

```
READCOL, '365nm@700 mAh_smooth.txt', lambdaled1, units1TAB, FORMAT='d,d' ;read LED file
lambdaled1c=lambdaled1*10.0^(-9.0d); put lambda in [m]
c365= (LCF0*10.0d^(-3.0d)*interpol(units1TAB,lambdaled1c,
lambda)/areacella);[W/micron/m^2]
```

```
READCOL, '380nm@700 mAh_smooth.txt', lambdaled2, units2TAB, FORMAT='d,d'
lambdaled2c=lambdaled2*10.0^(-9.0d)
c380= (LCF1*10.0d^(-3.0d)*interpol(units2TAB,lambdaled2c, lambda)/areacella)
```

```
READCOL, '400nm@700 mAh_smooth.txt', lambdaled3, units3TAB, FORMAT='d,d'
lambdaled3c=lambdaled3*10.0^(-9.0d)
c400= (LCF2*10.0d^(-3.0d)*interpol(units3TAB,lambdaled3c, lambda)/areacella)
```

```
READCOL, '420nm@700 mAh_smooth.txt', lambdaled4, units4TAB, FORMAT='d,d'
lambdaled4c=lambdaled4*10.0^(-9.0d)
c420= (LCF3*10.0d^(-3.0d)*interpol(units4TAB,lambdaled4c, lambda)/areacella)
```

```
READCOL, '447.5nm@700 mAh_smooth.txt', lambdaled5, units5TAB, FORMAT='d,d'
lambdaled5c=lambdaled5*10.0^(-9.0d)
c4475= (LCF4*10.0d^(-3.0d)*interpol(units5TAB,lambdaled5c, lambda)/areacella)
```

```
READCOL, '470nm@700 mAh_smooth.txt', lambdaled6, units6TAB, FORMAT='d,d'
lambdaled6c=lambdaled6*10.0^(-9.0d)
c470= (LCF5*10.0d^(-3.0d)*interpol(units6TAB,lambdaled6c, lambda)/areacella)
```

```
READCOL, '485nm@700 mAh_smooth.txt', lambdaled7, units7TAB, FORMAT='d,d'
lambdaled7c=lambdaled7*10.0^(-9.0d)
c485= (LCF6*10.0d^(-3.0d)*interpol(units7TAB,lambdaled7c, lambda)/areacella)
```

```
READCOL, '505nm@700 mAh_smooth.txt', lambdaled8, units8TAB, FORMAT='d,d'
lambdaled8c=lambdaled8*10.0^(-9.0d)
c505= (LCF7*10.0d^(-3.0d)*interpol(units8TAB,lambdaled8c, lambda)/areacella)
```

```
READCOL, '530nm@700 mAh_smooth.txt', lambdaled9, units9TAB, FORMAT='d,d'
lambdaled9c=lambdaled9*10.0^(-9.0d)
c530= (LCF8*10.0d^(-3.0d)*interpol(units9TAB,lambdaled9c, lambda)/areacella)
```

```
READCOL, '567.5nm@700 mAh_smooth.txt', lambdaled10, units10TAB, FORMAT='d,d'
lambdaled10c=lambdaled10*10.0^(-9.0d)
c5675= (LCF9*10.0d^(-3.0d)*interpol(units10TAB,lambdaled10c, lambda)/areacella)
```

```
READCOL, '590nm@700 mAh_smooth.txt', lambdaled11, units11TAB, FORMAT='d,d'
lambdaled11c=lambdaled11*10.0^(-9.0d)
c590= (LCF10*10.0d^(-3.0d)*interpol(units11TAB,lambdaled11c, lambda)/areacella)
```

```
READCOL, '627nm@700 mAh_smooth.txt', lambdaled12, units12TAB, FORMAT='d,d'
lambdaled12c=lambdaled12*10.0^(-9.0d)
c627= (LCF11*10.0d^(-3.0d)*interpol(units12TAB,lambdaled12c, lambda)/areacella)
```

```
READCOL, 'cold white@700mAh_smooth.txt', lambdaled13, units13TAB, FORMAT='d,d'
lambdaled13c=lambdaled13*10.0^(-9.0d)
ccw= (LCF12*10.0d^(-3.0d)*interpol(units13TAB,lambdaled13c, lambda)/areacella)
```

```
READCOL, '665nm@700 mAh_smooth.txt', lambdaled14, units14TAB, FORMAT='d,d'
lambdaled14c=lambdaled14*10.0^(-9.0d)
c665= (LCF13*10.0d^(-3.0d)*interpol(units14TAB,lambdaled14c, lambda)/areacella)
```

```

READCOL, '680nm@700 mAh_smooth.txt', lambdaled15, units15TAB, FORMAT='d,d'
lambdaled15c=lambdaled15*10.0^(-9.0d)
c680= (LCF14*10.0d^(-3.0d))*interpol(units15TAB,lambdaled15c, lambda)/areacella

READCOL, '700nm@700 mAh_smooth.txt', lambdaled16, units16TAB, FORMAT='d,d'
lambdaled16c=lambdaled16*10.0^(-9.0d)
c700= (LCF15*10.0d^(-3.0d))*interpol(units16TAB,lambdaled16c, lambda)/areacella

READCOL, '720nm@700 mAh_smooth.txt', lambdaled17, units17TAB, FORMAT='d,d'
lambdaled17c=lambdaled17*10.0^(-9.0d)
c720= (LCF16*10.0d^(-3.0d))*interpol(units17TAB,lambdaled17c, lambda)/areacella

READCOL, '740nm@700 mAh_smooth.txt', lambdaled18, units18TAB, FORMAT='d,d'
lambdaled18c=lambdaled18*10.0^(-9.0d)
c740= (LCF17*10.0d^(-3.0d))*interpol(units18TAB,lambdaled18c, lambda)/areacella

READCOL, '760nm@700 mAh_smooth.txt', lambdaled19, units19TAB, FORMAT='d,d'
lambdaled19c=lambdaled19*10.0^(-9.0d)
c760= (LCF18*10.0d^(-3.0d))*interpol(units19TAB,lambdaled19c, lambda)/areacella

READCOL, '780nm@700 mAh_smooth.txt', lambdaled20, units20TAB, FORMAT='d,d'
lambdaled20c=lambdaled20*10.0^(-9.0d)
c780= (LCF19*10.0d^(-3.0d))*interpol(units20TAB,lambdaled20c, lambda)/areacella

READCOL, '810nm@700 mAh_smooth.txt', lambdaled21, units21TAB, FORMAT='d,d'
lambdaled21c=lambdaled21*10.0^(-9.0d)
c810= (LCF20*10.0d^(-3.0d))*interpol(units21TAB,lambdaled21c, lambda)/areacella

READCOL, '830nm@700 mAh_smooth.txt', lambdaled22, units22TAB, FORMAT='d,d'
lambdaled22c=lambdaled22*10.0^(-9.0d)
c830= (LCF21*10.0d^(-3.0d))*interpol(units22TAB,lambdaled22c, lambda)/areacella

READCOL, '850nm@700 mAh_smooth.txt', lambdaled23, units23TAB, FORMAT='d,d'
lambdaled23c=lambdaled23*10.0^(-9.0d)
c850= (LCF22*10.0d^(-3.0d))*interpol(units23TAB,lambdaled23c, lambda)/areacella

READCOL, '880nm@700 mAh_smooth.txt', lambdaled24, units24TAB, FORMAT='d,d'
lambdaled24c=lambdaled24*10.0^(-9.0d)
c880= (LCF23*10.0d^(-3.0d))*interpol(units24TAB,lambdaled24c, lambda)/areacella

READCOL, '940nm@700 mAh_smooth.txt', lambdaled25, units25TAB, FORMAT='d,d'
lambdaled25c=lambdaled25*10.0^(-9.0d)
c940= (LCF24*10.0d^(-3.0d))*interpol(units25TAB,lambdaled25c, lambda)/areacella

```

```

;*****load color palette*****

```

```

DEVICE, DECOMPOSE = 0
TVLct, 255, 255, 255
TVLct, 255, 255, 255, 0
TVLct, 0, 0, 0, 1
TVLct, 255, 0, 0, 2
TVLct, 0, 255, 0, 3
TVLct, 0, 0, 255, 4
TVLct, 156, 138, 165, 5
TVLct, 155, 120, 80, 6
TVLct, 0, 130, 60, 7
TVLct, 85, 0, 200, 8
TVLct, 111, 38, 65, 9
tvlct, 50, 200, 0, 10 ; (dark green)
tvlct, 150, 150, 150, 11 ; (dark grigio)
tvlct, 200, 200, 200, 12 ; (light grigio)
tvlct, 255, 255, 255, 13 ; white
TVLct, 255, 194, 0, 14
TVLct, 139, 0, 0, 15
TVLct, 139, 35, 35, 16
TVLct, 238, 130, 238, 17
TVLct, 113, 0, 255, 18
TVLct, 248, 0, 211, 19

```

```

tv1ct,48,150,100, 20
tv1ct,200,148,150, 21
tv1ct,11,80,211, 22
tv1ct,60,15,130, 23
tv1ct,200,100,10, 24
tv1ct,110,89,111, 25

;*****trim LED spectra after interpolation with lambda
vector*****
;
bad=where(finite(c380) eq 0, nbad)
  if (nbad ge 1) then c380(bad)=0.0D

bad=where(finite(c400) eq 0, nbad)
  if (nbad ge 1) then c400(bad)=0.0D

bad=where(finite(c420) eq 0, nbad)
  if (nbad ge 1) then c420(bad)=0.0D

bad=where(finite(c4475) eq 0, nbad)
  if (nbad ge 1) then Y3(c4475)=0.0D

bad=where(finite(c470) eq 0, nbad)
  if (nbad ge 1) then c470(bad)=0.0D

bad=where(finite(c485) eq 0, nbad)
  if (nbad ge 1) then c485(bad)=0.0D

bad=where(finite(c505) eq 0, nbad)
  if (nbad ge 1) then c505(bad)=0.0D

bad=where(finite(c530) eq 0, nbad)
  if (nbad ge 1) then c530(bad)=0.0D

bad=where(finite(c5675) eq 0, nbad)
  if (nbad ge 1) then c5675(bad)=0.0D

bad=where(finite(c590) eq 0, nbad)
  if (nbad ge 1) then c590(bad)=0.0D

bad=where(finite(c627) eq 0, nbad)
  if (nbad ge 1) then c627(bad)=0.0D

bad=where(finite(ccw) eq 0, nbad)
  if (nbad ge 1) then ccw(bad)=0.0D

bad=where(finite(c665) eq 0, nbad)
  if (nbad ge 1) then c665(bad)=0.0D

bad=where(finite(c680) eq 0, nbad)
  if (nbad ge 1) then c680(bad)=0.0D

bad=where(finite(c700) eq 0, nbad)
  if (nbad ge 1) then c665(bad)=0.0D

  bad=where(finite(c720) eq 0, nbad)
  if (nbad ge 1) then c720(bad)=0.0D

bad=where(finite(c740) eq 0, nbad)
  if (nbad ge 1) then c740(bad)=0.0D

bad=where(finite(c760) eq 0, nbad)
  if (nbad ge 1) then c760(bad)=0.0D

  bad=where(finite(c780) eq 0, nbad)
  if (nbad ge 1) then c780(bad)=0.0D

bad=where(finite(c810) eq 0, nbad)
  if (nbad ge 1) then c810(bad)=0.0D

```



```

bad=where(finite(c830) eq 0, nbad)
if (nbad ge 1) then c830(bad)=0.0D

bad=where(finite(c850) eq 0, nbad)
if (nbad ge 1) then c850(bad)=0.0D

bad=where(finite(c880) eq 0, nbad)
if (nbad ge 1) then c880(bad)=0.0D

bad=where(finite(c940) eq 0, nbad)
if (nbad ge 1) then c940(bad)=0.0D

;*****

zero=where(c365 LT 0.00d, nzero)
if (nzero ge 1) then c365(zero)=0.0D

zerolambda=where(lambda LT min(lambdaled1c), nzerolambda)
if (nzerolambda ge 1) then c365(zerolambda)=0.0D

zerolambda=where(lambda GT max(lambdaled1c), nzerolambda)
if (nzerolambda ge 1) then c365(zerolambda)=0.0D

zero=where(c380 LT 0.00d, nzero)
if (nzero ge 1) then c380(zero)=0.0D

zerolambda=where(lambda LT min(lambdaled2c), nzerolambda)
if (nzerolambda ge 1) then c380(zerolambda)=0.0D

zerolambda=where(lambda GT max(lambdaled2c), nzerolambda)
if (nzerolambda ge 1) then c380(zerolambda)=0.0D

zero=where(c400 LT 0.00d, nzero)
if (nzero ge 1) then c400(zero)=0.0D

zerolambda=where(lambda LT min(lambdaled3c), nzerolambda)
if (nzerolambda ge 1) then c400(zerolambda)=0.0D

zerolambda=where(lambda GT max(lambdaled3c), nzerolambda)
if (nzerolambda ge 1) then c400(zerolambda)=0.0D

zero=where(c420 LT 0.0d, nzero)
if (nzero ge 1) then c420(zero)=0.0D

zerolambda=where(lambda LT min(lambdaled4c), nzerolambda)
if (nzerolambda ge 1) then c420(zerolambda)=0.0D

zerolambda=where(lambda GT max(lambdaled4c), nzerolambda)
if (nzerolambda ge 1) then c420(zerolambda)=0.0D

zero=where(c4475 LT 0.0d, nzero)
if (nzero ge 1) then c4475(zero)=0.0D

zerolambda=where(lambda LT min(lambdaled5c), nzerolambda)
if (nzerolambda ge 1) then c4475(zerolambda)=0.0D

zerolambda=where(lambda GT max(lambdaled5c), nzerolambda)
if (nzerolambda ge 1) then c4475(zerolambda)=0.0D

zero=where(c470 LT 0.0d, nzero)
if (nzero ge 1) then c470(zero)=0.0D

```

```

zerolambda=where(lambda LT min(lambdaled6c), nzerolambda)
if (nzerolambda ge 1) then c470(zerolambda)=0.0D

zerolambda=where(lambda GT max(lambdaled6c), nzerolambda)
if (nzerolambda ge 1) then c470(zerolambda)=0.0D

zero=where(c485 LT 0.0d, nzero)
if (nzero ge 1) then c485(zero)=0.0D

zerolambda=where(lambda LT min(lambdaled7c), nzerolambda)
if (nzerolambda ge 1) then c485(zerolambda)=0.0D

zerolambda=where(lambda GT max(lambdaled7c), nzerolambda)
if (nzerolambda ge 1) then c485(zerolambda)=0.0D

zero=where(c505 LT 0.0d, nzero)
if (nzero ge 1) then c505(zero)=0.0D

zerolambda=where(lambda LT min(lambdaled8c), nzerolambda)
if (nzerolambda ge 1) then c505(zerolambda)=0.0D

zerolambda=where(lambda GT max(lambdaled8c), nzerolambda)
if (nzerolambda ge 1) then c505(zerolambda)=0.0D

zero=where(c530 LT 0.0d, nzero)
if (nzero ge 1) then c530(zero)=0.0D

zerolambda=where(lambda LT min(lambdaled9c), nzerolambda)
if (nzerolambda ge 1) then c530(zerolambda)=0.0D

zerolambda=where(lambda GT max(lambdaled9c), nzerolambda)
if (nzerolambda ge 1) then c530(zerolambda)=0.0D

zero=where(c5675 LT 0.0d, nzero)
if (nzero ge 1) then c5675(zero)=0.0D

zerolambda=where(lambda LT min(lambdaled10c), nzerolambda)
if (nzerolambda ge 1) then c5675(zerolambda)=0.0D

zerolambda=where(lambda GT max(lambdaled10c), nzerolambda)
if (nzerolambda ge 1) then c5675(zerolambda)=0.0D

zero=where(c590 LT 0.0d, nzero)
if (nzero ge 1) then c590(zero)=0.0D

zerolambda=where(lambda LT min(lambdaled11c), nzerolambda)
if (nzerolambda ge 1) then c590(zerolambda)=0.0D

zerolambda=where(lambda GT max(lambdaled11c), nzerolambda)
if (nzerolambda ge 1) then c590(zerolambda)=0.0D

zero=where(c627 LT 0.0d, nzero)
if (nzero ge 1) then c627(zero)=0.0D

zerolambda=where(lambda LT min(lambdaled12c), nzerolambda)
if (nzerolambda ge 1) then c627(zerolambda)=0.0D

zerolambda=where(lambda GT max(lambdaled12c), nzerolambda)
if (nzerolambda ge 1) then c627(zerolambda)=0.0D

zero=where(ccw LT 0.0d, nzero)
if (nzero ge 1) then ccw(zero)=0.0D

```

```

zerolambda=where(lambda LT min(lambdaled13c), nzerolambda)
if (nzerolambda ge 1) then ccw(zerolambda)=0.0D

zerolambda=where(lambda GT max(lambdaled13c), nzerolambda)
if (nzerolambda ge 1) then ccw(zerolambda)=0.0D

zero=where(c665 LT 0.0d, nzero)
if (nzero ge 1) then c665(zero)=0.0D

zerolambda=where(lambda LT min(lambdaled14c), nzerolambda)
if (nzerolambda ge 1) then c665(zerolambda)=0.0D

zerolambda=where(lambda GT max(lambdaled14c), nzerolambda)
if (nzerolambda ge 1) then c665(zerolambda)=0.0D

zero=where(c680 LT 0.0d, nzero)
if (nzero ge 1) then c680(zero)=0.0D

zerolambda=where(lambda LT min(lambdaled15c), nzerolambda)
if (nzerolambda ge 1) then c680(zerolambda)=0.0D

zerolambda=where(lambda GT max(lambdaled15c), nzerolambda)
if (nzerolambda ge 1) then c680(zerolambda)=0.0D

zero=where(c700 LT 0.0d, nzero)
if (nzero ge 1) then c700(zero)=0.0D

zerolambda=where(lambda LT min(lambdaled16c), nzerolambda)
if (nzerolambda ge 1) then c700(zerolambda)=0.0D

zerolambda=where(lambda GT max(lambdaled16c), nzerolambda)
if (nzerolambda ge 1) then c700(zerolambda)=0.0D

zero=where(c720 LT 0.0d, nzero)
if (nzero ge 1) then c720(zero)=0.0D

zerolambda=where(lambda LT min(lambdaled17c), nzerolambda)
if (nzerolambda ge 1) then c720(zerolambda)=0.0D

zerolambda=where(lambda GT max(lambdaled17c), nzerolambda)
if (nzerolambda ge 1) then c720(zerolambda)=0.0D

zero=where(c740 LT 0.0d, nzero)
if (nzero ge 1) then c740(zero)=0.0D

zerolambda=where(lambda LT min(lambdaled18c), nzerolambda)
if (nzerolambda ge 1) then c740(zerolambda)=0.0D

zerolambda=where(lambda GT max(lambdaled18c), nzerolambda)
if (nzerolambda ge 1) then c740(zerolambda)=0.0D

zero=where(c760 LT 0.0d, nzero)
if (nzero ge 1) then c760(zero)=0.0D

zerolambda=where(lambda LT min(lambdaled19c), nzerolambda)
if (nzerolambda ge 1) then c760(zerolambda)=0.0D

zerolambda=where(lambda GT max(lambdaled19c), nzerolambda)
if (nzerolambda ge 1) then c760(zerolambda)=0.0D

zero=where(c780 LT 0.0d, nzero)
if (nzero ge 1) then c780(zero)=0.0D

zerolambda=where(lambda LT min(lambdaled20c), nzerolambda)
if (nzerolambda ge 1) then c780(zerolambda)=0.0D

```

```

zerolambda=where(lambda gT max(lambdaled20c), nzerolambda)
if (nzerolambda ge 1) then c780(zerolambda)=0.0D

```

```

zero=where(c810 LT 0.0d, nzero)
if (nzero ge 1) then c810(zero)=0.0D

```

```

zerolambda=where(lambda LT min(lambdaled21c), nzerolambda)
if (nzerolambda ge 1) then c810(zerolambda)=0.0D

```

```

zerolambda=where(lambda gT max(lambdaled21c), nzerolambda)
if (nzerolambda ge 1) then c810(zerolambda)=0.0D

```

```

zero=where(c830 LT 0.0d, nzero)
if (nzero ge 1) then c830(zero)=0.0D

```

```

zerolambda=where(lambda LT min(lambdaled22c), nzerolambda)
if (nzerolambda ge 1) then c830(zerolambda)=0.0D

```

```

zerolambda=where(lambda gT max(lambdaled22c), nzerolambda)
if (nzerolambda ge 1) then c830(zerolambda)=0.0D

```

```

zero=where(c850 LT 0.0d, nzero)
if (nzero ge 1) then c850(zero)=0.0D

```

```

zerolambda=where(lambda LT min(lambdaled23c), nzerolambda)
if (nzerolambda ge 1) then c850(zerolambda)=0.0D

```

```

zerolambda=where(lambda gT max(lambdaled23c), nzerolambda)
if (nzerolambda ge 1) then c850(zerolambda)=0.0D

```

```

zero=where(c880 LT 0.0d, nzero)
if (nzero ge 1) then c880(zero)=0.0D

```

```

zerolambda=where(lambda LT min(lambdaled24c), nzerolambda)
if (nzerolambda ge 1) then c880(zerolambda)=0.0D

```

```

zerolambda=where(lambda gT max(lambdaled24c), nzerolambda)
if (nzerolambda ge 1) then c880(zerolambda)=0.0D

```

```

zero=where(c940 LT 0.0d, nzero)
if (nzero ge 1) then c940(zero)=0.0D

```

```

zerolambda=where(lambda LT min(lambdaled25c), nzerolambda)
if (nzerolambda ge 1) then c940(zerolambda)=0.0D

```

```

zerolambda=where(lambda gT max(lambdaled25c), nzerolambda)
if (nzerolambda ge 1) then c940(zerolambda)=0.0D

```

```

;*****Define LEDs peaks*****

```

```

lambda_peak=DBLARR(25L)

```

```

ok=where(c365 eq max(c365), n_ok)
IF n_ok EQ 0L THEN stop
IF n_ok EQ 1L THEN BEGIN
lambda_peak(0)=lambda(ok)
ENDIF ELSE BEGIN
lambda_peak(0)=mean(lambda(ok))
ENDELSE

```

```

ok=where(c380 eq max(c380), n_ok)
IF n_ok EQ 0L THEN stop
IF n_ok EQ 1L THEN BEGIN

```

```

lambda_peak(1)=lambda(ok)
ENDIF ELSE BEGIN
lambda_peak(1)=mean(lambda(ok))
ENDELSE

ok=where(c400 eq max(c400),n_ok)
IF n_ok EQ 0L THEN stop
IF n_ok EQ 1L THEN BEGIN
lambda_peak(2)=lambda(ok)
ENDIF ELSE BEGIN
lambda_peak(2)=mean(lambda(ok))
ENDELSE

ok=where(c420 eq max(c420),n_ok)
IF n_ok EQ 0L THEN stop
IF n_ok EQ 1L THEN BEGIN
lambda_peak(3)=lambda(ok)
ENDIF ELSE BEGIN
lambda_peak(3)=mean(lambda(ok))
ENDELSE

ok=where(c4475 eq max(c4475),n_ok)
IF n_ok EQ 0L THEN stop
IF n_ok EQ 1L THEN BEGIN
lambda_peak(4)=lambda(ok)
ENDIF ELSE BEGIN
lambda_peak(4)=mean(lambda(ok))
ENDELSE

ok=where(c470 eq max(c470),n_ok)
IF n_ok EQ 0L THEN stop
IF n_ok EQ 1L THEN BEGIN
lambda_peak(5)=lambda(ok)
ENDIF ELSE BEGIN
lambda_peak(5)=mean(lambda(ok))
ENDELSE

ok=where(c485 eq max(c485),n_ok)
IF n_ok EQ 0L THEN stop
IF n_ok EQ 1L THEN BEGIN
lambda_peak(6)=lambda(ok)
ENDIF ELSE BEGIN
lambda_peak(6)=mean(lambda(ok))
ENDELSE

ok=where(c505 eq max(c505),n_ok)
IF n_ok EQ 0L THEN stop
IF n_ok EQ 1L THEN BEGIN
lambda_peak(7)=lambda(ok)
ENDIF ELSE BEGIN
lambda_peak(7)=mean(lambda(ok))
ENDELSE

ok=where(c530 eq max(c530),n_ok)
IF n_ok EQ 0L THEN stop
IF n_ok EQ 1L THEN BEGIN
lambda_peak(8)=lambda(ok)
ENDIF ELSE BEGIN
lambda_peak(8)=mean(lambda(ok))
ENDELSE

ok=where(c5675 eq max(c5675),n_ok)
IF n_ok EQ 0L THEN stop
IF n_ok EQ 1L THEN BEGIN
lambda_peak(9)=lambda(ok)
ENDIF ELSE BEGIN
lambda_peak(9)=mean(lambda(ok))
ENDELSE

```

```

ok=where(c590 eq max(c590),n_ok)
IF n_ok EQ 0L THEN stop
IF n_ok EQ 1L THEN BEGIN
lambda_peak(10)=lambda(ok)
ENDIF ELSE BEGIN
lambda_peak(10)=mean(lambda(ok))
ENDELSE

```

```

ok=where(c627 eq max(c627),n_ok)
IF n_ok EQ 0L THEN stop
IF n_ok EQ 1L THEN BEGIN
lambda_peak(11)=lambda(ok)
ENDIF ELSE BEGIN
lambda_peak(11)=mean(lambda(ok))
ENDELSE

```

```

ok=where(ccw eq max(ccw),n_ok)
IF n_ok EQ 0L THEN stop
IF n_ok EQ 1L THEN BEGIN
lambda_peak(12)=lambda(ok)
ENDIF ELSE BEGIN
lambda_peak(12)=mean(lambda(ok))
ENDELSE

```

```

ok=where(c665 eq max(c665),n_ok)
IF n_ok EQ 0L THEN stop
IF n_ok EQ 1L THEN BEGIN
lambda_peak(13)=lambda(ok)
ENDIF ELSE BEGIN
lambda_peak(13)=mean(lambda(ok))
ENDELSE

```

```

ok=where(c680 eq max(c680),n_ok)
IF n_ok EQ 0L THEN stop
IF n_ok EQ 1L THEN BEGIN
lambda_peak(14)=lambda(ok)
ENDIF ELSE BEGIN
lambda_peak(14)=mean(lambda(ok))
ENDELSE

```

```

ok=where(c700 eq max(c700),n_ok)
IF n_ok EQ 0L THEN stop
IF n_ok EQ 1L THEN BEGIN
lambda_peak(15)=lambda(ok)
ENDIF ELSE BEGIN
lambda_peak(15)=mean(lambda(ok))
ENDELSE

```

```

ok=where(c720 eq max(c720),n_ok)
IF n_ok EQ 0L THEN stop
IF n_ok EQ 1L THEN BEGIN
lambda_peak(16)=lambda(ok)
ENDIF ELSE BEGIN
lambda_peak(16)=mean(lambda(ok))
ENDELSE

```

```

ok=where(c740 eq max(c740),n_ok)
IF n_ok EQ 0L THEN stop
IF n_ok EQ 1L THEN BEGIN
lambda_peak(17)=lambda(ok)
ENDIF ELSE BEGIN
lambda_peak(17)=mean(lambda(ok))
ENDELSE

```

```

ok=where(c760 eq max(c760),n_ok)
IF n_ok EQ 0L THEN stop
IF n_ok EQ 1L THEN BEGIN
lambda_peak(18)=lambda(ok)
ENDIF ELSE BEGIN
lambda_peak(18)=mean(lambda(ok))
ENDELSE

```

```

ok=where(c780 eq max(c780),n_ok)
IF n_ok EQ 0L THEN stop
IF n_ok EQ 1L THEN BEGIN
lambda_peak(19)=lambda(ok)
ENDIF ELSE BEGIN
lambda_peak(19)=mean(lambda(ok))
ENDELSE

```

```

ok=where(c810 eq max(c810),n_ok)
IF n_ok EQ 0L THEN stop
IF n_ok EQ 1L THEN BEGIN
lambda_peak(20)=lambda(ok)
ENDIF ELSE BEGIN
lambda_peak(20)=mean(lambda(ok))
ENDELSE

```

```

ok=where(c830 eq max(c830),n_ok)
IF n_ok EQ 0L THEN stop
IF n_ok EQ 1L THEN BEGIN
lambda_peak(21)=lambda(ok)
ENDIF ELSE BEGIN
lambda_peak(21)=mean(lambda(ok))
ENDELSE

```

```

ok=where(c850 eq max(c850),n_ok)
IF n_ok EQ 0L THEN stop
IF n_ok EQ 1L THEN BEGIN
lambda_peak(22)=lambda(ok)
ENDIF ELSE BEGIN
lambda_peak(22)=mean(lambda(ok))
ENDELSE

```

```

ok=where(c880 eq max(c880),n_ok)
IF n_ok EQ 0L THEN stop
IF n_ok EQ 1L THEN BEGIN
lambda_peak(23)=lambda(ok)
ENDIF ELSE BEGIN
lambda_peak(23)=mean(lambda(ok))
ENDELSE

```

```

ok=where(c940 eq max(c940),n_ok)
IF n_ok EQ 0L THEN stop
IF n_ok EQ 1L THEN BEGIN
lambda_peak(24)=lambda(ok)
ENDIF ELSE BEGIN
lambda_peak(24)=mean(lambda(ok))
ENDELSE

```

```

FOR i_k=0L, 1-1L DO BEGIN
;
; ;*****
;

```

```

F_black_body0=F_black_body_matrix0
F_black_body1=F_black_body_matrix1
F_black_body2=F_black_body_matrix2

```

```

F_black_body3=F_black_body_matrix3
F_black_body4=F_black_body_matrix4

;interpolate stellar spectra with lambda_peak

F_l_pi_2_0=interpol((F_black_body0)*1.0D, lambda, lambda_peak)
F_l_pi_2_1=interpol((F_black_body1)*1.0D, lambda, lambda_peak)
F_l_pi_2_2=interpol((F_black_body2)*1.0D, lambda, lambda_peak)
F_l_pi_2_3=interpol((F_black_body3)*1.0D, lambda, lambda_peak)
F_l_pi_2_4=interpol((F_black_body4)*1.0D, lambda, lambda_peak)

;definition of the coeddcients for regress function

x1=interpol([c365], lambda, lambda_peak)
x2=interpol([c380], lambda, lambda_peak)
x3=interpol([c400], lambda, lambda_peak)
x4=interpol([c420], lambda, lambda_peak)
x5=interpol([c4475], lambda, lambda_peak)
x6=interpol([c470], lambda, lambda_peak)
x7=interpol([c485], lambda, lambda_peak)
x8=interpol([c505], lambda, lambda_peak)
x9=interpol([c530], lambda, lambda_peak)
x10=interpol([c5675], lambda, lambda_peak)
x11=interpol([c590], lambda, lambda_peak)
x12=interpol([c627], lambda, lambda_peak)
x13=interpol([ccw], lambda, lambda_peak)
x14=interpol([c665], lambda, lambda_peak)
x15=interpol([c680], lambda, lambda_peak)
x16=interpol([c700], lambda, lambda_peak)
x17=interpol([c720], lambda, lambda_peak)
x18=interpol([c740], lambda, lambda_peak)
x19=interpol([c760], lambda, lambda_peak)
x20=interpol([c780], lambda, lambda_peak)
x21=interpol([c810], lambda, lambda_peak)
x22=interpol([c830], lambda, lambda_peak)
x23=interpol([c850], lambda, lambda_peak)
x24=interpol([c880], lambda, lambda_peak)
x25=interpol([c940], lambda, lambda_peak)

;definition of the stellar classes for the regress function

y0=F_l_pi_2_0
y1=F_l_pi_2_1
y2=F_l_pi_2_2
y3=F_l_pi_2_3
y4=F_l_pi_2_4

;number on LED slots

w=[1,1,1,1,1,1,1,1,1,1,1,1,1,1,1,1,1,1,1,1,1,1,1]

;definition of the "x" vector

x=[[x1(0),x2(0),x3(0),x4(0),x5(0),x6(0),x7(0),x8(0),x9(0),x10(0),x11(0),x12(0),x13(0),x14(0),
x15(0),x16(0),x17(0), x18(0), x19(0), x20(0), x21(0),x22(0), x23(0), x24(0), x25(0)],
$,
[x1(1),x2(1),x3(1),x4(1),x5(1),x6(1),x7(1),x8(1),x9(1),x10(1),x11(1),x12(1),x13(1),x14(1),
x15(1), x16(1), x17(1), x18(1), x19(1), x20(1), x21(1),x22(1), x23(1), x24(1), x25(1)],
$,
[x1(2),x2(2),x3(2),x4(2),x5(2),x6(2),x7(2),x8(2),x9(2),x10(2),x11(2),x12(2),x13(2),x14(2),
x15(2), x16(2), x17(2), x18(2), x19(2), x20(2), x21(2),x22(2), x23(2), x24(2), x25(2)],
$,
[x1(3),x2(3),x3(3),x4(3),x5(3),x6(3),x7(3),x8(3),x9(3),x10(3),x11(3),x12(3),x13(3),x14(3),
x15(3), x16(3), x17(3), x18(3), x19(3), x20(3), x21(3),x22(3), x23(3), x24(3), x25(3)],
$,
[x1(4),x2(4),x3(4),x4(4),x5(4),x6(4),x7(4),x8(4),x9(4),x10(4),x11(4),x12(4),x13(4),x14(4),
x15(4), x16(4), x17(4), x18(4), x19(4), x20(4), x21(4),x22(4), x23(4), x24(4), x25(4)],
$,
$]

```



```

[x1(5),x2(5),x3(5),x4(5),x5(5),x6(5),x7(5),x8(5),x9(5),x10(5),x11(5),x12(5),x13(5),x14(5)
,x15(5),x16(5),x17(5),x18(5),x19(5),x20(5),x21(5),x22(5),x23(5),x24(5),x25(5)],
$,
[x1(6),x2(6),x3(6),x4(6),x5(6),x6(6),x7(6),x8(6),x9(6),x10(6),x11(6),x12(6),x13(6),x14(6)
,x15(6),x16(6),x17(6),x18(6),x19(6),x20(6),x21(6),x22(6),x23(6),x24(6),x25(6)],
$,
[x1(7),x2(7),x3(7),x4(7),x5(7),x6(7),x7(7),x8(7),x9(7),x10(7),x11(7),x12(7),x13(7),x14(7)
,x15(7),x16(7),x17(7),x18(7),x19(7),x20(7),x21(7),x22(7),x23(7),x24(7),x25(7)],
$,
[x1(8),x2(8),x3(8),x4(8),x5(8),x6(8),x7(8),x8(8),x9(8),x10(8),x11(8),x12(8),x13(8),x14(8)
,x15(8),x16(8),x17(8),x18(8),x19(8),x20(8),x21(8),x22(8),x23(8),x24(8),x25(8)],
$,
[x1(9),x2(9),x3(9),x4(9),x5(9),x6(9),x7(9),x8(9),x9(9),x10(9),x11(9),x12(9),x13(9),x14(9)
,x15(9),x16(9),x17(9),x18(9),x19(9),x20(9),x21(9),x22(9),x23(9),x24(9),x25(9)],
$,
[x1(10),x2(10),x3(10),x4(10),x5(10),x6(10),x7(10),x8(10),x9(10),x10(10),x11(10),x12(10),x
13(10),x14(10),x15(10),x16(10),x17(10),x18(10),x19(10),x20(10),x21(10),x22(10),
x23(10),x24(10),x25(10)], $
[x1(11),x2(11),x3(11),x4(11),x5(11),x6(11),x7(11),x8(11),x9(11),x10(11),x11(11),x12(11),x
13(11),x14(11),x15(11),x16(11),x17(11),x18(11),x19(11),x20(11),x21(11),x22(11),
x23(11),x24(11),x25(11)], $
[x1(12),x2(12),x3(12),x4(12),x5(12),x6(12),x7(12),x8(12),x9(12),x10(12),x11(12),x12(12),x
13(12),x14(12),x15(12),x16(12),x17(12),x18(12),x19(12),x20(12),x21(12),x22(12),
x23(12),x24(12),x25(12)], $
[x1(13),x2(13),x3(13),x4(13),x5(13),x6(13),x7(13),x8(13),x9(13),x10(13),x11(13),x12(13),x
13(13),x14(13),x15(13),x16(13),x17(13),x18(13),x19(13),x20(13),x21(13),x22(13),
x23(13),x24(13),x25(13)], $
[x1(14),x2(14),x3(14),x4(14),x5(14),x6(14),x7(14),x8(14),x9(14),x10(14),x11(14),x12(14),x
13(14),x14(14),x15(14),x16(14),x17(14),x18(14),x19(14),x20(14),x21(14),x22(14),
x23(14),x24(14),x25(14)], $
[x1(15),x2(15),x3(15),x4(15),x5(15),x6(15),x7(15),x8(15),x9(15),x10(15),x11(15),x12(15),x
13(15),x14(15),x15(15),x16(15),x17(15),x18(15),x19(15),x20(15),x21(15),x22(15),
x23(15),x24(15),x25(15)], $
[x1(16),x2(16),x3(16),x4(16),x5(16),x6(16),x7(16),x8(16),x9(16),x10(16),x11(16),x12(16),x
13(16),x14(16),x15(16),x16(16),x17(16),x18(16),x19(16),x20(16),x21(16),x22(16),
x23(16),x24(16),x25(16)], $
[x1(17),x2(17),x3(17),x4(17),x5(17),x6(17),x7(17),x8(17),x9(17),x10(17),x11(17),x12(17),x
13(17),x14(17),x15(17),x16(17),x17(17),x18(17),x19(17),x20(17),x21(17),x22(17),
x23(17),x24(17),x25(17)], $
[x1(18),x2(18),x3(18),x4(18),x5(18),x6(18),x7(18),x8(18),x9(18),x10(18),x11(18),x12(18),x
13(18),x14(18),x15(18),x16(18),x17(18),x18(18),x19(18),x20(18),x21(18),x22(18),
x23(18),x24(18),x25(18)], $
[x1(19),x2(19),x3(19),x4(19),x5(19),x6(19),x7(19),x8(19),x9(19),x10(19),x11(19),x12(19),x
13(19),x14(19),x15(19),x16(19),x17(19),x18(19),x19(19),x20(19),x21(19),x22(19),
x23(19),x24(19),x25(19)], $
[x1(20),x2(20),x3(20),x4(20),x5(20),x6(20),x7(20),x8(20),x9(20),x10(20),x11(20),x12(20),x
13(20),x14(20),x15(20),x16(20),x17(20),x18(20),x19(20),x20(20),x21(20),x22(20),
x23(20),x24(20),x25(20)], $
[x1(21),x2(21),x3(21),x4(21),x5(21),x6(21),x7(21),x8(21),x9(21),x10(21),x11(21),x12(21),x
13(21),x14(21),x15(21),x16(21),x17(21),x18(21),x19(21),x20(21),x21(21),x22(21),
x23(21),x24(21),x25(21)], $
[x1(22),x2(22),x3(22),x4(22),x5(22),x6(22),x7(22),x8(22),x9(22),x10(22),x11(22),x12(22),x
13(22),x14(22),x15(22),x16(22),x17(22),x18(22),x19(22),x20(22),x21(22),x22(22),
x23(22),x24(22),x25(22)], $
[x1(23),x2(23),x3(23),x4(23),x5(23),x6(23),x7(23),x8(23),x9(23),x10(23),x11(23),x12(23),x
13(23),x14(23),x15(23),x16(23),x17(23),x18(23),x19(23),x20(23),x21(23),x22(23),
x23(23),x24(23),x25(23)], $
[x1(24),x2(24),x3(24),x4(24),x5(24),x6(24),x7(24),x8(24),x9(24),x10(24),x11(24),x12(24),x
13(24),x14(24),x15(24),x16(24),x17(24),x18(24),x19(24),x20(24),x21(24),x22(24),
x23(24),x24(24),x25(24)]

```

```
;number of LEDs needed
```

```

result0=regress2(x,y0,w)
result1=regress2(x,y1,w)
result2=regress2(x,y2,w)
result3=regress2(x,y3,w)
result4=regress2(x,y4,w)

```

```
bad=WHERE(result0 LT 0, n_bad)
IF n_bad GE 1 THEN result0(bad)=0L
```

```
bad=WHERE(result1 LT 0, n_bad)
IF n_bad GE 1 THEN result1(bad)=0L
```

```
bad=WHERE(result2 LT 0, n_bad)
IF n_bad GE 1 THEN result2(bad)=0L
```

```
bad=WHERE(result3 LT 0, n_bad)
IF n_bad GE 1 THEN result3(bad)=0L
```

```
bad=WHERE(result4 LT 0, n_bad)
IF n_bad GE 1 THEN result4(bad)=0L
```

```
F_l_pi_best_2_0 = DBLARR(n_elements(lambda))
F_l_pi_best_2_1 = DBLARR(n_elements(lambda))
F_l_pi_best_2_2 = DBLARR(n_elements(lambda))
F_l_pi_best_2_3 = DBLARR(n_elements(lambda))
F_l_pi_best_2_4 = DBLARR(n_elements(lambda))
```

```
;regression function
```

```
FOR i_j=0L, n_elements(lambda)-1L DO BEGIN
F_l_pi_best_2_0(i_j) = c365(i_j)*result0(0) + c380(i_j) *result0(1) + c400(i_j)
*result0(2) + c420(i_j) *result0(3) + c4475(i_j) *result0(4) + c470(i_j) *result0(5) +
c485(i_j) *result0(6)+ c505(i_j) *result0(7) + c530(i_j) *result0(8) + c5675(i_j)
*result0(9) + c590(i_j) *result0(10) + c627(i_j) *result0(11)
+ccw(i_j)*result0(12)+c665(i_j) *result0(13)+ c680(i_j) *result0(14) +c700(i_j)
*result0(15) +c720(i_j) *result0(16)+ c740(i_j) *result0(17)+ c760(i_j) *result0(18)
+c780(i_j) *result0(19)+c810(i_j) *result0(20)+c830(i_j) *result0(21)+ c850(i_j)
*result0(22) + c880(i_j) *result0(23)+ c940(i_j) *result0(24)
ENDFOR
```

```
FOR i_j=0L, n_elements(lambda)-1L DO BEGIN
F_l_pi_best_2_1(i_j) = c365(i_j)*result1(0) + c380(i_j) *result1(1) + c400(i_j)
*result1(2) + c420(i_j) *result1(3) + c4475(i_j) *result1(4) + c470(i_j) *result1(5) +
c485(i_j) *result1(6)+ c505(i_j) *result1(7) + c530(i_j) *result1(8) + c5675(i_j)
*result1(9) + c590(i_j) *result1(10) + c627(i_j) *result1(11)
+ccw(i_j)*result1(12)+c665(i_j) *result1(13)+ c680(i_j) *result1(14) +c700(i_j)
*result1(15) +c720(i_j) *result1(16)+ c740(i_j) *result1(17)+ c760(i_j) *result1(18)
+c780(i_j) *result1(19)+c810(i_j) *result1(20)+c830(i_j) *result1(21)+ c850(i_j)
*result1(22) + c880(i_j) *result1(23)+ c940(i_j) *result1(24)
ENDFOR
```

```
FOR i_j=0L, n_elements(lambda)-1L DO BEGIN
F_l_pi_best_2_2(i_j) = c365(i_j)*result2(0) + c380(i_j) *result2(1) + c400(i_j)
*result2(2) + c420(i_j) *result2(3) + c4475(i_j) *result2(4) + c470(i_j) *result2(5) +
c485(i_j) *result2(6)+ c505(i_j) *result2(7) + c530(i_j) *result2(8) + c5675(i_j)
*result2(9) + c590(i_j) *result2(10) + c627(i_j) *result2(11)
+ccw(i_j)*result2(12)+c665(i_j) *result2(13)+ c680(i_j) *result2(14) +c700(i_j)
*result2(15) +c720(i_j) *result2(16)+ c740(i_j) *result2(17)+ c760(i_j) *result2(18)
+c780(i_j) *result2(19)+c810(i_j) *result2(20)+c830(i_j) *result2(21)+ c850(i_j)
*result2(22) + c880(i_j) *result2(23)+ c940(i_j) *result2(24)
ENDFOR
```

```
FOR i_j=0L, n_elements(lambda)-1L DO BEGIN
F_l_pi_best_2_3(i_j) = c365(i_j)*result3(0) + c380(i_j) *result3(1) + c400(i_j)
*result3(2) + c420(i_j) *result3(3) + c4475(i_j) *result3(4) + c470(i_j) *result3(5) +
c485(i_j) *result3(6)+ c505(i_j) *result3(7) + c530(i_j) *result3(8) + c5675(i_j)
*result3(9) + c590(i_j) *result3(10) + c627(i_j) *result3(11)
+ccw(i_j)*result3(12)+c665(i_j) *result3(13)+ c680(i_j) *result3(14) +c700(i_j)
*result3(15) +c720(i_j) *result3(16)+ c740(i_j) *result3(17)+ c760(i_j) *result3(18)
```

```

+c780(i_j) *result3(19)+c810(i_j) *result3(20)+c830(i_j) *result3(21)+ c850(i_j)
*result3(22) + c880(i_j) *result3(23)+ c940(i_j) *result3(24)
ENDFOR

FOR i_j=0L, n_elements(lambda)-1L DO BEGIN
F_l_pi_best_2_4(i_j) = c365(i_j)*result4(0) + c380(i_j) *result4(1) + c400(i_j)
*result4(2) + c420(i_j) *result4(3) + c4475(i_j) *result4(4) + c470(i_j) *result4(5) +
c485(i_j) *result4(6)+ c505(i_j) *result4(7) + c530(i_j) *result4(8) + c5675(i_j)
*result4(9) + c590(i_j) *result4(10) + c627(i_j) *result4(11)
+ccw(i_j)*result4(12)+c665(i_j) *result4(13)+ c680(i_j) *result4(14) +c700(i_j)
*result4(15) +c720(i_j) *result4(16)+ c740(i_j) *result4(17)+ c760(i_j) *result4(18)
+c780(i_j) *result4(19)+c810(i_j) *result4(20)+c830(i_j) *result4(21)+ c850(i_j)
*result4(22) + c880(i_j) *result4(23)+ c940(i_j) *result4(24)
ENDFOR

writecol, 'loopfitG0rv.txt', lambda,F_l_pi_best_2_0
writecol, 'loopfitG0rg.txt', lambda,F_l_pi_best_2_1
writecol, 'loopfitG0mg.txt', lambda,F_l_pi_best_2_2
writecol, 'loopfitG0maxg.txt', lambda,F_l_pi_best_2_3
writecol, 'loopfitG0em.txt', lambda,F_l_pi_best_2_4

;*****print the LED number needed to fit the spectra*****+

print, 'N° led (best fit)rv:', result0
print, 'N° led (best fit)rg:', result1
print, 'N° led (best fit)mg:', result2
print, 'N° led (best fit)maxg:', result3
print, 'N° led (best fit)em:', result4

lunghezzedonda=lambda_peak ;lambda corresponding to the LEDs' peaks

;*****

lambda_new=min(lambda) + findgen(1000)*((1.032*(10.0D^(-6.0D)))-min(lambda))/999.0D

;print a 2 column file with the LEDs peak wavelength and the number needed to fit

numeroledG0rv='numeroled_G0_atm_rv'+ strcompress(string(i_k),/remove_all)
numeroledG0rg='numeroled_G0_atm_rg'+ strcompress(string(i_k),/remove_all)
numeroledG0mg='numeroled_G0_atm_mg'+ strcompress(string(i_k),/remove_all)
numeroledG0maxg='numeroled_G0_atm_maxg'+ strcompress(string(i_k),/remove_all)
numeroledG0em='numeroled_G0_atm_em'+ strcompress(string(i_k),/remove_all)
;define the total number of led on the illuminator

totale_led=[5.0d, 15.0d,
10.0d,10.0d,10.0d,10.0d,7.0d,25.0d,10.0d,45.0d,20.0d,10.0d,14.0d,10.0d,14.0d,10.0d,11.0d,
8.0d,6.0d,8.0d,8.0d,15.0d,6.0d,16.0d,9.0d]

;FOR i_s=0L, n_elements(result0)-1L DO BEGIN
;printf, outfile, result0(i_s)
;
;ENDFOR

endfor

;printf, outfile, '*****
printf, outfile0, 100.0d*(result0)(0)/totale_led(0)
printf, outfile0, 100.0d*(result0)(1)/totale_led(1)
printf, outfile0, 100.0d*(result0)(2)/totale_led(2)
printf, outfile0, 100.0d*(result0)(3)/totale_led(3)
printf, outfile0, 100.0d*(result0)(4)/totale_led(4)
printf, outfile0, 100.0d*(result0)(5)/totale_led(5)
printf, outfile0, 100.0d*(result0)(6)/totale_led(6)

```



```

printf, outfile2, 100.0d*(result2) (20)/totale_led(20)
printf, outfile2, 100.0d*(result2) (21)/totale_led(21)
printf, outfile2, 100.0d*(result2) (22)/totale_led(22)
printf, outfile2, 100.0d*(result2) (23)/totale_led(23)
printf, outfile2, 100.0d*(result2) (24)/totale_led(24)

free_lun, outfile2

printf, outfile3, 100.0d*(result3) (0)/totale_led(0)
printf, outfile3, 100.0d*(result3) (1)/totale_led(1)
printf, outfile3, 100.0d*(result3) (2)/totale_led(2)
printf, outfile3, 100.0d*(result3) (3)/totale_led(3)
printf, outfile3, 100.0d*(result3) (4)/totale_led(4)
printf, outfile3, 100.0d*(result3) (5)/totale_led(5)
printf, outfile3, 100.0d*(result3) (6)/totale_led(6)
printf, outfile3, 100.0d*(result3) (7)/totale_led(7)
printf, outfile3, 100.0d*(result3) (8)/totale_led(8)
printf, outfile3, 100.0d*(result3) (9)/totale_led(9)
printf, outfile3, 100.0d*(result3) (10)/totale_led(10)
printf, outfile3, 100.0d*(result3) (11)/totale_led(11)
printf, outfile3, 100.0d*(result3) (12)/totale_led(12)
printf, outfile3, 100.0d*(result3) (13)/totale_led(13)
printf, outfile3, 100.0d*(result3) (14)/totale_led(14)
printf, outfile3, 100.0d*(result3) (15)/totale_led(15)
printf, outfile3, 100.0d*(result3) (16)/totale_led(16)
printf, outfile3, 100.0d*(result3) (17)/totale_led(17)
printf, outfile3, 100.0d*(result3) (18)/totale_led(18)
printf, outfile3, 100.0d*(result3) (19)/totale_led(19)
printf, outfile3, 100.0d*(result3) (20)/totale_led(20)
printf, outfile3, 100.0d*(result3) (21)/totale_led(21)
printf, outfile3, 100.0d*(result3) (22)/totale_led(22)
printf, outfile3, 100.0d*(result3) (23)/totale_led(23)
printf, outfile3, 100.0d*(result3) (24)/totale_led(24)

free_lun, outfile3

printf, outfile4, 100.0d*(result4) (0)/totale_led(0)
printf, outfile4, 100.0d*(result4) (1)/totale_led(1)
printf, outfile4, 100.0d*(result4) (2)/totale_led(2)
printf, outfile4, 100.0d*(result4) (3)/totale_led(3)
printf, outfile4, 100.0d*(result4) (4)/totale_led(4)
printf, outfile4, 100.0d*(result4) (5)/totale_led(5)
printf, outfile4, 100.0d*(result4) (6)/totale_led(6)
printf, outfile4, 100.0d*(result4) (7)/totale_led(7)
printf, outfile4, 100.0d*(result4) (8)/totale_led(8)
printf, outfile4, 100.0d*(result4) (9)/totale_led(9)
printf, outfile4, 100.0d*(result4) (10)/totale_led(10)
printf, outfile4, 100.0d*(result4) (11)/totale_led(11)
printf, outfile4, 100.0d*(result4) (12)/totale_led(12)
printf, outfile4, 100.0d*(result4) (13)/totale_led(13)
printf, outfile4, 100.0d*(result4) (14)/totale_led(14)
printf, outfile4, 100.0d*(result4) (15)/totale_led(15)
printf, outfile4, 100.0d*(result4) (16)/totale_led(16)
printf, outfile4, 100.0d*(result4) (17)/totale_led(17)
printf, outfile4, 100.0d*(result4) (18)/totale_led(18)
printf, outfile4, 100.0d*(result4) (19)/totale_led(19)
printf, outfile4, 100.0d*(result4) (20)/totale_led(20)
printf, outfile4, 100.0d*(result4) (21)/totale_led(21)
printf, outfile4, 100.0d*(result4) (22)/totale_led(22)
printf, outfile4, 100.0d*(result4) (23)/totale_led(23)
printf, outfile4, 100.0d*(result4) (24)/totale_led(24)

free_lun, outfile4

readcol, 'funzioneledbyte.txt', numero, I;, format='d,d'

readcol, 'G0rv.txt', perc0;, format='d,d'
readcol, 'G0rg.txt', perc1;, format='d,d'
readcol, 'G0mg.txt', perc2;, format='d,d'

```

```

readcol, 'G0maxg.txt', perc3;, format='d,d'
readcol, 'G0em.txt', perc4;, format='d,d'

val_min=1.0d
val_max=110.0d
n_elem=10000000.0d
I_n=val_min + findgen(n_elem)*((val_max-val_min)/(n_elem - 1.0D)) ; [m]

a=interpol(numero, I, I_n)

zero=where(a LT 0.0d, nzero)
if (nzero ge 1) then a(zero)=0.0D

zerolambda=where(I_n LT min(I), nzerolambda)
if (nzerolambda ge 1) then a(zerolambda)=0.0D

zerolambda=where(I_n gT max(I), nzerolambda)
if (nzerolambda ge 1) then a(zerolambda)=0.0D

plot, I_n, a, color=1

b0=interpol(a, I_n, perc0)
b1=interpol(a, I_n, perc1)
b2=interpol(a, I_n, perc2)
b3=interpol(a, I_n, perc3)
b4=interpol(a, I_n, perc4)

openw, outfilea, 'byte_e_spettro_G0_rv.txt', /get_lun ;Open the file to put results in
openw, outfileb, 'byte_e_spettro_G0_rg.txt', /get_lun ;Open the file to put results in
openw, outfilec, 'byte_e_spettro_G0_mg.txt', /get_lun ;Open the file to put results in
openw, outfiled, 'byte_e_spettro_G0_maxg.txt', /get_lun ;Open the file to put results in
openw, outfilee, 'byte_e_spettro_G0_em.txt', /get_lun ;Open the file to put results in

data0=dblarr(2,n_elements(lambda))
data0(0,*)=lambda*10.0d^(9.0d)
data0(1,*)=F_l_pi_best_2_0
bytes0=dblarr(1,n_elements(b0))
bytes0(0,*)=b0

data1=dblarr(2,n_elements(lambda))
data1(0,*)=lambda*10.0d^(9.0d)
data1(1,*)=F_l_pi_best_2_1
bytes1=dblarr(1,n_elements(b1))
bytes1(0,*)=b1

data2=dblarr(2,n_elements(lambda))
data2(0,*)=lambda*10.0d^(9.0d)
data2(1,*)=F_l_pi_best_2_2
bytes2=dblarr(1,n_elements(b2))
bytes2(0,*)=b2

data3=dblarr(2,n_elements(lambda))
data3(0,*)=lambda*10.0d^(9.0d)
data3(1,*)=F_l_pi_best_2_3
bytes3=dblarr(1,n_elements(b3))
bytes3(0,*)=b3

data4=dblarr(2,n_elements(lambda))
data4(0,*)=lambda*10.0d^(9.0d)
data4(1,*)=F_l_pi_best_2_4
bytes4=dblarr(1,n_elements(b4))
bytes4(0,*)=b4

printf, outfilea, round(bytes0)
printf, outfilea, data0

```



```

;
; xrange      2 element vector, lower and upper limit of integration
;             The use of XRANGE with a non-monitonic variation in x may
;             produce incorrect results.
;
; accumulate  if set, return value is a vector giving the accumulated
;             integral at each value of x. XRANGE can't be used when
;             this option is set.
;
; OUTPUT:     result of integration
;
; EXAMPLE:
;;           /4
;; find      | x dx
;;           /0
; x=findgen(5) & y=x
; print,integral(x,y)
; 8.00000                                ; answer for linear integrand is exact
;
;
;;           /5.5
;; find      | x^2 dx
;;           /0
;
; x=findgen(7) & y=x^2                    &$
; print,"    numerical    analytic" &$
; print,integral(x,y,xrange=[0,5.5]), 5.5^3/3
; 56.3750    55.4583
;
;; use more resolution in x to improve answer
;
; x=findgen(551)/100. & y=x^2            &$
; print,"    numerical    analytic" &$
; print,integral(x,y), 5.5^3/3
; 55.4584    55.4583                    ; much better
;
; author:    Paul Ricchiazzi                3NOV92
;           Institute for Computational Earth System Science
;           University of California, Santa Barbara
;
; REVISIONS:
; sep93: fixed error in treatment of xrange, added examples
; apr96: allow use of xrange with monitonically decreasing x
;-

if n_params() eq 0 then begin
  xhelp,'integral'
  return,0
endif

nn=n_elements(x)
if nn ne n_elements(y) then message,'x and y vectors must be same size'
dx=shift(x,-1)-x
yy=.5*(shift(y,-1)+y)

if keyword_set(accumulate) then begin
  sum=fltarr(nn)
  for i=1,nn-1 do sum(i)=sum(i-1)+dx(i-1)*yy(i-1)
  return,sum
endif

if n_elements(xrange) eq 0 then return,total(dx(0:nn-2)*yy(0:nn-2))

; rest of code is to treat end points when xrange is set...

;
xmin=min(xrange)
xmax=max(xrange)

```



```

ii=where(x ge xmin and x le xmax,nc)

if nc eq nn then return,total(dx(0:nn-2)*yy(0:nn-2))

n1=ii(0)

if n1 eq -1 then return,0.

n2=ii(nc-1)
sum=0.

; sum up points fully inside range

if n2 gt n1 then sum=total(dx(n1:n2-1)*yy(n1:n2-1))

; now add in rest of area inside integration limits

if n1 gt 0 then begin
  if x(n1) lt x(n2) then x1=xmin else x1=xmax
  y1=y(n1)+(x1-x(n1))*(y(n1+1)-y(n1))/(x(n1+1)-x(n1))
  sum1=.5*(y1+y(n1))*(x(n1)-x1)
  sum=sum+sum1
endif
if n2 lt nn-1 then begin
  if x(n1) lt x(n2) then x2=xmax else x2=xmin
  y2=y(n2)+(x2-x(n2))*(y(n2+1)-y(n2))/(x(n2+1)-x(n2))
  sum2=.5*(y2+y(n2))*(x2-x(n2))
  sum=sum+sum2
endif

return,sum

end

;+
; NAME:
;     REGRESS2
;
; PURPOSE:
;     Multiple linear regression fit.
;     Fit the function:
;      $Y(i) = A(0)*X(0,i) + A(1)*X(1,i) + \dots +$ 
;      $A(Nterms-1)*X(Nterms-1,i)$ 
;
; CATEGORY:
;     G2 - Correlation and regression analysis.
;
; CALLING SEQUENCE:
;     Result = REGRESS(X, Y, W [, YFIT, SIGMA, FTEST, R, RMUL, CHISQ])
;
; INPUTS:
;     X:   array of independent variable data. X must
;         be dimensioned (Nterms, Npoints) where there are Nterms
;         coefficients to be found (independent variables) and
;         Npoints of samples.
;
;     Y:   vector of dependent variable points, must have Npoints
;         elements.
;
;     W:   vector of weights for each equation, must be a Npoints
;         elements vector. For instrumental weighting
;          $w(i) = 1/\text{standard\_deviation}(Y(i))$ , for statistical
;         weighting  $w(i) = 1./Y(i)$ . For no weighting set  $w(i)=1$ ,
;         and also set the RELATIVE_WEIGHT keyword.
;
; OUTPUTS:
;     Function result = coefficients = vector of
;     Nterms elements. Returned as a column vector.

```

```

;
; OPTIONAL OUTPUT PARAMETERS:
;   Yfit:      array of calculated values of Y, Npoints elements.
;
;   Sigma:     Vector of standard deviations for coefficients.
;
;   Ftest:     value of F for test of fit.
;
;   Rmul:      multiple linear correlation coefficient.
;
;   R:         Vector of linear correlation coefficient.
;
;   Chisq:     Reduced chi squared.
;
; KEYWORDS:
;RELATIVE_WEIGHT: if this keyword is non-zero, the input weights
;                  (W vector) are assumed to be relative values, and not based
;                  on known uncertainties in the Y vector. This is the case for
;                  no weighting W(*) = 1.
;
; PROCEDURE:
;   Adapted from the program REGRES, Page 172, Bevington, Data Reduction
;   and Error Analysis for the Physical Sciences, 1969.
;
; MODIFICATION HISTORY:
;   Written, DMS, RSI, September, 1982.
;   Added RELATIVE_WEIGHT keyword, W. Landsman, August 1991
;   29-AUG-1994: H.C. Wen - Used simpler, clearer algorithm to determine
;               fit coefficients. The constant term, A0 is now just one
;               of the X(iterms,*) vectors, enabling the algorithm to
;               now return the sigma associated with this constant term.
;               I also made a special provision for the case when
;               Nterm = 1; namely, "inverting" a 1x1 matrix, i.e. scalar.
;   26-MAR-1996: Added the DOUBLE and CHECK keywords to the call to DETERM.
;   02-APR-1996: Test matrix singularity using second argument in INVERT
;               instead of call to DETERM.
;-
function REGRESS2, X, Y, W, Yfit, Sigma, Ftest, R, Rmul, Chisq, RELATIVE_WEIGHT=relative_weight

On_error, 2 ;Return to caller if an error occurs

NP = N_PARAMS ()
if (NP lt 3) or (NP gt 9) then $
    message, 'Must be called with 3-9 parameters: '+$
        'X, Y, W [, Yfit, Sigma, Ftest, R, RMul, Chisq]'
```

; Determine the length of these arrays and the number of sources

```

SX      = SIZE( X )
SY      = SIZE( Y )
nterm   = SX(1)
npts    = SY(1)

if (N_ELEMENTS(W) NE SY(1)) OR $
    (SX(0) NE 2) OR (SY(1) NE SX(2)) THEN $
    message, 'Incompatible arrays.'
```

```

WW      = REPLICATE(1., nterm) # W
curv    = ( X*WW ) # TRANSPOSE( X )
beta    = X # (Y*W)

if nterm eq 1 then begin
    sigma = 1./sqrt(curv)
    X_coef= beta/curv
endif else begin
    err   = INVERT( curv, status )

    if (status eq 1) then begin
        print, 'det( Curvature matrix )=0 .. Using REGRESS'
```

```

X1 = X
linechk = X(0,0) - X(0,fix( npts*randomu(seed) ))
if linechk eq 0 then begin
    print, 'Cannot determine sigma for CONSTANT'
    X1 = X1(1:nterm-1,*)
endif

coeff = REGRESS( X1,Y,W,Yfit,A0, Sigma,Ftest,R,Rmul,Chisq)

if linechk eq 0 then begin
    coeff = [A0,reform(coeff)]
    Sigma = [ 0,reform(Sigma)]
    R = [ 0,R]
endif
return, coeff
endif else if (status eq 2) then begin
    print, 'WARNING -- small pivot element used in matrix inversion.'
    print, '          significant accuracy probably lost.'
endif

diag = indgen( nterm )
sigma = sqrt( err( diag,diag ) )
X_coeff = err # beta
endelse

Yfit = TRANSPOSE(X_coeff # X)

dof = npts - nterm > 1
Chisq = TOTAL( (Y-Yfit)^2.*W )
Chisq = Chisq/dof

; To calculate the "test of fit" parameters, we revert back to the original
; cryptic routine in REGRESS1. Because the constant term (if any) is now
; included in the X variable, NPAR = NTERM_regress2 = NTERM_regress1 + 1.

if nterm eq 1 then goto, SKIP

SW = TOTAL(W) ;SUM OF WEIGHTS
YMEAN = TOTAL(Y*W)/SW ;Y MEAN
XMEAN = (X * (REPLICATE(1.,NTERM) # W)) # REPLICATE(1./SW,NPTS)
WMEAN = SW/NPTS
WW = W/WMEAN
;
NFREE = NPTS-1 ;DEGS OF FREEDOM
SIGMAY = SQRT(TOTAL(WW * (Y-YMEAN)^2)/NFREE) ;W*(Y(I)-YMEAN)
XX = X- XMEAN # REPLICATE(1.,NPTS) ;X(J,I) - XMEAN(I)
WX = REPLICATE(1.,NTERM) # WW * XX ;W(I) * (X(J,I)-XMEAN(I))
SIGMAX = SQRT( XX*WX # REPLICATE(1./NFREE,NPTS)) ;W(I) * (X(J,I)-XM) * (X(K,I)-XM)
R = WX # (Y - YMEAN) / (SIGMAX * SIGMAY * NFREE)

WW1 = WX # TRANSPOSE(XX)

ARRAY = INVERT(WW1/(NFREE * SIGMAX #SIGMAX))
A = (R # ARRAY)*(SIGMAY/SIGMAX) ;GET COEFFICIENTS

FREEN = NPTS-NTERM > 1 ;DEGS OF FREEDOM, AT LEAST 1.

CHISQ = TOTAL(WW*(Y-YFIT)^2)*WMEAN/FREEN ;WEIGHTED CHI SQUARED
IF KEYWORD_SET(relative_weight) then varnce = chisq $
else varnce = 1./wmean

RMUL = TOTAL(A*R*SIGMAX/SIGMAY) ;MULTIPLE LIN REG COEFF
IF RMUL LT 1. THEN FTEST = RMUL/(NTERM-1)/ ((1.-RMUL)/FREEN) ELSE FTEST=1.E6
RMUL = SQRT(RMUL)

SKIP: return, X_coeff

end

```

```

;+
; NAME:
;       MREGRESS
;
; PURPOSE:
;       Perform a multiple linear regression fit
;
; USAGE:
;       Result = MREGRESS(X, Y,                               $
;                       MEASURE_ERRORS=measure_errors,      $
;                       SIGMA=sigma,                        $
;                       INVERSE=inv,                        $
;                       STATUS=status)
;
; ARGUMENTS:
;   X:   (Input) The array of independent variable data. X must
;         be dimensioned as an array of Npoints by Nterms, where
;         there are Nterms coefficients (independent variables) to be
;         found and Npoints of samples.
;         Note that this array is transposed with respect to the
;         input of the IDL routine REGRESS.
;
;   Y:   (Input) The vector of dependent variable points. Y must have
;         Npoints elements.
;
; KEYWORDS:
;   MEASURE_ERRORS : Set this keyword to a vector containing standard
;                   measurement errors for each point Y[i]. This vector must be the same
;                   length as X and Y.
;
;                   For Gaussian errors (e.g. instrumental uncertainties), MEASURE_ERRORS
;                   should be set to the standard deviations of each point in Y.
;                   For Poisson or statistical weighting MEASURE_ERRORS should be
;                   set to sqrt(Y).
;
;   SIGMA : Set this keyword to a named variable to receive the errors
;           on the returned coefficients
;
;   INVERSE : Set this keyword to a named value to receive the structure
;             containing the covariance matrix and other terms that can be re-used
;             to solve the system with the same X and other Y.
;
;   STATUS : Set this keyword to a named variable to receive the status
;           of the operation. Possible status values are:
;           - 0 for successful completion,
;           - 1 for a singular array (which indicates that the inversion
;             is invalid), and
;           - 2 which is a warning that a small pivot element was used
;             and that significant accuracy was probably lost.
;           If STATUS is not specified then any error messages will be output
;           to the screen.
;
; RETURN:
;   MREGRESS returns a column vector of coefficients that has Nterms
;   elements.
;
; DESCRIPTION:
;   Adapted from the IDL program REGRESS
;
;   Perform a multiple linear regression fit:
;       
$$Y[i] = A[0]*X[0,i] + A[1]*X[1,i] + \dots + A[Nterms-1]*X[Nterms-1,i]$$

;
;   This is a variant of the IDL function REGRESS, where the
;   covariance matrix and other intermediate arrays can be saved
;   to solve faster the system with successive values of Y and
;   the same X.

```

```

;      An noticeable difference is also that MREGRESS does not
;      include a constant term (if necessary, the constant may be
;      included as one of the terms of X).
;
; HISTORY:
;      Written, Ph. Prugniel 2008/01/17 (from the IDL REGRESS)
;-
; CATEGORY:      ULY_UTIL
;-----
FUNCTION mregress, x, y, $
      MEASURE_ERRORS=measure_errors, $
      SIGMA=sigma, $
      INVERSE=inv, $
      STATUS=status

COMPILE_OPT idl2

ON_ERROR, 2          ;Return to caller if an error occurs
sy = SIZE(Y)          ;Get dimensions of x and y.
sx = SIZE(X)

ndimX = sx[0]
nterm = (ndimX EQ 1) ? 1 : sx[ndimX] ; # of terms (coefficients)
nptsX = sx[1]         ;# of observations (samples)
npts = sy[1]         ;# of observations (samples)

IF (nptsX NE npts) THEN MESSAGE, $
      'X and Y have incompatible dimensions.'
IF (ndimX EQ 1) THEN x = REFORM(x, npts, 1, /OVER) ; change X to a 2D array

nfree = npts-1       ;degs of freedom

invert = 0b
if n_tags(inv) gt 0 then if (size(inv.wx))[1] ne (size(y))[1] then invert = 1b

if n_tags(inv) le 0 or invert then begin
  weights = 1/measure_errors^2
  sw = TOTAL(weights)/npts
  weights = weights/sw
  wgt = REBIN(weights, npts, nterm)

; This commented block is the version with a constant term
; xmean = TOTAL(wgt*x, 1, DOUBLE=double)
; if (nterm gt 1) then $
;   xx = x - REBIN(transpose(xmean), npts, nterm) $ ;x(j,i) - xmean(i)
; else xx = x - xmean
; wx = TEMPORARY(wgt) * xx ;weights(i)*(x(j,i)-xmean(i))
; sigmax = SQRT(TOTAL(xx*wx, 1)/nfree) ;weights(i)*(x(j,i)-xm)*(x(k,i)-xm)
; ar = matrix_multiply(wx, xx, /ATRANSPOSE)/(nfree * sigmax #sigmax)

wx = TEMPORARY(wgt) * x ;weights(i)*x(j,i)

sigmax = SQRT(TOTAL(x*wx, 1)/nfree) ;weights(i)*x(j,i)*(x(k,i)-xm)

ar = matrix_multiply(wx, x, /ATRANSPOSE)/(nfree * sigmax #sigmax)

ar = INVERT(ar, status)
IF (status EQ 1L && ~ARG_PRESENT(status)) THEN BEGIN
  IF (ndimX EQ 1) THEN x = REFORM(x, /OVER) ; change X back to a vector
  MESSAGE, "Inversion failed due to singular array."
END
IF (status EQ 2L && ~ARG_PRESENT(status)) THEN BEGIN
  MESSAGE, /INFO, $
    "Inversion used a small pivot element. Results may be inaccurate."
endif

; error terms
sigma = ar[LINDGEN(nterm)*(nterm+1)]/(sw*nfree*sigmax^2)
neg = where(sigma lt 0, cnt) ; may have sigma^1<0 if small pivot

```

```

    if cnt gt 0 then sigma[neg] = 0
    sigma = sqrt(sigma)

    inv = {a:ar, ww:weights, wx:wx, sx:sigmax, sigma:sigma}
endif

; this commented block is the version with constant term
;ymean = TOTAL(y*inv.ww) ;y mean
;yy = y-ymean
;sigmay = SQRT(TOTAL(inv.ww * yy^2)*npts/nfree) ;weights*(y(i)-ymean)
;correlation = matrix_multiply(inv.wx, yy, /ATRANSPOSE) / (inv.sx * sigmay * nfree)

sigmay = SQRT(TOTAL(inv.ww * y^2)/nfree) ;weights*y(i)

correlation = matrix_multiply(inv.wx, y, /ATRANSPOSE) / (inv.sx*sigmay*nfree)
a = (correlation # inv.a)*(sigmay/inv.sx) ;get coefficients

;yfit = matrix_multiply(a,x, /BTRANSPOSE) ;compute fit
;const = ymean - TOTAL(a*xmean) ;constant term
;yfit = yfit + const ;add it in

IF (ndimX EQ 1) THEN x = REFORM(x, /OVER) ; change X back to a vector

return, a
END
;--- end ---

pro polyfit, xdata, ydata, degree, $
    coeffs, sigcoeffs, yfit, sigma, nr3bad, ncov, cov, $
    residbad=residbad, goodindx=goodindx, problem=problem, xmatrix=xmatrix
;+
;NAME:
;POLYFIT -- polynomial fit using standard least squares
;
;PURPOSE:
; Polynomial fits, like IDL's POLY_FIT, but returns sigmas of
; the coefficients, the fitted line, and the normalized covariance
; matrix also.
;
;CALLING SEQUENCE:
; POLYFIT, xdata, ydata, degree, $
; coeffs, sigcoeffs, yfit, sigma, nr3bad, ncov, cov, $
; residbad=residbad, goodindx=goodindx, problem=problem
;
;INPUTS:
; xdata: the x-axis data points.
; ydata: the y-axis data points.
; degree: the degree of the polynomial. e.g. linear fit has degree=1.
;KEYWORDS:
; residbad: if set, excludes points those residuals exceed residbad*sigma
; goodindx: the array of indices actually used in the fit.
; problem: nonzero if there was a problem with the fit.
; xmatrix: returns the xmatrix for diagnostic purposes
;
;OUTPUTS:
; coeffs: array of coefficients.
; sigcoeffs: me's of the coefficients.
; yfit: the fitted points evaluated at datax.
; sigma: the sigma (mean error) of the data points.
; nr3sig: the nr of datapoints lying more than 3 sigma away from the fit.
; ncov: the normalized covariance matrix.
; cov: the covariance matrix.
;
;HISTORY;
; 30 sep i tested to see if la_invert is better than invert.
;there is no essential diff, so we stick with invert.
;-

problem=0

```

```

x = double(xdata)
t = double(ydata)
ndata = n_elements(x)
goodindx= lindgen( ndata)
niter= 01
nr3bad = 01

ITERATE:
s = dblarr(degree+1, ndata, /nozero)

for ndeg = 0, degree do s[ndeg,*] = x^ndeg

ss = transpose(s) ## s
st = transpose(s) ## transpose(t)
ssi = invert(ss)
a = ssi ## st
bt = s ## a
resid = t - bt
yfit = reform( bt)
sigsq = total(resid^2)/(ndata-degree-1.)
sigarray = sigsq * ssi[lindgen(degree+1)*(degree+2)]
sigcoeffs = sqrt( abs(sigarray))
coeffs = reform( a)
sigma = sqrt(sigsq)
if keyword_set( residbad) then $
    badindx = where( abs(resid) gt residbad*sigma, nr3bad)
;stop

if ( (keyword_set( residbad)) and (nr3bad ne 0) ) then begin
goodindx = where( abs(resid) le residbad*sigma, nr3good)
IF NR3GOOD LE DEGREE+1 THEN BEGIN
    problem=-2
    goto, problemgood
ENDIF
x= x[goodindx]
t= t[goodindx]
goodindx= goodindx[ goodindx]
ndata= nr3good
niter= niter+ 11
goto, iterate
endif

PROBLEMGOOD: ; go here if there aren't enough good points left.

;stop

;TEST FOR NEG SQRTS...
indxsqrt = where( sigarray lt 0., countbad)
if (countbad ne 0) then begin
    print, countbad, ' negative sqrts in sigarray!'
    sigarray[indxsqrt] = -sigarray[indxsqrt]
    problem=-3
endif

cov=ssi

;DERIVE THE NORMALIZED COVARIANCE ARRAY...
doug = ssi[lindgen(degree+1)*(degree+2)]
doug = doug#doug
ncov = ssi/sqrt(doug)

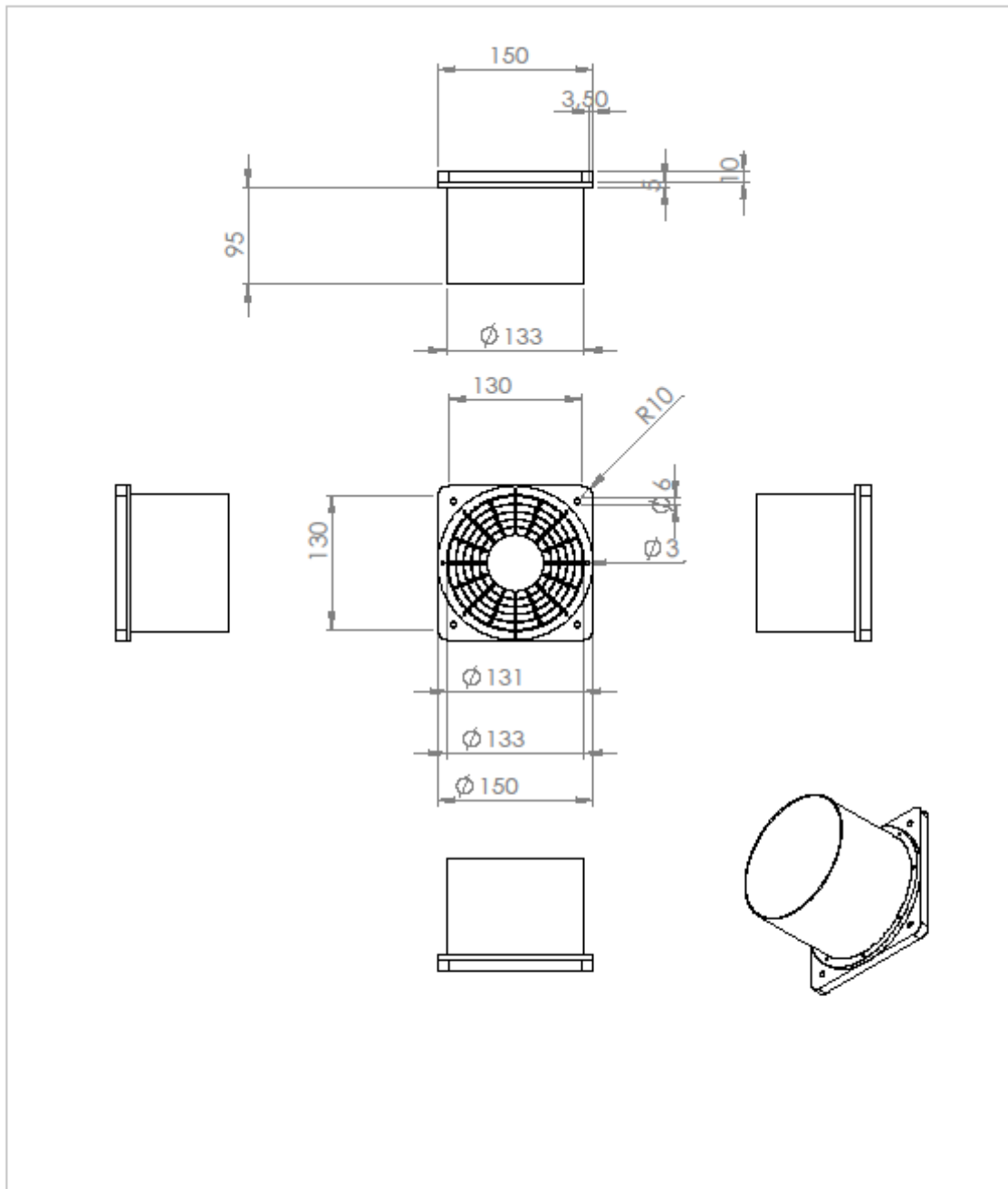
yfit= fltarr( n_elements( xdata))
for ndeg=0, degree do yfit= yfit+ coeffs[ ndeg]*xdata^ndeg

goodindx= goodindx
xmatrix=s
return
end

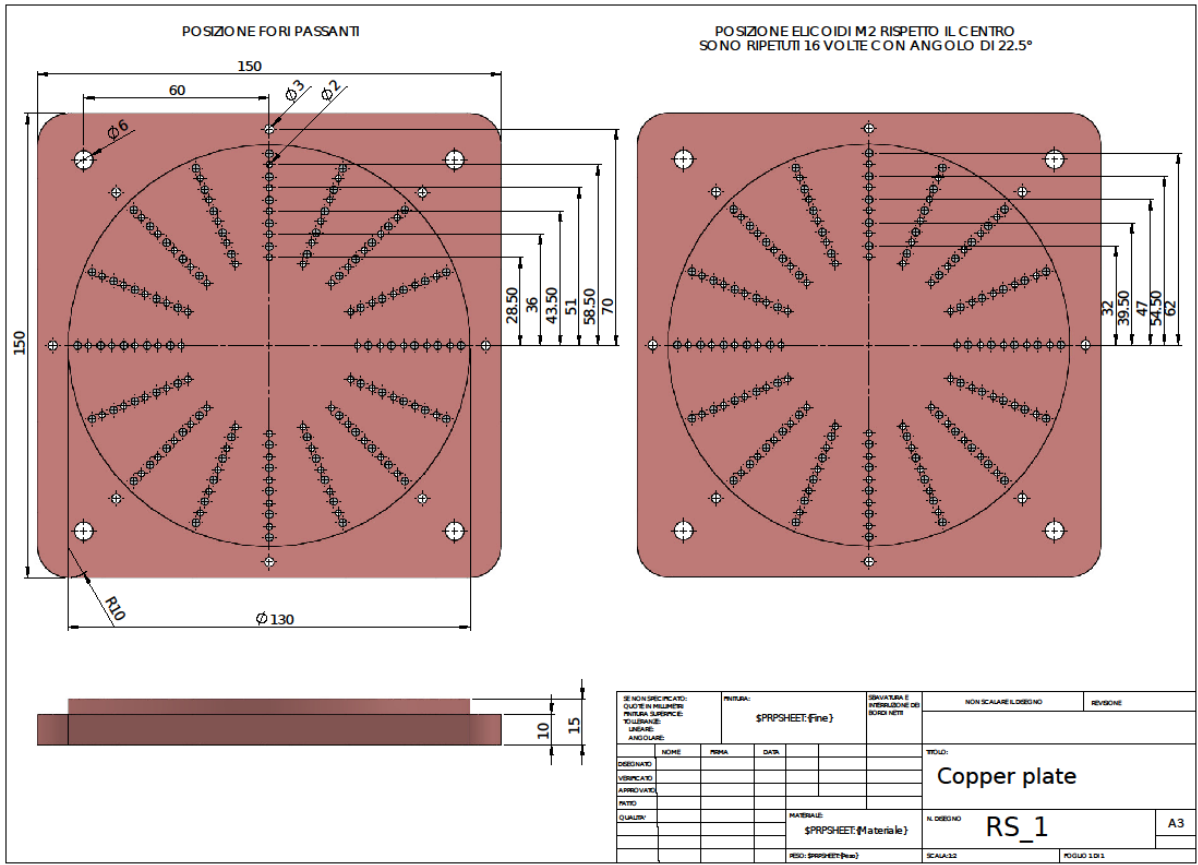
```

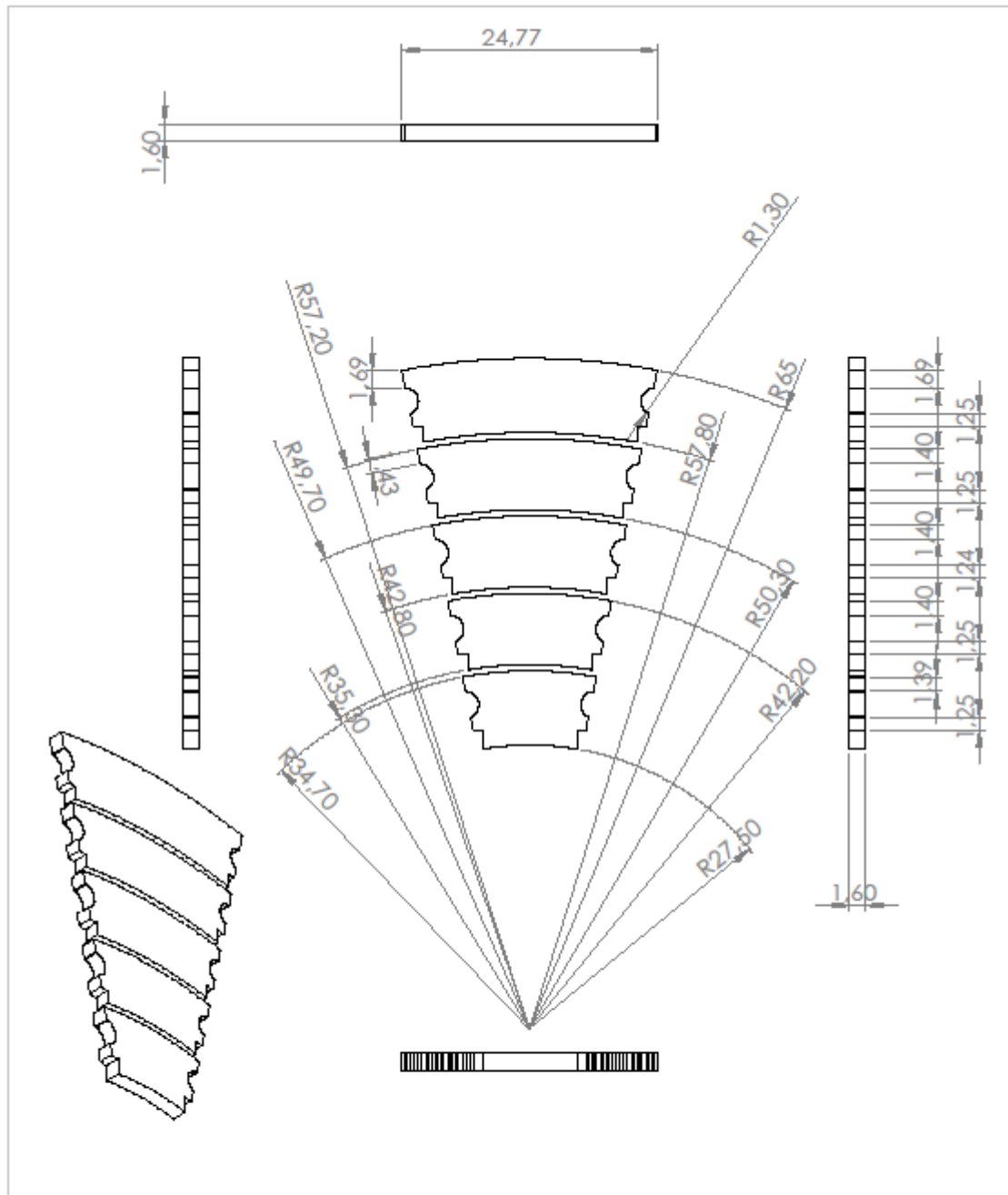
APPENDIX C: Starlight simulator building drawings

Hereafter will be attached the starlight simulator building drawings, starting from the ensemble RS_0 going through the copper plate RS_1 and the PCB wafers RS_2.



SE NON SPECIFICATO: QUOTE IN MILLIMETRI FINITURA SUPERFICIE: TOLLERANZE: LINEARE: ANGOLARE:		FINITURA: \$PRPSHEET:{Fine}		SBAVATURA E INTERRUZIONE DEI BORDI NETTI		NON SCALARE IL DISEGNO		REVISIONE	
DISEGNATO		NOME		FIRMA		DATA		TITOLO: Starlight simulator	
VERIFICATO									
APPROVATO									
FATTO									
QUALITA'								MATERIALE: \$PRPSHEET:{Materiale}	
								N. DISEGNO RS_0	
								SCALA:1:5	
								FOGLIO 1 DI 1	
								A4	

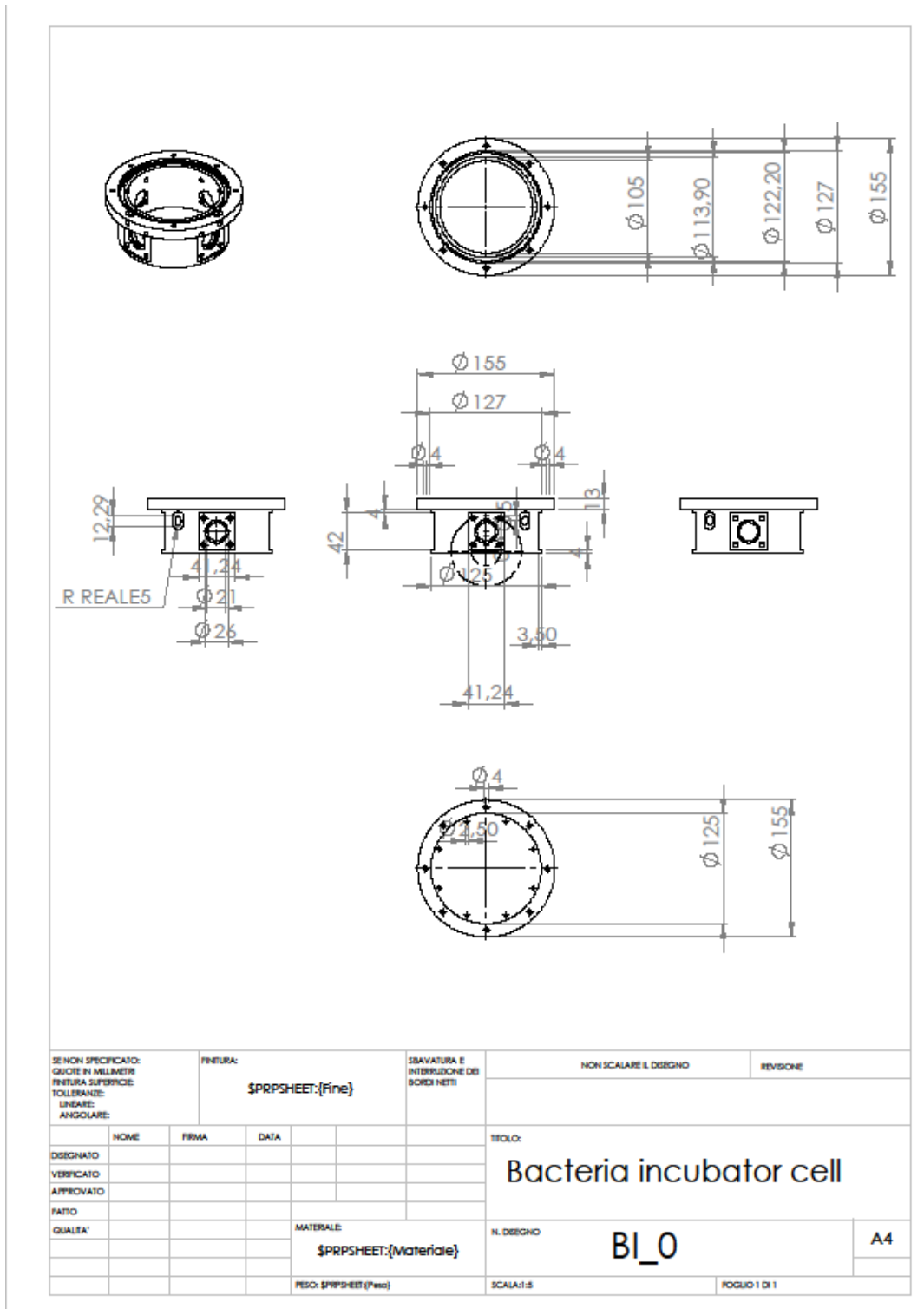


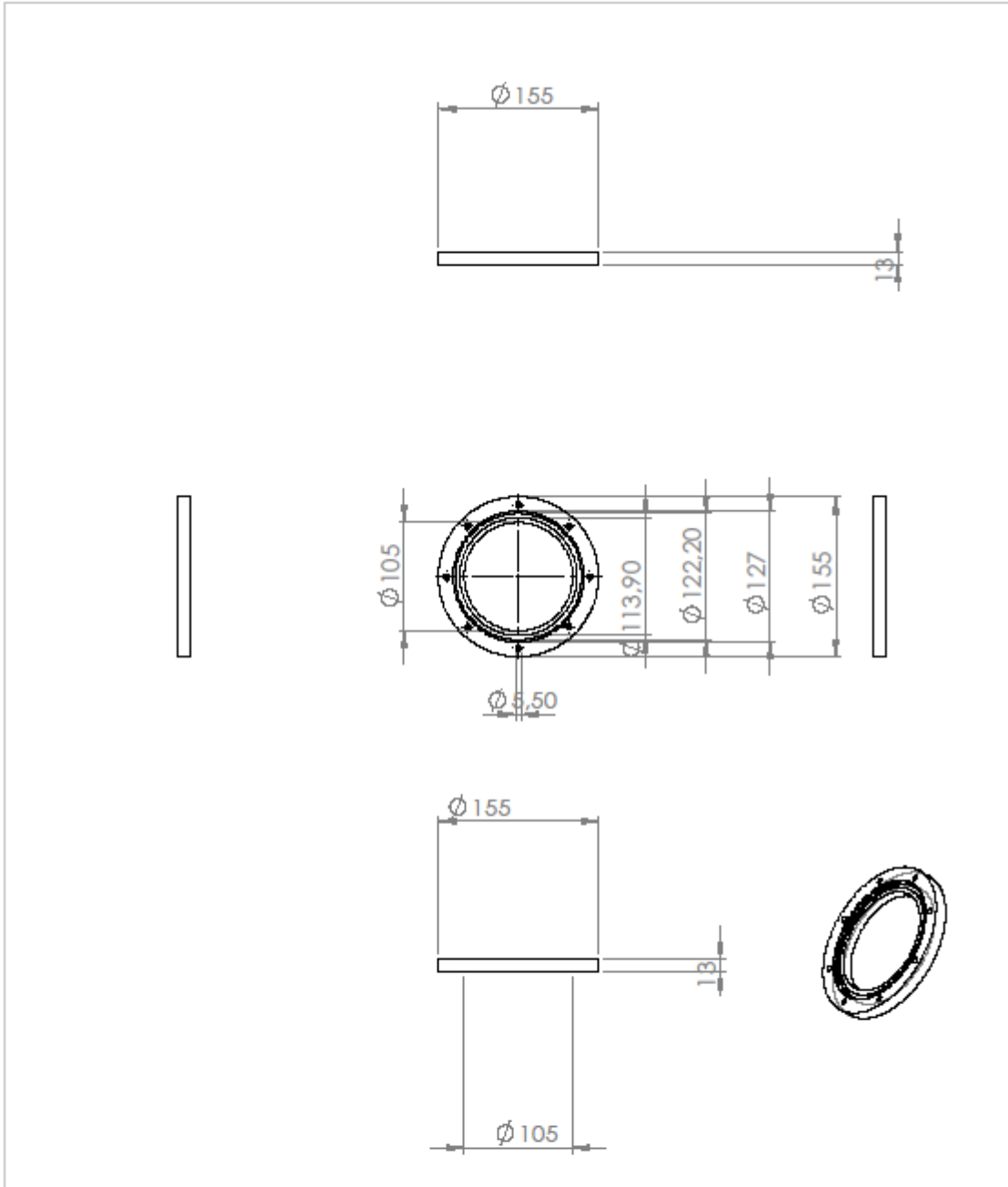


SE NON SPECIFICATO: QUOTE IN MILLIMETRI FINITURA SUPERFICIE: TOLLERANZE: LINEARE: ANGOLARE:		FINITURA: \$PRPSHEET:{Fine}		SBAVATURA E INTERRUZIONE DEI BORDI NETTI		NON SCALARE IL DISEGNO		REVISIONE	
DISEGNATO		FIRMA		DATA		TITOLO: PCB wafers			
VERIFICATO									
APPROVATO									
FATTO									
QUALITA'						MATERIALE: \$PRPSHEET:{Materiale}		N. DISEGNO RS_2	
						PESO: \$PRPSHEET:{Peso}		SCALA:2:1	
								FOGLIO 1 DI 1	
								A4	

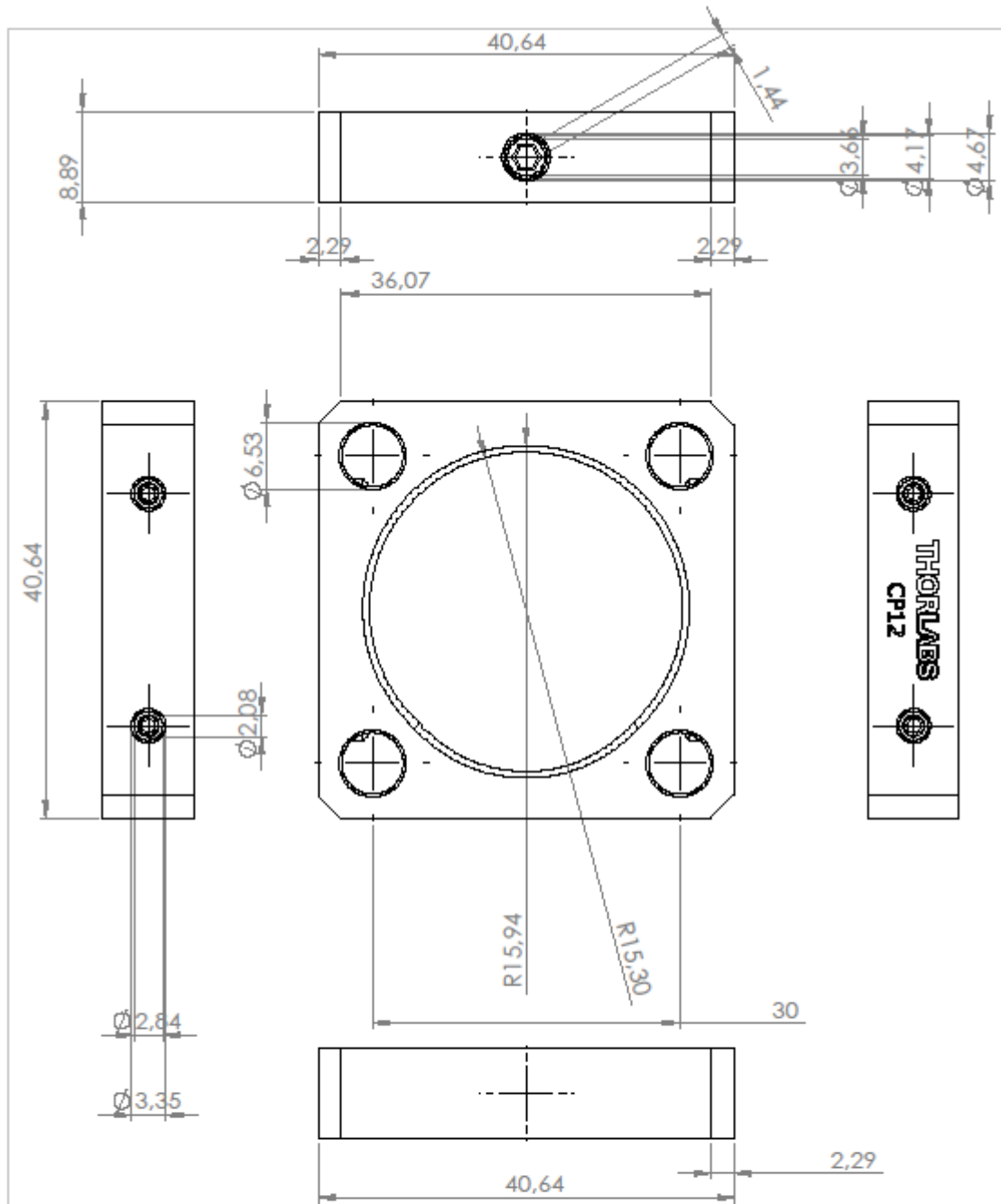
APPENDIX D: Bacteria gas cell building drawings

Hereafter will be attached the starlight simulator building drawings, starting from the main cell BI_0 going through the top window ring BI_1, the Thorlabs CP-12 BI_2a and the SM1L10 nosepieces BI_2b, the optical windows BI_3 and BI_4 and the gas fluxing nozzles BI_5.

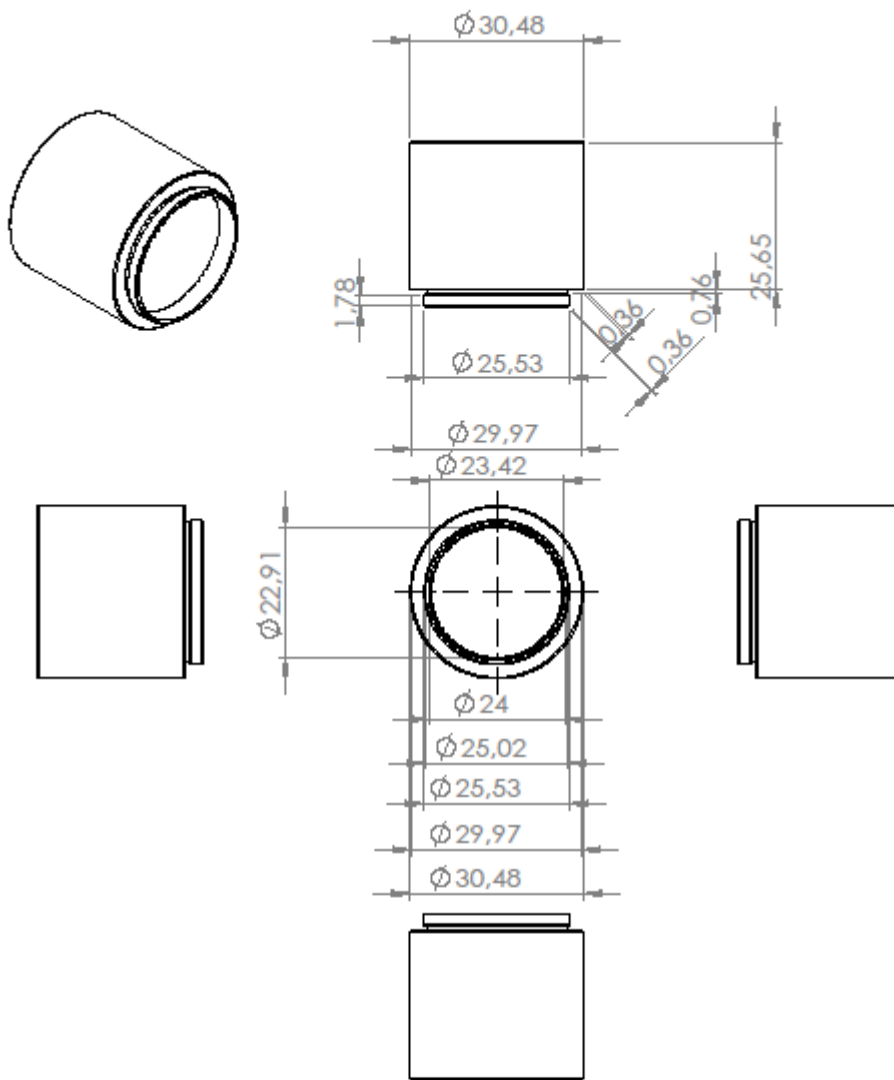




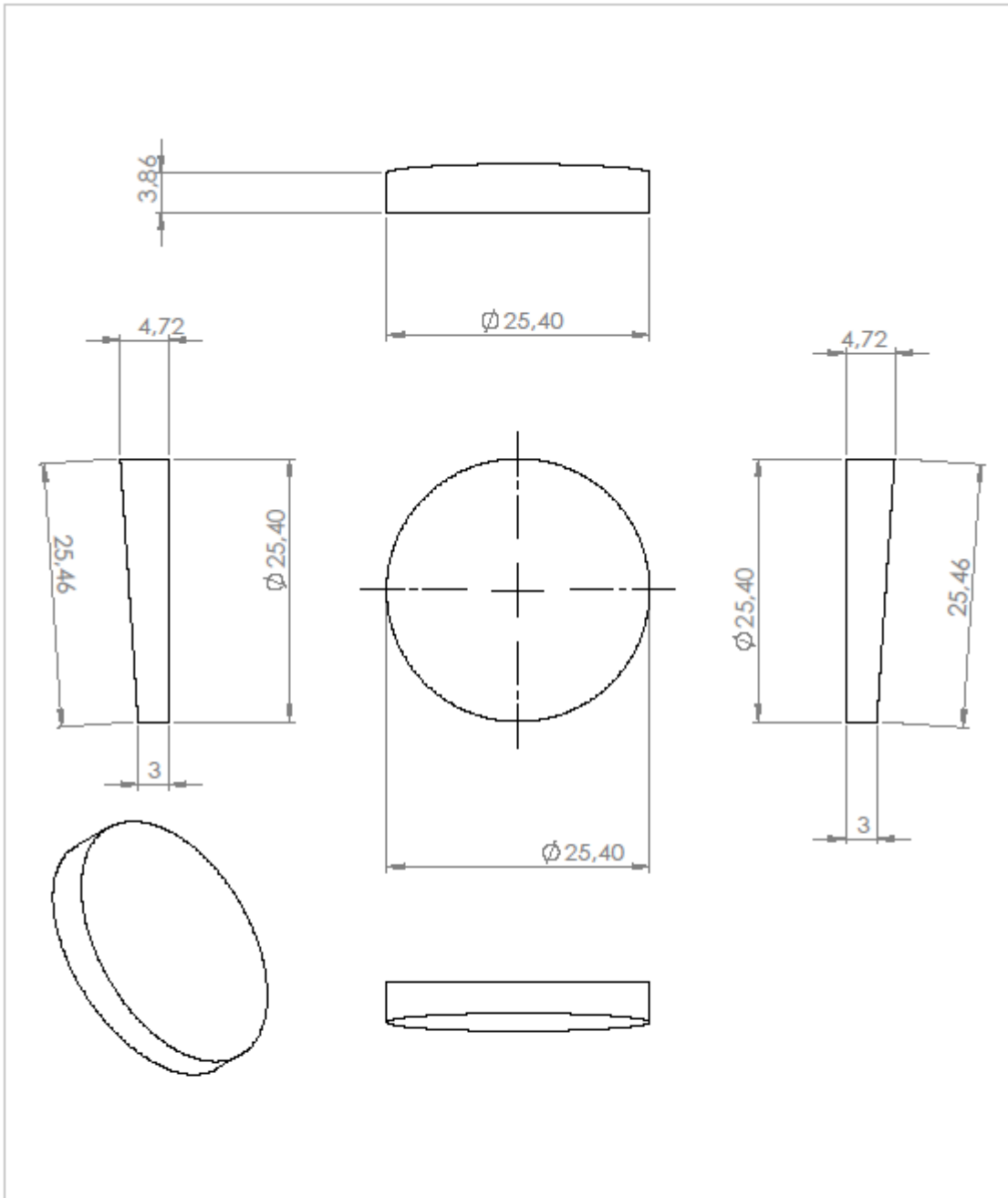
SE NON SPECIFICATO: QUOTE IN MILLIMETRI FINITURA SUPERFICIE: TOLLERANZE: LINEARE: ANGOLARE:		FINITURA: \$PRPSHEET:{Fine}		SBAVATURA E INTERSEZIONE DEI BORDI NETTI		NON SCALARE IL DISEGNO		REVISIONE	
DISEGNATO		FIRMA		DATA		TITOLO: Top window ring			
VERIFICATO									
APPROVATO									
FATTO									
QUALITA'						MATERIALE: \$PRPSHEET:{Materiale}		N. DISEGNO BI_1	
						PESO: \$PRPSHEET:{Peso}		SCALA:1:5	
								FOGLIO 1 DI 1	
								A4	



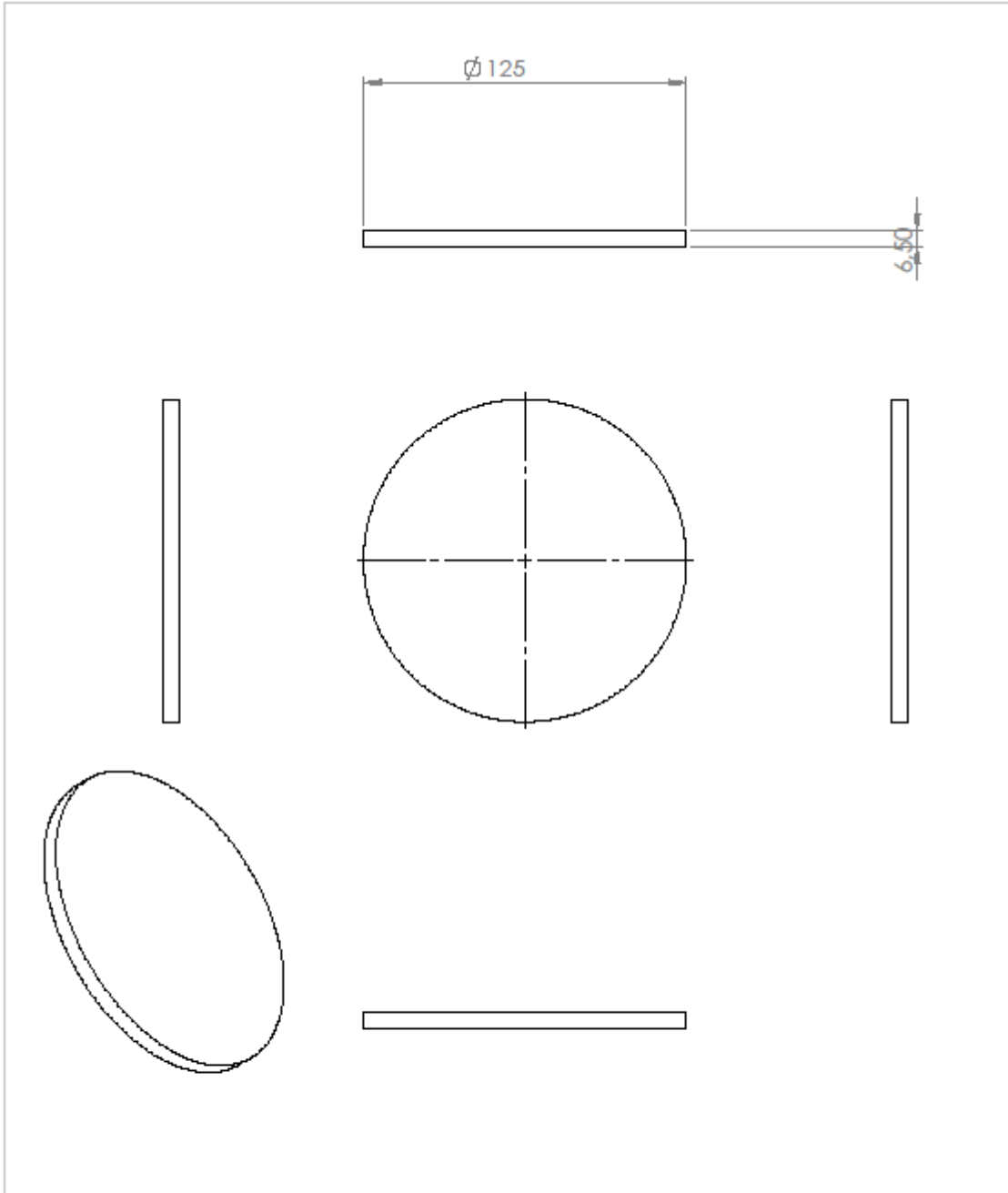
SE NON SPECIFICATO: QUOTE IN MILLIMETRI FINITURA SUPERFICIE: TOLLERANZE: LINEARE: ANGOLARE:		FINITURA: \$PRPSHEET:{Fine}		SBAVATURA E INTERRUZIONE DEI BORDI NETTI		NON SCALARE IL DISEGNO		REVISIONE	
DISEGNATO		FIRMA		DATA		TITOLO: Thorlabs CP-12			
VERIFICATO									
APPROVATO									
FATTO									
QUALITA'						MATERIALE: \$PRPSHEET:{Materiale}		N. DISEGNO BI_2a	
						PESO: \$PRPSHEET:{Peso}		SCALA: 2:1	
								FOGLIO 1 DI 1	
								A4	



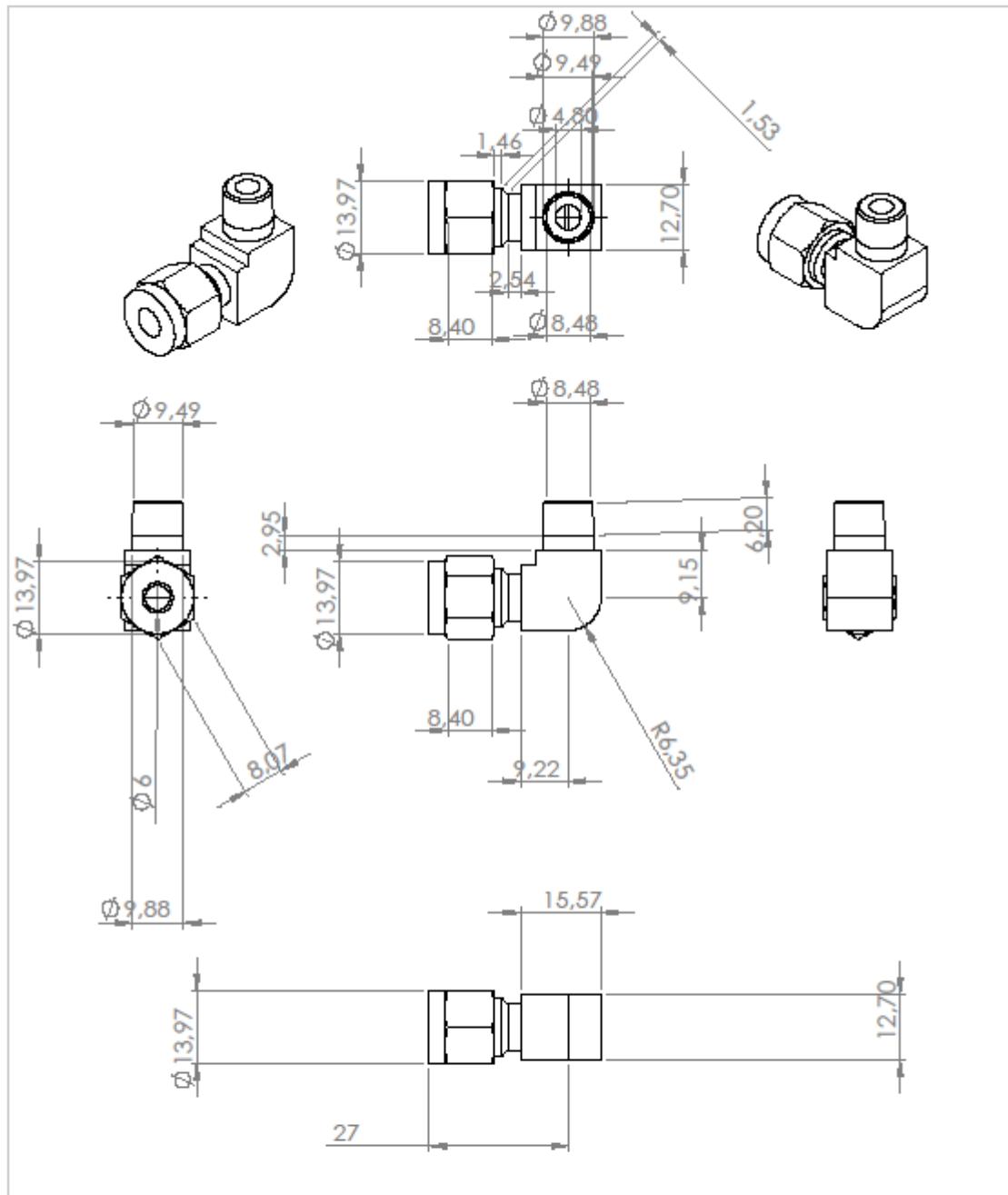
SE NON SPECIFICATO: QUOTE IN MILLIMETRI FINITURA SUPERFICIE: TOLLERANZE: LINEARE: ANGOLARE:		FINITURA: \$PRPSHEET:{Fine}		SBAVATURA E INTERRUZIONE DEI BORDI NETTI		NON SCALARE IL DISEGNO		REVISIONE	
DISEGNATO		FIRMA		DATA		TITOLO: Thorlabs SM1L10			
VERIFICATO						MATERIALE: \$PRPSHEET:{Materiale}		N. DISEGNO BI_2b	
APPROVATO						PESO: \$PRPSHEET:{Peso}		SCALA:1:1	
FATTO								FOGLIO 1 DI 1	
QUALITA'								A4	



SE NON SPECIFICATO: QUOTE IN MILLIMETRI FINITURA SUPERFICIE: TOLLERANZE: LINEARE: ANGOLARE:		FINITURA: \$PRPSHEET:{Fine}		SBAVATURA E INTERRUZIONE DEI BORDI NETTI		NON SCALARE IL DISEGNO		REVISIONE	
DISEGNATO		FIRMA		DATA		TITOLO: Wedge windows			
VERIFICATO						N. DISEGNO		BI_3	
APPROVATO								A4	
FATTO						MATERIALE: \$PRPSHEET:{Materiale}			
QUALITA'						PESO: \$PRPSHEET:{Peso}		SCALA: 2:1	
								FOGLIO 1 DI 1	



SE NON SPECIFICATO: QUOTE IN MILLIMETRI FINITURA SUPERFICIE: TOLLERANZE: LINEARE: ANGOLARE:		FINITURA: \$PRPSHEET:{Fine}		SBAVATURA E INTERRUZIONE DEI BORDI NETTI		NON SCALARE IL DISEGNO		REVISIONE	
DISEGNATO		FIRMA		DATA		TITOLO: Top Borofloat window			
VERIFICATO									
APPROVATO									
FATTO									
QUALITA'						MATERIALE: \$PRPSHEET:{Materiale}		N. DISEGNO BI_4	
						PESO: \$PRPSHEET:{Peso}		SCALA:1:2	
								FOGLIO 1 DI 1	
								A4	



SE NON SPECIFICATO: QUOTE IN MILLIMETRI FINITURA SUPERFICIE: TOLLERANZE: LINEARE: ANGOLARE:		FINITURA: \$PRPSHEET:{Fine}		SBAVATURA E INTERRUZIONE DEI BORDI NETTI		NON SCALARE IL DISEGNO		REVISIONE	
DISEGNATO		FIRMA		DATA		TITOLO: Gas fluxing nozzles			
VERIFICATO						N. DISEGNO		BI_5	
APPROVATO								A4	
FATTO									
QUALITA'						MATERIALE: \$PRPSHEET:{Materiale}			
						PESO: \$PRPSHEET:{Peso}		SCALA:1:1	
								FOGLIO 1 DI 1	

APPENDIX E: ESIs datasets

Hereafter can be seen a list of recently discovered exoplanets with the relative ESIs.

Planet Name	mass (EU)	radius (EU)	density (EU)	g (EU)	ve (EU)	a (AU)	Tsurf (K)	Teq (K)	ESIf	ESIs	ESIg
GJ 581 g	3.100	1.36	1.22	1.67	1.51	0.15	278.	248.	0.901	0.877	0.889
GJ 581 d	5.600	1.60	1.36	2.18	1.87	0.22	232.	202.	0.849	0.643	0.739
GJ 581 c	5.600	1.60	1.36	2.18	1.87	0.07	380.	350.	0.849	0.583	0.703
HD 69830 d	18.434	3.36	0.49	1.63	2.34	0.63	312.	282.	0.636	0.747	0.689
55 Cnc f	45.768	4.91	0.39	1.90	3.06	0.78	310.	280.	0.536	0.703	0.614
61 Vir d	22.884	3.68	0.46	1.69	2.50	0.48	375.	345.	0.612	0.555	0.583
GJ 581 e	1.700	1.16	1.10	1.27	1.21	0.03	591.	561.	0.954	0.297	0.532
HIP 57050 b	94.714	6.64	0.32	2.15	3.78	0.16	250.	220.	0.464	0.602	0.528
mu Ara d	165.876	8.38	0.28	2.36	4.45	0.92	327.	297.	0.413	0.588	0.493
HD 142 b	327.367	11.12	0.24	2.65	5.43	1.00	286.	256.	0.357	0.657	0.484
GJ 581 b	15.600	3.14	0.51	1.59	2.23	0.04	499.	469.	0.656	0.353	0.481
HD 37124 b	203.412	9.13	0.27	2.44	4.72	0.53	332.	302.	0.395	0.564	0.472
HD 96167 b	216.126	9.36	0.26	2.47	4.81	1.30	334.	304.	0.390	0.555	0.465
HD 108874 b	432.251	12.49	0.22	2.77	5.89	1.05	294.	264.	0.336	0.632	0.460
GJ 581 f	7.000	2.16	0.70	1.51	1.80	0.76	139.	109.	0.790	0.267	0.459
HD 210277 b	390.933	11.98	0.23	2.73	5.72	1.10	275.	245.	0.343	0.614	0.459
HD 147513 b	317.832	10.99	0.24	2.63	5.38	1.26	263.	233.	0.359	0.586	0.459
HD 69830 c	12.078	2.82	0.54	1.52	2.07	0.19	549.	519.	0.686	0.304	0.457
HD 188015 b	400.468	12.10	0.23	2.74	5.76	1.19	274.	244.	0.341	0.608	0.456
HD 142415 b	514.888	13.43	0.21	2.85	6.19	1.05	288.	258.	0.323	0.639	0.454
HD 114729 b	260.622	10.12	0.25	2.55	5.08	2.08	245.	215.	0.375	0.537	0.448
HD 82943 b	556.206	13.87	0.21	2.89	6.34	1.19	287.	257.	0.318	0.631	0.448
HD 34445 b	251.087	9.96	0.25	2.53	5.02	2.07	240.	210.	0.378	0.522	0.444
HD 216435 b	400.468	12.10	0.23	2.74	5.76	2.56	264.	234.	0.341	0.577	0.444
61 Vir c	18.212	3.34	0.49	1.63	2.33	0.22	541.	511.	0.638	0.303	0.440
HD 3651 b	63.566	5.63	0.36	2.01	3.36	0.28	450.	420.	0.502	0.381	0.437

HD 11964 c	193.877	8.95	0.27	2.42	4.66	3.34	221.	191.	0.399	0.468	0.432
HD 4203 b	657.912	14.87	0.20	2.97	6.65	1.16	299.	269.	0.306	0.594	0.426
HD 30562 b	410.003	12.22	0.22	2.75	5.80	2.30	251.	221.	0.340	0.534	0.426
HD 170469 b	212.947	9.30	0.26	2.46	4.79	2.24	219.	189.	0.391	0.459	0.424
mu Ara b	532.686	13.62	0.21	2.87	6.26	1.50	262.	232.	0.321	0.558	0.423
GJ 1214 b	5.689	2.71	0.29	0.77	1.45	0.01	548.	518.	0.542	0.329	0.423
HD 216770 b	206.591	9.19	0.27	2.45	4.74	0.46	383.	353.	0.394	0.452	0.422
HD 16141 b	73.101	5.96	0.34	2.06	3.50	0.35	462.	432.	0.489	0.361	0.420
HD 10647 b	295.584	10.66	0.24	2.60	5.27	2.03	228.	198.	0.365	0.476	0.417
kappa CrB b	572.097	14.03	0.21	2.91	6.39	2.70	319.	289.	0.316	0.548	0.416
HIP 14810 d	181.164	8.70	0.28	2.40	4.57	1.89	206.	176.	0.405	0.421	0.413
HD 73534 b	365.507	11.65	0.23	2.70	5.60	3.15	230.	200.	0.348	0.474	0.406
HD 134987 b	505.353	13.33	0.21	2.85	6.16	0.81	339.	309.	0.324	0.506	0.405
HD 164922 b	114.419	7.18	0.31	2.22	3.99	2.11	185.	155.	0.446	0.367	0.404
HD 153950 b	867.681	16.69	0.19	3.12	7.21	1.28	304.	274.	0.288	0.565	0.403
HIP 14810 c	406.825	12.18	0.23	2.74	5.78	0.55	358.	328.	0.340	0.475	0.402
HD 196885 b	820.006	16.30	0.19	3.09	7.10	2.37	267.	237.	0.291	0.551	0.401
HD 37124 d	198.327	9.03	0.27	2.43	4.69	1.64	202.	172.	0.397	0.404	0.400
HD 171028 b	581.632	14.13	0.21	2.91	6.42	1.29	337.	307.	0.314	0.504	0.398
HD 208487 b	143.024	7.88	0.29	2.30	4.26	0.49	440.	410.	0.426	0.371	0.397
HD 5319 b	616.594	14.48	0.20	2.94	6.53	1.75	334.	304.	0.310	0.508	0.397
HD 12661 b	731.013	15.54	0.19	3.03	6.86	0.83	324.	294.	0.299	0.523	0.395
HD 92788 b	1226.831	19.27	0.17	3.30	7.98	0.97	290.	260.	0.266	0.586	0.395
HD 205739 b	435.430	12.53	0.22	2.78	5.90	0.90	362.	332.	0.335	0.463	0.394
HD 125612 b	1017.062	17.83	0.18	3.20	7.56	1.20	273.	243.	0.277	0.559	0.394
HD 19994 b	533.957	13.63	0.21	2.87	6.26	1.42	348.	318.	0.320	0.483	0.393
HD 73526 c	794.579	16.09	0.19	3.07	7.03	1.05	323.	293.	0.293	0.521	0.391
HD 4208 b	254.265	10.01	0.25	2.54	5.04	1.70	205.	175.	0.377	0.405	0.391
HD 9446 c	578.454	14.10	0.21	2.91	6.41	0.65	346.	316.	0.315	0.484	0.391
HD 114783 b	314.653	10.94	0.24	2.63	5.36	1.20	213.	183.	0.360	0.423	0.390
55 Cnc c	53.714	5.24	0.37	1.95	3.20	0.24	535.	505.	0.519	0.285	0.385

HD 16175 b	1398.460	20.35	0.17	3.38	8.29	2.10	283.	253.	0.258	0.571	0.384
HD 45350 b	568.919	14.00	0.21	2.90	6.38	1.92	231.	201.	0.316	0.460	0.381
HD 75898 b	797.758	16.11	0.19	3.07	7.04	1.19	338.	308.	0.293	0.488	0.378
HD 82943 c	638.842	14.69	0.20	2.96	6.60	0.75	354.	324.	0.308	0.463	0.378
HD 23079 b	829.541	16.38	0.19	3.09	7.12	1.65	246.	216.	0.291	0.489	0.377
HD 183263 b	1172.799	18.91	0.17	3.28	7.88	1.52	264.	234.	0.269	0.524	0.375
HD 99492 b	34.644	4.37	0.42	1.81	2.82	0.12	590.	560.	0.566	0.246	0.373
16 Cyg B b	533.957	13.63	0.21	2.87	6.26	1.68	221.	191.	0.320	0.430	0.371
HD 175541 b	193.877	8.95	0.27	2.42	4.66	1.03	461.	431.	0.399	0.334	0.365
HD 28185 b	1811.641	22.67	0.16	3.53	8.94	1.03	279.	249.	0.243	0.547	0.365
HD 20868 b	632.485	14.63	0.20	2.96	6.58	0.95	223.	193.	0.309	0.430	0.364
HD 154857 b	572.097	14.03	0.21	2.91	6.39	1.20	381.	351.	0.316	0.417	0.363
HD 108874 c	323.553	11.07	0.24	2.64	5.41	2.68	195.	165.	0.358	0.367	0.362
HD 177830 b	406.825	12.18	0.23	2.74	5.78	1.00	407.	377.	0.340	0.386	0.362
HD 95089 b	381.398	11.85	0.23	2.71	5.67	1.51	419.	389.	0.345	0.371	0.358
6 Lyn b	762.796	15.82	0.19	3.05	6.95	2.20	368.	338.	0.296	0.430	0.357
HD 136418 b	635.664	14.66	0.20	2.96	6.59	1.32	382.	352.	0.308	0.412	0.356
HD 213240 b	1430.243	20.54	0.16	3.39	8.35	2.03	256.	226.	0.257	0.493	0.356
HD 148427 b	305.119	10.80	0.24	2.61	5.32	0.93	443.	413.	0.362	0.344	0.353
HD 180902 b	508.531	13.36	0.21	2.85	6.17	1.39	407.	377.	0.324	0.379	0.351
HD 8574 b	670.625	14.99	0.20	2.98	6.69	0.77	386.	356.	0.305	0.403	0.350
CoRoT-9 b	266.979	11.78	0.16	1.92	4.76	0.41	407.	377.	0.297	0.409	0.349
HD 40979 b	1055.201	18.10	0.18	3.22	7.64	0.81	358.	328.	0.275	0.436	0.346
HD 4308 b	12.872	2.89	0.53	1.54	2.11	0.12	731.	701.	0.678	0.174	0.344
HD 11506 b	1093.341	18.37	0.18	3.24	7.72	2.43	231.	201.	0.273	0.433	0.344
HD 12661 c	498.996	13.26	0.21	2.84	6.14	2.56	198.	168.	0.325	0.361	0.343
HD 128311 b	692.873	15.20	0.20	3.00	6.75	1.10	208.	178.	0.302	0.383	0.340
HD 52265 b	359.150	11.56	0.23	2.69	5.58	0.49	458.	428.	0.350	0.321	0.335
HD 10697 b	2027.767	23.75	0.15	3.59	9.24	2.16	254.	224.	0.237	0.471	0.334
HD 196050 b	953.495	17.35	0.18	3.17	7.41	2.50	217.	187.	0.282	0.396	0.334

HD 6434 b	152.559	8.10	0.29	2.33	4.34	0.15	532.	502.	0.420	0.265	0.334
HD 167042 b	508.531	13.36	0.21	2.85	6.17	1.30	433.	403.	0.324	0.343	0.333
HD 222582 b	2463.196	25.76	0.14	3.71	9.78	1.35	263.	233.	0.227	0.488	0.333
HD 23596 b	2285.211	24.96	0.15	3.67	9.57	2.72	258.	228.	0.231	0.478	0.332
HD 231701 b	343.258	11.35	0.24	2.67	5.50	0.53	467.	437.	0.353	0.311	0.332
HD 86264 b	2224.823	24.69	0.15	3.65	9.50	2.86	256.	226.	0.232	0.474	0.332
HD 33564 b	2892.269	27.53	0.14	3.82	10.25	1.10	306.	276.	0.218	0.503	0.331
HD 169830 c	1284.040	19.64	0.17	3.33	8.09	3.60	226.	196.	0.263	0.412	0.329
HD 181342 b	1048.845	18.06	0.18	3.22	7.62	1.78	383.	353.	0.276	0.392	0.329
HD 50499 b	543.492	13.74	0.21	2.88	6.29	3.86	190.	160.	0.319	0.336	0.327
HD 73526 b	921.712	17.11	0.18	3.15	7.34	0.66	400.	370.	0.284	0.370	0.324
HD 216437 b	667.447	14.96	0.20	2.98	6.68	2.70	195.	165.	0.305	0.343	0.323
HD 192263 b	228.839	9.58	0.26	2.49	4.89	0.15	521.	491.	0.385	0.266	0.320
HD 114386 b	394.111	12.02	0.23	2.73	5.73	1.65	174.	144.	0.343	0.298	0.319
HD 38801 b	3400.800	29.45	0.13	3.92	10.75	1.70	311.	281.	0.210	0.483	0.319
HD 2039 b	1557.376	21.28	0.16	3.44	8.56	2.20	224.	194.	0.252	0.400	0.317
HD 206610 b	699.230	15.25	0.20	3.01	6.77	1.68	438.	408.	0.302	0.327	0.314
HD 89744 b	2539.476	26.08	0.14	3.73	9.87	0.89	338.	308.	0.225	0.438	0.314
30 Ari B b	3140.178	28.49	0.14	3.87	10.50	0.99	326.	296.	0.214	0.454	0.312
HD 202206 c	775.510	15.92	0.19	3.06	6.98	2.55	191.	161.	0.295	0.329	0.312
HD 37124 c	217.079	9.38	0.26	2.47	4.81	3.19	153.	123.	0.390	0.248	0.311
HD 69830 b	10.488	2.66	0.56	1.48	1.99	0.08	828.	798.	0.703	0.137	0.311
HD 7924 b	9.217	1.84	1.48	2.73	2.24	0.06	875.	845.	0.805	0.119	0.310
HD 190360 c	18.116	3.34	0.49	1.63	2.33	0.13	780.	750.	0.638	0.150	0.309
HD 89307 b	565.741	13.97	0.21	2.90	6.37	3.27	177.	147.	0.316	0.297	0.307
HD 141937 b	3082.968	28.28	0.14	3.86	10.45	1.52	245.	215.	0.215	0.431	0.304
HD 73267 b	972.565	17.50	0.18	3.18	7.46	2.20	191.	161.	0.280	0.322	0.301
HAT-P-13 c	4608.561	33.42	0.12	4.13	11.75	1.19	315.	285.	0.196	0.460	0.300
HD 50554 b	1557.376	21.28	0.16	3.44	8.56	2.38	209.	179.	0.252	0.356	0.299
HD 154672 b	1595.516	21.50	0.16	3.45	8.62	0.60	397.	367.	0.250	0.357	0.299
HD 210702 b	635.664	14.66	0.20	2.96	6.59	1.17	474.	444.	0.308	0.288	0.298

HD 169830 b	915.356	17.06	0.18	3.14	7.33	0.81	444.	414.	0.284	0.312	0.298
HD 190360 b	477.383	13.01	0.22	2.82	6.06	3.92	165.	135.	0.329	0.267	0.296
HD 39091 b	3289.559	29.05	0.13	3.90	10.65	3.29	240.	210.	0.212	0.413	0.296
HD 212771 b	731.013	15.54	0.19	3.03	6.86	1.22	465.	435.	0.299	0.293	0.296
HD 202206 b	5530.273	36.06	0.12	4.25	12.39	0.83	313.	283.	0.188	0.457	0.293
HD 11964 b	34.961	4.39	0.41	1.82	2.82	0.23	758.	728.	0.565	0.151	0.292
HD 72659 b	940.782	17.26	0.18	3.16	7.39	4.16	183.	153.	0.282	0.300	0.291
HD 117618 b	56.574	5.36	0.37	1.97	3.25	0.18	714.	684.	0.514	0.164	0.290
HD 4313 b	731.013	15.54	0.19	3.03	6.86	1.19	477.	447.	0.299	0.281	0.290
HD 192699 b	794.579	16.09	0.19	3.07	7.03	1.16	471.	441.	0.293	0.285	0.289
HD 134987 c	260.622	10.12	0.25	2.55	5.08	5.80	145.	115.	0.375	0.223	0.289
HD 117207 b	654.733	14.84	0.20	2.97	6.64	3.78	166.	136.	0.306	0.260	0.282
HD 102117 b	54.667	5.28	0.37	1.96	3.22	0.15	753.	723.	0.518	0.148	0.277
HD 9446 b	222.482	9.47	0.26	2.48	4.85	0.19	618.	588.	0.388	0.194	0.275
HD 106252 b	2164.434	24.41	0.15	3.63	9.42	2.61	197.	167.	0.234	0.315	0.271
HD 128311 c	1020.240	17.85	0.18	3.20	7.56	1.76	171.	141.	0.277	0.265	0.271
HD 13931 b	597.524	14.29	0.20	2.93	6.47	5.15	156.	126.	0.313	0.235	0.271
mu Ara e	576.547	14.08	0.21	2.91	6.40	5.24	154.	124.	0.315	0.232	0.270
HD 70642 b	635.664	14.66	0.20	2.96	6.59	3.30	157.	127.	0.308	0.237	0.270
HD 74156 c	2552.189	26.14	0.14	3.74	9.88	3.85	201.	171.	0.225	0.321	0.269
HD 187123 c	632.485	14.63	0.20	2.96	6.58	4.89	155.	125.	0.309	0.233	0.268
HD 62509 b	921.712	17.11	0.18	3.15	7.34	1.69	500.	470.	0.284	0.254	0.268
HD 38529 c	5625.623	36.31	0.12	4.27	12.45	3.69	234.	204.	0.187	0.379	0.266
HD 183263 c	1214.117	19.19	0.17	3.30	7.96	4.25	170.	140.	0.267	0.257	0.262
mu Ara c	10.555	2.67	0.56	1.49	1.99	0.09	974.	944.	0.702	0.097	0.262
HD 145377 b	1830.711	22.76	0.16	3.53	8.97	0.45	454.	424.	0.243	0.281	0.261
CoRoT-7 c	8.391	1.79	1.46	2.62	2.17	0.05	1042.	1012.	0.813	0.083	0.259
HD 33283 b	104.884	6.93	0.32	2.19	3.89	0.17	737.	707.	0.454	0.147	0.258
61 Vir b	5.085	1.56	1.34	2.09	1.81	0.05	1093.	1063.	0.857	0.077	0.258
81 Cet b	1684.508	21.99	0.16	3.48	8.76	2.50	473.	443.	0.247	0.265	0.256

18 Del b	3273.667	28.99	0.13	3.90	10.63	2.60	427.	397.	0.212	0.296	0.250
HD 1461 b	7.596	1.74	1.43	2.50	2.09	0.06	1086.	1056.	0.822	0.076	0.250
HD 168443 c	5752.755	36.65	0.12	4.28	12.53	2.91	214.	184.	0.186	0.329	0.247
rho CrB b	330.545	11.17	0.24	2.65	5.44	0.22	650.	620.	0.356	0.170	0.246
HD 217107 c	791.401	16.06	0.19	3.07	7.02	5.27	144.	114.	0.294	0.198	0.241
HD 179079 b	25.427	3.84	0.45	1.72	2.57	0.11	956.	926.	0.600	0.095	0.239
HD 178911 B b	1999.798	23.62	0.15	3.59	9.21	0.32	502.	472.	0.238	0.235	0.236
HAT-P-11 b	25.744	5.07	0.20	1.00	2.25	0.05	823.	793.	0.401	0.135	0.233
HD 87883 b	565.741	13.97	0.21	2.90	6.37	3.60	130.	100.	0.316	0.170	0.232
14 Her b	1474.739	20.81	0.16	3.41	8.42	2.77	150.	120.	0.255	0.203	0.227
HD 224693 b	225.661	9.53	0.26	2.49	4.87	0.23	749.	719.	0.387	0.133	0.227
HD 139357 b	3102.038	28.35	0.14	3.86	10.46	2.36	487.	457.	0.215	0.237	0.226
HD 74156 b	597.524	14.29	0.20	2.93	6.47	0.29	650.	620.	0.313	0.162	0.225
HD 131664 b	5768.647	36.69	0.12	4.28	12.54	3.17	187.	157.	0.186	0.263	0.221
70 Vir b	2364.669	25.32	0.15	3.69	9.67	0.48	525.	495.	0.229	0.213	0.221
HD 30177 b	2914.517	27.62	0.14	3.82	10.28	3.86	163.	133.	0.218	0.221	0.220
55 Cnc b	261.893	10.14	0.25	2.55	5.08	0.12	760.	730.	0.374	0.128	0.219
HD 17156 b	1020.876	11.48	0.67	7.75	9.43	0.16	830.	800.	0.526	0.088	0.215
HD 130322 b	343.258	11.35	0.24	2.67	5.50	0.09	749.	719.	0.353	0.128	0.213
55 Cnc d	1218.885	19.22	0.17	3.30	7.97	5.77	133.	103.	0.266	0.165	0.209
HD 49674 b	36.551	4.47	0.41	1.83	2.86	0.06	1035.	1005.	0.560	0.078	0.209
55 Cnc e	7.628	1.74	1.44	2.51	2.09	0.04	1300.	1270.	0.821	0.051	0.204
HD 108147 b	82.954	6.28	0.33	2.10	3.63	0.10	969.	939.	0.476	0.084	0.201
HD 11977 b	2078.620	24.00	0.15	3.61	9.31	1.93	599.	569.	0.236	0.169	0.200
GJ 86 b	1274.505	19.58	0.17	3.32	8.07	0.11	663.	633.	0.264	0.145	0.196
HD 114762 b	3502.506	29.82	0.13	3.94	10.84	0.30	564.	534.	0.209	0.180	0.194
HAT-P-15 b	618.501	12.03	0.36	4.27	7.17	0.10	852.	822.	0.413	0.091	0.194
HD 168443 b	2549.011	26.12	0.14	3.73	9.88	0.30	604.	574.	0.225	0.164	0.192
HD 168746 b	73.101	5.96	0.34	2.06	3.50	0.07	1049.	1019.	0.489	0.072	0.187
HD 102195 b	143.024	7.88	0.29	2.30	4.26	0.05	993.	963.	0.426	0.077	0.181
GJ 179 b	260.622	10.12	0.25	2.55	5.08	2.41	89.	59.	0.375	0.084	0.177

WASP-10 b	972.565	12.12	0.55	6.62	8.96	0.04	977.	947.	0.483	0.064	0.175
CoRoT-6 b	940.782	13.08	0.42	5.50	8.48	0.09	960.	930.	0.431	0.067	0.170
CoRoT-7 b	4.799	1.68	1.01	1.69	1.69	0.02	1685.	1655.	0.917	0.029	0.163
HD 46375 b	79.140	6.16	0.34	2.08	3.58	0.04	1181.	1151.	0.481	0.055	0.162
HD 81688 b	858.146	16.61	0.19	3.11	7.19	0.81	870.	840.	0.288	0.087	0.158
42 Dra b	1233.187	19.31	0.17	3.31	7.99	1.19	827.	797.	0.266	0.094	0.158
HD 195019 b	1175.978	18.94	0.17	3.28	7.88	0.14	835.	805.	0.269	0.092	0.157
14 And b	1525.593	21.10	0.16	3.43	8.51	0.83	803.	773.	0.253	0.098	0.157
HD 32518 b	966.209	17.45	0.18	3.17	7.44	0.59	871.	841.	0.281	0.086	0.155
HD 217107 b	422.716	12.37	0.22	2.76	5.85	0.07	998.	968.	0.337	0.069	0.153
HD 162020 b	4370.187	32.69	0.13	4.09	11.57	0.07	701.	671.	0.198	0.116	0.152
HD 38529 b	247.909	9.91	0.25	2.52	5.00	0.13	1114.	1084.	0.379	0.057	0.147
HD 76700 b	62.613	5.59	0.36	2.00	3.35	0.05	1332.	1302.	0.504	0.043	0.146
HD 219828 b	20.977	3.55	0.47	1.67	2.43	0.05	1516.	1486.	0.621	0.034	0.146
HAT-P-3 b	190.381	9.99	0.19	1.91	4.37	0.04	1082.	1052.	0.333	0.063	0.145
HD 83443 b	127.133	7.51	0.30	2.26	4.12	0.04	1247.	1217.	0.436	0.047	0.143
11 UMi b	3337.234	29.22	0.13	3.91	10.69	1.54	787.	757.	0.211	0.095	0.141
OGLE-TR-111 b	171.629	12.09	0.10	1.18	3.77	0.05	965.	935.	0.231	0.084	0.140
Kepler-4 b	24.473	4.01	0.38	1.52	2.47	0.05	1505.	1475.	0.558	0.035	0.139
HAT-P-12 b	67.063	10.76	0.05	0.58	2.50	0.04	906.	876.	0.177	0.108	0.138
HIP 14810 b	1233.187	19.31	0.17	3.31	7.99	0.07	950.	920.	0.266	0.070	0.136
51 Peg b	148.745	8.01	0.29	2.32	4.31	0.05	1289.	1259.	0.422	0.043	0.134
HD 102272 b	1875.207	22.99	0.15	3.55	9.03	0.61	908.	878.	0.241	0.074	0.134
HD 68988 b	603.880	14.35	0.20	2.93	6.49	0.07	1083.	1053.	0.312	0.056	0.132
XO-5 b	410.361	12.22	0.22	2.75	5.80	0.05	1164.	1134.	0.340	0.049	0.130
CoRoT-4 b	228.839	13.35	0.10	1.28	4.14	0.09	1006.	976.	0.223	0.075	0.130
HD 189733 b	365.507	12.92	0.17	2.19	5.32	0.03	1143.	1113.	0.295	0.053	0.125
WASP-7 b	305.119	10.27	0.28	2.89	5.45	0.06	1292.	1262.	0.392	0.040	0.125
WASP-16 b	271.746	11.31	0.19	2.12	4.90	0.04	1222.	1192.	0.320	0.047	0.122
HD 187123 b	165.273	8.37	0.28	2.36	4.44	0.04	1384.	1354.	0.413	0.036	0.122

HD 75289 b	133.489	7.66	0.30	2.28	4.18	0.05	1431.	1401.	0.432	0.034	0.121
WASP-2 b	269.204	11.70	0.17	1.97	4.80	0.03	1212.	1182.	0.301	0.048	0.120
XO-1 b	286.049	13.29	0.12	1.62	4.64	0.05	1136.	1106.	0.251	0.056	0.118
HD 88133 b	69.923	5.85	0.35	2.04	3.46	0.05	1583.	1553.	0.493	0.028	0.118
OGLE-TR-113 b	394.111	12.46	0.20	2.54	5.63	0.02	1255.	1225.	0.324	0.042	0.117
HD 185269 b	298.762	10.71	0.24	2.61	5.28	0.08	1333.	1303.	0.364	0.037	0.117
XO-2 b	181.164	10.92	0.14	1.52	4.07	0.04	1234.	1204.	0.281	0.048	0.116
HAT-P-2 b	2777.850	13.35	1.17	15.58	14.43	0.07	1398.	1368.	0.544	0.024	0.115
HD 73256 b	594.345	14.26	0.21	2.92	6.46	0.04	1256.	1226.	0.313	0.040	0.112
HD 149026 b	113.148	6.85	0.35	2.41	4.07	0.04	1635.	1605.	0.476	0.025	0.109
HD 179949 b	301.940	10.76	0.24	2.61	5.30	0.04	1429.	1399.	0.363	0.032	0.107
HAT-P-16 b	1332.669	14.46	0.44	6.37	9.60	0.04	1516.	1486.	0.427	0.023	0.099
HAT-P-14 b	699.230	13.47	0.29	3.86	7.21	0.06	1477.	1447.	0.367	0.027	0.099
HAT-P-1 b	166.544	13.66	0.07	0.89	3.49	0.06	1213.	1183.	0.183	0.052	0.098
WASP-22 b	177.986	12.57	0.09	1.13	3.76	0.05	1330.	1300.	0.219	0.041	0.095
CoRoT-2 b	1052.023	16.44	0.24	3.89	8.00	0.03	1436.	1406.	0.321	0.028	0.094
HD 86081 b	476.748	13.01	0.22	2.82	6.06	0.04	1517.	1487.	0.329	0.027	0.093
WASP-26 b	324.188	14.81	0.10	1.48	4.68	0.04	1321.	1291.	0.221	0.039	0.093
XO-3 b	3747.237	13.66	1.47	20.09	16.57	0.05	1592.	1562.	0.504	0.017	0.093
WASP-14 b	2455.251	14.13	0.87	12.30	13.19	0.04	1721.	1691.	0.538	0.015	0.091
OGLE-TR-182 b	336.902	16.50	0.08	1.24	4.52	0.05	1265.	1235.	0.187	0.044	0.091
HAT-P-5 b	336.902	14.14	0.12	1.69	4.88	0.04	1437.	1407.	0.244	0.032	0.089
WASP-5 b	520.291	13.14	0.23	3.01	6.29	0.03	1614.	1584.	0.336	0.023	0.087
HD 209458 b	203.412	15.49	0.05	0.85	3.63	0.05	1344.	1314.	0.162	0.041	0.081
Kepler-6 b	212.629	14.85	0.06	0.96	3.79	0.05	1404.	1374.	0.179	0.036	0.081
tau Boo b	1239.544	19.36	0.17	3.31	8.01	0.05	1545.	1515.	0.265	0.023	0.079
HAT-P-13 b	270.157	14.36	0.09	1.31	4.34	0.04	1535.	1505.	0.213	0.029	0.078
HAT-P-9 b	247.909	15.71	0.06	1.00	3.97	0.05	1428.	1398.	0.174	0.035	0.078
HAT-P-6 b	335.948	14.92	0.10	1.51	4.75	0.05	1560.	1530.	0.222	0.027	0.077
CoRoT-5 b	148.427	15.58	0.04	0.61	3.09	0.05	1347.	1317.	0.136	0.042	0.076
Kepler-5 b	671.896	16.06	0.16	2.61	6.47	0.05	1683.	1653.	0.273	0.020	0.075

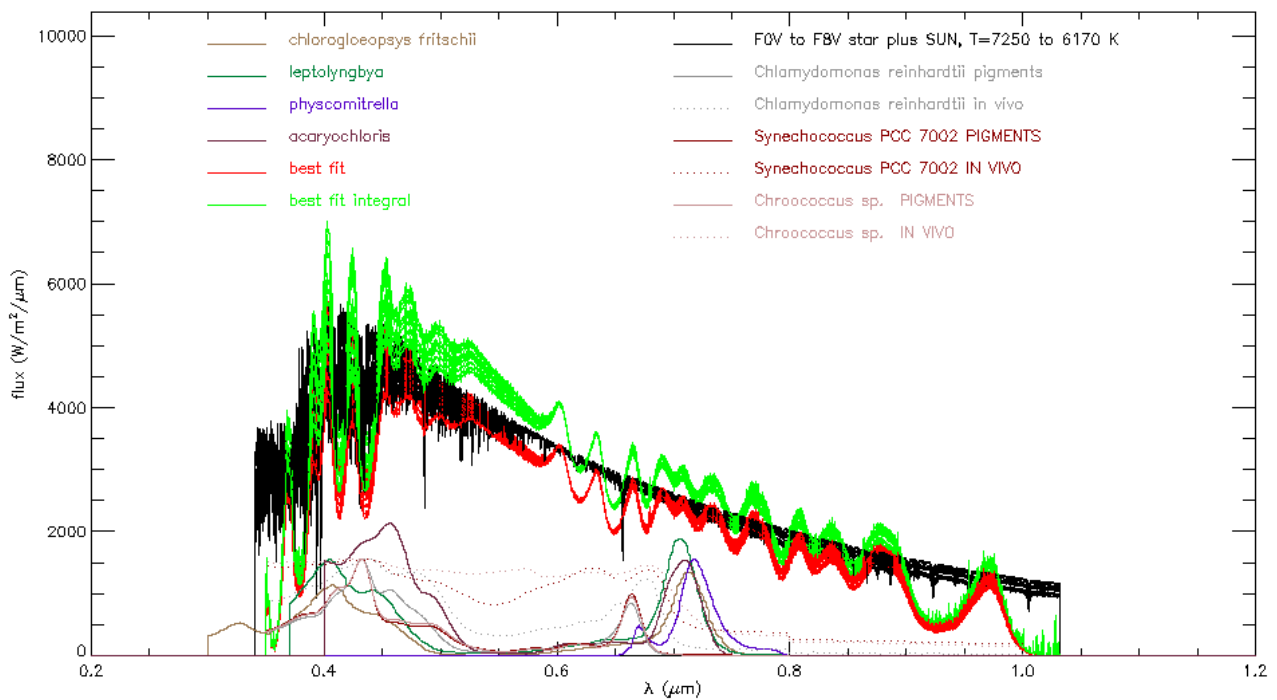
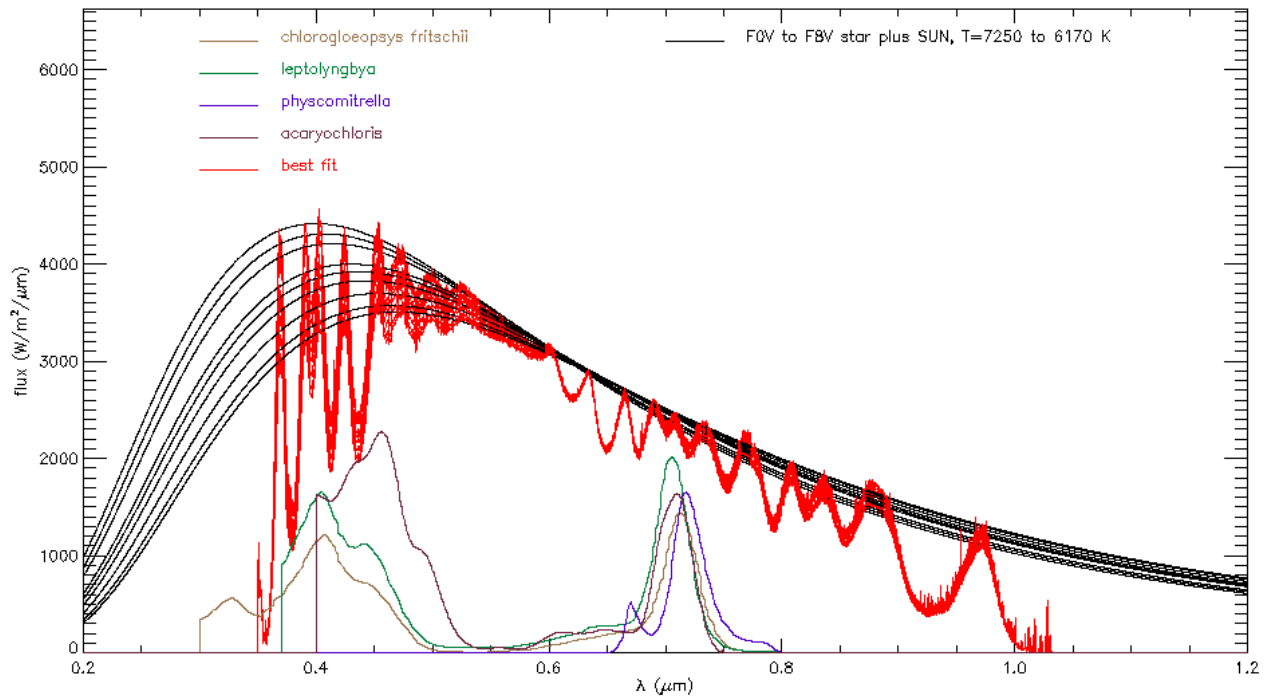
HAT-P-4 b	216.126	14.25	0.07	1.06	3.90	0.04	1573.	1543.	0.194	0.028	0.073
HAT-P-8 b	483.104	16.83	0.10	1.71	5.36	0.05	1588.	1558.	0.215	0.025	0.073
OGLE-TR-211 b	238.374	14.14	0.08	1.19	4.11	0.05	1612.	1582.	0.206	0.026	0.073
CoRoT-3 b	6884.236	11.33	4.73	53.60	24.65	0.06	1585.	1555.	0.337	0.015	0.072
OGLE-TR-132 b	371.863	14.03	0.13	1.89	5.15	0.03	1842.	1812.	0.259	0.018	0.067
Kepler-8 b	191.653	15.92	0.05	0.76	3.47	0.05	1550.	1520.	0.149	0.030	0.067
WASP-3 b	654.733	16.32	0.15	2.46	6.34	0.03	1845.	1815.	0.262	0.016	0.066
WASP-15 b	172.265	16.02	0.04	0.67	3.28	0.05	1542.	1512.	0.140	0.030	0.065
Kepler-7 b	137.621	16.59	0.03	0.50	2.88	0.06	1454.	1424.	0.117	0.036	0.065
WASP-4 b	356.448	15.89	0.09	1.41	4.74	0.02	1745.	1715.	0.205	0.020	0.065
OGLE-TR-10 b	216.126	19.30	0.03	0.58	3.35	0.04	1415.	1385.	0.112	0.037	0.064
WASP-19 b	365.507	14.70	0.12	1.69	4.99	0.02	1857.	1827.	0.237	0.017	0.064
WASP-1 b	273.335	16.65	0.06	0.99	4.05	0.04	1651.	1621.	0.165	0.024	0.064
WASP-18 b	3314.985	13.07	1.48	19.40	15.93	0.02	2218.	2188.	0.508	0.008	0.063
OGLE-TR-56 b	413.181	13.47	0.17	2.28	5.54	0.02	2074.	2044.	0.291	0.013	0.061
CoRoT-1 b	327.367	16.72	0.07	1.17	4.43	0.03	1765.	1735.	0.180	0.020	0.060
HAT-P-7 b	572.097	15.95	0.14	2.25	5.99	0.04	1981.	1951.	0.256	0.014	0.060
WASP-17 b	155.738	19.53	0.02	0.41	2.83	0.05	1533.	1503.	0.092	0.032	0.054
WASP-12 b	448.143	20.09	0.06	1.11	4.73	0.02	2331.	2301.	0.152	0.010	0.039

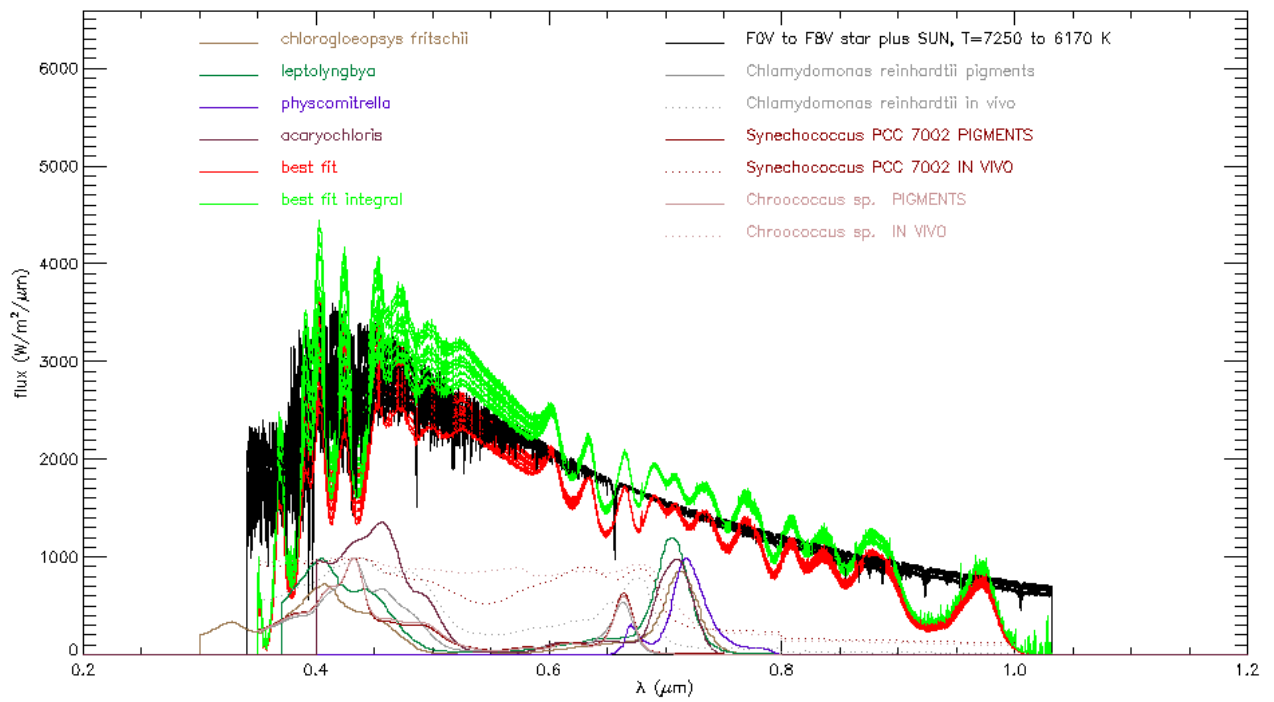
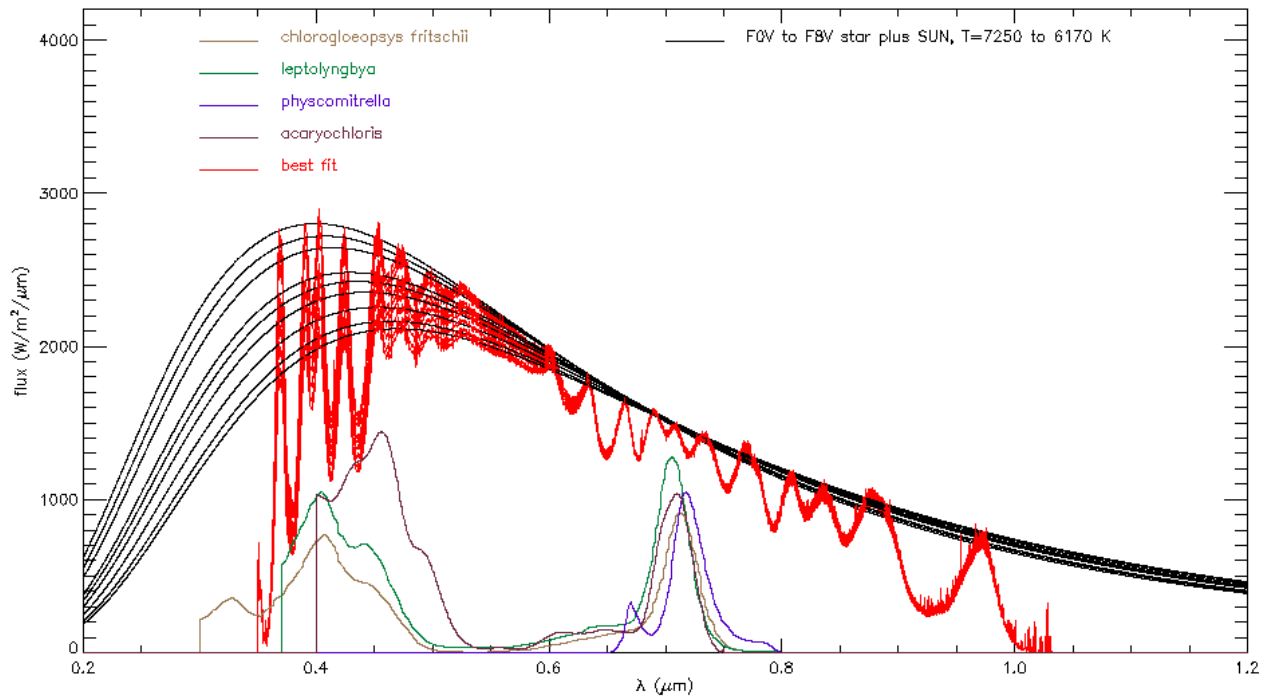
Here, ESI_{int} , ESI_{sur} , ESI_{grav} and ESI are the Earth Similarity Index for the internal composition of the planet, the surface and the gravity, and the total one. EU means Earth Units.

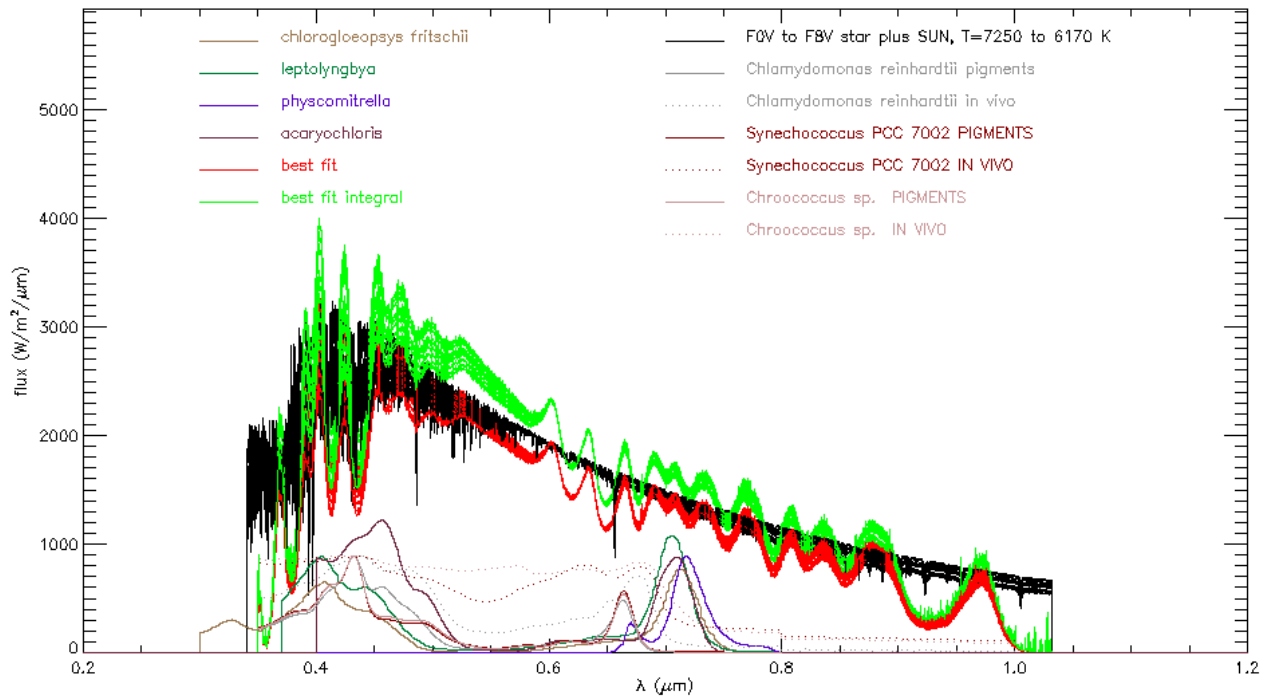
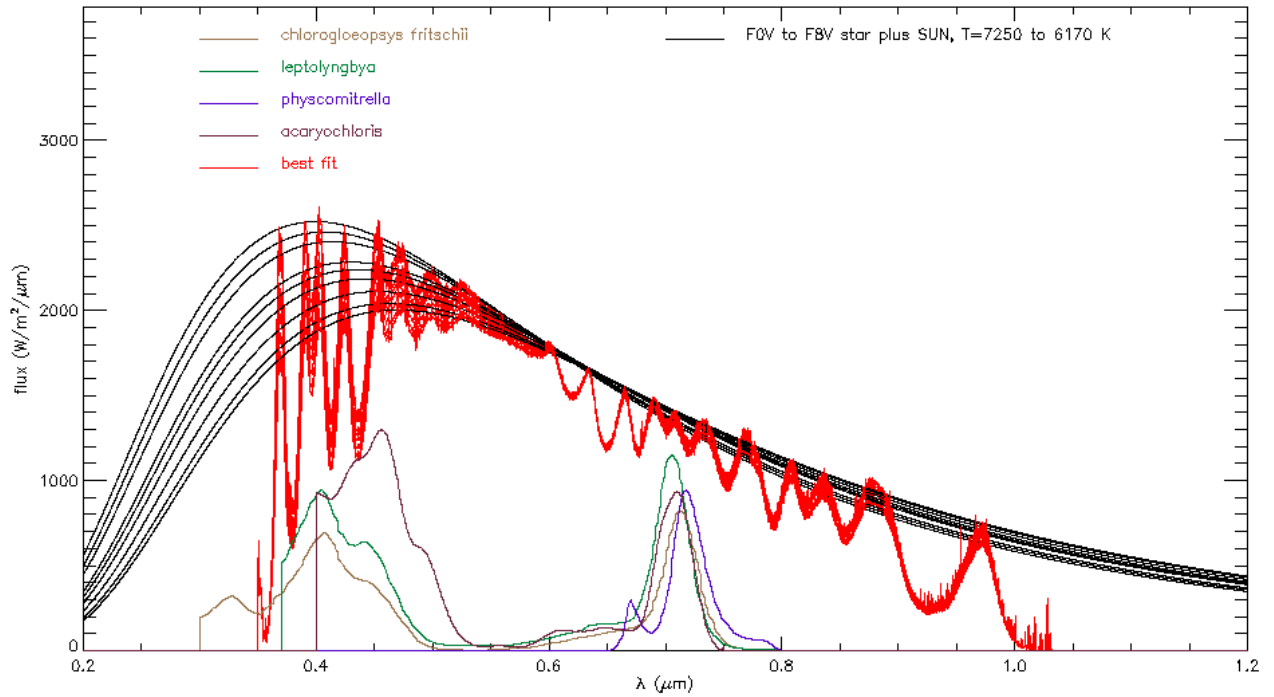
APPENDIX F: Stellar simulations

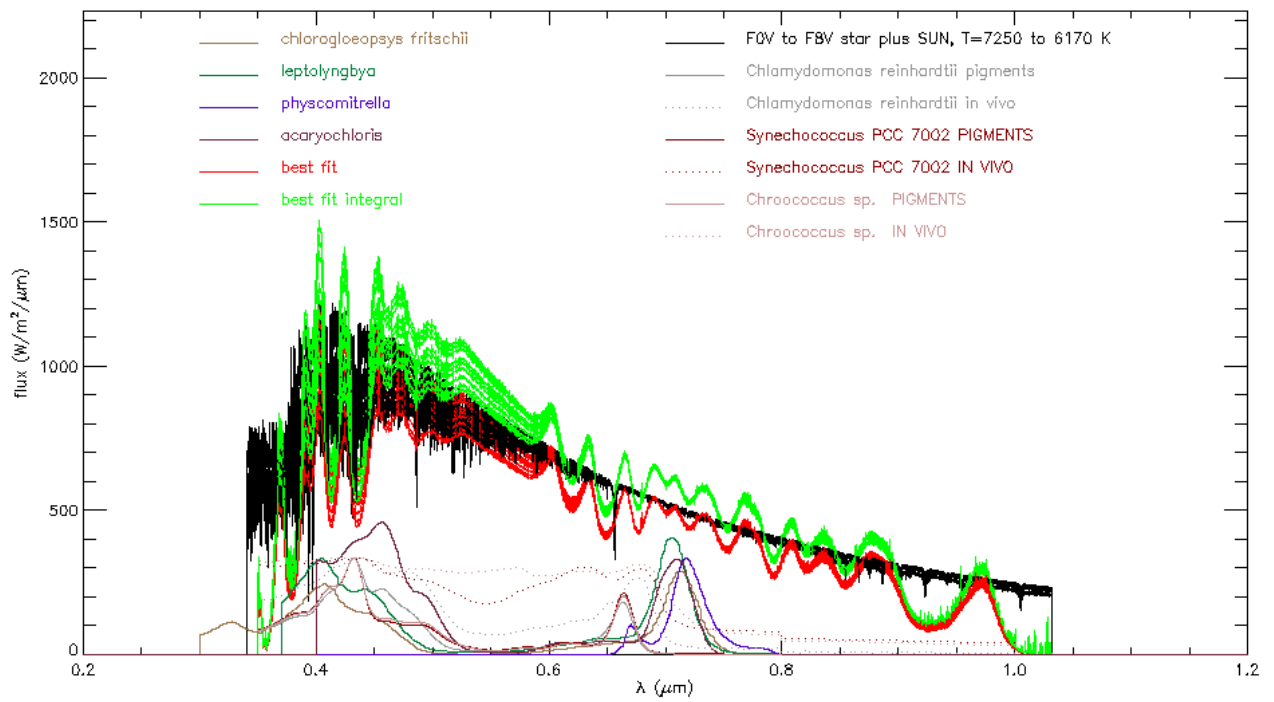
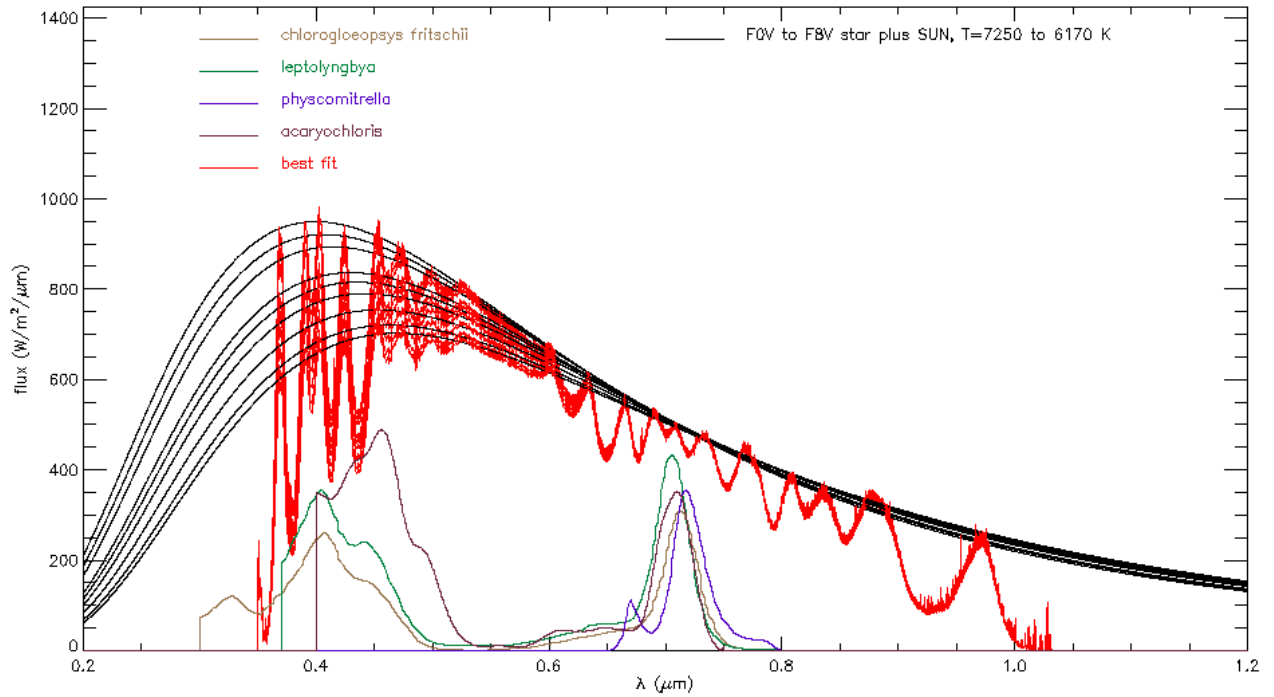
F.1: F type stars

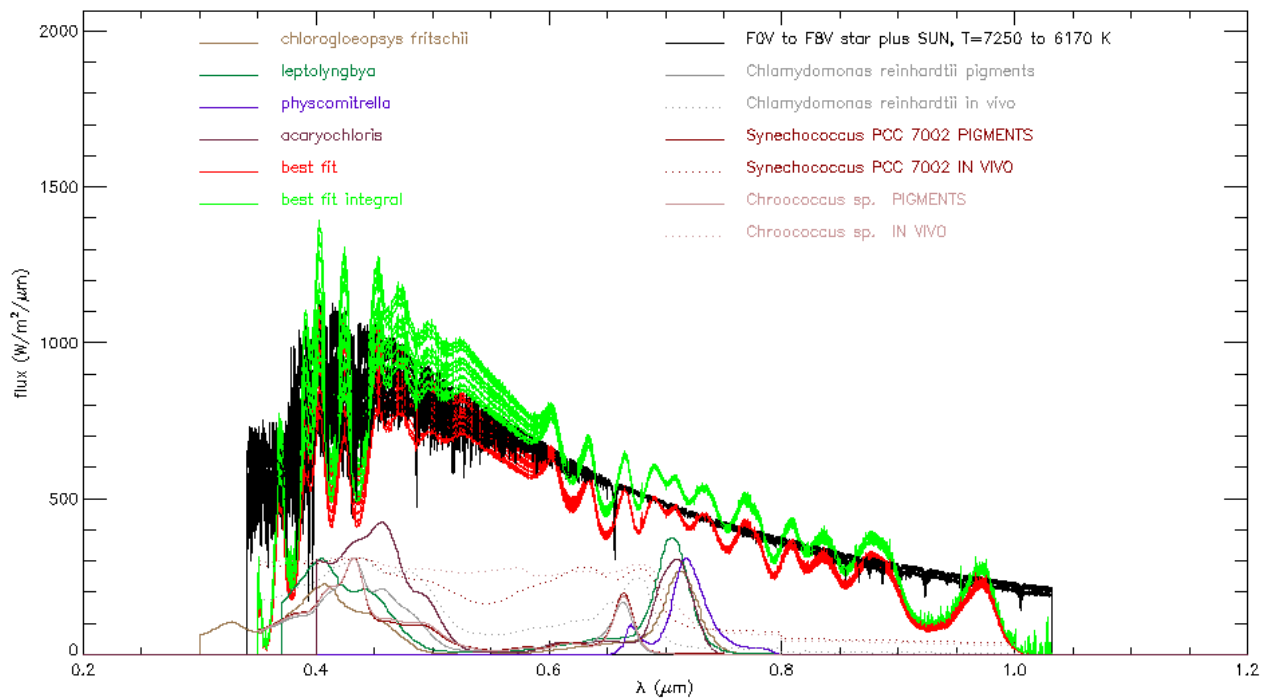
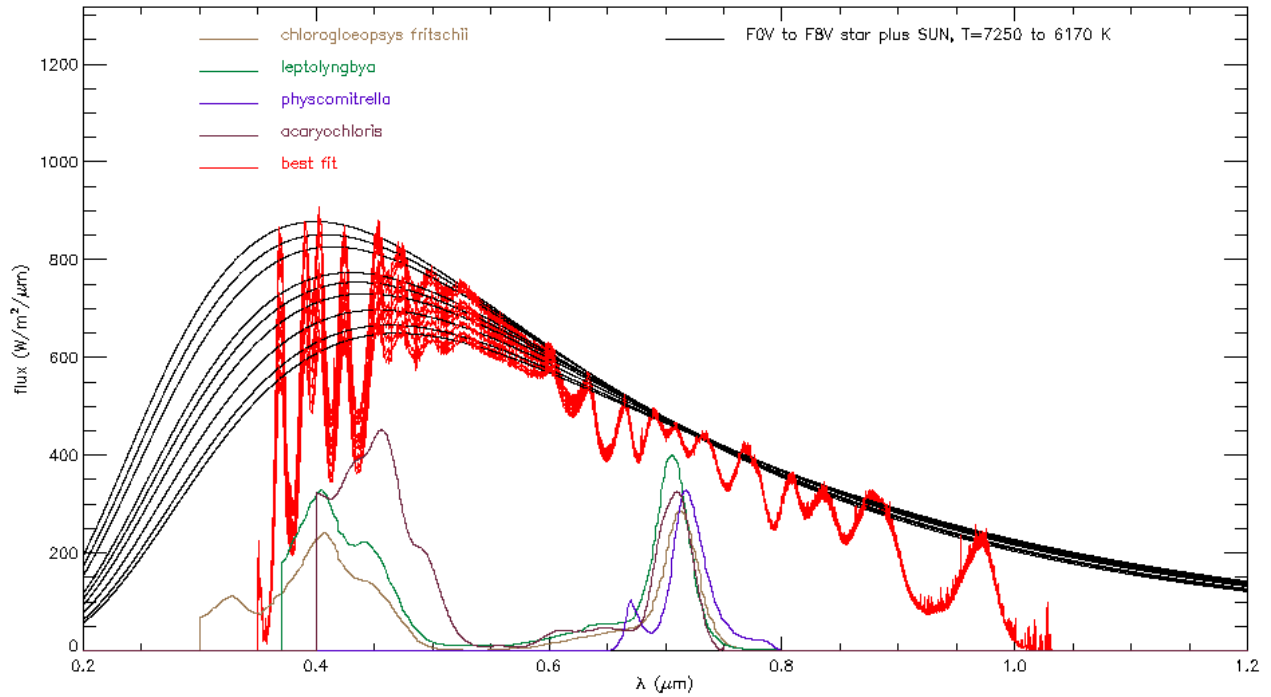
In these pictures are illustrated the simulations of F type stars and their fit with LED palette as well as the black body fit. The red line represents the spectrum fit, the green line is the integral fit.







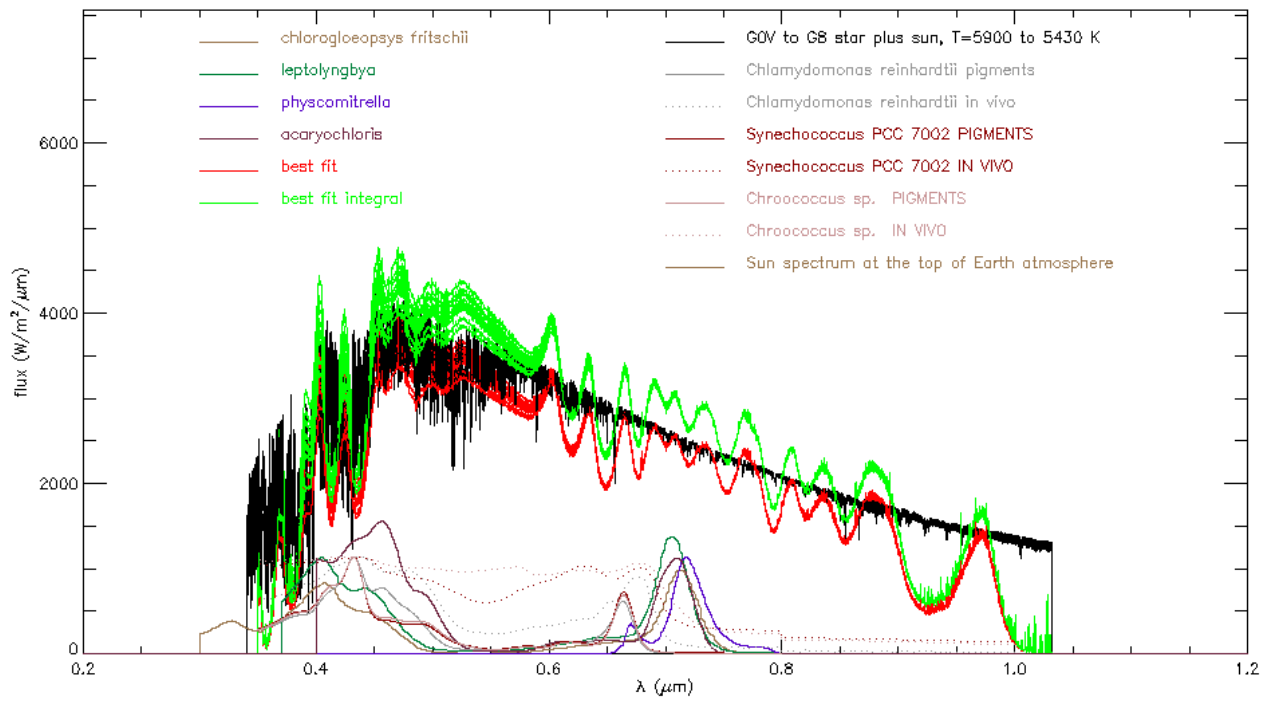
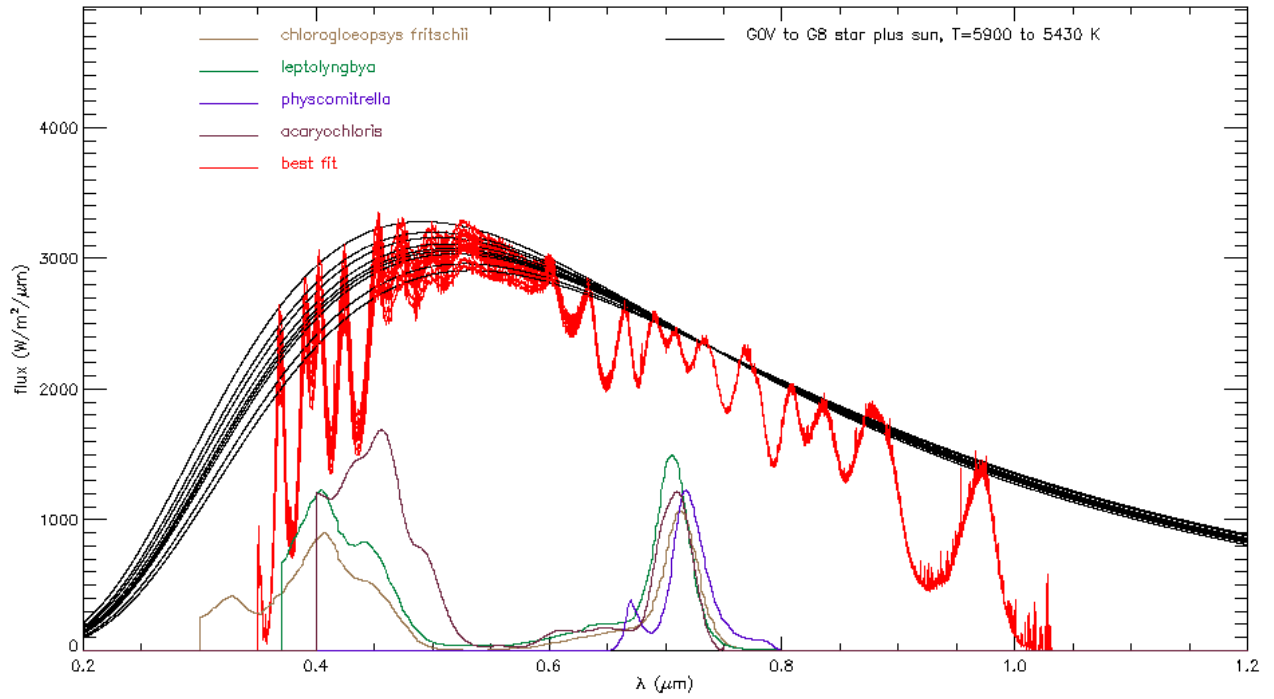


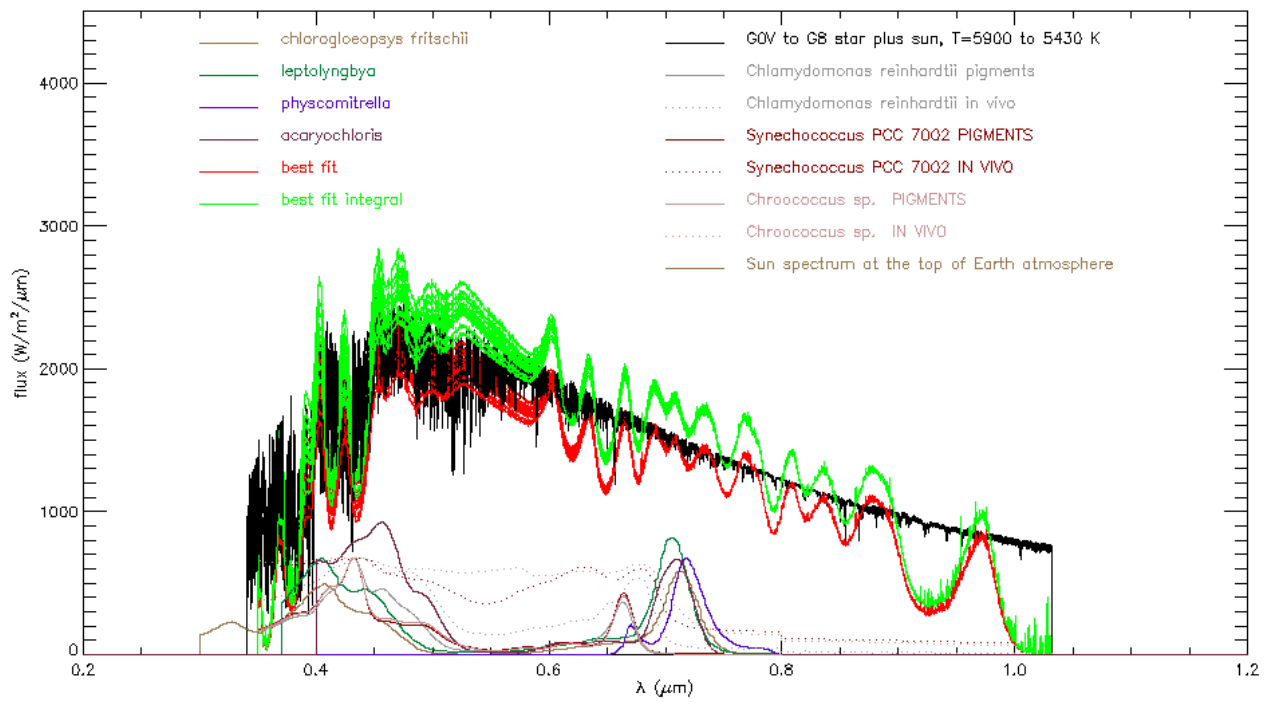
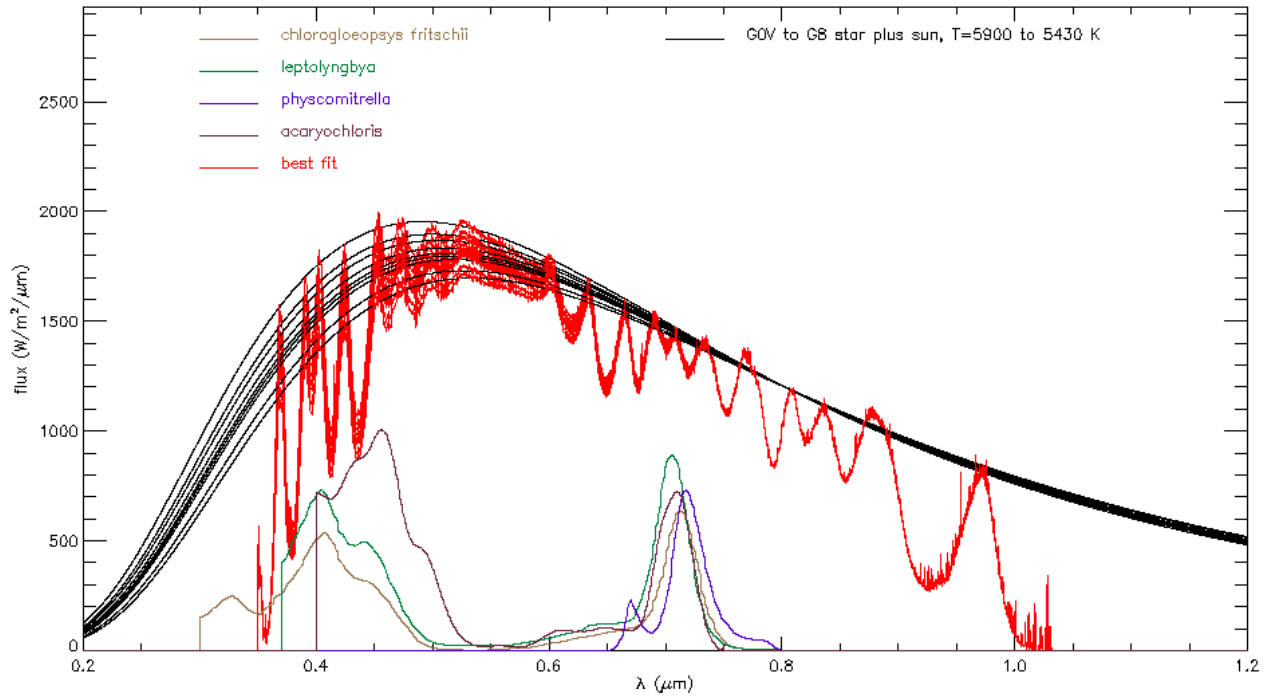


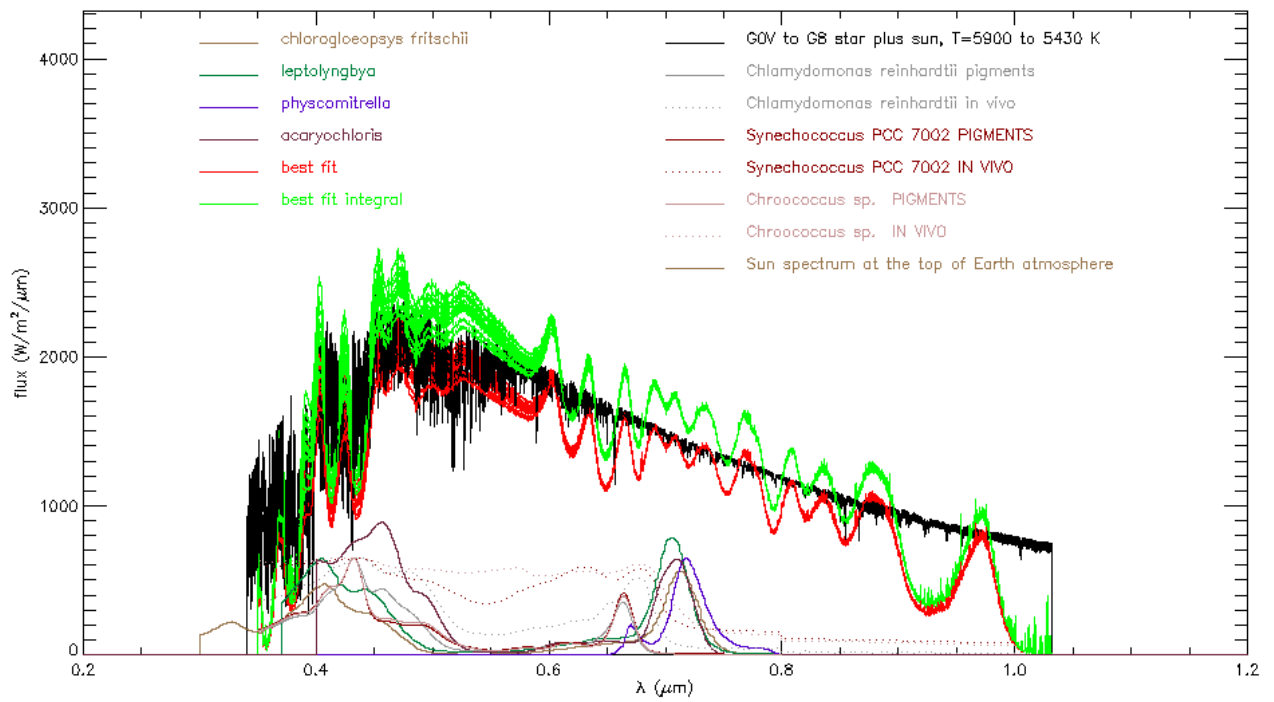
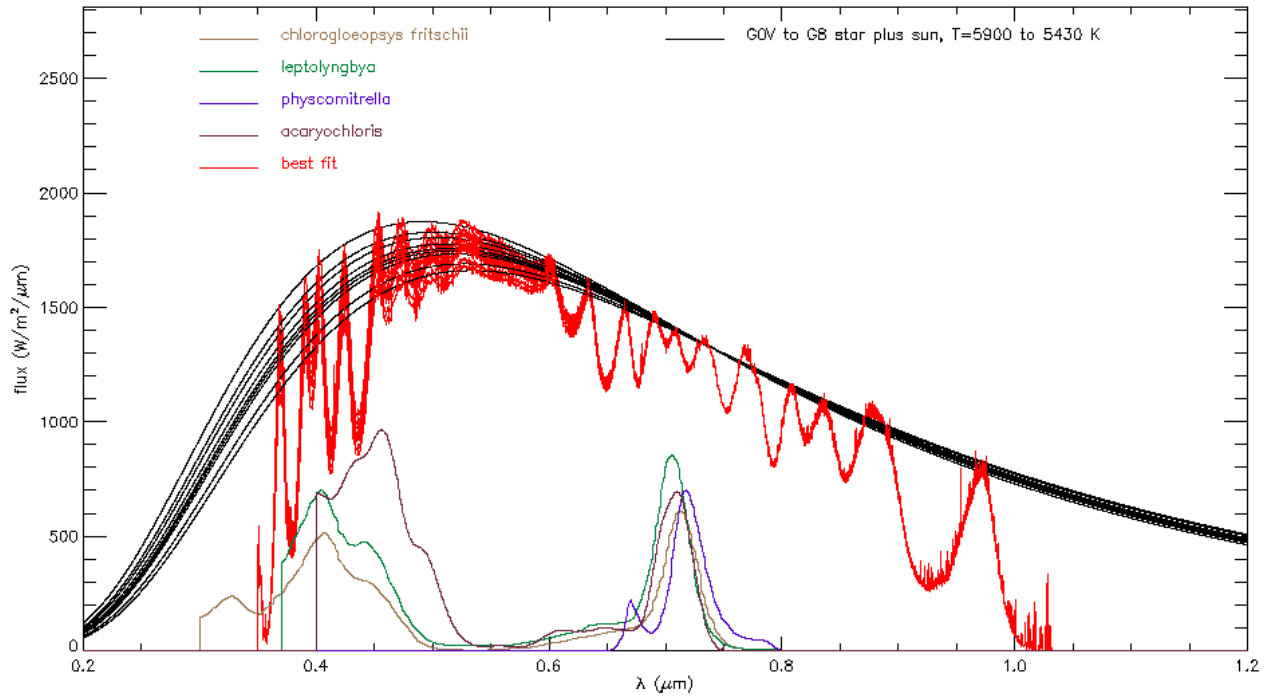
Figures F.1, F.2, F.3, F.4, F.5, F.6, F.7, F.8, F.9, F.10: Simulations of F type stars and their fit with LED palette as well as the black body fit. The red line represents the spectrum fit, the green line is the integral fit.

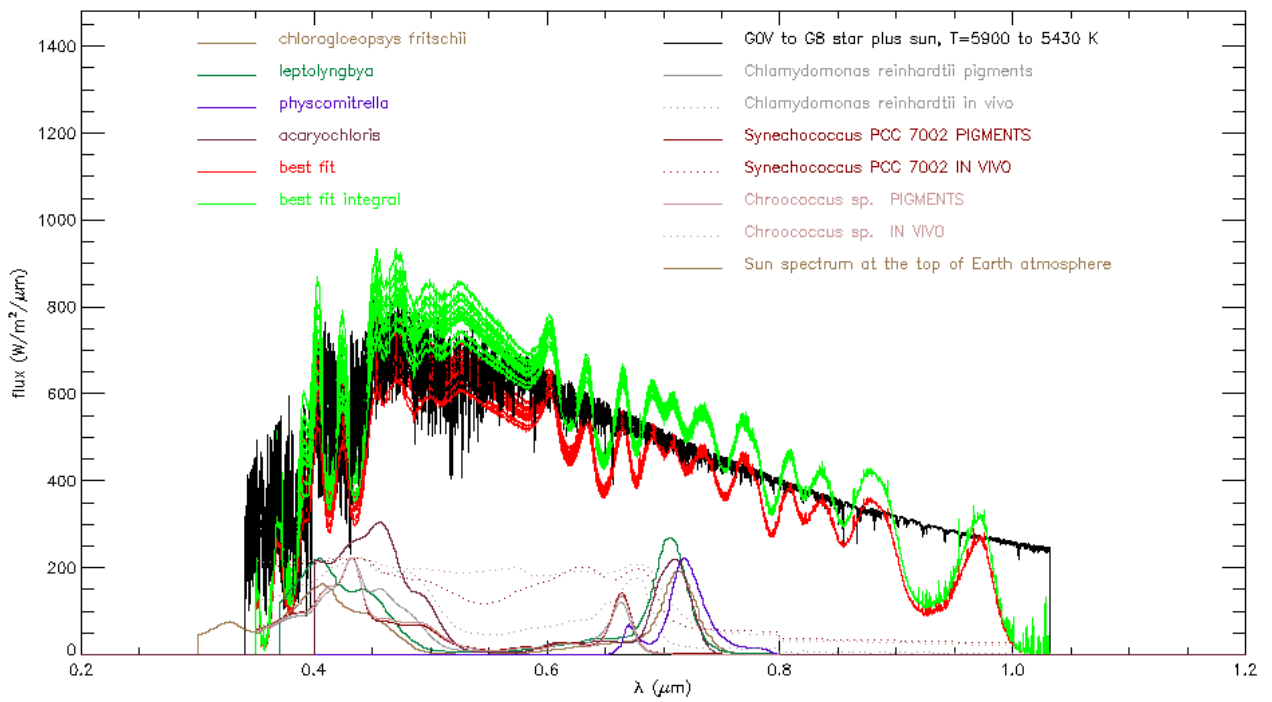
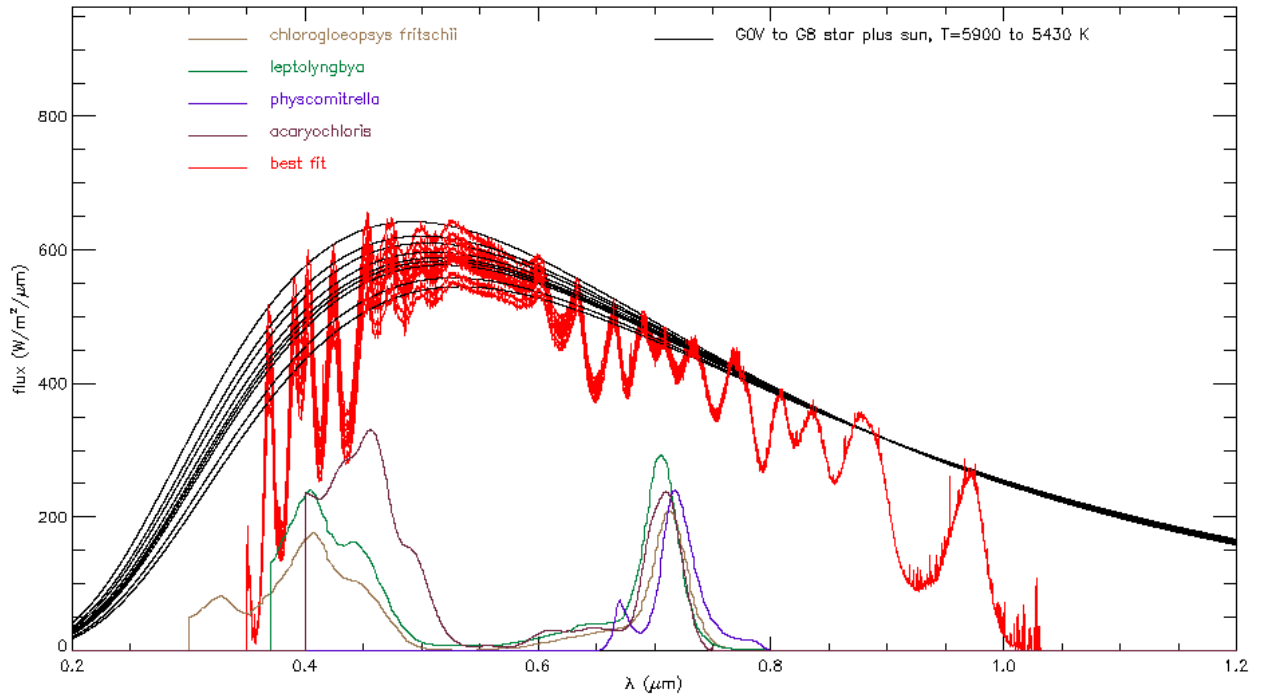
F.2: G type stars

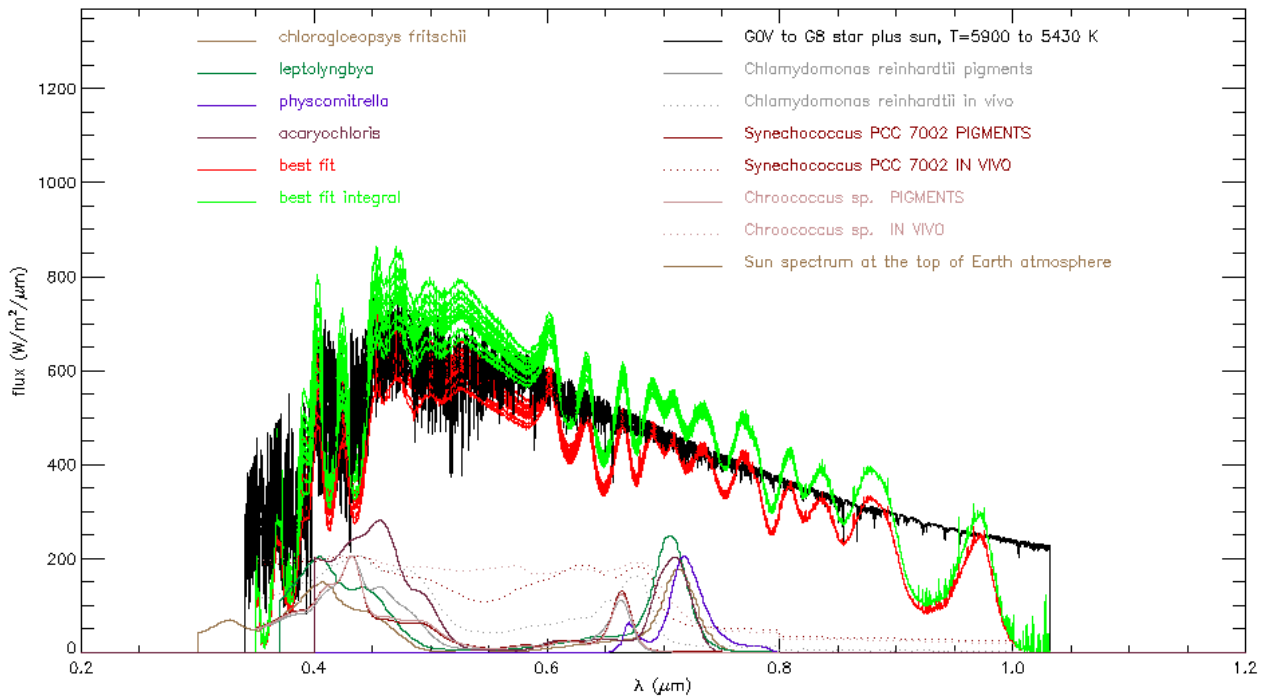
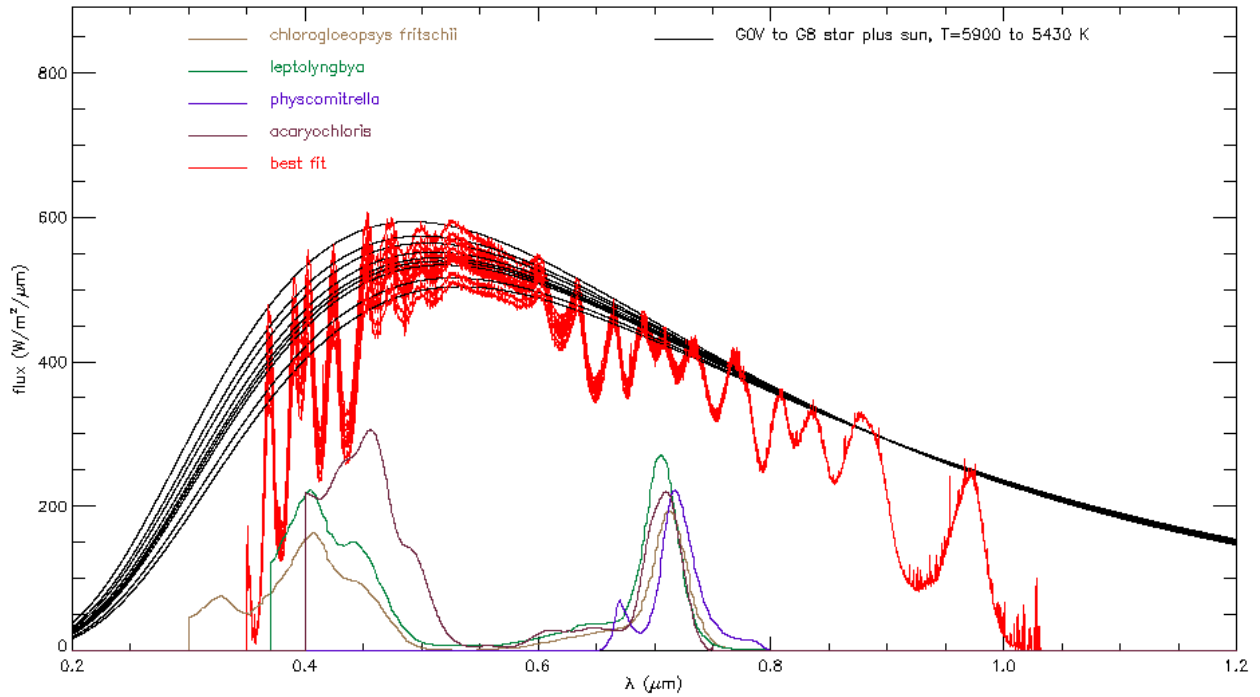
In these pictures are illustrated the simulations of G type stars and their fit with LED palette as well as the black body fit. The red line represents the spectrum fit, the green line is the integral fit.







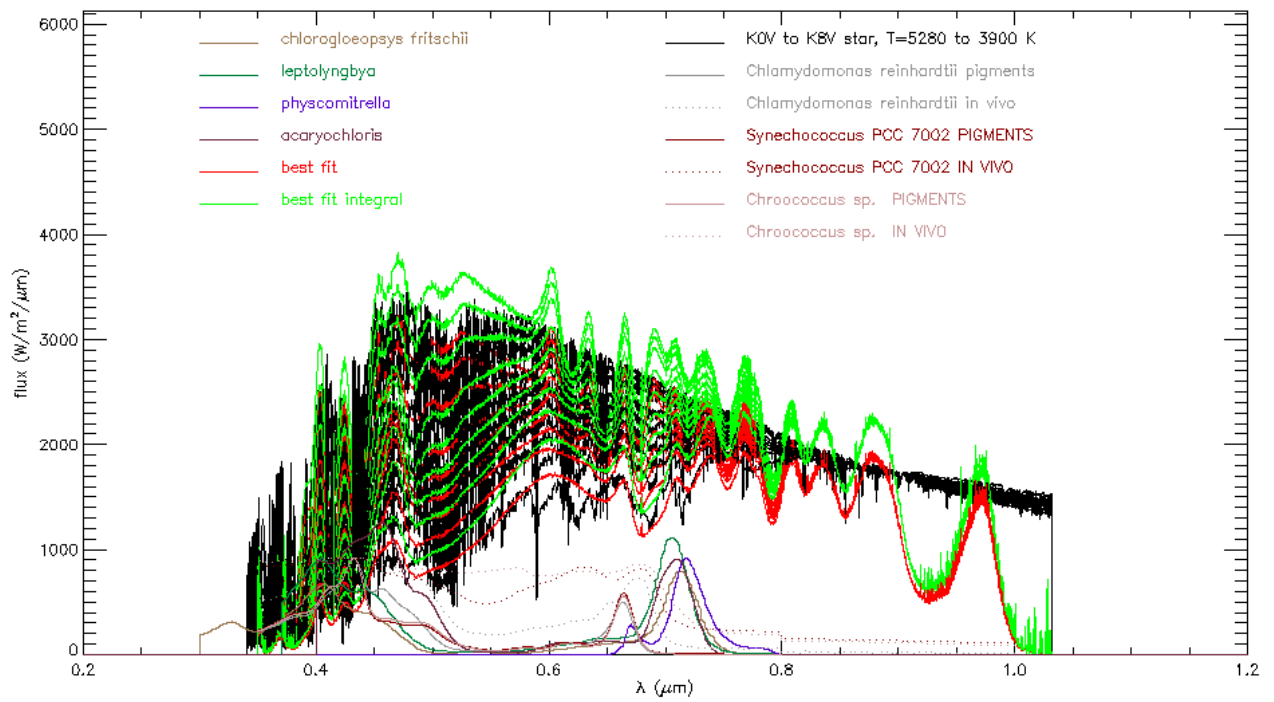
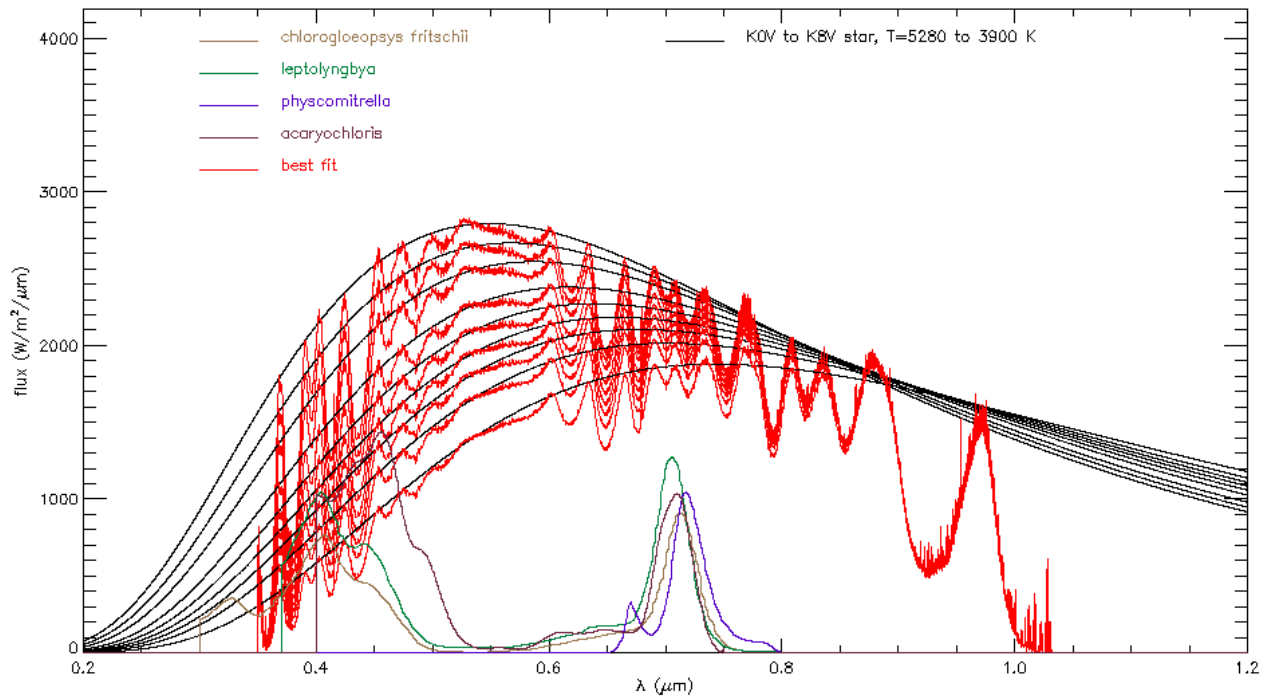


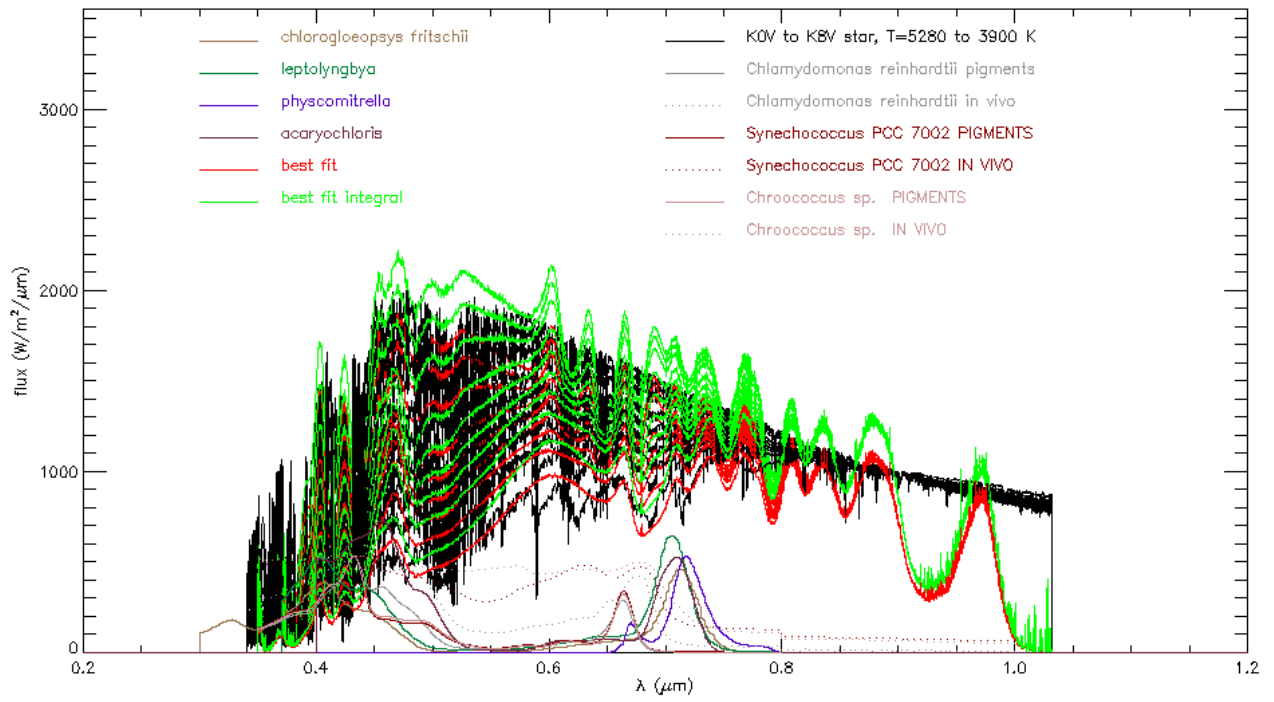
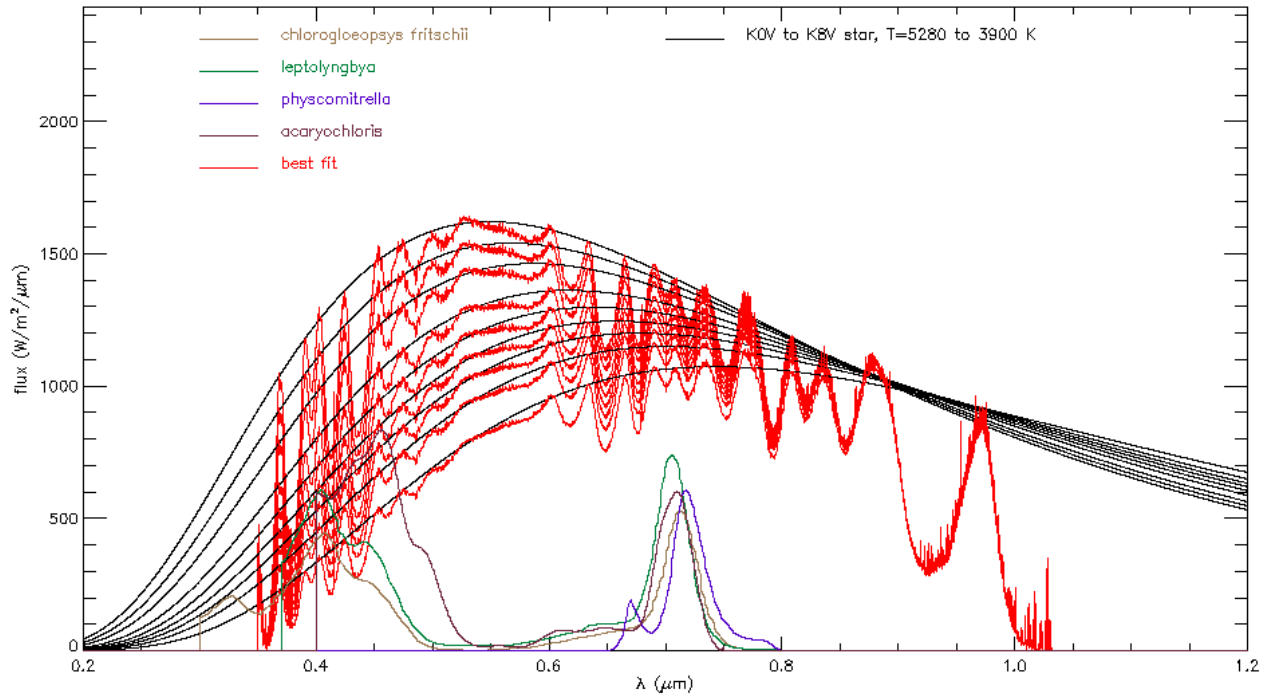


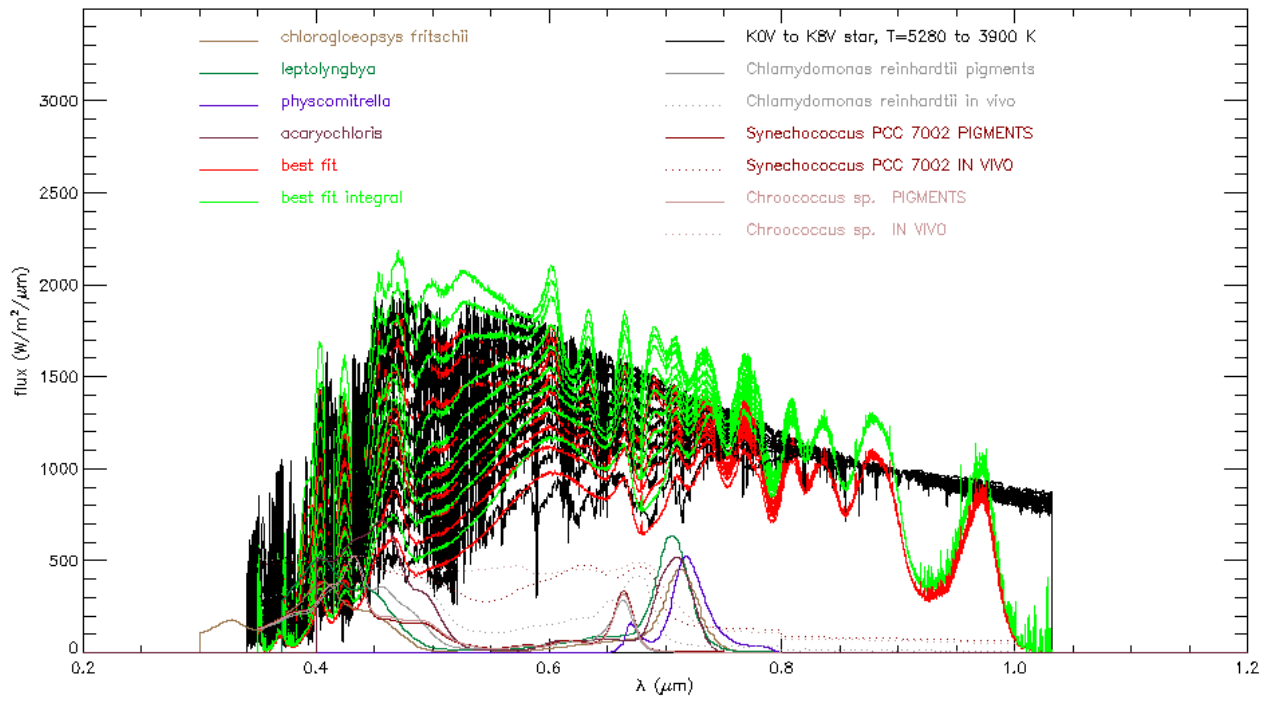
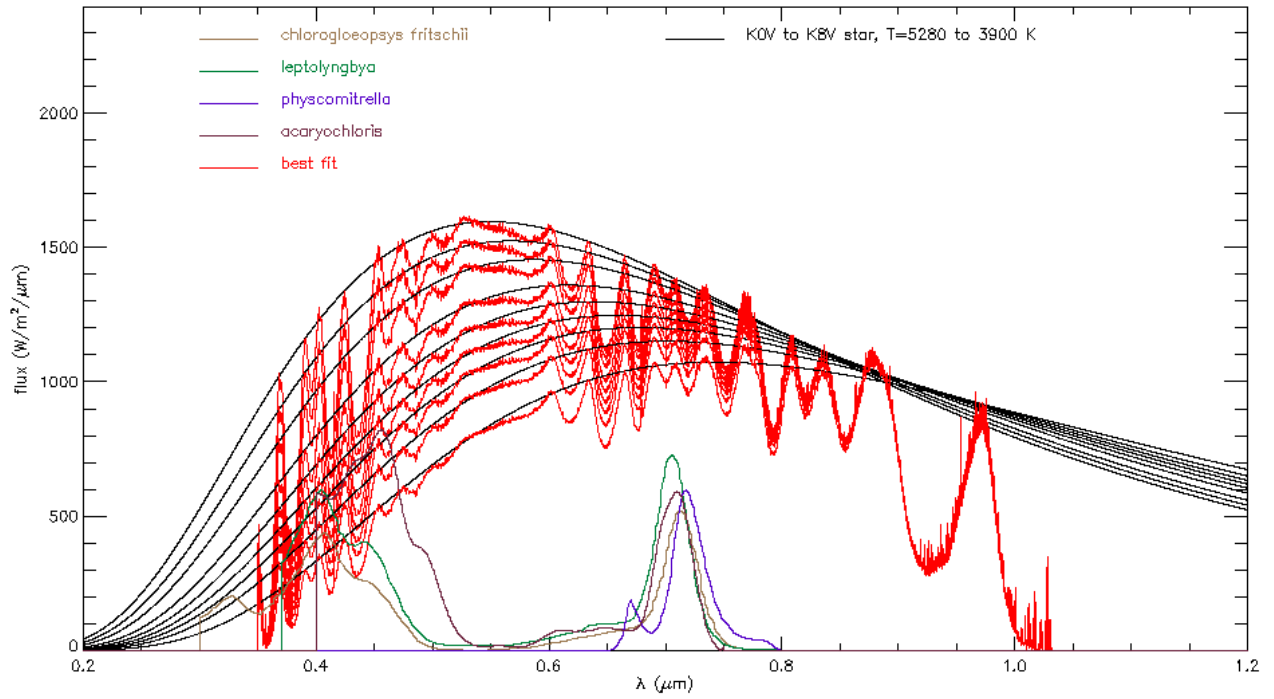
Figures F.11, F.12, F.13, F.14, F.15, F.16, F.17, F.18, F.19, F.20: Simulations of G type stars and their fit with LED palette as well as the black body fit. The red line represents the spectrum fit, the green line is the integral fit.

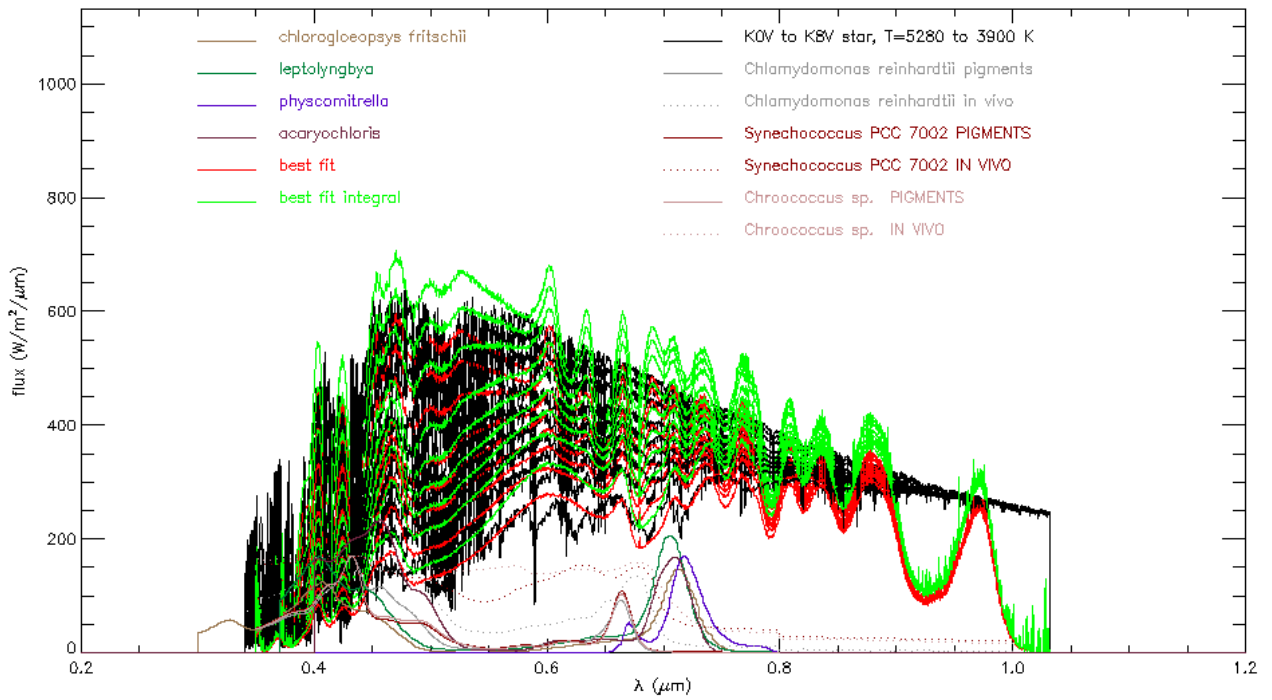
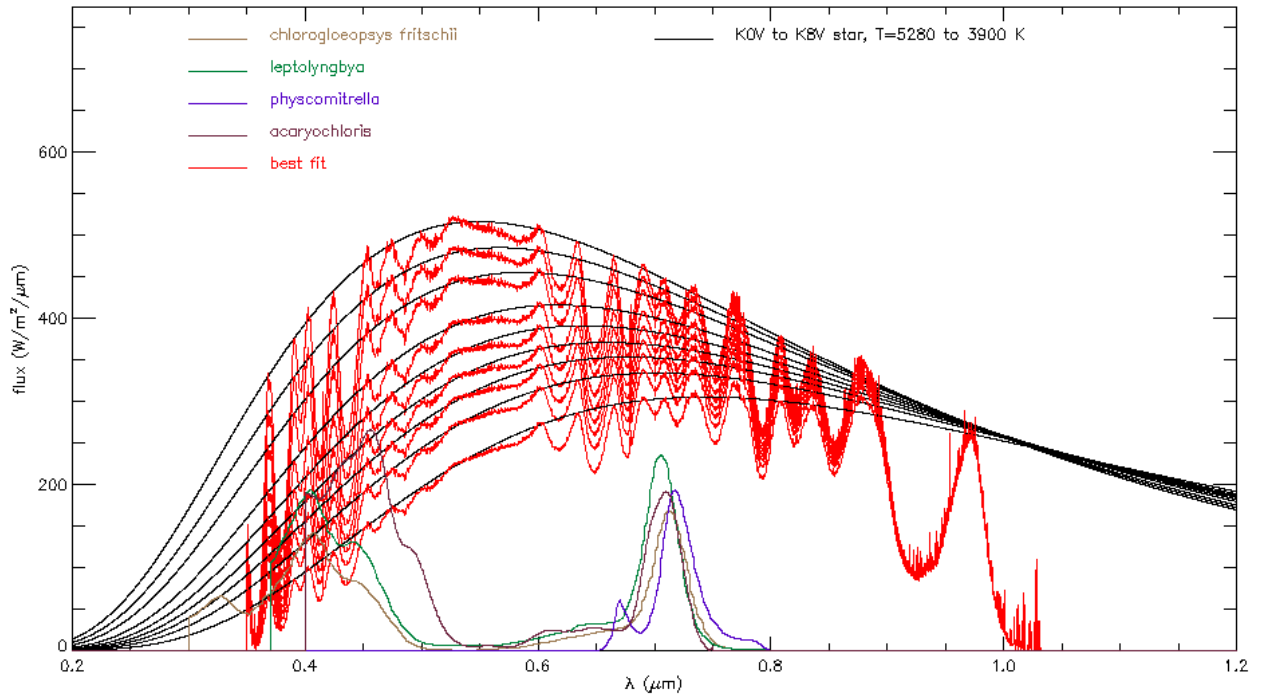
F.3: K type stars

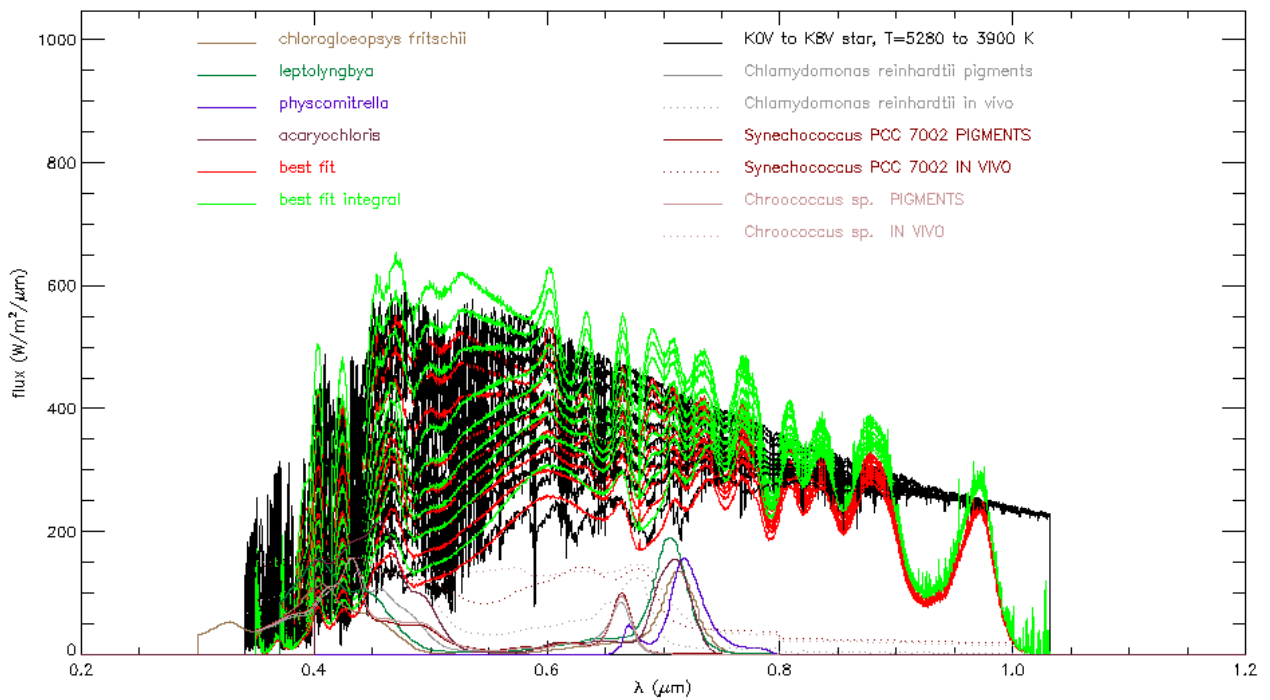
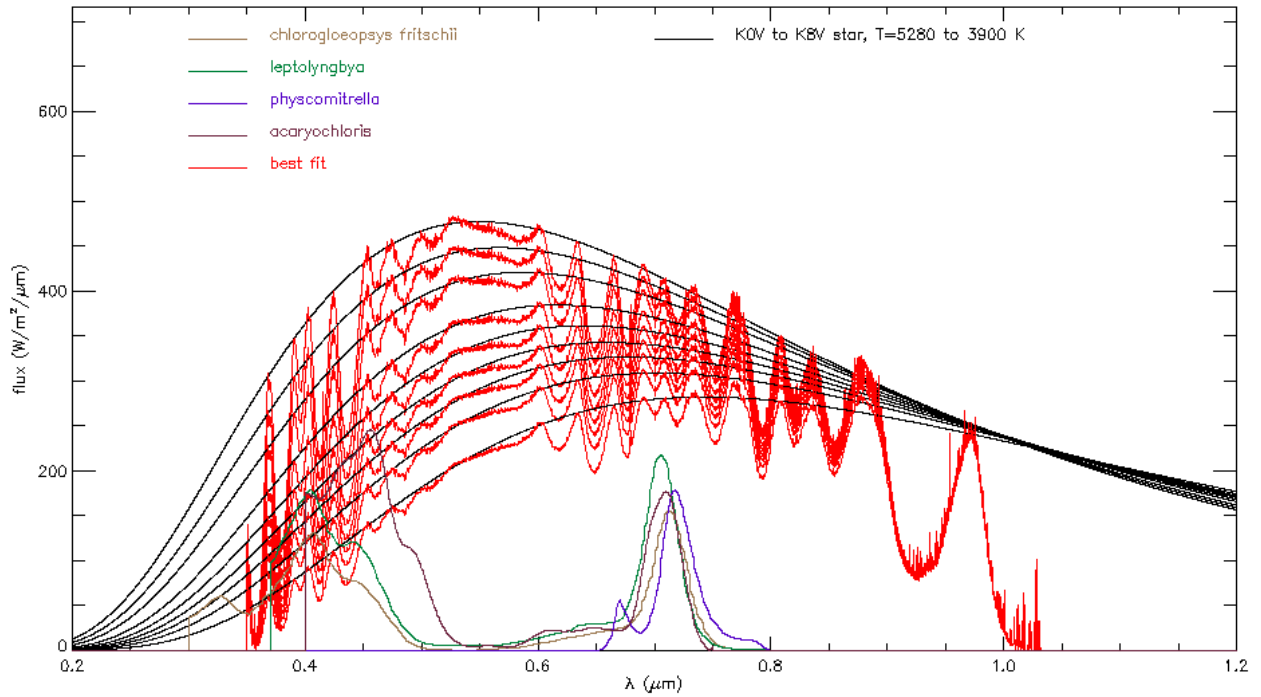
In these pictures are illustrated the simulations of K type stars and their fit with LED palette as well as the black body fit. The red line represents the spectrum fit, the green line is the integral fit.







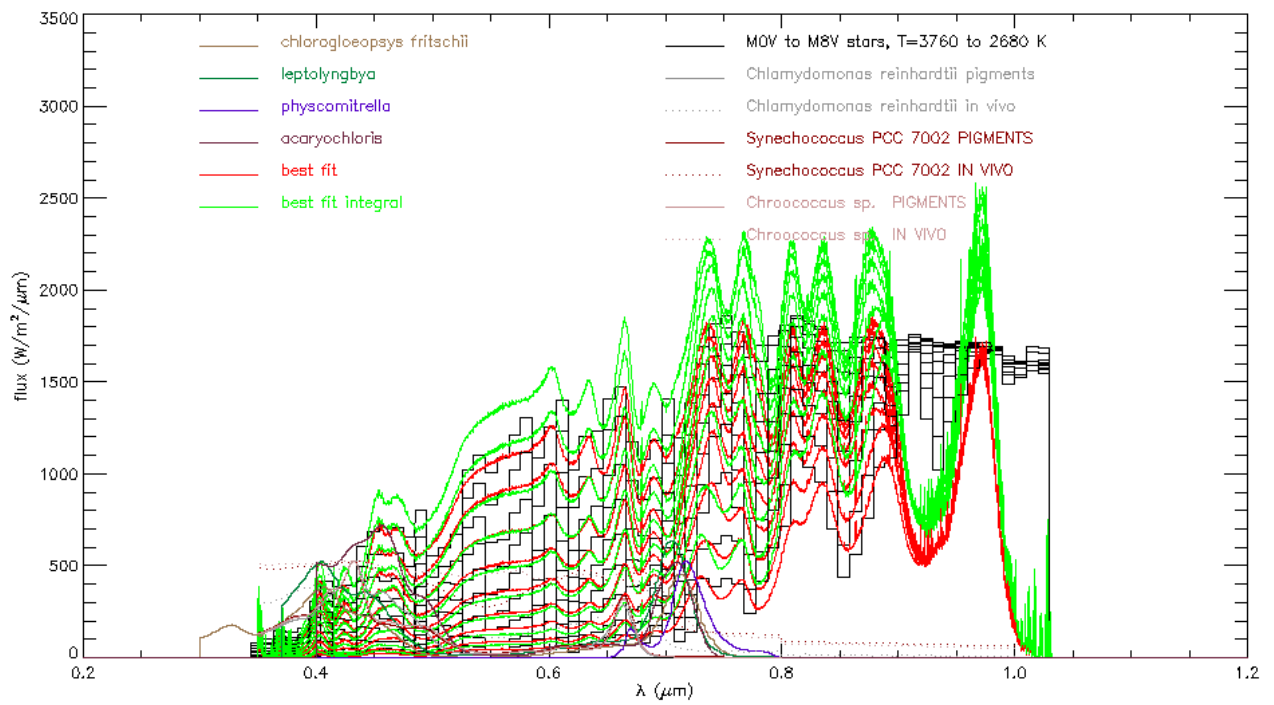
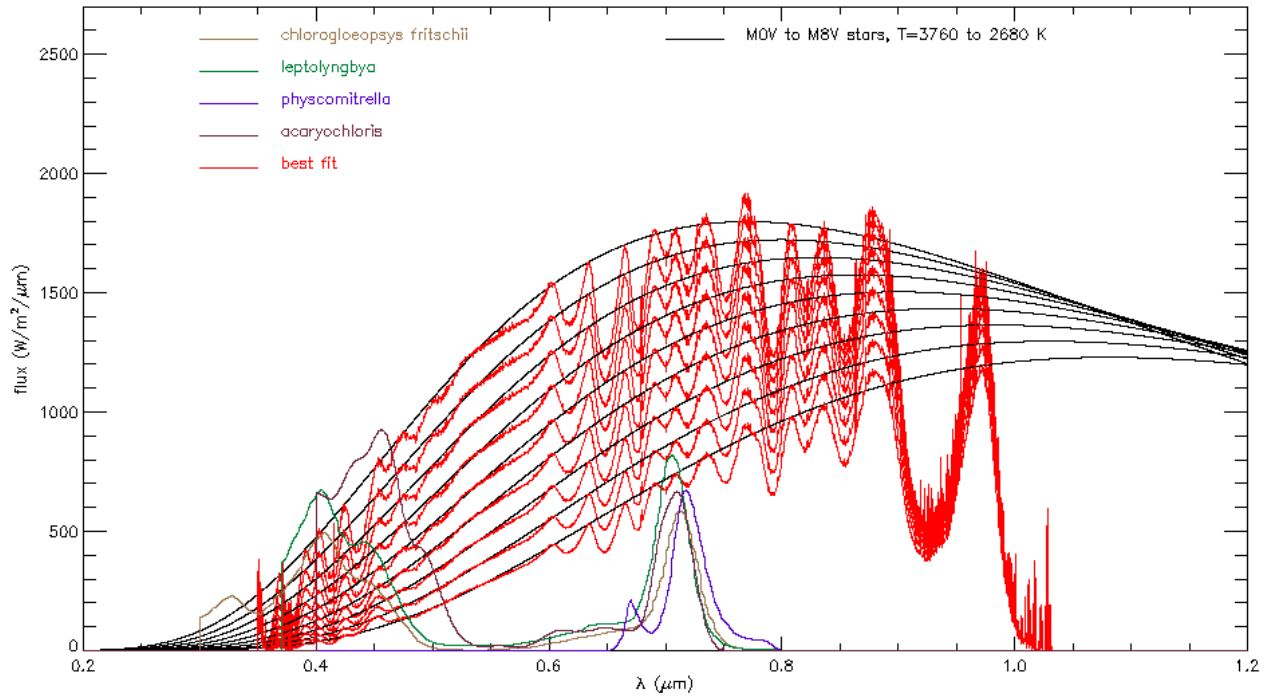


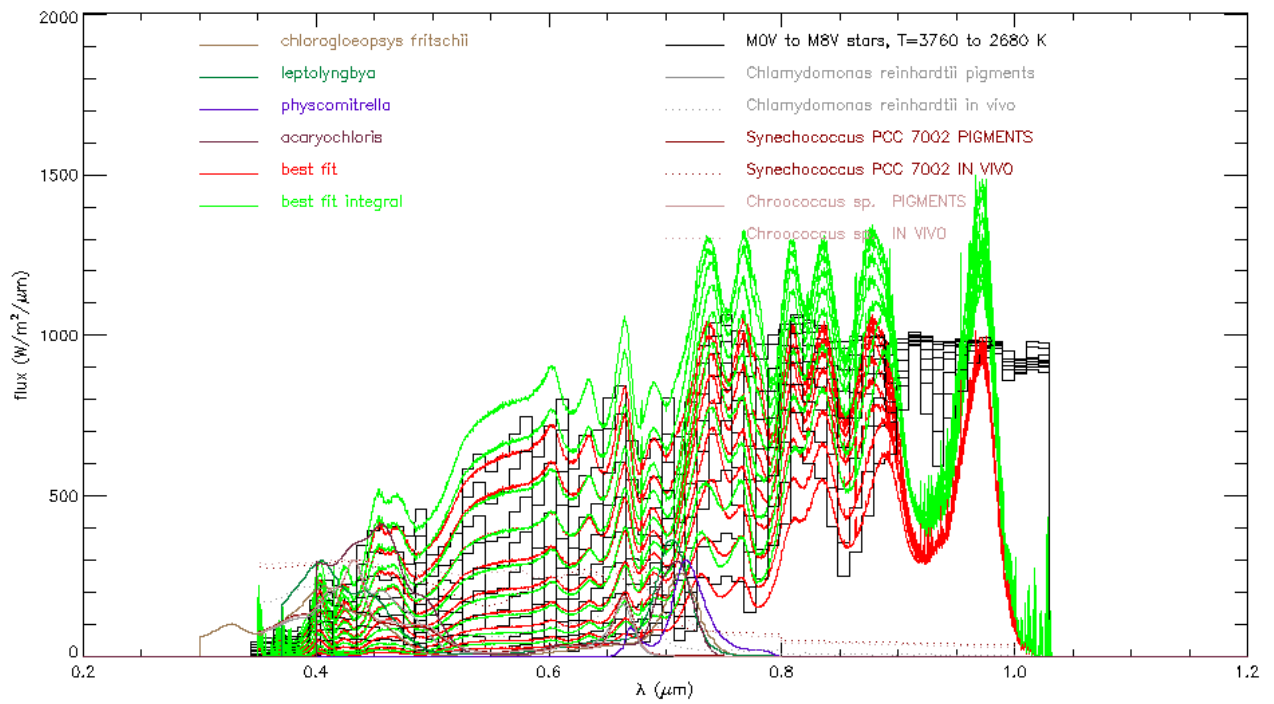
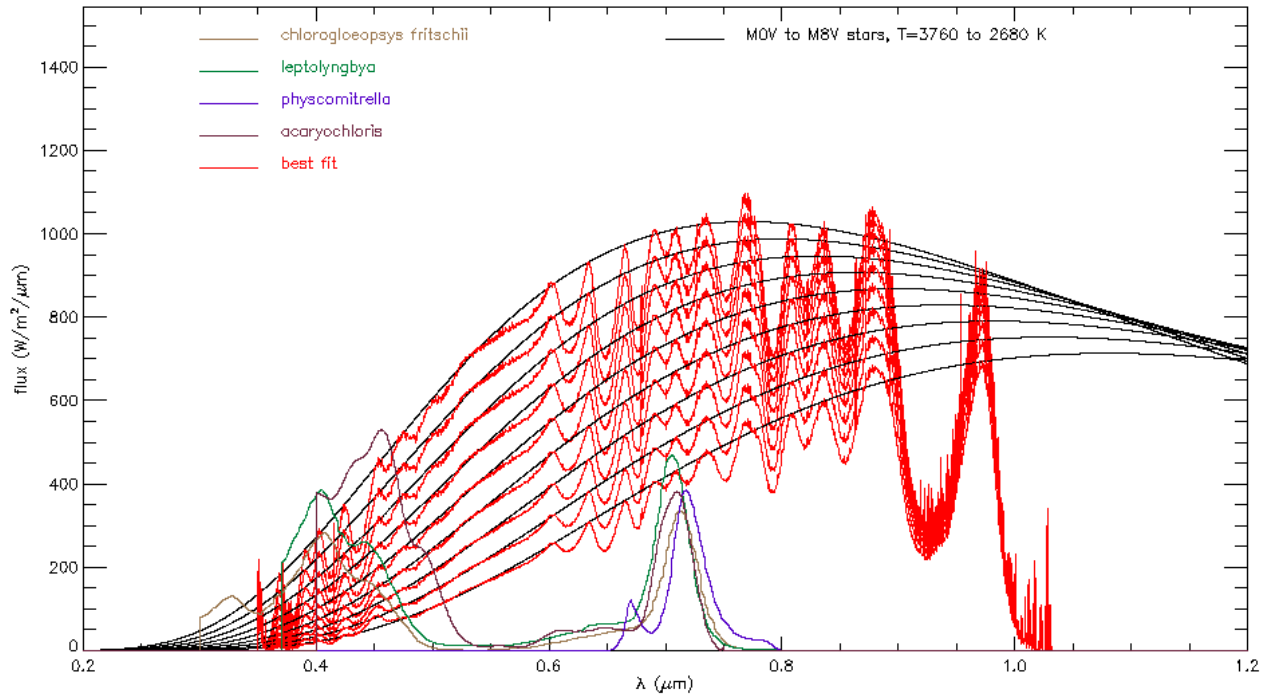


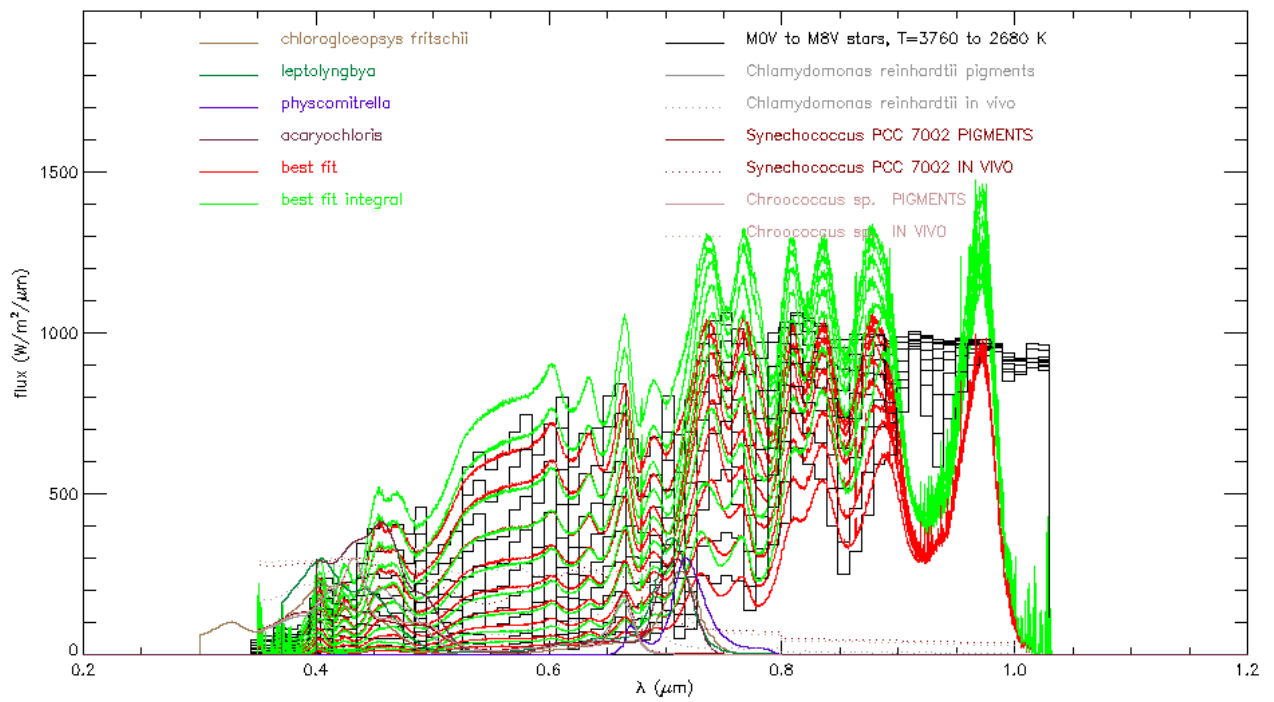
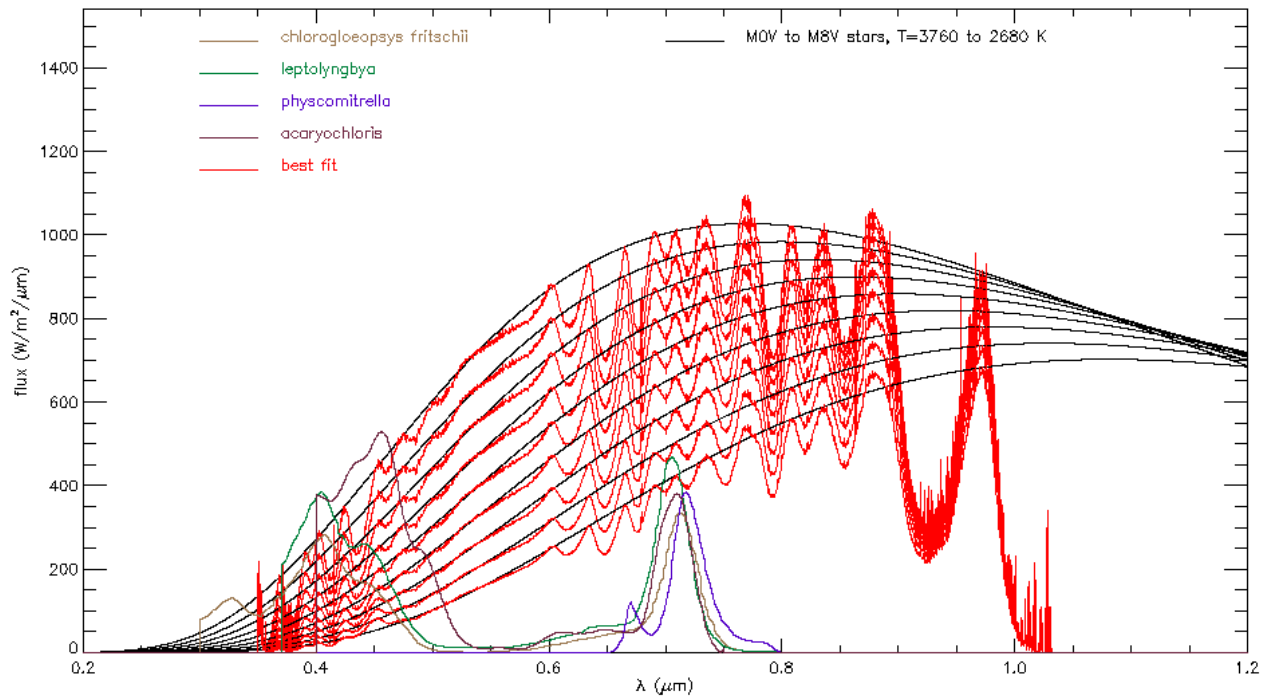
Figures F.21, F.22, F.23, F.24, F.25, F.26, F.27, F.28, F.29, F.30: Simulations of G type stars and their fit with LED palette as well as the black body fit. The red line represents the spectrum fit, the green line is the integral fit.

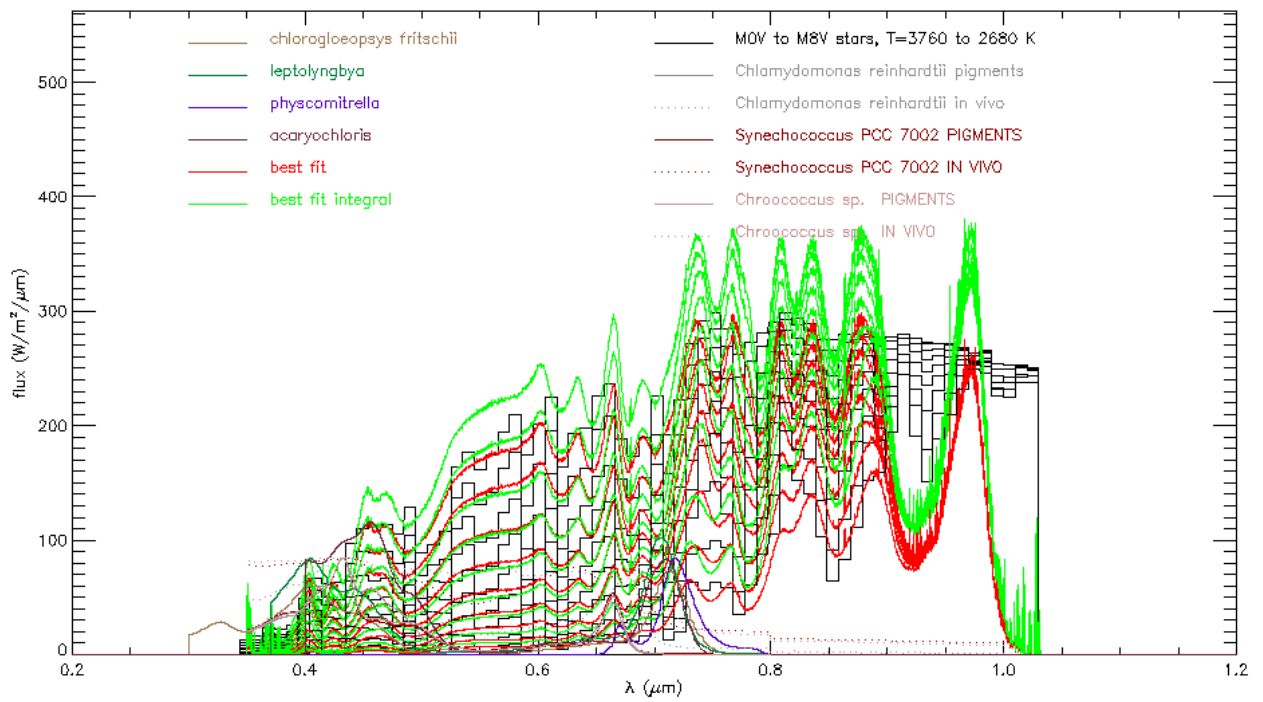
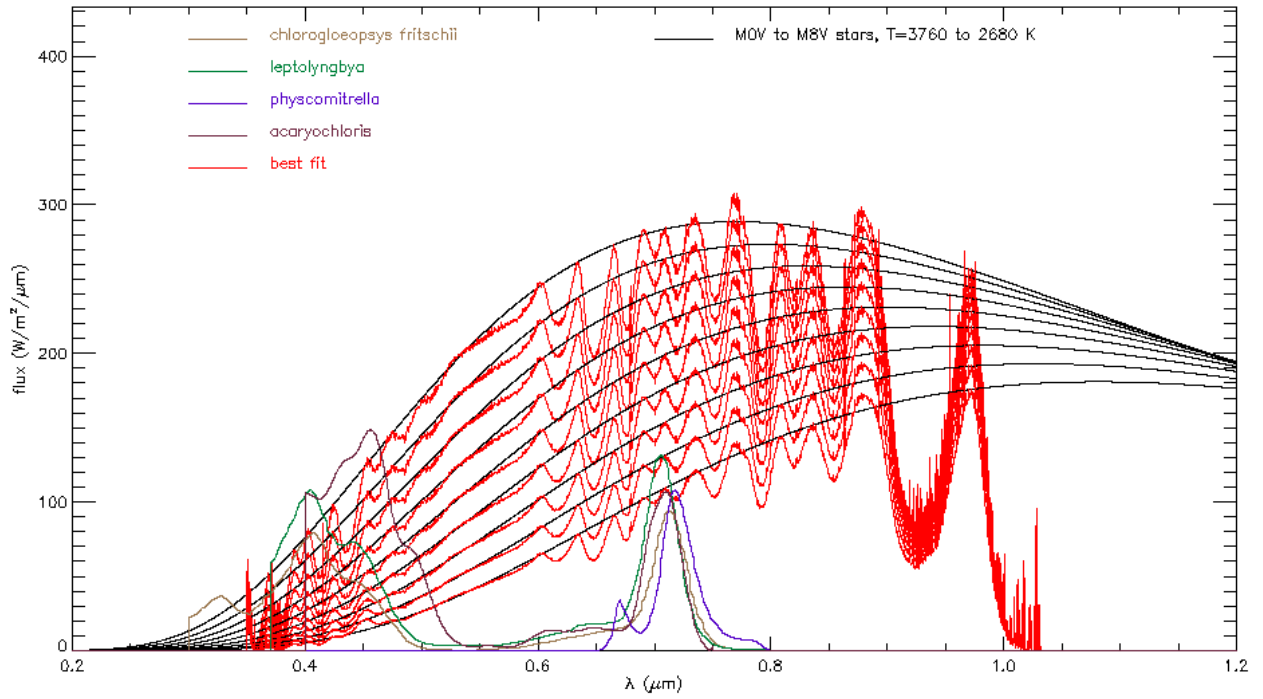
F.4: M type stars

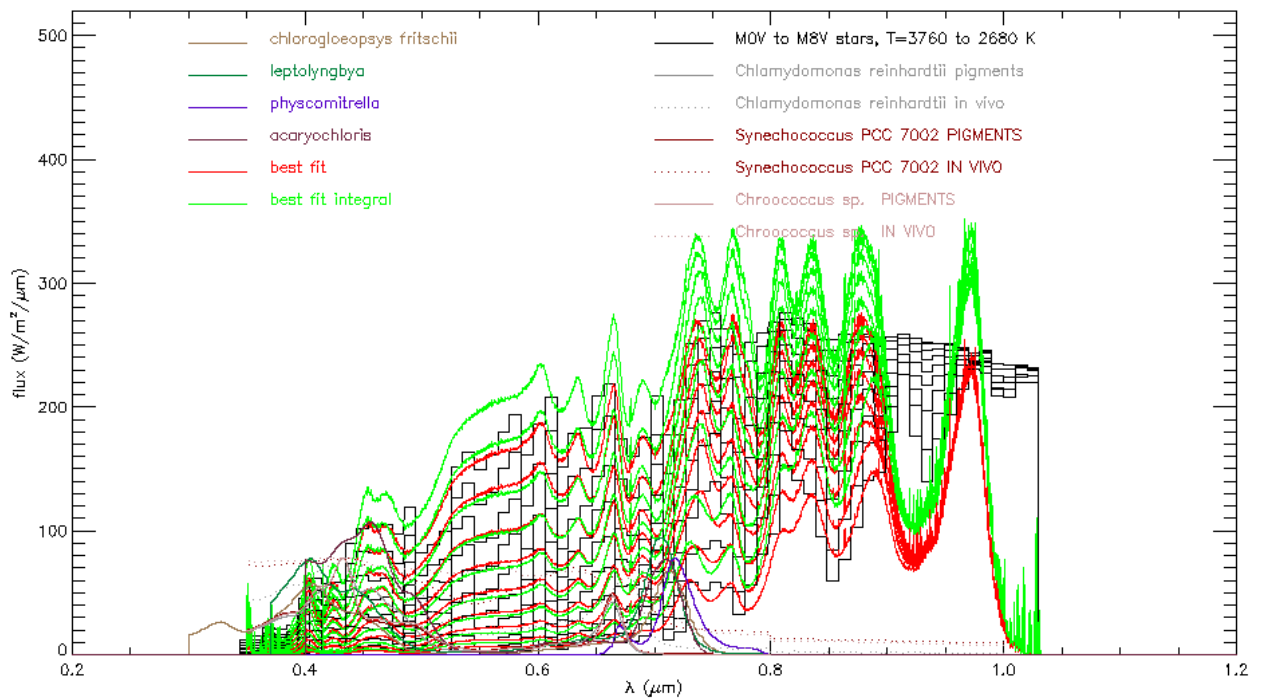
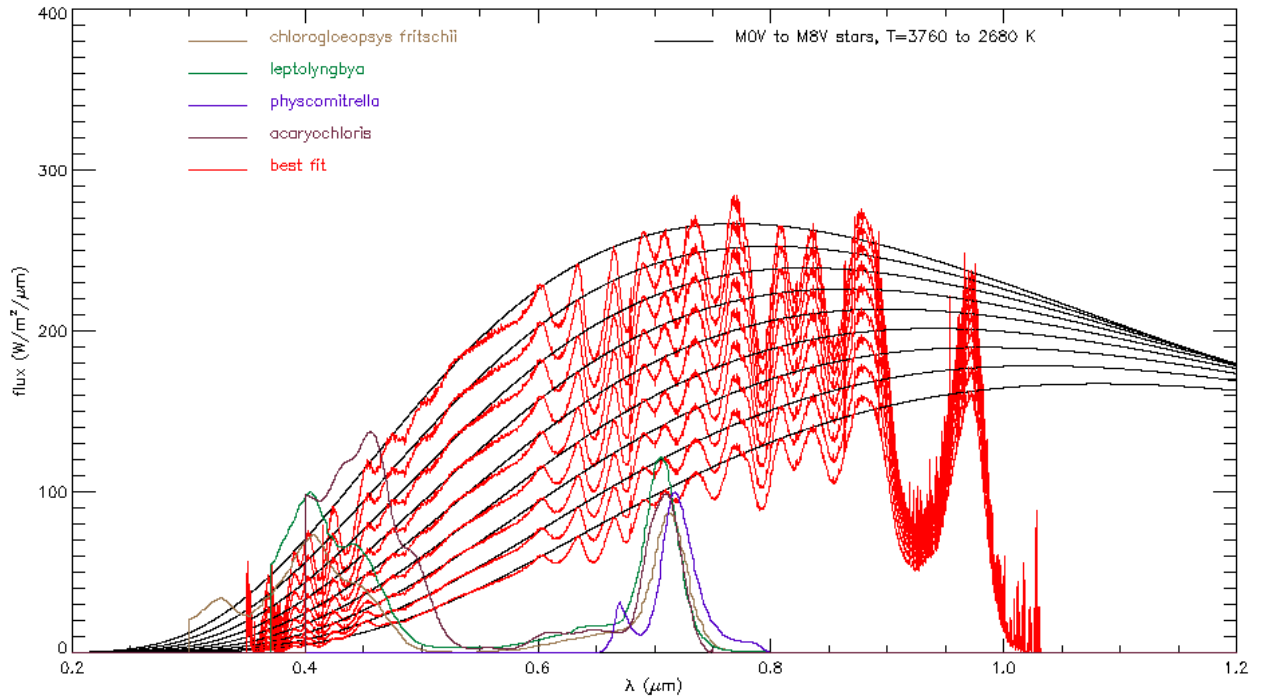
In these pictures are illustrated the simulations of M type stars and their fit with LED palette as well as the black body fit. The red line represents the spectrum fit, the green line is the integral fit.





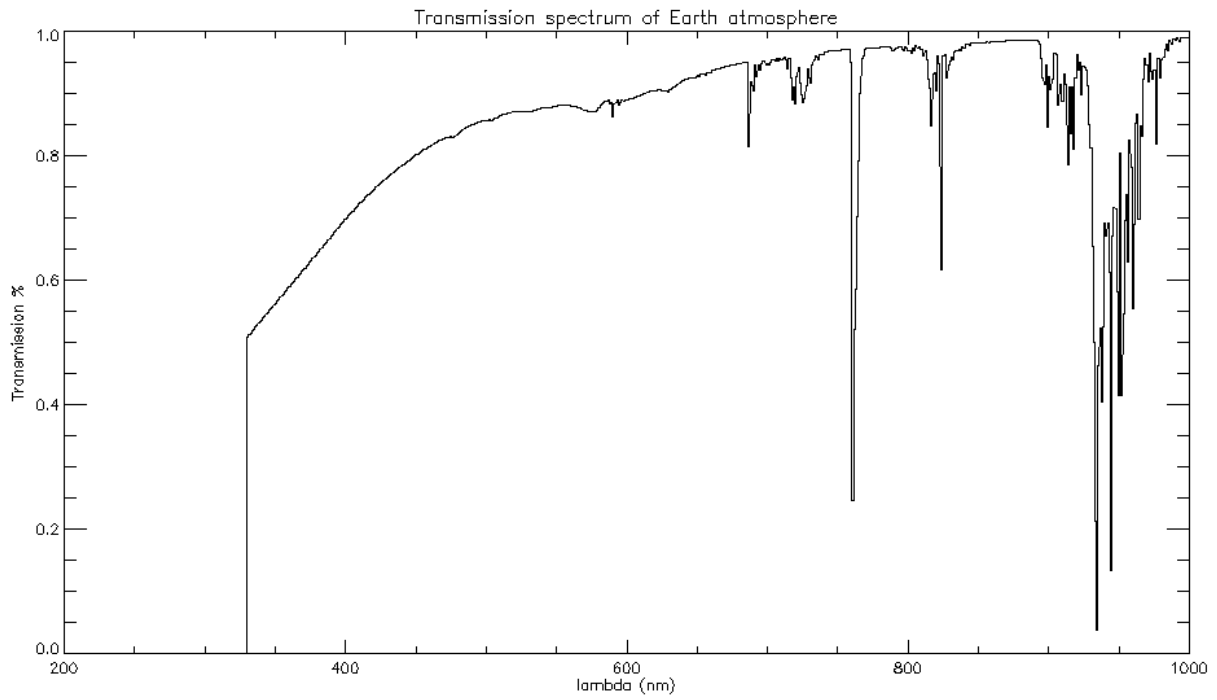






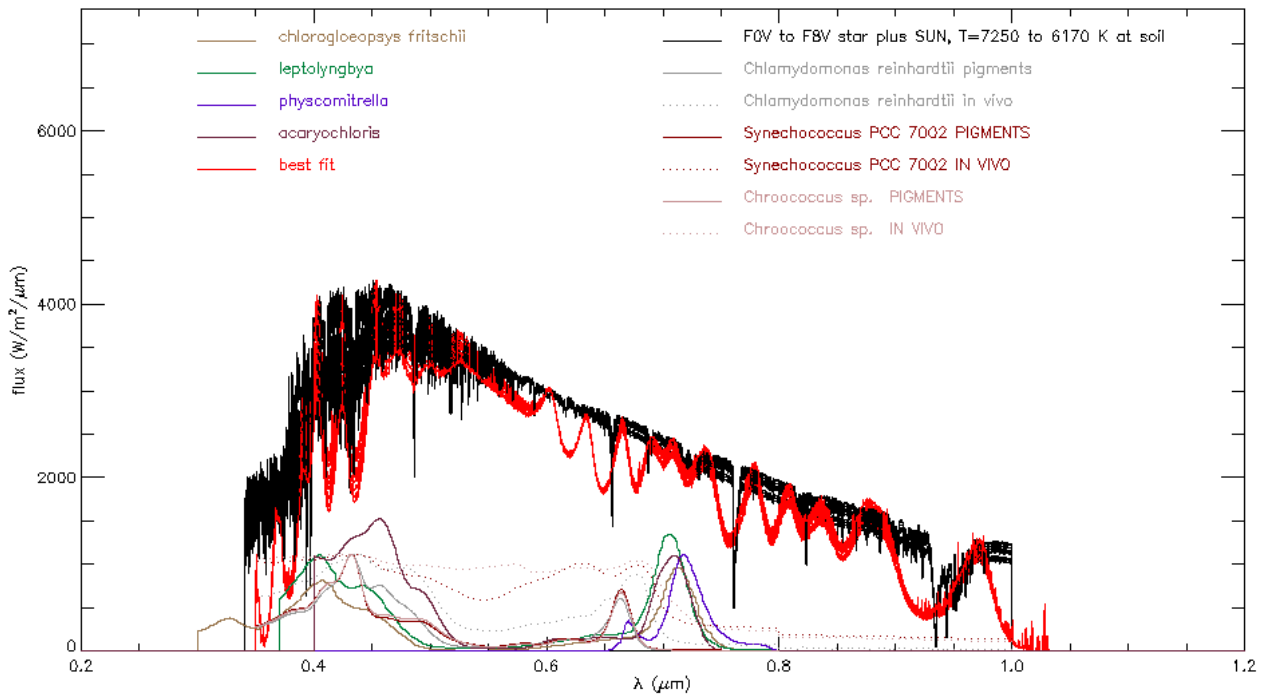
Figures F.21, F.32, F.33, F.34, F.35, F.36, F.37, F.38, F.39, F.40: Simulations of G type stars and their fit with LED palette as well as the black body fit. The red line represents the spectrum fit, the green line is the integral fit.

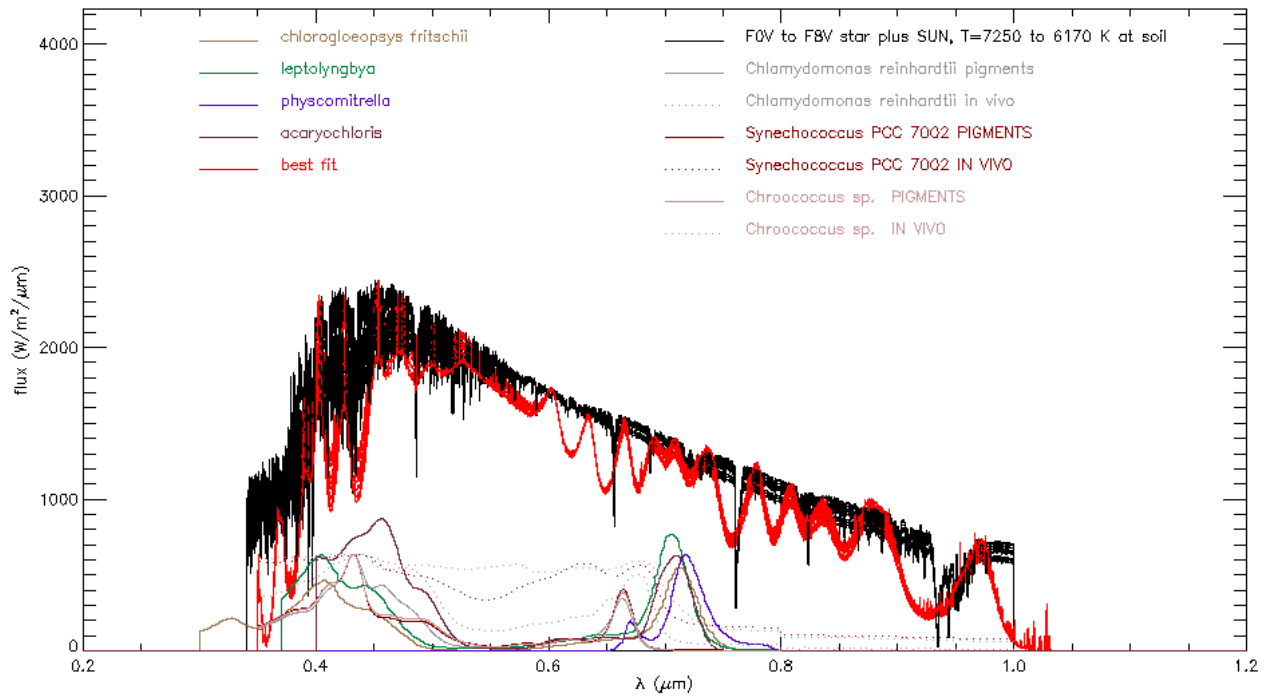
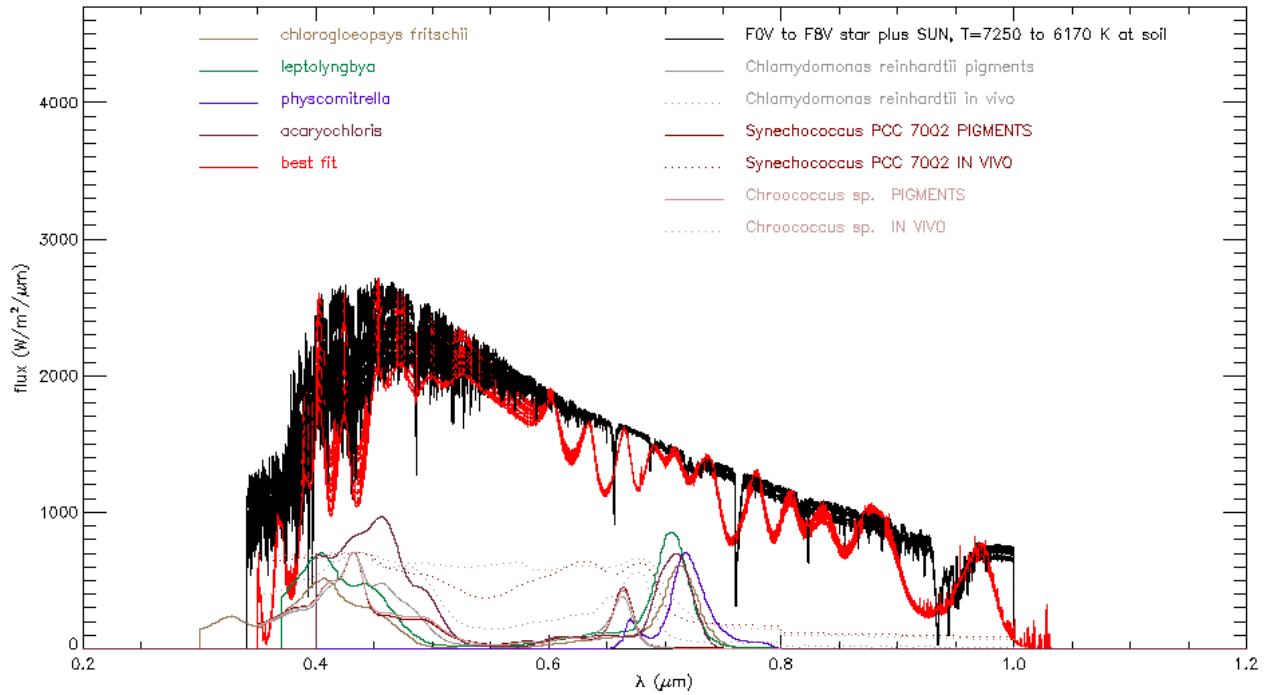
In figure form F.42 to F.63 can be seen the same simulations but filtered by the Earth's atmosphere (figure 6.41).

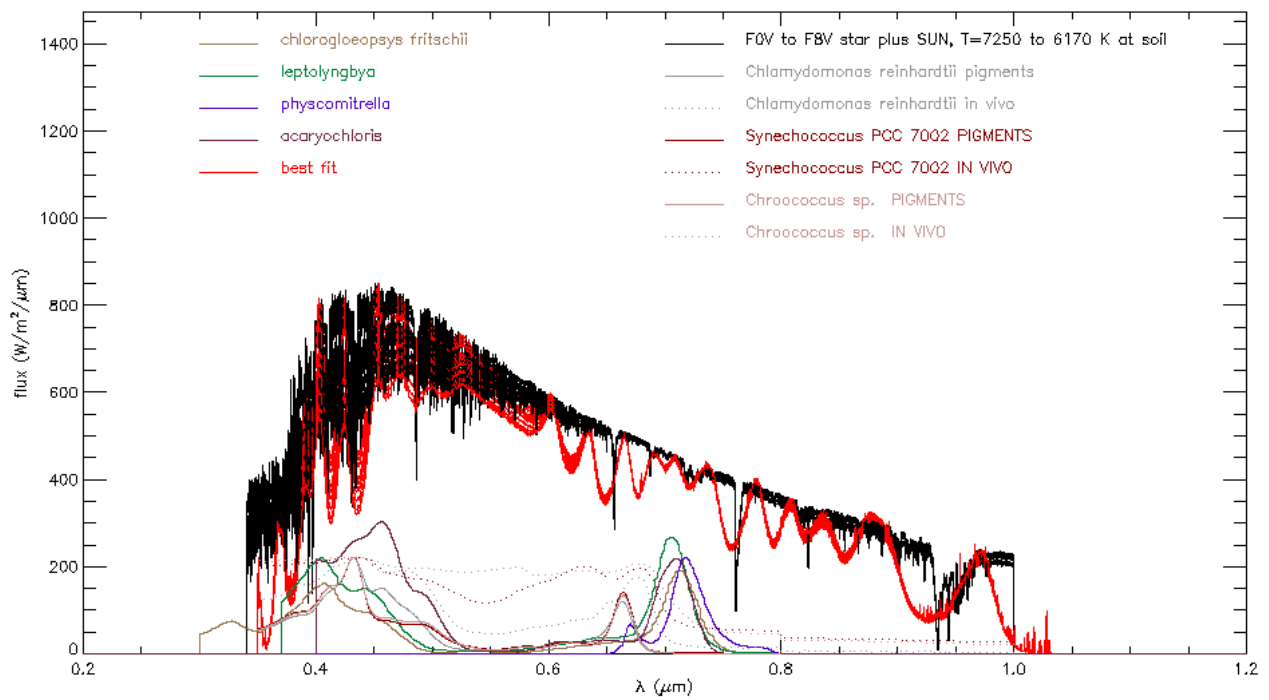
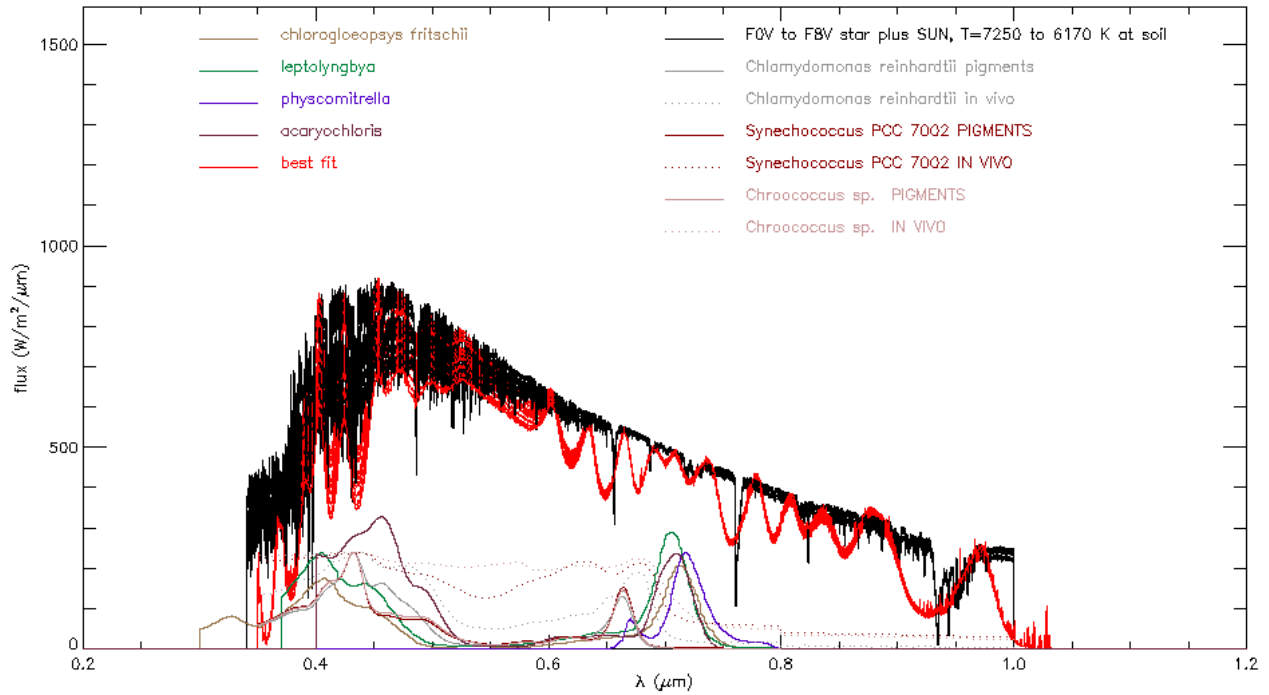


F.5: Filtered F stars

Figure F.41: Spectrum of the Earth's atmosphere

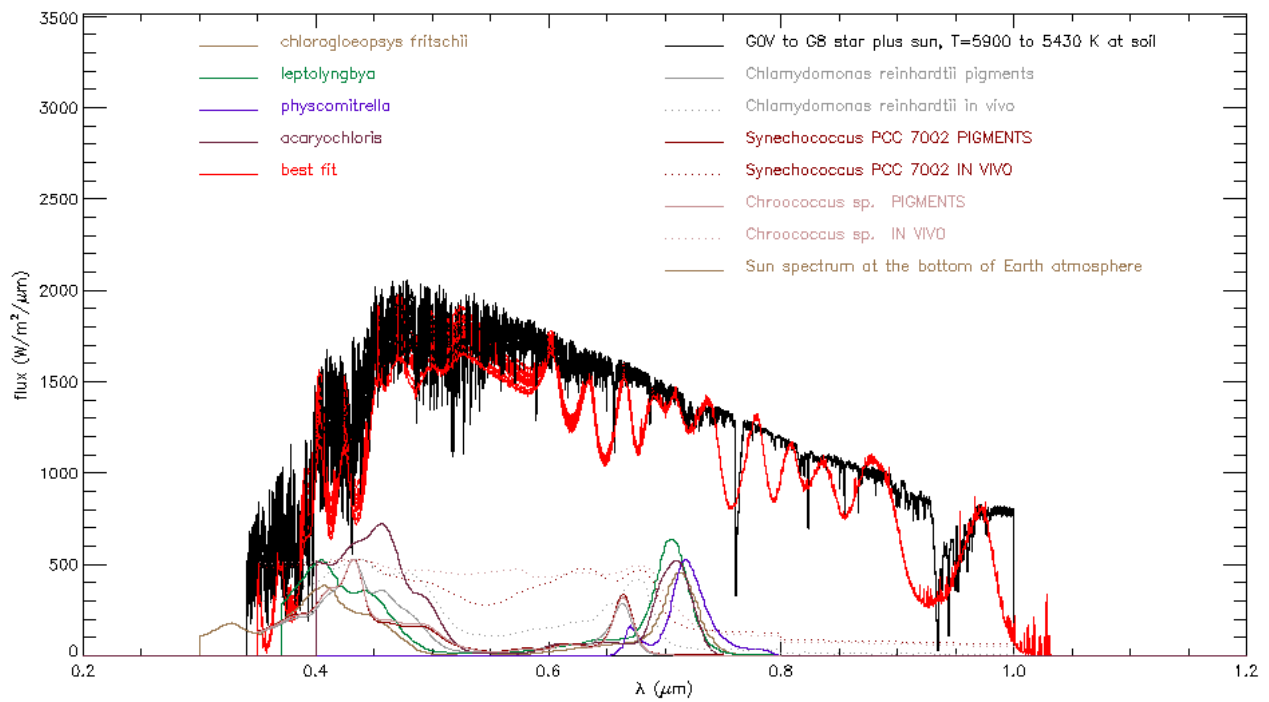
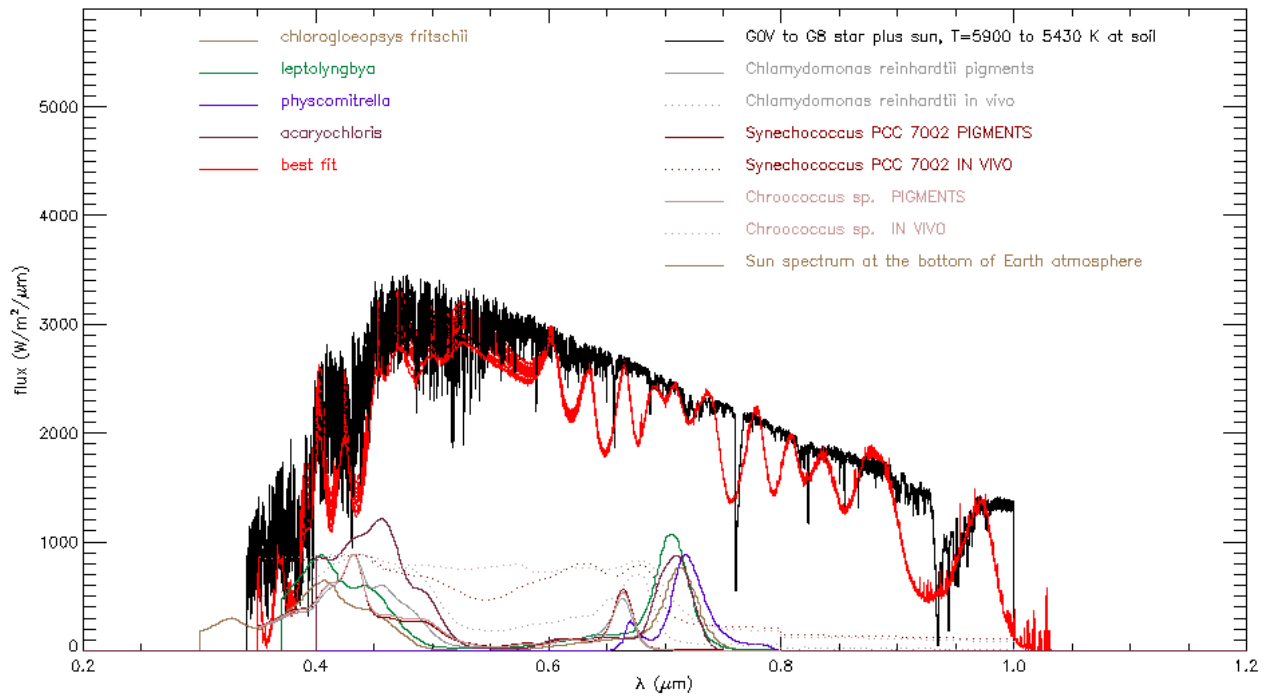


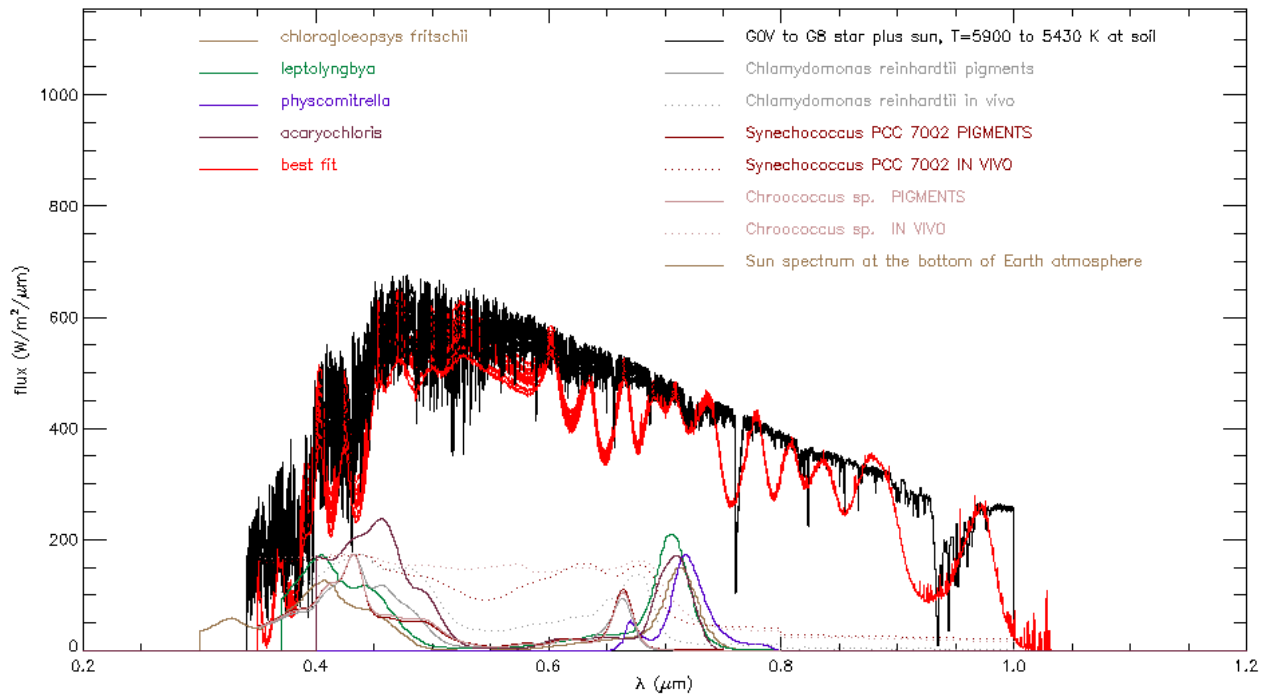
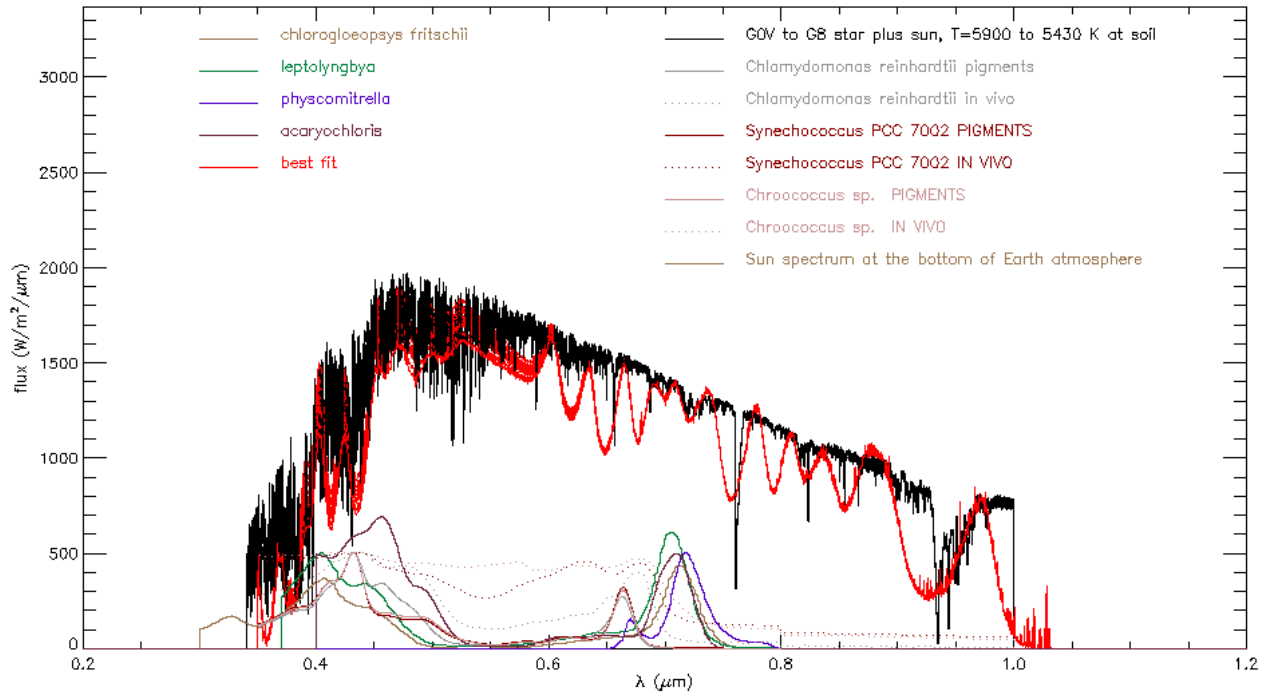


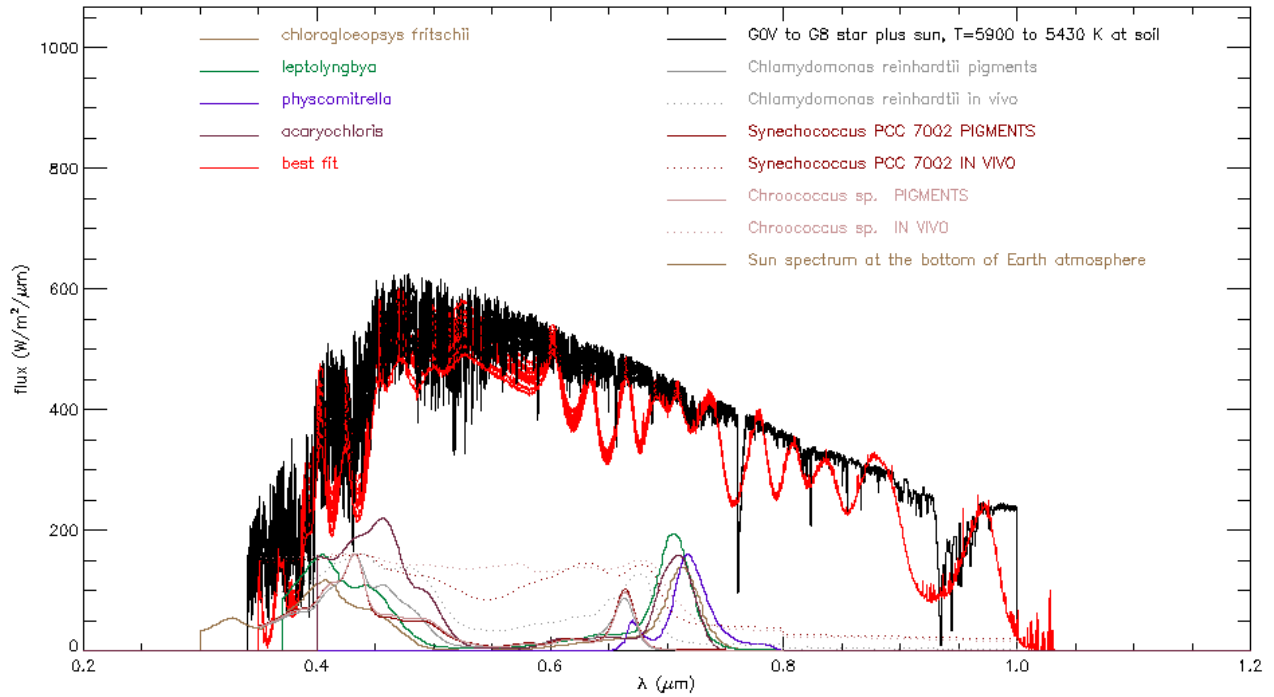


Figures F.42, F.43, F.44, F.45 and F.46: Simulations of F type stars and their fit with LED palette as well as the black body fit. The red line represents the spectrum fit

F.6: Filtered G stars

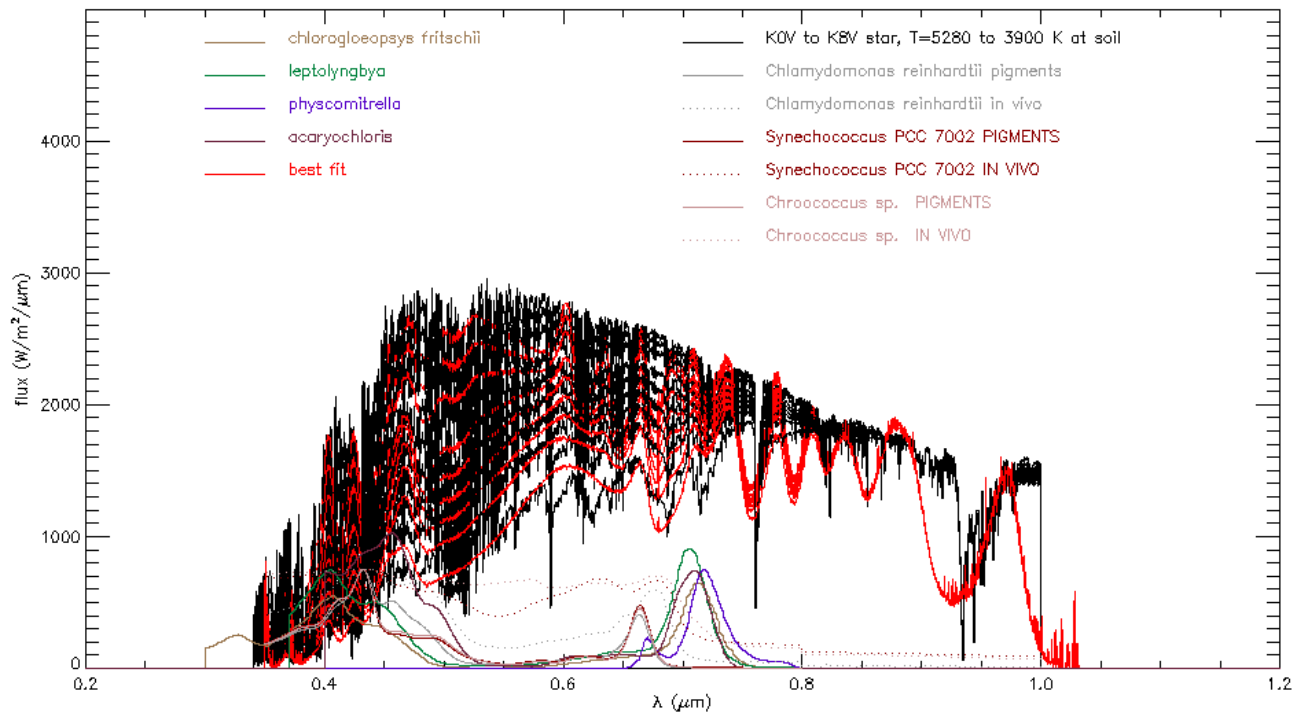


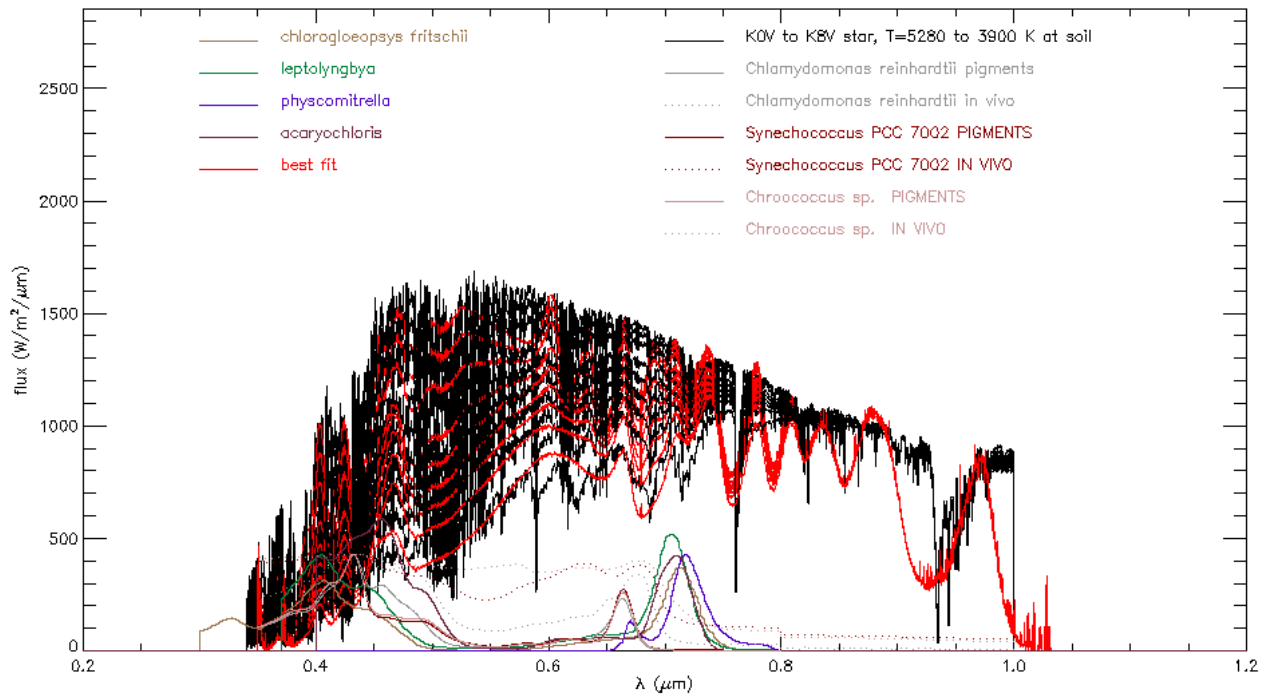
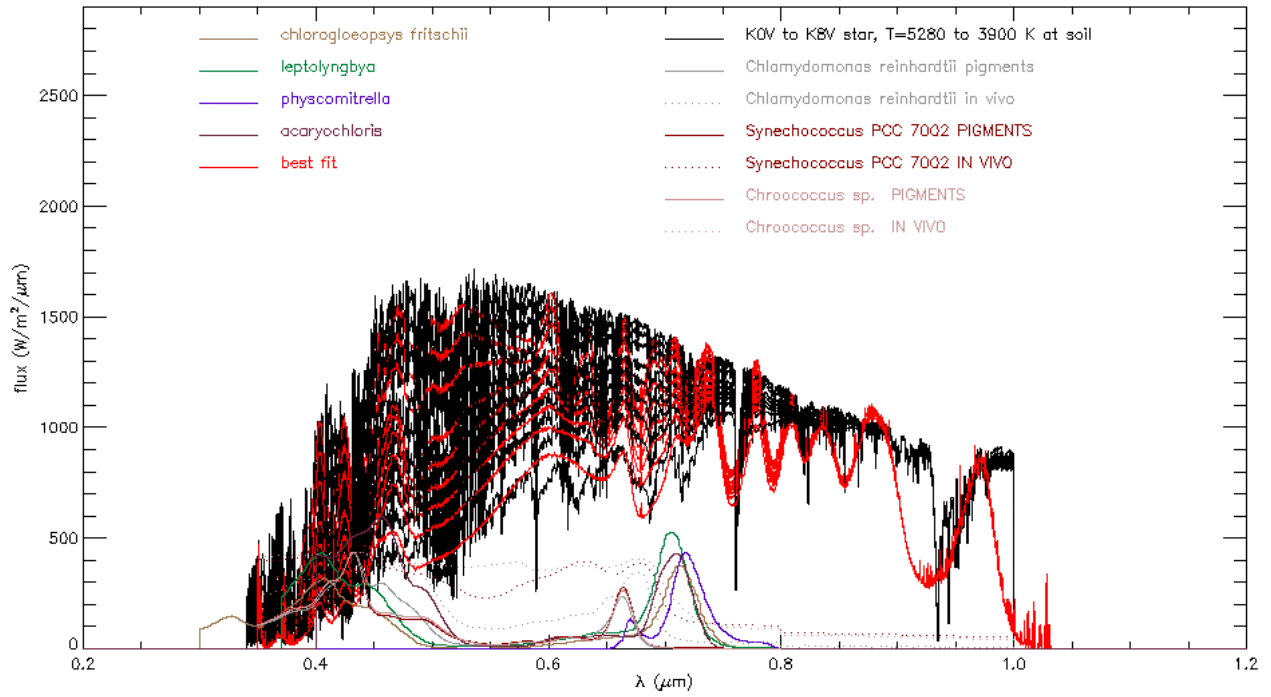


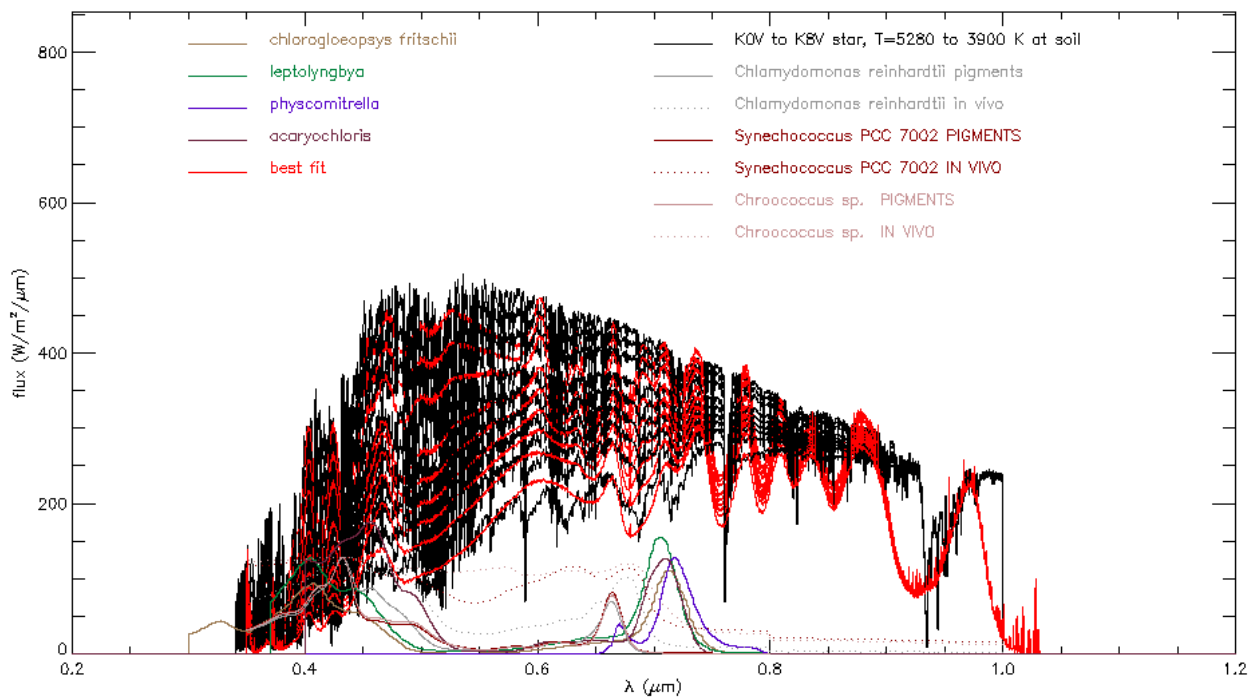
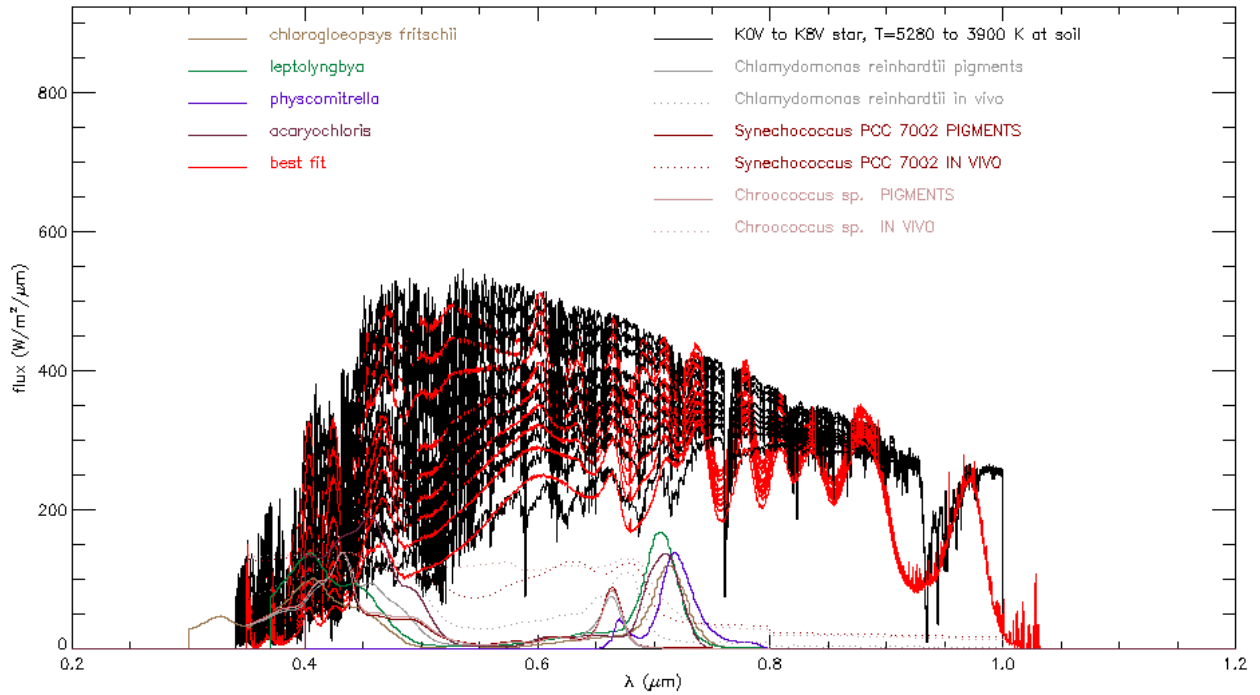


Figures F.47, F.48, F.49, F.505 and F.51: Simulations of G type stars and their fit with LED palette as well as the black body fit. The red line represents the spectrum fit.

F.7: Filtered K stars

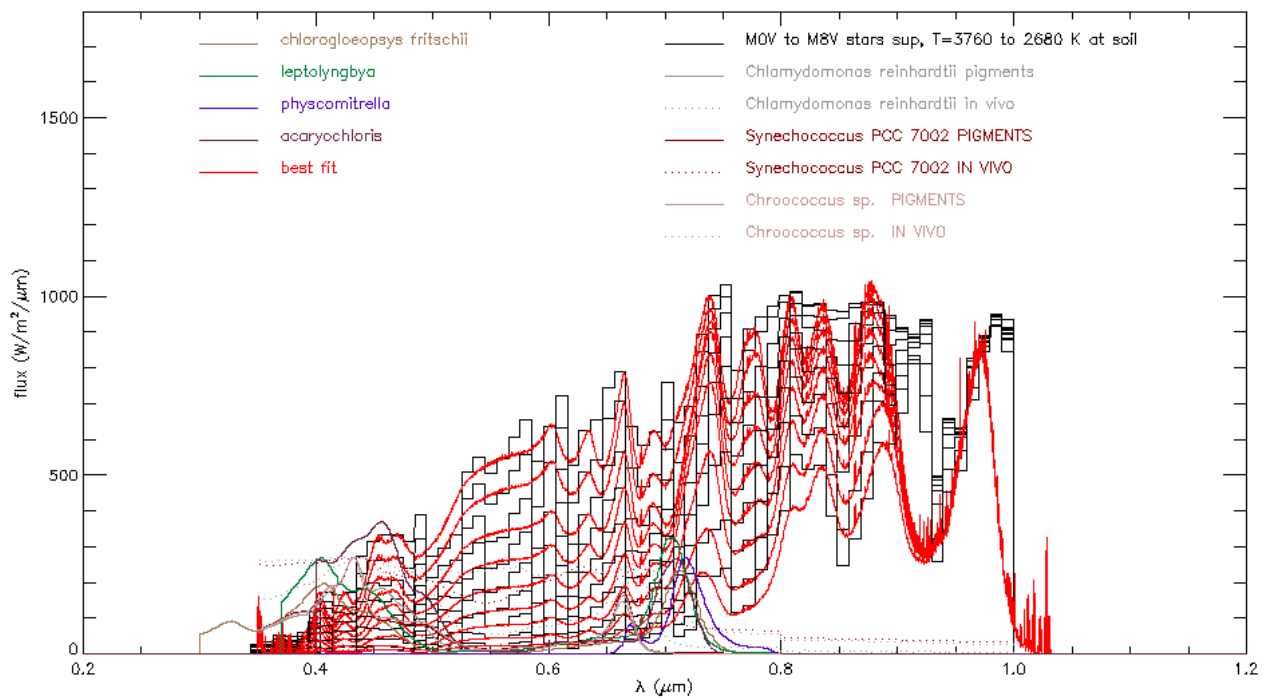
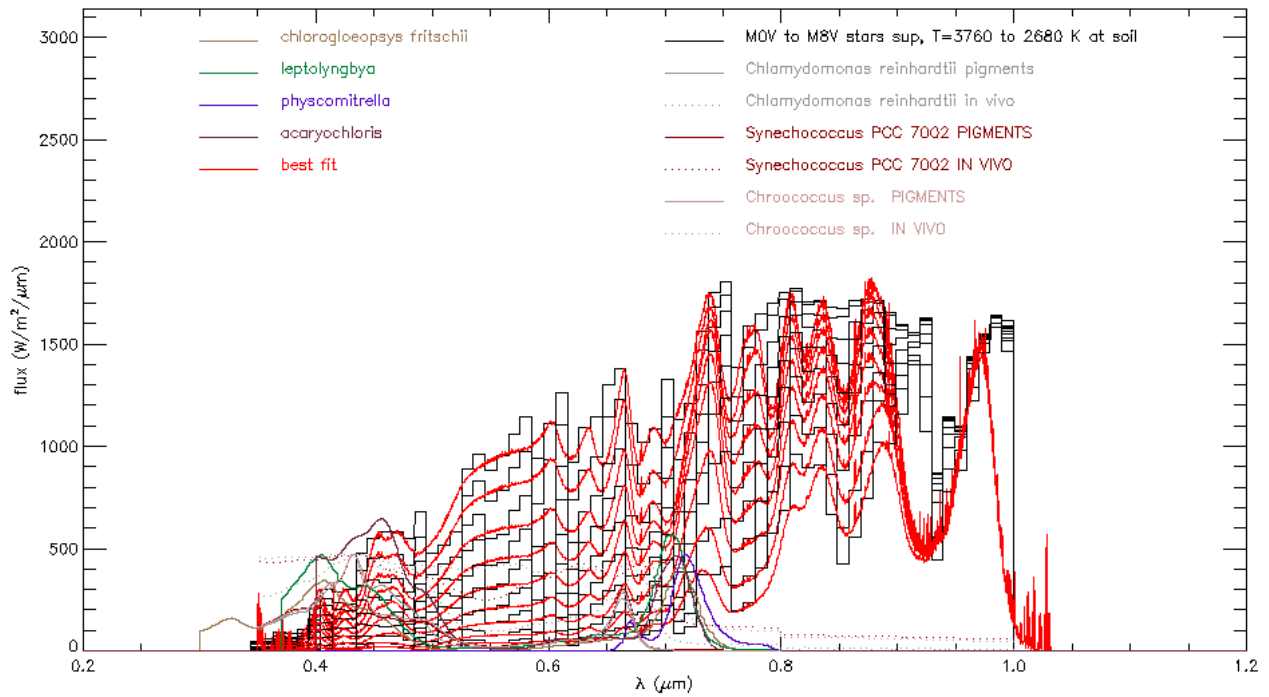


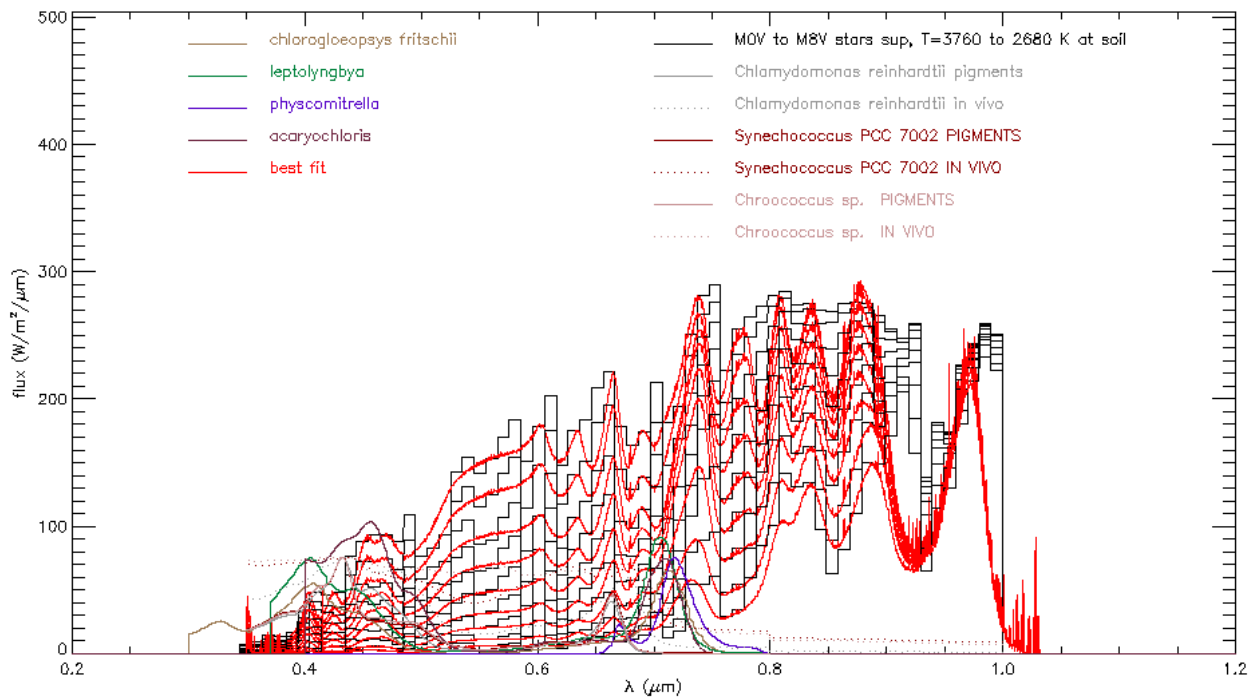
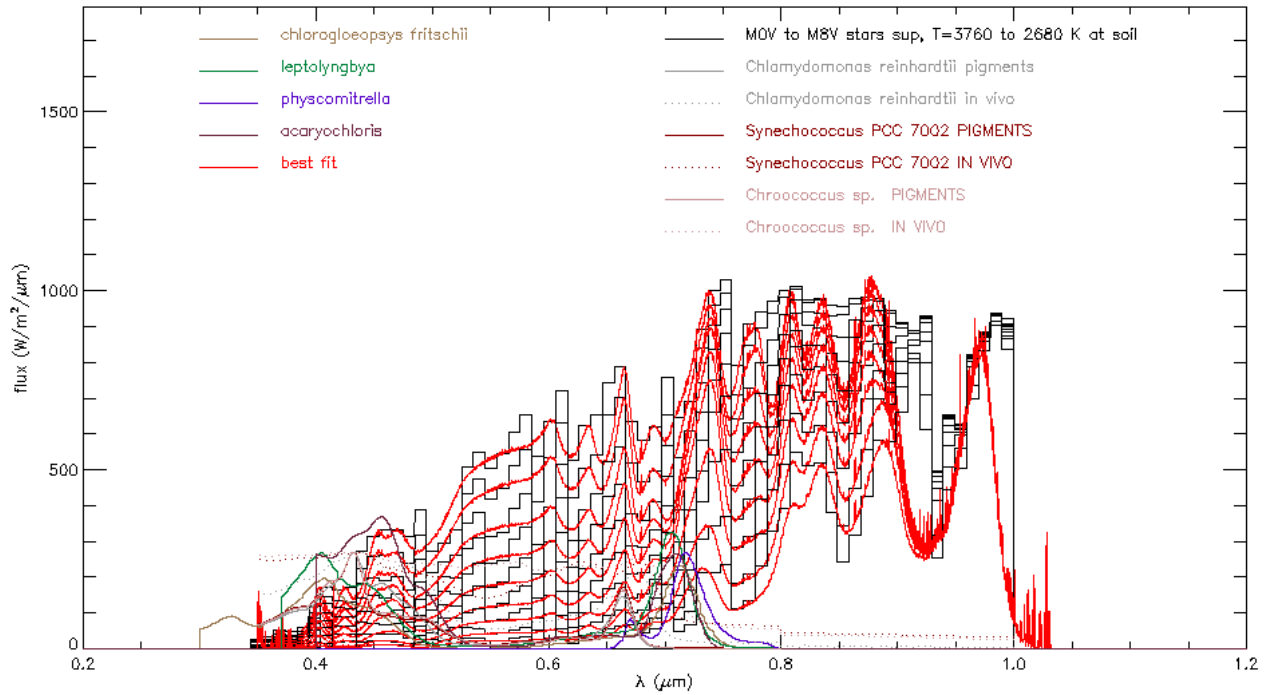


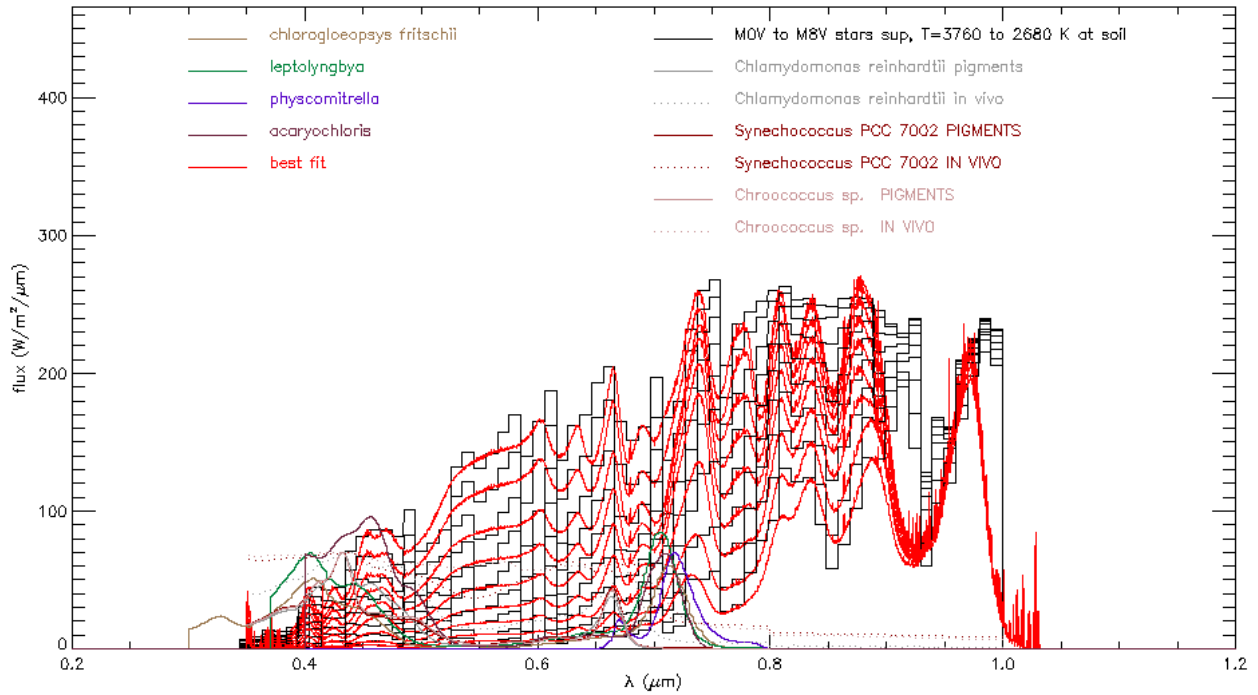


Figures F.52, F.53, F.54, F.55 and F.56: Simulations of K type stars and their fit with LED palette as well as the black body fit. The red line represents the spectrum fit

F.8: Filtered M stars







Figures F.57, F.58, F.59, F.60 and F.61: Simulations of M type stars and their fit with LED palette as well as the black body fit. The red line represents the spectrum fit.

F.9: Europa simulations

In these picture is illustrated the simulation of the solar spectrum at the top of Europa's atmosphere and its fit with LED palette. The red line represents the spectrum fit.

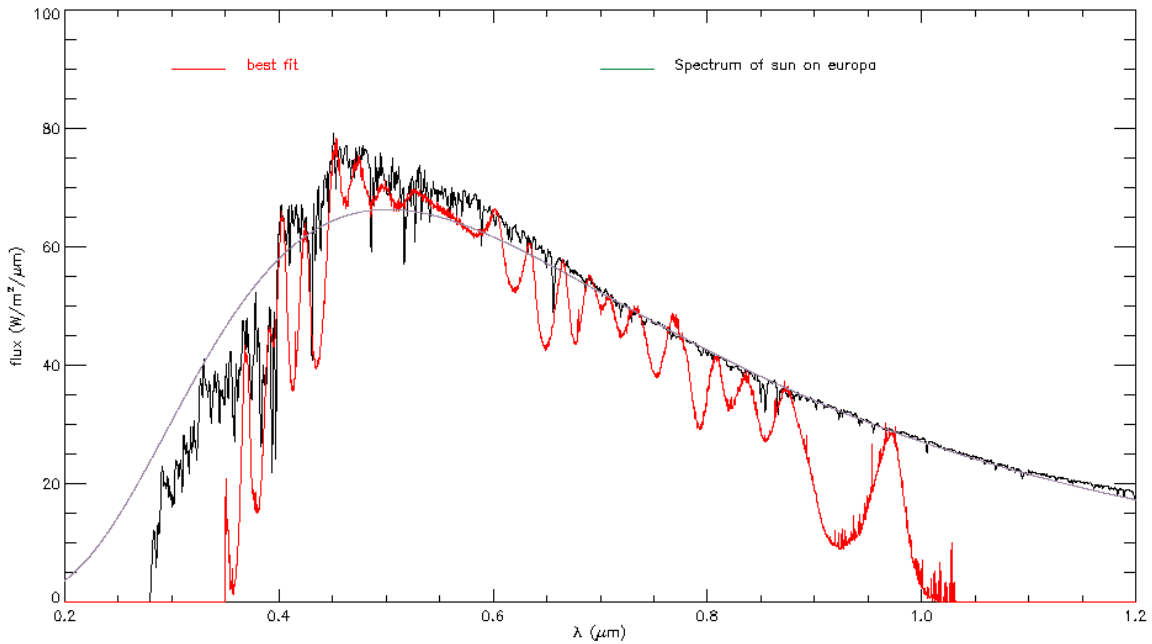


Figure F.62: Solar spectrum at the top of Europa's atmosphere and its fit with LED palette. The red line represents the spectrum fit

The data used for this simulations are $R_*=695800000$ m, Solar radius, $d=1.4266032*10^{12}$ m, $d_{e-s}=149600000000$ m distance from Earth to Sun

F.10: Titanus simulations

In these picture is illustrated the simulation of the solar spectrum at the top of Titanus atmosphere and its fit with LED palette. The red line represents the spectrum fit.

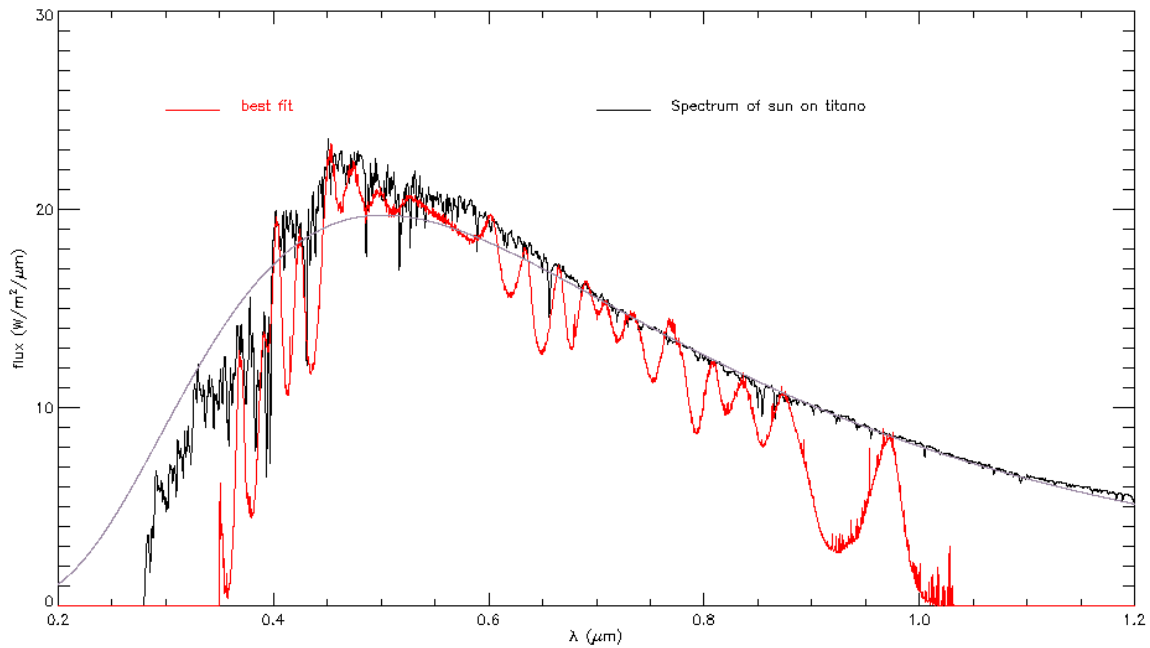


Figure F.63: Solar spectrum at the top of Titanus atmosphere and its fit with LED palette. The red line represents the spectrum fit

The data used for this simulations are $R_*=695800000$ m, Solar radius, $d=7.7774099*10^{11}$ m, $d_{e-s}=149600000000$ m distance from Earth to Sun.

APPENDIX G: PPFD conversion table

Hereafter the conversion table of the PPFD. The formula used here is:

$$\text{PPFD}[\text{mol of photons m}^{-2}\text{s}^{-1}] = \frac{10^6}{E_{\text{mol photons}}} \text{PPFD}[\text{W m}^{-2}] = \frac{\lambda}{N_A h c} \text{PPFD}[\text{W m}^{-2}] \quad (\text{F.1})$$

Wavelength (nm)	Energy of one photon (J/photons)	Energy of a mole of photon (J/mol_photons)	1/Energy of a mole of photon (mol_photons/J)
400	4,96606E-19	299105,9183	3,3433E-06
410	4,84494E-19	291810,653	3,42688E-06
420	4,72958E-19	284862,7812	3,51046E-06
430	4,61959E-19	278238,0663	3,59404E-06
440	4,5146E-19	271914,4748	3,67763E-06
450	4,41428E-19	265871,9318	3,76121E-06
460	4,31831E-19	260092,1081	3,84479E-06
470	4,22644E-19	254558,2343	3,92837E-06
480	4,13839E-19	249254,9386	4,01196E-06
490	4,05393E-19	244168,1039	4,09554E-06
500	3,97285E-19	239284,7426	4,17912E-06
510	3,89495E-19	234592,8857	4,2627E-06
520	3,82005E-19	230081,4848	4,34629E-06
530	3,74797E-19	225740,3255	4,42987E-06
540	3,67856E-19	221559,9498	4,51345E-06
550	3,61168E-19	217531,5878	4,59703E-06
560	3,54719E-19	213647,0959	4,68062E-06
570	3,48496E-19	209898,9019	4,7642E-06
580	3,42487E-19	206279,956	4,84778E-06
590	3,36682E-19	202783,6863	4,93136E-06
600	3,31071E-19	199403,9588	5,01495E-06
610	3,25643E-19	196135,0421	5,09853E-06
620	3,20391E-19	192971,5743	5,18211E-06
630	3,15306E-19	189908,5341	5,26569E-06
640	3,10379E-19	186941,2139	5,34928E-06
650	3,05604E-19	184065,1958	5,43286E-06
660	3,00973E-19	181276,3298	5,51644E-06
670	2,96481E-19	178570,7136	5,60002E-06
680	2,92121E-19	175944,6742	5,6836E-06
690	2,87888E-19	173394,752	5,76719E-06
700	2,83775E-19	170917,6847	5,85077E-06
710	2,79778E-19	168510,3939	5,93435E-06
720	2,75892E-19	166169,9723	6,01793E-06
730	2,72113E-19	163893,6719	6,10152E-06
740	2,68436E-19	161678,8931	6,1851E-06
750	2,64857E-19	159523,175	6,26868E-06
760	2,61372E-19	157424,1864	6,35226E-06
770	2,57977E-19	155379,717	6,43585E-06
780	2,5467E-19	153387,6698	6,51943E-06

Wavelength (nm)	Energy of one photon (J/photons)	Energy of a mole of photon (J/mol_photons)	1/Energy of a mole of photon (mol_photons/J)
790	2,51446E-19	151446,0543	6,60301E-06
800	2,48303E-19	149552,9791	6,68659E-06
810	2,45238E-19	147706,6465	6,77018E-06
820	2,42247E-19	145905,3464	6,85376E-06
830	2,39328E-19	144147,4512	6,93734E-06
840	2,36479E-19	142431,4106	7,02092E-06
850	2,33697E-19	140755,7474	7,10451E-06
860	2,3098E-19	139119,0531	7,18809E-06
870	2,28325E-19	137519,984	7,27167E-06
880	2,2573E-19	135957,2574	7,35525E-06
890	2,23194E-19	134429,6482	7,43884E-06
900	2,20714E-19	132935,9859	7,52242E-06
910	2,18288E-19	131475,1513	7,606E-06
920	2,15916E-19	130046,074	7,68958E-06
930	2,13594E-19	128647,7295	7,77316E-06
940	2,11322E-19	127279,1371	7,85675E-06
950	2,09097E-19	125939,3571	7,94033E-06
960	2,06919E-19	124627,4892	8,02391E-06
970	2,04786E-19	123342,6702	8,10749E-06
980	2,02696E-19	122084,0719	8,19108E-06
990	2,00649E-19	120850,8999	8,27466E-06
1000	1,98643E-19	119642,3913	8,35824E-06
1010	1,96676E-19	118457,8135	8,44182E-06
1020	1,94748E-19	117296,4628	8,52541E-06
1030	1,92857E-19	116157,6626	8,60899E-06
1040	1,91002E-19	115040,7624	8,69257E-06
1050	1,89183E-19	113945,1364	8,77615E-06
1060	1,87399E-19	112870,1827	8,85974E-06
1070	1,85647E-19	111815,3215	8,94332E-06
1080	1,83928E-19	110779,9949	9,0269E-06
1090	1,82241E-19	109763,665	9,11048E-06
1100	1,80584E-19	108765,8139	9,19407E-06
1110	1,78957E-19	107785,942	9,27765E-06
1120	1,77359E-19	106823,5679	9,36123E-06
1130	1,7579E-19	105878,2269	9,44481E-06
1140	1,74248E-19	104949,4709	9,52839E-06
1150	1,72733E-19	104036,8672	9,61198E-06
1160	1,71244E-19	103139,998	9,69556E-06
1170	1,6978E-19	102258,4599	9,77914E-06
1180	1,68341E-19	101391,8631	9,86272E-06
1190	1,66927E-19	100539,831	9,94631E-06
1200	1,65535E-19	99701,99937	1,00299E-05
1210	1,64167E-19	98878,01623	1,01135E-05
1220	1,62822E-19	98067,54101	1,01971E-05
1230	1,61498E-19	97270,24426	1,02806E-05
1240	1,60196E-19	96485,80713	1,03642E-05

Wavelength (nm)	Energy of one photon (J/photons)	Energy of a mole of photon (J/mol_photons)	1/Energy of a mole of photon (mol_photons/J)
1250	1,58914E-19	95713,92099	1,04478E-05
1260	1,57653E-19	94954,28701	1,05314E-05
1270	1,56411E-19	94206,61577	1,0615E-05
1280	1,55189E-19	93470,6269	1,06985E-05
1290	1,53986E-19	92746,04871	1,07821E-05
1300	1,52802E-19	92032,61787	1,08657E-05
1310	1,51636E-19	91330,07911	1,09493E-05
1320	1,50487E-19	90638,18487	1,10329E-05
1330	1,49355E-19	89956,69506	1,11165E-05
1340	1,48241E-19	89285,37674	1,12E-05
1350	1,47143E-19	88624,00387	1,12836E-05
1360	1,46061E-19	87972,35708	1,13672E-05
1370	1,44995E-19	87330,22338	1,14508E-05
1380	1,43944E-19	86697,39596	1,15344E-05
1390	1,42908E-19	86073,67397	1,1618E-05
1400	1,41888E-19	85458,8623	1,17015E-05
1410	1,40881E-19	84852,77136	1,17851E-05
1420	1,39889E-19	84255,21691	1,18687E-05
1430	1,38911E-19	83666,01987	1,19523E-05
1440	1,37946E-19	83085,00612	1,20359E-05
1450	1,36995E-19	82512,00636	1,21194E-05
1460	1,36057E-19	81946,8559	1,2203E-05
1470	1,35131E-19	81389,39457	1,22866E-05
1480	1,34218E-19	80839,4665	1,23702E-05
1490	1,33317E-19	80296,92001	1,24538E-05
1500	1,32428E-19	79761,60747	1,25374E-05
1510	1,31551E-19	79233,38517	1,26209E-05
1520	1,30686E-19	78712,11316	1,27045E-05
1530	1,29832E-19	78197,65517	1,27881E-05
1540	1,28989E-19	77689,87845	1,28717E-05
1550	1,28156E-19	77188,65368	1,29553E-05
1560	1,27335E-19	76693,85488	1,30389E-05
1570	1,26524E-19	76205,35924	1,31224E-05
1580	1,25723E-19	75723,04709	1,3206E-05
1590	1,24932E-19	75246,80176	1,32896E-05
1600	1,24152E-19	74776,5095	1,33732E-05
1610	1,2338E-19	74312,05938	1,34568E-05
1620	1,22619E-19	73853,34321	1,35403E-05
1630	1,21867E-19	73400,25546	1,36239E-05
1640	1,21124E-19	72952,69317	1,37075E-05
1650	1,20389E-19	72510,55588	1,37911E-05
1660	1,19664E-19	72073,74554	1,38747E-05
1670	1,18948E-19	71642,16646	1,39583E-05
1680	1,1824E-19	71215,72524	1,40418E-05
1690	1,1754E-19	70794,33065	1,41254E-05
1700	1,16849E-19	70377,89364	1,4209E-05

Wavelength (nm)	Energy of one photon (J/photons)	Energy of a mole of photon (J/mol_photons)	1/Energy of a mole of photon (mol_photons/J)
1710	1,16165E-19	69966,32725	1,42926E-05
1720	1,1549E-19	69559,54651	1,43762E-05
1730	1,14822E-19	69157,46843	1,44598E-05
1740	1,14162E-19	68760,01195	1,45433E-05
1750	1,1351E-19	68367,09782	1,46269E-05
1760	1,12865E-19	67978,64863	1,47105E-05
1770	1,12227E-19	67594,58869	1,47941E-05
1780	1,11597E-19	67214,84404	1,48777E-05
1790	1,10974E-19	66839,34234	1,49612E-05
1800	1,10357E-19	66468,01288	1,50448E-05
1810	1,09747E-19	66100,78651	1,51284E-05
1820	1,09144E-19	65737,59559	1,5212E-05
1830	1,08548E-19	65378,37398	1,52956E-05
1840	1,07958E-19	65023,05695	1,53792E-05
1850	1,07374E-19	64671,58118	1,54627E-05
1860	1,06797E-19	64323,88472	1,55463E-05
1870	1,06226E-19	63979,90694	1,56299E-05
1880	1,05661E-19	63639,5885	1,57135E-05
1890	1,05102E-19	63302,87131	1,57971E-05
1900	1,04549E-19	62969,69851	1,58807E-05
1910	1,04001E-19	62640,01444	1,59642E-05
1920	1,0346E-19	62313,76457	1,60478E-05
1930	1,02924E-19	61990,89553	1,61314E-05
1940	1,02393E-19	61671,35504	1,6215E-05
1950	1,01868E-19	61355,09188	1,62986E-05
1960	1,01348E-19	61042,0559	1,63821E-05
1970	1,00834E-19	60732,19795	1,64657E-05
1980	1,00325E-19	60425,46988	1,65493E-05
1990	9,98204E-20	60121,82451	1,66329E-05
2000	9,93213E-20	59821,21558	1,67165E-05
2010	9,88272E-20	59523,59779	1,68001E-05
2020	9,83379E-20	59228,92671	1,68836E-05
2030	9,78535E-20	58937,1588	1,69672E-05
2040	9,73738E-20	58648,25135	1,70508E-05
2050	9,68988E-20	58362,16252	1,71344E-05
2060	9,64284E-20	58078,85124	1,7218E-05
2070	9,59626E-20	57798,27728	1,73016E-05
2080	9,55012E-20	57520,40113	1,73851E-05
2090	9,50443E-20	57245,18409	1,74687E-05
2100	9,45917E-20	56972,58817	1,75523E-05
2110	9,41434E-20	56702,57609	1,76359E-05
2120	9,36993E-20	56435,1113	1,77195E-05
2130	9,32594E-20	56170,15791	1,7803E-05
2140	9,28236E-20	55907,68073	1,78866E-05
2150	9,23919E-20	55647,64519	1,79702E-05
2160	9,19642E-20	55390,01738	1,80538E-05

Wavelength (nm)	Energy of one photon (J/photons)	Energy of a mole of photon (J/mol_photons)	1/Energy of a mole of photon (mol_photons/J)
2170	9,15404E-20	55134,76403	1,81374E-05
2180	9,11205E-20	54881,85245	1,8221E-05
2190	9,07044E-20	54631,25057	1,83045E-05
2200	9,02921E-20	54382,92689	1,83881E-05
2210	8,98835E-20	54136,85047	1,84717E-05
2220	8,94787E-20	53892,99097	1,85553E-05
2230	8,90774E-20	53651,31854	1,86389E-05
2240	8,86797E-20	53411,8039	1,87225E-05
2250	8,82856E-20	53174,41829	1,8806E-05
2260	8,7895E-20	52939,13343	1,88896E-05
2270	8,75078E-20	52705,92156	1,89732E-05
2280	8,7124E-20	52474,75541	1,90568E-05
2290	8,67435E-20	52245,60818	1,91404E-05
2300	8,63664E-20	52018,45354	1,92239E-05
2310	8,59925E-20	51793,2656	1,93075E-05
2320	8,56218E-20	51570,01894	1,93911E-05
2330	8,52543E-20	51348,68856	1,94747E-05
2340	8,489E-20	51129,24989	1,95583E-05
2350	8,45288E-20	50911,67878	1,96419E-05
2360	8,41706E-20	50695,9515	1,97254E-05
2370	8,38154E-20	50482,0447	1,9809E-05
2380	8,34633E-20	50269,93543	1,98926E-05
2390	8,31141E-20	50059,60114	1,99762E-05
2400	8,27678E-20	49851,01964	2,00598E-05
2410	8,24243E-20	49644,1691	2,01434E-05
2420	8,20837E-20	49439,02807	2,02269E-05
2430	8,17459E-20	49235,57544	2,03105E-05
2440	8,14109E-20	49033,79046	2,03941E-05
2450	8,10786E-20	48833,6527	2,04777E-05
2460	8,0749E-20	48635,14208	2,05613E-05
2470	8,04221E-20	48438,23884	2,06448E-05
2480	8,00978E-20	48242,92352	2,07284E-05
2490	7,97762E-20	48049,177	2,0812E-05
2500	7,9457E-20	47856,98045	2,08956E-05
2510	7,91405E-20	47666,31535	2,09792E-05
2520	7,88264E-20	47477,16346	2,10628E-05
2530	7,85149E-20	47289,50684	2,11463E-05
2540	7,82058E-20	47103,32784	2,12299E-05
2550	7,78991E-20	46918,60906	2,13135E-05
2560	7,75948E-20	46735,3334	2,13971E-05
2570	7,72929E-20	46553,48401	2,14807E-05
2580	7,69933E-20	46373,04431	2,15643E-05
2590	7,6696E-20	46193,99796	2,16478E-05
2600	7,6401E-20	46016,32889	2,17314E-05
2610	7,61083E-20	45840,02127	2,1815E-05
2620	7,58178E-20	45665,05951	2,18986E-05

Wavelength (nm)	Energy of one photon (J/photons)	Energy of a mole of photon (J/mol_photons)	1/Energy of a mole of photon (mol_photons/J)
2630	7,55295E-20	45491,42825	2,19822E-05
2640	7,52434E-20	45319,11239	2,20657E-05
2650	7,49595E-20	45148,09702	2,21493E-05
2660	7,46777E-20	44978,36748	2,22329E-05
2670	7,4398E-20	44809,90933	2,23165E-05
2680	7,41204E-20	44642,70832	2,24001E-05
2690	7,38448E-20	44476,75045	2,24837E-05
2700	7,35713E-20	44312,02189	2,25672E-05
2710	7,32999E-20	44148,50904	2,26508E-05
2720	7,30304E-20	43986,19849	2,27344E-05
2730	7,27629E-20	43825,07703	2,2818E-05
2740	7,24973E-20	43665,13164	2,29016E-05
2750	7,22337E-20	43506,34949	2,29852E-05
2760	7,1972E-20	43348,71793	2,30687E-05
2770	7,17121E-20	43192,22451	2,31523E-05
2780	7,14542E-20	43036,85694	2,32359E-05
2790	7,11981E-20	42882,60312	2,33195E-05
2800	7,09438E-20	42729,4511	2,34031E-05

Table 3.12: Wavelength (nm), Energy of one photon (J/photons), Energy of a mole of photon (J/mol_photons) and conversion factor 1/Energy of a mole of photon (mol_photons/J).

Bibliography

- Abe, Y. & Matsui, T. 1988, *Journal of Atmospheric Sciences*, 45, 3081
- Adams, E. R., Seager, S., Elkins-Tanton, L.: Ocean Planet or Thick Atmosphere: On the Mass-Radius Relationship for Solid Exoplanets with Massive Atmospheres, *Astrophys. Journal*, 673, 1160-1164, 2008
- Allard F, Hauschildt PH. 1995a. See Tinney 1995, pp. 32–44
- Allard F, Hauschildt PH. 1995b. *Ap. J.* 445:433–50
- Allard F., Hauschildt P. H., Alexander D. R., Starrfield S. 1997. Model atmospheres of very low mass stars and brown dwarfs. *Annu. Rev. Astron. Astrophys.* 35, 137–177 (doi:10.1146/annurev.astro.35.1.137) doi: 10.1146/annurev.astro.35.1.137. [Cross Ref]
- Alonso, Roi; et al.: "TrES-1: The Transiting Planet of a Bright K0V Star". *The Astrophysical Journal Letters* 613, 2004
- Amos, J., "Plato planet-hunter in pole position". *BBC News*, 29 January, 2014.
- Ångström, A. K. 1924. Solar and terrestrial radiation. *Q. J. R. Meteorol. Soc.* 50, 121–126.
- Antal, T., Harju, E., Pihlgren, L., Lastusaari, M., Tyystjärvi, T., Hölsä, J. and Tyystjärvi, E. 2012. Use of near-infrared radiation for oxygenic photosynthesis via photon up-conversion. *International Journal of Hydrogen Energy* 37 (10): 8859–8863.
- Archetti, M., Döring, T.F., Hagen, S.B., Hughes, N.M., Leather, S.R., Lee, D.W., Lev-Yadun, S., Manetas, Y., Ougham, H.J., Schaberg, P.G., and Thomas, H. (2009) Unravelling the evolution of autumn colours: an interdisciplinary approach. *Trends Ecol Evol* 24:166–173
- Audard, M; Gudel, M; Drake, JJ; Kashyap, "VL Extreme-Ultraviolet flare activity in late-type stars", *The Astrophysical Journal*, Volume 541, Issue 1, pp. 396-409
- M. Audard et al., "Extreme-ultraviolet flare activity in late-type stars", *ASTROPHYS J*, 541(1), 2000, pp. 396-409
- Aurnou, J.M., (2004) Secrets of the deep. *Nature*, 428, 134-135.
- Avago Technologies, Inc. Retrieved May 30, 2010. "Data Sheet — HLMP-1301, T-1 (3 mm) Diffused LED Lamps".
- Bada, J.L., Bigham, C., and Miller, S.L. (1994) Impact melting of frozen oceans on the early Earth: implications for the origin of life. *Proc. Natl. Acad. Sci. U S A* 91, 1248–1250.
- Bahcall, J. N., Pinsonneault, M. H., & Basu, Sarbani. 2001. *ApJ*, 555, 90
- Ball, P. (2004) Water, water, everywhere. *Nature* 427(6969), 19–20.
- Bambach, R.K. (1999) Energetics in the global marine fauna: a connection between terrestrial diversification and change in the marine biosphere. *GEOBIOS* 32(2), 131–144.
- Baraffe, I., Chabrier, G., Allard, F., & Hauschildt, P. 1998, *A&A*, 337, 403

- Baraffe, I., Homeier, D., Allard, F., Chabrier, G.: "New evolutionary models for pre-main sequence and main sequence low-mass stars down to the hydrogen-burning limit", *Astronomy & Astrophysics*, Volume 577, id.A42, 2015
- Barnes, J.R. and Cameron, A.C. (2001) Starspot patterns on the M dwarfs HK Aqr and RE 1816 +541. *Monthly Notices R. Astron. Soc.* 326, 950–958.
- Batalha N.H., Rowe J.F., Bryson S.T., : Planetary Candidates Observed by Kepler. III. Analysis of the First 16 Months of Data, 2011, *Ap. J. Supp. Ser.*, 204, 24
- Battista, J. R. 1997, "Against all odds: The survival strategies of *Deinococcus radiodurans*", *Annual Review of Microbiology*, vol. 51, pp. 203-224.
- Behrendt L, Schrameyer V, Qvortrup K, Lundin L, Sørensen SJ, Larkum AW, Kühl M.: "Biofilm growth and near-infrared radiation-driven photosynthesis of the chlorophyll d-containing cyanobacterium *Acaryochloris marina*.", *Appl Environ Microbiol.* 2012 Jun;78(11):3896-904. doi: 10.1128/AEM.00397-12. Epub 2012 Mar 30.
- Beja, O., Spudich, E. N., Spudich, J. L., Leclerc, M., & DeLong, E. F. 2001, Proteorhodopsin phototrophy in the ocean *Nature* 411, 786-789
- Ben-Itzhak, I., Krishnamurthi, V., Carnes, K.D., Aliabadi, H., Knudsen, H., Mikkelsen, U., and Essry, B.D., "Ionization and excitation of hydrogen molecules by fast proton impact.", *J. Phys. B. Atmos. Mol. Opt. Phys.* 29, L21–L28., (1996)
- Benner, S.A., Ricardo, A., and Carrigan, M.A.: "Is there a common chemical model for life in the universe?" *Curr. Opin. Chem. Biol.* 8, 672–689, (2004)
- Biller, Liu, Wahhaj, et al.: "The Gemini NICI Planet-Finding Campaign: The Frequency of Planets around Young Moving Group Stars", *ApJ*, 777, 160, 2013
- Billi, D., Viaggiu, E., Cockell, C. S., Rabbow, E., Horneck, G. and Onofri, S.: "Damage Escape and Repair in Dried *Chroococcidiopsis* spp. from Hot and Cold Deserts Exposed to Simulated Space and Martian Conditions.", *Astrobiology* 1 (0): 65–73. 2011
- Blankenship, R.E., Madigan, M.T., and Bauer, C.E.: "Anoxygenic Photosynthetic Bacteria.", Kluwer Academic Publishers, Dordrecht, The Netherlands. (1995)
- Blankenship, R.E.: "Molecular Mechanisms of Photosynthesis", Blackwell Science, Oxford, UK,(2002)
- Boeshaar PC.. "The spectral classification of M dwarf stars.", PhD thesis. Ohio State Univ., Columbus, OH. 1976
- Borucki W. J., Koch D.G., Barsi G., et al.: "Characteristics of planetary candidates observed by Kepler , II: Analysis of the first four months of data", *Ap. J.*, 736, 19
- Boss, A.P.: "Rapid formation of gas giant planets around M dwarf stars." *Astrophys. J.* 643(1), 501–508. (2006a)
- Bowling, D. R., Sargent, S.D., Tanner, B.D., and Ehleringer, J.R.:"Tunable diode laser absorption spectroscopy for stable isotope studies of ecosystem–atmosphere CO₂ exchange", *Agricultural and forest meteorology*, 118, 1-19, (2003)
- Brock, T.D. and Freeze, H.: "*Thermus aquaticus* gen. n. and sp. n., a non-sporulating extreme thermophile.", *J Bacteriol*, 98:289–297, (1969)

- Burrows A, Liebert J. 1993. *Mod. Phys. Rev.* 65:301
- Burrows, A., Hubbard, W.B., Lunine, J.I., and Liebert, J.: "The theory of brown dwarfs and extrasolar planets.", *Rev. Mod. Phys.* 73, 719–765, (2001)
- Cain J.C., Beaumont P., Holter W., Wang Z., Nevanlinna H (1995): "The magnetic bode fallacy." *J Geophys Res* 100:9439
- Canfield, D.E., Rosing, M.T., and Bjerrum, C. (2006) Early anaerobic metabolisms. *Philos. Trans. R. Soc. B Biol. Sci.* 361(1474), 1819–1834.
- Canganella, F. & Wiegel, J., (2011), "Extremophiles: from abyssal to terrestrial ecosystems and possibly beyond", *Naturwissenschaften*, vol. 98, no. 4, pp. 253-279.
- Carroll, S.B. (2001): "Chance and necessity: the evolution of morphological complexity and diversity." *Nature* 409(6823), 1102–1109.
- Catling, D. C., K. J. Zahnle, and C. P. McKay 2001. : "Biogenic methane, hydrogen escape, and the irreversible oxidation of early Earth." *Science* 293, 839–843.
- Catling, D.C., Glein, C.R., Zahnle, K.J., and McKay, C.P. (2005) "Why O₂ is required by complex life on habitable planets and the concept of planetary oxygenation time." *Astrobiology* 5(3), 415–438.
- Cavicchioli, R. 2002, "Extremophiles and the search for extraterrestrial life", *Astrobiology*, vol. 2, no. 3, pp. 281-292.
- Chakraborty, A. et al.: "First light results from PARAS: the PRL Echelle Spectrograph." *Proc. SPIE* 7735, 77354N (2010).
- Cherchneff I, Barker JR. 1992. *Ap. J.* 394:703–16
- Chittka, L. and Raine, N.E. (2006) : "Recognition of flowers by pollinators.", *Curr Opin Plant Biol* 9:428–435.
- Cleaves, H.J. and Miller, S.L. (1998): "Oceanic protection of prebiotic organic compounds from UV radiation." *Proc. Natl. Acad. Sci. U S A* 95, 7260–7263.
- Charbonneau, D., Allen L.E., Megeath S.T. et al.: "Detection of Thermal Emission from an Extrasolar Planet", *ApJ.*, 626, 523, 2005
- Chauvin, G.; Lagrange, A.-M.; Dumas, C.; Zuckerman, B.; Mouillet, D.; Song, I.; Beuzit, J.-L.; Lowrance, P.: "Giant planet companion to 2MASSW J1207334-393254", *Astronomy and Astrophysics*, Volume 438, Issue 2, August I 2005, pp.L25-L28
- Chen, M., Telfer, A., Lin, S., Pascal, A., Larkum, A.W.D., Barber, J., and Blankenship, R.E. (2005): "The nature of the photosystem II reaction centre in the chlorophyll d containing prokaryote, *Acaryochloris marina*." *Photochem. Photobiol. Sci.* 4(12), 1060–1064.
- Churkina, G., Nemry, B., Ruimy, A., and Schloss, A.L. (1999): "Comparing global models of terrestrial net primary productivity (NPP): overview and key results.", *Global Change Biol.* 5 (Suppl. 1), 1–15.

Cockell C.S., Kaltenecker L., and Raven J. A.: "Cryptic Photosynthesis—Extrasolar Planetary Oxygen Without a Surface Biological Signature, *Astrobiology*." September 2009, 9(7): 623-636. doi:10.1089/ast.2008.0273.

Cockell, C.S. (2002): "Photobiological uncertainties in the Archaean and post-Archaean world.", *Int. J. Astrobiol.* 1, 31–38.

Cockell, C.S., and Raven, J.A. (2004), "Zones of photosynthetic potential on Mars and the early Earth.", *Icarus* 169, 300-310.

Cockell, C. S., Kaltenecker, L., & Raven, J. A. 2009, "Cryptic Photosynthesis-Extrasolar Planetary Oxygen Without a Surface Biological Signature", *Astrobiology*, vol. 9, no.7, pp. 623-636

Coelho, S.: "Iron dust helps oceans to fix nitrogen", 2 November 2009, Natural Environment Research Council, NEWS FROM THE NATURAL WORLD: PLANET EARTH ONLINE

Coulson, K. L. 1975: "Solar and Terrestrial Radiation." Academic Press, New York.

Cox, M.M. and Battista, J.R. (2005): "Deinococcus radiodurans—the consummate survivor.", *Nat Rev Microbiol* 3:882–892.

Cramer, W., Kicklighter, D.W., Bondeau, A., Moore, B.I.,

Crisp, D. (1997): "Absorption of sunlight by water vapor in cloudy conditions: a partial explanation for the cloud absorption anomaly.", *Geophys. Res. Lett.* 24(5), 571–574.

Dartnell, L. (2011): "Biological constraints on habitability.", *Astronomy & Geophysics* 52:1.25–1.28.

DasSarma, S. (2006): "Extreme halophiles are models for astrobiology.", *Microbe Wash DC* 1:120–126.

Davi H, Barbaroux C, Dufréne E, et al.: "Modelling leaf mass per area in forest canopy as affected by prevailing radiation conditions.", *Ecol Model* 2008;211:339–49.

Davidge TJ, Boeshaar PC. 1993. *Ap. J. Lett.* 403:L47–L50

Davis SP. 1994:" In *Molecules in the Stellar Environment*", ed. UG Jørgensen, *Lect. Notes Phys.*, pp. 397–411. Berlin/Heidelberg: Springer-Verlag

Decker, K.L.M., Potter, C.S., Bebout, B.M., Des Marais, D.J., Carpenter, S., Discipulo, M., Hoehler, T.M., Miller, S.R., Thamdrup, B., Turk, K.A., and Visscher, P.T. (2005): "Mathematical simulation of the diel O, S, and C biogeochemistry of a hypersaline microbial mat.", *FEMS Microbiol. Ecol.* 52(3), 377–395.

Deguchi, Shigeru; Hirokazu Shimoshige, Mikiko Tsudome, Sada-atsu Mukai, Robert W. Corkery, Susumu Ito, and Koki Horikoshi (2011). "Microbial growth at hyperaccelerations up to 403,627 xg". *Proceedings of the National Academy of Sciences* 108 (19): 7997. doi:10.1073/pnas.1018027108. Retrieved 28 April 2011.

Delfosse, X., Forveille, T., Segransan, T., Beuzit, J.-L., Udry, S., Perrier, C., and Mayor, M. (2000): "Accurate masses of very low mass stars. IV. Improved mass-luminosity relations.", *Astron. Astrophys.* 364, 217–224.

Del Giorgio, P.A., Williams, P. le B. (2005): "The global significance of respiration in aquatic ecosystems"; from the single cell to the biosphere. In: *Respiration in Aquatic Systems*. (del Giorgio, P. and Williams, P. le B., eds), Oxford University Press, Oxford, pp 36-46.

Des Marais, D.J. (2000): "When did photosynthesis emerge on Earth?", *Science* 289(5485), 1703–1705.

DesMarais D.J., Harwit M.O., Jucks K.W., Kasting J.F., Lin D.N.C., Lunine J.I., Schneider J., Seager S., TraubW.A., Woolf N.J. (2002): "Remote sensing of planetary properties and biosignatures on extrasolar terrestrial planets.", *Astrobiology* 2:153 dialight.com.

"Dialight Micro LED SMD LED "598 SERIES" Datasheet"

Dismukes, G.C., Klimov, V.V., Baranov, S.V., Kozlov, Y.N., DasGupta, J., and Tyryshkin, A. (2001): "The origin of atmospheric oxygen on Earth: the innovation of oxygenic photosynthesis."; *Proc. Natl. Acad. Sci. U S A* 98(5), 2170–2175.

Dole, S. H.: 1964, "Habitable Planets for Man", London, Blaisdell Publishing Company.

Domagal-Goldman, S.D., Meadows, V.S., Claire, M.W., and Kasting, J.F. (2011): "Using biogenic sulphur gases as remotely detectable biosignatures on anoxic planets.", *Astrobiology* 11:419–441.

Domagal-Goldman, S. D., Meadows, V. S., Claire, M. W., & Kasting, J. F. 2011, *Astrobiology*, 11, 419
Efremov, A. A.; Bochkareva, N. I.; Gorbunov, R. I.; Lavrinovich, D. A.; Rebane, Y. T.; Tarkhin, D. V.; Shreter, Y. G. (2006). "Effect of the joule heating on the quantum efficiency and choice of thermal conditions for high-power blue InGaN/GaN LEDs". *Semiconductors* 40 (5): 605. doi:10.1134/S1063782606050162.

Efremov, A. A.; Bochkareva, N. I.; Gorbunov, R. I.; Lavrinovich, D. A.; Rebane, Y. T.; Tarkhin, D. V.; Shreter, Y. G. (2006). "Effect of the joule heating on the quantum efficiency and choice of thermal conditions for high-power blue InGaN/GaN LEDs". *Semiconductors* 40 (5): 605. doi:10.1134/S1063782606050162.

Ehrenreich, A. and Widdel, F. (1994): "Anaerobic oxidation of ferrous iron by purple bacteria, a new type of phototrophic metabolism."; *Appl. Environ. Microbiol.* 60(12), 4517–4526.

Emerson, R., Chalmers, R., and Cederstrand, C. (1957): "Some factors influencing the long-wave limit of photosynthesis." *Proc. Natl. Acad. Sci. U S A* 43, 133–143.

EnergyDaily. Retrieved on March 16, 2012.: "The LED's dark secret.", energy.ltgovernors.com, "LED Lighting Explained: Questions and Answers".

energy.ltgovernors.com. "In depth: Advantages of LED Lighting". energy.ltgovernors.com.

Eraso, J.M. and Kaplan, S. (2001): "Photoautotrophy. *Encyclopaedia of Life Sciences*", Nature Publishing Group, London.

Erculiani M.,S., Claudi, R., Giro, E., Galletta, G., D'alessandro; M., Farisato, G., Lessio, L., Micela, G., Billi, D., "Interpreting EChO's future data: biological laboratory estimates under M star's planetary surface conditions" *Proc. SPIE* 9143, *Space Telescopes and Instrumentation 2014: Optical, Infrared, and Millimeter Wave*, 914355 (August 2, 2014); doi:10.1117/12.2055854

- Erokhina, L. G., Shatilovich, A. V., Kaminskaya, O. P. and Gilichinskii, D. A. 2002: "The Absorption and Fluorescence Spectra of the Cyanobacterial Phycobionts of Cryptoendolithic Lichens in the High-Polar Regions of Antarctica."; *Microbiology* 71 (5): 601–607.
- Falkowski P. G. and Raven J. A.: "Aquatic photosynthesis", Blackwell Science, 1997
- Fegley BJ, Lodders K. 1996. *Ap. J. Lett.* 472:L37–L39
- Ferreira, A. C., Nobre, M. F., Moore, E., Rainey, F. A., Battista, J. R., & da Costa, M. S. 1999, "Characterization and radiation resistance of new isolates of *Rubrobacter radiotolerans* and *Rubrobacter xylanophilus*", *Extremophiles*, vol. 3, no. 4, pp. 235-238.
- Field, C.B., Behrenfeld, M.J., Randerson, J.T., and Falkowski, P. (1998) Primary production in the biosphere: integrating terrestrial and oceanic components. *Science* 281, 237-240.
- Fleagle, R. G., and J. A. Businger 1963: "An Introduction to Atmospheric Physics.", Academic Press, New York.
- Fogg, M., J., "An estimate of the prevalence of biocompatible and habitable planets", *J. Br., Interplanet. Soc.* 45, 3-12, 1992
- Forget, F.; Leconte, J., " Possible climates on terrestrial exoplanets", *Philosophical Transactions of the Royal Society A: Mathematical, Physical and Engineering Sciences*, vol. 372, issue 2014, pp. 20130084-20130084
- Friedmann, E.I., Kappen, L., Meyer, M.A., and Nienow, J.A. (1993): "Long-term productivity in the cryptoendolithic microbial community of the Ross Desert", *Antarctica. Microb. Ecol.* 25, 51-69.
- Fulton L., Michael; Dummer, Richard S.: "Advanced Large Area Deposition Technology for Astronomical and Space Applications". *Vacuum & Coating Technology* (December 2011): 43–47.
- Galletta, G., D'Alessandro, M., Bertoloni, G., Fanti, G., Dainese, E., Pelizzo, M., Ferri, F., Pavarin D., Bettanini C., Bianchini G., Debei, S.: "LISA: Mars and the limits of life", 2007, *Mem. S.A.It.* Vol. 78, 608
- Gan, F., Shen, G. and Bryant, D.A., "Occurrence of Far-Red Light Photoacclimation (FaRLiP) in Diverse Cyanobacteria", *Life* 2015, 5, 4-24; doi:10.3390/life5010004
- Gan,F. and Bryant, D.A., "Adaptive and acclimative responses of cyanobacteria to far-red light", *Environmental Microbiology* (Impact Factor: 6.2). 07/2015; DOI: 10.1111/1462-2920.12992
- D. Garoli e M. Pelizzo, "Misure irradiazione UV all'interno di LISA,". Università degli Studi di Padova, Tech. Rep., 2007.
- Gasol, J.M., Pinhassi, J., Alonso-Sàez, L., Ducklow, H., Herndl, G.J., Koblížek, M., Luo, Y., Moràn, X.A.G., Reinthaler, T., and Simon, M. (2008): "Towards a better understanding of microbial carbon flux in the sea." *Aquat Microb Ecol* 53:21–38.
- Geballe TR, Kulkarni SR, Woodward CE, Sloan GC. 1996. *Ap. J. Lett.* 467:L101–4
- Gershberg, R.E. and Shakhovskaya, N.I. (1983): "Characteristics of activity energetics of the UV Ceti-type flare stars.", *Astrophys. Space Sci.* 95, 235–253.
- Gilbert W (1986): "Origin of life: the RNA world.", *Nature* 319:618

- Glud , R.N. et al., "High rates of microbial carbon turnover in sediments in the deepest oceanic trench on Earth," *Nature Geosciences*, doi: 10.1038/ngeo1773, 2013.
- Goldblatt, C., Claire, M. W., Lenton, T. M., et al. 2009, *Nature Geoscience*, 2, 891
- Gomes, J. and Steiner, W.: "Extremophiles and Extremozymes", *Food Technol. Biotechnol.* 42 (4) 223–235 (2004)
- Gorton, H.L., Williams, W.E., and Vogelmann, T.C. (2001): "The light environment and cellular optics of snow alga *Chlamydomonas nivalis* ", (Bauer) Wille. *Photochem. Photobiol.* 73(6), 611–620.
- Grant, L. (1987): "Diffuse and specular characteristics of leaf reflectance.", *Remote Sensing Environ.* 22(2), 309–322.
- Gray, R.O. and Corbally, C.J., " *Stellar Spectral Classification*", Princeton university press, 2009, Grenfell, J. L., Gebauer, S., von Paris, P., et al. 2011, *Icarus*, 211, 81
- Grißmeier J-M, Stadelmann A, Motschmann U, Belisheva NK, Lammer H, Biernat HK (2005): "Cosmic ray impact on extrasolar Earth-like planets in close-in habitable zones.", *Astrobiology* 5:587
- Grimm, B., Porra, R.J., Rüdiger, W., and Scheer, H., eds. (2006): "Advances in Photosynthesis and Respiration, Vol. 25: Chlorophylls and Bacteriochlorophylls: Biochemistry, Biophysics, Functions and Applications.", Springer, Dordrecht, The Netherlands.
- Gurevitch J, Schuepp PH.: "Boundary layer properties of highly dissected leaves: an investigation using an electrochemical fluid tunnel.", *Plant Cell Environ* 1990;13:783–92.
- Haberle, R., C. McKay, D. Tyler, and R. Reynolds,: "Can synchronously rotating planets support an atmosphere?", In *Circumstellar Habitable Zones*. Travis House, Menlo Park, CA, 1996.
- Haisch, K., Lada, E., and Lada, C. (2001): "Circumstellar disks in the IC 348 cluster.", *Astron. J.* 121(4), 2065–2074.
- Harm, W. (1980): "Biological Effects of Ultraviolet Radiation", Cambridge University Press, Cambridge, UK.
- Hart M. H., (1978) The evolution of the atmosphere of the earth. *Icarus* 33:23
- Hauschildt, P. H., Allard, F., & Baron, E. 1999, *ApJ*, 512, 377
- Hawley, S.L. and Pettersen, B.R. (1991): "The great flare of 1985 April 12 on AD Leonis.", *Astrophys. J.* 378, 725–741.
- Haurwitz, B. 1948: Insolation in relation to cloud type.", *J. Meteorol.* 5, 110–113.
- Heath, M.J., Doyle, L.R., Joshi, M.M., and Haberle, R.M. (1999): "Habitability of planets around M dwarf stars.", *Orig. Life Evol. Biosph.* 29, 405–424.
- Heber U, Bilger W, Bligny R, Lange OL (2000): "Phototolerance of lichens, mosses and higher plants in an alpine environment: analysis of photoreactions.", *Planta* 211:770–780
- Hecht, E. (2002).: "Optics (4 ed.)", Addison Wesley. p. 591. ISBN 0-19-510818-3.
- Hedges, J.I. (1992): "Global biogeochemical cycles: progress and problems.", *Marine Chemistry* 39, 67-93.

- Hegde S.S. and Kaltenegger L.: "Colors of extreme exo-Earth environments. ", *Astrobiology* 13(1):47-56 (2013) PMID 23252379
- Hellemans, Alexander (18 January 2007): "COROT sees first light.", *Physics World* (online edition) (IOP Publishing). Retrieved 2 August 2008
- Henry TJ, Kirkpatrick JD, Simons DA. 1994. *Astron. J.* 108:1437–44
- Hillenbrand, L.A. and White, R.J. (2004): "An assessment of dynamical mass constraints on pre-main sequence evolutionary tracks.", *Astrophys. J.* 604, 741–757.
- Hoehler, T.M., B. M. Bebout, and D. J. Des Marais 2001: "The role of microbial mats in the production of reduced gases on the early Earth.", *Nature* 412, 324–327.
- Holman, M.J. and Wiegert, P.A. (1999): "Long-term stability of planets in binary systems.", *Astron J* 117:621–628.
- Holton, J. R. 1992., "An Introduction to Dynamic Meteorology", Ch. 2., Academic Press, San Diego
- Hoskins, B. J., and A. J. Simmons 1975: "A multi-layer model and the, semi-implicit method.", *Q. J. R. Meteorol. Soc.* 101, 637–655.
- Howard, Andrew W. and Johnson, John Asher and Marcy, Geoffrey W. and Fischer, Debra A. and Wright, Jason T. and Bernat, David and Henry, Gregory W. and Peek, Kathryn M. G. and Isaacson, Howard and Apps, Kevin and Endl, Michael and Cochran, William D. and Valenti, Jeff A. and Anderson, Jay and Piskunov, Nikolai E.,: "The California Planet Survey. I. Four New Giant Exoplanets", *The California Planet Survey. I. Four New Giant Exoplanets. Astrophysical Journal*, 721 (2). pp. 1467-1481. ISSN 0004-637X, 2010
- Hu, Y., & Ding, F. 2011, *A&A*, 526, A135
- Huang, S.S.,: *The Problem of Life in the Universe and the Mode of Star Formation*, Publications of the Astronomical Society of the Pacific, Vol. 71, No. 422, p.421, 1959-1960
- Ida, S.; Lin, D.,: "Toward a Deterministic Model of Planetary Formation. I. A Desert in the Mass and Semimajor Axis Distributions of Extrasolar Planets", *ApJ*, 604, 388, 2004
- Igamberdiev, A.U. and Lea, P.J. (2006): "Land plants equilibrate O₂ and CO₂ concentrations in the atmosphere.", *Photosynthesis Res.* 87(2), 177–194.
- International Dark-Sky Association. May 4, 2010: "Visibility, Environmental, and Astronomical Issues Associated with Blue-Rich White Outdoor Lighting. "
- Irwin AW. 1987. *Astron. Astrophys.* 182:348– 58
- Irwin AW. 1988. *Astron. Astrophys. Suppl.* 74:145–60
- Ishiwatari, M., Takehiro, S.-I., Nakajima, K., & Hayashi, Y. 2002, *Journal of Atmospheric Sciences*, 59, 3223
- Izumiura, H., : "An East-Asian Extra-Solar Planet Search Network", *Journal of the Korean Astronomical Society*, vol. 38, no. 2, pp. 81-84, 2005

- Jagger, J. (1985): "Solar-UV Actions on Living Cells", Praeger Scientific, New York.
- James, I. N., and Gray, L. J. 1986: "Concerning the effect of surface drag on the circulation of a baroclinic planetary atmosphere.", *Q. J. R. Meteorol. Soc.* 112, 1231–1250.
- Jiao, Y., Kappler, A., Croal, L.R., and Newman, D.K. (2005): "Isolation and characterization of a genetically tractable photoautotrophic Fe(II)-oxidizing bacterium, *Rhodospseudomonas palustris* strain TIE-1.", *Appl. Environ. Microbiol.* 71(8), 4487–4496.
- Jöckel, P., Brenninkmeijer, C.A.M., Lawrence, M.G., and Siegmund, P. (2003): "The detection of solar proton produced ¹⁴CO. *Atmos. Chem. Phys. Discuss.* 3, 1733–1752.
- John Mather (2006). "JWST Science".
- Jones HRA, Longmore AJ, Jameson RF, Mountain CM. 1994. *MNRAS* 267:413–23
- Joshi, M. (2003): "Climate model studies of synchronously rotating planets.", *Astrobiology* 3(2), 415–427.
- Joshi, M.M., Haberle, R.M., and Reynolds, R.T. (1997): "Simulations of the atmospheres of synchronously rotating terrestrial planets orbiting M dwarfs: conditions for atmospheric collapse and the implications for atmospheric habitability.", *Icarus* 129, 450–465.
- Junge, K., Eicken, H., Swanson, B.D., and Deming, J.W. (2006): "Bacterial incorporation of leucine into protein down to 20 degrees C with evidence for potential activity in sub-eutectic saline ice formations.", *Cryobiology* 52(3), 417–429.
- Joshi, M. M., S. R. Lewis, P. L. Read, and D. C. Catling "Western boundary currents in the martian atmosphere: Numerical simulations and observational evidence.", 1995, *J. Geophys. Res.*, 100,, 5485–5500.
- Kakani, V.G., Reddy, K.R., Zhao, D., and Sailaja, K. (2003): "Field crop responses to ultraviolet-B radiation: a review", *Agric. Forest Meteorol.* 120(1–4), 191–218.
- Kaltenegger, L., Selsis, F. (2007) Biomarkers set in context, in *Extrasolar Planets*. In: DvorakR (ed) *Extrasolar planets*. Wiley-VCH, Berlin, pp 75–98
- Kaltenegger, L., Segura, A., & Mohanty, S. 2011, *ApJ*, 733, 35
- Karnieli, A., Kidron, G.J., Glaesser, C., and Ben-Dor, E. (1999): "Spectral characteristics of cyanobacteria soil crust in semiarid environments.", *Remote Sensing Environ.* 69(1), 67–75.
- Kasper, M., et al. (2008). "EPICS: the exoplanet imager for the E-ELT". *Adaptive Optics Systems - Proceedings of the SPIE*, Volume 7015. SPIE. pp. 70151S–70151S–12.
- Kasting, J.F. and Pollack, J.B. (1983): "Loss of water from Venus. I: Hydrodynamic escape of hydrogen. " *Icarus* 53, 479–508.
- Kasting, J. F., Pollack, J. B., & Crisp, D. 1984, *J. Atmosph. Chem.*, 1, 403
- Kasting, J. F. 1987, *Precambrian Res.*, 34, 205
- Kasting, J. F. 1988, *Icarus*, 74, 472
- Kasting, J. F. 1991, *Icarus*, 94, 1

Kasting, J.F., Whitmire, D.P., and Reynolds, R.T. (1993): "Habitable zones around main sequence stars." *Icarus* 101, 108–128.

Kasting, J., F., Kopparapu, R., Ramirez, R., M., Harman C.: "Remote Life Detection Criteria, Habitable Zone Boundaries, and the Frequency of Earth-like Planets around M and Late-K Stars", *Proc Natl Acad Sci U S A* 2014 Sep 25;111(35):12641-6. Epub 2013 Nov 25.

Kaula, W.M. (1995) Venus reconsidered. *Science* 270, 1460–1464.

Ke, B. (2001) *Advances in Photosynthesis, Vol. 10: "Photosynthesis: Photobiochemistry and Photobiophysics"*, Kluwer Academic Publishers, Dordrecht, The Netherlands.

Kettle, A.J., Rhee, T.S., von Hobe, M., Poulton, A., Aiken, J., and Andreae, M.O. (2001): Assessing the flux of different volatile sulphur gases from the ocean to the atmosphere. *J Geophys Res* 106:12193–12209.

Kharecha, P., Kasting, J.F., and Siefert, J.L. (2005): "A coupled atmosphere-ecosystem model of the early Archean Earth.", *Geobiology* 3:53–76.

Kiang, N. Y., J. Siefert, Govindjee, R. E. Blankenship and V. S. Meadows (2007): "Spectral signatures of photosynthesis I: Review of Earth organisms." *Astrobiology*, 7(1) 222-51

Kiang, N.Y., Segura, A., Siefert, J., Tinetti, G., Govindjee, Blankenship, R.E., Cohen, M., Siefert, J., Crisp, D., and Meadows, V.S. (2007): "Spectral signatures of photosynthesis. II. Coevolution with other starts and the atmosphere on extrasolar worlds. *Astrobiology* 7(1), 252–274. (b)

Kiang, N.Y., 2008: "The color of plants on other worlds.", *Sci. Amer.*, 298, 48-55.

Kimura, H., Asada, R., Masta, A., and Naganuma, T. (2003): "Distribution of microorganisms in the subsurface of the Manus Basin hydrothermal vent field in Papua New Guinea.", *Appl Environ Microbiol* 69:644–648.

Kirkpatrick JD, Beichman CA. 1995. *Bull. Am. Astron. Soc.* 187:7512

Kirkpatrick JD, Henry TJ, Simons DA. 1995. *Astron. J.* 109:797–807

Klassen, J.L. (2010): "Phylogenetic and evolutionary patterns in microbial carotenoid biosynthesis are revealed by comparative genomics.", *PloS One* 5, doi:10.1371/journal.pone.0011257.

Knutson, H., A., et al. "Friends of Hot Jupiters. I. A Radial Velocity Search for Massive, Long-period Companions to Close-in Gas Giant Planets", *The Astrophysical Journal* 2014 785 126

Koch, D., Gould, A. : "Kepler Mission". NASA. March 14, 2009.

Kopparapu, R.K., Ramirez, R., Kasting, J.K., Eymet, V., Robinson, T.D., Mahadevan, S., Terrien, R.C., Domagal-Goldman, S., Meadows, V. and Deshpande, R., "Habitable Zones Around Main-Sequence Stars: New Estimates", *Astrophysical Journal*, 765, 131, 2013

Lada, C.J., Muench, A.A., Luhman, K.L., Allen, L., Hartmann, L., Megeath, T., Myers, P., Fazio, G., Wood, K., Muzerolle, J., Rieke, G., Siegler, N., and Young, E. (2006): "Spitzer observations of IC 348: the disk population at 2–3 million years.", *Astron. J.* 131, 1574.

Lammer H (2007) Preface: M Star planet habitability. *Astrobiology* 7(1):27

Lammer, H., Bredehöft, J. H., Coustenis, A., Khodachenko, M. L., Kaltenecker, L., Grasset, O., Priour, D., Raulin, F., Ehrenfreund, P., Yamauchi, M., Wahlund, J., E., Grießmeier, J., M., Stangl, G., Cockell, C., S.,

- Kulikov, Yu. N., Grenfell, J. L., Rauer, H.: "What makes a planet habitable?", *The Astronomy and Astrophysics Review*, June 2009, Volume 17, Issue 2, pp 181-249
- Lafrenière, D.; Marois, C.; Doyon, R., Nadeau, D.; Artigau, É.,: "A New Algorithm for Point-Spread Function Subtraction in High-Contrast Imaging: A Demonstration with Angular Differential Imaging," *The Astrophysical Journal*, Volume 660, Issue 1, pp. 770-780, 2007.
- Lammer H, Lichtenegger HIM, Kulikov YN, Grießmeier J-M, Terada N, Erkaev NV, Biernat HK, Khodachenko ML, Ribas I, Penz T, Selsis F (2007): "Coronal mass ejection (CME) activity of low mass M stars as an important factor for the habitability of terrestrial exoplanets. II. CME-induced ion pick up of Earth-like exoplanets in close-in habitable zones.", *Astrobiology* 7:185
- Lammer, H.; Bredehöft, J. H.; Coustenis, A.; Khodachenko, M. L.; Kaltenegger, L.; Grasset, O.; Prieur, D.; Raulin, F.; Ehrenfreund, P.; Yamauchi, M.; Wahlund, J.-E.; Grießmeier, J.-M.; Stangl, G.; Cockell, C. S.; Kulikov, Yu. N.; Grenfell, J. L.; Rauer, H., 2009: "What makes a planet habitable?" *The Astronomy and Astrophysics Review*, Volume 17, Issue 2, pp.181-249
- Larkum, A.W.D. and Veski, M. (2003): "Algal plastids: their fine structure and properties. In *Advances in Photosynthesis and Respiration*", Vol. 14: *Photosynthesis in Algae*, edited by A.W.D. Larkum, S.E. Douglas, and J.A. Raven, Kluwer Academic Publishers, Dordrecht, The Netherlands, pp. 11–28.
- Larkum, A.W.D. and Kühl, M. (2005): "Chlorophyll d: the puzzle resolved.", *Trends Plant Sci.* 10(8), 355–357
- Laughlin, G., Bodenheimer, P. and Adams, F. C.: 1997, 'The End of the Main Sequence', *Ap. J.* 482, 420–432. Detection (Cambridge England: Cambridge University Press).
- Laughlin, G., Bodenheimer, P., and Adams, F.C. (2004): "The core accretion model predicts few Jovian-mass planets orbiting red dwarfs.", *Astrophys. J. Lett.* 612, 73–76.
- LEDS Magazine. November 17, 2006. Retrieved February 17, 2008. "Seoul Semiconductor launches AC LED lighting source Acriche".
- Léger A, Selsis F, Sotin C, Guillot T, Despois D, Mawet D, Ollivier M, Labèque FA, Valette Brachet C, Chazelas B, Lammer H (2004), "A new family of planets? Ocean-Planets". *Icarus* 169:499
- Leggett SK, Allard F, Berriman G, Dahn CC, Hauschildt PH. 1996. *Ap. J. Suppl.* 104: 117
- Leggett, S. K. et al.: "Spectral energy distributions for disk and halo M dwarfs.", *Astrophys. J.* 535, 965-974 (2000).
- Leggett, S. K., Allard, F., Geballe, T. R., Hauschildt, P. H., & Schweitzer, A.: "Infrared Spectra and Spectral Energy Distributions of Late-M- and L-Dwarfs", 2001, *ApJ*, 548, 908.
- Lide, D. R. 1997, "CRC Handbook of Chemistry and Physics", (Boca Raton, FL: CRC Press).
- Liebert J, Kirkpatrick JD, Beichman C, Reid IN, Monet DC, Dahn CC. 1995. *Bull. Am. Astron. Soc.* 187:7502
- Liebert, J., Kirkpatrick, J.D., Reid, I.N., and Fisher, M.D. (1999): "A 2MASS ultracool M dwarf observed in a spectacular flare.", *Astrophys. J.* 519, 345–353.

- Lincoln TA, Joyce GF (2009): "Self-sustained replication of an RNA enzyme.", *Science*. doi:10.1126/science.1167856
- Lindberg, P., Lindblad, P. and Cournac, L. 2004: "Gas Exchange in the Filamentous Cyanobacterium *Nostoc punctiforme* Strain ATCC 29133 and Its Hydrogenase-Deficient Mutant Strain NHM5.", *Applied and Environmental Microbiology* 70 (4): 2137–2145.
- Littler, M.M., Littler, D.S., Blair, S.M., and Norris, J.M. (1986): "Deep-water plant communities from an uncharted seamount off San Salvador Island, Bahamas—distribution, abundance, and primary productivity.", *Deep-Sea Res. A Oceanogr. Res.* 33(7), 881–892
- Liu, M.C. (2004): "Substructure in the circumstellar disk around the young star AU Microscopii.", *Science* 305(5689), 1442–1444.
- Lodders, K. and Fegley, B. (1998): "The Planetary Scientists's Companion", Oxford University Press, New York.
- López-Morales, M., Morrell, N. I., Butler, R. P., & Seager, S. 2006, *Pub. Astron. Soc. Pac.*, 118, 1506
- Lusk, C.H., Warton, D.I.: "Global meta-analysis shows that relationships of leaf mass per area with species shade tolerance depend on leaf habit and ontogeny.", *New Phytol* 2007;176:764–74.
- McClellan, K.H., Winson, M.K., Fish, L., Taylor, A., Chhabra, S.R., Camara, M., Daykin, M., Lamb, J.H., Swift, S., Bycroft, B.W., Stewart, G.S.A.B., and Williams, P. (1997): "Quorum sensing and *Chromobacterium violaceum*: exploitation of violacein production and inhibition for the detection of Nacylhomoserine lactones.", *Microbiology* 143:3703–3711.
- Mayor, M., Bonfils, X., Forveille, T., et al. 2009, *A&A*, 507, 487
- Mackwell, S.J., Zimmerman, M.E., and Kohlstedt, D.L. (1998): "High-temperature deformation of dry diabase with application to tectonics on Venus. *J. Geophys. Res.* 103, 975–984.
- Madigan M. T., Marris B. L., *Extremophiles*, *Sci. Am.* 276 (1997) 66–71.
- Magrin, D., Munari, M., Pagano, I., Piazza, D., Ragazzoni, R. et al.: "PLATO: detailed design of the telescope optical units." in *Space Telescopes and Instrumentation 2010: Optical, Infrared, and Millimeter Wave*, Edited by Oschmann, Jacobus M., Jr.; Clampin, Mark C.; MacEwen, Howard A. *Proceedings of the SPIE*, Volume 7731, pp. 773124-8 (2010)
- Manning, W.M. and Strain, H.H. (1943): "Chlorophyll d: a green pigment in red algae.", *J. Biol. Chem.* 151(1), 1–19.
- Marion, G. M., Fritsen, C. H., Eicken, H., & Payne, M. C. 2003, "The search for life on Europa: Limiting environmental factors, potential habitats, and Earth analogues", *Astrobiology*, vol. 3, no. 4, pp. 785-811.
- Marois, C., MacIntosh, B., et al. : "Direct Imaging of Multiple Planets Orbiting the Star HR 8799". *Science* 322 (5906): 1348–52.
- Martín, E.L., Rebolo, R., Zapatero Osorio, M.R. 1996. *Ap. J.* 469:706
- Martin, B.: "NM Tech Exoplanet Search: Is Earth Alone?". QRKE. Retrieved 2014-04-21.

- Mattimore, V. & Battista, J. R. 1996: "Radioresistance of *Deinococcus radiodurans*: Functions necessary to survive ionizing radiation are also necessary to survive prolonged desiccation", *Journal of Bacteriology*, vol. 178, no. 3, pp. 633-637.
- McDonald, M.S. (2003) *Photobiology of Higher Plants*, John Wiley & Sons Ltd., Chichester, UK.
- McKay, C.P. (2000): "Thickness of tropical ice and photosynthesis on a snowball Earth. *Geophys. Res. Lett.* 27, 2153–2156.
- Meeks, J.C. and Castenholz, R.W. (1971): "Growth and photosynthesis in an extreme thermophile, *Synechococcus lividus* (Cyanophyta).", *Arch Mikrobiol* 78:25–41.
- Meierhenrich UJ, Muñoz Caro GM, Bredehöft JH, Jessberger EK, Thiemann WH-P (2004): "Identification of diamino acids in the murchison meteorite.", *Proc Natl Acad Sci USA* 101:9182–9186
- Meyer, J.-M. (2000): "Pyoverdines: pigments, siderophores and potential taxonomic markers of fluorescent *Pseudomonas* species.", *Arch Microbiol* 174:135–142.
- Mielke ,S. P., Kiang, N. Y., Blankenship , R. E., Gunner , M. R., Mauzerall, D.: "Efficiency of photosynthesis in a Chl d-utilizing cyanobacterium is comparable to or higher than that in Chl a-utilizing oxygenic species." *Biochim Biophys Acta*. 2011 September; 1807(9): 1231–1236. Published online 2011 June 25. doi: 10.1016/j.bbabi.2011.06.007
- Miller, S.R., Wingard, C.E., and Castenholz, R.W. (1998): "Effects of visible light and UV radiation on photosynthesis in a population of a hot spring cyanobacterium, a *Synechococcus* sp., subjected to high-temperature stress." *Appl. Environ. Microbiol.* 64(10), 3893–3899.
- Miller, S.R., Augustine, S., Olson, T.L., Blankenship, R.E., Selker, J., and Wood, A.M. (2005): "Discovery of a freeliving chlorophyll d-producing cyanobacterium with a hybrid proteobacterial cyanobacterial small-subunit rRNA gene.", *Proc. Natl. Acad. Sci. U S A* 102(3), 850–855.
- Minniti, D.; et al. (2009). "Low Mass Companions for Five Solar-Type Stars from the Magellan Planet Search Program". *Astrophysical Journal* 693 (2): 1424–1430.
- Mitra-Kraev, U., Harra, L.K., Güdel, M., Audard, M., Branduardi-Raymont, G., Kay, H.R.M., Mewe, R., Raassen, A.J.J., and van Driel-Gesztelyi, L. (2005): "Relationship between X-ray and ultraviolet emission of flares from dMe stars observed by XMM-Newton.", *Astron. Astrophys.* 431, 679–686.
- Miyashita, H., Ikemoto, H., Kurano, N., Adachi, K., Chihara, M., and Miyachi, S. (1996): "Chlorophyll d as a major pigment.", *Nature* 383(6599), 402.
- Montechario, M. and Giordano, M. (2006): "Effect of prolonged dark incubation on pigments and photosynthesis of the cave dwelling cyanobacterium *Phormidium autumnale* (Oscillatoriales, Cyanobacteria).", *Phycologia* 45:704–710.
- Montechario, M., Hirschmugl, C.J., Raven, J.A., and Giordano, M. (2006): "Homoeostasis of cell composition in prolonged darkness.", *Plant Cell Environ* 30:2198–2204.
- Montgomery, R. and Laughlin, G. (2006) : "forming earths around low mass stars.", *Astrobiology* 6(1), 157.
- Moran, J.J., House, C.H., Vrentas, J.M., and Freeman, K. (2008): "Methyl sulphide production by a novel carbon monoxide metabolism in *Methanosarcina acetivorans*.", *Appl Environ Microbiol* 74:540–542.

- Morbidelli, A., Chambers, J., Lunine, J.I., Petit, J.M., Robert, F., Valsecchi, G.B., and Cyr, K.E. (2000): "Source regions and timescales for the delivery of water to the Earth." *Meteoritics Planet. Sci.* 35, 1309–1320.
- Mueller, D.R., Vincent, W.F., Bonilla, S., and Laurion, I. (2005): "Extremotrophs, extremophiles and broadband pigmentation strategies in a high arctic ice shelf ecosystem.", *FEMS Microbiol. Ecol.* 53(1), 73–87.
- Mulkidjanian, A.Y. and Junge, W. (1997): "On the origin of photosynthesis as inferred from sequence analysis: a primordial UV-protector as common ancestor of reaction centres and antenna proteins.", *Photosynthesis Res.* 51(1), 27–42.
- Narra, P. and Zinger, D.S. (2004). "An effective LED dimming approach". *Industry Applications Conference, 2004. 39th IAS Annual Meeting. Conference Record of the 2004 IEEE* 3: 1671–1676.
- Neale L, Tennyson J. 1995. *Ap. J. Lett.* 454:L169
- Nelson DR (2004): "Earth's formation and first billion years. In: Eriksson PG et al (eds) *The Precambrian Earth: tempos and events.*", *Dev Precambrian Geol* 12:3
- Nienow, J.A. and Friedmann, E.I. (1993): "Terrestrial lithophytic (rock) communities.", In *Antarctic Microbiology*, 343-412, Wiley-Liss, New York
- Nisbet, E.G. and Fowler, C.M.R. (1999): "Archaean metabolic evolution of microbial mats.", *Proc. R. Soc. Lond. B* 266(1436), 2375–2382.
- Niinemets Ü, Portsmouth A, Tobias M. : "Leaf size modifies support biomass distribution between stems, petioles and mid-ribs in temperate plants.", *New Phytol* 2006;171:91–104.
- Niinemets Ü, Portsmouth A, Tobias M.: "Leaf shape and venation pattern alter the support investments within leaf lamina in temperate species: a neglected source of leaf physiological differentiation?", *Funct Ecol* 2007;21:28–40.
- Niinemets Ü, Portsmouth A, Tena D, et al.: "Do we underestimate the importance of leaf size in plant economics? Disproportional scaling of support costs within the spectrum of leaf physiognomy.", *Ann Bot (Lond)* 2007;100:283–303.
- Nisbet, E.G., Cann, J.R., Lee, C., and Dover, V. (1995): "Origins of photosynthesis.", *Nature* 373(6514), 479–480.
- Nobel, P.S. (1974): "Introduction to Biophysical Plant Physiology", W.H. Freeman and Company, San Francisco.
- Nobel, P.S. (1999): "Physicochemical and Environmental Plant Physiology", Academic Press, San Diego.
- North, G. R., Cahalan, R. F., & Coakley, Jr., J. A., "Energy balance climate models", *Reviews of Geophysics and Space Physics*, 19, 91, 1981
- Nutzman P., Charbonneau D.,: "Design considerations for a ground-based transit search for habitable planets orbiting M dwarfs", *PASP*, 120, 317, 2008
- Oesterhelt, D. & Stoekenius, W. 1971, "Rhopsin-like protein from the purple membrane of *Halobacterium halobium*", *Nature* 233, 149-152

- O'Malley-James J.T., Raven J.A., Cockell C.S., Greaves J.S. (2012): "Life and Light: Exotic Photosynthesis in Binary and Multiple Star Systems", *Astrobiology* 12(2): 115-124
- Olson, J.M. (2006): "Photosynthesis in the Archean era.", *Photosynthesis Res.* 99(2), 109–117.
- Oren, A., Stambler, N., and Dubinsky, Z. (1992): "On the red coloration of saltern crystallizer ponds.", *International Journal of Salt Lake Research* 1:77–89.
- Oren, A. and Dubinsky, Z. (1994): "On the red coloration of saltern crystallizer ponds. II. Additional evidence for the contribution of halobacterial pigments.", *International Journal of Salt Lake Research* 3:9–13.
- Oren, A. (2009): "Saltern evaporation ponds as model systems for the study of primary production processes under hypersaline conditions.", *Aquat Microb Ecol* 56:193–204.
- Overbye, Dennis (May 12, 2013). "Finder of New Worlds". *The New York Times*.
- Overbye, Dennis (January 6, 2015). "As Ranks of Goldilocks Planets Grow, Astronomers Consider What's Next". *The New York Times*.
- Overmann, J. and Garcia-Pichel, F. (2000): "The Phototrophic Way of Life. The Prokaryotes", Release 3.2 7/25/2000, edited by M. Dworkin, Springer-Verlag, New York, <http://link.springer-ny.com/link/service/books/10125/>.
- Painter, T.H., Duval, B., Thomas, W.H., Mendez, M., Heintzelman, S., and Dozier, J. (2001): "Detection and quantification of snow algae with an airborne imaging spectrometer.", *Appl Environ Microbiol* 67:5267–5272.
- Paul et al.: "BMC Plant growth strategies are remodeled by spaceflight", *Plant Biology*, 2012, 12:232
- Paytan A, Mackey KR, Chen Y, Lima ID, Doney SC, Mahowald N, Labiosa R.: "Toxicity of atmospheric aerosols on marine phytoplankton." *Post AF., Proc Natl Acad Sci U S A.* 2009 Mar 24; 106(12):4601-5
- Pavlov, A. A., Kasting, J. F., Brown, L. L., Rages, K. A., & Freedman, R. 2000, *J. Geophys. Res.*, 105, 11981
- Perruchot; et al.: "The SOPHIE spectrograph: design and technical key-points for high throughput and high stability", 2008, *Proceedings of the SPIE* 7014: 70140J.
- Pickup M, Westoby M, Basden A.: "Dry mass costs of deploying leaf area in relation to leaf size.", *Funct Ecol* 2005;19:88–97.
- Pierrehumbert, R. 2010: "Principles of Planetary Climate", (Cambridge University Press)
- Pilcher, C.B. (2003): "Biosignatures of early earths.", *Astrobiology* 3:471–486.
- Poensgen, T. (January 22, 2013): "InfiniLED MicroLEDs achieve Ultra-High Light Intensity." infiniled.com High Power Point Source White Led NVSx219A. [Nichia.co.jp](http://nichia.co.jp), November 2, 2010.
- Price CA, Enquist BJ.: "Scaling mass and morphology in leaves: an extension of the WBE model.", *Ecology* 2007;88:1132–41.
- Proteau, P.J., Gerwick, W.H., Garcia-Pichel, F., and Castenholz, R. (1993): "The structure of scytonemin, an ultraviolet sunscreen pigment from the sheaths of cyanobacteria.", *Experientia* 49:825–829.

Puxley, P., Hippel, T., Takamiya, M., and Volk, K. (2008): "Definition of an Astronomical Source in the ITC", Gemini Observatory, The United States Gemini Office, Tucson, AZ. Available online at <http://www.gemini.edu/nearirresources?q=node/10257>.

Raloff, J. (May 27, 2006). "Light Impacts: Science News". Sciencenews.org.

Rasool, S.,I., DeBergh, C., "The runaway greenhouse and the accumulation of CO₂ in the Venus atmosphere", *Nature*, 266, 1037-1039, 1970

Rauer, H., Erikson, A., Kabath, P., Hedelt, P., Boer, M., Carone, L., Csizmadia, S., Eig Müller, P., Paris, P. v., Renner, S., Tournois, G., Titz, R., & Voss, H. 2010, *AJ*, 139,53

Raven, J.A. (1984): "A cost-benefit analysis of photon absorption by photosynthetic unicells.", *New Phytol.* 98(4), 593–625.

Raven, J.A. (1995): "The early evolution of land plants: aquatic ancestors and atmospheric interactions.", *Bot J. Scot.* 47, 151-175.

Raven, J. A., and P. G. Falkowski 1999: "Oceanic sinks for atmospheric CO₂.", *Plant Cell Environ.* 22, 741–755.

Raven, J. A., J. E. Kübler, and J. Beardall, (2000): "Put out the light, and then put out the light.", *J. Mar. Biol. Assoc. UK* 80, 1–27.

Raven, J.A., Beardall, J., Flynn, K.J., and Maberly, S.C. (2009): "Phagotrophy in the origins of photosynthesis in eukaryotes and as a complementary mode of nutrition in phototrophs: relation to Darwin's insectivorous plants.", *J Exp Bot* 60:3975–3987.

Raymond, S., Meadows, V., and Scalo, J. (2006): "Earth with a red sun: terrestrial planet formation and habitability around low mass stars.", *Astrobiology* 6(1), 121.

Reeburgh, W.S. (1997): "Figures summarizing the global cycles of biogeochemically important elements. ", *Bull. Ecol. Soc. Am.* 78(4), 260–267.

Regenauer-Lieb K, Yuen DA, Branlund J (2001): "The initiation of subduction: criticality by addition of water?", *Science* 294:578

Reich, P.B., Walters, M.B., Ellsworth, D.S.: "From tropics to tundra: a global convergence in plant functioning.", *Proc Natl Acad Sci USA* 1997;94:13730–4.

Reid IN, Hawley SL, Mateo M. 1995b. *MNRAS* 272:828

Reid IN. 1994. *Astrophys. Space Sci.* 217:57

Reid, I.N., Kirkpatrick, J.D., Liebert, J., Gizis, J.E., Dahn, C.C., and Monet, D.G. (2002). "High-resolution spectroscopy of ultracool M dwarfs.", *Astron. J.* 124, 519–540.

Rietmeijer, F.J.M., Nuth, J.A. III, and Karner, J.M. (1999): "Metastable eutectic, gas to solid, condensation in the FeOFe₂O₃-SiO₃ system.", *Phys. Chem. Chem. Phys.* 1, 1511–1516.

Rietmeijer, F.J.M., Hallenbeck, S.L., Nuth, J.A. III, and Karner, J.M. (2002a): "Amorphous magnesiosilicate smokes annealed in vacuum: the evolution of magnesium silicates in circumstellar and cometary dust.", *Icarus* 156(1), 269–286.

- Rietmeijer, F.J.M., Nuth, J.A. III, Karner, J.M., and Hallenbeck, S.L. (2002b): "Gas-to-solid condensation in a Mg- SiO-H₂-O₂ vapor: metastable eutectics in the MgO-SiO₂ phase diagram.", *Phys. Chem. Chem. Phys.* 4, 546–551.
- Rivera, E., Lissauer, J.J., Butler, R.P., Marcy, G.W., Vogt, S.S., Fischer, D.A., et al. (2005): A \sim 7.5 Earth-mass planet orbiting the nearby star, GJ 876. *Astrophys. J.* 634, 625–640.
- Roberts, P.H. and Glatzmaier, G.A. (2000): "Geodynamo theory and simulations.", *Rev. Mod. Phys.* 72, 1081-1123.
- Rossi SCF, Marciel WJ, Benevides-Soares P. 1985. *Astron. Astrophys.* 148:93
- Rothschild, L.J., Giver, L.J., White, M.R. and Mancinelli, R.L. (1994): "Metabolic activity of microorganisms in evaporites.", *J. Phycol.* 30, 431-438.
- Rusch, D.W., Gérard, J.-C., Solomon, S., Crutzen, P.J., and Reid, G.C. (1981): "The effect of particle precipitation events on the neutral and ion chemistry of the middle atmosphere—1.", *Odd nitrogen. Planet. Space Sci.* 29, 767–774.
- Russel CT (1993): "Magnetic fields of the terrestrial planets.", *J Geophys Res* 98:18681
- Sack L, Cowan PD, Jaikumar N, et al.: "The 'hydrology' of leaves: coordination of structure and function in temperate woody species.", *Plant Cell Environ* 2003;26:1343–56.
- Sack L, Frole K.. "Leaf structural diversity is related to hydraulic capacity in tropical rain forest trees. *Ecology* 2006;87:483–91.
- Saito, T., Terato, H., and Yamamoto, O. (1994): "Pigments of *Rubrobacter radiotolerans*. *Arch Microbiol* 162:414–421.
- Saito, T., Miyabe, Y., Ide, H., and Yamamoto, O. (1997): "Hydroxyl radical scavenging ability of bacterioruberin. *Radiation Physics and Chemistry* 50:267–269.
- Sauval, A.J., Tatum, J.B.. 1984. *Ap. J. Suppl.* 56:193
- Scalo, J., Kaltenegger, L., Segura, A.G., Fridlund, M., Ribas, I., Kulikov Yu, N., Grenfell, J.L., Rauer, H., Odert, P., Leitzinger, M., Selsis, F., Khodachenko, M.L., Eiroa, C., Kasting, J., Lammer, H., (2007): "M stars as targets for terrestrial exoplanet searchers and biosignature detection.", *Astrobiology* 7:85. doi:19.1089/ast.2006.0000
- Scheer, H. (2003): "The Pigments. Light-Harvesting Antennas in Photosynthesis", Kluwer, Dordrecht, The Netherlands.
- Schilling, G, "Europe Downscales Monster Telescope to Save Money". *Science Insider*, 2011
- Schlesinger, W.H., Phippen, J.S., Wallenstein, M.D., Hofmockel, K.S., Klepeis, D.M., and Mahall, B.E. (2003): "Community composition and photosynthesis by photoautotrophs under quartz pebbles, Southern Mohave Desert.", *Ecology* 84, 3222-3231.
- Schopf JW (2004): "Biologic History and the Cardinal Rule.", *American Geophysical Union, Fall Meeting 2004*, abstract #U44A-01
- Schwieterman, E.W. , Cockell,C. S. Meadows , V. S.: "Nonphotosynthetic Pigments as Potential Biosignatures", *Astrobiology*. May 2015, 15(5): 341-361.

Schulze-Makuch, D., Méndez, A., Fairén, A. G., von Paris, P., Turse, C., Boyer, G., Davila, A. F., Resendes de Sousa António, M., Irwin, L. N., and Catling, D. (2011): "A Two-Tiered Approach to Assess the Habitability of Exoplanets.", *Astrobiology* 11(10): 1041-1052.

Sciencedaily.com (January 13, 2009). Retrieved on March 16, 2012. "Smart Lighting: New LED Drops The 'Droop'."

Seager, S., Turner, E.L., Schafer, J., and Ford, E.B. (2005): "Vegetation's red edge: a possible spectroscopic biosignature of extraterrestrial plants.", *Astrobiology* 5(3), 372–390.

Seager, S., Schrenk, M., Bains, W.,: "An Astrophysical View of Earth-Based Metabolic Biosignature Gases", *Astrobiology*. January 2012, 12(1): 61-82. doi:10.1089/ast.2010.0489.

Seager, S.; Mallén-Ornelas, G.: "A Unique Solution of Planet and Star Parameters from an Extrasolar Planet Transit Light Curve", *The Astrophysical Journal*, Volume 585, Issue 2, pp. 1038-1055, 2003

Segura, A., Krelow, K., Kasting, J.F., Sommerlatt, D., Meadows, V., Crisp, D., Cohen, M., and Mlawer, E. (2003): "Ozone concentrations and ultraviolet fluxes on Earth-like planets around other stars.", *Astrobiology* 3(4), 689–708.

Segura, A., Kasting, J.F., Meadows, V., Cohen, M., Scalo, J., Crisp, D., Butler R.A.H., and Tinetti, G. (2005): "Biosignatures from Earth-like planets around M dwarfs.", *Astrobiology* 5(6), 706–725.

Selsis et al. (2007): "Habitable planets around the star Gl 581?.", *Astronomy and Astrophysics* 476 (3): 1373 – 1387. DOI:10.1051/0004-6361:20078091

Shiple, B., Lechowicz, M.J., Wright, I.J. et al.: "Fundamental tradeoffs generating the worldwide leaf economics spectrum.", *Ecology*. 2006;87:535–

Sicilia-Aguilar, A., Hartmann, L.W., Hernandez, J. Briceno, C., and Calvet, N. (2005): "Young stars in Trumpler 37 and NGC 7160.", *Astron. J.* 130, 188–209.

Sleep, N. H. 2001. Oxygenating the atmosphere. *Nature* 410, 317–319.

Solovchenko, A.E. and Merzlyak, M.N. (2008): "Screening of visible and UV radiation as a photoprotective mechanism in plants.", *Russ J Plant Physiol* 55:719–737.

Solomatov VS (2004): "Initiation of subduction by small-scale convection.", *J. Geophys Res* 109. doi:10.1029/2003JB002628

Solomon, S., Rusch, D.W., Gerard, J.-C., Reid, G.C., and Crutzen, P.J. (1981): "The effect of particle precipitation events on the neutral and ion chemistry of the MA: II. Odd hydrogen.", *Planet. Space Sci.* 29, 885–892.

Solomon, S. C., and J. W. Head, 1991, "Fundamental issues in the geology and geophysics of Venus," *Science*, v. 252, p. 252-260.

Southam, G., Rothschild, L. J., & Westall, F. 2007, "The geology and habitability of terrestrial planets: Fundamental requirements for life", *Space Science Reviews*, vol. 129, no. 1-3, pp. 7-34.

Sharp CM, Huebner WF. 1990. *Ap. J. Suppl.* 72:417

- Stevens, D. J., Gaudi, B. S.; "A Posteriori Transit Probabilities". Publications of the Astronomical Society of the Pacific 125: 933–950, 2013
- Stevenson D.J., 1983: "Planetary magnetic fields.", Rep Prog Phys 46:555
- Stevenson D.J., 2003: "Planetary magnetic fields.", Earth Planet Sci Lett 208:1
- Stevenson, R., August 2009: "The LED's Dark Secret: Solid-state lighting won't supplant the lightbulb until it can overcome the mysterious malady known as droop.", IEEE Spectrum
- Takenaka A, Takahashi K, Kohyama T.: "Optimal leaf display and biomass partitioning for efficient light capture in an understorey palm, *Licuala arbuscula*.", Funct Ecol 2001;15:660–8.
- Tarter, J.C et al., (2007): "A Reappraisal of The Habitability of Planets around M Dwarf Stars." Astrobiology 7,30-65.
- text.com. January 15, 2007. Retrieved September 3, 2007. "Blue LEDs: A health hazard?"
- Tian, B., Sun, Z., Xu, Z., Shen, S., Wang, H., and Hua, Y. (2008): "Carotenoid 3',4'-desaturase is involved in carotenoid biosynthesis in the radioresistant bacterium *Deinococcus radiodurans*.", Microbiology 154:3697–3706.
- Tijhuis, L., van Loosdrecht, M. C. M., & Heijnen, J. J. 1993, Biotechnology and Bioengineering, 42, 509
- Tian, F., Toon, O.B., Pavlov, A.A., and De Sterck, H. (2005): "A hydrogen-rich early Earth atmosphere." Science 308, 1014–1017.
- Tinetti, G., Meadows, V.S., Crisp, D., Fong, W., Fishbein, E., Turnbull, M., and Bibring, J.P. (2006a) "Detectability of planetary characteristics in disk-averaged spectra. I: The Earth model.", Astrobiology 6(1), 34–47.
- Tinetti, G., Meadows, V.S., Crisp, D., Kiang, N.Y., Kahn, B., Velusamy, T., Bosc, E., and Turnbull, M. (2006b): "Detectability of planetary characteristics in disk-averaged spectra. II. Synthetic spectra and light curves of the Earth.", Astrobiology 6(6), 881–900.
- Tinetti, G., Rashby, S., and Yung, Y.L. (2006c): "Detectability of red-edge shifted vegetation on M-star terrestrial planets.", Astrophys. J. Lett. 644(2), L129–L132.
- Toon, O. B., McKay, C. P., Ackerman, T. P., & Santhanam, K. 1989, J. Geophys. Res., 94, 16287
- Trissl, H.-W. (1993): "Long-wavelength absorbing antenna pigments and heterogeneous absorption bands concentrate excitons and increase absorption cross section.", Photosynthesis Res. 35(3), 247–263.
- Tsuji T, Ohnaka K, Aoki W. 1995. See Tinney 1995, pp. 45–52
- Tucker, C.J. (1976): "Sensor design for monitoring vegetation canopies. Photogram. Eng. Remote Sensing 42(11), 1399–1410.
- Tsukaya, H.: "Leaf shape: genetic controls and environmental factors.", The International Journal of Developmental Biology [2005, 49(5-6):547-555]
- Valencia, D., O'Connell, R. J., Sasselov, D. "Internal structure of massive terrestrial planets.", Icarus 181, 545-554, (2006)
- Valencia, D, O'Connell R. J., Sasselov D. D.: "Inevitability of plate tectonics on Super-Earths." ApJ

670:L45, (2007)

Vance, S., Christensen, L.E., Webster, C.R., and Sung, K. (2011): "Volatile organic sulphur compounds as biomarkers complementary to methane: infrared absorption spectroscopy of CH₃SH enables in-situ measurements on Earth and Mars. *Planet Space Sci* 59:299–303.

Vardavas, I. M., & Carver, J. H. 1984, *Planet. Space Sci.*, 32, 1307

Venil, C. and Lakshmanaperumalsamy, P. (2009): "An insightful overview on microbial pigment, prodigiosin. *Electronic Journal of Biology* 5:49–61.

Vince-Pure, D.: "Photocontrol of stem elongation in light-grown plants of *Fuchsia hybrida*", *Planta*, 7. I. 1977, Volume 133, Issue 2, pp. 149-156

Visentin, R. 2009: "Master degree in Natural sciences: Studio sulla sopravvivenza di endospore batteriche in ambiente marziano.", Università degli studi di Padova

Vladilo, G., Murante, G., Silva, L., Provenzale, A., Ferri, G., & Ragazzini, G., 2013: "The Habitable Zone of Earth-like Planets with Different Levels of atmospheric pressure", *ApJ* 767 65 doi:10.1088/0004-637X/767/1/65

Vladilo, G., Silva, L., Murante, G., Filippi, L., and Provenzale, A. , "Modelling the surface temperature of Earth-like planets", *The Astrophysical Journal* 804 (1) 50 (2015)

Von Paris, P., Gebauer, S., Godolt, M., et al. 2010, *A&A*, 522, A23: "Spectroscopic characterization of the atmospheres of potentially habitable planets: GL 581 d as a model case study", 23 September 2011 von PARIS Ph., CABRERA J., GODOLT M., GRENFELL J., HEDEL T. P. & 3 additional authors . *Astron. & Astrophys.*, 534, A26

Weber AL, Miller SL (1981): "Reasons for the occurrence of the twenty coded protein amino acids.", *J Mol Evol* 17:273–284

West, A.A., Hawley, S.L., Walkowicz, L.M., Covey, K.R., Silvestri, N.M., Raymond, S.N., Harris, H.C., Munn, J.A., McGehee, P.M., Ivezić, Z., and Brinkmann, J. (2004): "Spectroscopic properties of cool stars in the Sloan Digital Sky Survey: an analysis of magnetic activity and a search for subdwarfs.", *Astrophys. J.* 128, 426–436.

Wetherill, G.W. (1994): "Possible consequences of absence of “Jupiters” in planetary systems.", *Astrophys. Space Sci.* 212, 23–32.

Whitman, W.B., Coleman, D.C., and Wiebe, W.J. (1998): "Prokaryotes: the unseen majority."; *Proc. Natl. Acad. Sci. U S A* 95(12), 6578–6583.

Whittaker, R.H. (1975): "Communities and ecosystems.", Macmillian Publishing, New York, p. 224.

Whitmire, D., P., Matese, J.,J., and Tomley, L., J., "A brown dwarf companion as an explanation of the asymmetry in Beta Pictoris disk", *Astronom. Astrophys.* 203, L13-L15, 1991

Whitton, B. A.: "Ecology of Cyanobacteria II - Their Diversity in Space and Time.", Springer Netherlands, 2012.

- Williams, W.E., Gorton, H.L., and Vogelmann, T.C. (2003): "Surface gas-exchange processes of snow algae.", *Proc Natl Acad Sci USA* 100:562–566.
- Williams, P., Winzer, K., Chan, W.C., and Càmara, M. (2007): "Look who's talking: communication and quorum sensing in the bacterial world.", *Philos Trans R Soc Lond B Biol Sci* 362: 1119–1134.
- Winn, N., J.: "Transits and occultations", Chapter of the graduate-level textbook, *EXOPLANETS*, ed. S. Seager, University of Arizona Press (Tucson, AZ), 2010
- Whitney, C.: "Exoplanets Soon to Glean in the Eye of NESSI". NASA (California: Jet Propulsion Laboratory). Retrieved 2014-04-21.
- Wood, B.E., Müller, H.-R., Zank, G.P., Linsky, J.L., and Redfield, S. (2005): "New mass loss measurements from astrospheric Ly-alpha absorption.", *Astrophys. J.* 628, L143–L146.
- Wolszczan, A. (1994). "Confirmation of Earth Mass Planets Orbiting the Millisecond Pulsar PSR B1257+12". *Science* 264 (5158): 538–542.
- Wolstencroft, R.D. and Raven, J.A. (2002) : "photosynthesis: likelihood of occurrence and possibility of detection on Earth-like planets.", *Icarus* 157(2), 535–548.
- Wordsworth, R., Forget, F., Selsis, F., et al. 2010b, *A&A*, 522, A22
- Wordsworth, R. D., Forget, F., Selsis, F., et al. 2011, *ApJ*, 733, L48
- Worthey, J. A. "How White Light Works". LRO Lighting Research Symposium, Light and Color. Retrieved October 6, 2007.
- Woyke, T., Teeling, H., Ivanova, N.N., Huntzman, M., Richter, M., Gloeckner, F.O., Boffelli, D., Anderson, I.J., Barry, K.W., Shapiro, H.J., Szeto, E., Kyrpides, N.C., Musmann, M., Amann, R., Bergin, C., Ruehland, C., Rubin, E.M., and Dubilier, N. (2006): "Symbiosis insights through metagenomic analysis of a microbial consortium.", *Nature* doi:10.1038/nature05192.
- Wright IJ, Reich PB, Westoby M, et al.: "The worldwide leaf economics spectrum.", *Nature* 2004;428:821–7.
- Xu F., Guo W., Xu W., Wei Y., Wang R. 2009: "Leaf morphology correlates with water and light availability: What consequences for simple and compound leaves?", *Progress in Natural Science* 19 1789-1798.
- Zhang, Y.C., Rossow, W.B., Lacis, A.A., Oinas, V., and Mischenko, M.I. (2004): "Calculation of radiative fluxes from the surface to top of atmosphere based on ISCCP and other global data sets: refinements of the radiative transfer model and the input data.", *J. Geophys. Res. Atmos.* 109(D19105) doi:10.1029/2003JD004457.
- Zwietering, M. H. , Jongenburger, I. , Rombouts, F. M. and van 't Riet, K.: "Modelling of the Bacterial Growth Curve", *Appl. Environ. Microbiol.* 1990, 56(6):1875.

